frontiers | Research Topics

Cells, biomaterials, and biophysical stimuli for bone, cartilage, and muscle regeneration, volume II

Edited by
Lorenzo Fassina, Nora Bloise, Murugan Ramalingam and Livia Visai

Published in
Frontiers in Bioengineering and Biotechnology

ISSN 1664-8714
ISBN 978-2-8325-4958-2
DOI 10.3389/978-2-8325-4958-2

About Frontiers

Frontiers is more than just an open access publisher of scholarly articles: it is a pioneering approach to the world of academia, radically improving the way scholarly research is managed. The grand vision of Frontiers is a world where all people have an equal opportunity to seek, share and generate knowledge. Frontiers provides immediate and permanent online open access to all its publications, but this alone is not enough to realize our grand goals.

Frontiers journal series

The Frontiers journal series is a multi-tier and interdisciplinary set of open-access, online journals, promising a paradigm shift from the current review, selection and dissemination processes in academic publishing. All Frontiers journals are driven by researchers for researchers; therefore, they constitute a service to the scholarly community. At the same time, the *Frontiers journal series* operates on a revolutionary invention, the tiered publishing system, initially addressing specific communities of scholars, and gradually climbing up to broader public understanding, thus serving the interests of the lay society, too.

Dedication to quality

Each Frontiers article is a landmark of the highest quality, thanks to genuinely collaborative interactions between authors and review editors, who include some of the world's best academicians. Research must be certified by peers before entering a stream of knowledge that may eventually reach the public - and shape society; therefore, Frontiers only applies the most rigorous and unbiased reviews. Frontiers revolutionizes research publishing by freely delivering the most outstanding research, evaluated with no bias from both the academic and social point of view. By applying the most advanced information technologies, Frontiers is catapulting scholarly publishing into a new generation.

What are Frontiers Research Topics?

Frontiers Research Topics are very popular trademarks of the *Frontiers journals series*: they are collections of at least ten articles, all centered on a particular subject. With their unique mix of varied contributions from Original Research to Review Articles, Frontiers Research Topics unify the most influential researchers, the latest key findings and historical advances in a hot research area.

Find out more on how to host your own Frontiers Research Topic or contribute to one as an author by contacting the Frontiers editorial office: frontiersin.org/about/contact

Cells, biomaterials, and biophysical stimuli for bone, cartilage, and muscle regeneration, volume II

Topic editors

Lorenzo Fassina — University of Pavia, Italy
Nora Bloise — University of Pavia, Italy
Murugan Ramalingam — University of the Basque Country, Spain
Livia Visai — University of Pavia, Italy

Citation

Fassina, L., Bloise, N., Ramalingam, M., Visai, L., eds. (2024). *Cells, biomaterials, and biophysical stimuli for bone, cartilage, and muscle regeneration, volume II*. Lausanne: Frontiers Media SA. doi: 10.3389/978-2-8325-4958-2

Table of contents

frontiers | Frontiers in Bioengineering and Biotechnology

TYPE Editorial
PUBLISHED 20 May 2024
DOI 10.3389/fbioe.2024.1427256

OPEN ACCESS

EDITED AND REVIEWED BY
Hasan Uludag,
University of Alberta, Canada

*CORRESPONDENCE
Lorenzo Fassina,
lorenzo.fassina@unipv.it
Nora Bloise,
nora.bloise@unipv.it
Murugan Ramalingam,
rmurug2000@gmail.com
Livia Visai,
livia.visai@unipv.it

RECEIVED 03 May 2024
ACCEPTED 09 May 2024
PUBLISHED 20 May 2024

CITATION
Fassina L, Bloise N, Ramalingam M and Visai L (2024), Editorial: Cells, biomaterials, and biophysical stimuli for bone, cartilage, and muscle regeneration, volume II.
Front. Bioeng. Biotechnol. 12:1427256.
doi: 10.3389/fbioe.2024.1427256

Editorial: Cells, biomaterials, and biophysical stimuli for bone, cartilage, and muscle regeneration, volume II

Lorenzo Fassina[1]*, Nora Bloise[2,3]*, Murugan Ramalingam[4,5,6,7,8]* and Livia Visai[2,3]*

[1]Department of Electrical, Computer and Biomedical Engineering, Centre for Health Technologies (CHT), University of Pavia, Pavia, Italy, [2]Department of Molecular Medicine, Centre for Health Technologies (CHT), INSTM UdR of Pavia, University of Pavia, Pavia, Italy, [3]UOR6 Nanotechnology Laboratory, Department of Prevention and Rehabilitation in Occupational Medicine and Specialty Medicine, ICS Maugeri IRCCS, Pavia, Italy, [4]Joint Research Laboratory (JRL) on Bioprinting and Advanced Pharma Development, A Joint Venture of TECNALIA and University of the Basque Country (UPV/EHU), Centro de Investigación Lascaray Ikergunea, Vitoria-Gasteiz, Spain, [5]NanoBioCel Group, Department of Pharmacy and Food Sciences, Faculty of Pharmacy, University of the Basque Country (UPV/EHU), Vitoria-Gasteiz, Spain, [6]IKERBASQUE, Basque Foundation for Science, Bilbao, Spain, [7]Bioaraba Health Research Institute, Vitoria-Gasteiz, Spain, [8]Biomedical Research Networking Centre in Bioengineering, Biomaterials and Nanomedicine (CIBER-BBN), Institute of Health Carlos III, Madrid, Spain

KEYWORDS

tissue engineering, regeneration, bone, cartilage, muscle

Editorial on the Research Topic
Cells, biomaterials, and biophysical stimuli for bone, cartilage, and muscle regeneration, volume II

Over the last few years, a variety of Tissue Engineering strategies have been developed to improve the regeneration of bone, cartilage, and skeletal muscle. Numerous studies have proven that physical factors (e.g., external forces, electromagnetic waves, electric fields, ultrasounds, lasers, fluid flow shear stresses, mechanical vibrations, mechanical deformations, and biomaterials' features), as well as biochemical factors, may induce cells to reprogram their functions and dynamically adapt to the microenvironment conditions. In this context, many efforts are dedicated to engineer the biomaterial scaffolds, the physical stimuli, and the biochemical cues to whom the mammalian cells respond in terms of proliferation, differentiation, and production of extracellular matrix.

Effective regeneration of bone, cartilage, and skeletal muscle defects often presents significant challenges, particularly in patients with decreased tissue regeneration ability due to extensive trauma, diseases, or aging. To this regard, in the present Research Topic, 90 Authors from all over the world decided to publish their outstanding and promising results.

In particular, Wu et al. showed that, during the mineralization period of distraction osteogenesis in a rat model, the injection of rat bone marrow mesenchymal stem cells, which were differentiated by recombinant rat platelet-derived growth factor BB (rrPDGF-BB), can successfully promote the bone regeneration inside the distraction space.

Ren et al. made a comprehensive review regarding the action performed by the mesenchymal stem cells through their exosomes (MSC-Exos), thus highlighting that MSC-Exos are effective in promoting the osteogenesis.

In addition, Liu et al. thoroughly reviewed a growing evidence indicating that the microRNAs delivered by small extracellular vesicles originating from mesenchymal stem cells can enhance the bone regeneration.

Jaber et al. developed a powerful *in silico* approach to evaluate, in pre-clinical studies, the design of scaffolds for the bone regeneration within long bone large defects; their approach could lead to optimized architectures of 3D printed implants for bone regeneration. In particular, they simulated *in silico* that PCL strut-like scaffolds appear superior to gyroid ones in terms of bone regeneration despite their large surface curvatures.

Moreover, Sanaei et al. showed that, in endoprosthetic reconstruction surgery, reducing the prosthesis modulus by inclusion of an open-space lattice has a positive effect on bone tissue particularly within the periprosthetic zones; the improved mechanics appears to also have a positive effect on the osteointegration.

Gao et al. systematically reviewed the physiological mechanisms underlying the mandibular flexure, discussing different concurrent deformation types, moreover, they explored the deep implications of mandibular flexure on clinical aspects such as bone absorption around dental implants.

Dabaghi et al. evaluated the regeneration capability of a human-derived demineralized scaffold for the meniscal regeneration; overall, the results suggest that the new scaffold could be used as a promising biocompatible graft material for the meniscal tissue regeneration.

Luo et al. synthesized biocompatible RGD conjugated-sonosensitizer-nanoparticles to regulate the chondrogenic differentiation of bone marrow mesenchymal stem cells; such nanoparticles have the ability to generate a moderate level of ROS via an ultrasound treatment: this leads to an enhanced chondrogenic differentiation and to the buildup of cartilage extracellular matrix.

In addition, Qiang et al. showed that the sequential release of Bevacizumab (an inhibitor of the vascular endothelial growth factor) followed by insulin-like growth factor-1 (a cartilage repair factor), both delivered from microspheres contained in a hydrogel, can effectively improve the cartilage regeneration in a rabbit model of proximal tibial growth plate injury. In particular, they proposed a novel approach, where the inhibition of osteogenic differentiation and bone bridge formation is prioritized before promoting the chondrogenic differentiation.

On the other hand, Gao et al. studied, *in vitro*, the creep deformation of articular cartilage under the physiological loads occurring in daily activities such as standing, single-leg lunge, and the stance phase of gait; their *in vitro* model together with a viscoelastic constitutive law was employed to predict the creep-recovery behavior of the cartilage. If not fully recovered in time, the creep deformation may induce some damage in the cartilage; as a consequence, these findings could provide new understandings of normal joint function and cartilage pathology.

Mahdavi-Jouibari et al. focused on stem cells from human exfoliated deciduous teeth, which have a clear chondrogenic differentiation potential together with minimal immunogenicity and can be an interesting option for cartilage regeneration.

Finally, Wang et al. reviewed the role of macrophage polarization in tendon healing, focusing on insights from animal models; in particular, the review explores the complex role of macrophages in tendon pathology, detailing how various macrophage phenotypes contribute to both healing and adhesions' formation. The review also searches the potential of modulating the macrophage activity to enhance the tendon repair and to minimize the adhesions.

Author contributions

LF: Writing–original draft, Writing–review and editing. NB: Writing–original draft, Writing–review and editing. MR: Writing–original draft, Writing–review and editing. LV: Writing–original draft, Writing–review and editing.

Funding

The authors declare that no financial support was received for the research, authorship, and/or publication of this article.

Conflict of interest

The authors declare that the research was conducted in the absence of any commercial or financial relationships that could be construed as a potential conflict of interest.

The authors declared that they were an editorial board member of Frontiers, at the time of submission. This had no impact on the peer review process and the final decision.

Publisher's note

frontiers | Frontiers in Bioengineering and Biotechnology

TYPE Original Research
PUBLISHED 23 September 2022
DOI 10.3389/fbioe.2022.995266

OPEN ACCESS

EDITED BY
Jin Nam,
University of California, Riverside,
United States

REVIEWED BY
Maria Jose Gomez-Benito,
University of Zaragoza, Spain
Manuel Doblare,
University of Zaragoza, Spain

*CORRESPONDENCE
Sara Checa,
sara.checa@charite.de

SPECIALTY SECTION
This article was submitted to Biomechanics,
a section of the journal
Frontiers in Bioengineering and Biotechnology

RECEIVED 15 July 2022
ACCEPTED 06 September 2022
PUBLISHED 23 September 2022

CITATION
Jaber M, Poh PSP, Duda GN and Checa S (2022), PCL strut-like scaffolds appear superior to gyroid in terms of bone regeneration within a long bone large defect: An in silico study.
Front. Bioeng. Biotechnol. 10:995266.
doi: 10.3389/fbioe.2022.995266

PCL strut-like scaffolds appear superior to gyroid in terms of bone regeneration within a long bone large defect: An *in silico* study

Mahdi Jaber[1,2], Patrina S. P. Poh[1], Georg N. Duda[1,3] and Sara Checa[1]*

[1]Berlin Institute of Health at Charité – Universitätsmedizin Berlin, Julius Wolff Institute, Berlin, Germany, [2]Berlin-Brandenburg School for Regenerative Therapies, Berlin, Germany, [3]BIH Center for Regenerative Therapies, Berlin, Germany

The treatment of large bone defects represents a major clinical challenge. 3D printed scaffolds appear as a promising strategy to support bone defect regeneration. The 3D design of such scaffolds impacts the healing path and thus defect regeneration potential. Among others, scaffold architecture has been shown to influence the healing outcome. Gyroid architecture, characterized by a zero mean surface curvature, has been discussed as a promising scaffold design for bone regeneration. However, whether gyroid scaffolds are favourable for bone regeneration in large bone defects over traditional strut-like architecture scaffolds remains unknown. Therefore, the aim of this study was to investigate whether gyroid scaffolds present advantages over more traditional strut-like scaffolds in terms of their bone regeneration potential. Validated bone defect regeneration principles were applied in an *in silico* modeling approach that allows to predict bone formation in defect regeneration. Towards this aim, the mechano-biological bone regeneration principles were adapted to allow simulating bone regeneration within both gyroid and strut-like scaffolds. We found that the large surface curvatures of the gyroid scaffold led to a slower tissue formation dynamic and conclusively reduced bone regeneration. The initial claim, that an overall reduced zero mean surface curvature would enhance bone formation, could not be confirmed. The here presented approach illustrates the potential of *in silico* tools to evaluate in pre-clinical studies scaffold designs and eventually lead to optimized architectures of 3D printed implants for bone regeneration.

KEYWORDS

mechano-biology, bone defect healing, 3D-printed scaffold design, bone tissue engineering, gyroid, TPMS

1 Introduction

The treatment of large bone defects represents a major clinical challenge. Current treatment strategies, such as autologous bone grafting, although clinically successful, have substantial drawbacks and limitations; e.g., the need for additional surgical access to the donor site, limited availability of adequate bone to fill a critical-sized defect and subsequent morbidity of the donor site (Roddy et al., 2018).

Porous scaffolds made from biomaterials and printed in 3D to match the patient-specific defect dimensions have a high potential to overcome the above mentioned limitations and solve the medical need in treating critical size large bone defects (Pobloth et al., 2018). Different scaffold designs have been experimentally tested, both *in vitro* and in pre-clinical studies (Cobos et al., 2000; Reichert et al., 2012; Lovati et al., 2016; Shah et al., 2016; Reznikov et al., 2019). It has been shown that, among others, scaffold material, pore size, porosity, permeability and overall stiffness influence the healing outcome (Schlichting et al., 2008; Mitsak et al., 2011; Pobloth et al., 2018; Wei et al., 2020).

Recently, triply periodic minimal surfaces (TPMS) scaffolds have gained high interest in tissue engineering. They are thought to resemble the bone microarchitecture due to their biomimetic geometry (Dong and Zhao, 2021). TPMS scaffolds are characterized by a mean surface curvature of zero (Jinnai et al., 2002), similar to what has been reported for trabecular bone (Abueidda et al., 2019). In addition, the surface area to volume ratio of TPMS scaffolds is relatively high compared to other scaffold designs (Lu et al., 2020; du Plessis et al., 2018). This higher surface area of TPMS scaffolds has been shown to contribute to enhanced cell adhesion, support migration on such surfaces, and enable proliferation (Yoo, 2014; Vijayavenkataraman et al., 2018).

TPMS can adopt different configurations. Among them, gyroid is the most popular for creating architectures with robust mechanical performance (Abueidda et al., 2019). Gyroid has no planes of reflection symmetry and no straight line segments lying on its surface (Karcher, 1989; Große-Brauckmann and Wohlgemuth, 1996). Interestingly, gyroid architectures are found in nature, e.g., in mitochondria's inner membranes (Cui et al., 2020) and butterfly wings (Michielsen and Stavenga, 2008). Moreover, the continuous curvature of their struts has been suggested to be beneficial avoiding concentration of mechanical stresses (Yánez et al., 2020). Gyroid scaffolds were shown to exhibit high permeability when compared to other TPMS scaffolds (Castro et al., 2019a; Santos et al., 2020). In addition, compared to other TPMS scaffolds, gyroid scaffolds show high stiffness (Yang et al., 2019), crucial for maintaining a stable mechanical environment, which makes them especially interesting for bone regeneration applications (Glatt et al., 2017).

Although numerous experimental and numerical studies have been performed on scaffolds with gyroid architecture in recent years, most of these studies have been limited to analysing their mechanical properties (Melchels et al., 2010b; Dalaq et al., 2016; Yánez et al., 2018; Castro et al., 2019b; Alizadeh-Osgouei et al., 2021). For example, several studies have investigated the influence of the pore size of gyroid scaffolds on their overall mechanical properties (Ma et al., 2019; Alizadeh-Osgouei et al., 2021; Caiazzo et al., 2021). Only a few *in vitro* studies have investigated cellular behaviour within gyroid scaffolds. Melchels et al. (2010a) showed that their open architecture facilitates cell infiltration into the scaffold, which has been attributed to the zero-mean curvature (Rajagopalan and Robb, 2006). In addition, very few *in vivo* studies have investigated the bone regeneration potential of gyroid scaffolds. Kelly et al. (2021) investigated the potential of gyroid scaffolds in a rat femoral defect; however, they didn't compare its healing outcome to a different scaffold design. Van hede et al. (2022) showed that gyroid scaffolds lead to slightly more bone formation when compared to traditional strut-like scaffolds within a skull bone defect. However, bone regeneration within a skull defect occurs under highly reduced mechanical conditions. So far, whether gyroid scaffolds present advantages over traditional scaffolds (e.g., strut-like scaffolds) in large long bone defects, remains unknown.

Ongoing research is moving towards the use of approaches that satisfy the 3Rs principle, i.e., reduction, replacement and refinement (Viceconti and Dall'Ara, 2019). *In silico* approaches offer the unique opportunity to investigate virtually, potential mechanisms behind biological processes and even to investigate interactions that are difficult or even impossible to measure experimentally. In addition, they allow testing of potential treatment strategies, reducing the need for pre-clinical experiments (Viceconti and Dall'Ara, 2019; Jean-Quartier et al., 2018). In the field of bone regeneration, numerous computer models have been developed and validated for their potential to predict regeneration in uneventful bone healing conditions (Byrne et al., 2011; Checa et al., 2011; Vetter et al., 2012; Repp et al., 2015; Borgiani et al., 2019). Recently, these models have been further developed and validated in their potential to predict bone regeneration within scaffolds (Perier-Metz et al., 2020; Perier-Metz et al., 2022). However, they have never investigated bone regeneration within gyroid scaffolds.

The aim of this study was to investigate whether gyroid scaffolds would be favourable for bone regeneration over more traditional scaffolds, i.e., a strut-like scaffold, applying principles of bone formation in an *in silico* modelling approach. The bone regeneration potential of a gyroid scaffold as well as the influence of mechanical cues and cellular dynamics throughout the regeneration was compared with that of a more traditional strut-like design to assess the suggested benefits of a gyroid architecture compared with more traditional designs. We hypothesized that a gyroid scaffold design would promote cellular activities

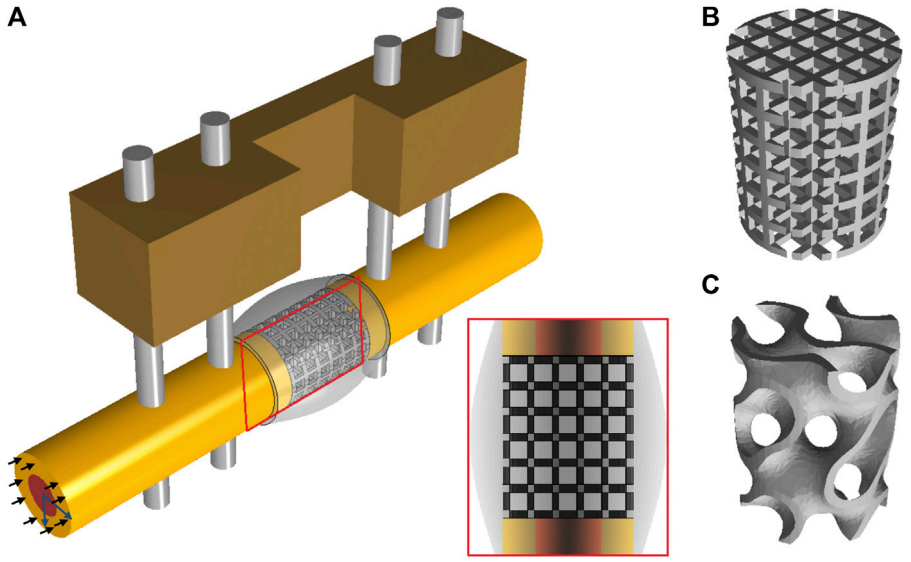

FIGURE 1
(A) CAD model simulating a large bone defect in the rat femur stabilized with an external fixator. In the defect a strut-like **(B)** or a gyroid **(C)** scaffold was virtually inserted. The black arrows represent the compressive loads and the blue arrows represent the tangential loads inducing bending.

involved in bone regeneration and therefore show enhanced bone regeneration compared to a strut-like configuration, as predicted by an *in silico* model.

2 Materials and methods

2.1 *In silico* bone regeneration model

A previously described bone regeneration computer model able to explain experimentally observed scaffold-supported bone regeneration in a large bone defect (Perier-Metz et al., 2020; Perier-Metz et al., 2022) was adapted to investigate bone regeneration within gyroid scaffolds. The computer model combined finite element (FE) analysis to determine the mechanical environment within the scaffold, and an agent-based model (ABM) describing the biological processes taking place during bone regeneration (Perier-Metz et al., 2020). Scaffolds were virtually inserted into a critical size large bone defect in the rat femur to mimic an *in vivo* experimental setup, so that the model could be used to inform a potential future pre-clinical study. This experimental setup has been previously used to investigate bone regeneration within large bone defects both *in vivo* (Schwarz et al., 2013) and *in silico* (Borgiani et al., 2021).

2.1.1 Finite element model

A 3D finite element model was created to assess the mechanical environment inside the large bone defect and scaffold pores. The FE model was developed in ABAQUS/Standard 2019 (Simulia, Dassault Systemes). The model simulated a large bone defect in the rat femur stabilized with an external fixator, following previous experimental studies (Schwarz et al., 2013). The computer model included the cortical bone, the marrow cavity, the external fixator and the scaffold fitted in the defect region surrounded by a callus. The geometry of the bone was modelled as a hollow cylinder representing the cortical bone and an internal marrow cavity. The large bone defect was replicated by opening a 5-mm-wide gap in the middle of the bone. The geometry of the model is based on a previous computer model (Borgiani et al., 2021) that approximated the callus dimensions based on histological data (Schwarz et al., 2013). To better assess the regeneration potential of the gyroid scaffold, scaffolds with two different architectures and with the same overall geometry (height 5 mm and radius 2 mm) and porosity (79%) were developed: one having a more traditional strut-like architecture and the other having a gyroid configuration (Figure 1). The strut-like scaffold (Figure 1B) was directly modelled using ABAQUS/Standard 2019 with a pore size of 0.54 mm, resulting in a surface area to volume ratio of 3.74. The gyroid scaffold (Figure 1C) was created in Rhinoceros 3D (Robert McNeel & Associates) with a pore size of 0.56 mm and a surface area to volume ratio of 2.35. The surface geometry was then imported into ABAQUS/Standard 2019 where it was converted from a shell (.stl) to a solid (.sat) using the "create a geometry from mesh" software plugin. The dimensions of all the parts of the model are reported in Supplementary Data.

All biological tissues were modelled as poroelastic materials with properties given in Table 1. The fixator, the nails and the

TABLE 1 Tissue material properties [adapted from (Checa et al., 2011)].

Material properties	Granulation tissue	Fibrous tissue	Cartilage	Immature bone	Mature bone	Cortical bone	Bone marrow
Young's modulus (MPa)	0.2	2	10	1,000	5,000	5,000	2
Permeability (10^{-14} s m^4/N)	1	1	0.5	10	37	0.001	1
Poisson's ratio	0.167	0.167	0.3	0.3	0.3	0.3	0.167
Bulk modulus grain (MPa)	2,300	2,300	3,700	13,940	13,940	13,920	2,300
Bulk modulus fluid (MPa)	2,300	2,300	2,300	2,300	2,300	3,200	2,300

scaffolds were considered linear elastic isotropic and modelled identical in both scaffold designs. Scaffolds were assumed to be made of Polycaprolactone (PCL), a material highly investigated for scaffold applications (Dwivedi et al., 2020), while the fixator and the nails were assumed to be made of Polyether-ether-ketone (PEEK) and titanium, respectively, following a previous pre-clinical experimental study (Schwarz et al., 2013). Therefore, the material properties of Polyether-ether-ketone: PEEK (E = 3,800 MPa, v = 0.3), titanium: Ti (E = 111,000 MPa, v = 0.3), and Polycaprolactone: PCL (E = 350 MPa, v = 0.33) were assigned to the fixator, the nails and the scaffolds, respectively.

Mechanical loading conditions aimed to simulate the peak load under normal walking conditions. An axial compressive load of 14.7 N [corresponding to 6 body weight (BW)] was applied at the proximal bone side (Wehner et al., 2010) (Figure 1). In addition, two tangential forces of 1.8 N were applied on the proximal bone surface in the antero/posterior and in the medial/lateral directions thereby inducing bending loads (corresponding to 10.7 BW mm of moment at the femoral mid-shaft) (Wehner et al., 2010) (Figure 1). The distal part was fully constrained. A pore pressure boundary condition was constrained to be zero on the external surface of the callus domain.

The model was meshed using three-dimensional quadratic tetrahedral elements (C3D10 MP) with an average mesh size of 0.50 mm for the whole model except for the scaffold and the callus region, which had an average mesh size of 0.20 mm.

Scaffolds were assumed to experience bulk degradation where scaffold's volume is preserved, as reported for PCL (Pitt et al., 1981). To model this, the mechanical properties of the polymer were assumed to be linearly related to its molecular weight (Adachi et al., 2006). Scaffold degradation was then simulated using the following equation:

$$E = E_0 e^{-kt}$$

With E the updated Young's modulus, E_0 the initial Young's modulus, k the degradation rate per day and t for time. A degradation rate of 0.003 day^{-1} was assumed as reported for PCL material in an *in vivo* setting (Pitt et al., 1981).

2.1.2 Agent-based computer model to investigate cellular activity within the scaffold pores

An agent-based computer model was implemented using C++, where the space occupied by the scaffold and the regenerating tissue region (scaffold pores) was discretized into a 3D grid (spacing 10 μm) in which each of the positions within the scaffold pores represents a potential space a cell could occupy. This means that the space occupied by each element in the FE model would contain a number of agents in the agent based model. Since each agent size is 10 × 10 × 10 um^3, the FE callus dimensions (x = 6mm, y = 6 mm and z = 7.2 mm) were translated into the ABM to 600 agents in the x direction, 600 agents in the y direction and 720 agents in the z direction; resulting in a total of 259200000 agents in the 3D grid. The following cell phenotypes were included: mesenchymal cells (MSC), fibroblasts, chondrocytes, immature osteoblasts and mature osteoblasts. The model simulates cellular processes including migration, proliferation, differentiation and apoptosis. Cell differentiation, proliferation and apoptosis are regulated by a mechanical stimulus based on octahedral shear strain and fluid flow extracted from the FE model (Checa et al., 2011) (Table 2). Cell differentiation was modelled to occur only on top of existing surfaces (scaffold or newly formed tissues), simulating surface-guided bone regeneration within scaffolds (Perier-Metz et al., 2020). In addition, different cellular processes are modelled to occur at different rates (Table 3).

To simulate the invasion of MSCs from the marrow cavity and periosteum, 30% of the agent-based positions along the periosteum and marrow cavity were initially seeded with MSCs (Checa et al., 2011). In addition, following Perier-Metz et al. (2020), the scaffold pores were assumed to be filled with bone graft (Finkemeier, 2002). The bone grafting effect on the bone regeneration process was modelled by limiting progenitor cell migration and proliferation to the regions containing graft (scaffold pores) after a latency period (14 days) (Perier-Metz et al., 2020).

TABLE 2 Mechano-regulation algorithms for progenitor cell differentiation [adapted from (Checa et al., 2011)].

Stimulus: $S = \frac{\gamma}{a} + \frac{v}{b}$	Bone resorption	Mature osteoblast	Immature osteoblast	Chondrocyte	Fibroblast
γ: shear strain, v: fluid velocity					
a = 0.0375[a], b = 0.003 mm/s[a]					
Thresholds[a,b]	S≤0.01	0.01<S≤2.53	2.53<S≤3	3<S≤5	S>5

[a](Huiskes et al., 1997).
[b](Lacroix and Prendergast, 2002).

TABLE 3 Cell activity rates [adapted from (Checa et al., 2011)].

Cell type	Proliferation rate (/day)	Apoptosis rate (/day)	Differentiation rate (/day)	Migration speed (μm/h)
MSC	0.60	0.05	0.30	30
Fibroblasts	0.55	0.05	—	30
Chondrocytes	0.20	0.10	—	—
Osteoblasts	0.30	0.16	—	—

TABLE 4 Summary of the bone healing simulations and scaffold characteristics.

Name	Architecture	Porosity (%)	Degradation	Pore size	Number of nodes	Number of elements
Gyroid scaffold	Gyroid	79	Normal	0.54	417,684	301,748
Strut-like scaffold	Strut-like	79	Normal	0.56	372,137	267,151
Highly degradable scaffold	Gyroid	79	Fast	0.56	417,684	301,748
Non-degradable scaffold	Gyroid	79	—	0.56	417,684	301,748
Gyroid scaffold with lower porosity	Gyroid	69	Normal	0.5	443,353	320,911
Strut-like scaffold with lower porosity	Strut-like	69	Normal	0.49	368,107	263,877

Cells were simulated to produce the corresponding extracellular matrix (osteoblasts: bone, chondrocytes: cartilage and fibroblasts: fibrous tissue), so that each cell position was assumed to account for corresponding extracellular matrix deposition. Extracellular matrix deposition is modelled as cell differentiation of MSCs into another cell type and a change in tissue material properties in the FE model; which were updated iteratively (1 iteration = 1 day). All differentiated cells inside each single element contributed to the element material properties, following a rule of mixtures (Lacroix and Prendergast, 2002). In addition, the contribution of each differentiated cell to the specific element material properties were averaged over the last ten iterations to account for the delay in actual ECM deposition (Lacroix and Prendergast, 2002). Therefore, the agent-based and the FE models interacted through the level of mechanical signals (from the FEM to the ABM) and the corresponding changes in tissue material properties (from the ABM to the FEM).

2.1.3 Scaffold design evaluations

The effect of each scaffold parameter was assessed following common experimental setups in which all variable factors (eg. material type, porosity, pore size. . .) in an experimental group (eg. gyroid scaffold) and a comparison control group (eg. strut-like scaffold) are kept the same except for one variable factor (eg. architecture) that differs between the two groups. Accordingly, several scaffold design effects were investigated (Table 4):

- Scaffold architecture effect: To examine the influence of the scaffold architecture on bone tissue regeneration, two scaffolds were modelled by assuming the same scaffold porosity and material parameters and varying the scaffold architecture. A model with a gyroid architecture was compared to a model with a strut-like architecture (Figure 1).
- Scaffold degradation effect: Since the degradation rate of PCL material is very slow, the effect of degradation on the bone regeneration process was expected to be minimal.

Thereby, to investigate the effect of scaffold degradation on the regeneration process, the influence of a highly degradable scaffold (k = 0.03 per day) on bone regeneration was compared to the effect of a non-degradable scaffold, both with the same gyroid design.

- Porosity effect: To examine the influence of scaffold porosity on the bone regeneration process, both gyroid and strut-like scaffolds were modelled with a lower porosity of ~69% and compared with the 79% porous scaffolds. The gyroid scaffold with 69% porosity had a pore size of 0.5 mm and a surface area to volume ratio of 2.43, while the strut-like scaffold had a pore size of 0.49 mm and a surface area to volume ratio of 4.3.

2.2 Output data analysis

2.2.1 Overall scaffold stiffness computation

A virtual compression test was performed to compute the overall stiffness of the scaffolds and their changes over the healing process. The compression test was done by applying a vertical force (F = 15 N) at the top surface of the scaffolds and outputting the resultant average vertical displacement.

2.2.2 Tissue regeneration

Tissue distribution in a longitudinal section through the middle of the scaffold (Figure 1A) was evaluated and represented in a similar manner to histological sections. Tissue patterning was evaluated at 4 time points: 0-, 4-, 8-, and 12-weeks post-surgery. Moreover, the relative area occupied by the different tissue types within the mid-section in the callus and the total volume of the different tissue types within the scaffold pores were quantified daily until 12 weeks.

Cellular activities happening within the scaffold pores were quantified by measuring the total number of cells that migrated (regardless of distance travelled), proliferated, differentiated to other cell types and died daily until 12 weeks. All MSCs and fibroblasts are potential migrating cells but only those that manage to change position within one iteration are considered migrating cells. The cell were assigned a migrating speed of 30 microns/hr which is equivalent to 720 microns/day. Also, the average speed of the cells (MSCs and fibroblasts) was quantified by dividing the average distance travelled by the cells by the number of cells that travelled per day.

2.2.3 Mechanical stimulus

In order to investigate the changes in the mechanical conditions within the scaffold pores during tissue regeneration, the mechanical stimulus (based on octahedral shear strain and fluid flow) distribution was computed 0-, 4-, 8-, and 12-weeks post-surgery, for each of the scaffold designs investigated.

3 Results

3.1 Predicted tissue formation over the course of healing

3.1.1 Gyroid vs. strut-like scaffolds

Initial mechanical stimuli distribution within the gyroid and strut-like scaffolds were different, despite being under the same external mechanical load (Figure 2A). Initially, in both scaffold designs, most of the tissue volume was under mechanical stimuli beneficial for bone formation; however, the distribution across the defect highly varied (Figure 2A). Higher mechanical signals beneficial for cartilage and fibrous tissue formation were detected at the contact region between the cortical bone and scaffold in both scaffold designs (Figure 2A).

These differences in the mechanical behavior of the scaffolds and the induced strains within the scaffold pores resulted in a divergence of the bone healing progression. In the strut-like scaffold, bone tissue started to form within the scaffold pores, simultaneously starting from the top and bottom surfaces and slowly progressing towards the core region by intramembranous ossification. Only small regions of fibrocartilage layers that would surround the scaffold walls were predicted. However, in the gyroid scaffolds, large fibrous tissue volumes were predicted to initially form surrounding the highly curved scaffold surfaces, with bone formation predicted to occur in regions far from those surfaces (Figure 2A). For the gyroid scaffolds, fibrous tissue was predicted to be slowly replaced by bone over the course of healing.

The healing outcome was also considerably different between the two scaffolds. After 12 weeks, bony bridging was observed in the strut-like scaffold, which had already entered the remodeling phase, whereas void regions were observed within the scaffold core of the gyroid scaffold. Overall, quantitatively more bone formation was predicted within the strut-like scaffold compared with the gyroid scaffold (Figures 2A.

The *in silico* longitudinal compression test of the scaffolds showed that during healing the strut-like scaffold provided a higher total stiffness compared the gyroid scaffold (Figure 2C).

3.1.2 Degradation effect

Initially, the mechanical stimuli within the fast degradable and non-degradable gyroid scaffolds were comparable (Figure 3A). With the loss of the mechanical stiffness of a fast degradable scaffold over time, a noticeable difference in the mechanical stimuli distribution between a fast degradable and a non-degradable scaffold was observed (Figure 3A). The non-degradable scaffold led to more regions beneficial for bone formation, whereas the fast degradable scaffold resulted in more regions beneficial for fibrous tissue formation (Figure 3A). Across the early healing stages, the amount of predicted regenerated tissue within both scaffold configurations differed slightly (Figures 3A. However, at late

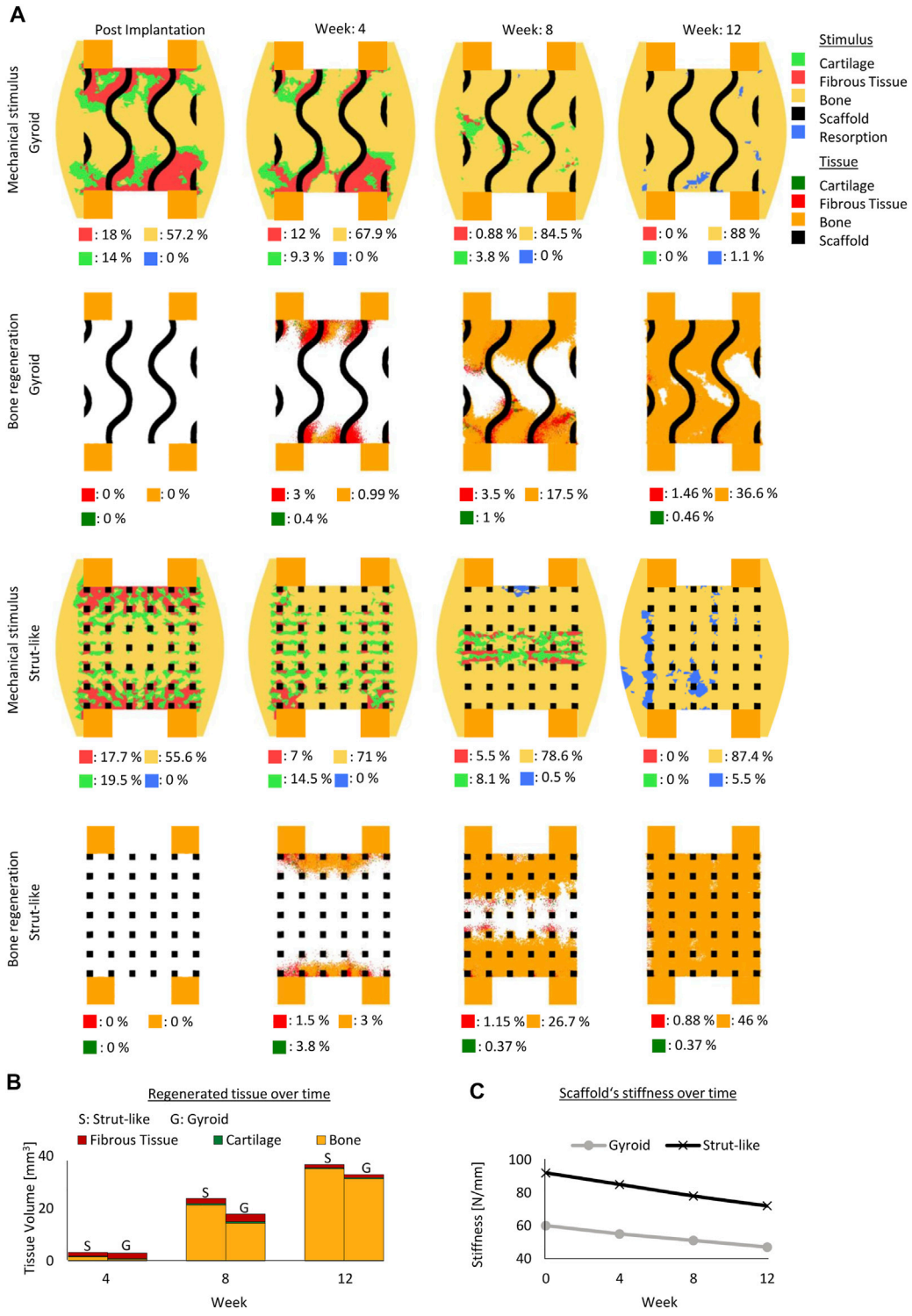

FIGURE 2
Predicted bone, cartilage and fibrous tissue within the scaffold pores at 4, 8 and 12 weeks of healing for scaffolds with strut-like and gyroid architecture with 79% porosity. **(A)**: Longitudinal cross sections of the callus from Figure 1A with quantified tissue regeneration in the 2D section, mechanical stimulus distribution over time using a strut-like scaffold, predicted tissue distribution over time using a strut-like scaffold, mechanical stimulus distribution over time using a gyroid scaffold and predicted tissue distribution over time using a gyroid scaffold. **(B)**: Total tissue volume predicted within the scaffold pores at different stages of healing. **(C)**: Mechanical stiffness of scaffolds computed from compression tests at different stages of healing.

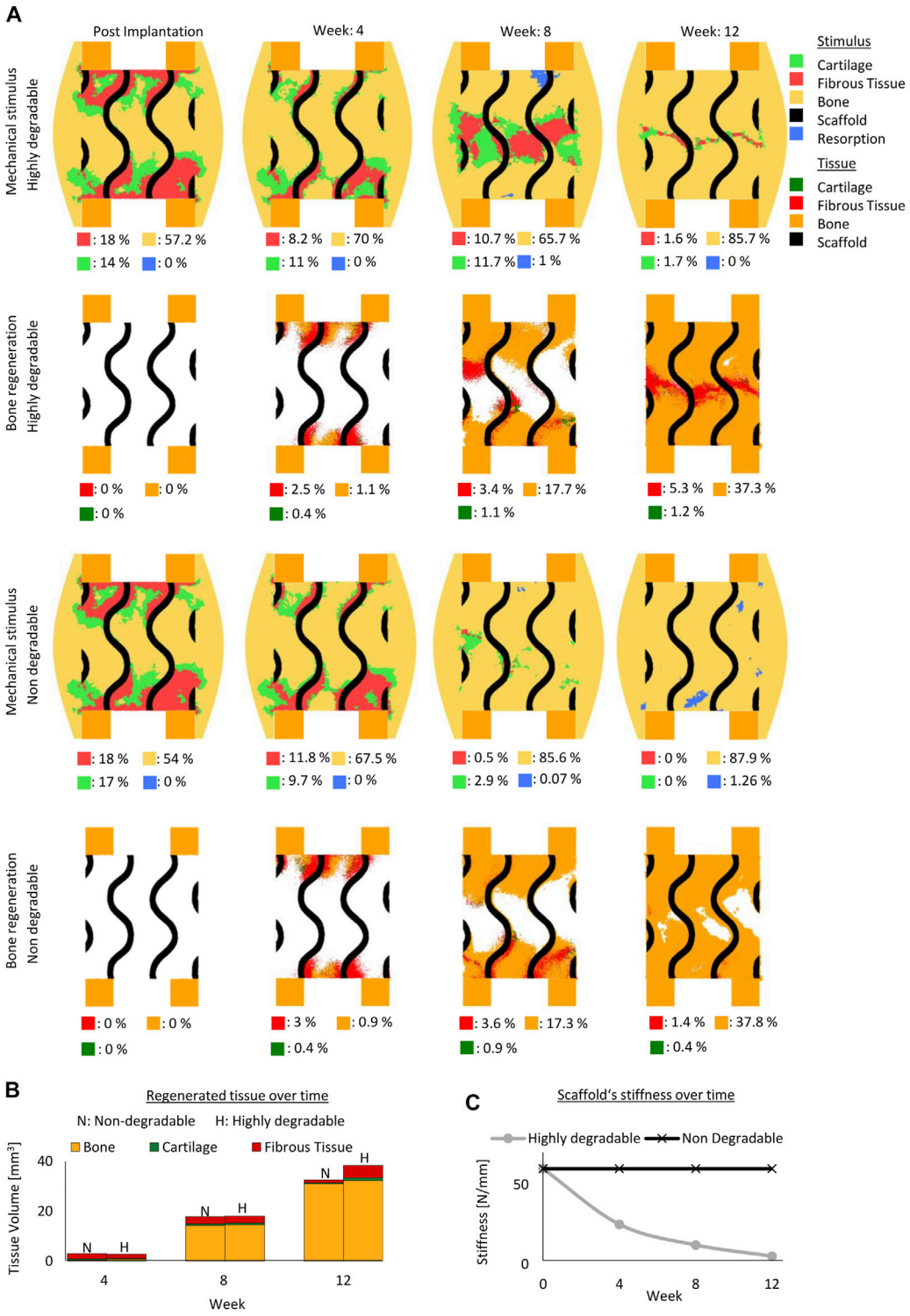

FIGURE 3
Predicted bone, cartilage and fibrous tissue within the scaffold pores at 4, 8 and 12 weeks of healing for scaffolds with non- and highly degradable scaffolds with 79% porosity. **(A)**: Longitudinal cross sections of the callus from Figure 1A with quantified tissue regeneration in the 2D section, mechanical stimulus distribution over time using a non-degradable scaffold, predicted tissue distribution over time using a non-degradable scaffold, mechanical stimulus distribution over time using a highly degradable and predicted tissue distribution over time using a highly degradable. **(B)**: Total tissue volume predicted within the scaffold pores at different stages of healing. **(C)**: Mechanical stiffness of scaffolds computed from compression tests at different stages of healing.

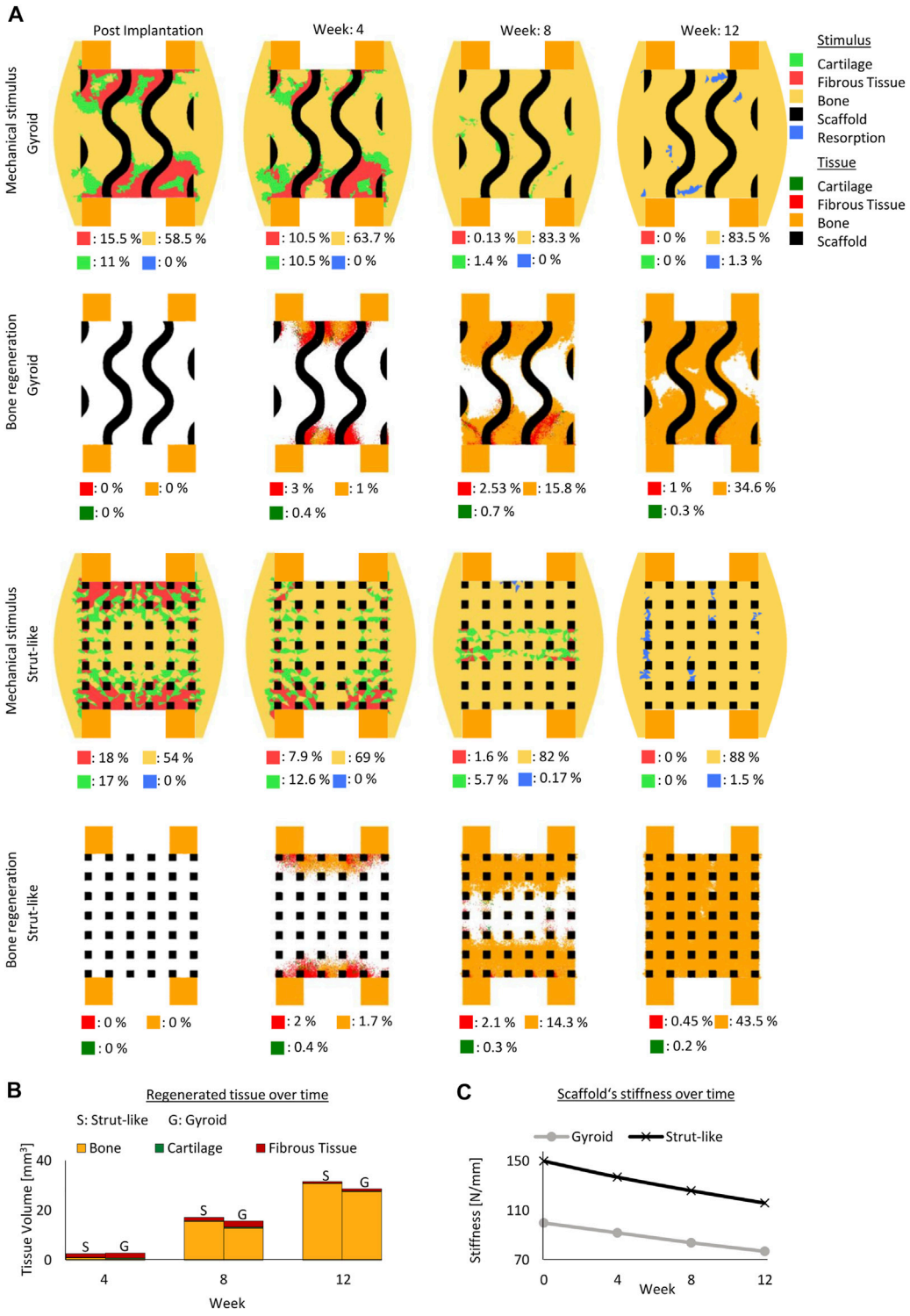

FIGURE 4
Predicted bone, cartilage and fibrous tissue within the scaffold pores at 4, 8 and 12 weeks of healing for scaffolds with strut-like and gyroid architecture with 69% porosity. **(A)**: Longitudinal cross sections of the callus from Figure 1A with quantified tissue regeneration in the 2D section, mechanical stimulus distribution over time using a strut-like scaffold, predicted tissue distribution over time using a strut-like scaffold, mechanical stimulus distribution over time using gyroid scaffold and predicted tissue distribution over time using a gyroid scaffold. **(B)**: Total tissue volume predicted within the scaffold pores at different stages of healing. **(C)**: Mechanical stiffness of scaffolds computed from compression tests at different stages of healing.

stages of healing, the total amount of tissue regenerated highly varied (Figures 3A. After 12 weeks, the highly degradable scaffold yielded only slightly more bone tissue compared to the non-degradable scaffold, however it resulted in considerably more fibrous tissue. While a layer of fibrous tissue was observed at the end of the regeneration process in the highly degradable scaffold, regions with remaining voids were found in a non-degradable scaffold (Figures 3A.

In addition, even though the fast degradable scaffold was undergoing an exponential decay in its mechanical stiffness reaching 5 N/mm at the end of the regeneration process (initially 60N/mm) (Figure 3C), the formation of tissue at the early stages of healing maintained a stable mechanical environment beneficial for new bone formation within the defect region.

3.1.3 Porosity effect

In the gyroid design, a scaffold with 69% porosity resulted in initial mechanical stimuli similar to a scaffold with 79% porosity (Figures 2A, 4A). With both porosities, most of the predicted tissue forming during the regeneration process was predicted to be bone. With the higher porosity scaffold more bone was formed compared to the one with the lower porosity scaffold (Figures 2A, 4A) Although, the predicted mechanical stimulus within both scaffold porosities continued to be similar during the regeneration process (Figures 2A, 4A), the model with lower porosity yielded less bone and fibrocartilage tissue due to slower tissue formation penetrating the scaffold and resulting in overall less tissue formation (Figures 2A, 4A. The mechanical stimuli in both scaffolds predicted mostly bone formation with distinct certain regions in the resorption zone at the end of the regeneration process (Figures 2A, 4A).

Similarly, in the strut-like designs, the mechanical stimuli were comparable for both scaffold porosities settings across the regeneration process (Figures 2A, 4A).While bone bridging was observed within the higher porosity scaffold at the end of the regeneration process, void regions at the center of the defect were observed within the lower porosity scaffold (Figures 2A, 4A).

In both scaffold design, a 10% reduction in scaffold porosity led to an increase of 40% in the overall scaffold stiffness (Figure 4C).

3.2 Analysis of cellular activity

The cellular activities including MSC migration, osteoblast proliferation and differentiation, and fibroblast differentiation were quantified per day in different scaffold designs.

3.2.1 Mesenchymal cells migration

Initially, the number of predicted MSCs migrating was similar in all scaffold configurations, however, higher MSC migration was predicted around the 3rd week in strut-like scaffolds. The cell migration continued to increase over the following weeks, with a higher increase within the strut-like compared with the gyroid scaffolds (Figure 5A). At the 8th–9th week, a decrease in the cell migration was predicted until the end of the regeneration process, for all scaffold designs. In addition to scaffold architecture, scaffold porosity showed a strong effect on MSC migration. Scaffolds with higher porosity showed increased migration, especially during the middle phase of the regeneration process (Figure 5).

3.2.2 Osteoblasts proliferation

Initially, the number of predicted osteoblasts proliferating was similar in all scaffold configurations. Whereas strut-like and gyroid scaffolds had comparable osteoblastic proliferation behaviour, over the course of the healing, higher osteoblastic proliferation was observed within the strut-like scaffold. In both scaffold architectures, the number of osteoblasts proliferating increased until the 9–10th week, from this time point, a decrease in the number of osteoblasts proliferation was observed until the end of the regeneration process. Similar to MSC migration, increase in the scaffold porosity lead to increase osteoblast proliferation in both scaffold architectures, however the effect was larger in the strut-like design (Figure 5B).

3.2.3 Osteoblasts differentiation

Initially, the number of MSCs differentiated into osteoblasts was similar in all scaffold configurations, however at the later stages of regeneration considerably more osteoblastic differentiation was predicted to occur within the strut-like scaffolds. In strut-like scaffolds, a considerable increase in osteoblast differentiation was predicted around the 8th–9th week, where a much lower peak was predicted around the 10th week within the gyroid scaffolds. Similar to MSC migration and osteoblast proliferation, increase scaffold porosity led to increase osteoblast differentiation in both scaffold architectures, however the effect was larger in the strut-like design (Figure 5C).

3.2.4 Fibroblasts differentiation

The number of MSCs differentiated into fibroblasts increased during the initial healing period in all scaffolds configurations (Figure 5D), however, higher fibroblast differentiation was predicted around the 4th week in gyroid scaffolds. From this time point, fibroblasts differentiation decreased until the end of the regeneration process. However, the strut-like scaffold showed a different trend, where at around the 6th–8th week had a second increase, followed by a decrease until the end of the regeneration process. Furthermore, lower fibroblast differentiation was predicted within the scaffolds with lower porosity, with higher difference within the strut-like design (Figure 5D).

Quantification of other cellular activities over the course of regeneration for the different scaffold designs is provided in Supplementary Data. The cellular activities include fibroblasts,

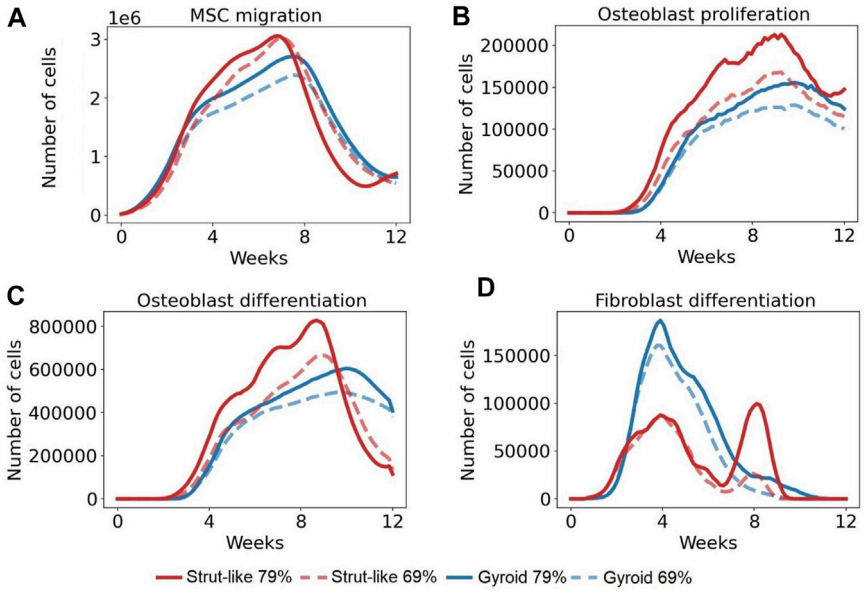

FIGURE 5
The number of the total cells per day across time in several cellular activities. **(A)**: Total number of MSCs that migrated per day in 12 weeks **(B)**: Total number of osteoblasts that proliferated per day in 12 weeks. **(C)**: Total number of MSCs that differentiated into osteoblasts per day in 12 weeks **(D)**: Total number MSCs that differentiated into fibroblasts per day in 12 weeks.

chondrocytes and MSCs proliferation, fibroblasts, chondrocytes and osteoblasts apoptosis, fibroblasts and MSCs average speed during migration, MSCs differentiation into chondrocytes and number of migrated fibroblasts.

Cumulative number of proliferated, differentiated and dead cells is reported in Supplementary Data.

4 Discussion

In the recent years, gyroid architectures have gained a lot of interest in tissue engineering for their high potential to be used as scaffolds in the treatment of large bone defects (Castro et al., 2019b; Yang et al., 2019; Jin et al., 2020). However, so far there has been no study to investigate whether they present advantages over traditional scaffolds for their bone regeneration potential. In this study, we use the power of computer modelling approaches to investigate whether a gyroid as a scaffold architecture presents an advantage, in terms of healing outcome, over a traditional scaffold with a strut-like architecture. Contrary to our initial hypothesis, our results showed reduced predicted healing outcome in gyroid compared to strut-like scaffolds.

In this study, we adapted a previously described bone regeneration computer model, which was able to explain experimentally observed scaffold-supported bone regeneration for two different scaffold designs in two independent pre-clinical studies of bone regeneration within large bone defects (Perier-Metz et al., 2020; Perier-Metz et al., 2022), to predict bone regeneration within a large bone defect supported with a gyroid scaffold. The model was previously able to explain bone regeneration within a titanium honeycomb scaffold and a PCL strut-like scaffold, where surface-scaffold guidance was identified as an important mechanism during scaffold supported regeneration (Pobloth et al., 2018; Perier-Metz et al., 2020; Perier-Metz et al., 2022; Pobloth et al., 2018). Other mechanoregulation theories have been previously proposed to explain the mechanobiological regulation of bone regeneration (Carter et al., 1998; Claes and Heigele, 1999; Prendergast et al., 1997). Mechanical stimuli based on hydrostatic stress and tensile strain, mechanical strains and hydrostatic pressure, and octahedral strain and fluid velocity have all been proposed as potential regulators. Computer modeling approaches have been used to test those theories and their potential to predict *in vivo* tissue regeneration, where it has been shown that most of those theories result in comparable tissue regeneration prediction, which in general agrees with experimental observations (Geris et al., 2003; Isaksson et al., 2006b; Postigo et al., 2014). In this study, we quantified regions under tension and compression strains and found that tensile strains were higher at the scaffold bone interface, while compressive strains were higher between the scaffold walls (Supplementary Data).

Unfortunately, experimental studies on scaffold-supported bone regeneration within gyroid scaffolds are very limited. To the authors knowledge, the only *in vivo* study that compared the bone healing potential of a gyroid scaffold to a strut-like scaffold is the one by Van hede et al. (2022), where a skull defect was used as defect model. Since skull bone has different developmental and regenerative mechanisms than long bones (Lim et al., 2013), those *in vivo* observations cannot be compared to the computer model predictions presented here. *In vitro* experiments of cellular function within gyroid scaffolds have been mainly performed to test different biomaterials or 3D printing techniques, where in general it has been reported that cells are able to penetrate and proliferate within gyroid scaffolds (Melchels et al., 2010a; Tsai et al., 2015; Ataee et al., 2019; Diez-Escudero et al., 2020; Spece et al., 2020; Chen et al., 2021; Noroozi et al., 2022). Spece et al. (2020) compared cellular activity within gyroid and strut-like scaffolds in terms of ALP activity, where they showed higher ALP activity in strut-like scaffolds. These findings agree with the higher osteoblast activity in strut-like scaffolds predicted in this study.

In this study, gyroid and strut-like scaffolds of the same porosity and almost the same pore size were compared in terms of predicted bone regeneration. In the gyroid scaffolds, the pore size does not describe the distance between surfaces, in fact in the scaffolds investigated here the distance between the surfaces for the gyroid scaffolds were approximately twice the pore size. This has a major impact not only in reducing the overall mechanical properties but also in the surface area to volume ratio and the cellular behaviour. Reduced surface area to volume ratio was determined in the gyroid compared with the strut-like scaffolds for a given porosity. In this study, we predicted reduced cell proliferation in gyroid compared to strut-like scaffolds, where strut-like scaffolds had a larger surface area to volume ratio. This is in agreement with experimental studies that reported faster cell growth for shorter distance between scaffold inner surfaces (Van Bael et al., 2012; Liu et al., 2020).

Since various polymeric materials used as scaffold materials experience degradation (Pitt and Zhong-wei, 1987), degradation due to hydrolysis undergoing exponential decay was implemented in the model (Adachi et al., 2006). Given that PCL degrades very slowly (degradation rate constant: 0.003 per day) (Pitt et al., 1981), the effect of its degradation on tissue formation was negligible. The effect of scaffold degradation on tissue regeneration was marked by comparing a highly degradable (0.03 per day) to a non-degradable scaffold. Although, this degradation rate is unrealistic for PCL, the scaffold material properties were kept constant to isolate the effect of degradation. The highly degradable scaffold resulted in more soft tissue and overall tissue formation compared with the non-degradable scaffold. Scaffold degradation was predicted to affect bone regeneration by decreasing the scaffold's mechanical stiffness allowing for higher deformations promoting soft tissue formation within the defect region. Our results showed that a highly degradable scaffold led to more bone regeneration, which is in agreement with experiments done on polymeric scaffolds where they found that at 3 months, the maximum amount of bone was observed in the scaffold with the highest degradability (Huang et al., 2019).

In this study, scaffolds with two different porosities (69% and 79%), both for gyroid and strut-like designs, were investigated. We found that while there was a substantial difference in the overall mechanical properties of the scaffolds, in agreement with experimental studies (Baino and Fiume, 2019), the mechanical environment within the scaffold pores for different porosities was similar. However, due to larger pores sizes in the scaffolds with higher porosities, more penetration of the cells was predicted, leading to more bone regeneration. This is also in agreement with experimental findings (Lee et al., 2019). Pobloth et al. (2018) showed that scaffolds with lower porosity but with the same architecture yield less bone and slower healing dynamics. Furthermore, we found a lower influence of scaffold porosity on tissue regeneration in the gyroid compared to the strut-like scaffold which could be explained by the smaller changes in surface area to volume ratio with changes in porosity in those scaffolds.

In addition, our results show reduced mechanical stiffness in the gyroid compared with the strut-like scaffolds, in agreement with numerical studies (Ali and Sen, 2017). With the same porosity, the strut-like scaffold was stiffer than the gyroid scaffold; however, the former scaffold showed considerably more bone formation than the latter. Previous *in vivo* studies have shown that softer scaffolds can enhance bone regeneration (Pobloth et al., 2018). This study shows that the scaffold architecture can have a higher impact on bone formation than overall scaffold stiffness.

Our study presents some limitations. First, in contrast to studies suggesting higher surface area to volume ratio for the gyriod scaffold (Lu et al., 2020; du Plessis et al., 2018), in this study, the gyroid scaffold had lower surface area to volume ratio. This is because in our models, to keep the porosity and pore size similar in both the gyroid and strut-like scaffolds, the number of scaffold unit cells was different for each scaffold design which led to lower surface area to volume ratio in the gyroid scaffold as compared to the strut-like scaffold. Previous studies have shown that by fixing the porosity and varying the unit cells of the scaffold, the scaffold mechanical properties are altered (Jian et al., 2015) and consequently, the bone regeneration (Pobloth et al., 2018). We performed additional simulations to investigate the effect of the number of scaffold unit cells. For a given porosity, we found that increasing the number of unit cells increases the surface area to volume ratio and enhances bone regeneration, both in gyroid and strut-like configurations (Supplementary Data). However, although the gyroid scaffold presented higher surface to volume ratio (gyroid: 3.32 and strut-like: 2.58), the strut-like scaffold still resulted in more bone formation compared to the gyroid scaffold for comparable number of unit cells (Supplementary Data). A further limitation relates

to the size of the parametric analysis performed. In this study, each scaffold design parameter was studied across two variations only (architecture: gyroid and strut-like; porosity: 79 % and 69%; degradation: degradable and non-degradable). Although, the number of models were sufficient to test this study's main hypothesis on whether gyroid scaffold outperform strut-like scaffolds, further studies with higher ranges of scaffold design parameters could give a better understanding on the interplay between the scaffolds design parameters and identify which scaffold design parameter has the highest impact on the bone regeneration. Finally, among the limitations of the study is using the same degradation rate in all scaffold configurations. Wu and Ding (2005) showed that increasing the pore size or decreasing the porosity lead to an increase in the rate of degradation in PLGA materials. However, since the material used here is PCL, which has a very slow degrading rate, this effect does not influence the results.

In conclusion, here we used a computer model of scaffold-supported bone regeneration, that was previously able to explain bone regeneration within two different scaffold designs in two experimental setups, to predict, for the first time, the bone regeneration potential of PCL gyroid scaffolds in long bone large defects. Computer model predictions suggest slower healing dynamics and reduced bone tissue formation in gyroid compared with strut-like scaffolds. Future studies should focus on the experimental validation of these findings so that they can be used for the optimization of scaffold design to support bone regeneration in long bone large defects.

Data availability statement

The original contributions presented in the study are included in the article/Supplementary Material; further inquiries can be directed to the corresponding author.

Author contributions

MJ, PP, GD, and SC designed the study. MJ developed the computational models and collected the data. MJ and SC interpreted the data and drafted the manuscript. All authors read and revised the manuscript and approved its content.

Funding

This study was funded by the BMBF, SyMBoD project 01ZX 1910A.

Conflict of interest

The authors declare that the research was conducted in the absence of any commercial or financial relationships that could be construed as a potential conflict of interest.

Publisher's note

All claims expressed in this article are solely those of the authors and do not necessarily represent those of their affiliated organizations, or those of the publisher, the editors and the reviewers. Any product that may be evaluated in this article, or claim that may be made by its manufacturer, is not guaranteed or endorsed by the publisher.

Supplementary material

The Supplementary Material for this article can be found online at: https://www.frontiersin.org/articles/10.3389/fbioe.2022.995266/full#supplementary-material

References

Abueidda, D. W., Elhebeary, M., Shiang, C. S., Andrew)Pang, S., Abu Al-Rub, R. K., et al. (2019). Mechanical properties of 3D printed polymeric Gyroid cellular structures: Experimental and finite element study. *Mat. Des.* 165, 107597. doi:10.1016/j.matdes.2019.107597

Adachi, T., Osako, Y., Tanaka, M., Hojo, M., and Hollister, S. J. (2006). Framework for optimal design of porous scaffold microstructure by computational simulation of bone regeneration. *Biomaterials* 27, 3964–3972. doi:10.1016/j.biomaterials.2006.02.039

Ali, D., and Sen, S. (2017). Finite element analysis of mechanical behavior, permeability and fluid induced wall shear stress of high porosity scaffolds with gyroid and lattice-based architectures. *J. Mech. Behav. Biomed. Mat.* 75, 262–270. doi:10.1016/j.jmbbm.2017.07.035

Alizadeh-Osgouei, M., Li, Y., Vahid, A., Ataee, A., and Wen, C. (2021). High strength porous PLA gyroid scaffolds manufactured via fused deposition modeling for tissue-engineering applications. *Smart Mat. Med.* 2, 15–25. doi:10.1016/j.smaim.2020.10.003

Ataee, A., Li, Y., and Wen, C. (2019). A comparative study on the nanoindentation behavior, wear resistance and *in vitro* biocompatibility of SLM manufactured CP–Ti and EBM manufactured Ti64 gyroid scaffolds. *Acta Biomater.* 97, 587–596. doi:10.1016/j.actbio.2019.08.008

Baino, F., and Fiume, E. (2019). Elastic mechanical properties of 45S5-based bioactive glass-ceramic scaffolds. *Mater. (Basel)* 12, 3244. doi:10.3390/ma12193244

Borgiani, E., Duda, G. N., Willie, B. M., and Checa, S. (2021). Bone morphogenetic protein 2-induced cellular chemotaxis drives tissue patterning during critical-sized bone defect healing: An *in silico* study. *Biomech. Model. Mechanobiol.* 20, 1627–1644. doi:10.1007/s10237-021-01466-0

Borgiani, E., Figge, C., Kruck, B., Willie, B. M., Duda, G. N., and Checa, S. (2019). Age-related changes in the mechanical regulation of bone healing are explained by altered cellular mechanoresponse. *J. Bone Min. Res.* 34, 1923–1937. doi:10.1002/jbmr.3801

Byrne, D. P., Lacroix, D., and Prendergast, P. J. (2011). Simulation of fracture healing in the tibia: Mechanoregulation of cell activity using a lattice modeling approach. *J. Orthop. Res.* 29, 1496–1503. doi:10.1002/jor.21362

Caiazzo, F., Alfieri, V., and Bujazha, B. D. (2021). Additive manufacturing of biomorphic scaffolds for bone tissue engineering. *Int. J. Adv. Manuf. Technol.* 113, 2909–2923. doi:10.1007/s00170-021-06773-5

Carter, D. R., Blenman, P. R., and Beaupre, G. S. (1988). Correlations between mechanical stress history and tissue differentiation in initial fracture healing. *J. Orthop. Res.* 6 (5), 736–748. doi:10.1002/jor.1100060517

Castro, A. P. G., Pires, T., Santos, J. E., Gouveia, B. P., and Fernandes, P. R. (2019a). Permeability versus design in TPMS scaffolds. *Mater. (Basel)* 12, 1313. doi:10.3390/ma12081313

Castro, A. P. G., Ruben, R. B., Gonçalves, S. B., Pinheiro, J., Guedes, J. M., and Fernandes, P. R. (2019b). Numerical and experimental evaluation of TPMS Gyroid scaffolds for bone tissue engineering. *Comput. Methods Biomech. Biomed. Engin.* 22, 567–573. doi:10.1080/10255842.2019.1569638

Checa, S., Prendergast, P. J., and Duda, G. N. (2011). Inter-species investigation of the mechano-regulation of bone healing: Comparison of secondary bone healing in sheep and rat. *J. Biomech.* 44, 1237–1245. doi:10.1016/j.jbiomech.2011.02.074

Chen, W., Yang, J., Kong, H., Helou, M., Zhang, D., Zhao, J., et al. (2021). Fatigue behaviour and biocompatibility of additively manufactured bioactive tantalum graded lattice structures for load-bearing orthopaedic applications. *Mater. Sci. Eng. C* 130, 112461. doi:10.1016/j.msec.2021.112461

Claes, L. E., and Heigele, C. A. (1999). Magnitudes of local stress and strain along bony surfaces predict the course and type of fracture healing. *J. Biomech.* 32 (3), 255–266. doi:10.1016/S0021-9290(98)00153-5

Cobos, J. A., Lindsey, R. W., and Gugala, Z. (2000). The cylindrical titanium mesh cage for treatment of a long bone segmental defect: Description of a new technique and report of two cases. *J. Orthop. Trauma* 14, 54–59. doi:10.1097/00005131-200001000-00011

Cui, C., Deng, Y., and Han, L. (2020). Bicontinuous cubic phases in biological and artificial self-assembled systems. *Sci. China Mat.* 63, 686–702. doi:10.1007/s40843-019-1261-1

Dalaq, A. S., Abueidda, D. W., Abu Al-Rub, R. K., and Jasiuk, I. M. (2016). Finite element prediction of effective elastic properties of interpenetrating phase composites with architectured 3D sheet reinforcements. *Int. J. Solids Struct.* 83, 169–182. doi:10.1016/j.ijsolstr.2016.01.011

Diez-Escudero, A., Harlin, H., Isaksson, P., and Persson, C. (2020). Porous polylactic acid scaffolds for bone regeneration: A study of additively manufactured triply periodic minimal surfaces and their osteogenic potential. *J. Tissue Eng.* 11, 204173142095654. doi:10.1177/2041731420956541

Dong, Z., and Zhao, X. (2021). Application of TPMS structure in bone regeneration. *Eng. Regen.* 2, 154–162. doi:10.1016/j.engreg.2021.09.004

du Plessis, A., Yadroitsava, I., Yadroitsev, I., le Roux, S. G., and Blaine, D. C. (2018). Numerical comparison of lattice unit cell designs for medical implants by additive manufacturing. *Virtual Phys. Prototyp.* 13, 266–281. doi:10.1080/17452759.2018.1491713

Dwivedi, R., Kumar, S., Pandey, R., Mahajan, A., Nandana, D., Katti, D. S., et al. (2020). Polycaprolactone as biomaterial for bone scaffolds: Review of literature. *J. Oral Biol. Craniofac. Res.* 10, 381–388. doi:10.1016/j.jobcr.2019.10.003

Finkemeier, C. G. (2002). Bone-grafting and bone-graft substitutes. *J. Bone Jt. Surgery-American Volume* 84, 454–464. doi:10.2106/00004623-200203000-00020

Geris, L., van Oosterwyck, H., vander Sloten, J., Duyck, J., and Naert, I. (2003). Assessment of mechanobiological models for the numerical simulation of tissue differentiation around immediately loaded implants. *Comput. Methods Biomech. Biomed. Engin.* 6, 277–288. doi:10.1080/1025584031000163441 2

Glatt, V., Evans, C. H., and Tetsworth, K. (2017). A concert between biology and biomechanics: The influence of the mechanical environment on bone healing. *Front. Physiol.* 7, 678. doi:10.3389/fphys.2016.00678

Große-Brauckmann, K., and Wohlgemuth, M. (1996). The gyroid is embedded and has constant mean curvature companions. *Calc. Var. Partial Differ. Equ.* 4, 499–523. doi:10.1007/BF01261761

Huang, J., Xia, X., Zou, Q., Ma, J., Jin, S., Li, J., et al. (2019). The long-term behaviors and differences in bone reconstruction of three polymer-based scaffolds with different degradability. *J. Mat. Chem. B* 7, 7690–7703. doi:10.1039/c9tb02072a

Huiskes, R., Van Driel, W. D., Prendergast, P. J., and Søballe, K. (1997). A biomechanical regulatory model for periprosthetic fibrous-tissue differentiation. *J. Mat. Sci. Mat. Med.* 8, 785–788. doi:10.1023/A:1018520914512

Isaksson, H., Wilson, W., van Donkelaar, C. C., Huiskes, R., and Ito, K. (2006b). Comparison of biophysical stimuli for mechano-regulation of tissue differentiation during fracture healing. *J. Biomech.* 39, 1507–1516. doi:10.1016/J.JBIOMECH.2005.01.037

Jean-Quartier, C., Jeanquartier, F., Jurisica, I., and Holzinger, A. (2018). *In silico* cancer research towards 3R. *BMC Cancer* 18, 408. doi:10.1186/s12885-018-4302-0

Jian, Y. T., Yang, Y., Tian, T., Stanford, C., Zhang, X. P., and Zhao, K. (2015). Effect of pore size and porosity on the biomechanical properties and cytocompatibility of porous NiTi alloys. *PLoS One* 10, e0128138. doi:10.1371/journal.pone.0128138

Jin, Y., Kong, H., Zhou, X., Li, G., and Du, J. (2020). Design and characterization of sheet-based gyroid porous structures with bioinspired functional gradients. *Mater. (Basel)* 13, 3844. doi:10.3390/ma13173844

Jinnai, H., Watashiba, H., Kajihara, T., Nishikawa, Y., Takahashi, M., and Ito, M. (2002). Surface curvatures of trabecular bone microarchitecture. *Bone* 30, 191–194. doi:10.1016/S8756-3282(01)00672-X

Karcher, H. (1989). The triply periodic minimal surfaces of Alan Schoen and their constant mean curvature companions. *Manuscr. Math.* 64, 291–357. doi:10.1007/BF01165824

Kelly, C. N., Lin, A. S., Leguineche, K. E., Shekhar, S., Walsh, W. R., Guldberg, R. E., et al. (2021). Functional repair of critically sized femoral defects treated with bioinspired titanium gyroid-sheet scaffolds. *J. Mech. Behav. Biomed. Mat.* 116, 104380. doi:10.1016/j.jmbbm.2021.104380

Lacroix, D., and Prendergast, P. J. (2002). A mechano-regulation model for tissue differentiation during fracture healing: Analysis of gap size and loading. *J. Biomech.* 35, 1163–1171. doi:10.1016/S0021-9290(02)00086-6

Lee, D. J., Kwon, J., Kim, Y., Wang, X., Wu, T. J., Lee, Y. T., et al. (2019). Effect of pore size in bone regeneration using polydopamine-laced hydroxyapatite collagen calcium silicate scaffolds fabricated by 3D mould printing technology. *Orthod. Craniofac. Res.* 22, 127–133. doi:10.1111/ocr.12261

Lim, J., Lee, J., Yun, H. S., Shin, H. I., and Park, E. K. (2013). Comparison of bone regeneration rate in flat and long bone defects: Calvarial and tibial bone. *Tissue Eng. Regen. Med.* 10, 336–340. doi:10.1007/S13770-013-1094-9

Liu, F., Ran, Q., Zhao, M., Zhang, T., Zhang, D. Z., and Su, Z. (2020). Additively manufactured continuous cell-size gradient porous scaffolds: Pore characteristics, mechanical properties and biological responses *in vitro*. *Mater. (Basel)* 13, 2589. doi:10.3390/ma13112589

Lovati, A. B., Lopa, S., Recordati, C., Talò, G., Turrisi, C., Bottagisio, M., et al. (2016). *In vivo* bone formation within engineered hydroxyapatite scaffolds in a sheep model. *Calcif. Tissue Int.* 99, 209–223. doi:10.1007/S00223-016-0140-8

Lu, Y., Cheng, L. L., Yang, Z., Li, J., and Zhu, H. (2020). Relationship between the morphological, mechanical and permeability properties of porous bone scaffolds and the underlying microstructure. *PLoS One* 15, e0238471. doi:10.1371/journal.pone.0238471

Ma, S., Tang, Q., Feng, Q., Song, J., Han, X., and Guo, F. (2019). Mechanical behaviours and mass transport properties of bone-mimicking scaffolds consisted of gyroid structures manufactured using selective laser melting. *J. Mech. Behav. Biomed. Mat.* 93, 158–169. doi:10.1016/j.jmbbm.2019.01.023

Melchels, F. P. W., Barradas, A. M. C., Van Blitterswijk, C. A., De Boer, J., Feijen, J., and Grijpma, D. W. (2010a). Effects of the architecture of tissue engineering scaffolds on cell seeding and culturing. *Acta Biomater.* 6, 4208–4217. doi:10.1016/j.actbio.2010.06.012

Melchels, F. P. W., Bertoldi, K., Gabbrielli, R., Velders, A. H., Feijen, J., and Grijpma, D. W. (2010b). Mathematically defined tissue engineering scaffold architectures prepared by stereolithography. *Biomaterials* 31, 6909–6916. doi:10.1016/j.biomaterials.2010.05.068

Michielsen, K., and Stavenga, D. G. (2008). Gyroid cuticular structures in butterfly wing scales: Biological photonic crystals. *J. R. Soc. Interface* 5, 85–94. doi:10.1098/rsif.2007.1065

Mitsak, A. G., Kemppainen, J. M., Harris, M. T., and Hollister, S. J. (2011). Effect of polycaprolactone scaffold permeability on bone regeneration *in vivo*. *Tissue Eng. Part A* 17, 1831–1839. doi:10.1089/ten.tea.2010.0560

Noroozi, R., Shamekhi, M. A., Mahmoudi, R., Zolfagharian, A., Asgari, F., Mousavizadeh, A., et al. (2022). *In vitro* static and dynamic cell culture study of novel bone scaffolds based on 3D-printed PLA and cell-laden alginate hydrogel. *Biomed. Mat.* 17, 045024. doi:10.1088/1748-605X/AC7308

Perier-Metz, C., Duda, G. N., and Checa, S. (2020). Mechano-biological computer model of scaffold-supported bone regeneration: Effect of bone graft and scaffold structure on large bone defect tissue patterning. *Front. Bioeng. Biotechnol.* 8, 585799. doi:10.3389/fbioe.2020.585799

Perier-Metz, C., Cipitria, A., Hutmacher, D. W., Duda, G. N., and Checa, S. (2022). An *in silico* model predicts the impact of scaffold design in large bone defect regeneration. *Acta Biomater.* 145, 329–341. doi:10.1016/J.ACTBIO.2022.04.008

Prendergast, P. J., Huiskes, R., and Soballe, K. (1997). ESB Research Award 1996. Biophysical stimuli on cells during tissue differentiation at implant interfaces. *J. Biomech.* 30 (06), 539–548. doi:10.1016/S0021-9290(96)00140-6

Pitt, C. G., Chasalow, F. I., Hibionada, Y. M., Klimas, D. M., and Schindler, A. (1981). Aliphatic polyesters. I. The degradation of poly(ϵ-caprolactone) *in vivo*. *J. Appl. Polym. Sci.* 26, 3779–3787. doi:10.1002/app.1981.070261124

Pitt, C. G., and Zhong-wei, G. (1987). Modification of the rates of chain cleavage of poly(ϵ-caprolactone) and related polyesters in the solid state. *J. Control. Release* 4, 283–292. doi:10.1016/0168-3659(87)90020-4

Pobloth, A. M., Checa, S., Razi, H., Petersen, A., Weaver, J. C., Chmidt-Bleek, K., et al. (2018). Mechanobiologically optimized 3D titanium-mesh scaffolds enhance bone regeneration in critical segmental defects in sheep. *Sci. Transl. Med.* 10, eaam8828. doi:10.1126/SCITRANSLMED.AAM8828

Postigo, S., Schmidt, H., Rohlmann, A., Putzier, M., Simón, A., Duda, G., et al. (2014). Investigation of different cage designs and mechano-regulation algorithms in the lumbar interbody fusion process - a finite element analysis. *J. Biomech.* 47, 1514–1519. doi:10.1016/J.JBIOMECH.2014.02.005

Rajagopalan, S., and Robb, R. A. (2006). Schwarz meets Schwann: Design and fabrication of biomorphic and durataxic tissue engineering scaffolds. *Med. Image Anal.* 10, 693–712. doi:10.1016/j.media.2006.06.001

Reichert, J. C., Cipitria, A., Epari, D. R., Saifzadeh, S., Krishnakanth, P., Berner, A., et al. (2012). A tissue engineering solution for segmental defect regeneration in load-bearing long bones. *Sci. Transl. Med.* 4, 141ra93. doi:10.1126/SCITRANSLMED.3003720

Repp, F., Vetter, A., Duda, G. N., and Weinkamer, R. (2015). The connection between cellular mechanoregulation and tissue patterns during bone healing. *Med. Biol. Eng. Comput.* 53, 829–842. doi:10.1007/s11517-015-1285-8

Reznikov, N., Boughton, O. R., Ghouse, S., Weston, A. E., Collinson, L., Blunn, G. W., et al. (2019). Individual response variations in scaffold-guided bone regeneration are determined by independent strain- and injury-induced mechanisms. *Biomaterials* 194, 183–194. doi:10.1016/J.BIOMATERIALS.2018.11.026

Roddy, E., DeBaun, M. R., Daoud-Gray, A., Yang, Y. P., and Gardner, M. J. (2018). Treatment of critical-sized bone defects: Clinical and tissue engineering perspectives. *Eur. J. Orthop. Surg. Traumatol.* 28, 351–362. doi:10.1007/S00590-017-2063-0

Santos, J., Pires, T., Gouveia, B. P., Castro, A. P. G., and Fernandes, P. R. (2020). On the permeability of TPMS scaffolds. *J. Mech. Behav. Biomed. Mat.* 110, 103932. doi:10.1016/j.jmbbm.2020.103932

Schlichting, K., Schell, H., Kleemann, R. U., Schill, A., Weiler, A., Duda, G. N., et al. (2008). Influence of scaffold stiffness on subchondral bone and subsequent cartilage regeneration in an ovine model of osteochondral defect healing. *Am. J. Sports Med.* 36, 2379–2391. doi:10.1177/0363546508322899

Schwarz, C., Wulsten, D., Ellinghaus, A., Lienau, J., Willie, B. M., and Duda, G. N. (2013). Mechanical load modulates the stimulatory effect of BMP2 in a rat nonunion model. *Tissue Eng. Part A* 19, 247–254. doi:10.1089/ten.tea.2012.0265

Shah, F. A., Omar, O., Suska, F., Snis, A., Matic, A., Emanuelsson, L., et al. (2016). Long-term osseointegration of 3D printed CoCr constructs with an interconnected open-pore architecture prepared by electron beam melting. *Acta Biomater.* 36, 296–309. doi:10.1016/J.ACTBIO.2016.03.033

Spece, H., Yu, T., Law, A. W., Marcolongo, M., and Kurtz, S. M. (2020). 3D printed porous PEEK created via fused filament fabrication for osteoconductive orthopaedic surfaces. *J. Mech. Behav. Biomed. Mat.* 109, 103850. doi:10.1016/j.jmbbm.2020.103850

Tsai, M. C., Hung, K. C., Hung, S. C., and Hsu, S. H. (2015). Evaluation of biodegradable elastic scaffolds made of anionic polyurethane for cartilage tissue engineering. *Colloids Surfaces B Biointerfaces* 125, 34–44. doi:10.1016/j.colsurfb.2014.11.003

Van Bael, S., Chai, Y. C., Truscello, S., Moesen, M., Kerckhofs, G., Van Oosterwyck, H., et al. (2012). The effect of pore geometry on the *in vitro* biological behavior of human periosteum-derived cells seeded on selective laser-melted Ti6Al4V bone scaffolds. *Acta Biomater.* 8, 2824–2834. doi:10.1016/j.actbio.2012.04.001

Van hede, D., Liang, B., Anania, S., Barzegari, M., Verlée, B., Nolens, G., et al. (2022). 3D-Printed synthetic hydroxyapatite scaffold with in silico optimized macrostructure enhances bone formation *in vivo*. *Adv. Funct. Mat.* 32, 2105002. doi:10.1002/adfm.202105002

Vetter, A., Witt, F., Sander, O., Duda, G. N., and Weinkamer, R. (2012). The spatio-temporal arrangement of different tissues during bone healing as a result of simple mechanobiological rules. *Biomech. Model. Mechanobiol.* 11, 147–160. doi:10.1007/s10237-011-0299-x

Viceconti, M., and Dall'Ara, E. (2019). From bed to bench: How *in silico* medicine can help ageing research. *Mech. Ageing Dev.* 177, 103–108. doi:10.1016/j.mad.2018.07.001

Vijayavenkataraman, S., Zhang, L., Zhang, S., Fuh, J. Y. H., and Lu, W. F. (2018). Triply periodic minimal surfaces sheet scaffolds for tissue engineering applications: An optimization approach toward biomimetic scaffold design. *ACS Appl. Bio Mat.* 1, 259–269. doi:10.1021/acsabm.8b00052

Wehner, T., Wolfram, U., Henzler, T., Niemeyer, F., Claes, L., and Simon, U. (2010). Internal forces and moments in the femur of the rat during gait. *J. Biomech.* 43, 2473–2479. doi:10.1016/j.jbiomech.2010.05.028

Wei, S., Ma, J. X., Xu, L., Gu, X. S., and Ma, X. L. (2020). Biodegradable materials for bone defect repair. *Mil. Med. Res.* 7, 54. doi:10.1186/s40779-020-00280-6

Wu, L., and Ding, J. (2005). Effects of porosity and pore size on *in vitro* degradation of three-dimensional porous poly(D, L-lactide-co-glycolide) scaffolds for tissue engineering. *J. Biomed. Mat. Res. A* 75, 767–777. doi:10.1002/JBM.A.30487

Yánez, A., Cuadrado, A., Martel, O., Afonso, H., and Monopoli, D. (2018). Gyroid porous titanium structures: A versatile solution to be used as scaffolds in bone defect reconstruction. *Mat. Des.* 140, 21–29. doi:10.1016/j.matdes.2017.11.050

Yánez, A., Fiorucci, M. P., Cuadrado, A., Martel, O., and Monopoli, D. (2020). Surface roughness effects on the fatigue behaviour of gyroid cellular structures obtained by additive manufacturing. *Int. J. Fatigue* 138, 105702. doi:10.1016/j.ijfatigue.2020.105702

Yang, E., Leary, M., Lozanovski, B., Downing, D., Mazur, M., Sarker, A., et al. (2019). Effect of geometry on the mechanical properties of Ti-6Al-4V gyroid structures fabricated via slm: A numerical study. *Mat. Des.* 184, 108165. doi:10.1016/j.matdes.2019.108165

Yoo, D. J. (2014). Advanced porous scaffold design using multi-void triply periodic minimal surface models with high surface area to volume ratios. *Int. J. Precis. Eng. Manuf.* 15, 1657–1666. doi:10.1007/s12541-014-0516-5

frontiers | Frontiers in Bioengineering and Biotechnology

TYPE Original Research
PUBLISHED 10 January 2023
DOI 10.3389/fbioe.2022.1085062

OPEN ACCESS

EDITED BY
Massimiliano Zingales,
University of Palermo, Italy

REVIEWED BY
Cevat Erisken,
Nazarbayev University, Kazakhstan
Matteo Berni,
Rizzoli Orthopedic Institute (IRCCS), Italy

*CORRESPONDENCE
Yansong Tan,
tomorrow2012@163.com
Chunqiu Zhang,
zhang_chunqiu@126.com

SPECIALTY SECTION
This article was submitted to Biomechanics, a section of the journal Frontiers in Bioengineering and Biotechnology

RECEIVED 31 October 2022
ACCEPTED 28 December 2022
PUBLISHED 10 January 2023

CITATION
Gao L, Liu G, Tan Y, Li R, Zhang C, Gao H and Zhao B (2023), Creep-recovery behaviors of articular cartilage under uniaxial and biaxial tensile loadings. *Front. Bioeng. Biotechnol.* 10:1085062. doi: 10.3389/fbioe.2022.1085062

Creep-recovery behaviors of articular cartilage under uniaxial and biaxial tensile loadings

Lilan Gao[1,2], Gang Liu[1,2], Yansong Tan[1,2]*, Ruixin Li[3], Chunqiu Zhang[1,2]*, Hong Gao[4] and Bingjie Zhao[1,2]

[1]Tianjin Key Laboratory for Advanced Mechatronic System Design and Intelligent Control, School of Mechanical Engineering, Tianjin University of Technology, Tianjin, China, [2]National Demonstration Center for Experimental Mechanical and Electrical Engineering Education, Tianjin University of Technology, Tianjin, China, [3]Tianjin Stomatological Hospital, The Affiliated Stomatological Hospital of Nankai University, Tianjin Key Laboratory of Oral and Maxillofacial Function Reconstruction, Tianjin, China, [4]School of Chemical Engineering and Technology, Tianjin University, Tianjin, China

Creep deformation in cartilage can be observed under physiological loads in daily activities such as standing, single-leg lunge, the stance phase of gait. If not fully recovered in time, it may induce irreversible damage in cartilage and further lead to early osteoarthritis. In this study, 36 cruciform-shape samples in total from 18 bulls were employed to conduct the uniaxial and biaxial creep-recovery tests by using a biaxial cyclic testing system. Effects of stress level (σ = .5, 1.0, 1.5 MPa) and biaxial stress ratio (B = 0, .3, .5, 1.0) on creep-recovery behaviors of cartilage were characterized. And then, a viscoelastic constitutive model was employed to predict its creep-recovery behaviors. The results showed that the creep strain and its three components, namely instantaneous elastic strain, delayed elastic strain and viscous flow strain, increase with the increasing stress level or with the decreasing biaxial stress ratio. Compared with uniaxial creep-recovery, biaxial creep-recovery exhibits a smaller creep strain, a faster recovery rate of creep strain and a smaller residual strain. Besides, the built viscoelastic model can be used to describe the uniaxial creep-recovery behaviors of cartilage as a good correlation between the fitted results and test results is achieved. The findings are expected to provide new insights into understanding normal joint function and cartilage pathology.

KEYWORDS

articular cartilage, biaxial loading, stress ratio, creep-recovery, strain ratio

Highlights

- Creep-recovery behaviors are explored at different stress levels and biaxial stress ratios.
- Creep strain and its components increase with stress level.
- A biaxial stress ratio of 1 imposes the smallest creep strain.
- Increasing biaxial stress ratio accelerates the recovery of creep strain and decreases the residual strain.
- The higher the biaxial stress ratio, the smaller the viscous flow strain and the delayed elastic strain.

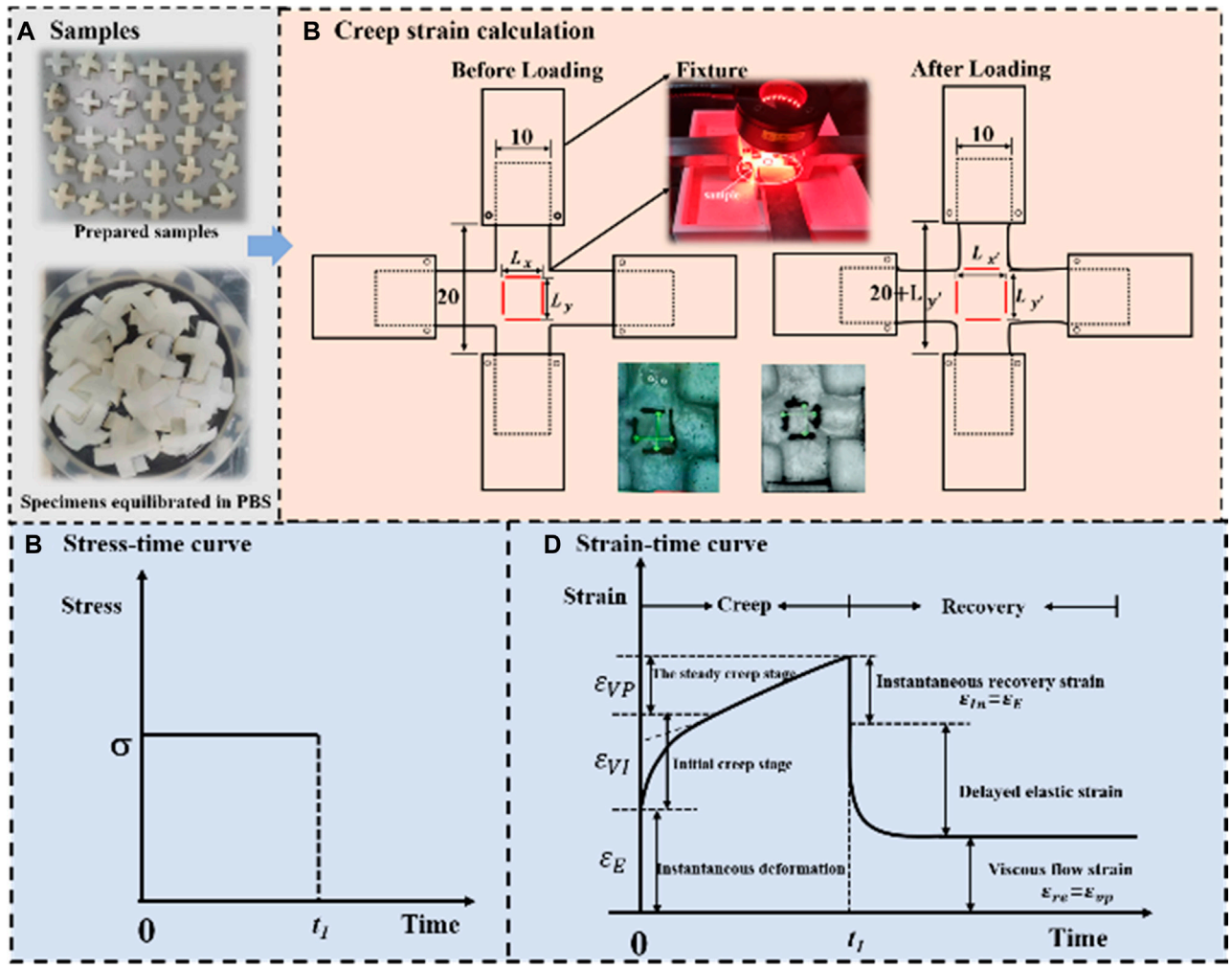

GRAPHICAL ABSTRACT

1 Introduction

Articular cartilage has the functions to absorb shocks, transmit loads and sustain complex mechanical loading histories, thus maintaining dynamic mechanical equilibrium of knee joint in daily activities. As a kind of fluid saturated porous material, articular cartilage exhibits viscoelastic responses under mechanical loads. And creep is observed in cartilage when the mechanical load is held constant during standing, single-leg lunge (Hosseini et al., 2010; Choi et al., 2016; Qiu et al., 2016), the stance phase of gait (Liu et al., 2010; Li et al., 2014) and so on. Creep deformation under physiological loads may serve as a functional indicator for cartilage healthy. The majority of creep deformation in cartilage can recover timely. However, long term overloading may cause irreversible deformation, further induce damage in cartilage and lead to early osteoarthritis (Roos et al., 1998; Felson, 2013; Martel-Pelletier et al., 2016; Georgiev and Angelov, 2019; Peters et al., 2022). Studying the creep and creep-recovery behaviors of articular cartilage are helpful for understanding the normal joint function and cartilage pathology.

In vivo creep tests were usually conducted by applying 50%–150% body weight on the joint for 300–900 s (Herberhold et al., 1998; Herberhold et al., 1999; Hosseini et al., 2010; Choi et al., 2016; Uzuner et al., 2020), and the creep deformations of cartilage were measured *in vivo* by using imaging techniques like computed tomography (CT), magnetic resonance (MR), dual fluoroscopic imaging (DF). Herberhold et al. found that the creep deformation had high inter-individual variability (Herberhold et al., 1998; 1999). Hosseini et al. found the cartilage deformation of human tibiofemoral increases sharply in the first 20 s and almost held constant beyond 50 s when a constant full body weight was quickly applied and maintained for 300 s (Hosseini et al., 2010). Choi et al. studied the time-dependent creep behavior of tibial cartilage by applying a load of 75% body weight on limb and they reported that the creep deformation increased rapidly over the first minute and kept stable after 5 min (Choi et al., 2016). Uzuner et al. reported a substantial increase in cartilage deformation when joint loading increased from nil to 75% body weight and a continued small increase over time when the joint loading was held constant (Uzuner et al., 2020). *In vivo* experimental data help to understand the deformation characters of cartilage under physiological loads. However, technical limitations impede the accurate measurement of creep recovery in the physiological range and it non-etheless has significant difficulty to quantitatively analyze the creep-recovery deformation law of cartilage.

To cover the shortage of *in vivo* tests, *in vitro* creep tests are widely used to investigate the creep and creep-recovery behaviors

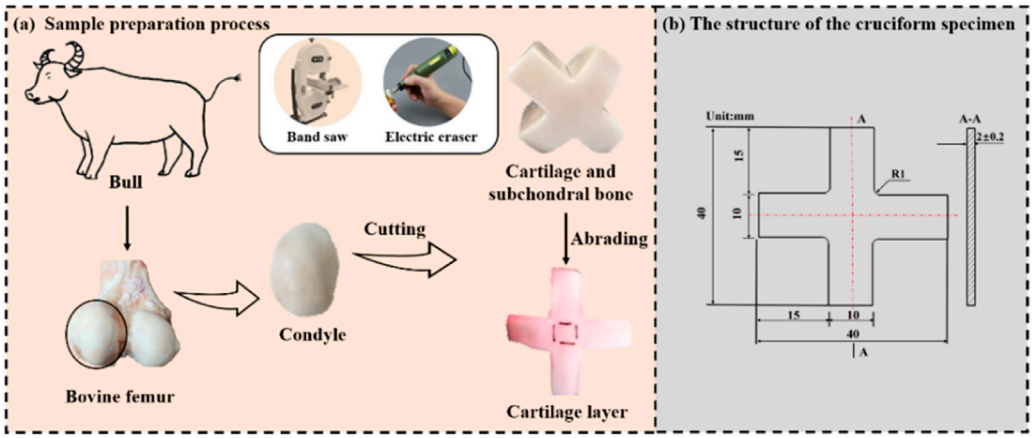

FIGURE 1
(A) Sample preparation process; **(B)** the structure of the cruciform specimen.

of cartilage. Athanasiou et al. and Stolberg et al. employed the indentation test system to characterize the creep-recovery behavior of cartilage and they found that the initial creep rate is larger than the initial recovery rate and more than 95% of the creep deformation could recovered within 90 min (Athanasiou et al., 1991; Stolberg-Stolberg et al., 2018). Boettcher et al. found that the cartilage deformation increased with the increasing stress. (Boettcher et al., 2016). Cutclife and DeFrate validated the use of the recovery response for mechanical characterization of cartilage in a controlled, *ex vivo* environment (Cutcliffe and DeFrate, 2020). Reuter and Hurschler used a biphasic 3D-FE-based method to determine the biomechanical properties of equine articular cartilage (Reuter and Hurschler., 2021). In our previous study, the depth-dependent creep strain of cartilage under uniaxial compressive load was investigated by an optimized digital image correlation (DIC) technique (Si et al., 2022). And the creep deformation could accelerate the fatigue damage of cartilage in knee joint (Gao et al., 2019). It should be mentioned that these studies on the creep-recovery behaviors of articular cartilage were probed under uniaxial loading.

The cartilage with freely squeezing and stretching *in vivo* is subjected to biaxial or even multiaxial loads, and however literature provides limited data on these. Thus, it is of great significance to study the biaxial or multiaxial creep-recovery behaviors of cartilage. The goal of this study is to investigate the creep-recovery behaviors of articular cartilage under biaxial tensile load. The hypothesize is that changing the stress state from uniaxial loading to biaxial loading has a significant effect on creep deformation of cartilage. To verify the hypothesize, both the uniaxial and biaxial creep-recovery experiments were conducted by using a biaxial cyclic testing system. Effects of stress level and biaxial stress ratio on cartilage creep-recovery were characterized. Creep strain components were analyzed and compared at different loading conditions. Additionally, the creep-recovery behaviors of cartilage were predicted by mathematical models. This study is original because it provides the first insight into the effect of biaxial constraint on tensile creep behavior of cartilage. The results could help to explore intrinsic mechanical properties of articular cartilage and to prevent cartilage damage.

2 Materials and methods

2.1 Sample preparation

In total, 36 cruciform-shape samples from 18 bulls (around 8 months) were prepared for mechanical tests. The cruciform-shape samples were selected as test samples since they were widely used in biaxial tests to measure in plane mechanical properties of anisotropic material (Leotoing et al., 2013; Lamkanfi et al., 2015; Chen et al., 2022) and the sample preparation process in this study is similar to literature (Kamalanathan and Broom, 1993). As shown in Figure 1A , firstly, the cartilage with subchondral bone was harvested from the medial and lateral femoral trochleae of each femur. Secondly, the cruciform shape was marked on the cartilage with subchondral bone. Thirdly, the cartilage with subchondral bone was cut into the cruciform shape by a band saw. Finally, the subchondral bone was removed from cartilage by cutting with the band saw and abrading with an electric eraser (Si et al., 2022). Thus, the cruciform-shape cartilage sample with the thickness of 2.00 mm ± .2 mm was obtained. Figure 1B shows the specific structural dimensions of the cruciform specimen. It should be mentioned that since the curvature structure of cartilage induced by the orientation of collagen fibrils may affect the results, all the samples were cut from the same position of the femur. The pre-prepared samples were wrapped in gauze moistened with phosphate buffered saline and placed in a refrigerator at −20°C to preserve the collagen fibers intact of cartilage samples. Prior to tests, the samples were defrosted by being immersed in phosphate Buffered Saline (PBS, pH 7.4) for 12 h at room temperature.

2.2 Experimental description

Three kinds of mechanical tests, namely the uniaxial tensile tests, the uniaxial creep recovery tests and the biaxial creep recovery tests were conducted on the biaxial dynamic mechanical testing system (IPBF-300, CARE Measurement & Control Co., Ltd., China). For uniaxial tensile and uniaxial creep-recovery tests, only one side of the

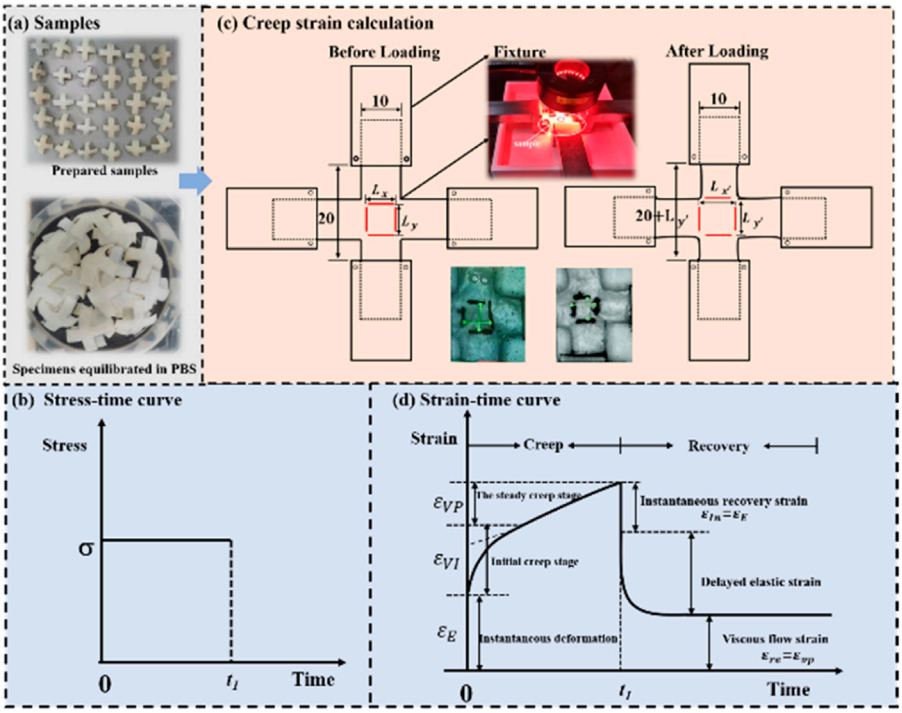

FIGURE 2
(A) Samples; **(B)** stress-time curve; **(C)** creep strain calculation; **(D)** stress-time curve.

specimen was loaded, leaving the other side of the specimen freely shrinking; for biaxial creep-recovery tests, both loading axes were loaded and recovered at the same time. The uniaxial tensile tests were performed at different strain rates of .01%/s, .1%/s and 1%/s considering the limit of physiological strain rate of articular cartilage (Huang et al., 2003; Li et al., 2003; Li and Herzog, 2004). As reported that the deformation of cartilage under physiological loads is no larger than 30% with the average deformation value lower than 20%. Thus, the rate-dependent tensile tests were stopped when the strain reached 20% (Liu et al., 2010; Wang et al., 2015).

The stress on the cartilage was .535 MPa in double leg stance and .953 MPa in single leg stance (Qiu et al., 2016). In order to approximate the *in vivo* stress state, both uniaxial and biaxial creep-recovery tests were carried out at different stress levels σ of .5, 1.0 and 1.5 MPa. In addition, for the biaxial creep-recovery tests, the different biaxial stress ratios (denoted as B, indicates the ratio of stress in one loading direction to that in the other direction) of .3, .5 and 1.0 were applied. It can be seen that the biaxial stress ratio B) of uniaxial creep tests is 0 and $B = 1$ means that the cartilage is in an equi-biaxial stress state. For all the creep-recovery test conditions mentioned above, the creep time was 2,400 s and followed by the strain recovery (at 0 MPa) time of 3,600 s to make sure that most creep deformation of cartilage has recovered (Eckstein et al., 1999; Erisken et al., 2010).

All the tests were conducted at room temperature with a preload of 0.1 N being applied before tests to keep the samples align with the axis of loading. Besides, to prevent cartilage samples from drying (Erisken et al., 2008), an air humidifier was placed near the sample and a sprayer was employed to spray the PBS solution on the surface of sample every 5 min during tests (Si et al., 2022).

2.3 Image and data analysis

During mechanical tests, the load and displacement of the central area (10 mm × 10 mm) were recorded by the mechanical sensor and the digital image correlation (DIC) system equipped by the biaxial dynamic mechanical testing machine. The tensile stress of cartilage is the load divided by the cross-sectional area. The measurement of strain is similar with that reported in literatures (Kamalanathan and Broom, 1993; Lin et al., 2017; Lin et al., 2018; Zhang et al., 2019). As shown in Figure 2C, two pairs of thin lines were drawn in the middle local mark section of cruciform sample. A optical camera was applied to measure the variation of distance between fine lines. The distances between two pairs of marked lines were recorded as length L_x and L_y (before loading) and L_x'; L_y' (after loading). Thus, the strain in x-axis and y-axis directions was calculated as:

$$\varepsilon_x = \frac{L_x' - L_x}{L_x},\ \varepsilon_y = \frac{L_y' - L_y}{L_y} \tag{1}$$

Only the strain in x-axis is recorded for uniaxial mechanical tests. For the creep-recovery tests, as shown in Figure 1D, the creep strain is divided into three components, namely instantaneous elastic strain ε_e, delayed elastic strain ε_D and viscous flow strain ε_V.

2.4 Statistical analysis

Considering the random error of experiments, three samples were repeated by the same person under the same loading condition, and test data were used in data analysis. The figures were plotted in Origin 2018 and the statistical analyses were performed using SPSS

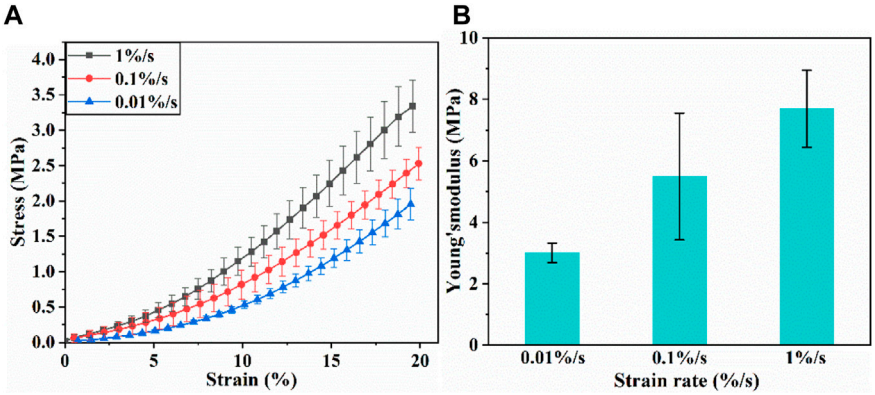

FIGURE 3
(A) Tensile stress-strain curves of articular cartilage; **(B)** Young's modulus of articular cartilage.

22.0. R-squared value was used to indicate the agreement between the test result and its prediction. A one-way analysis of variance (ANOVAs) was employed to detect significant differences between different testing conditions. The statistical results were significant if $p < .05$.

3 Theoretical model

The viscoelastic constitutive model Eq. 2 introduced by Lou and Schapery is used to describe the unconfined mechanical behavior of cartilage (Lou and Schapery, 1971). The constitutive model under uniaxial loading can be expressed as

$$\varepsilon = g_0 A(0)\sigma + g_1 \int_0^t \Delta A(\psi - \psi') \frac{dg_2\sigma}{d\tau} d\tau \tag{2}$$

Where $A(0)$ is initial components of linear viscoelastic creep compliance, and $\Delta A(\psi)$ is transient components of linear viscoelastic creep compliance. t is the loading time. g_0, g_1 and g_2 are three stress-dependent material parameters and their changes reflect the third and higher order stress-dependence of Gibbs free energy. The converted time ψ is expressed as

$$\psi = \psi(t) = \int_0^t \frac{dt'}{a_\sigma}, \quad \psi' = \psi(\tau) = \int_0^\tau \frac{dt'}{a_\sigma} \tag{3}$$

Here a_σ is the time-scale factor, which reflects the relevance of free energy, stress and temperature. In this study we assume that a_σ depends only on the applied stress.

When the step-stress input $\sigma[H(t) - H(t - t_1)]$ (Figure 2B) is applied, Eq. 2 yields the creep strain

$$\varepsilon_c = g_0 A(0)\sigma + g_1 g_2 \Delta A\left(\frac{t}{a_\sigma}\right)\sigma, \quad 0 < t < t_1 \tag{4}$$

And the recovery strain can be expressed as

$$\varepsilon_r = g_2[\Delta A(\psi) - \Delta A(\psi - \psi_1)]\sigma, \quad t > t_1 \tag{5}$$

Where in Eq. (5)

$$\psi_1 = t_1/a_\sigma, \ \psi = t_1/a_\sigma + t - t_1 \tag{6}$$

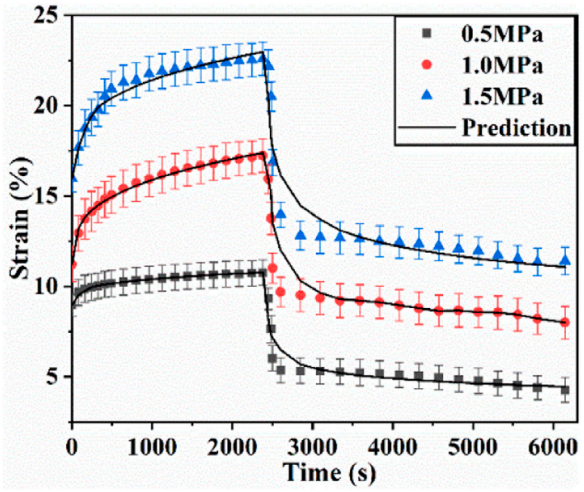

FIGURE 4
Uniaxial creep-recovery curves of cartilage at different stress levels.

The creep strain at t_1 (just before unloading) can be described as follows in Eq. (7). At the moment after unloading the initial strain in recovery phase can be described as follows in Eq. (8).

$$\varepsilon_{c1} = \varepsilon(t_1) = g_0 A(0)\sigma + g_1 g_2 \Delta A(\psi_1)\sigma \tag{7}$$

$$\varepsilon_r(t_1) = \varepsilon_1' = g_2 \Delta A(\psi_1)\sigma \tag{8}$$

Therefore, the strain jump value at $t = t_1$ can be expressed as

$$\delta\varepsilon_1 = \varepsilon_{c1} - \varepsilon_1' = g_0 A(0)\sigma + (g_1 - 1) g_2 \Delta A(\psi_1)\sigma \tag{9}$$

The transient component of linear viscoelastic creep compliance is expressed as

$$\Delta A(\psi) = C\psi^n \tag{10}$$

Where C is creep coefficient, n is creep index.

By substituting Eq. (10) into Eq. (4), we obtain the non-linear viscoelastic creep model.

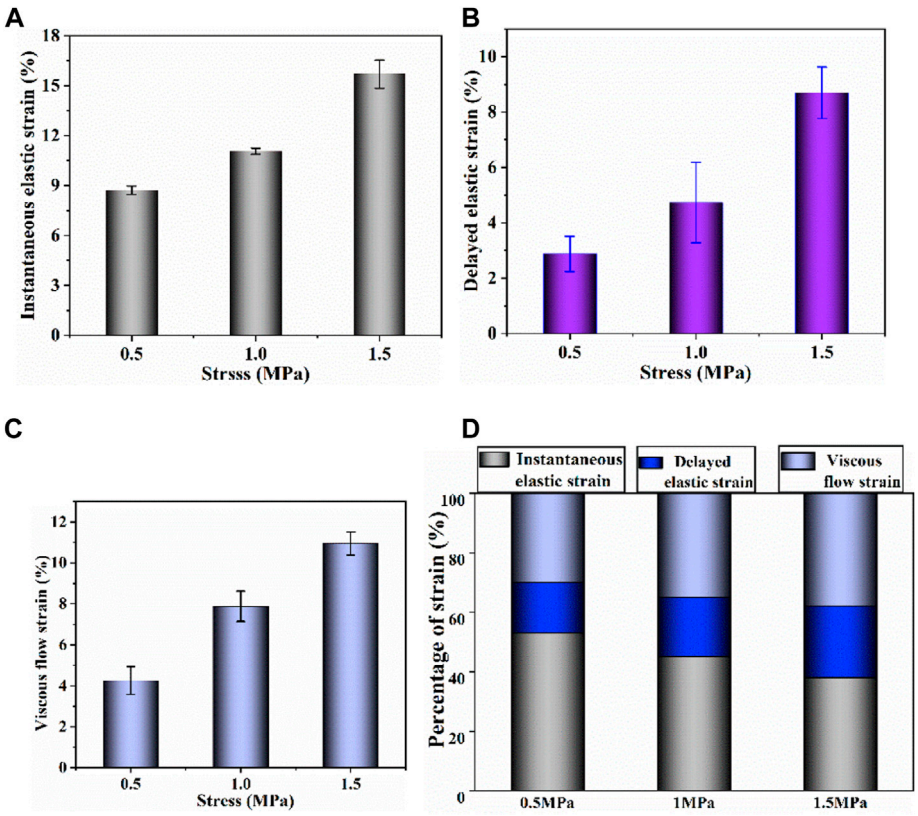

FIGURE 5
(A–C) Instantaneous elastic strain, delayed elastic strain and viscous flow strain components of uniaxial creep strain, respectively; **(D)** percentage of each strain component at different stress.

$$\varepsilon_c = g_0 A(0)\sigma + C\frac{g_1 g_2}{a_\sigma^n} t^n \sigma \tag{11}$$

By substituting Eq. (10) into Eq. (5), we obtain the expression of recovery strain:

$$\varepsilon_r = \frac{\Delta\varepsilon_c}{g_1}\left[(1 + a_\sigma\lambda)^n - (a_\sigma\lambda)^n\right] \tag{12}$$

Where in Eq. (12)

$$\lambda = \frac{t - t_1}{t_1} \tag{13}$$

and

$$\Delta\varepsilon_c = \varepsilon(t_1) - \varepsilon_0 = g_1 g_2 c {\psi_1}^n \sigma \tag{14}$$

It is noted that the parameters in creep model Eq. 11 and recovery model (Eqs. 12–14 were obtained by fitting the test data with the non-linear least square method in the software origin 2018. Thus, the uniaxial creep-recovery strains of cartilage can be fitted by the built model.

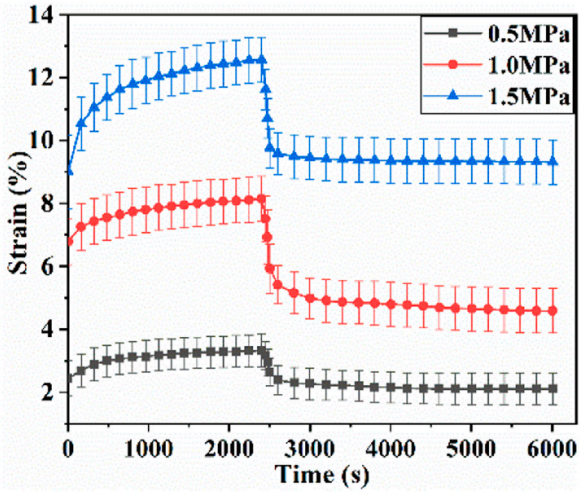

FIGURE 6
Biaxial creep-recovery curves of articular cartilage at different stress levels.

4 Results

4.1 Tensile properties of articular cartilage at different strain rates

Figure 3A shows the stress-strain curves of articular cartilage at different strain rates. The stress-strain curves are not coincident, indicating that the tensile behavior of articular cartilage is strain rate-dependent. According to literature (Korhonen et al., 2002), and considering the error in data at the very beginning of the

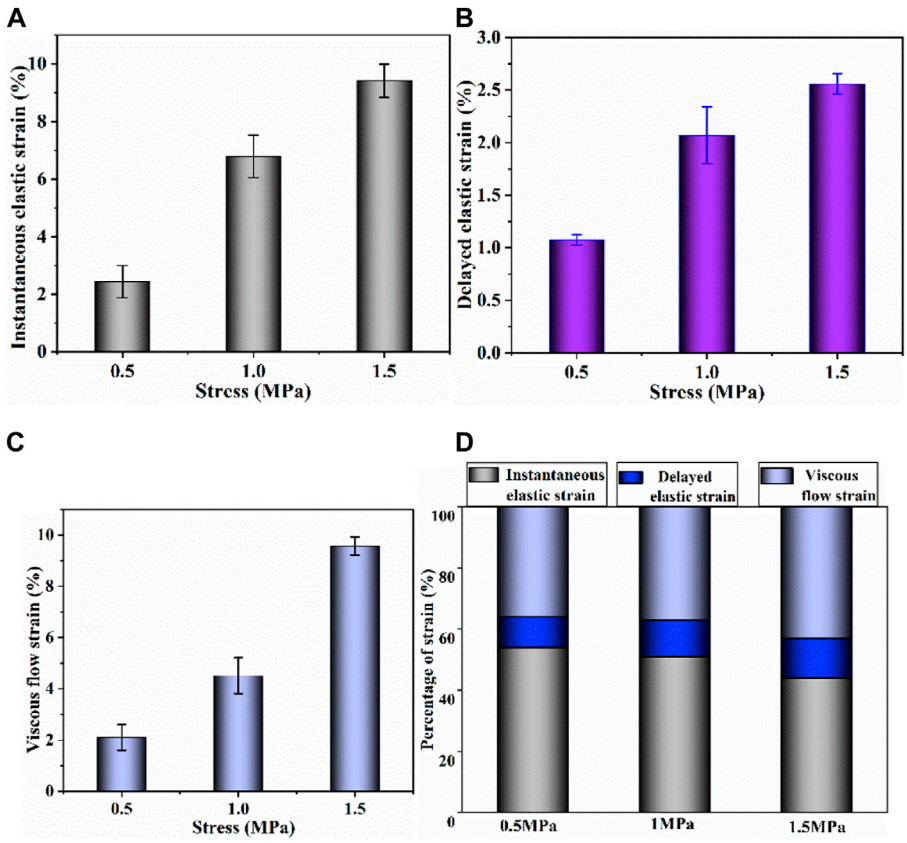

FIGURE 7
(A–C) Instantaneous elastic strain, delayed elastic strain and viscous flow strain components of biaxial creep strain, respectively; **(D)** percentage of each biaxial strain component at different stress levels.

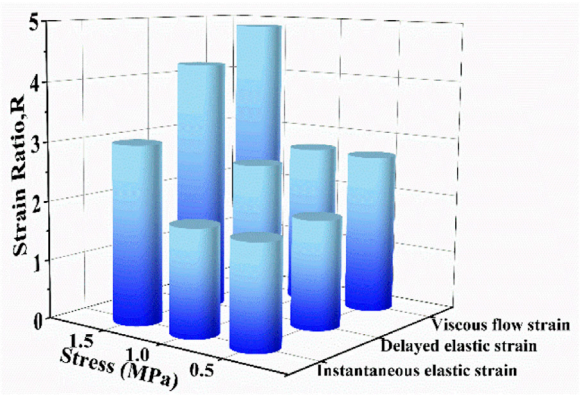

FIGURE 8
The strain ratio as a function of stress level for instantaneous elastic strain, delayed elastic strain and viscous flow strain.

experiments, the Young's modulus of cartilage was determined by calculating the slope of linear range of stress-strain curve when the strain value is 1%–5%. Effect of strain rate on Young's modulus is shown in Figure 3B. Young's modulus increases obviously with the increase of strain rate.

4.2 Uniaxial creep-recovery behaviors of articular cartilage at different stress levels

The uniaxial creep-recovery curves of cartilage at different stress levels are shown in Figure 4. In the phase of creep, the creep strain at each stress level increases rapidly at first, and followed by the decrease of growth rate with creep time. The creep strain increases with the increase of stress level ($p < .05$). In the phase of recovery ($\sigma = 0$ MPa), the strain decreases rapidly at the beginning, and then the declining rate decreases with recovery time. When the recovery time is 2,400 s, the strain decreases to 45.1%, 50.3% and 53.5% of initial recovery strain at stress level of .5, 1.0, 1.5 MPa. When the recovery time is 3,600 s, the recovery strain decreases to 39.5%, 46.4% and 50.5% of initial recovery strain. Enough unloading time is beneficial for creep recovery. And longer recovery time is required for creep recovery at higher stress level.

Simultaneously, the creep strains and recovery strains at different stress levels have also been fitted by the theoretical creep-recovery model (Eq. (11) and Eq, 12. Figure 4 demonstrates the comparisons of test results and fitting results. There are good agreements between them (R > .8).

Based on the creep strain classification in Figure 2D, each component at different stress levels is compared in Figure 5. It is noted that the increase of stress level results in an increase in all strain

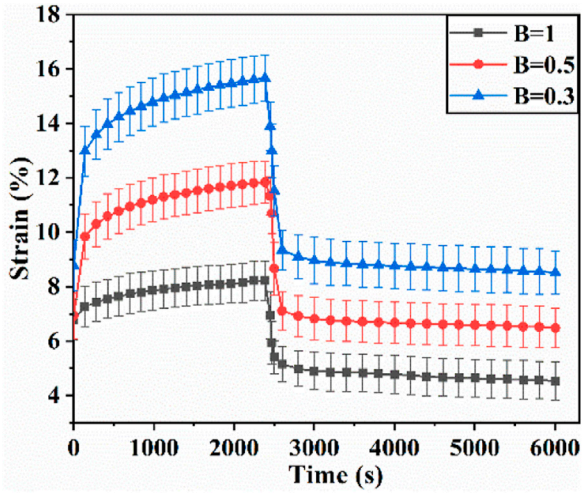

FIGURE 9
Biaxial creep-recovery curves of articular cartilage at different stress ratio.

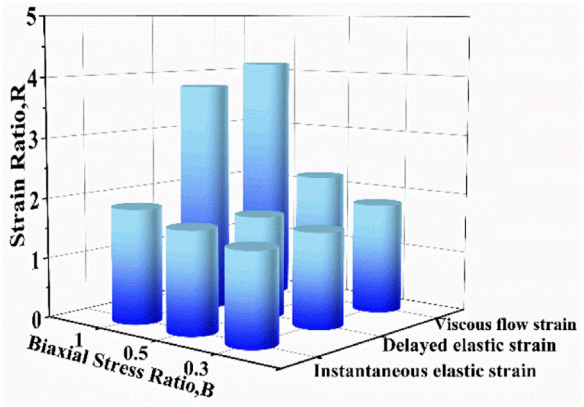

FIGURE 11
The strain ratio as a function of biaxial stress ratio for instantaneous elastic strain, delayed elastic strain and viscous flow strain.

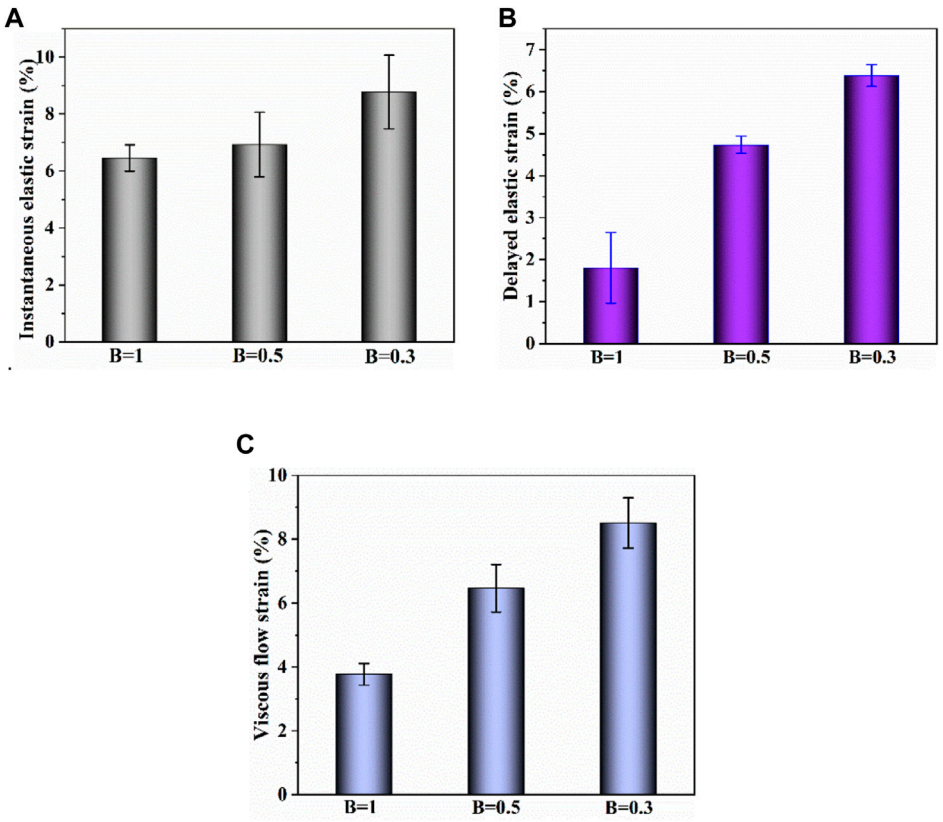

FIGURE 10
(A–C) Instantaneous elastic strain, delayed elastic strain and viscous flow strain components of biaxial creep strain, respectively.

components. As shown in Figure 5D, by comparing the percentage of each strain component, the contribution of each strain component at different stress levels was evaluated. Decrease in proportion of instantaneous elastic strain and increase in proportions of delayed elastic strain and viscous flow strain are observed with the increase of stress level.

4.3 Biaxial creep-recovery behaviors of articular cartilage at different stress levels

Biaxial creep-recovery tests with different stress levels were carried out at $B = 1.0$. Only the creep-recovery behavior in x-axis (along the split line of cartilage) was chosen for discussion since the creep-recovery responses in two axes are similar. Figure 6 shows the biaxial creep-recovery strain curves at different stress levels. Similar to uniaxial creep response in Figure 4, both biaxial creep strain and the biaxial residual strain increase with the increase of stress level ($p < .05$). The biaxial creep strain is smaller than the uniaxial creep strain, indicating that the equi-biaxial loading enforces constraint on the accumulation of biaxial creep strain. Similarity, the biaxial recovered strain is less than the uniaxial recovered strain at the same stress level, which is illustrated by analyzing the percentages of creep strain components (Figure 7). The recovered strain mainly includes the intantaneous elastic strain and delayed elastic strain (Figure 2D). As shown in Figure 7D, the percentages of biaxial delayed elastic strain with .5, 1.0, 1.5 MPa are 10%, 12%, 13%, which are smaller than those of 17%, 20%, 24% under uniaxial loading. In addition, the percentages of instantaneous elastic strain under biaxial loading are almost as large as those under uniaxial loading. Differences in percentages of these creep strain components suggest that biaxial loading serves to suppress the delayed elastic strain, resulting in the smaller biaxial recovered strain and thus the larger residual strain in biaxial creep-recovery tests.

To further quantify the effect of biaxial stress level on creep strain, the strain ratio R was proposed and it is defined as uniaxial creep strain component divided by corresponding biaxial creep strain component. Figure 8 compares the strain ratios of instantaneous elastic strain, delayed elastic strain and viscous flow strain at different stress levels. It is found that all strain ratios at different stress levels are larger than 1, which means that each uniaxial creep strain component is larger than the corresponding biaxial creep strain component. At the same stress level, the strain ratio of viscous flow strain is larger than that of the other two components. The strain ratio increases with the increase of stress level by focusing on certain creep strain component. Compared with .5 MPa and 1.0 MPa, 1.5 MPa exhibits the most remarkable increase in all three creep strain components. Besides, the strain ratios of viscous flow strain and delayed elastic strain experience greater increase than that of instantaneous, regardless the stress level. Consequently, biaxial loading reduces the creep strain by retarding viscous flow strain and delayed elastic strain, especially at high stress of 1.5 MPa.

4.4 Effect of biaxial stress ratio on biaxial creep-recovery behavior

Figure 9 shows the creep-recovery responses of cartilage at different biaxial stress ratios. The biaxial creep strain decreases with increase of biaxial stress ratio ($p < .05$), indicating that the stronger the biaxial constraint, the smaller the creep strain. Besides, the larger biaxial creep strain shows the smaller residual strain. As shown in Figures 10A–C, increasing biaxial stress ratio B from .3 to 1.0 brings a large reduction of each creep component, leading to the decreasing of creep and recovered strain. In particular, the delayed elastic strain decreases from 4.74 to 1.81 with biaxial stress ratio from $B = .5$ to $B = 1.0$, corresponding to a 72% reduction.

In addition, the strain ratios of instantaneous elastic strain, delayed elastic strain and viscous flow strain at different stress ratios were compared in Figure 11. At the same stress level, the strain ratio of instantaneous elastic strain is smaller than that of the other two components. The strain ratio of instantaneous elastic strain rises slightly with the rise of biaxial stress ratio. By comparison, the strain ratios of delayed elastic strain and viscous flow strain show the more remarkable increase with the rise of biaxial stress ratio, especially when the biaxial stress ratio increase from $B = .5$ to $B = 1.0$. The results indicate that biaxial loading limits creep deformation of cartilage by inhibiting its delayed elastic strain and viscous flow strain, and the equi-biaxial stress state imposes the largest constriction.

5 Discussions

In daily activities, articular cartilage is subjected to long time biaxial loads or multiaxial loads. The creep deformation is induced in cartilage under mechanical loads due to the alternation of unequal fluid exudation and imbibition within its matrix. Once unloaded, most of the creep deformation will gradually recover with time. Uniaxial creep-recovery of cartilage have been well described in previous studies (Gao et al., 2019; Cutcliffe and DeFrate, 2020). However, seldom has any study focused on biaxial or multiaxial creep-recovery of cartilage. Thus, we probed the creep-recovery behaviors of articular cartilage by comparing uniaxial and biaxial tensile loading results.

The creep strain evolution of cartilage consists of two parts, namely initial creep stage and the steady creep stage. In initial creep stage, the uniaxial and biaxial creep strain showed a similar evolution that the creep strain increased rapidly at the beginning, and gradually tended to be stable with time (Figure 4; Figure 6; Figure 9). The rapid increase of strain in initial creep stage for cartilage is due to the rapid outflow of interstitial fluid. When the unbound fluid in cartilage is squeezed out, the burden of supporting tensile load is gradually shifted to the collagen network. The cartilage becomes more resistant to deformation and the next creep stage starts. In steady creep stage, the increase rate of creep strain stays constant. The creep strain evolution observed in this study is similar with that reported by Hosseini et al. and Choi et al. as they found that the creep deformation *in vivo* kept stable after a rapid growth (Hosseini et al., 2010; Choi et al., 2016). However, it should be mentioned that there is no accurate cut-off point between the first creep stage and the steady creep stage since the creep deformation of cartilage varies with different physiological loads (Schoenbauer et al., 2015; Wang et al., 2015; Chan et al., 2016; Choi et al., 2016). Compared with uniaxial creep, biaxial creep exhibits smaller strain at the same stress level, especially at high stress level of 1.5 MPa. It is found that biaxial loading reduces the creep strain through retarding all creep strain components (Figure 5; Figure 7), especially through retarding delayed elastic strain and viscous flow strain (Figure 8). The smaller strain under biaxial creep is ascribed to the higher constraint imposed by the equi-biaxial stress state, as higher constraints can increase the stiffness of the cartilage and restrict the rapid outflow of interstitial fluid.

Generally, the deformation of articular cartilage can be fully recovered within a sufficient period of unloading time due to the viscoelastic properties of articular cartilage (Torzilli, 1984; Athanasiou et al., 1994). Eckstein et al. suggested at least 90 min of rest might be required to allow articular cartilage to fully recover according to the

imaging based studies (Eckstein et al., 1999). Erisken et al. reported that 1,000 s was sufficient for the compressive stress to relax in bovine cartilage (Erisken et al., 2010). In this study, it is found that both uniaxial and biaxial strain have not been fully recovered with the residual strains left when the recovery time is 3,600 s. Compared with uniaxial loading, biaxial loading shows a smaller residual strain (Figure 4; Figure 6; Figure 9), due to the significant decrease in the viscous flow strain at equi-biaxial stress state (Figure 5C; Figure 7C). The residual strain, as viscous flow strain, is slow to recover. Thus, more time may be needed for the residual creep deformation to recover.

It is very likely for cartilage to experience non-uniform stress distribution in daily activities due to its curvature structure, thickness variation, diffusion kinetics and other factors (Kamalanathan and Broom, 1993). Kamalanathan and Broom reported that the tissue was significantly stiffer, i.e. more strain limiting, along the split-line direction than across it. They found that the tissue was significantly stiffer, i.e. more strain limiting, along the split-line direction than across it and the anisotropic strain-limiting response of the fibrillar array will result in fibrils acting more collectively along the less extensible direction than across it. Obviously, the stress state of cartilage under physiological load is not equi-biaxial. To better understand how biaxial constraint influences biaxial creep behavior, we studied the effect of biaxial stress ratio on creep-recovery behavior of cartilage (Figure 8). Both creep strain and recovered strain decrease with the increase of biaxial stress ratio due to the reason that the larger the biaxial stress ratio, the stronger the biaxial constraint. The equi-biaxial stress state ($B = 1$) imposes the largest biaxial constraint. Thus, when the biaxial stress ratio B is 1.0, the lowest creep and recovery strain is induced in cartilage. Increasing the biaxial stress ratio from .3 to 1.0 causes a decrease in all creep strain components, especially in delayed elastic strain (Figure 9; Figure 10). Furthermore, less proportion of delayed elastic strain results in less time to reach steady recovery state (Figure 8) since delayed elastic strain is slow to recover. In addition, the higher constraint was imposed by the larger biaxial stress ratio, which in turn increases the stiffness of cartilage (Lin et al., 2017; Zhang et al., 2019) resulting in the smaller creep strain and residual strain.

Viscoelastic (Leipzig and Athanasiou, 2005; Si et al., 2022), biphasic (Huang et al., 2003) and poroviscoelastic models (Wang et al., 2001) are employed to describe mechanical behaviors of cartilage in literature. Leipzig and Athanasiou used the viscoelastic model to describe the mechanical behaviors of cartilage cells (Leipzig and Athanasiou, 2005). Gao et al. employed the non-linear viscoelastic constitutive model to predict the depth-dependent creep behaviors of cartilage under compression (Gao et al., 2014). The viscoelastic constitutive model employed in this study is proposed by Lou and sharper (Lou and Schapery, 1971). It has the outstanding advantage of retaining the single time integral form even in the non-linear range. And the non-linear effects are expressed by means of stress-dependent material functions determined experimentally. It has been applied to predict the mechanical behaviors of cracked cartilage and exhibits good results (Si et al., 2022). In this study, the proposed viscoelastic model with the consideration of irrecoverable deformation was developed to describe the uniaxial creep-recovery behaviors of cartilage and a good consistence between test data and fitted data is obtained.

6 Conclusion

The study probed the uniaxial and biaxial creep-recovery behaviors of articular cartilage. Changing the stress state from uniaxial loading to biaxial loading, creep strain decreases significantly under the same stress level. Increasing biaxial stress ratio (from $B = .3–1$) causes notable decrease in creep strain. During the recovery process of creep, it takes less time for the biaxial strain than the uniaxial strain to reach the steady recovery state. The cartilage with higher stress level or smaller biaxial stress ratio shows larger residual strain, indicating that the cartilage damage may be accelerated at higher stress level or at smaller biaxial stress ratio. These results provide a new sight for cartilage creep and are significant to improve the durability of cartilage in daily activities.

Data availability statement

The original contributions presented in the study are included in the article/supplementary material, further inquiries can be directed to the corresponding authors.

Author contributions

LG: Writing—original draft, Methodology. GL: Writing—original draft, Investigation. YT: Writing—review and editing. RL: Software. CZ: Methodology, Supervision. HG: Supervision. BZ: Supervision.

Acknowledgments

The authors gratefully acknowledge the financial support from National Natural Science Foundation of China (Nos. 32271371, 12072235), Tianjin Natural Science Foundation (Nos. 21JCQNJC01310 and 21JCYBJC00940) and Technical Innovation Guidance Project of Tianjin Science and Technology Bureau (No. 22YDTPJC00440).

Conflict of interest

The authors declare that the research was conducted in the absence of any commercial or financial relationships that could be construed as a potential conflict of interest.

Publisher's note

References

Athanasiou, K. A., Agarwal, A., and Dzida, F. J. (1994). Comparative study of the intrinsic mechanical properties of the human acetabular and femoral head cartilage. *J. Orthop. Res.* 12, 340–349. doi:10.1002/jor.1100120306

Athanasiou, K. A., Rosenwasser, M. P., Buckwalter, J. A., Malinin, T. I., and Mow, V. C. (1991). Interspecies comparisons of *in situ* intrinsic mechanical properties of distal femoral cartilage. *J. Orthop. Res.* 9, 330–340. doi:10.1002/jor.1100090304

Boettcher, K., Kienle, S., Nachtsheim, J., Burgkart, R., Hugel, T., and Lieleg, O. (2016). The structure and mechanical properties of articular cartilage are highly resilient towards transient dehydration. *Acta Biomater.* 29, 180–187. doi:10.1016/j.actbio.2015.09.034

Chan, D. D., Cai, L. Y., Butz, K. D., Trippel, S. B., Nauman, E. A., and Neu, C. P. (2016). *In vivo* articular cartilage deformation: Noninvasive quantification of intratissue strain during joint contact in the human knee. *Sci. Rep.* 6, 19220. doi:10.1038/srep19220

Chen, J. X., Zhang, J. H., and Zhao, H. W. (2022). Quantifying alignment deviations for the in-plane biaxial test system via a shape-optimised cruciform specimen. *Materials* 15, 4949. doi:10.3390/ma15144949

Choi, J. H., Mcwalter, E. J., Datta, S., Mueller, K., Maier, A., Fahrig, R., et al. (2016). Tibial cartilage creep during weight bearing:*in vivo* 3D CT assessment. *Osteoarthr. Cartil.* 24, S104. doi:10.1016/j.joca.2016.01.210

Cutcliffe, H. C., and Defrate, L. E. (2020). Comparison of cartilage mechanical properties measured during creep and recovery. *Sci. Rep.* 10, 1547. doi:10.1038/s41598-020-58220-2

Eckstein, F., Tieschky, M., Faber, S., Englmeier, K. H., and Reiser, M. (1999). Functional analysis of articular cartilage deformation, recovery, and fluid flow following dynamic exercise *in vivo*. *Anat. Embryology* 200, 419–424. doi:10.1007/s004290050291

Erisken, C., Kalyon, D. M., and Wang, H. J. (2008). Functionally graded electrospun polycaprolactone and beta-tricalcium phosphate nanocomposites for tissue engineering applications. *Biomaterials* 29, 4065–4073. doi:10.1016/j.biomaterials.2008.06.022

Erisken, C., Kalyon, D. M., and Wang, H. J. (2010). Viscoelastic and biomechanical properties of osteochondral tissue constructs generated from graded polycaprolactone and beta-tricalcium phosphate composites. *J. Biomechanical Engineering-Transactions Asme* 132, 091013. doi:10.1115/1.4001884

Felson, D. T. (2013). Osteoarthritis as a disease of mechanics. *Osteoarthr. Cartil.* 21, 10–15. doi:10.1016/j.joca.2012.09.012

Gao, L. L., Liu, D. D., Gao, H., Lv, L. W., and Zhang, C. Q. (2019). Effects of creep and creep-recovery on ratcheting strain of articular cartilage under cyclic compression. *Mater. Sci. Eng. C-Materials Biol. Appl.* 94, 988–997. doi:10.1016/j.msec.2018.10.047

Gao, L. L., Zhang, C. Q., Gao, H., Liu, Z. D., and Xiao, P. P. (2014). Depth and rate dependent mechanical behaviors for articular cartilage: Experiments and theoretical predictions. *Mater. Sci. Eng. C-Materials Biol. Appl.* 38, 244–251. doi:10.1016/j.msec.2014.02.009

Georgiev, T., and Angelov, A. K. (2019). Modifiable risk factors in knee osteoarthritis: Treatment implications. *Rheumatol. Int.* 39, 1145–1157. doi:10.1007/s00296-019-04290-z

Herberhold, C., Faber, S., Stammberger, T., Steinlechner, M., Putz, R., Englmeier, K. H., et al. (1999). *In situ* measurement of articular cartilage deformation in intact femoropatellar joints under static loading. *J. Biomechanics* 32, 1287–1295. doi:10.1016/s0021-9290(99)00130-x

Herberhold, C., Stammberger, T., Faber, S., Putz, R., Englmeier, K. H., Reiser, M., et al. (1998). An MR-based technique for quantifying the deformation of articular cartilage during mechanical loading in an intact cadaver joint. *Magnetic Reson. Med.* 39, 843–850. doi:10.1002/mrm.1910390522

Hosseini, A., Van De Velde, S. K., Kozanek, M., Gill, T. J., Grodzinsky, A. J., Rubash, H. E., et al. (2010). *In-vivo* time-dependent articular cartilage contact behavior of the tibiofemoral joint. *Osteoarthr. Cartil.* 18, 909–916. doi:10.1016/j.joca.2010.04.011

Huang, C. Y., Soltz, M. A., Kopacz, M., Mow, V. C., and Ateshian, G. A. (2003). Experimental verification of the roles of intrinsic matrix viscoelasticity and tension-compression nonlinearity in the biphasic response of cartilage. *J. Biomechanical Engineering-Transactions Asme* 125, 84–93. doi:10.1115/1.1531656

Kamalanathan, S., and Broom, N. D. (1993). The biomechanical ambiguity of the articular surface. *J. Anat.* 183, 567–578.

Korhonen, R. K., Laasanen, M. S., Toyras, J., Rieppo, J., Hirvonen, J., Helminen, H. J., et al. (2002). Comparison of the equilibrium response of articular cartilage in unconfined compression, confined compression and indentation. *J. Biomechanics* 35, 903–909. doi:10.1016/s0021-9290(02)00052-0

Lamkanfi, E., Van Paepegem, W., and Degrieck, J. (2015). Shape optimization of a cruciform geometry for biaxial testing of polymers. *Polym. Test.* 41, 7–16. doi:10.1016/j.polymertesting.2014.09.016

Leipzig, N. D., and Athanasiou, K. A. (2005). Unconfined creep compression of chondrocytes. *J. Biomechanics* 38, 77–85. doi:10.1016/j.jbiomech.2004.03.013

Leotoing, L., Guines, D., Zidane, I., and Ragneau, E. (2013). Cruciform shape benefits for experimental and numerical evaluation of sheet metal formability. *J. Mater. Process. Technol.* 213, 856–863. doi:10.1016/j.jmatprotec.2012.12.013

Li, J. S., Tsai, T. Y., Wang, S. B., Li, P. Y., Kwon, Y. M., Freiberg, A., et al. (2014). Prediction of *in vivo* knee joint kinematics using a combined dual fluoroscopy imaging and statistical shape modeling technique. *J. Biomechanical Engineering-Transactions Asme* 136, 124503. doi:10.1115/1.4028819

Li, L. P., Buschmann, M. D., and Shirazi-Adl, A. (2003). Strain-rate dependent stiffness of articular cartilage in unconfined compression. *J. Biomechanical Engineering-Transactions Asme* 125, 161–168. doi:10.1115/1.1560142

Li, L. P., and Herzog, W. (2004). Strain-rate dependence of cartilage stiffness in unconfined compression: The role of fibril reinforcement versus tissue volume change in fluid pressurization. *J. Biomechanics* 37, 375–382. doi:10.1016/s0021-9290(03)00263-x

Lin, Q., Shi, S. W., Wang, L., Chen, S., Chen, X., and Chen, G. (2017). In-plane biaxial cyclic mechanical behavior of proton exchange membranes. *J. Power Sources* 360, 495–503. doi:10.1016/j.jpowsour.2017.06.040

Lin, Q., Shi, S. W., Wang, L., Chen, X., and Chen, G. (2018). Biaxial fatigue crack propagation behavior of perfluorosulfonic-acid membranes. *J. Power Sources* 384, 58–65. doi:10.1016/j.jpowsour.2018.02.002

Liu, F., Kozanek, M., Hosseini, A., Van De Velde, S. K., Gill, T. J., Rubash, H. E., et al. (2010). *In vivo* tibiofemoral cartilage deformation during the stance phase of gait. *J. Biomechanics* 43, 658–665. doi:10.1016/j.jbiomech.2009.10.028

Lou, Y. C., and Schapery, R. A. (1971). Viscoelastic characterization of a nonlinear fiber-reinforced plastic. *J. Compos. Mater.* 5, 208–234. doi:10.1177/002199837100500206

Martel-Pelletier, J., Barr, A. J., Cicuttini, F. M., Conaghan, P. G., Cooper, C., Goldring, M. B., et al. (2016). Osteoarthritis. *Nat. Rev. Dis. Prim.* 2, 16072. doi:10.1038/nrdp.2016.72

Peters, A. E., Geraghty, B., Bates, K. T., Akhtar, R., Readioff, R., and Comerford, E. (2022). Ligament mechanics of ageing and osteoarthritic human knees. *Front. Bioeng. Biotechnol.* 10, 954837. doi:10.3389/fbioe.2022.954837

Qiu, L. L., Ma, X. M., Gao, L. L., Men, Y. T., and Zhang, C. Q. (2016). Analysis of the mechanical state of the human joint with defect cartilage in standing. *J. Mech. Med. Biol.* 16, 1640021. doi:10.1142/s0219519416400212

Reuter, T., and Hurschler, C. (2021). Comparison of biphasic material properties of equine articular cartilage estimated from stress relaxation and creep indentation tests. *Curr. Dir. Biomed. Eng.* 7, 363–366. doi:10.1515/cdbme-2021-2092

Roos, E. M., Roos, H. P., Ekdahl, C., and Lohmander, L. S. (1998). Knee injury and osteoarthritis outcome score (KOOS) - validation of a Swedish version. *Scand. J. Med. Sci. Sports* 8, 439–448. doi:10.1111/j.1600-0838.1998.tb00465.x

Schoenbauer, E., Szomolanyi, P., Shiomi, T., Juras, V., Zbyn, S., Zak, L., et al. (2015). Cartilage evaluation with biochemical MR imaging using *in vivo* Knee compression at 3 T-comparison of patients after cartilage repair with healthy volunteers. *J. Biomechanics* 48, 3349–3355. doi:10.1016/j.jbiomech.2015.06.016

Si, Y. P., Tan, Y. S., Gao, L. L., Li, R. X., Zhang, C. Q., Gao, H., et al. (2022). Mechanical properties of cracked articular cartilage under uniaxial creep and cyclic tensile loading. *J. Biomechanics* 134, 110988. doi:10.1016/j.jbiomech.2022.110988

Stolberg-Stolberg, J., Foehr, P., Pflieger, I., Kuntz, L., Von Deimling, C., Obermeier, A., et al. (2018). Analysis of cartilage creep recovery using a highly dynamic closed-loop test system. *J. Bionic Eng.* 15, 1057–1066. doi:10.1007/s42235-018-0093-x

Torzilli, P. A. (1984). Mechanical response of articular-cartilage to an oscillating load. *Mech. Res. Commun.* 11, 75–82. doi:10.1016/0093-6413(84)90100-9

Uzuner, S., Li, L. P., Kucuk, S., and Memisoglu, K. (2020). Changes in knee joint mechanics after medial meniscectomy determined with a poromechanical model. *J. Biomechanical Engineering-Transactions Asme* 142, 101006. doi:10.1115/1.4047343

Wang, C. C. B., Hung, C. T., and Mow, V. C. (2001). An analysis of the effects of depth-dependent aggregate modulus on articular cartilage stress-relaxation behavior in compression. *J. Biomechanics* 34, 75–84. doi:10.1016/s0021-9290(00)00137-8

Wang, H. S., Koff, M. F., Potter, H. G., Warren, R. F., Rodeo, S. A., and Maher, S. A. (2015). An MRI-compatible loading device to assess knee joint cartilage deformation: Effect of preloading and inter-test repeatability. *J. Biomechanics* 48, 2934–2940. doi:10.1016/j.jbiomech.2015.08.006

Zhang, C., Shi, S. W., Lin, Q., Wang, L., and Chen, X. (2019). Interplay between temperature and biaxial loading on creep behavior of perfluorosulfonic-acid membranes. *J. Power Sources* 444, 227309. doi:10.1016/j.jpowsour.2019.227309

frontiers | Frontiers in Bioengineering and Biotechnology

TYPE Review
PUBLISHED 06 February 2023
DOI 10.3389/fbioe.2023.1136453

OPEN ACCESS

EDITED BY
Yunfeng Lin,
Sichuan University, China

REVIEWED BY
Bei Li,
The Fourth Military Medical University, China
Bingdong Sui,
Air Force Medical University, China

*CORRESPONDENCE
Liqun Yang,
yanglq@lnszjk.com.cn
Muxin Zhao,
zhaomuxin@126.com

†These authors have contributed equally to this work and share first authorship

SPECIALTY SECTION
This article was submitted to Biomaterials, a section of the journal Frontiers in Bioengineering and Biotechnology

RECEIVED 05 January 2023
ACCEPTED 24 January 2023
PUBLISHED 06 February 2023

CITATION
Ren S, Lin Y, Liu W, Yang L and Zhao M (2023), MSC-Exos: Important active factor of bone regeneration.
Front. Bioeng. Biotechnol. 11:1136453.
doi: 10.3389/fbioe.2023.1136453

MSC-Exos: Important active factor of bone regeneration

Sihang Ren[1,2,3†], Yuyang Lin[1†], Wenyue Liu[1], Liqun Yang[3,4*] and Muxin Zhao[1*]

[1]Department of Plastic Surgery, The Second Hospital of Dalian Medical University, Dalian, China, [2]Department of Plastic Surgery, The First Hospital of China Medical University, Shenyang, China, [3]NHC Key Laboratory of Reproductive Health and Medical Genetics (China Medical University), Liaoning Research Institute of Family Planning (The Affiliated Reproductive Hospital of China Medical University), Shenyang, China, [4]Department of Biomaterials, Shengjing Hospital of China Medical University, Shenyang, China

Bone defect and repair is a common but difficult problem in restorative and reconstructive surgery. Bone tissue defects of different sizes caused by different reasons bring functional limitations and cosmetic deformities to patients. Mesenchymal stem cells (MSC), a major hotspot in the field of regeneration in recent years, have been widely used in various studies on bone tissue regeneration. Numerous studies have shown that the bone regenerative effects of MSC can be achieved through exosome-delivered messages. Although its osteogenic mechanism is still unclear, it is clear that MSC-Exos can directly or indirectly support the action of bone regeneration. It can act directly on various cells associated with osteogenesis, or by carrying substances that affect cellular activators or the local internal environment in target cells, or it can achieve activation of the osteogenic framework by binding to materials. Therefore, this review aims to summarize the types and content of effective contents of MSC-Exos in bone regeneration, as well as recent advances in the currently commonly used methods to enable the binding of MSC-Exos to the framework and to conclude that MSC-Exos is effective in promoting osteogenesis.

KEYWORDS

MSC-Exos, bone regenaration, mesenchyaml stem cells, osteogenic cells, biomaterials

1 Introduction

Bone regeneration is an extremely complex repair process. The combination of cells, growth factors and structural framework is essential for bone regeneration (Battafarano et al., 2021). Bone repair is delayed or stopped if these three elements are affected or absent for various reasons within the individual with a bone defect. In adult individuals, a bone defect of 2 cm is the threshold value, and bone defects exceeding 2 cm are difficult to heal on their own without external forces. In order to break the limit, the study aims to fundamentally reconstruct the homeostasis of the three elements of bone regeneration and simulate the normal bone regeneration process *in vivo* (Sobacchi et al., 2013).

Mesenchymal stem cells are pluripotent non-hematopoietic stem cells with self-renewal capacity (Xia et al., 2019). MSCs are not only abundant, which can be found in bone marrow, adipose, muscle, peripheral blood, umbilical cord, placenta, fetal tissue, and amniotic fluid (Brown et al., 2019), but also involved in tissue repair, immunomodulation and anti-inflammation by controlling immune response, angiogenesis, cell proliferation, migration, invasion and survival (Heo et al., 2019). Previous studies suggested that MSC could be a source of cells in bone regeneration, but recent studies have shown that MSCs are not only the cellular basis for osteogenesis, but also parental cells for the release of various factors (Du et al., 2019). However, recent studies have shown that MSC is not only the

cellular basis for osteogenesis, but also an activator and fusion agent for the release of various factors, or structural frameworks, making MSC an "all-rounder" in osteogenesis. This ability is fully reflected by the fact that exosomes concentrate the active components of MSC and stimulate the maximum osteogenic potential of MSC, while discarding the ethical issues, immune resistance (EL Andaloussi et al., 2013) and the inconvenience of excessive cell size (Verweij et al., 2019).

Exosomes are small vesicles secreted by cells that mediate intercellular communication through paracrine and other means (Schott et al., 2021). Exosomes are influenced by parental cells (Xia et al., 2019) and the carriage of these substances results in exosomes from different sources with specific and unchangeable parental characteristics (Wang et al., 2018a). Furthermore, spectrum-specific exosomes have a greater impact on the differentiation of MSCs than extracellular matrix, and osteoblast-derived exosomes containing osteogenic factors can reverse the lipogenic differentiation potential of MSCs cultured in lipogenic medium (Kargozar et al., 2019). These vesicles, which can be secreted by almost all living cells, are important carriers of information between osteoblasts and other cells, or between cells and the microenvironment (Peng et al., 2020). The secreted exosomes could be taken up by recipient cells *via* endocytosis, ligand-receptor interaction (where both the ligand and the receptor are not clearly uncovered) or fusion then the contained bioactive cargos are transferred to modify gene expression, signaling, and overall functions and behaviors of recipient cells. Artificially interfered with exosomes can contain RNA, enzymes, therapeutic genes or drugs and other contents (Basso and Bonetto, 2016). Therefore, the effective application and potential development of MSC-Exos is an important topic and a necessary tool in the field of bone regeneration. By reviewing the various contributions of MSC-Exos in osteogenesis in recent years, we acknowledge the significant contribution of MSC-Exos in osteogenesis and also find the limitations and defects due to its low yield, difficulties in purification or difficulties in targetin.

2 Effect of MSC-Exos on osteogenesis-related cells and active factors

In the process of osteogenesis, cellular components are the basis of the whole process, including osteoblasts, osteoclasts, osteocytes, and chondrocytes (Kim and Mikos, 2021). The positive effect of MSC exosomes on the proliferation and/or migration of multiple cell types *in vitro*, including osteoblasts, osteocytes, MSCs and endothelial cells (Jia et al., 2020). The Effects of mesenchymal stem cell-derived exosomes on osteogenesis-related cells and their active factors are summarized in Table 1; Figure 1. Activation of the core cells can effectively promote the initiation and rapid progression of the osteogenic process (Li et al., 2018). In turn, the effect on macrophages provides beneficial regulation of the inflammatory environment of bone regeneration (Schlundt et al., 2021). Therefore, it can be assumed that the primary effect of MSC-Exos on cells lies in the direct action on osteogenic cells (Liu et al., 2021a). The active factors of the osteogenic elements are considered to be more important components than cells. In conjunction with the trend of being "cell-free", the effective use of osteogenic factors and tissue frameworks plays a key role.

2.1 MSC-Exos act on MSC

Information transfer between MSCs through MSC-Exos is the initial direction in MSC-Exos research (Zhu et al., 2019). When jaw BMSC-Exos was co-cultured with iliac BMSC, it was found that ALP and osteogenic gene expression were upregulated, while siRNA against Rab27a blocked this osteogenic effect, and it was concluded that Exo interacted between BMSC-J as well as BMSC-I to upregulate maxillary BMSC osteogenic ability (Li et al., 2019). When human dental pulp stem cells (hPDSCs) were co-cultured with human stem cells (hADSC), the phenotype of osteoblast was upregulated and was able to upregulate the MAPK pathway, leading to phosphorylation of ERK1/2 as well as JNK, thus promoting hADSC osteogenic differentiation (Jin et al., 2020). MSC-derived sEVs increase the expression of VEGFA and VEGFR2 in MSCs and thus may facilitate osteogenesis and angiogenesis of bone regeneration (Pizzicannella et al., 2019a; Pizzicannella et al., 2019b). MSC-Exos induces osteogenic differentiation by using its cargo. hADSC-Exo, which is predifferentiated in osteogenic medium, may act on different targets of osteogenesis by altering its miRNA expression profile at different stages of culture and induce MSC differentiation towards osteoblasts by activating different pathways including PI3K/Akt as well as MAPK and thus initiate osteogenesis and promote bone regeneration (Zhai et al., 2020).

2.2 MSC-Exos act on osteoblasts

BMSC-Exo is able to carry the LncRNA MALAT1 and act as a sponge for miR-34c to promote SATB2 expression, while silencing of SATB2 is able to reduce ALP activity in osteoblasts and mineralized nodules (Yang et al., 2019). In osteoporotic rats, BMSC-Exos-miRNA-935 was able to act on osteoblasts to regulate STAT1 pathway, promoting ALP synthesis and osteoblast proliferation and differentiation, thereby inhibiting osteoporosis progression in OVX rats (Zhang et al., 2021a). After TNF-α acts on primary osteoblasts, it can upregulate the expression of miRNA-141-5p, thereby inhibiting osteogenesis. As a sponge, lncRNA-KCNQ1OT1 inhibits the block of primary osteoblast proliferation by miRNA-141-5p. ADSC-lncRNA-KCNQ1OT1 acts as the sponge of miRNA-214, and inhibits its expression, thereby upregulating BMP2 expression and promoting osteogenic differentiation of BMSC (Wang et al., 2019). In addition, lncRNA-HOTAIR targeting miRNA-138 and lncRNA-LOXLT-AS1 targeting miRNA-196a-5p have been found to play a regulatory role in osteogenesis (Wang et al., 2021a).

2.3 MSC-Exos act on osteoclasts

BMSC-Exos-miRNA-335 acts on VapB (vesicle associated membrane protein-associated protein B), and inhibition of its expression can target activation of the Wnt/β-catenin pathway and promote fracture recovery. VapB is a key target for regulating PLcr2-Ca^{2+}-NFAT signaling, and inhibition of this signaling inhibits osteoclast differentiation and stabilizes fracture ends (Hu et al., 2021). The Wnt pathway is a classical pathway of osteogenesis. ADSC-Exo-miRNA-130a-3p mediates the SIRT7/Wnt/β-catenin axis, targets silencing of SIRT mRNA, and activates the Wnt pathway, thereby preventing β-catenin from being degraded and entering the nucleus completes its process of promoting osteogenic

TABLE 1 Effect of exosomes derived from mesenchymal stem cells on osteogenic associated cells.

Source	Target cells	Effect	Reference
jaw-BMSC	MSC	upregulate maxillary BMSC-ilium osteogenic ability	Li et al. (2019)
hPDSCs		promote hADSC osteogenic differentiation	Jin et al. (2020)
hGMSC		bringing miR-296 and miR-210 to promote bone regeneration of calvaria defects, associated with vascularization increasing	Pizzicannella et al. (2019a), Pizzicannella et al. (2019b)
hPDLSC			Zhai et al. (2020)
hMSCs		bringing osteogenic miRNAs to induce MSC differentiation towards osteoblasts	Yang et al. (2019)
BMSC	Osteoblasts	bringing LncRNA MALAT1 to promote SATB2 expression (silencing of SATB2 is able to reduce ALP activity in osteoblasts)	Zhang et al. (2021a)
BMSC		bringing miRNA-935 to promote osteoblast proliferation and differentiation	Wang et al. (2019), Wang et al. (2021a)
BMSC-Exo with KCNQ1OT1 knockdown		inhibit the block of primary osteoblast proliferation	Wang et al. (2021a)
lnc-KCNQ1OT1-modified ADSCs-Exos		attenuate cytotoxicity and apoptosis of TNF-α-induced primary osteoblasts	Hu et al. (2021)
BMSC-Exo	Osteoclasts	bringing miRNA-335 to inhibit osteoclast differentiation and stabilizes fracture	Yang et al. (2020a)
OMSC-Exo		bringing miR-206-3p to inhibit osteoclastogenesis and promote osteogenic differentiation	Guo et al. (2021a)
MSC	Chondrocytes	enhance chondrocytes migration, proliferation, chondrogenic differentiation and matrix synthesis ability	Otsuru et al. (2018), Zhang et al. (2018)
infrapatellar fat pad (IPFP) MSCs-derived exosomes		bringing miR-100-5p to regulatedchondrocyte autophagy, thereby inhibiting apoptosis	Wu et al. (2019)
hiPS-MSC		bringing miRNA-135b to romote cell proliferation and inhibit apoptosis	Zhang et al. (2020)
MSC		attenuate inflammation and restoring matrix homeostasis in alleviating TMJ osteoarthritis	Zhang et al. (2019)
MSC	Osteocytes	anti-apoptotic effects onosteocytes and bone marrow MSCs	Yin et al. (2017)
LLLI-ADSC-exo		inhibits hypoxia-induced apoptosis and promotes bone defect repair	Zhu et al. (2017)
PSC-derived EVs		suppress osteocytes shRNA expression	Xu et al. (2019a)
ADSC	endothelial cells	bringing miRNA125a to promote the formation of endothelial tip cells and angiogenesis	Liang et al. (2016)
ADSC		bringing miRNA-21 to promote endothelial cell vascularization	An et al. (2019)
ADSC		bringing miRNA-21 and miRNA322 to promote angiogenesis	Kato et al. (2021)
HUVEC-Exo		bringing miRNA-423-5p to promote proliferation, migration and tube formation	Xu et al. (2019b)
ADSC		bringing LncRNA SNHG9 to inhibiting the inflammatory response and apoptosis, upregulate endothelial cell function	Song et al. (2020)
MSC	Macrophages	reduce the pro-inflammatory marker expression and ROS production	Zhang et al. (2022)
MSCs-Exo derived form orofacial bone		bringing miR-223 and miR-let-7c to promote polarization to M2 macrophages	Yuan et al. (2017)
ADSC	T cells	bringing miR-20a to promote the differentiation of Th17 and Treg from naive $CD4^+$ T cell	Bolandi et al. (2020)

gene expression (Yang et al., 2020a). The orofacial MSC appears to be unique in orofacial skeletal development. OMSCs are derived from neural crest cells (NCCs). The results confirmed that miRNA-206-3p is an important downstream factor of GATA4 (GATA-binding protein 4: transcription factor that regulates the expression of RUNX2 and TGF-β). Under the action of GATA4, upregulates miRNA-206-3p, promotes NFATc1 (nuclear factor of activated T cell cytoplasm 1) expression and suppresses BMP3 expression, thereby inhibiting osteoclastogenesis and promoting osteogenic differentiation (Guo et al., 2021a).

2.4 MSC-Exos act on chondrocytes

Chondrocytes treated with MSC-derived small extracellular vesicles (sEVs) enhanced migration, proliferation, chondrogenic

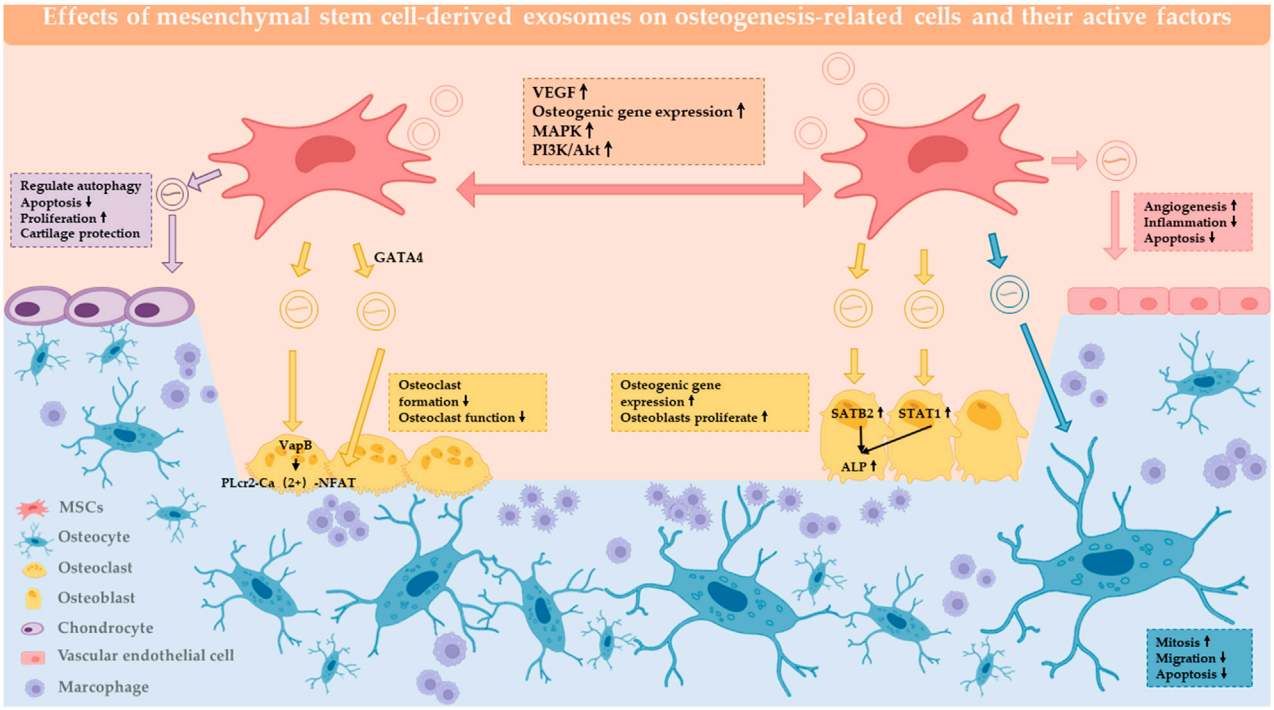

FIGURE 1
Effect of MSC-Exos on osteogenesis-related cells and active factors. MSC-EXOs act on MSCs, osteoblasts, osteoclasts, chondrocytes, osteocytes, endothelial cells, and the local immune microenvironment to have a positive impact on bone regeneration.

differentiation and matrix synthesis ability (Otsuru et al., 2018; Zhang et al., 2018). This cascade of responses induced by MSC-derived sEVs leads to the stimulation of multiple cellular responses, such as cell survival, proliferation, differentiation and migration, which facilitated tissue repair (Chew et al., 2019). Recently, it was reported that targeting mTOR signaling in chondrocytes mediated by MSC-derived sEVs as an alternative mechanism for chondroprotection. The results showed that MSC-derived sEVs downregulated mTOR signaling, and regulated IL-1-mediated chondrocyte autophagy, thereby inhibiting apoptosis and regulating cellular metabolism for matrix production (Wu et al., 2019). In a mouse OA model induced by IL-1β and collagenase, MSC-Exos was able to promote COL2A1 and proteoglycan expression and resist IL-1β-induced chondrocyte proliferation inhibition and apoptosis. Further study revealed that lncRNA-KLF3-AS1 and miRNA-206 are competitive endogenous RNAs (ceRNAs), and miRNA-206 can promote the expression of GIT1 (G-protein coupled receptor kinase interacting protein 1) lncRNA-KLF3-AS1 acts as a sponge for miRNA-206 and inhibits the expression of miRNA-206, thus achieving a protective effect against cartilage damage. In addition, hiPS-MSC-Exo acts on the PDCD4 (programmed cell death protein 4) gene *via* miRNA-135b, activating the downstream caspase-3 pathway, promoting OCN expression, promoting cell proliferation and inhibiting apoptosis (Zhang et al., 2020). MSC-Exos alleviate TMJ osteoarthritis by attenuating inflammation and restoring matrix homeostasis through the mechanism of Adenosine, a receptor for receptor cells, binds to the CD73 ligand on the surface of the MSC-Exos membrane, causing the release of Exo contents into chondrocytes and activating the Akt/ERK/AMPK pathway, thereby regulating matrix homeostasis (Zhang et al., 2019).

2.5 MSC-Exos act on osteocytes

MSC exosomes have anti-apoptotic effects on osteocytes and bone marrow MSCs, producing proliferation-promoting, migration-promoting, anti-apoptotic effects on MSCs after low-intensity laser irradiation (Yin et al., 2017). ADSC-secreted Exo (LLLI-ADSC-Exo) inhibits hypoxia-induced apoptosis and promotes bone defect repair (Zhu et al., 2017). Human perivascular stem cell (PSC)-derived EVs promote mitosis, cell migration, and suppress osteoblast shRNA expression through tetra-transmembrane proteins to achieve pro-osteogenic effects (Xu et al., 2019a).

2.6 MSC-Exos act on endothelial cells

ADSC-Exo-miRNA125a is able to bind to the 3′UTR target of delta-like4 (DDL4), thereby promoting the formation of endothelial tip cells and angiogenesis (Liang et al., 2016). Also, ADSC-miRNA-21 acts on the PTEN pathway to promote endothelial cell vascularization, while exerting a similar effect (An et al., 2019).

Meanwhile, bone regeneration repair in a rat cranial defect model was achieved by PLGA/PDA scaffold mounted with Exo in the experiment *in vivo*. Under the action of GW4869, ADSC-Exo promoted the entry of ADSC-exo-miRNA-21, miRNA-27b, miRNA322, and let-7i into endothelial cells through the ESCRT-independent pathway, where miRNA-21 inhibited PTEN as well as Smad7 pathway, and miRNA-322 inhibited Cul-2 pathway, thus promoting angiogenesis (Kato et al., 2021). Therapeutic effect of human umbilical cord MSC exosomes in osteonecrosis, attributing the anti-apoptotic and pro-survival effects of MSC exosomes to miR-

21-mediated downregulation of PTEN (phosphatase and tensin homolog) and AKT (protein kinase B) phosphorylation (Kuang et al., 2019). In a model of hindlimb ischemia, ADSC-Exo promotes M2 polarisation, inhibits iNOS expression and time-as well as dose-dependently upregulates arginase 1 (Arg-1) levels, in which miRNA-21 plays a major role and inhibits Akt phosphorylation as well as CSF-1 secretion, and through this mode of action, promotes vascular regeneration in the ischaemic limb (Zhu et al., 2020). MiRNA-423-5p acts on the sufu of HUVECs, promoting their proliferation, migration and tube formation (Xu et al., 2019b). BMSC-Exos promotes HUVEC proliferation, migration and regulates the Hippo pathway through the YAP target, promoting angiogenesis, and by transporting lysophosphatidic acid (LPA) and autocrine motility factors (ATX) also act on the Hippo pathway, prompting YAP/TAZ in complex with TEAD to direct nuclear gene expression and induce cartilage reconstruction in temporomandibular joint osteoarthritis (Wang et al., 2021b). LncRNA SNHG9 enters endothelial cells *via* ADSC-Exo and then targets and inhibits TRADD mRNA (TNF-R1-associated death domain), causing TRADD protein degradation, inhibiting the inflammatory response and apoptosis, thereby upregulating endothelial cell function (Song et al., 2020). Angiogenesis is a critical step in osteogenesis and a key target for the treatment of ischemic bone diseases.

2.7 MSC-Exos act in the osteoimmune microenvironment

Osteoimmunology reveals that the immune system and the skeletal system are closely linked and share many commonalities in terms of cytokines, receptors and signaling. Immune cells often play the role of regulators in the formation of the local bone microenvironment: by regulating the expression of various factors, they regulate osteogenic differentiation, osteolytic differentiation, fibrosis, vascularisation and other processes closely related to bone regeneration (Schmidt-Bleek et al., 2014; Chen et al., 2016). The release of regulatory factors by immune cells can influence the osteogenic and osteolytic processes in bone tissue. Macrophages play an important role in the regulation of the bone immune microenvironment. The different subtypes of macrophages correspond to the stages of fracture healing. In the inflammatory phase, activated M1 macrophages perform phagocytosis and produce pro-inflammatory cytokines such as TNF, IL-1β, IL-6 and IL-12 to promote early and mid-stage osteogenesis. In the late phase, alternative activated M2 macrophages release pro-regenerative cytokines such as IL-10, TGF-β, BMP2, and VEGF to establish an anti-inflammatory environment and promote osteochondral differentiation and angiogenesis (Shin et al., 2021). Zhang et al. (2022) developed bioactive 3D PLA-Exo scaffolds and found significantly lower expression of pro-inflammatory markers and reactive oxygen species (ROS) compared to the PLA scaffold group. After co-culture of exosomes from jawbone-derived OMMSCs with macrophages, increased miR-223 in macrophages could be achieved by inhibiting Pknox1 expression, polarizing macrophages toward the M2 type (Yuan et al., 2017). It has also been shown that ADSC-Exos containing miR-10a promotes the differentiation of naive $CD4^+$ T cells towards Th17 and Treg (Bolandi et al., 2020).

3 MSC-Exos in combination with biomaterials for bone defect repair

Currently, most bone defects are repaired with bone replacement materials (Carriel et al., 2018), which are not optimally suited to replacement due to their biological inertness, foreign body reactions and the additional damage caused after placement. The combination of biomaterials with MSC-Exos enables adhesion between cells and implants and is now used as a method for *in vivo* experiments in scientific research in the direction of osteogenesis, not only for testing the osteogenic effect of MSC-Exos, but also for clinical transformation. MSC-Exo is mostly combined with biological material by co-incubation. Among the biomaterials, the more mature materials can be divided into natural polymers, synthetic polymers, metal and inorganic non-metal materials (Ren et al., 2022a). The Classification of biomaterials combined with MSC-EXOs are summarized in Figure 2.

3.1 Natural material

3.1.1 Hydroxyapatite scaffold

Pouya et al. synthesized and characterized hydroxyapatite (HA) scaffold, following the osteogenesis and angiogenesis of HA scaffold with or without endometrial mesenchymal stem cells (hEnSCs) derived exosomes were investigated in rat with calvaria defect (Youseflee et al., 2022). Studies have shown that Alg (alginate)/HA is inferior to Alg/hydroxyapatite (Hap) in terms of mechanical properties, cytocompatibility and induction of cell differentiation in MSC (Yu et al., 2017). Therefore, some studies have chosen to use periumbilical stem cell-Exo co-embedded with hydroxyapatite (HAP) in HA-Alg for bone regeneration (Yang et al., 2020b). Some studies have also used this Exo combined with novel coral hydroxyapatite (CHA), filamentous protein (SF), glycolic chitosan (GCS) and bifunctional polyethylene glycol (DF-PEG) to form a novel self-healing hydrogel, which was successfully used for the repair of bone defects in mice (Wang et al., 2020a). MSC-Exos wrapped hydrogels form MSC-Exos-HAGel + nanohydroxy apatite-poly (hHP) to form uMSCEXO/Gel/nHP, which promotes angiogenesis by promoting endothelial cell proliferation and migration. In-depth studies have found that miRNA-21 is the target for intercellular communication and promotes the notch/DLL4 pathway to achieve pro-angiogenic purposes (Bohner et al., 2020).

3.1.2 β-tricalcium phosphate

β-tricalcium phosphate (β-TCP) is resorbable, osteoconductive and osteoinductive, making it one of the most potent bone graft substitutes (Zhang et al., 2016). Exosomes can enhance the osteoinductivity of β-TCP by activating the PI3K/Akt signaling pathway in hBMSCs, which implies that the exosome/β-TCP scaffold has better osteogenic activity than the β-TCP scaffold (Ying et al., 2020). And BMSC-Exoss-HIF1α combined with β-TCP scaffolds could repair critical-sized bone defects by promoting new bone regeneration and neovascularization (Nikhil and Kumar, 2022).

3.1.3 Composite natural scaffold

Aman et al. prepared two types of cryogels, namely chitosan-gelatin-chondroitin sulfate (CGC) for articular cartilage and nanohydroxyapatite-gelatin (HG) for subchondral bone (Bahar

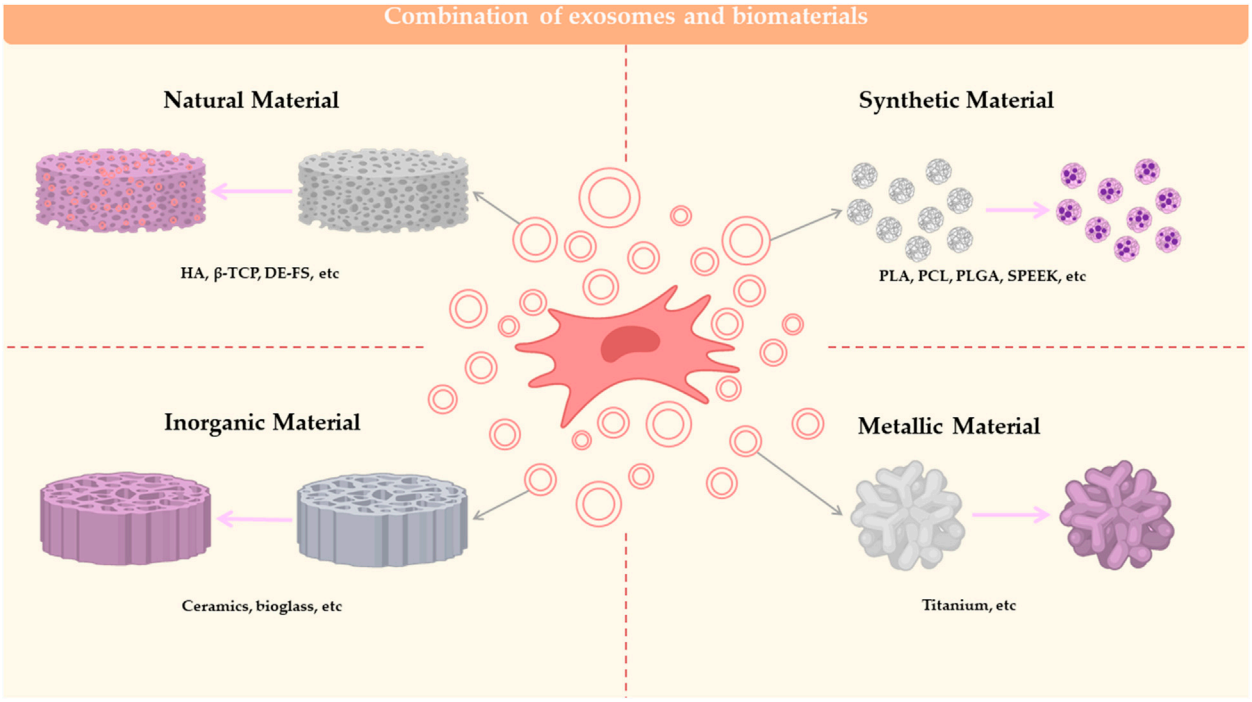

FIGURE 2
Combination of exosomes and biomaterials. Biomaterials combined with MSC-EXO for bone defect repair can be classified into 4 categories: natural material, synthetic material, inorganic material and metallic material.

et al., 2022).A novel bilayer cryogel manufactured using a single process of two layers (CGC as top layer and HG as the bottom layer) to mimic osteochondral units. The CS/HA/Exo combination is a new therapy for bone defect repair to induce bone formation. The CS scaffold significantly promoted bone regeneration compared to the control (Wang et al., 2022).

3.1.4 Others

Exosomes derived from osteogenic differentiated BMSC (OBMSC) are osteogenic, leading to the proposal of a novel exosomal decellularized fish scale (DE-FS) scaffold for promoting bone regeneration *in vivo*. The DE-FS scaffold is obtained through a process of decellularization and decalcification and has high biocompatibility and low immune rejection. The intrinsically anisotropic structure of DE-FS enhances the adhesion and proliferation of BMSCs *in vitro* (Zhang et al., 2022).

3.2 Synthetic material

3.2.1 PLA scaffolds

Zhang et al. developed bioactive 3D PLA scaffolds based on exosomes to enhance their osteogenic and immunomodulatory potential (Zhang et al., 2022). PLA (polylactic acid)-10CaSi (calcium silicate) was produced by the thermal phase separation technique Porous scaffolds were placed in HBSS and immersed for 28 days. The surface micromorphology of the scaffolds was studied by ESEM-EDX and the exo-rich complex was used for bone regeneration with good results (Gandolfi et al., 2020). Zha et al. (2021) used ATDC5-derived exosomes to encapsulate the VEGF gene and construct gene-activated engineered exosomes. The specific exosome anchor peptide CP05 was used as a flexible joint to effectively combine engineered exosome nanoparticles with 3D-printed porous bone scaffolds. It was also verified that the CP05 anchor peptide (PCL-CP05)-modified 3D printed PCL scaffold could effectively induce massive vascularized bone regeneration.

3.2.2 PCL scaffolds

Chondroprogenitor cell-derived (ATDC5) exosome plays a key role in osteogenic induction and vascular remodeling of large segmental bone defects by transfecting VEGF plasmid and binding to GPI, CP05 and CD63 to form a composite 3D scaffold material of ATDC5-Exo-VEGF-GPI CP05 using PCL as a scaffold (Zha et al., 2021). In addition, S-GSNO and MSC-Exos-modified PCL, GSNO modulates fibrin structure, limits Plt activity, inhibits coagulation and thrombosis, and GSNO alters blood coagulation structure, thus providing a critical contribution to early blood scab formation and early bone regeneration (Wang et al., 2020b).

3.2.3 PLGA scaffolds

Li et al. (2018) demonstrated the development of a polydopamine-encapsulated PLGA scaffold to achieve controlled release of hASC-Exos and repair of cranial defects in mice. Gao et al. adsorbed hypoxic Exosomes onto the surface of injectable porous poly (lactide-co-glycolide) (PLGA) microspheres with bioinspired polydopamine (PDA) coating (PMS-PDA microspheres) to induce vascularized bone regeneration in 5-mm rat calvarial defect (Gao et al., 2022). Swanson et al. (2020) improved encapsulation and controlled release of poly (lactic acid-glycolic acid) (PLGA) and poly (ethylene glycol)

(PEG) triblock copolymer microsphere exosomes on a tunable time scale.

3.2.4 Sulfonated polyetheretherketone scaffolds

Bone marrow stem cell (BMSC)-derived exosomes contain a variety of signaling molecules and have been proven to have immunomodulatory functions. Fan et al. (2021) developed a BMSC-derived Exos functionalized implant that accelerates osseointegration through immunomodulation. BMSC-Exoss is reversibly incorporated onto tannic acid (TA)-modified sulfonated polyetheretherketone (SPEEK) *via* strong interactions of TA with biomolecules. The slow release of exosomes from SPEEK can be phagocytosed by co-cultured cells, which can effectively improve the biocompatibility of SPEEK.

3.3 Inorganic non-metallic materials

Sr replaces Casi ceramics into BMSC to promote endocytosis of Exo-carrying miRNA-146a by HUVECs, allowing miRNA-146a to promote angiogenesis by inhibiting Smad4 and Nf2 pathways in target cells. This alternative approach greatly reduces rejection through the release of anti-inflammatory factors, and is of great clinical application (Liu et al., 2021b). The use of lithium-containing glass ceramics co-cultured with BMSC produced Li-BGC-BMSC-Exos, which highly expresses miRNA130a, promotes endothelial cell proliferation, migration and angiogenesis by inhibiting PTEN protein expression, as well as Akt activation (Liu et al., 2019). In addition, ionic products from bioglass acting on MSC were found to promote the expression of nSMase2 as well as Rab7a, thereby promoting endothelial cell proliferation, migration and angiogenesis by promotion of exosomes genesis and the ability to increase the content of miRNA-1290 and decrease the content of miRNA-342-5p in the output exosomes and promote the expression of vasoactive factors such as VEGF, thus promoting angiogenesis. This study, although focusing on novel biomaterials, provides constructive insights into the mechanisms of Exo product action in promoting Exo genesis (Zhang et al., 2016). BMSC and ADSC from different sources were screened for BMSC-Oi-Exo in osteoinduction medium or normal medium with increased levels of miRNA-328a, miRNA31a-5p, let-7c-5p, and let-7c-5p, and activation of BMP through miRNA regulation of BMP induction by BMPR2/Acvr 2b Smad1/5/9 phosphorylation. The Exo lyophilized formulation is also bound to the material by binding to a hierarchical porous bioactive glass scaffold to achieve maintenance of bioactivity and slow release (Liu et al., 2021c).

3.4 Metal scaffolds

Due to the limited duration of Exo activity *in vivo*, some studies have shifted the focus to maintaining the long-term stability and osteogenic ability of Exo *in vivo*. It was found that the combination of Ti-pyrrole -biotin forms a Bio-ppy-Ti complex, followed by the addition of streptavidin (SA), with ADSC-evs. The combination forms a novel biomaterial that exerts an efficient and stable bone-enabling effect (Chen et al., 2019). Alternatively, lyophilization techniques were used to address the problems of low cell implantation rate and short cell life span during Ti cage osteoinduction (Bari et al., 2021). A complex Gr-Ti scaffold was prepared using ADSC-derived Exos. The results showed that the Gr-Ti scaffold had low toxicity and good biocompatibility and promoted the adhesion and osteogenic differentiation of ADSCs. Exosomes play a role in promoting osteogenic differentiation of ADSCs: mRNA levels of RUNX2, ALP, and Osterix were significantly higher in the Gr-Ti/Exos group than in the Gr-Ti group, and this process was associated with the Wnt signaling pathway. Gr-Ti scaffolds with ADSC and ADSC-derived Exos successfully repaired mandibular defects in rabbits. The bone density and flexural strength were significantly higher in the Gr-Ti/Exos group than in the Gr-Ti group (Sun et al., 2022).

4 Regulators of MSC-Exos production

Exosomes are tiny EVs as their small yields hinder the expansion of basic research in exogenous analysis. Intracellular calcium levels, external stress, cytoskeletal blockade, drug effects, gene expression factors and other factors all affect EXOs production (Liu and Su, 2019). Therefore, it is of great significance for its practical application in the future to increase its output through the engineering production of exosomes.

4.1 MSC pretreatment

The characteristics of exosomes vary with the source of MSCs. When the MSC is subjected to different external effects, it transmits different signaling factors to exosomes to guide exosomes to work. Thus, treatment of the MSC can influence the formation, secretion and cargo of the exosome from the initiation. The Pretreatment of mesenchymal stem cells are summarized in Figure 3.

4.1.1 Physical alterations

4.1.1.1 Temperature

By changing the ambient temperature of cultured cells (42°C and 37°C), it was found that the surface markers CD9 and CD63 were more significantly expressed in the 42°C group. And that bone regeneration experiments using heat stress-induced ADSC-Exo with β-TCP (tricalcium phosphate) as a carrier were more effective than using β-TCP alone or using the ADSC with β-TCP (Akdeniz-Dogan et al., 2021).

4.1.1.2 Stress

BMSC under cyclic mechanical stress (CMS) regulates osteogenic differentiation *via* HDAC1 and Dnmt 3b epigenetically, while RUNX2-sensitive miRNA-103a is upregulated by stress in BMSC, and CMS-BMSC-Exo inhibits osteoclast formation and function by suppressing the NF-kB pathway, in the same way that acting on periodontal membrane exosome inhibits IL-1β production in M, thereby suppressing apoptosis and inhibiting bone formation (Xiao et al., 2021). The rotary cell culture system (RCCS) provides a novel mechanical environment for HUMSCs, and the different speeds of RCCS can increase exosome production within 196 h at the beginning of culture, and RCCS acts on HUMSCs through the microgravity and fluid shear of the RCCS, resulting in high expression of lncRNA-H19. lncRNA-H19 is a highly conserved sequence involved in stem cell formation and function. is a highly conserved sequence involved in stem cell differentiation, embryonic growth and tumorigenesis. This

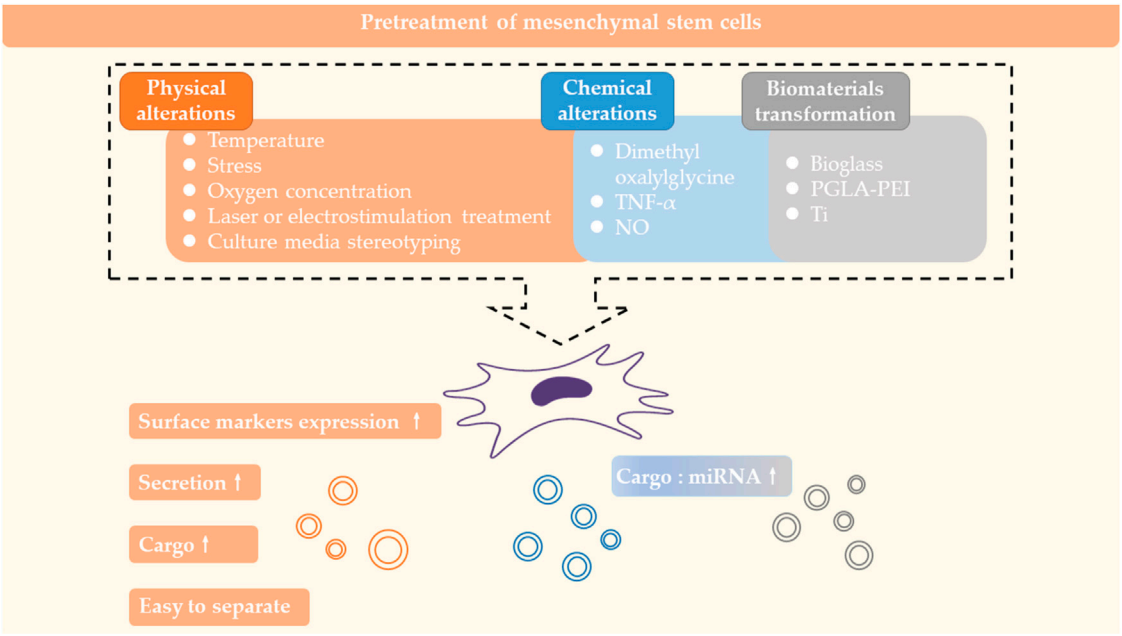

FIGURE 3
Pretreatment of mesenchymal stem cells. Physical and chemical alterations of MSCs or cultivation of MSCs with kinds of biomaterials can affect the formation, secretion and carrying of exosomes.

highly expressed lncRNA H19 is released *via* exosomes and acts on chondrocytes to promote chondrocyte proliferation, anti-apoptosis, ECM formation and function (Yan et al., 2021).

4.1.1.3 Culture media stereotyping

Bioreactors act on PDSCs, ADSCs, and SMSCs within 2D or 3D culture media through fluidic and tensile forces, and act on Yes-associated-protein (YAP) through mechanical stimulation, thereby activating the Wnt pathway and promoting the secretion and production of osteogenic exo (Guo et al., 2021b). Dental pulp pluripotent stem cells (DPPSC) are considered to be an important source of stem cells in the field of bone regeneration, and 3D culture promotes Nanog expression and osteogenesis, as well as the isolation of exosomes, providing a serum-free environment that excludes the influence of serum-derived exosomes on experimental result (Faruqu et al., 2020).

4.1.1.4 Oxygen concentration

Hypoxia-pretreated ADSC-Exo was able to promote angiogenesis in adipose grafts thereby promoting ADSC as well as adipose graft survival (Han et al., 2018). Using MLO-Y4 as a model, the environment of hypoxia and serum deprivation triggered increased apoptosis by ROS. hADSC-Exo was able to inhibit RANKL expression, thereby suppressing osteoclast-mediated osteoclastogenesis, and by upregulating Bcl-2/Bax, inhibiting ROS and reducing cytochrome enzyme production, thereby resisting apoptosis in the hypoxic environment (Ren et al., 2019). It has even been suggested that Evs in hypoxic environments are important factors in regenerative medicine. This effect is induced by HIF-1α, which hydroxylates and cleaves HIF-1α in a normoxic environment *via* prolyl hydroxylases (PHDs) on proline residues. In contrast, under hypoxia, PHDs require oxygen in conjunction with α-ketoglutarate and Fe, so HIF-1α hydroxylation is reduced and stabilized and translocated in the nucleus, activating hypoxia-sensitive genes that regulate cell cycle, apoptosis and cell differentiation (Imanirad et al., 2014). In contrast, MSC under hypoxic conditions exhibit reduced Mit activity, increased glucose depletion, reduced Mit autophagy, reduced ROS, lower telomeric shortening rates, and decreased cellular senescence overall (Noronha et al., 2019). Therefore, the influence of hypoxia has been incorporated in various studies on MSC-Exos and the hypoxic state of animal models or cultured cells has been achieved by atmospheric hypoxia, chemical hypoxia or other methods to interfere with the mechanism of action of MSC-Exos.

4.1.1.5 Laser or electrostimulation treatment

After low-intensity laser irradiation, it produced proliferation-promoting, migration-promoting and anti-apoptotic effects on MSC (Yin et al., 2017). Exosomes secreted by ADSC (LLLI-ADSC-Exo) was able to inhibit hypoxia-induced apoptosis in osteoblasts 40 and promote bone defect repair (Wang et al., 2018b). In contrast, after radiation treatment of hPMSC, miRNA-23a levels in extracted Exo decreased, thereby inhibiting the CXCL12 (chemokine 12) pathway in BMSC and thus inhibiting BMSC osteogenesis (Zhuang and Zhou, 2020). ESCRT-III-related protein Alix stimulated ADSC in the microgrooved matrix, promoting secretion of EVs, upregulation of miRNA pro-angiogenesis, and increased secretion of growth factors (Ji et al., 2021).

4.1.2 Chemical alterations

Dimethyl oxalylglycine-stimulated human bone marrow mesenchymal stem cell-derived exosomes enhance bone regeneration through angiogenesis by targeting the AKT/mTOR pathway (Liang et al., 2019). Inflammatory preconditioning of ADSC-Exo has immunosuppressive properties (Domenis et al.,

2018). Pretreatment of ADSC with TNF-α, which mimics the acute inflammatory microenvironment, promotes Wnt3a expression and enhances osteogenic gene expression in ADSC-CM by pretreating parental cells with Exo (Lu et al., 2017). Alternatively, Exo production was promoted by TNF-α acting on human dental pulp MSCs carrying miRNA-1260b, which inhibited osteoclastogenesis due to Wnt5a and promoted M2 polarization, thereby inhibiting periodontal inflammatory bone loss (Nakao et al., 2021). In addition, it has been shown that controlled Nitric Oxide releasing acts on PMSC to promote exo-miRNA-126 release as well as VEGF expression and acts on EC to promote angiogenesis and indirectly promote osteogenesis (Du et al., 2017).

4.1.3 Biomaterials transformation

The use of lithium-containing glass ceramics co-cultured with BMSC produced Li-BGC-BMSC-Exo with high expression of miRNA130a, which promoted endothelial cell proliferation, migration and angiogenesis by inhibiting PTEN protein expression, as well as Akt activation (Liu et al., 2019). In addition, ionic products in bioglass acting on MSC were found to promote the expression of nSMase2 as well as Rab7a, thus promoting Exo output by promoting Exo genesis, and were able to increase the content of miRNA-1290 in the output Exo, decreasing the content of miRNA-342-5p, and promote the expression of vasoactive factors such as VEGF, thus promoting angiogenesis, the study, while focusing on novel biomaterials, also provided constructive insights into the mechanisms of Exo promotion by the action of ionic products (Bohner et al., 2020). The composite particles made by using PLGA and PEI as coating materials and cyanine 5.5 as an indicator, in which SPIO magnetic nanoparticles were encapsulated, promoted the secretion of Exo under dynamic-induced endocytosis and were able to carry a variety of miRNAs including miRNA-2127, achieving antioxidant, regeneration, proliferation and immune (Park et al., 2020). M-Exo isolated under BMP2 stimulation was co-cultured with nanotube implants and was able to promote osteogenesis (Wei et al., 2019). It was shown that there are two structures of micro/nanostructured hierarchical titanium topographies, reticular and tubular, both of which can extend the diffusion area of BMSC on the Ti surface and promote BMSC osteogenesis *in vitro*, with the key targets being SMPD3 (sphingomyelin phosphodiesterase 3) and Rab27b (the small GTPase Rab27), which promotes Exo biogenesis and secretion to improve osseointegration (Zhang et al., 2021b).

4.2 MSC-Exos pretreatment

Exosome engineering summarises the common methods used regarding Exo treatment, such as freeze-thaw cycles, sonication, electroporation, extrusion, click chemistry, antibody, etc (Choi et al., 2021; Khayambashi et al., 2021). In contrast to the osteogenic modification of MSC-Exo, current research is more inclined to develop new ideas and methods while verifying the effectiveness and safety of the original methods.

It has been shown that ADSC-Exo proteins obtained by different isolation methods are characterized differently. Studies comparing ultracentrifugation (UC), size exclusion chromatography (SEC), Exo Quick-TC precipitation and Exo Quick-TC ULTRA isolation methods found that all proteins were involved in integrin pathways and inflammatory pathways, but the UC method also involved in cholecystokinin-R (CCKR) signaling pathway, ROS, and angiogenesis; qEV favored CCKR, EGF-R, and cytoskeletal regulation; TC favored cytoskeleton, angiogenesis, EGF-R, and PDGF-R; and Tcu appeared to be similar to TC but with a slightly lesser role for PDGF-R and concluded that different isolation methods of ADSC-Exo had different effects on LPS-stimulated cells differently, and if studies in related fields are conducted, the TCU method is recommended to promote greater tube formation function (Huang et al., 2021).

The modification of the exosome can be divided into two aspects: cargo filling and exosome membrane modification, but of course, not being bound to natural sources of exosomes, one also sets out to reassemble the components of the exosome thus engineering the production of exosomes.

4.2.1 Cargo filling

The role of MSC-Exo is largely dependent on the modulation of target cells and environments by the active factors carried by its contents, therefore enrichment of the contents in the exosome will be central to enhancing the osteogenic role of the Exo.

4.2.1.1 Electroporation

With regard to Exo modification, electroporation is the more common practice, using a PBS solution to dilute the exosome extracted from MSC and then mixing it with the target contents in an electroporation buffer. After electroporation, the electroporation solution is aspirated and placed in a new RNase-free Eppendorf tube and kept at 37°C for 30 min to restore the integrity of the exosome membrane. Subsequently, the solution was centrifuged at 10,000 × g for 2 h to remove excess target contents (Duan et al., 2021). However, it was found that membrane defects in the Exo triggered by electroporation were still difficult to repair in a short period of time, promptly by resting, thus triggering adverse effects on the structural integrity and function of the Exo (Khayambashi et al., 2021). However, it has been shown that electroporation can inactivate exo-let-7 in preosteoblasts, thereby inhibiting osteogenesis (Liu and Su, 2019).

4.2.1.2 Freeze-dried

The use of freeze-dried ADSC-Exos and GMP-compliant pharmaceuticals can be used to modulate immunity (Choi et al., 2019). And the freeze-dried method is generally not used alone, but mostly in combination with biological materials. For example, in experiments with GMSC-Exos to promote wound healing, chitosan solution was mixed with silk fibroin solution and then the chitosan-silk fibroin emulsion was incubated at −20°C for 12 h, then at −70°C for 6 h and then lyophilized in a vacuum freeze dryer for 48 h to obtain a chitosan/silk fibroin hydrogel sponge that was effective for wound healing (Bari et al., 2019).

4.2.1.3 Freeze-thaw cycles

A mixture of exosome and liposome is designed using membrane fusion of the exosome and liposome. Exosomes and liposomes are prepared separately and then mixed in equal volume ratios. the mixture is frozen in liquid nitrogen and thawed at room temperature for 15 min. The freeze-thaw cycle is repeated several times and the resulting mixture is a mixture of exosomes and liposomes. This method allows for the carriage of membrane surface proteins and markers and membrane fusion (Shi et al., 2017).

4.2.2 Membranes modification

4.2.2.1 Click chemistry

Atomic transfer radical polymerization for the packaging of Exo has also been successful (Sato et al., 2016), with PLGA (polylactic acid-ethanolic acid copolymer) + PEG (polyethylene glycol) forming triblock copolymer microspheres and assembling Exo by droplet microfluidics to form a controlled mineralized Exo, which is combined with the aqueous and organic phases to make an Exo scaffold, thus making a cell-promoting craniofacial bone regeneration free material 75. A study combined HUVEC-Exo with new coral hydroxyapatite (CHA), filamentous protein (SF), glycolic chitosan (GCS) and bifunctional polyethylene glycol (DF-PEG) to make a composite hydrogel to promote bone regeneration. It was found that the new composite had more new bone tissue and morphogenetic protein 2 (BMP-2) and the highest microvascular density 61. Another study used exosome-encapsulated dexamethasone sodium phosphate (Dex) nanoparticles (Exo/Dex) with a folic acid (FA)-polyethylene glycol (PEG)-cholesterol modified (Chol) compound on its surface to achieve an active targeted drug delivery system (Lathwal et al., 2021).

4.2.2.2 Receptor-ligand

After the study selected bone marrow stromal cell target bone (ST)-derived Exo (Ste-Exos) and clarified its characteristic action of promoting BMSC osteogenesis, ste-exos was modified to improve its difficulty in improving postmenopausal osteoporosis in OVX mice after intravenous administration *in vivo*, and the targeted delivery of Exo was achieved through the assembly of Ste-Exos and aptamer complexes to form a complex targeting BMSC (Yan et al., 2020).

4.2.2.3 Electrostatic interaction

The anionic environment in the joint cavity results in minimal utilization of MSC-Evs in intra-articular injectables. A study used a new cationic amphiphilic macromolecule: e-polylysine-polyethylene distearyl phosphatidylethanolamine to modify MSC-Evs, reversing their surface charge, and the method maintains the integrity of the Evs with no interference with the cargo, resulting in good stability in the presence of anionic macromolecule interference (Luo et al., 2019).

4.2.2.4 Hydrophobic insertion

IL-10 pretreatment of immature DC (imDC) induces tolDex, the Dex that inhibits inflammation in osteoarthritis. The study used tolerogenic DC (tolDC)-derived exosome to immobilise ROS-sensitive thioredoxin (TK)-embedded polyethylene glycol (PEG) joints on the exosome surface using a hydrophobic insertion method. This processing method was used to achieve targeted delivery of the exosome to mature DCs, reduce CD40 expression levels and counteract the inflammatory response of osteoarthritis. In addition, the presence of PEG was found to prolong the duration of action of the exosome in the circulation as well as in inflamed joints (Feng et al., 2021a).

4.2.3 New attempts

Some studies have even artificialized Exo, using nanoporous membranes, microfluidics and other techniques to extract cell fragmentation, adding specific exosome cargo and designing a mimetic of Exo for replacing biological sources of Exo that are less abundant and have more uncontrollable factors in the organism (Lee et al., 2021).

Combined with the current research progress, based on the improvement of each key step of MSC-Exo, and the trend of mainstream research ideas, we can roughly deduce the scheme of exo optimization: firstly, to provide a 3D culture environment for MSC and to encapsulate the active ingredients of MSC-Exo by modifying the contributing bone factors, to select a suitable vector for the specificity of different sites of bone defects The vector is selected for the specificity of the bone defect at different sites, and the target binding of Exo is enhanced by means of receptors and ligands to promote the maximization of Exo function. In the future, researchers may need to integrate multiple approaches to develop standardized and consistent quality procedures and propose methods for large-scale production of MSC-Exo.

5 Future perspectives

When we look for clinical applications of bone regeneration biomaterials, we are used to evaluating them in terms of safety, biocompatibility, the difficulty of preparation, price and convenience of use, so it is particularly important to build an evaluation system for biomaterials for bone defect repair.

The combination of exosomes and biomaterial scaffolds while maintaining the activity of the exosomes is the challenge of this technology, which has been solved by hydrogels, lyophilization and surface modification of the scaffold material. Recent literature has focused on keywords such as 3D bioprinting, composite scaffolds and multi-porous scaffolds, which may reveal future research hotspots in this field. However, it is important to notice that we should not stiffly composite exosomes and scaffolds at the expense of the properties of both themselves.

The advantages of combining exosomes with biological scaffolds are: 1) the enrichment of exosomes; 2) the storage of exosomes; 3) the avoidance of ethics due to “cell-free”, which is the current research trend and facilitates clinical translation. Although exosomes have a promising application in bone tissue repair, there are also many constraints that hinder their development, as they are difficult to extract, with low yields, low target utilization, and often difficult to act accurately in complex *in vivo* environments. The existing research focuses on 1) the mechanism of MSC-Exos osteogenesis in different sources and environments, and 2) the modification and functional enhancement of MSC-Exos.

As for materials, they should not only act as a carrier, but should intervene at all stages of exosome production. For example, combining different properties of materials to promote the secretion of exosomes containing active ingredients from parental cells, or the isolation or accumulation of exosomes through the adsorption of materials, and also researchers have focused on how to achieve functional substitution of exosomes through the exploration of lipophilic materials, thus enabling the mass production of exosomes.

Although MSC-Exos were promising therapeutic agents, the research on the efficacy of MSC-Exos on bone regeneration is still in its infancy. Numerous *in vitro* trials have demonstrated the effectiveness of MSC-Exo in bone disease, (Feng et al., 2021b), while most experiments *in vivo* have been conducted on small animals (including rats, mice and rabbits), validating the effectiveness of MSC-Exo on bone regeneration in animal models of bone defects and diseases such as osteonecrosis and

osteoporosis (Tan et al., 2020), supporting the basis for clinical translation of MSC therapeutic agents (Ren et al., 2022b). However, the clinical trials of MSC-Exo is still limited. www.clinicaltrials.gov lists 7 clinical trials of exosomes in relation to bone, 3 of which describe the use of exosomes as an early diagnostic tool and 2 for clinical treatment. One is attempting to verify whether transplantation of hASCs-CM and a synthetic bone substitute can facilitate maxillary bone repair, and another is attempting to verify the feasibility of intradiscal injection of PRP with exosomes derived from blood for the treatment of chronic low back pain but has not yet published results. As the translation of MSC-Exo-based therapies from preclinical studies to the clinic requires a number of key parameters, including the establishment of optimal MSC culture conditions and exosome production, isolation and storage protocols to provide batch-to-batch consistency, optimal dosing and exosome dosing schedules, and the development of potency assays to allow efficacy evaluation (Mendt et al., 2019). More clinical trials remain to be conducted.

In addition, we should also focus on enhancing the compliance of MSC-Exosomes and the immunomodulatory effects of MSC-Exosomes on bone regeneration. Bone regeneration is not only about bone defects caused by trauma and fractures, but also about bone loss caused by systemic diseases such as osteoporosis, femoral necrosis or drugs. Therefore, it is not enough to combine exosomes with biomaterials, but also to focus on the concentration enhancement and targeted presentation of exosomes in circulation, and thus to maximize the contribution of exosomes to the three basic elements of bone regeneration.

6 Conclusion

The production of MSC-Exos can be achieved by direct action on various osteogenic cells or by carrying substances that affect cellular activity factors or the local internal environment in target cells, or by binding to biological materials to activate the osteogenic framework. The generation of MSC-Exos can be achieved by pretreatment of its parental cells and exosome contents and membranes with a view to obtaining the possibility of mass production of MSC-Exos.

Author contributions

SR and YL were responsible for the project design, data collection, results in analysis, manuscript preparation, and literature search. WL was responsible for the literature search and preparation of the manuscript. LY was responsible for the project design, data analysis, the content of the article, and funding collection. MZ was responsible for the project design, manuscript preparation, and funding collection.

Funding

This work was sponsored by the Natural Science Foundation of Liaoning Province (2022-YGJC-69) and the support program for excellent young scholars of China Medical University.

Conflict of interest

The authors declare that the research was conducted in the absence of any commercial or financial relationships that could be construed as a potential conflict of interest.

Publisher's note

References

Akdeniz-Dogan, Z., Sendur, S., Karademir-Yilmaz, B., Bugdayci, O., Cilingir-Kaya, O. T., Yilmaz-Goler, A. M., et al. (2021). The role of extracellular vesicles secreted from thermal stress-induced adipose-derived stem cells on bone regeneration. *J. Craniofac Surg.* 32 (6), 2245–2250. doi:10.1097/scs.0000000000007901

An, Y., Zhao, J., Nie, F., Qin, Z., Xue, H., Wang, G., et al. (2019). Exosomes from adipose-derived stem cells (ADSCs) overexpressing miR-21 promote vascularization of endothelial cells. *Sci. Rep.* 9 (1), 12861. doi:10.1038/s41598-019-49339-y

Bahar, D., Gonen, Z. B., Gumusderelioglu, M., Onger, M., Tokak, E., Ozturk-Kup, F., et al. (2022). Repair of rat calvarial bone defect by using exosomes of umbilical cord–derived mesenchymal stromal cells embedded in chitosan/hydroxyapatite scaffolds. *Int. J. Oral Maxillofac. Implants* 37 (5), 943–950. doi:10.11607/jomi.9515

Bari, E., Perteghella, S., Catenacci, L., Sorlini, M., Croce, S., Mantelli, M., et al. (2019). Freeze-dried and GMP-compliant pharmaceuticals containing exosomes for acellular mesenchymal stromal cell immunomodulant therapy. *Nanomedicine Lond. Engl.* 14 (6), 753–765. doi:10.2217/nnm-2018-0240

Bari, E., Tartara, F., Cofano, F., di Perna, G., Garbossa, D., Perteghella, S., et al. (2021). Freeze-dried secretome (lyosecretome) from mesenchymal stem/stromal cells promotes the osteoinductive and osteoconductive properties of titanium cages. *Int. J. Mol. Sci.* 22 (16), 8445. doi:10.3390/ijms22168445

Basso, M., and Bonetto, V. (2016). Extracellular vesicles and a novel form of communication in the brain. *Front. Neurosci.* 10, 127. doi:10.3389/fnins.2016.00127

Battafarano, G., Rossi, M., De Martino, V., Marampon, F., Borro, L., Secinaro, A., et al. (2021). Strategies for bone regeneration: From graft to tissue engineering. *Int. J. Mol. Sci.* 22 (3), 1128. doi:10.3390/ijms22031128

Bohner, M., Santoni, B. L. G., and Döbelin, N. (2020). β-tricalcium phosphate for bone substitution: Synthesis and properties. *Acta Biomater.* 113, 23–41. doi:10.1016/j.actbio.2020.06.022

Bolandi, Z., Mokhberian, N., Eftekhary, M., Sharifi, K., Soudi, S., Ghanbarian, H., et al. (2020). Adipose derived mesenchymal stem cell exosomes loaded with miR-10a promote the differentiation of Th17 and Treg from naive CD4+ T cell. *Life Sci.* 259, 118218. doi:10.1016/j.lfs.2020.118218

Brown, C., McKee, C., Bakshi, S., Walker, K., Hakman, E., Halassy, S., et al. (2019). Mesenchymal stem cells: Cell therapy and regeneration potential. *J. Tissue Eng. Regen. Med.* 13 (9), 1738–1755. doi:10.1002/term.2914

Carriel, V., Geuna, S., and Alaminos, M. (2018). *Ex vivo* and *in vivo* stem cells-based tissue engineering strategies for their use in regenerative medicine. *Stem Cells Int.* 2018, 1–2. doi:10.1155/2018/7143930

Chen, L., Mou, S., Li, F., Zeng, Y., Sun, Y., Horch, R. E., et al. (2019). Self-assembled human adipose-derived stem cell-derived extracellular vesicle-functionalized biotin-doped polypyrrole titanium with long-term stability and potential osteoinductive ability. *ACS Appl. Mater Interfaces* 11 (49), 46183–46196. doi:10.1021/acsami.9b17015

Chen, Z., Klein, T., Murray, R. Z., Crawford, R., Chang, J., Wu, C., et al. (2016). Osteoimmunomodulation for the development of advanced bone biomaterials. *Mater Today* 19 (6), 304–321. doi:10.1016/j.mattod.2015.11.004

Chew, J. R. J., Chuah, S. J., Teo, K. Y. W., Zhang, S., Lai, R. C., Fu, J. H., et al. (2019). Mesenchymal stem cell exosomes enhance periodontal ligament cell functions and promote periodontal regeneration. *Acta Biomater.* 89, 252–264. doi:10.1016/j.actbio.2019.03.021

Choi, H., Choi, Y., Yim, H. Y., Mirzaaghasi, A., Yoo, J. K., and Choi, C. (2021). Biodistribution of exosomes and engineering strategies for targeted delivery of therapeutic exosomes. *Tissue Eng. Regen. Med.* 18 (4), 499–511. doi:10.1007/s13770-021-00361-0

Choi, S. Y., Han, E. C., Hong, S. H., Kwon, T. G., Lee, Y., and Lee, H. J. (2019). Regulating osteogenic differentiation by suppression of exosomal MicroRNAs. *Tissue Eng. Part A* 25 (15-16), 1146–1154. doi:10.1089/ten.tea.2018.0257

Domenis, R., Cifu, A., Quaglia, S., Pistis, C., Moretti, M., Vicario, A., et al. (2018). Pro inflammatory stimuli enhance the immunosuppressive functions of adipose mesenchymal stem cells-derived exosomes. *Sci. Rep.* 8 (1), 13325. doi:10.1038/s41598-018-31707-9

Du, W., Su, L., Zhang, N., and Wang, H. (2019). Exosomes derived from preadipocytes improve osteogenic differentiation, potentially via reduced miR223 expression. *Mol. Med. Rep.* 19 (2), 951–958. doi:10.3892/mmr.2018.9760

Du, W., Zhang, K., Zhang, S., Wang, R., Nie, Y., Tao, H., et al. (2017). Enhanced proangiogenic potential of mesenchymal stem cell-derived exosomes stimulated by a nitric oxide releasing polymer. *Biomaterials* 133, 70–81. doi:10.1016/j.biomaterials.2017.04.030

Duan, L., Xu, X., Xu, L., Chen, H., Li, X., Alahdal, M., et al. (2021). Exosome-mediated drug delivery for cell-free therapy of osteoarthritis. *Curr. Med. Chem.* 28 (31), 6458–6483. doi:10.2174/1875533xmtexenjqg4

EL Andaloussi, S., Mager, I., Breakefield, X. O., and Wood, M. J. A. (2013). Extracellular vesicles: Biology and emerging therapeutic opportunities. *Nat. Rev. Drug Discov.* 12 (5), 347–357. doi:10.1038/nrd3978

Fan, L., Guan, P., Xiao, C., Wen, H., Wang, Q., Liu, C., et al. (2021). Exosome-functionalized polyetheretherketone-based implant with immunomodulatory property for enhancing osseointegration. *Bioact. Mater* 6 (9), 2754–2766. doi:10.1016/j.bioactmat.2021.02.005

Faruqu, F. N., Zhou, S., Sami, N., Gheidari, F., Lu, H., and Al-Jamal, K. T. (2020). Three-dimensional culture of dental pulp pluripotent-like stem cells (DPPSCs) enhances Nanog expression and provides a serum-free condition for exosome isolation. *FASEB Bioadv* 2 (7), 419–433. doi:10.1096/fba.2020-00025

Feng, K., Xie, X., Yuan, J., Gong, L., Zhu, Z., Zhang, J., et al. (2021). Reversing the surface charge of MSC-derived small extracellular vesicles by εPL-PEG-DSPE for enhanced osteoarthritis treatment. *J. Extracell. Vesicles* 10 (13), e12160. doi:10.1002/jev2.12160

Feng, Z. Y., Zhang, Q. Y., Tan, J., and Xie, H. Q. (2021). Techniques for increasing the yield of stem cell-derived exosomes: What factors may be involved? *Sci. China Life Sci.* 65, 1325–1341. doi:10.1007/s11427-021-1997-2

Gandolfi, M. G., Gardin, C., Zamparini, F., Ferroni, L., Esposti, M. D., Parchi, G., et al. (2020). Mineral-doped poly(L-lactide) acid scaffolds enriched with exosomes improve osteogenic commitment of human adipose-derived mesenchymal stem cells. *Nanomater. (Basel)* 10 (3), 432. doi:10.3390/nano10030432

Gao, Y., Yuan, Z., Yuan, X., Wan, Z., Yu, Y., Zhan, Q., et al. (2022). Bioinspired porous microspheres for sustained hypoxic exosomes release and vascularized bone regeneration. *Bioact. Mater* 14, 377–388. doi:10.1016/j.bioactmat.2022.01.041

Guo, S., Debbi, L., Zohar, B., Samuel, R., Arzi, R. S., Fried, A. I., et al. (2021). Stimulating extracellular vesicles production from engineered tissues by mechanical forces. *Nano Lett.* 21 (6), 2497–2504. doi:10.1021/acs.nanolett.0c04834

Guo, S., Gu, J., Ma, J., Xu, R., Wu, Q., Meng, L., et al. (2021). GATA4-driven miR-206-3p signatures control orofacial bone development by regulating osteogenic and osteoclastic activity. *Theranostics* 11 (17), 8379–8395. doi:10.7150/thno.58052

Han, Y. D., Bai, Y., Yan, X. L., Ren, J., Zeng, Q., Li, X. d., et al. (2018). Co-transplantation of exosomes derived from hypoxia-preconditioned adipose mesenchymal stem cells promotes neovascularization and graft survival in fat grafting. *Biochem. Biophys. Res. Commun.* 497 (1), 305–312. doi:10.1016/j.bbrc.2018.02.076

Heo, J. S., Choi, Y., and Kim, H. O. (2019). Adipose-derived mesenchymal stem cells promote M2 macrophage phenotype through exosomes. *Stem Cells Int.* 2019, 1–10. doi:10.1155/2019/7921760

Hu, H., Wang, D., Li, L., Yin, H., He, G., and Zhang, Y. (2021). Role of microRNA-335 carried by bone marrow mesenchymal stem cells-derived extracellular vesicles in bone fracture recovery. *Cell death Dis.* 12 (2), 156. doi:10.1038/s41419-021-03430-3

Huang, L. H., Rau, C. S., Wu, S. C., Wu, Y., Wu, C. J., Tsai, C., et al. (2021). Identification and characterization of hADSC-derived exosome proteins from different isolation methods. *J. Cell Mol. Med.* 25 (15), 7436–7450. doi:10.1111/jcmm.16775

Imanirad, P., Solaimani Kartalaei, P., Crisan, M., Vink, C., Yamada-Inagawa, T., de Pater, E., et al. (2014). HIF1α is a regulator of hematopoietic progenitor and stem cell development in hypoxic sites of the mouse embryo. *Stem Cell Res.* 12 (1), 24–35. doi:10.1016/j.scr.2013.09.006

Ji, Y., Han, W., Fu, X., Li, J., Wu, Q., and Wang, Y. (2021). Improved small extracellular vesicle secretion of rat adipose-derived stem cells by micro grooved substrates through upregulation of the ESCRT-III-associated protein Alix. *Adv. Healthc. Mater* 10 (16), 2101876. doi:10.1002/adhm.202101876

Jia, Y., Qiu, S., Xu, J., Kang, Q., and Chai, Y. (2020). Exosomes secreted by young mesenchymal stem cells promote new bone formation during distraction osteogenesis in older rats. *Calcif. Tissue Int.* 106 (5), 509–517. doi:10.1007/s00223-019-00656-4

Jin, Q., Li, P., Yuan, K., Zhao, F., Zhu, X., Zhang, P., et al. (2020). Extracellular vesicles derived from human dental pulp stem cells promote osteogenesis of adipose-derived stem cells via the MAPK pathway. *J. Tissue Eng.* 11, 204173142097556. doi:10.1177/2041731420975569

Kargozar, S., Mozafari, M., Hamzehlou, S., Brouki Milan, P., Kim, H. W., and Baino, F. (2019). Bone tissue engineering using human cells: A comprehensive review on recent trends, current prospects, and recommendations. *Appl. Sci.* 9 (1), 174. doi:10.3390/app9010174

Kato, T., Kato, K., Shimizu, Y., Takefuji, M., and Murohara, T. (2021). Treatment with adipose-derived regenerative cells enhances ischemia-induced angiogenesis via exosomal microRNA delivery in mice. *Nagoya J. Med. Sci.* 83 (3), 465–476. doi:10.18999/nagjms.83.3.465

Khayambashi, P., Iyer, J., Pillai, S., Upadhyay, A., Zhang, Y., and Tran, S. (2021). Hydrogel encapsulation of mesenchymal stem cells and their derived exosomes for tissue engineering. *Int. J. Mol. Sci.* 22 (2), 684. doi:10.3390/ijms22020684

Kim, Y. S., and Mikos, A. G. (2021). Emerging strategies in reprogramming and enhancing the fate of mesenchymal stem cells for bone and cartilage tissue engineering. *J. Control Release* 330, 565–574. doi:10.1016/j.jconrel.2020.12.055

Kuang, M. J., Huang, Y., Zhao, X. G., Zhang, R., Ma, J. x., Wang, D. c., et al. (2019). Exosomes derived from Wharton's jelly of human umbilical cord mesenchymal stem cells reduce osteocyte apoptosis in glucocorticoid-induced osteonecrosis of the femoral head in rats via the miR-21-PTEN-AKT signalling pathway. *Int. J. Biol. Sci.* 15 (9), 1861–1871. doi:10.7150/ijbs.32262

Lathwal, S., Yerneni, S. S., Boye, S., Muza, U. L., Takahashi, S., Sugimoto, N., et al. (2021). Engineering exosome polymer hybrids by atom transfer radical polymerization. *Proc. Natl. Acad. Sci. U. S. A.* 118 (2), e2020241118. doi:10.1073/pnas.2020241118

Lee, E. S., Sul, J. H., Shin, J. M., Shin, S., Lee, J. A., Kim, H. K., et al. (2021). Reactive oxygen species-responsive dendritic cell-derived exosomes for rheumatoid arthritis. *Acta Biomater.* 128, 462–473. doi:10.1016/j.actbio.2021.04.026

Li, W., Liu, Y., Zhang, P., Tang, Y., Zhou, M., Jiang, W., et al. (2018). Tissue-engineered bone immobilized with human adipose stem cells-derived exosomes promotes bone regeneration. *ACS Appl. Mater Interfaces* 10 (6), 5240–5254. doi:10.1021/acsami.7b17620

Li, X., Zheng, Y., Hou, L., Zhou, Z., Huang, Y., Zhang, Y., et al. (2019). Exosomes derived from maxillary BMSCs enhanced the osteogenesis in iliac BMSCs. *Oral Dis.* 26 (1), 131–144. doi:10.1111/odi.13202

Liang, B., Liang, J. M., Ding, J. N., Xu, J., Xu, J. G., and Chai, Y. M. (2019). Dimethyloxaloylglycine-stimulated human bone marrow mesenchymal stem cell-derived exosomes enhance bone regeneration through angiogenesis by targeting the AKT/mTOR pathway. *Stem Cell Res. Ther.* 10 (1), 335. doi:10.1186/s13287-019-1410-y

Liang, X., Zhang, L., Wang, S., Han, Q., and Zhao, R. C. (2016). Exosomes secreted by mesenchymal stem cells promote endothelial cell angiogenesis by transferring miR-125a. *J. Cell Sci.* 129 (11), 2182–2189. doi:10.1242/jcs.170373

Liu, A., Lin, D., Zhao, H., Chen, L., Cai, B., Lin, K., et al. (2021). Optimized BMSC-derived osteoinductive exosomes immobilized in hierarchical scaffold via lyophilization for bone repair through Bmpr2/Acvr2b competitive receptor-activated Smad pathway. *Biomaterials* 272, 120718. doi:10.1016/j.biomaterials.2021.120718

Liu, C., and Su, C. (2019). Design strategies and application progress of therapeutic exosomes. *Theranostics* 9 (4), 1015–1028. doi:10.7150/thno.30853

Liu, L., Guo, S., Shi, W., Liu, Q., Huo, F., Wu, Y., et al. (2021). Bone marrow mesenchymal stem cell-derived small extracellular vesicles promote periodontal regeneration. *Tissue Eng. Part A* 27 (13-14), 962–976. doi:10.1089/ten.tea.2020.0141

Liu, L., Liu, Y., Feng, C., Chang, J., Fu, R., Wu, T., et al. (2019). Lithium-containing biomaterials stimulate bone marrow stromal cell-derived exosomal miR-130a secretion to promote angiogenesis. *Biomaterials* 192, 523–536. doi:10.1016/j.biomaterials.2018.11.007

Liu, L., Yu, F., Li, L., Zhou, L., Zhou, T., Xu, Y., et al. (2021). Bone marrow stromal cells stimulated by strontium-substituted calcium silicate ceramics: Release of exosomal miR-146a regulates osteogenesis and angiogenesis. *Acta Biomater.* 119, 444–457. doi:10.1016/j.actbio.2020.10.038

Lu, Z., Chen, Y., Dunstan, C., Roohani-Esfahani, S., and Zreiqat, H. (2017). Priming adipose stem cells with tumor necrosis factor-alpha preconditioning potentiates their exosome efficacy for bone regeneration. *Tissue Eng. Part A* 23 (21-22), 1212–1220. doi:10.1089/ten.tea.2016.0548

Luo, Z. W., Li, F. X., Liu, Y. W., Rao, S. S., Yin, H., Huang, J., et al. (2019). Aptamer-functionalized exosomes from bone marrow stromal cells target bone to promote bone regeneration. *Nanoscale* 11 (43), 20884–20892. doi:10.1039/c9nr02791b

Mendt, M., Rezvani, K., and Shpall, E. (2019). Mesenchymal stem cell-derived exosomes for clinical use. *Bone Marrow Transplant.* 54 (S2), 789–792. doi:10.1038/s41409-019-0616-z

Nakao, Y., Fukuda, T., Zhang, Q., Sanui, T., Shinjo, T., Kou, X., et al. (2021). Exosomes from TNF-alpha-treated human gingiva-derived MSCs enhance M2 macrophage polarization and inhibit periodontal bone loss. *Acta Biomater.* 122, 306–324. doi:10.1016/j.actbio.2020.12.046

Nikhil, A., and Kumar, A. (2022). Evaluating potential of tissue-engineered cryogels and chondrocyte derived exosomes in articular cartilage repair. *Biotechnol. Bioeng.* 119 (2), 605–625. doi:10.1002/bit.27982

Noronha, N. C., Mizukami, A., Caliári-Oliveira, C., Cominal, J. G., Rocha, J. L. M., Covas, D. T., et al. (2019). Priming approaches to improve the efficacy of mesenchymal stromal cell-based therapies. *Stem Cell Res. Ther.* 10 (1), 131. doi:10.1186/s13287-019-1224-y

Otsuru, S., Desbourdes, L., Guess, A. J., Hofmann, T. J., Relation, T., Kaito, T., et al. (2018). Extracellular vesicles released from mesenchymal stromal cells stimulate bone growth in osteogenesis imperfecta. *Cytotherapy* 20 (1), 62–73. doi:10.1016/j.jcyt.2017.09.012

Park, D. J., Yun, W. S., Kim, W., Park, J. E., Lee, S. H., Ha, S., et al. (2020). Improvement of stem cell-derived exosome release efficiency by surface-modified nanoparticles. *J. Nanobiotechnology* 18 (1), 178. doi:10.1186/s12951-020-00739-7

Peng, H., Ji, W., Zhao, R., Yang, J., Lu, Z., Li, Y., et al. (2020). Exosome: A significant nano-scale drug delivery carrier. *J. Mater Chem. B* 8 (34), 7591–7608. doi:10.1039/d0tb01499k

Pizzicannella, J., Diomede, F., Gugliandolo, A., Chiricosta, L., Bramanti, P., Merciaro, I., et al. (2019). 3D printing PLA/gingival stem cells/EVs upregulate miR-2861 and -210 during osteoangiogenesis commitment. *Int. J. Mol. Sci.* 20 (13), 3256. doi:10.3390/ijms20133256

Pizzicannella, J., Gugliandolo, A., Orsini, T., Fontana, A., Ventrella, A., Mazzon, E., et al. (2019). Engineered extracellular vesicles from human periodontal-ligament stem cells increase VEGF/VEGFR2 expression during bone regeneration. *Front. physiology* 10, 512. doi:10.3389/fphys.2019.00512

Ren, L., Song, Z. J., Cai, Q. W., Chen, R. x., Zou, Y., Fu, Q., et al. (2019). Adipose mesenchymal stem cell-derived exosomes ameliorate hypoxia/serum deprivation-induced osteocyte apoptosis and osteocyte-mediated osteoclastogenesis *in vitro*. *Biochem. Biophys. Res. Commun.* 508 (1), 138–144. doi:10.1016/j.bbrc.2018.11.109

Ren, S., Guo, S., Yang, L., and Wang, C. (2022). Effect of composite biodegradable biomaterials on wound healing in diabetes. *Front. Bioeng. Biotechnol.* 10, 1060026. doi:10.3389/fbioe.2022.1060026

Ren, S., Wang, C., and Guo, S. (2022). Review of the role of mesenchymal stem cells and exosomes derived from mesenchymal stem cells in the treatment of orthopedic disease. *Med. Sci. Monit.* 28, e935937. doi:10.12659/msm.935937

Sato, Y. T., Umezaki, K., Sawada, S., Mukai, S. a., Sasaki, Y., Harada, N., et al. (2016). Engineering hybrid exosomes by membrane fusion with liposomes. *Sci. Rep.* 6, 21933. doi:10.1038/srep21933

Schlundt, C., Fischer, H., Bucher, C. H., Rendenbach, C., Duda, G. N., and Schmidt-Bleek, K. (2021). The multifaceted roles of macrophages in bone regeneration: A story of polarization, activation and time. *Acta Biomater.* 133, 46–57. doi:10.1016/j.actbio.2021.04.052

Schmidt-Bleek, K., Schell, H., Lienau, J., Schulz, N., Hoff, P., Pfaff, M., et al. (2014). Initial immune reaction and angiogenesis in bone healing. *J. Tissue Eng. Regen. Med.* 8 (2), 120–130. doi:10.1002/term.1505

Schott, N. G., Friend, N. E., and Stegemann, J. P. (2021). Coupling osteogenesis and vasculogenesis in engineered orthopedic tissues. *Tissue Eng. Part B Rev.* 27 (3), 199–214. doi:10.1089/ten.teb.2020.0132

Shi, Q., Qian, Z., Liu, D., Sun, J., Wang, X., Liu, H., et al. (2017). GMSC-derived exosomes combined with a chitosan/silk hydrogel sponge accelerates wound healing in a diabetic rat skin defect model. *Front. physiology* 8, 904. doi:10.3389/fphys.2017.00904

Shin, R. L.-Y., Lee, C. W., Shen, O. Y. J., Xu, H., and Lee, O. K. S. (2021). The crosstalk between mesenchymal stem cells and macrophages in bone regeneration: A systematic review. *Stem Cells Int.* 2021, 1–21. doi:10.1155/2021/8835156

Sobacchi, C., Schulz, A., Coxon, F. P., Villa, A., and Helfrich, M. H. (2013). Osteopetrosis: Genetics, treatment and new insights into osteoclast function. *Nat. Rev. Endocrinol.* 9 (9), 522–536. doi:10.1038/nrendo.2013.137

Song, Y., Li, H., Ren, X., and Feng, C. (2020). SNHG9, delivered by adipocyte-derived exosomes, alleviates inflammation and apoptosis of endothelial cells through suppressing TRADD expression. *Eur. J. Pharmacol.* 872, 172977. doi:10.1016/j.ejphar.2020.172977

Sun, X., Yang, S., Tong, S., and Guo, S. (2022). Study on exosomes promoting the osteogenic differentiation of ADSCs in graphene porous titanium alloy scaffolds. *Front. Bioeng. Biotechnol.* 10, 905511. doi:10.3389/fbioe.2022.905511

Swanson, W. B., Zhang, Z., Xiu, K., Gong, T., Eberle, M., Wang, Z., et al. (2020). Scaffolds with controlled release of pro-mineralization exosomes to promote craniofacial bone healing without cell transplantation. *Acta Biomater.* 118, 215–232. doi:10.1016/j.actbio.2020.09.052

Tan, S. H. S., Wong, J., Sim, S., Tjio, C., Wong, K., Chew, J., et al. (2020). Mesenchymal stem cell exosomes in bone regenerative strategies—A systematic review of preclinical studies. *Mater. Today Bio* 7, 100067. doi:10.1016/j.mtbio.2020.100067

Verweij, F. J., Revenu, C., Arras, G., Dingli, F., Loew, D., Pegtel, D. M., et al. (2019). Live tracking of inter-organ communication by endogenous exosomes *in vivo*. *Dev. Cell* 48 (4), 573–589.e4. doi:10.1016/j.devcel.2019.01.004

Wang, C. G., Liao, Z., Xiao, H., Liu, H., Hu, Y. H., Liao, Q. D., et al. (2019). LncRNA KCNQ1OT1 promoted BMP2 expression to regulate osteogenic differentiation by sponging miRNA-214. *Exp. Mol. pathology* 107, 77–84. doi:10.1016/j.yexmp.2019.01.012

Wang, L., Wang, J., Zhou, X., Sun, J., Zhu, B., Duan, C., et al. (2020). A new self-healing hydrogel containing hucMSC-derived exosomes promotes bone regeneration. *Front. Bioeng. Biotechnol.* 8, 564731. doi:10.3389/fbioe.2020.564731

Wang, M., Yuan, Q., and Xie, L. (2018). Mesenchymal stem cell-based immunomodulation: Properties and clinical application. *Stem Cells Int.* 2018, 1–12. doi:10.1155/2018/3057624

Wang, S. Z., Jia, J., and Chen, C. H. (2021). lncRNA-KCNQ1OT1: A potential target in exosomes derived from adipose-derived stem cells for the treatment of osteoporosis. *Stem Cells Int.* 2021, 1–17. doi:10.1155/2021/7690006

Wang, X., Ao, J., Lu, H., Zhao, Q., Ma, Y., Zhang, J., et al. (2020). <p>Osteoimmune modulation and guided osteogenesis promoted by barrier membranes incorporated with S-nitrosoglutathione (GSNO) and mesenchymal stem cell-derived exosomes</p>. *Int. J. Nanomedicine* 15, 3483–3496. doi:10.2147/ijn.s248741

Wang, Y., Kong, B., Chen, X., Liu, R., Zhao, Y., Gu, Z., et al. (2022). BMSC exosome-enriched acellular fish scale scaffolds promote bone regeneration. *J. Nanobiotechnology* 20 (1), 444. doi:10.1186/s12951-022-01646-9

Wang, Y., Zhao, M., Li, W., Yang, Y., Zhang, Z., Ma, R., et al. (2021). BMSC-derived small extracellular vesicles induce cartilage reconstruction of temporomandibular joint osteoarthritis via autotaxin-YAP signaling Axis. *Front. Cell Dev. Biol.* 9, 656153. doi:10.3389/fcell.2021.656153

Wang, Y. H., Wu, J. Y., Kong, S. C., Chiang, M. H., Ho, M. L., Yeh, M. L., et al. (2018). Low-power laser irradiation and human adipose-derived stem cell treatments promote bone regeneration in critical-sized calvarial defects in rats. *PLoS One* 13 (4), e0195337. doi:10.1371/journal.pone.0195337

Wei, F., Li, M., Crawford, R., Zhou, Y., and Xiao, Y. (2019). Exosome-integrated titanium oxide nanotubes for targeted bone regeneration. *Acta Biomater.* 86, 480–492. doi:10.1016/j.actbio.2019.01.006

Wu, J., Kuang, L., Chen, C., Yang, J., Zeng, W. N., Li, T., et al. (2019). miR-100-5p-abundant exosomes derived from infrapatellar fat pad MSCs protect articular cartilage and ameliorate gait abnormalities via inhibition of mTOR in osteoarthritis. *Biomaterials* 206, 87–100. doi:10.1016/j.biomaterials.2019.03.022

Xia, X., Chan, K. F., Wong, G. T. Y., Wang, P., Liu, L., Yeung, B. P. M., et al. (2019). Mesenchymal stem cells promote healing of nonsteroidal anti-inflammatory drug-related peptic ulcer through paracrine actions in pigs. *Sci. Transl. Med.* 11 (516), eaat7455. doi:10.1126/scitranslmed.aat7455

Xiao, F., Zuo, B., Tao, B., Wang, C., Li, Y., Peng, J., et al. (2021). Exosomes derived from cyclic mechanical stretch-exposed bone marrow mesenchymal stem cells inhibit RANKL-induced osteoclastogenesis through the NF-κB signaling pathway. *Ann. Transl. Med.* 9 (9), 798. doi:10.21037/atm-21-1838

Xu, F., Xiang, Q., Huang, J., Chen, Q., Yu, N., Long, X., et al. (2019). Exosomal miR-423-5p mediates the proangiogenic activity of human adipose-derived stem cells by targeting Sufu. *Stem Cell Res. Ther.* 10 (1), 106. doi:10.1186/s13287-019-1196-y

Xu, J., Wang, Y., Hsu, C. Y., Gao, Y., Meyers, C. A., Chang, L., et al. (2019). Human perivascular stem cell-derived extracellular vesicles mediate bone repair. *Elife* 8, e48191. doi:10.7554/elife.48191

Yan, F., Zhong, Z., Wang, Y., Feng, Y., Mei, Z., Li, H., et al. (2020). Exosome-based biomimetic nanoparticles targeted to inflamed joints for enhanced treatment of rheumatoid arthritis. *J. Nanobiotechnology* 18 (1), 115. doi:10.1186/s12951-020-00675-6

Yan, L., Liu, G., and Wu, X. (2021). Exosomes derived from umbilical cord mesenchymal stem cells in mechanical environment show improved osteochondral activity via upregulation of LncRNA H19. *J. Orthop. Transl.* 26, 111–120. doi:10.1016/j.jot.2020.03.005

Yang, S., Guo, S., Tong, S., and Sun, X. (2020). Exosomal miR-130a-3p regulates osteogenic differentiation of Human Adipose-Derived stem cells through mediating SIRT7/Wnt/β-catenin axis. *Cell Prolif.* 53 (10), e12890. doi:10.1111/cpr.12890

Yang, S., Zhu, B., Yin, P., Zhao, L., Wang, Y., Fu, Z., et al. (2020). Integration of human umbilical cord mesenchymal stem cells-derived exosomes with hydroxyapatite-embedded hyaluronic acid-alginate hydrogel for bone regeneration. *ACS Biomater. Sci. Eng.* 6 (3), 1590–1602. doi:10.1021/acsbiomaterials.9b01363

Yang, X., Yang, J., Lei, P., and Wen, T. (2019). LncRNA MALAT1 shuttled by bone marrow-derived mesenchymal stem cells-secreted exosomes alleviates osteoporosis through mediating microRNA-34c/SATB2 axis. *Aging* 11 (20), 8777–8791. doi:10.18632/aging.102264

Yin, K., Zhu, R., Wang, S., and Zhao, R. C. (2017). Low-Level laser effect on proliferation, migration, and antiapoptosis of mesenchymal stem cells. *Stem Cells Dev.* 26 (10), 762–775. doi:10.1089/scd.2016.0332

Ying, C., Wang, R., Wang, Z., Tao, J., Yin, W., Zhang, J., et al. (2020). BMSC-exosomes carry mutant HIF-1α for improving angiogenesis and osteogenesis in critical-sized calvarial defects. *Front. Bioeng. Biotechnol.* 8, 565561. doi:10.3389/fbioe.2020.565561

Youseflee, P., Ranjbar, F. E., Bahraminasab, M., Ghanbari, A., Faradonbeh, D. R., Arab, S., et al. (2022). Exosome loaded hydroxyapatite (HA) scaffold promotes bone regeneration in calvarial defect: An *in vivo* study. *Cell Tissue Bank*. doi:10.1007/s10561-022-10042-4

Yu, H., Cauchois, G., Louvet, N., Chen, Y., Rahouadj, R., and Huselstein, C. (2017). Comparison of MSC properties in two different hydrogels. Impact of mechanical properties. *Biomed. Mater Eng.* 28 (1), S193–S200. doi:10.3233/bme-171641

Yuan, L., Cao, Y., Yang, Z., Sun, J., Pan, G., Qian, J., et al. (2017). Exosomes secreted by mesenchymal stem cells derived from orofacial bone regulate the function of macrophage. *J. Pract. Stomatology* 33 (03), 344–348.

Zha, Y., Li, Y., Lin, T., Chen, J., Zhang, S., and Wang, J. (2021). Progenitor cell-derived exosomes endowed with VEGF plasmids enhance osteogenic induction and vascular remodeling in large segmental bone defects. *Theranostics* 11 (1), 397–409. doi:10.7150/thno.50741

Zhai, M., Zhu, Y., Yang, M., and Mao, C. (2020). Human mesenchymal stem cell derived exosomes enhance cell-free bone regeneration by altering their miRNAs profiles. *Adv. Sci. (Weinh).* 7 (19), 2001334. doi:10.1002/advs.202001334

Zhang, J., Liu, X., Li, H., Chen, C., Hu, B., Niu, X., et al. (2016). Exosomes/tricalcium phosphate combination scaffolds can enhance bone regeneration by activating the PI3K/Akt signaling pathway. *Stem Cell Res. Ther.* 7 (1), 136. doi:10.1186/s13287-016-0391-3

Zhang, S., Chuah, S. J., Laial, R. C., Hui, J. H. P., Lim, S. K., and Toh, W. S. (2018). MSC exosomes mediate cartilage repair by enhancing proliferation, attenuating apoptosis and modulating immune reactivity. *Biomaterials* 156, 16–27. doi:10.1016/j.biomaterials.2017.11.028

Zhang, S., Teo, K. Y. W., Chuah, S. J., Lai, R. C., Lim, S. K., and Toh, W. S. (2019). MSC exosomes alleviate temporomandibular joint osteoarthritis by attenuating inflammation and restoring matrix homeostasis. *Biomaterials* 200, 35–47. doi:10.1016/j.biomaterials.2019.02.006

Zhang, X., You, J. M., Dong, X. J., and Wu, Y. (2020). Administration of mircoRNA-135b-reinforced exosomes derived from MSCs ameliorates glucocorticoid-induced osteonecrosis of femoral head (ONFH) in rats. *J. Cell Mol. Med.* 24 (23), 13973–13983. doi:10.1111/jcmm.16006

Zhang, Y., Cao, X., Li, P., Fan, Y., Zhang, L., Ma, X., et al. (2021). microRNA-935-modified bone marrow mesenchymal stem cells-derived exosomes enhance osteoblast proliferation and differentiation in osteoporotic rats. *Life Sci.* 272, 119204. doi:10.1016/j.lfs.2021.119204

Zhang, Y., Huo, M., Wang, Y., Xiao, L., Wu, J., Ma, Y., et al. (2022). A tailored bioactive 3D porous poly(lactic-acid)-exosome scaffold with osteoimmunomodulatory and osteogenic differentiation properties. *J. Biol. Eng.* 16 (1), 22. doi:10.1186/s13036-022-00301-z

Zhang, Z., Xu, R., Yang, Y., Liang, C., Yu, X., Liu, Y., et al. (2021). Micro/nano-textured hierarchical titanium topography promotes exosome biogenesis and secretion to improve osseointegration. *J. Nanobiotechnology* 19 (1), 78. doi:10.1186/s12951-021-00826-3

Zhu, C. T., Li, T., Hu, Y. H., Zou, M., -Guo, Q., and Qu, X. W. (2017). Exosomes secreted by mice adipose-derived stem cells after low-level laser irradiation treatment reduce apoptosis of osteocyte induced by hypoxia. *Eur. Rev. Med. Pharmacol. Sci.* 21 (24), 5562–5570. doi:10.26355/eurrev_201712_13993

Zhu, D., Johnson, T. K., Wang, Y., Thomas, M., Huynh, K., Yang, Q., et al. (2020). Macrophage M2 polarization induced by exosomes from adipose-derived stem cells contributes to the exosomal proangiogenic effect on mouse ischemic hindlimb. *Stem Cell Res. Ther.* 11 (1), 162. doi:10.1186/s13287-020-01669-9

Zhu, Y., Jia, Y., Wang, Y., Xu, J., and Chai, Y. (2019). Impaired bone regenerative effect of exosomes derived from bone marrow mesenchymal stem cells in type 1 diabetes. *STEM CELLS Transl. Med.* 8 (6), 593–605. doi:10.1002/sctm.18-0199

Zhuang, X. M., and Zhou, B. (2020). Exosome secreted by human gingival fibroblasts in radiation therapy inhibits osteogenic differentiation of bone mesenchymal stem cells by transferring miR-23a. *Biomed. Pharmacother.* 131, 110672. doi:10.1016/j.biopha.2020.110672

frontiers | Frontiers in Bioengineering and Biotechnology

TYPE Review
PUBLISHED 13 February 2023
DOI 10.3389/fbioe.2023.1021024

OPEN ACCESS

EDITED BY
Mona Kamal Marei,
Alexandria University, Egypt

REVIEWED BY
Brunella Grigolo,
Laboratory of RAMSES, Rizzoli Orthopedic Institute (IRCCS), Italy
Sarah Yasser,
Tanta University, Egypt

*CORRESPONDENCE
Ezatolah Kazeminejad,
Dr. Kazeminejad@goums.ac.ir
Ayyoob Khosravi,
khosravia@goums.ac.ir

†These authors have contributed equally to this work

SPECIALTY SECTION
This article was submitted to Tissue Engineering and Regenerative Medicine, a section of the journal Frontiers in Bioengineering and Biotechnology

RECEIVED 16 August 2022
ACCEPTED 30 January 2023
PUBLISHED 13 February 2023

CITATION
Mahdavi-Jouibari F, Parseh B, Kazeminejad E and Khosravi A (2023), Hopes and opportunities of stem cells from human exfoliated deciduous teeth (SHED) in cartilage tissue regeneration. *Front. Bioeng. Biotechnol.* 11:1021024. doi: 10.3389/fbioe.2023.1021024

Hopes and opportunities of stem cells from human exfoliated deciduous teeth (SHED) in cartilage tissue regeneration

Forough Mahdavi-Jouibari[1†], Benyamin Parseh[2,3†], Ezatolah Kazeminejad[2,4*] and Ayyoob Khosravi[2,5*]

[1]Department of Medical Biotechnology, Faculty of Advanced Medical Technologies, Golestan University of Medical Sciences, Gorgan, Iran, [2]Stem Cell Research Center, Golestan University of Medical Sciences, Gorgan, Iran, [3]Faculty of Advanced Medical Technologies, Golestan University of Medical Sciences, Gorgan, Iran, [4]Dental Research Center, Golestan University of Medical Sciences, Gorgan, Iran, [5]Department of Molecular Medicine, Faculty of Advanced Medical Technologies, Golestan University of Medical Sciences, Gorgan, Iran

Cartilage lesions are common conditions, affecting elderly and non-athletic populations. Despite recent advances, cartilage regeneration remains a major challenge today. The absence of an inflammatory response following damage and the inability of stem cells to penetrate into the healing site due to the absence of blood and lymph vessels are assumed to hinder joint repair. Stem cell-based regeneration and tissue engineering have opened new horizons for treatment. With advances in biological sciences, especially stem cell research, the function of various growth factors in the regulation of cell proliferation and differentiation has been established. Mesenchymal stem cells (MSCs) isolated from different tissues have been shown to increase into therapeutically relevant cell numbers and differentiate into mature chondrocytes. As MSCs can differentiate and become engrafted inside the host, they are considered suitable candidates for cartilage regeneration. Stem cells from human exfoliated deciduous teeth (SHED) provide a novel and non-invasive source of MSCs. Due to their simple isolation, chondrogenic differentiation potential, and minimal immunogenicity, they can be an interesting option for cartilage regeneration. Recent studies have reported that SHED-derived secretome contains biomolecules and compounds that efficiently promote regeneration in damaged tissues, including cartilage. Overall, this review highlighted the advances and challenges of cartilage regeneration using stem cell-based therapies by focusing on SHED.

KEYWORDS

mesenchymal stem cells, cartilage, regenerative medicine, tooth banking, SHED

Introduction

Articular cartilage lesions, reported in nearly 36% of athletes and 63% of non-athletes, become more prevalent with advancing age and inadequate physical activity in young people (Fernandes et al., 2020). The lack of nerves and lymph makes the articular cartilage a particular tissue in the body (Sophia Fox et al., 2009; Simon and Jackson, 2018). Due to the absence of a vasculature which results in the reduced ability of cartilage tissue to repair themselves, these tissues cannot access growth factors required for cell regeneration (Zainal Ariffin et al., 2012). Despite recent advances, treatment of damaged cartilage seems

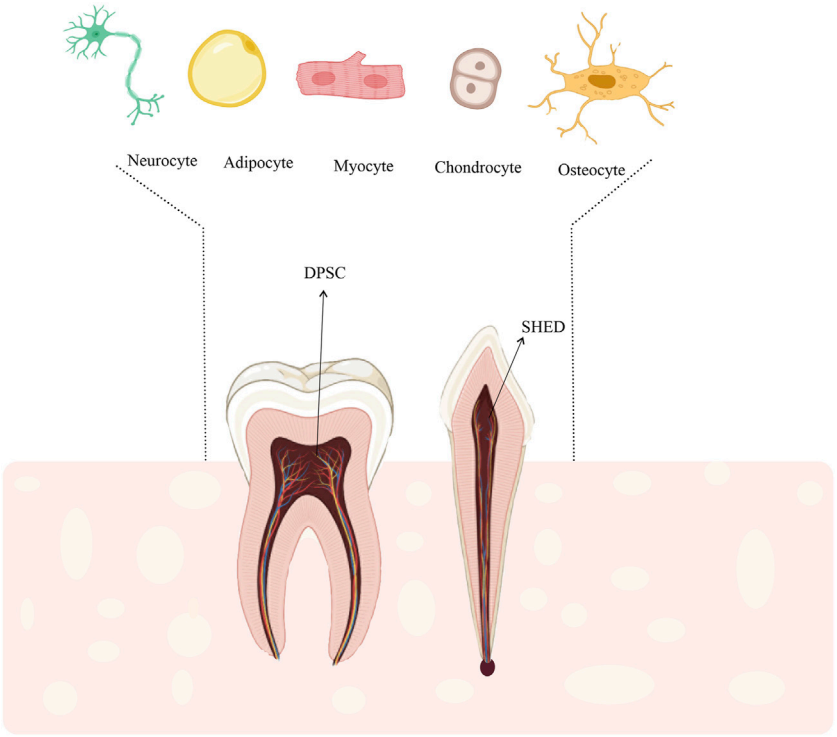

FIGURE 1
DPSCs and SHED could differentiate into other specified cells such as, adipocytes, myocytes, osteocytes, and chondrocytes. Therefore, SHED could be a suitable stem cell source for cell-based regenerative therapies including cartilage regeneration.

unattainable (Frenkel and Di Cesare, 2004; Murphy et al., 2020). Owing to its inherent characteristics, cartilage has minimal access to humoral agents and potential restoration cells after injury (Hardingham et al., 2002; Frenkel and Di Cesare, 2004). Common treatments for damaged tissues include microfracture (Steadman et al., 2003), excision and drilling (Insall, 1967), chondrocyte, and osteochondral transplantation (autograft and allograft) (Pinski et al., 2016; Jackson et al., 2019). Although these procedures can alleviate the symptoms of patients, fibrocartilage tissues may develop which are mechanically distinct from a normal cartilage tissue (Simon and Jackson, 2018).

Cell-based therapies provide a novel approach in regenerative medicine to treat and repair damaged cartilage tissues. The use of mesenchymal stem cell (MSCs) and autologous chondrocyte implantation (ACI) is more common in cell therapy, and tissue regeneration approaches. ACI is a two-stage procedure involving arthroscopic removal of healthy cartilage, expansion of produced cells (cell culture-expanded), and the implantation of new cartilage (Niemeyer et al., 2014; Fernandes et al., 2018; To et al., 2019; Fernandes et al., 2020). However, differentiated cartilage cells have limited proliferative potential, and access to an adequate number of cells for transplantation is a major challenge. Additionally, the proliferative capacity of autologous cartilage cells decreases with aging, which may act as a significant barrier to the treatment of age-related cartilage disorders such as osteoarthritis (OA) (Dozin et al., 2002). Generally, MSCs are excellent candidates for regenerative medicine as they have advantages over other stem cells, and there are no ethical issues related to their production (Wei et al., 2013; Lv et al., 2014). MSCs have a fibroblast-like morphology and clonogenic capacity. Friedenstein first identified these cells in the rat bone marrow (BM) in 1966 (Friedenstein et al., 1966). Recently MSCs have been isolated from tissues including the BM (Shi and Gronthos, 2003; Soleimani et al., 2012), Adipose (Zuk et al., 2002), dental pulp (Gronthos et al., 2000; Pierdomenico et al., 2005), human exfoliated deciduous teeth (Miura et al., 2003), periodontal ligament (Seo et al., 2004), and umbilical cord (Kern et al., 2006).

Microarray analysis showed that the dental pulp stem cells (DPSCs) and BM-MSCs express similar genes (Shi et al., 2001; Tamaki et al., 2013; Shen et al., 2019). One of the main differences between these two types of cellular sources is the high proliferation of DPSC compared to BM-MSC (Nakamura et al., 2009; Karaöz et al., 2011; Shen et al., 2019). On the other hand, repeated studies have shown that stem cells from human exfoliated deciduous teeth (SHED) have higher proliferation and survival potentials compared to other dental sources (Majumdar et al., 2016). Other advantages of SHED include painless cell collection and minimal risk of invasion (Kawashima, 2012; Fernandes et al., 2020). More importantly, SHED and DPSC have been shown to differentiate into mesodermal (Ishkitiev et al., 2010; Nourbakhsh et al., 2011; Gugliandolo and Mazzon, 2022; Kok et al., 2022), ectodermal, and endodermal lineage (Ishkitiev et al., 2010; Gugliandolo and Mazzon, 2022; Kok et al., 2022) (Figure 1). Despite the very high morphological similarity of deciduous cells to DPSCs, studies suggest that SHED has higher rates of differentiation and proliferation than DPSC (Nakamura et al.,

2009; Wang et al., 2012). The proliferation rate of SHED is higher than that of DPSC, and the proliferation rate of DPSC is higher than that of BM-MSCs (SHED > DPSC > BM-MSC) (Huang et al., 2009). Regardless of their remarkable proliferative properties, these cells are used to reduce the risk of oncogenesis and modulate the immune system (Dai et al., 2019; Shen et al., 2019; Taguchi et al., 2019; Khosravi, 2020). Moreover, SHED-derived MSCs can be an available and potential source for tissue engineering and regenerative medicine (Wang et al., 2012; Taguchi et al., 2019). The present review aimed to introduce SHED as a viable option for cartilage regeneration.

Cartilage lesions

While damage to articular cartilage is not life-threatening, it causes pain as it progresses and leads to a significant loss of movement, affecting the individual's life (Semião, 2017). Depending on the underlying causes, two different phenotypes of cartilage damage have been categorized. Focal lesions are well-defined abnormalities that are commonly caused by trauma, osteonecrosis, or osteochondritis dissecans. Also, degenerative lesions are usually caused by osteoarthritis, meniscus injuries, deformities, or ligament instability (Falah et al., 2010). Morphological and biochemical changes in the tissue, caused by senescence, impair the mechanical properties and reduce the ability of chondrocytes to preserve the articular cartilage; besides, changes in the secretory phenotypes of cells can be detected (Loeser, 2009; Anderson and Loeser, 2010; Lotz and Loeser, 2012). The effects of these lesions on the synthesis and secretion of chemokines, cytokines, and proteases need to be characterized.

Cartilage regeneration

Tissue engineering

In the past, humans used to replace missing body parts with dead or artificial things of their own construction (Abdullah et al., 2013). Generally, the root cause of many diseases, neurological disorders, heart failure, and OA, is the absence of a significant cell population of cells that our bodies cannot replace (Murry and Keller, 2008). Although the application different surgical techniques have led to considerable progress, repair of damaged cartilage *via* proliferation or synthesis of natural hyaline has yet to be achieved (Niemeyer et al., 2014; Richter et al., 2016; Lee and Wang, 2017; Fernandes et al., 2018; Yang et al., 2018). Recent research has focused on the potential use of tissue and stem cell engineering in repair and reconstruction of bodily components (Nardi, 2009). It seems that by implementing the available tissue engineering knowledge and using suitable cells, tissue or organ reconstruction can be attained by scaffolding and morphogenic signals necessary for cell induction (Estrela et al., 2011; Zhang et al., 2019; Weizel et al., 2020). Stem cell-based tissue engineering has been recently advocated for cartilage repair (Pelttari et al., 2006; Craft et al., 2015; Guzzo and O'Sullivan, 2016; Nam et al., 2018).

Stem cell therapy

It is well accepted that mature cartilage cannot be restored. The failure is caused by an insufficient inflammatory response following damage and the inability of stem cells to migrate to the injury site owing to the absence of arteries or lymph. However, in previous research when adult human chondrocytes were isolated from the native matrix and transplanted to human and animal models with cartilage defects or *ex vivo* culture conditions, they could produce cartilage-like extracellular matrix (ECM) (Ebihara et al., 2012; Van Pham, 2017). The discovery of stem cells has resulted in the development of novel therapeutic techniques for regenerating damaged tissues, as the distinguishing features of all stem cells after birth include multiplicity and self-renewal (Bianco et al., 2008). The direct injection of the cells into the affected area both prevents damage and causes tissue regeneration. Overall, the outcome of cell therapy is determined by the extent of the injury, injection method, mechanism of release, and dosage (Van Pham, 2017).

Stem cell types for cartilage regeneration

Stem cells are derived from two primary sources: tissue-specific stem cells or adult stem cells (ASCs) (Bonab et al., 2006) and pluripotent embryonic stem cells (ESCs) (Thomson et al., 1998). With recent advances, researchers have been able to produce induced pluripotent stem cells (iPSCs) from embryonic and adult origin through reprogramming and defined protein and gene factors (Takahashi et al., 2007). Research on ESCs, iPSCs, and ASC, are at various stages of cartilage regeneration (Van Pham, 2017). The ESCs are derived from the intracellular body in the blastocyst stage. The iPSCs can be developed by reprogramming somatic cells. The ASC can be derived from different body tissues (Wang et al., 2017). Both ESCs and iPSCs can proliferate and develop into three germ layers, which are, ectoderm, mesoderm, and endoderm (Lee et al., 2013; Cheng et al., 2014). The ASC, can be classified into multipotent and unipotent types. Multipotent cells are divided into various types such as MSCs that can develop into chondrocytes, osteocytes, and adipocytes. On the other hand, unipotent stem cells can develop into only 1 cell lineage, such as satellite stem cells from skeletal muscle or epidermis (Dulak et al., 2015). Due to the absence of ethical restrictions and high availability, most clinical trials utilize MSC as a therapeutic agent for cartilage repair (Van Pham, 2017; Rathan et al., 2019). Overall, selection of the right source of MSCs depends on availability, easy preparation, and cartilaginous potential of each resource. Although there are many studies on the use of ESCs and iPSCs, there are still ethical and safety issues (i.e., immune stimulation, teratoma, and tumor) for the clinical application of these sources (Orth et al., 2014).

Embryonic stem cells (ESCs)

In 1998, Thomson was the first to isolate human ESCs with significant telomerase expression. These cells can develop into all three germ layers, namely, ectoderm (i.e., neural epithelium, stratified squamous epithelium, and embryonic ganglia), mesoderm (i.e., bone, cartilage, smooth and striated muscle), and

endoderm (i.e., gut epithelium) (Thomson et al., 1998). The identification of ESCs has revolutionized the field by introducing human embryogenesis and providing an unlimited potential source of therapeutic cells to treat various diseases (Van Pham, 2017; Sozen et al., 2018). According to a study by (Kramer et al. (2000), on mice, embryonic cell differentiation can be modulated *in vitro* into chondrocytes by transforming growth factor-β family (TGF-β1, BMP-2, and BMP-4). Additionally, (Nakayama et al. (2003) reported that ESCs produce different mesoderm cells when stimulated with BMP4. Among the derived cells, those expressing PDGFRα + or flk-1 showed cartilaginous activity in the presence of TGF-β3 and expressed cartilage-specific genes in seven-to 16-day culture. However, cells derived from early human embryos have raised significant ethical concerns as they inhibit embryonic development. Other challenges of this cellular resource include the immunization of ESCs in clinical applications (Van Pham, 2017).

Induced pluripotent stem cells (iPSCs)

In 2006, Yamanaka et al. established iPSCs. Under ESC culture conditions, pluripotent stem cells from embryonic or adult mouse fibroblasts were generated using four transcription factors, including Oct3/4, Sox2, c-Myc, and Klf4. Homeobox protein Nanog has been confirmed to be unanticipatedly unneeded (Takahashi and Yamanaka, 2006; Nam et al., 2018; Karagiannis et al., 2019). In 2007, a comparable method for human fibroblasts was reported to generate human iPSCs by combining various components (Takahashi et al., 2007; Karagiannis et al., 2019). Generally, iPSCs have similar proliferation, replication, and gene expression characteristics to ESCs. However, unlike ESCs, these cellular resources are associated with no ethical limitations, as they are unique to each patient and can be easily produced from the individual's somatic cells (Li et al., 2016; Nam et al., 2018). Although these cells are reproducible, the efficiency of the procedure is poor, with only nearly 1% of transfected fibroblasts transforming into iPSCs (Yamanaka, 2009). The iPSCs have been used in previous research to generate various therapeutic cells (Van Pham, 2017). Ko et al. (2014) conducted a study to determine the cartilaginous characteristics of human pluripotent stem cells and to evaluate the difference in cartilage formation between iPSCs and BM-derived MSCs. They used undifferentiated iPSCs to produce embryoid bodies (EBs). Following the dissociation of EBs into single cells, cartilage culture was performed in the presence of alginate hydrogel. Chondro-induced iPSCs were implanted in animals with osteochondral abnormalities and assessed 12 weeks. In chondrocytes generated by iPSCs, embryonic markers Nanog, SSEA4, and Oct3/4 disappeared, whereas BMP-4 emerged as a mesodermal marker. The main challenge of utilizing iPSCs for therapeutic and *in vitro* applications is achieving the required uniform cell differentiation and a single-sort cell lineage (Lietman, 2016). Therefore, to establish successful treatments for cartilage repair using iPSCs, a standard differentiation procedure with highly repeatable differentiation efficiency is required. Nevertheless, concerns about cancer in iPSCs, should be addressed in preclinical investigations using animal models (Van Pham, 2017).

Mesenchymal stem cells (MSC)

The MSC_S can differentiate into specific cells within a lineage (Dua et al., 2003; Strauer and Kornowski, 2003). The benefits of these stem cells include low immune system activation, lack of tumorigenicity, and minimal ethical issues (Seyhoun et al., 2019). However, limited differentiation is a significant barrier against the therapeutic application of MSCs (Zuk et al., 2002; Szychlinska et al., 2017). It is known that MSCs migrate through cerebrospinal fluid toward damaged spinal cord tissue and integrate with the host tissue following migration. These cells are expected to play a promising role in tissue regeneration for cell-based therapy (Satake et al., 2004; Woo et al., 2020; Zhang et al., 2020). The International Society for Cell Therapy (ISCT) has recommended three criteria for classifying MSCs, which are as follows (Fernandes et al., 2020): MSCs must be adherent under conventional culture conditions (Simon and Jackson, 2018), they express surface antigens such as CD105, CD90, CD73, and they do not express CD45, CD34, CD14 (CD11b), CD19 (CD79a), and HLA-DR (Sophia Fox et al., 2009). The MSCs can differentiate into osteogenic, chondrogenic, and adipogenic cell lineage according to these criteria (Dominici et al., 2006). It is well established that MSCs can be found in almost all post-natal tissues and may be obtained from various tissues such as skeletal muscle (Williams et al., 1999), BM (Haynesworth et al., 1992), umbilical cord (Erices et al., 2000), placenta (In't Anker et al., 2004), and adipocyte (Halvorsen et al., 2000; Go et al., 2020). The first isolated human dental MSCs were derived from pulp tissue (Gronthos et al., 2000). Followed by other dental MSCs such as SHED (Miura et al., 2003), periodontal ligament stem cells (PDLSCs) (Seo et al., 2004), and dental follicle progenitor/stem cells (DFPSCs) (Morsczeck et al., 2005) with ectomesenchymal origin have been identified. These cells have different differentiation potentials, replication rates, and surface marker properties (Morsczeck et al., 2005; Strioga et al., 2012; Abu Kasim et al., 2015; Anitua et al., 2018; Yamada et al., 2019). Dental stem cells express specific markers expressed by ESCs and MSCs, such as oct4, CD106, STRO-1, and NANOG (Gronthos et al., 2000; Ferro et al., 2012). Under certain stimuli, these clonogenic cells can differentiate into different cells, such as neurons, adipocytes, odontoblasts (Miura et al., 2003; Pivoriūnas et al., 2010; Wang et al., 2010), osteocytes, and chondrocytes (Dai et al., 2012).

Tissue reservoirs of MSCs

Bone marrow

The MSCs originate from the BM and differentiate into various mesodermal cell types, including bone, cartilage, adipose, and muscles (Prockop, 1997). The MSCs from the BM tissue can be used to repair the cartilage, making this tissue one of the most common sources of MSCs. It should be noted that BM-MSCs are extremely rare; consequently, they are not the richest source of stem cells (Bonab et al., 2006). Besides, the number of BM-MSCs decreases with advancing age, and cell therapy becomes more difficult. Aspiration, on the other hand, involves an invasive and painful process of cell removal from the BM and increases the risk of

infection (Dao et al., 2017). According to investigations by McCarthy et al. (2012), BM-MSCs are prone to the formation of osteophytes, which are subchondral bone overgrowths. They may also develop hypertrophic cartilage phenotypes and eventually differentiate into calcified cartilage; accordingly, research into other MSC types is ongoing.

Adipose tissue

Zuk et al. (2001) discovered ADSCs by liposuction in 2001. ADSCs can be distinguished from BM-MSCs by their differentiation capacity, cell surface markers, and abundance in the body. Since more stem cells can be derived from the adipose tissue than BM, ADSCs have a significant functional advantage over BM-MSCs (Aust et al., 2004; Oedayrajsingh-Varma et al., 2006). The isolation of MSCs from the adipose tissue consists of a number of simple processes that can be performed by anyone with cell culture laboratory experience (Estes et al., 2010). The limitations of the adipose tissue are its lower capacity for cartilage development compared to BM and the presence of embryonic markers, such as Oct-4, Nodal, and Utf-1 (Jonidi Shariatzadeh et al., 2018).

Wharton's jelly

The MSCs derived from Wharton's jelly have significant applications in regenerative medicine. These MSCs express markers of both EMSCs and MSCs and may be collected painlessly and safely from the donor site. These cells have other benefits, including rapid proliferation, limitless multipotency, minimal immunogenicity, and most importantly, lack of tumorigenicity (Fong et al., 2010; Gauthaman et al., 2012). The Wharton's jelly has been successfully differentiated into the chondrogenic lineage in different studies using chondrogenic factors (Wang et al., 2011; Reppel et al., 2015); however, this source may have high initial banking costs (Moise, 2005).

Stem cells from human exfoliated deciduous teeth (SHED)

Multiple populations of MSCs have been identified and isolated from dental and oral tissues, including PDLSCs, DPSCs, papillary apical stem cells (SCAP), DFPSCs, gum-derived stem cells (GMSCs), and SHED. Due to their easy accessibility, DPSCs and SHED have received the greatest attention (Yang et al., 2019; Shi et al., 2020). In this regard, a study of oral stem cells and BM-MSCs reported that SHED has the highest reproductive potential, followed by GMSCs, while BM-MSCs had the lowest reproductive potential (Li et al., 2018). Masako Miura et al. isolated SHED in 2003. Generally, SHED can be easily obtained from readily available dental pulp tissue with no major ethical concerns and provide adequate cells for clinical applications due to strong proliferation and telomerase expression (Miura et al., 2003). Similar to DPSCs, SHED expresses different markers, including CD13, CD44, CD73, CD90, CD146, CD166, and STRO-1 (Miura et al., 2003; Govindasamy et al., 2010; Akpinar et al., 2014), but not CD34, CD45, or HLA-DR (Karaöz et al., 2010; Akpinar et al., 2014). Another hallmark that indicates the mesenchymal origin of these cells is the lack of markers associated with the monocytic and hematopoietic lineage. The SHED and DPSCs, similar to ESCs, have been shown to have pluripotency markers, including Oct-4, Nanog, Sox-2, as well as insulin-like growth factor-1 receptor (IGF1R) (Karaöz et al., 2010; Kaukua et al., 2015). These transcription factors are essential for cell proliferation and self-renewal. Studies suggest that Oct-4 and Nanog regulate MSC proliferation and differentiation (Tsai and Hung, 2012). Although SHED has some similarities to DPSCs, they have different gene expression pattern (Galler et al., 2008; Nakamura et al., 2009). SHED has higher levels of pluripotent markers, such as Oct-4, Nanog, and Sox-2 compared to DPSC (Govindasamy et al., 2010). Compared to DPSC and even BM-MSCs, SHED also has a higher proliferation rate (Miura et al., 2003; Nakamura et al., 2009). Moreover, the mineralization ability of SHED is higher than that of DPSC. The mRNA expression levels of inflammatory cytokines, such as interleukin-6 (IL-6), and other proteins such as matrix metalloproteinase 1 (MMP1), tissue inhibitor of metalloproteinase 1 (TIMP1), MMP2, and TIMP2, were significantly higher than in $DPSC_S$ (Wang et al., 2012).

Immune-modulatory properties of SHED

Recently, major attention has been paid to the immunomodulatory characteristics of dental MSCs. According to previous research, the application of allogeneic cells may result in host immune system rejection due to tissue incompatibility. Nevertheless, MSCs can modulate the immune system by secreting soluble factors, enzyme expression, and cell-to-cell interaction (Pierdomenico et al., 2005; Li et al., 2014; Woo et al., 2020). Yamaza et al. (2010) discovered that SHED had a significant effect on the suppression of the T-helper 17 cells *in vitro* compared to the immunomodulatory properties of BM-MSCs. Moreover, de Sá Silva et al. (2014) found that when monocyte-derived dendritic Cells (moDCs) were cultivated on SHED, the production of pro-inflammatory cytokines namely IL-2, interferon-λ (IFN-λ), and tumor necrosis factor-α (TNF-α) decreased while the expression of IL-10 as anti-inflammatory cytokine, increased. Additionally, Yu-Yang Dai et al. performed *in vivo* and *in vitro* investigations on the immunomodulatory properties of SHED for the treatment of allergic rhinitis (AR). In the SHED administration group, the Th2-mediated responses, nasal symptoms, and inflammatory responses significantly decreased. Besides, peripheral blood mononuclear cells (PBMCs) from AR patients were cultivated with SHED and BM-MSCs in the presence of phytohemagglutinin. It was found that SHED inhibited T-cell proliferation, decreased the production of mediators including IL-4 and IL-17A, and increased the Th1/Th2 ratio by stimulating Treg cell expansion (Dai et al., 2019). Numerous studies have confirmed the immunomodulatory effects of SHED *in vivo*. In this regard, (Gao et al. (2018) demonstrated that the injection of SHED in the mouse periodontitis model caused bone regeneration and led to the suppression of the inflammatory response, as well as immune response modulation. They proposed that the therapeutic effects of SHED were caused by the polarization of M2 macrophages. According to previous findings, SHED modulates the immune system by regulating

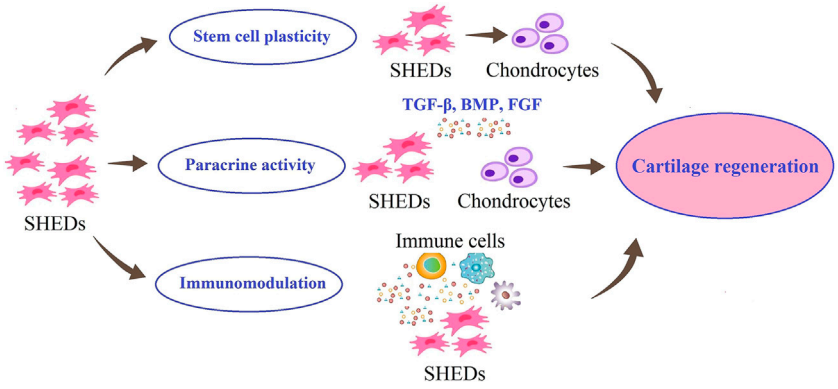

FIGURE 2
Possible roles of SHED in cartilage regeneration. SHED can proliferate and differentiate into chondrocytes. Also, SHED can secrete different growth factors, to maintain chondrocyte phenotypes and promote their proliferation. In addition, SHED have immunomodulatory effects on the lesion site.

immune cell proliferation and differentiation and adjusting the expression of pro-inflammatory and anti-inflammatory mediators.

Tumorigenicity risk of SHED

In most settings, genomic changes are an inevitable phase of *in vitro* stem cell culture. The frequency of these changes, which increases over time in the culture, represents at least one general process of increased tumorigenicity (Maitra et al., 2005), which is a particularly critical gap in the application of these cells. Overall, stem cell tumorigenicity is the primary barrier to the safe application of stem cell-based regenerative medicine. Although some of adult stem cell therapies may appear safe, they have limited applications for the treatment of human disease (Knoepfler, 2009). According to a recent study in 2020 by Yuk Wah Chan et al., despite the tremendous therapeutic potentials of adipose-derived stem cells (ADSCs), they spontaneously fused with breast cancer cells (BCC); these hybrids exhibit surface antigen markers of cancer stem cells (CSCs) and showed strong *in vivo* tumorigenic capacity. CSCs are a rare population in tumors with high metastatic potential and resistance to treatment (Khosravi et al., 2021). Recent studies have shown the ability of MSCs to regulate CSCs through increased tumor-initiating abilities, enhance the resistance of CSCs to chemotherapy and drive the metastatic *preferences* of CSCs to specific tissues (Cuiffo and Karnoub, 2012). Therefore, the predilection of MSCs to cooperate with CSCs in tumor initiation, progression and metastasis should be further investigated. Several studies have reported that ADSCs or MSC increase the BCC migration and proliferation either through mediators and growth factor secretion or directly *via* cell fusion (Chan et al., 2020). Wen-Ching Shen et al., in a study on tumorigenesis in BM cells and DPSCs, found that a higher PTEN expression in DP-MSCs relative to BM-MSCs was responsible for differences in the lineage linkage and tumorigenesis of these two cell types. Moreover, the PTEN promoter in BM-MSCs exhibited higher DNA methylation levels compared to DP-MSCs, besides enrichment of histone H3 lysine 9 dimethylation (H3K9Me2,) mediated by enhanced Dnmt3b and G9a expression. The results showed how multiple epigenetic variables influence the lineage linkage and tumorigenesis in various ways. According to the findings, these variables need to be considered in the development of treatments based on stem cells (Shen et al., 2019).

SHED-based strategies for cartilage regeneration

The selection and development of SHED-based strategies for regeneration of damaged cartilage tissues require understanding the molecular mechanisms involved in cartilage regeneration. These strategies are shown schematically in Figure 2.

The first strategy can be the use of endogenous MSCs of damaged cartilage. Previous studies have shown that the quantity and potency of endogenous MSCs are insufficient to regenerate cartilage repair completely (Baraniak and McDevitt, 2010). Considering the possibility of migration of transplanted MSCs to damaged areas and differentiation into target cells (Pan et al., 2020), researchers are looking for exogenous MSCs with promising potential for migration, proliferation, and differentiation into chondrocytes. SHED have been reported to have the chondrogenic differentiation ability in both *in vitro* and *in vivo* models, suggesting their potential of them in cartilage regeneration (Chen et al., 2014).

The second strategy in cartilage regeneration is to use the therapeutic effects of SHED through their paracrine effects. Extracellular vesicles (EVs), exosomes and soluble growth factors, known as the secretome or serum-free conditioned media of SHED have been shown in numerous studies to have a modulatory effect on other cells or tissues, demonstrating the efficacy of cell-free based stem cell therapy in cartilage regeneration and maintain chondrocyte phenotypes and promote their proliferation (Guo and Yu, 2022). SHED can promote the proliferation of chondrocytes and the production of cartilage matrix by releasing nutritional factors, such as transforming growth factor beta (TGF-β), bone morphogenetic

proteins (BMPs), and fibroblast growth factors (FGFs) (Bar et al., 2021).

A damaged cartilage is exposed to a progressive inflammatory environment. Evidence suggests that remodeling and reconstruction in the cartilage lesions that results from cell transplantation depends not only on differentiation potential but also on anti-inflammatory paracrine mechanism that reduce inflammation at the lesion site (Guo and Yu, 2022). The third strategy in cartilage regeneration could involve the role of SHED in modulating the immune response in the cartilage repair process. Yamaza et al. (2010) showed that the optimal therapeutic effect of SHED may be due to their immunomodulatory effects of them in terms of recovering the Tregs/Th17 ratio and reducing Th17 cell levels in peripheral blood. Studies have also shown that SHED have low expression of major histocompatibility complex class I (MHC I) and negative expression of major histocompatibility complex class II (MHC II) (Dai et al., 2019). These properties could support the use of SHED for immune modulation in clinical practice.

Efficacy of SHED in cartilage regeneration

Regenerative medicine for functional tissue restoration has evolved from *ex vivo* tissue engineering to induction and intra-tissue restoration. Multidisciplinary approaches to cell biology and evolution, bioengineering, immunology, and genomic and proteomic elements of molecular biology have led to significant advances in regenerative medicine and tissue engineering (Naranjo et al., 2016). Also, biotechnology and regenerative medicine advances, along with the application of stem cells for tissue regeneration have resulted in significant medical progress (Sylvester and Longaker, 2004). The optimal cellular source for tissue engineering should be available and easily expanded *in vitro*. For instance, cartilage regeneration must produce significant extracellular matrix components without becoming dedifferentiated; chondrocytes and stem cells have been reported to be the primary resource for this purpose (Sharma and Elisseeff, 2004; Kock et al., 2012). Lars Patterson from the University of Gothenburg published research in 1987 which revealed that chondrocytes might be stimulated to proliferate *in vitro* and then utilized to repair cartilage lesions in the joint from which they have been originated. This method was developed by Genzyme Laboratories in Cambridge, UK, where arthroscopically obtained cells are still sent for culture (Manfredini et al., 2007). The only method approved by the Food and Drug Administration (FDA) for cartilage tissue engineering is the Carticel transplantation of *in vitro* expanded autologous chondrocytes (Wood et al., 2006; Camarero-Espinosa et al., 2016). This strategy utilizes the cartilage cells, conducts *in vitro* expansion, and implants the cells in the operated knee (Manfredini et al., 2007). Because differentiated cells cannot reflect all phenotypic changes in the tissue, the application of chondrocytes for tissue engineering is not ideal. Besides, the application and implantation of a clonal or immortal cell lineage can result in tumor development due to the unlimited proliferation of these cells (Camarero-Espinosa et al., 2016).

Some adverse effects of Carticel methods are graft failure, delamination, and tissue hypertrophy (Wood et al., 2006). Basic scientific studies and clinical trials have been conducted to apply stem cells and growth factors to restore damaged tissues (Strauer and Kornowski, 2003). Stem cells with paracrine activity and the release of vesicles and exosomes play a vital role in tissue regeneration and repair (Ando et al., 2014; Kay et al., 2017; Bjørge et al., 2018; Niazi et al., 2020). Dental epithelial cells and MSCs are great resources employed in dentistry and various regenerative medical disciplines. However, if these biological resources are not employed properly, they should be discarded (Xiao and Nasu, 2014; Mattei et al., 2021). The SHED can differentiate into bone, generate teeth, and develop into various non-dental mesenchymal cell lineages *in vitro* (Abdullah et al., 2013; Mattei et al., 2021). Ishikawa et al. demonstrated that injecting SHED-conditioned medium (SHED-CM) into mice could decrease symptoms of cartilage disease *via* the paracrine mechanism. It has been shown that SHED-CM suppresses inflammation and bone degradation. Therefore, it may provide an anti-inflammatory and restorative therapy for individuals with rheumatoid arthritis (Ishikawa et al., 2016). In a study by Werle et al. (2016), comparing the rate of proliferation and differentiation between healthy deciduous teeth and decayed deciduous teeth, the two sources of SHED had similar proliferation rates. Both cells expressed CD90, CD73, and CD29 markers, whereas the CD45, CD34, CD14, and HLA-DR were negative; they could differentiate into bone, cartilage, and adipose tissue cell lineages. Additionally, Chen et al. (2014) evaluated cartilage differentiation potential of SHED. In this study, SHED was cultured in a cartilage differentiation medium containing TGF-b3, basic fibroblast growth factor (bFGF), dexamethasone, insulin, and ascorbate phosphate for 2 weeks. The expanded SHED grown on the β-tricalcium phosphate (β-TCP) scaffold was transplanted into the subcutaneous space on the back of nude mice. Chondrogenesis was studied using Safranin O staining and toluidine blue staining. They also evaluated type II collagen and aggrecan *via* immunohistochemistry. The results revealed the *in vitro* and *in vivo* differentiation capacity of SHED into cartilage.

Signaling molecules involved in chondrogenesis during cartilage development

MSCs originate from the mesoderm and form the appendicular skeleton (Camarero-Espinosa et al., 2016). Skeletal development is divided into four stages, the first of which is the migration of cells to the eventual skeletal site. Tissue interactions (epithelial-mesenchymal) occur in the following step. Cell condensation and differentiation into osteoblasts or chondroblasts are the final steps in the process. The cell condensation stage is critical for bone morphogenesis and mesenchymal tissues (Hall and Miyake, 2000; Chan et al., 2021). MSCs increase mitosis during organ development due to cell-cell or cell-substrate interactions, resulting in cell condensation (Camarero-Espinosa et al., 2016). The cartilaginous anlage is formed when stem cells in the condensation develop into chondrocytes, which produce an abundance of ECM proteins such as collagen types II, IX, and XI and proteoglycans (Demoor et al., 2014). During the endochondral ossification process, chondrocytes in the condensation zone become hypertrophic and express markers of terminal differentiation markers including type X collagen, Runt-related transcription factor 2 (RUNX-2), Indian

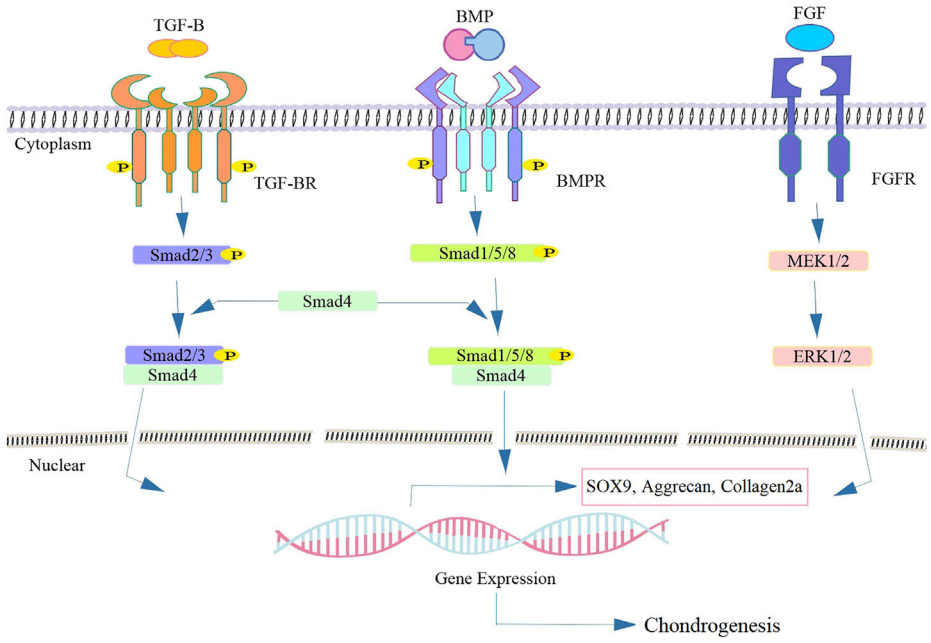

FIGURE 3
Schematics of representative signaling biomolecules present in SHED-CM responsible for cartilage regeneration. Following the binding of the TGF-β or BMP ligand to TGF-β-RII, leads to the phosphorylation of TGF-β-RI and subsequent phosphorylation and activation of the intracellular Smad superfamily. The heterocomplex of Smad4 and other co-activators translocate to the nucleus and thereby regulating the target gene expression such as sox9 involved in cartilage regeneration. FGF binds to FGFR and activates the downstream cascade and leading to the expression of the chondrogenic markers *via* activation of the MEK/ERK signaling pathway.

hedgehog (Ihh) and MMP-13 (Mariani et al., 2014; Kwon et al., 2016). Several complicated regulatory mechanisms such as BMP, FGF, TGF-β, and Wnt signaling pathways are involved in chondrocyte destiny, determining whether they retain cartilage form or undergo hypertrophic maturation prior to ossification (Minina et al., 2002). Several TGF-β isoforms are activated during the cartilage regeneration process (van der Kraan and van den Berg, 2007). Proteoglycan and type II collagen are produced at a higher rate as a result of this activation, which also prevents ECM degradation (Darling and Athanasiou, 2005; Pogue and Lyons, 2006). TGF-β promotes cell proliferation and upregulated cartilage-specific genes such as glycosaminoglycans (GAG), aggrecan, and type II collagen. It has been demonstrated that SRY-related high-mobility-group box transcription factor (SOX) 9 mediated transcription is stimulated by TGF-β-activated Smad3/4 (Furumatsu et al., 2009; Kwon et al., 2016). TGF-β operates as a stimulator during the first stages of chondrogenesis but as an inhibitor throughout the suppressing the production of osteocalcin, MMP-13, type X collagen, and vascular endothelial growth factor (VEGF) in advanced phases of chondrocyte differentiation and prevents differentiate into hypertrophic chondrocytes (Mackie et al., 2008; Mariani et al., 2014).

In embryonic skeletal development, BMPs are growth factors required for cartilage formation (Tsumaki et al., 2002). BMPs control the growth and resorption of cartilage as a member of the TGF family. BMPs signaling pathway is transduced Smad1/5/8 whereas Smad2/3 are responsible for mediating TGF-β signaling (De Caestecker, 2004) (Figure 3). Prechondrogenic condensation and chondrocyte maturation begin with the activation of BMP signaling (Mihelic et al., 2004). BMP-2 has been confirmed to have a substantial anabolic impact on cartilage. It has been shown that the upregulation of type II collagen by chondrocytes seeded in alginate, stimulates proteoglycan production in murine cartilage (Gründer et al., 2004). Regarding the protective impact of BMPs in cartilage regeneration; it has been demonstrated BMPs are related to matrix degradation and chondrocyte hypertrophy (Leboy et al., 2001). However, enhanced matrix turnover may be useful in replenishing matrix molecules during cartilage matrix regeneration. Enhanced matrix turnover may be useful in replenishing matrix molecules during cartilage matrix regeneration (Blaney Davidson et al., 2007). BMP-2 regulates the expression and function of SOX9 to enhance chondrocyte proliferation and matrix production, and regulate chondrogenesis (Zehentner et al., 1999). FGF2, also known as bFGF, is another factor involved in the healing of cartilage lesions. It is present in the pericellular matrix of cartilage at relatively high concentrations (Chia et al., 2009). FGFs enhance the amount of SOX9 expression and upregulate the type II collagen gene expression through increase the activity of SOX9-dependent, chondrocyte-specific enhancer elements (Figure 3). It binds to cell receptors and promotes anabolic signaling pathways, resulting in reduced aggrecanase activity, without any significant change in the proteoglycan composition (Fortier et al., 2011).

SHED-CM promote cartilage regeneration

Cell-free therapies have been recently employed in tissue engineering and regenerative medicine to eliminate any concerns

TABLE 1 Advantages and disadvantages of stem cells from umbilical cord blood and SHED.

	Advantages	Disadvantages	References
Umbilical cord blood stem cells banking	1. The collection is simple and painless and not time-consuming	1. Slow engraftment	Moise, 2005; Waller-Wise (2011)
	2. No donor attribution (no risk for mother or child)	2. Large inventory product (high up-front costs; units may become "outdated" due to changes in banking standards	
	3. Higher proliferative capacity	3. Limited cell dose	
	4. Low risk for transmission of infection, Lower rate of acute graft-vs-host disease	4. Autologous donation may have limited benefits owing to hereditary disorders, Storage issues	
	5. Less expensive than bone marrow harvest and less rejection risk		
Stem cells from exfoliated deciduous teeth banking	1. There was no immunological response or tissue rejection, no immunosuppressive treatment was required, and the risk of transmitting disease was considerably decreased	1. Long-term clinical trials are still needed to evaluate the oncogenic potential	Arthur et al. (2008), Mao (2008), Shi et al. (2005), Cordeiro et al. (2008), Mao et al. (2006), Arora et al. (2009)
	2. For both the child and the parent, it is simple and painless	2. The study is mostly focused on animal models, but human research trials are still required to determine the same outcomes in humans	
	3. Less than one-third of the cost of cord blood storage	3. To be applied therapeutically, large numbers are needed	
	4. Not vulnerable to the same ethical considerations as embryonic stem cells	5. Compared to embryonic stem cells, they have a lower potency	
	5. For multiple tissue regeneration such as connective tissues, dental tissues, neural tissue, and bone marrow can be used		

related to the use of stem cells (Vizoso et al., 2017; Harrell et al., 2019; Kumar et al., 2019; González-González et al., 2020; Parseh et al., 2022). Activated chondrocytes in the damaged site produce more cartilage, proinflammatory mediators, catabolic enzymes, and oxidative stress stimulators. This causes the cartilage matrix to degrade and induce chondrocyte apoptosis or necrosis by activating the NF-kB pathway, which results in severe articular injury and functional disability (Lo Monaco et al., 2020; Palamà et al., 2020). NF-kB transcription factors regulate a variety of immunological responses, survival, cellular differentiation, and growth in both healthy and malignant situations. Activation of NF-kB in chondrocytes controls the production of several matrix-degrading enzymes, affecting the quantity and remodeling of ECM proteins. It also has indirect beneficial impacts in terminal chondrocyte maturation through the expression of RUNX-2, the downstream transcription factor associated with the differentiation of chondrocyte to osteoblast development. Different factors including mechanical stress, inflammatory mediators such as TNF-α or IL-1β, aging, fibronectin fragments, and Toll-like membrane receptors can activate NF-kB in OA chondrocytes (Mariani et al., 2014).

The SHED-CM can reduce inflammation in cartilage defects, as it contains anti-inflammatory cytokines (e.g., IL-4 and IL-10), downregulates the NF-kB pathway, and significantly diminishes the expression of proinflammatory cytokines (e.g., IL-1 and TNF-α), besides nitric oxide synthesis (Muhammad et al., 2020; Bar et al., 2021). Additionally, it has been demonstrated that SHED-CM contains a number of growth factors, including TGF-β1, FGF-2, BMP-2 and BMP-4, which are crucial for cartilage regeneration (Bar et al., 2021) TGF-β has the potential to influence SHED activities, including proliferation, collagen turnover, and differentiation. These processes occur *via* TGF-β receptor binding and are differentially controlled by TAK1, MEK/ERK, p38, and ALK5/Smad2/3 signaling (Chang et al., 2020).

Muhammad et al. (2020) in a study on SHED-CM in cartilage regeneration, found that it enhances the expression of aggrecan and type II collagen in OA chondrocytes. The SHED-CM protected cartilage cells by enhancing matrix proteins and suppressing MMP-13 production. This work shows that soluble paracrine components in SHED-CM have an anabolic effect on chondrocytes by downregulating NF-kB signaling and catabolic activity. Ogasawara et al. (2020) studied the effect of SHED-CM on a model of temporomandibular joint osteoarthritis (TMJOA). In this study, it was demonstrated that SHED-CM can hinder cartilage degradation, reduce inflammation, enhance cellular proliferation, promote cartilage regeneration, and prevent TMJOA development through mechanical stress.

Tooth banking

Accessibility and low invasion concerns are two advantages of deciduous teeth over other tissue or fluid. However, this great resource is only available to youngsters with deciduous teeth. The preservation of these cells is a major challenge when SHED is used therapeutically (Volponi et al., 2010). Since the isolation of SHED is complicated, conservation and banking strategies must be developed for clinical applications. Stem cell cryopreservation has valuable

advantages, including long-term storage, differentiation potential retention, contaminants control for safety and quality, and dosage adjustment of cell treatment in therapeutic interventions; therefore, attention has been shifted toward banking (Hubel, 1997; Papaccio et al., 2006). It is important to realize that stem cells may keep their primary properties, such as long-term tissue regeneration after cryopreservation. The use of a magnetic field during freezing has been also shown to boost the vitality of frozen cells. Ice crystals develop during freezing and cause excessive disruptions in osmosis and the plasma membrane (Pilbauerová and Suchánek, 2018). Overall, the application of a magnetic field minimizes cytotoxicity and the dimethyl sulfoxide content in freezing media, resulting in improved cell performance following thawing (Lin et al., 2015). The number of specific stem cell preservation banks for deciduous teeth has increased in North America, the United Kingdom, and India. In 2004, the University of Hiroshima in Japan developed the first dental banks (Kaku et al., 2010). In a study by Zhang et al. (2006) even after freezing, dental pulp stem cells could be employed as a source of multipotent stem cells for tissue regeneration and cell-based treatment. Since the first hematopoietic stem cell transplantation from umbilical cord blood (UCB) bank in 1988, public and family UCB bank have been developed worldwide (Mayani et al., 2020). There are a number of hematologic, pediatric, genetic, immunological, and oncological disorders that have been successfully treated using UBC, as a rich source of hematopoietic stem cells (Lubin and Shearer, 2007). It has been suggested that current banking methods are not valid due to a lack of validated tissue processing regulations (e.g., volume reduction, red blood cell removal, and plasma removal) (Smith and Thomson, 2000). Dental stem cell banking is rapidly finding its place in stem cell-based therapies, similar to UCB which has been cryopreserved for at last 2 decades. The advantages and disadvantages of using umbilical cord stem cells and deciduous teeth are summarized in Table 1.

Challenges

Cell-based therapies have several challenges, including cell implantation time, migration, survival, rejection, and immunological incompatibility (Pearse and Bunge, 2006). On the other hand, the characteristics of self-renewability and plasticity are critical hallmarks of cancer cells. The concept that the transplanted stem cells may lose control and facilitate tumor development is a threatening and irreversible side effect (Knoepfler, 2009; Vicente-Duenas et al., 2009). Although SHED is a valuable autologous resource for restoring damaged tissue, it is only available to children who have lost their deciduous teeth. Therefore, commercial SHED banking, which is relatively new method compared to other types of banking, attempts to keep these important cells and utilizes them to cure disease and restore tissue in adulthood. Meanwhile, dental stem cells are often involved in neoplasia; therefore, mechanisms that allow these stem cells to undergo self-renewal, differentiation, and cancer should be investigated (Xiao and Nasu, 2014). Overall, stem cells provide significant opportunities owing to their differentiation into different lineages and regeneration of multiple tissues. Still, the use of SHED in cartilage tissue engineering has not expanded, and so far, no specific application has been reported (Barry and Murphy, 2004; Barry and Murphy, 2013).

Conclusion

Cartilage, when severely damaged, cannot restore and regenerate itself due to the absence of nerves, lymph, and arteries (Van Pham, 2017). Because of the unpredictability of conventional surgical procedures and the relative improvement of injured tissue, the use of stem cells and cartilage tissue engineering has received more attention. Currently, stem cell transplantation is a promising approach for cartilage restoration (Orth et al., 2014; Murphy et al., 2020). The MSCs are the most reliable source in stem cell-based regenerative medicine. As reviewed in this article, SHED exhibits phenotypes of MSCs, such as expression of MSCs-related markers, self-renewal, multipotency, and immunoregulatory effects. This cellular source can be recruited for cell-based regeneration in cartilage disorders.

Author contributions

FM-J and BP wrote the first draft of the manuscript. AK and EN edited the manuscript. All authors read and approved the final manuscript.

Acknowledgments

We thank Mrs. Mahdavi-Jouibari for editing the manuscript and correction of grammatical errors and English improvement.

Conflict of interest

The authors declare that the research was conducted in the absence of any commercial or financial relationships that could be construed as a potential conflict of interest.

Publisher's note

References

Abdullah, M. F., Ponnuraj, K. T., and Mokhtar, K. I. (2013). DPSCs and SHED in tissue engineering and regenerative medicine. *Open Stem Cell J.* 4, 1–6. doi:10.2174/1876893801304010001

Abu Kasim, N. H., Govindasamy, V., Gnanasegaran, N., Musa, S., Pradeep, P. J., Srijaya, T. C., et al. (2015). Unique molecular signatures influencing the biological function and fate of post-natal stem cells isolated from different sources. *J. tissue Eng. Regen. Med.* 9 (12), E252–E266. doi:10.1002/term.1663

Akpinar, G., Kasap, M., Aksoy, A., Duruksu, G., Gacar, G., and Karaoz, E. (2014). Phenotypic and proteomic characteristics of human dental pulp derived mesenchymal stem cells from a natal, an exfoliated deciduous, and an impacted third molar tooth. *Stem Cells Int.* 2014, 1–19. doi:10.1155/2014/457059

Anderson, A. S., and Loeser, R. F. (2010). Why is osteoarthritis an age-related disease? *Best Pract. Res. Clin. rheumatology* 24 (1), 15–26. doi:10.1016/j.berh.2009.08.006

Ando, Y., Matsubara, K., Ishikawa, J., Fujio, M., Shohara, R., Hibi, H., et al. (2014). Stem cell-conditioned medium accelerates distraction osteogenesis through multiple regenerative mechanisms. *Bone* 61, 82–90. doi:10.1016/j.bone.2013.12.029

Anitua, E., Troya, M., and Zalduendo, M. (2018). Progress in the use of dental pulp stem cells in regenerative medicine. *Cytotherapy* 20 (4), 479–498. doi:10.1016/j.jcyt.2017.12.011

Arora, V., Arora, P., and Munshi, A. (2009). Banking stem cells from human exfoliated deciduous teeth (SHED): Saving for the future. *J. Clin. Pediatr. Dent.* 33 (4), 289–294. doi:10.17796/jcpd.33.4.y887672r0j703654

Arthur, A., Rychkov, G., Shi, S., Koblar, S. A., and Gronthos, S. (2008). Adult human dental pulp stem cells differentiate toward functionally active neurons under appropriate environmental cues. *Stem cells* 26 (7), 1787–1795. doi:10.1634/stemcells.2007-0979

Aust, L., Devlin, B., Foster, S., Halvorsen, Y., Hicok, K., Du Laney, T., et al. (2004). Yield of human adipose-derived adult stem cells from liposuction aspirates. *Cytotherapy* 6 (1), 7–14. doi:10.1080/14653240310004539

Bar, J. K., Lis-Nawara, A., and Grelewski, P. G. (2021). Dental pulp stem cell-derived secretome and its regenerative potential. *Int. J. Mol. Sci.* 22 (21), 12018. doi:10.3390/ijms222112018

Baraniak, P. R., and McDevitt, T. C. (2010). Stem cell paracrine actions and tissue regeneration. *Regen. Med.* 5 (1), 121–143. doi:10.2217/rme.09.74

Barry, F., and Murphy, M. (2013). Mesenchymal stem cells in joint disease and repair. *Nat. Rev. Rheumatol.* 9 (10), 584–594. doi:10.1038/nrrheum.2013.109

Barry, F. P., and Murphy, J. M. (2004). Mesenchymal stem cells: Clinical applications and biological characterization. *Int. J. Biochem. Cell Biol.* 36 (4), 568–584. doi:10.1016/j.biocel.2003.11.001

Bianco, P., Robey, P. G., and Simmons, P. J. (2008). Mesenchymal stem cells: Revisiting history, concepts, and assays. *Cell stem Cell* 2 (4), 313–319. doi:10.1016/j.stem.2008.03.002

Bjørge, I., Kim, S., Mano, J., Kalionis, B., and Chrzanowski, W. (2018). Extracellular vesicles, exosomes and shedding vesicles in regenerative medicine–a new paradigm for tissue repair. *Biomaterials Sci.* 6 (1), 60–78. doi:10.1039/c7bm00479f

Blaney Davidson, E. N., Vitters, E. L., van Lent, P. L., Van de Loo, F. A., van den Berg, W. B., and van der Kraan, P. M. (2007). Elevated extracellular matrix production and degradation upon bone morphogenetic protein-2 (BMP-2) stimulation point toward a role for BMP-2 in cartilage repair and remodeling. *Arthritis Res. Ther.* 9 (5), R102–R111. doi:10.1186/ar2305

Bonab, M. M., Alimoghaddam, K., Talebian, F., Ghaffari, S. H., Ghavamzadeh, A., and Nikbin, B. (2006). Aging of mesenchymal stem cell *in vitro*. *BMC Cell Biol.* 7 (1), 14–17. doi:10.1186/1471-2121-7-14

Camarero-Espinosa, S., Rothen-Rutishauser, B., Foster, E. J., and Weder, C. (2016). Articular cartilage: From formation to tissue engineering. *Biomaterials Sci.* 4 (5), 734–767. doi:10.1039/c6bm00068a

Chan, W. C. W., Tan, Z., To, M. K. T., and Chan, D. (2021). Regulation and role of transcription factors in osteogenesis. *Int. J. Mol. Sci.* 22 (11), 5445. doi:10.3390/ijms22115445

Chan, Y. W., So, C., Yau, K. L., Chiu, K. C., Wang, X., Chan, F. L., et al. (2020). Adipose-derived stem cells and cancer cells fuse to generate cancer stem cell-like cells with increased tumorigenicity. *J. Cell. physiology* 235 (10), 6794–6807. doi:10.1002/jcp.29574

Chang, H-H., Chen, I-L., Wang, Y-L., Chang, M-C., Tsai, Y-L., Lan, W-C., et al. (2020). Regulation of the regenerative activity of dental pulp stem cells from exfoliated deciduous teeth (SHED) of children by TGF-β1 is associated with ALK5/Smad2, TAK1, p38 and MEK/ERK signaling. *Aging (Albany NY)* 12 (21), 21253–21272. doi:10.18632/aging.103848

Chen, K., Xiong, H., Xu, N., Shen, Y., Huang, Y., and Liu, C. (2014). Chondrogenic potential of stem cells from human exfoliated deciduous teeth *in vitro* and *in vivo*. *Acta Odontol. Scand.* 72 (8), 664–672. doi:10.3109/00016357.2014.888756

Cheng, A., Hardingham, T. E., and Kimber, S. J. (2014). Generating cartilage repair from pluripotent stem cells. *Tissue Eng. Part B Rev.* 20 (4), 257–266. doi:10.1089/ten.teb.2012.0757

Chia, S. L., Sawaji, Y., Burleigh, A., McLean, C., Inglis, J., Saklatvala, J., et al. (2009). Fibroblast growth factor 2 is an intrinsic chondroprotective agent that suppresses ADAMTS-5 and delays cartilage degradation in murine osteoarthritis. *Arthritis & rheumatism official J. Am. Coll. rheumatology.* 60 (7), 2019–2027. doi:10.1002/art.24654

Cordeiro, M. M., Dong, Z., Kaneko, T., Zhang, Z., Miyazawa, M., Shi, S., et al. (2008). Dental pulp tissue engineering with stem cells from exfoliated deciduous teeth. *J. Endod.* 34 (8), 962–969. doi:10.1016/j.joen.2008.04.009

Craft, A. M., Rockel, J. S., Nartiss, Y., Kandel, R. A., Alman, B. A., and Keller, G. M. (2015). Generation of articular chondrocytes from human pluripotent stem cells. *Nat. Biotechnol.* 33 (6), 638–645. doi:10.1038/nbt.3210

Cuiffo, B. G., and Karnoub, A. E. (2012). Mesenchymal stem cells in tumor development: Emerging roles and concepts. *Cell adhesion Migr.* 6 (3), 220–230. doi:10.4161/cam.20875

Dai, J., Wang, J., Lu, J., Zou, D., Sun, H., Dong, Y., et al. (2012). The effect of co-culturing costal chondrocytes and dental pulp stem cells combined with exogenous FGF9 protein on chondrogenesis and ossification in engineered cartilage. *Biomaterials* 33 (31), 7699–7711. doi:10.1016/j.biomaterials.2012.07.020

Dai, Y-Y., Ni, S-Y., Ma, K., Ma, Y-S., Wang, Z-S., and Zhao, X-L. (2019). Stem cells from human exfoliated deciduous teeth correct the immune imbalance of allergic rhinitis via Treg cells *in vivo* and *in vitro*. *Stem Cell Res. Ther.* 10 (1), 39–14. doi:10.1186/s13287-019-1134-z

Dao, T. T-T., Vu, N. B., Pham, L. H., Gia, L. V., Le, H. T-N., Phi, L. T., et al. (2017). "*In vitro* production of cartilage tissue from rabbit bone marrow-derived mesenchymal stem cells and polycaprolactone scaffold," in *Tissue engineering and regenerative medicine* (Berlin, Germany: Springer), 45–60.

Darling, E. M., and Athanasiou, K. A. (2005). Growth factor impact on articular cartilage subpopulations. *Cell tissue Res.* 322 (3), 463–473. doi:10.1007/s00441-005-0020-4

De Caestecker, M. (2004). The transforming growth factor-β superfamily of receptors. *Cytokine & growth factor Rev.* 15 (1), 1–11. doi:10.1016/j.cytogfr.2003.10.004

de Sá Silva, F., Ramos, R. N., de Almeida, D. C., Bassi, E. J., Gonzales, R. P., Miyagi, S. P. H., et al. (2014). Mesenchymal stem cells derived from human exfoliated deciduous teeth (SHED) induce immune modulatory profile in monocyte-derived dendritic cells. *PLoS One* 9 (5), e98050. doi:10.1371/journal.pone.0098050

Demoor, M., Ollitrault, D., Gomez-Leduc, T., Bouyoucef, M., Hervieu, M., Fabre, H., et al. (2014). Cartilage tissue engineering: Molecular control of chondrocyte differentiation for proper cartilage matrix reconstruction. *Biochimica Biophysica Acta (BBA)-General Subj.* 1840 (8), 2414–2440. doi:10.1016/j.bbagen.2014.02.030

Dominici, M., Le Blanc, K., Mueller, I., Slaper-Cortenbach, I., Marini, F., Krause, D., et al. (2006). Minimal criteria for defining multipotent mesenchymal stromal cells. The International Society for Cellular Therapy position statement. *Cytotherapy* 8 (4), 315–317. doi:10.1080/14653240600855905

Dozin, B., Malpeli, M., Camardella, L., Cancedda, R., and Pietrangelo, A. (2002). Response of young, aged and osteoarthritic human articular chondrocytes to inflammatory cytokines: Molecular and cellular aspects. *Matrix Biol.* 21 (5), 449–459. doi:10.1016/s0945-053x(02)00028-8

Dua, H. S., Joseph, A., Shanmuganathan, V., and Jones, R. (2003). Stem cell differentiation and the effects of deficiency. *Eye* 17 (8), 877–885. doi:10.1038/sj.eye.6700573

Dulak, J., Szade, K., Szade, A., Nowak, W., and Józkowicz, A. (2015). Adult stem cells: Hopes and hypes of regenerative medicine. *Acta Biochim. Pol.* 62 (3), 329–337. doi:10.18388/abp.2015_1023

Ebihara, G., Sato, M., Yamato, M., Mitani, G., Kutsuna, T., Nagai, T., et al. (2012). Cartilage repair in transplanted scaffold-free chondrocyte sheets using a minipig model. *Biomaterials* 33 (15), 3846–3851. doi:10.1016/j.biomaterials.2012.01.056

Erices, A., Conget, P., and Minguell, J. J. (2000). Mesenchymal progenitor cells in human umbilical cord blood. *Br. J. Haematol.* 109 (1), 235–242. doi:10.1046/j.1365-2141.2000.01986.x

Estes, B. T., Diekman, B. O., Gimble, J. M., and Guilak, F. (2010). Isolation of adipose-derived stem cells and their induction to a chondrogenic phenotype. *Nat. Protoc.* 5 (7), 1294–1311. doi:10.1038/nprot.2010.81

Estrela, C., Alencar, A. H. G., Kitten, G. T., Vencio, E. F., and Gava, E. (2011). Mesenchymal stem cells in the dental tissues: Perspectives for tissue regeneration. *Braz. Dent. J.* 22 (2), 91–98. doi:10.1590/s0103-64402011000200001

Falah, M., Nierenberg, G., Soudry, M., Hayden, M., and Volpin, G. (2010). Treatment of articular cartilage lesions of the knee. *Int. Orthop.* 34 (5), 621–630. doi:10.1007/s00264-010-0959-y

Fernandes, T. L., Cortez de SantAnna, J. P., Frisene, I., Gazarini, J. P., Gomes Pinheiro, C. C., Gomoll, A. H., et al. (2020). Systematic review of human dental pulp stem cells for cartilage regeneration. *Tissue Eng. Part B Rev.* 26, 1–12. doi:10.1089/ten.TEB.2019.0140

Fernandes, T. L., Kimura, H. A., Pinheiro, C. C. G., Shimomura, K., Nakamura, N., Ferreira, J. R., et al. (2018). Human synovial mesenchymal stem cells good

manufacturing practices for articular cartilage regeneration. *Tissue Eng. Part C. Methods* 24 (12), 709–716. doi:10.1089/ten.tec.2018.0219

Ferro, F., Spelat, R., D'Aurizio, F., Puppato, E., Pandolfi, M., Beltrami, A. P., et al. (2012). Dental pulp stem cells differentiation reveals new insights in Oct4A dynamics. *PloS one* 7 (7), e41774. doi:10.1371/journal.pone.0041774

Fong, C-Y., Subramanian, A., Biswas, A., Gauthaman, K., Srikanth, P., Hande, M. P., et al. (2010). Derivation efficiency, cell proliferation, freeze–thaw survival, stem-cell properties and differentiation of human Wharton's jelly stem cells. *Reprod. Biomed. online* 21 (3), 391–401. doi:10.1016/j.rbmo.2010.04.010

Fortier, L. A., Barker, J. U., Strauss, E. J., McCarrel, T. M., and Cole, B. J. (2011). The role of growth factors in cartilage repair. *Clin. Orthop. Relat. Research®* 469 (10), 2706–2715. doi:10.1007/s11999-011-1857-3

Frenkel, S. R., and Di Cesare, P. E. (2004). Scaffolds for articular cartilage repair. *Ann. Biomed. Eng.* 32 (1), 26–34. doi:10.1023/b:abme.0000007788.41804.0d

Furumatsu, T., Ozaki, T., and Asahara, H. (2009). Smad3 activates the Sox9-dependent transcription on chromatin. *Int. J. Biochem. Cell Biol.* 41 (5), 1198–1204. doi:10.1016/j.biocel.2008.10.032

Galler, K. M., Cavender, A., Yuwono, V., Dong, H., Shi, S., Schmalz, G., et al. (2008). Self-assembling peptide amphiphile nanofibers as a scaffold for dental stem cells. *Tissue Eng. Part A* 14 (12), 2051–2058. doi:10.1089/ten.tea.2007.0413

Gao, X., Shen, Z., Guan, M., Huang, Q., Chen, L., Qin, W., et al. (2018). Immunomodulatory role of stem cells from human exfoliated deciduous teeth on periodontal regeneration. *Tissue Eng. Part A* 24 (17-18), 1341–1353. doi:10.1089/ten.tea.2018.0016

Gauthaman, K., Fong, C-Y., Suganya, C-A., Subramanian, A., Biswas, A., Choolani, M., et al. (2012). Extra-embryonic human Wharton's jelly stem cells do not induce tumorigenesis, unlike human embryonic stem cells. *Reprod. Biomed. online* 24 (2), 235–246. doi:10.1016/j.rbmo.2011.10.007

Go, G., Jeong, S-G., Yoo, A., Han, J., Kang, B., Kim, S., et al. (2020). Human adipose–derived mesenchymal stem cell–based medical microrobot system for knee cartilage regeneration *in vivo*. *Sci. Robotics* 5 (38), eaay6626. doi:10.1126/scirobotics.aay6626

González-González, A., García-Sánchez, D., Dotta, M., Rodríguez-Rey, J. C., and Pérez-Campo, F. M. (2020). Mesenchymal stem cells secretome: The cornerstone of cell-free regenerative medicine. *World J. stem cells* 12 (12), 1529–1552. doi:10.4252/wjsc.v12.i12.1529

Govindasamy, V., Abdullah, A. N., Ronald, V. S., Musa, S., Aziz, Z. A. C. A., Zain, R. B., et al. (2010). Inherent differential propensity of dental pulp stem cells derived from human deciduous and permanent teeth. *J. Endod.* 36 (9), 1504–1515. doi:10.1016/j.joen.2010.05.006

Gronthos, S., Mankani, M., Brahim, J., Robey, P. G., and Shi, S. (2000). Postnatal human dental pulp stem cells (DPSCs) *in vitro* and *in vivo*. *Proc. Natl. Acad. Sci.* 97 (25), 13625–13630. doi:10.1073/pnas.240309797

Gründer, T., Gaissmaier, C., Fritz, J., Stoop, R., Hortschansky, P., Mollenhauer, J., et al. (2004). Bone morphogenetic protein (BMP)-2 enhances the expression of type II collagen and aggrecan in chondrocytes embedded in alginate beads. *Osteoarthr. Cartil.* 12 (7), 559–567. doi:10.1016/j.joca.2004.04.001

Gugliandolo, A., and Mazzon, E. (2022). Dental mesenchymal stem cell secretome: An intriguing approach for neuroprotection and neuroregeneration. *Int. J. Mol. Sci.* 23 (1), 456. doi:10.3390/ijms23010456

Guo, R., and Yu, J. (2022). Multipotency and immunomodulatory benefits of stem cells from human exfoliated deciduous teeth. *Front. Dent. Med.* 3, 805875. doi:10.3389/fdmed.2022.805875

Guo, X., Zheng, Q., Yang, S., Shao, Z., Yuan, Q., Pan, Z., et al. (2006). Repair of full-thickness articular cartilage defects by cultured mesenchymal stem cells transfected with the transforming growth factor β1 gene. *Biomed. Mater.* 1 (4), 206–215. doi:10.1088/1748-6041/1/4/006

Guzzo, R. M., and O'Sullivan, M. B. (2016). Human pluripotent stem cells: Advances in chondrogenic differentiation and articular cartilage regeneration. *Curr. Mol. Biol. Rep.* 2 (3), 113–122. doi:10.1007/s40610-016-0041-7

Hall, B. K., and Miyake, T. (2000). All for one and one for all: Condensations and the initiation of skeletal development. *Bioessays* 22 (2), 138–147. doi:10.1002/(sici)1521-1878(200002)22:2<138::aid-bies5>3.0.co;2-4

Halvorsen, Y., Wilkison, W., and Gimble, J. (2000). Adipose-derived stromal cells—Their utility and potential in bone formation. *Int. J. Obes.* 24 (4), S41–S44. doi:10.1038/sj.ijo.0801503

Hardingham, T., Tew, S., and Murdoch, A. (2002). Tissue engineering: Chondrocytes and cartilage. *Arthritis Res. Ther.* 4 (3), S63–S68. doi:10.1186/ar561

Harrell, C. R., Fellabaum, C., Jovicic, N., Djonov, V., Arsenijevic, N., and Volarevic, V. (2019). Molecular mechanisms responsible for therapeutic potential of mesenchymal stem cell-derived secretome. *Cells* 8 (5), 467. doi:10.3390/cells8050467

Haynesworth, S., Goshima, J., Goldberg, V., and Caplan, A. (1992). Characterization of cells with osteogenic potential from human marrow. *Bone* 13 (1), 81–88. doi:10.1016/8756-3282(92)90364-3

Huang, G-J., Gronthos, S., and Shi, S. (2009). Mesenchymal stem cells derived from dental tissues vs. those from other sources: Their biology and role in regenerative medicine. *J. Dent. Res.* 88 (9), 792–806. doi:10.1177/0022034509340867

Hubel, A. (1997). Parameters of cell freezing: Implications for the cryopreservation of stem cells. *Transfus. Med. Rev.* 11 (3), 224–233. doi:10.1053/tmrv.1997.0110224

In't Anker, P. S., ScherjonSAKleijburg-van der Keur, C., de Groot-Swings, G. M., Claas, F. H., Fibbe, W. E., et al. (2004). Isolation of mesenchymal stem cells of fetal or maternal origin from human placenta. *Stem cells* 22 (7), 1338–1345. doi:10.1634/stemcells.2004-0058

Insall, J. (1967). Intra-articular surgery for degenerative arthritis of the knee: A report of the work of the late KH pridie. *J. bone Jt. Surg. Br. volume* 49 (2), 211–228. doi:10.1302/0301-620x.49b2.211

Ishikawa, J., Takahashi, N., Matsumoto, T., Yoshioka, Y., Yamamoto, N., Nishikawa, M., et al. (2016). Factors secreted from dental pulp stem cells show multifaceted benefits for treating experimental rheumatoid arthritis. *Bone* 83, 210–219. doi:10.1016/j.bone.2015.11.012

Ishkitiev, N., Yaegaki, K., Calenic, B., Nakahara, T., Ishikawa, H., Mitiev, V., et al. (2010). Deciduous and permanent dental pulp mesenchymal cells acquire hepatic morphologic and functional features *in vitro*. *J. Endod.* 36 (3), 469–474. doi:10.1016/j.joen.2009.12.022

Jackson, A. T., Drayer, N. J., Samona, J., Dukes, C. A., Chen, C. S., Arrington, E. A., et al. (2019). Osteochondral allograft transplantation surgery for osteochondral lesions of the talus in athletes. *J. Foot Ankle Surg.* 58 (4), 623–627. doi:10.1053/j.jfas.2018.11.020

Jonidi Shariatzadeh, F., Gheydari, K., Solouk, A., and Bonakdar, S. (2018). Use of stem cells in cartilage tissue regeneration and engineering: A review. *Pathobiology Res.* 21 (1), 41–63.

Kaku, M., Kamada, H., Kawata, T., Koseki, H., Abedini, S., Kojima, S., et al. (2010). Cryopreservation of periodontal ligament cells with magnetic field for tooth banking. *Cryobiology* 61 (1), 73–78. doi:10.1016/j.cryobiol.2010.05.003

Karagiannis, P., Takahashi, K., Saito, M., Yoshida, Y., Okita, K., Watanabe, A., et al. (2019). Induced pluripotent stem cells and their use in human models of disease and development. *Physiol. Rev.* 99 (1), 79–114. doi:10.1152/physrev.00039.2017

Karaöz, E., Demircan, P. C., Sağlam, Ö., Aksoy, A., Kaymaz, F., and Duruksu, G. (2011). Human dental pulp stem cells demonstrate better neural and epithelial stem cell properties than bone marrow-derived mesenchymal stem cells. *Histochem. Cell Biol.* 136 (4), 455–473. doi:10.1007/s00418-011-0858-3

Karaöz, E., Doğan, B. N., Aksoy, A., Gacar, G., Akyüz, S., Ayhan, S., et al. (2010). Isolation and *in vitro* characterisation of dental pulp stem cells from natal teeth. *Histochem. Cell Biol.* 133 (1), 95–112. doi:10.1007/s00418-009-0646-5

Kaukua, N., Chen, M., Guarnieri, P., Dahl, M., Lim, M. L., Yucel-Lindberg, T., et al. (2015). Molecular differences between stromal cell populations from deciduous and permanent human teeth. *Stem Cell Res. Ther.* 6 (1), 59–14. doi:10.1186/s13287-015-0056-7

Kawashima, N. (2012). Characterisation of dental pulp stem cells: A new horizon for tissue regeneration? *Archives oral Biol.* 57 (11), 1439–1458. doi:10.1016/j.archoralbio.2012.08.010

Kay, A. G., Long, G., Tyler, G., Stefan, A., Broadfoot, S. J., Piccinini, A. M., et al. (2017). Mesenchymal stem cell-conditioned medium reduces disease severity and immune responses in inflammatory arthritis. *Sci. Rep.* 7 (1), 18019–18111. doi:10.1038/s41598-017-18144-w

Kern, S., Eichler, H., Stoeve, J., Klüter, H., and Bieback, K. (2006). Comparative analysis of mesenchymal stem cells from bone marrow, umbilical cord blood, or adipose tissue. *Stem cells* 24 (5), 1294–1301. doi:10.1634/stemcells.2005-0342

Khosravi, A. (2020). Biological characteristics of stem cells from human exfoliated deciduous teeth (SHED) and its therapeutic applications in regenerative medicine. *Jorjani Biomed. J.* 8 (2), 1–3. doi:10.52547/jorjanibiomedj.8.2.1

Khosravi, A., Jafari, S. M., and Asadi, J. (2021). Knockdown of TAZ decrease the cancer stem properties of ESCC cell line YM-1 by modulation of Nanog, OCT-4 and SOX2. *Gene* 769, 145207. doi:10.1016/j.gene.2020.145207

Knoepfler, P. S. (2009). Deconstructing stem cell tumorigenicity: A roadmap to safe regenerative medicine. *Stem cells* 27 (5), 1050–1056. doi:10.1002/stem.37

Ko, J-Y., Kim, K-I., Park, S., and Im, G-I. (2014). *In vitro* chondrogenesis and *in vivo* repair of osteochondral defect with human induced pluripotent stem cells. *Biomaterials* 35 (11), 3571–3581. doi:10.1016/j.biomaterials.2014.01.009

Kock, L., van Donkelaar, C. C., and Ito, K. (2012). Tissue engineering of functional articular cartilage: The current status. *Cell tissue Res.* 347 (3), 613–627. doi:10.1007/s00441-011-1243-1

Kok, Z. Y., Alaidaroos, N. Y., Alraies, A., Colombo, J. S., Davies, L. C., Waddington, R. J., et al. (2022). Dental pulp stem cell heterogeneity: Finding superior quality "needles" in a dental pulpal "haystack" for regenerative medicine-based applications. *Stem Cells Int.* 2022, 1–20. doi:10.1155/2022/9127074

Kramer, J., Hegert, C., Guan, K., Wobus, A. M., Müller, P. K., and Rohwedel, J. (2000). Embryonic stem cell-derived chondrogenic differentiation *in vitro*: Activation by BMP-2 and BMP-4. *Mech. Dev.* 92 (2), 193–205. doi:10.1016/s0925-4773(99)00339-1

Kumar, P., Kandoi, S., Misra, R., Vijayalakshmi, S., Rajagopal, K., and Verma, R. S. (2019). The mesenchymal stem cell secretome: A new paradigm towards cell-free therapeutic mode in regenerative medicine. *Cytokine & growth factor Rev.* 46, 1–9. doi:10.1016/j.cytogfr.2019.04.002

Kwon, H., Paschos, N. K., Hu, J. C., and Athanasiou, K. (2016). Articular cartilage tissue engineering: The role of signaling molecules. *Cell. Mol. Life Sci.* 73 (6), 1173–1194. doi:10.1007/s00018-015-2115-8

Leboy, P. S., Grasso-Knight, G., D'Angelo, M., Volk, S. W., Lian, J. B., Drissi, H., et al. (2001). Smad-Runx interactions during chondrocyte maturation. *JBJS* 83 (1), S1–S15. doi:10.2106/00004623-200100001-00003

Lee, A. S., Tang, C., Rao, M. S., Weissman, I. L., and Wu, J. C. (2013). Tumorigenicity as a clinical hurdle for pluripotent stem cell therapies. *Nat. Med.* 19 (8), 998–1004. doi:10.1038/nm.3267

Lee, W. Y., and Wang, B. (2017). Cartilage repair by mesenchymal stem cells: Clinical trial update and perspectives. *J. Orthop. Transl.* 9, 76–88. doi:10.1016/j.jot.2017.03.005

Li, J., Xu, S. Q., Zhao, Y. M., Yu, S., Ge, L. H., and Xu, B. H. (2018). Comparison of the biological characteristics of human mesenchymal stem cells derived from exfoliated deciduous teeth, bone marrow, gingival tissue, and umbilical cord. *Mol. Med. Rep.* 18 (6), 4969–4977. doi:10.3892/mmr.2018.9501

Li, Y., Liu, T., Van Halm-Lutterodt, N., Chen, J., Su, Q., and Hai, Y. (2016). Reprogramming of blood cells into induced pluripotent stem cells as a new cell source for cartilage repair. *Stem Cell Res. Ther.* 7 (1), 31–11. doi:10.1186/s13287-016-0290-7

Li, Z., Jiang, C. M., An, S., Cheng, Q., Huang, Y. F., Wang, Y. T., et al. (2014). Immunomodulatory properties of dental tissue-derived mesenchymal stem cells. *Oral Dis.* 20 (1), 25–34. doi:10.1111/odi.12086

Lietman, S. A. (2016). Induced pluripotent stem cells in cartilage repair. *World J. Orthop.* 7 (3), 149. doi:10.5312/wjo.v7.i3.149

Lin, S-L., Chang, W-J., Lin, C-Y., Hsieh, S-C., Lee, S-Y., Fan, K-H., et al. (2015). Static magnetic field increases survival rate of dental pulp stem cells during DMSO-free cryopreservation. *Electromagn. Biol. Med.* 34 (4), 302–308. doi:10.3109/15368378.2014.919588

Lo Monaco, M., Gervois, P., Beaumont, J., Clegg, P., Bronckaers, A., Vandeweerd, J-M., et al. (2020). Therapeutic potential of dental pulp stem cells and leukocyte-and platelet-rich fibrin for osteoarthritis. *Cells* 9 (4), 980. doi:10.3390/cells9040980

Loeser, R. F. (2009). Aging and osteoarthritis: The role of chondrocyte senescence and aging changes in the cartilage matrix. *Osteoarthr. Cartil.* 17 (8), 971–979. doi:10.1016/j.joca.2009.03.002

Lotz, M., and Loeser, R. F. (2012). Effects of aging on articular cartilage homeostasis. *Bone* 51 (2), 241–248. doi:10.1016/j.bone.2012.03.023

Lubin, B. H., and Shearer, W. T. (2007). Cord blood banking for potential future transplantation. *Pediatrics* 119 (1), 165–170. doi:10.1542/peds.2006-2901

Lv, F-J., Tuan, R. S., Cheung, K. M., and Leung, V. Y. (2014). Concise review: The surface markers and identity of human mesenchymal stem cells. *Stem cells* 32 (6), 1408–1419. doi:10.1002/stem.1681

Mackie, E., Ahmed, Y., Tatarczuch, L., Chen, K-S., and Mirams, M. (2008). Endochondral ossification: How cartilage is converted into bone in the developing skeleton. *Int. J. Biochem. Cell Biol.* 40 (1), 46–62. doi:10.1016/j.biocel.2007.06.009

Maitra, A., Arking, D. E., Shivapurkar, N., Ikeda, M., Stastny, V., Kassauei, K., et al. (2005). Genomic alterations in cultured human embryonic stem cells. *Nat. Genet.* 37 (10), 1099–1103. doi:10.1038/ng1631

Majumdar, D., Kanafi, M., Bhonde, R., Gupta, P., and Datta, I. (2016). Differential neuronal plasticity of dental pulp stem cells from exfoliated deciduous and permanent teeth towards dopaminergic neurons. *J. Cell. Physiology* 231 (9), 2048–2063. doi:10.1002/jcp.25314

Manfredini, M., Zerbinati, F., Gildone, A., and Faccini, R. (2007). Autologous chondrocyte implantation: A comparison between an open periosteal-covered and an arthroscopic matrix-guided technique. *Acta Orthop. Belg.* 73 (2), 207–218.

Mao, J., Giannobile, W., Helms, J., Hollister, S., Krebsbach, P., Longaker, M., et al. (2006). Craniofacial tissue engineering by stem cells. *J. Dent. Res.* 85 (11), 966–979. doi:10.1177/154405910608501101

Mao, J. J. (2008). Stem cells and the future of dental care. *N. Y. State Dent. J.* 74 (2), 20–24.

Mariani, E., Pulsatelli, L., and Facchini, A. (2014). Signaling pathways in cartilage repair. *Int. J. Mol. Sci.* 15 (5), 8667–8698. doi:10.3390/ijms15058667

Mattei, V., Martellucci, S., Pulcini, F., Santilli, F., Sorice, M., and Delle Monache, S. (2021). Regenerative potential of DPSCs and revascularization: Direct, paracrine or autocrine effect? *Stem Cell Rev. Rep.* 17, 1635–1646. doi:10.1007/s12015-021-10162-6

Mayani, H., Wagner, J. E., and Broxmeyer, H. E. (2020). Cord blood research, banking, and transplantation: Achievements, challenges, and perspectives. *Bone marrow Transplant.* 55 (1), 48–61. doi:10.1038/s41409-019-0546-9

McCarthy, H. E., Bara, J. J., Brakspear, K., Singhrao, S. K., and Archer, C. W. (2012). The comparison of equine articular cartilage progenitor cells and bone marrow-derived stromal cells as potential cell sources for cartilage repair in the horse. *Veterinary J.* 192 (3), 345–351. doi:10.1016/j.tvjl.2011.08.036

Mihelic, R., Pecina, M., Jelic, M., Zoricic, S., Kusec, V., Simic, P., et al. (2004). Bone morphogenetic protein–7 (osteogenic protein–1) promotes tendon graft integration in anterior cruciate ligament reconstruction in sheep. *Am. J. sports Med.* 32 (7), 1619–1625. doi:10.1177/0363546504263703

Minina, E., Kreschel, C., Naski, M. C., Ornitz, D. M., and Vortkamp, A. (2002). Interaction of FGF, Ihh/Pthlh, and BMP signaling integrates chondrocyte proliferation and hypertrophic differentiation. *Dev. Cell* 3 (3), 439–449. doi:10.1016/s1534-5807(02)00261-7

Miura, M., Gronthos, S., Zhao, M., Lu, B., Fisher, L. W., Robey, P. G., et al. (2003). Shed: Stem cells from human exfoliated deciduous teeth. *Proc. Natl. Acad. Sci.* 100 (10), 5807–5812. doi:10.1073/pnas.0937635100

Moise, K. J., Jr (2005). Umbilical cord stem cells. *Obstetrics Gynecol.* 106 (6), 1393–1407. doi:10.1097/01.aog.0000188388.84901.e4

Morsczeck, C., Götz, W., Schierholz, J., Zeilhofer, F., Kühn, U., Möhl, C., et al. (2005). Isolation of precursor cells (PCs) from human dental follicle of wisdom teeth. *Matrix Biol.* 24 (2), 155–165. doi:10.1016/j.matbio.2004.12.004

Muhammad, S. A., Nordin, N., Hussin, P., Mehat, M. Z., Abu Kasim, N. H., and Fakurazi, S. (2020). Protective effects of stem cells from human exfoliated deciduous teeth derived conditioned medium on osteoarthritic chondrocytes. *PloS one* 15 (9), e0238449. doi:10.1371/journal.pone.0238449

Murphy, M. P., Koepke, L. S., Lopez, M. T., Tong, X., Ambrosi, T. H., Gulati, G. S., et al. (2020). Articular cartilage regeneration by activated skeletal stem cells. *Nat. Med.* 26 (10), 1583–1592. doi:10.1038/s41591-020-1013-2

Murry, C. E., and Keller, G. (2008). Differentiation of embryonic stem cells to clinically relevant populations: Lessons from embryonic development. *Cell* 132 (4), 661–680. doi:10.1016/j.cell.2008.02.008

Nakamura, S., Yamada, Y., Katagiri, W., Sugito, T., Ito, K., and Ueda, M. (2009). Stem cell proliferation pathways comparison between human exfoliated deciduous teeth and dental pulp stem cells by gene expression profile from promising dental pulp. *J. Endod.* 35 (11), 1536–1542. doi:10.1016/j.joen.2009.07.024

Nakayama, N., Duryea, D., Manoukian, R., Chow, G., and Han, C-y. E. (2003). Macroscopic cartilage formation with embryonic stem-cell-derived mesodermal progenitor cells. *J. Cell Sci.* 116 (10), 2015–2028. doi:10.1242/jcs.00417

Nam, Y., Rim, Y. A., Lee, J., and Ju, J. H. (2018). Current therapeutic strategies for stem cell-based cartilage regeneration. *Stem cells Int.* 2018, 1–20. doi:10.1155/2018/8490489

Naranjo, J. D., Scarritt, M. E., Huleihel, L., Ravindra, A., Torres, C. M., and Badylak, S. F. (2016). Regenerative medicine: Lessons from mother nature. *Regen. Med.* 11 (8), 767–775. doi:10.2217/rme-2016-0111

Nardi, N. (2009). Methodology, biology and clinical applications of mesenchymal stem cells. *Front. Biosci. (Landmark Ed.* 14, 4281–4298. doi:10.2741/3528

Niazi, V., Parseh, B., Ahani, M., Karami, F., Gilanchi, S., Atarodi, K., et al. (2020). Communication between stromal and hematopoietic stem cell by exosomes in normal and malignant bone marrow niche. *Biomed. Pharmacother.* 132, 110854. doi:10.1016/j.biopha.2020.110854

Niemeyer, P., Salzmann, G., Feucht, M., Pestka, J., Porichis, S., Ogon, P., et al. (2014). First-generation versus second-generation autologous chondrocyte implantation for treatment of cartilage defects of the knee: A matched-pair analysis on long-term clinical outcome. *Int. Orthop.* 38 (10), 2065–2070. doi:10.1007/s00264-014-2368-0

Nourbakhsh, N., Soleimani, M., Taghipour, Z., Karbalaie, K., Mousavi, S-B., Talebi, A., et al. (2011). Induced *in vitro* differentiation of neural-like cells from human exfoliated deciduous teeth-derived stem cells. *Int. J. Dev. Biol.* 55 (2), 189–195. doi:10.1387/ijdb.103090nn

Oedayrajsingh-Varma, M., Van Ham, S., Knippenberg, M., Helder, M., Klein-Nulend, J., Schouten, T., et al. (2006). Adipose tissue-derived mesenchymal stem cell yield and growth characteristics are affected by the tissue-harvesting procedure. *Cytotherapy* 8 (2), 166–177. doi:10.1080/14653240600621125

Ogasawara, N., Kano, F., Hashimoto, N., Mori, H., Liu, Y., Xia, L., et al. (2020). Factors secreted from dental pulp stem cells show multifaceted benefits for treating experimental temporomandibular joint osteoarthritis. *Osteoarthr. Cartil.* 28 (6), 831–841. doi:10.1016/j.joca.2020.03.010

Orth, P., Rey-Rico, A., Venkatesan, J. K., Madry, H., and Cucchiarini, M. (2014). Current perspectives in stem cell research for knee cartilage repair. *Stem cells cloning Adv. Appl.* 7, 1–17. doi:10.2147/sccaa.s42880

Palamà, M. E. F., Shaw, G. M., Carluccio, S., Reverberi, D., Sercia, L., Persano, L., et al. (2020). The secretome derived from mesenchymal stromal cells cultured in a xeno-free medium promotes human cartilage recovery *in vitro*. *Front. Bioeng. Biotechnol.* 8, 90. doi:10.3389/fbioe.2020.00090

Pan, H., Lam, P. K., Tong, S. W., Leung, K. K., Teoh, A. Y., and Ng, E. K. (2020). Mesenchymal stem cells combined with tissue fusion technology promoted wound healing in porcine bowel anastomosis. *Stem cells Int.* 2020, 1–14. doi:10.1155/2020/5142797

Papaccio, G., Graziano, A., d'Aquino, R., Graziano, M. F., Pirozzi, G., Menditti, D., et al. (2006). Long-term cryopreservation of dental pulp stem cells (SBP-DPSCs) and their differentiated osteoblasts: A cell source for tissue repair. *J. Cell. physiology* 208 (2), 319–325. doi:10.1002/jcp.20667

Parseh, B., Khosravi, A., Fazel, A., Ai, J., Ebrahimi-Barough, S., Verdi, J., et al. (2022). 3-Dimensional model to study apoptosis induction of activated natural killer cells conditioned medium using patient-derived colorectal cancer organoids. *Front. Cell Dev. Biol.* 10, 895284. doi:10.3389/fcell.2022.895284

Pearse, D. D., and Bunge, M. B. (2006). Designing cell-and gene-based regeneration strategies to repair the injured spinal cord. *J. neurotrauma* 23 (3-4), 437–452. doi:10.1089/neu.2006.23.437

Pelttari, K., Winter, A., Steck, E., Goetzke, K., Hennig, T., Ochs, B. G., et al. (2006). Premature induction of hypertrophy during *in vitro* chondrogenesis of human mesenchymal stem cells correlates with calcification and vascular invasion after ectopic transplantation in SCID mice. *Arthritis & Rheumatism Official J. Am. Coll. Rheumatology* 54 (10), 3254–3266. doi:10.1002/art.22136

Pierdomenico, L., Bonsi, L., Calvitti, M., Rondelli, D., Arpinati, M., Chirumbolo, G., et al. (2005). Multipotent mesenchymal stem cells with immunosuppressive activity can be easily isolated from dental pulp. *Transplantation* 80 (6), 836–842. doi:10.1097/01.tp.0000173794.72151.88

Pilbauerová, N., and Suchánek, J. (2018). Cryopreservation of dental stem cells. *Acta Medica* 61 (1), 1–7. doi:10.14712/18059694.2018.16

Pinski, J. M., Boakye, L. A., Murawski, C. D., Hannon, C. P., Ross, K. A., and Kennedy, J. G. (2016). Low level of evidence and methodologic quality of clinical outcome studies on cartilage repair of the ankle. *Arthrosc. J. Arthrosc. Relat. Surg.* 32 (1), 214–222. e1. doi:10.1016/j.arthro.2015.06.050

Pivoriūnas, A., Surovas, A., Borutinskaitė, V., Matuzevičius, D., Treigytė, G., Savickienė, J., et al. (2010). Proteomic analysis of stromal cells derived from the dental pulp of human exfoliated deciduous teeth. *Stem cells Dev.* 19 (7), 1081–1093. doi:10.1089/scd.2009.0315

Pogue, R., and Lyons, K. (2006). BMP signaling in the cartilage growth plate. *Curr. Top. Dev. Biol.* 76, 1–48. doi:10.1016/S0070-2153(06)76001-X

Prockop, D. J. (1997). Marrow stromal cells as stem cells for nonhematopoietic tissues. *Science* 276 (5309), 71–74. doi:10.1126/science.276.5309.71

Rathan, S., Dejob, L., Schipani, R., Haffner, B., Möbius, M. E., and Kelly, D. J. (2019). Fiber reinforced cartilage ECM functionalized bioinks for functional cartilage tissue engineering. *Adv. Healthc. Mater.* 8 (7), 1801501. doi:10.1002/adhm.201801501

Reppel, L., Schiavi, J., Charif, N., Leger, L., Yu, H., Pinzano, A., et al. (2015). Chondrogenic induction of mesenchymal stromal/stem cells from Wharton's jelly embedded in alginate hydrogel and without added growth factor: An alternative stem cell source for cartilage tissue engineering. *Stem Cell Res. Ther.* 6 (1), 260–313. doi:10.1186/s13287-015-0263-2

Richter, D. L., Schenck, R. C., Jr, Wascher, D. C., and Treme, G. (2016). Knee articular cartilage repair and restoration techniques: A review of the literature. *Sports health* 8 (2), 153–160. doi:10.1177/1941738115611350

Satake, K., Lou, J., and Lenke, L. G. (2004). Migration of mesenchymal stem cells through cerebrospinal fluid into injured spinal cord tissue. *Spine* 29 (18), 1971–1979. doi:10.1097/01.brs.0000138273.02820.0a

Semião, A. F. P. (2017). *Strategies for chondrogenic differentiation of human induced pluripotent stem cells*. Lisbon, Portugal: Technico lisboa.

Seo, B-M., Miura, M., Gronthos, S., Bartold, P. M., Batouli, S., Brahim, J., et al. (2004). Investigation of multipotent postnatal stem cells from human periodontal ligament. *Lancet* 364 (9429), 149–155. doi:10.1016/s0140-6736(04)16627-0

Seyhoun, I., Hajighasemlou, S., Ai, J., Hosseinzadeh, F., Mirmoghtadaei, M., Seyhoun, S. M., et al. (2019). Novel combination of mesenchymal stem cell-conditioned medium with sorafenib have synergistic antitumor effect of hepatocellular carcinoma cells. *Asian Pac. J. Cancer Prev. APJCP* 20 (1), 263–267. doi:10.31557/apjcp.2019.20.1.263

Sharma, B., and Elisseeff, J. H. (2004). Engineering structurally organized cartilage and bone tissues. *Ann. Biomed. Eng.* 32 (1), 148–159. doi:10.1023/b:abme.0000007799.60142.78

Shen, W-C., Lai, Y-C., Li, L-H., Liao, K., Lai, H-C., Kao, S-Y., et al. (2019). Methylation and PTEN activation in dental pulp mesenchymal stem cells promotes osteogenesis and reduces oncogenesis. *Nat. Commun.* 10 (1), 2226–2313. doi:10.1038/s41467-019-10197-x

Shi, S., Bartold, P., Miura, M., Seo, B., Robey, P., and Gronthos, S. (2005). The efficacy of mesenchymal stem cells to regenerate and repair dental structures. *Orthod. craniofacial Res.* 8 (3), 191–199. doi:10.1111/j.1601-6343.2005.00331.x

Shi, S., and Gronthos, S. (2003). Perivascular niche of postnatal mesenchymal stem cells in human bone marrow and dental pulp. *J. bone mineral Res.* 18 (4), 696–704. doi:10.1359/jbmr.2003.18.4.696

Shi, S., Robey, P., and Gronthos, S. (2001). Comparison of human dental pulp and bone marrow stromal stem cells by cDNA microarray analysis. *Bone* 29 (6), 532–539. doi:10.1016/s8756-3282(01)00612-3

Shi, X., Mao, J., and Liu, Y. (2020). Pulp stem cells derived from human permanent and deciduous teeth: Biological characteristics and therapeutic applications. *Stem cells Transl. Med.* 9 (4), 445–464. doi:10.1002/sctm.19-0398

Simon, T. M., and Jackson, D. W. (2018). Articular cartilage: Injury pathways and treatment options. *Sports Med. Arthrosc. Rev.* 26, 31–39. doi:10.1097/00132585-200609000-00006

Smith, F. O., and Thomson, B. G. (2000). Umbilical cord blood collection, banking, and transplantation: Current status and issues relevant to perinatal caregivers. *Birth* 27 (2), 127–135. doi:10.1046/j.1523-536x.2000.00127.x

Soleimani, M., Abbasnia, E., Fathi, M., Sahraei, H., Fathi, Y., and Kaka, G. (2012). The effects of low-level laser irradiation on differentiation and proliferation of human bone marrow mesenchymal stem cells into neurons and osteoblasts—An *in vitro* study. *Lasers Med. Sci.* 27 (2), 423–430. doi:10.1007/s10103-011-0930-1

Sophia Fox, A. J., Bedi, A., and Rodeo, S. A. (2009). The basic science of articular cartilage: Structure, composition, and function. *Sports health* 1 (6), 461–468. doi:10.1177/1941738109350438

Sozen, B., Amadei, G., Cox, A., Wang, R., Na, E., Czukiewska, S., et al. (2018). Self-assembly of embryonic and two extra-embryonic stem cell types into gastrulating embryo-like structures. *Nat. Cell Biol.* 20 (8), 979–989. doi:10.1038/s41556-018-0147-7

Steadman, J. R., Briggs, K. K., Rodrigo, J. J., Kocher, M. S., Gill, T. J., and Rodkey, W. G. (2003). Outcomes of microfracture for traumatic chondral defects of the knee: Average 11-year follow-up. *Arthrosc. J. Arthrosc. Relat. Surg.* 19 (5), 477–484. doi:10.1053/jars.2003.50112

Strauer, B. E., and Kornowski, R. (2003). Stem cell therapy in perspective. *Mini-Review Expert Opin. Circ.* 107, 929–934. doi:10.1161/01.cir.0000057525.13182.24

Strioga, M., Viswanathan, S., Darinskas, A., Slaby, O., and Michalek, J. (2012). Same or not the same? Comparison of adipose tissue-derived versus bone marrow-derived mesenchymal stem and stromal cells. *Stem cells Dev.* 21 (14), 2724–2752. doi:10.1089/scd.2011.0722

Sylvester, K. G., and Longaker, M. T. (2004). Stem cells: Review and update. *Archives Surg.* 139 (1), 93–99. doi:10.1001/archsurg.139.1.93

Szychlinska, M. A., Stoddart, M. J., D'Amora, U., Ambrosio, L., Alini, M., and Musumeci, G. (2017). Mesenchymal stem cell-based cartilage regeneration approach and cell senescence: Can we manipulate cell aging and function? *Tissue Eng. Part B Rev.* 23 (6), 529–539. doi:10.1089/ten.teb.2017.0083

Taguchi, T., Yanagi, Y., Yoshimaru, K., Zhang, X-Y., Matsuura, T., Nakayama, K., et al. (2019). Regenerative medicine using stem cells from human exfoliated deciduous teeth (SHED): A promising new treatment in pediatric surgery. *Surg. today* 49 (4), 316–322. doi:10.1007/s00595-019-01783-z

Takahashi, K., Tanabe, K., Ohnuki, M., Narita, M., Ichisaka, T., Tomoda, K., et al. (2007). Induction of pluripotent stem cells from adult human fibroblasts by defined factors. *Cell* 131 (5), 861–872. doi:10.1016/j.cell.2007.11.019

Takahashi, K., and Yamanaka, S. (2006). Induction of pluripotent stem cells from mouse embryonic and adult fibroblast cultures by defined factors. *Cell* 126 (4), 663–676. doi:10.1016/j.cell.2006.07.024

Tamaki, Y., Nakahara, T., Ishikawa, H., and Sato, S. (2013). *In vitro* analysis of mesenchymal stem cells derived from human teeth and bone marrow. *Odontology* 101 (2), 121–132. doi:10.1007/s10266-012-0075-0

Thomson, J. A., Itskovitz-Eldor, J., Shapiro, S. S., Waknitz, M. A., Swiergiel, J. J., Marshall, V. S., et al. (1998). Embryonic stem cell lines derived from human blastocysts. *science* 282 (5391), 1145–1147. doi:10.1126/science.282.5391.1145

To, K., Zhang, B., Romain, K., Mak, C., and Khan, W. (2019). Synovium-derived mesenchymal stem cell transplantation in cartilage regeneration: A PRISMA review of *in vivo* studies. *Front. Bioeng. Biotechnol.* 7, 314. doi:10.3389/fbioe.2019.00314

Tsai, C-C., and Hung, S-C. (2012). Functional roles of pluripotency transcription factors in mesenchymal stem cells. *Cell cycle* 11 (20), 3711–3712. doi:10.4161/cc.22048

Tsumaki, N., Nakase, T., Miyaji, T., Kakiuchi, M., Kimura, T., Ochi, T., et al. (2002). Bone morphogenetic protein signals are required for cartilage formation and differently regulate joint development during skeletogenesis. *J. Bone Mineral Res.* 17 (5), 898–906. doi:10.1359/jbmr.2002.17.5.898

van der Kraan, P., and van den Berg, W. (2007). TGF-beta and osteoarthritis. *Osteoarthr. Cartil.* 15 (6), 597–604. doi:10.1016/j.joca.2007.02.005

Van Pham, P. (2017). *Bone and cartilage regeneration*. Berlin, Germany: Springer International Publishing.

Vicente-Duenas, C., de Diego, J. G., Rodriguez, F., Jimenez, R., and Cobaleda, C. (2009). The role of cellular plasticity in cancer development. *Curr. Med. Chem.* 16 (28), 3676–3685. doi:10.2174/092986709789105019

Vizoso, F. J., Eiro, N., Cid, S., Schneider, J., and Perez-Fernandez, R. (2017). Mesenchymal stem cell secretome: Toward cell-free therapeutic strategies in regenerative medicine. *Int. J. Mol. Sci.* 18 (9), 1852. doi:10.3390/ijms18091852

Volponi, A. A., Pang, Y., and Sharpe, P. T. (2010). Stem cell-based biological tooth repair and regeneration. *Trends Cell Biol.* 20 (12), 715–722. doi:10.1016/j.tcb.2010.09.012

Waller-Wise, R. (2011). Umbilical cord blood: Information for childbirth educators. *J. Perinat. Educ.* 20 (1), 54–60. doi:10.1891/1058-1243.20.1.54

Wang, J., Wang, X., Sun, Z., Wang, X., Yang, H., Shi, S., et al. (2010). Stem cells from human-exfoliated deciduous teeth can differentiate into dopaminergic neuron-like cells. *Stem cells Dev.* 19 (9), 1375–1383. doi:10.1089/scd.2009.0258

Wang, L., Zhao, L., and Detamore, M. S. (2011). Human umbilical cord mesenchymal stromal cells in a sandwich approach for osteochondral tissue engineering. *J. Tissue Eng. Regen. Med.* 5 (9), 712–721. doi:10.1002/term.370

Wang, M., Yuan, Z., Ma, N., Hao, C., Guo, W., Zou, G., et al. (2017). Advances and prospects in stem cells for cartilage regeneration. *Stem Cells Int.* 2017, 1–16. doi:10.1155/2017/4130607

Wang, X., Sha, X-J., Li, G-H., Yang, F-S., Ji, K., Wen, L-Y., et al. (2012). Comparative characterization of stem cells from human exfoliated deciduous teeth and dental pulp stem cells. *Archives oral Biol.* 57 (9), 1231–1240. doi:10.1016/j.archoralbio.2012.02.014

Wei, X., Yang, X., Han, Z., Qu, F., Shao, L., and Shi, Y. (2013). Mesenchymal stem cells: A new trend for cell therapy. *Acta Pharmacol. Sin.* 34 (6), 747–754. doi:10.1038/aps.2013.50

Weizel, A., Distler, T., Schneidereit, D., Friedrich, O., Bräuer, L., Paulsen, F., et al. (2020). Complex mechanical behavior of human articular cartilage and hydrogels for cartilage repair. *Acta Biomater.* 118, 113–128. doi:10.1016/j.actbio.2020.10.025

Werle, S. B., Lindemann, D., Steffens, D., Demarco, F. F., de Araujo, F. B., Pranke, P., et al. (2016). Carious deciduous teeth are a potential source for dental pulp stem cells. *Clin. Oral Investig.* 20 (1), 75–81. doi:10.1007/s00784-015-1477-5

Williams, J. T., Southerland, S. S., Souza, J., Calcutt, A. F., and Cartledge, R. G. (1999). Cells isolated from adult human skeletal muscle capable of differentiating into multiple mesodermal phenotypes. *Am. Surg.* 65 (1), 22–26. doi:10.1177/000313489906500106

Woo, C. H., Kim, H. K., Jung, G. Y., Jung, Y. J., Lee, K. S., Yun, Y. E., et al. (2020). Small extracellular vesicles from human adipose-derived stem cells attenuate cartilage degeneration. *J. Extracell. vesicles* 9 (1), 1735249. doi:10.1080/20013078.2020.1735249

Wood, J. J., Malek, M. A., Frassica, F. J., Polder, J. A., Mohan, A. K., Bloom, E. T., et al. (2006). Autologous cultured chondrocytes: Adverse events reported to the United States Food and Drug administration. *JBJS* 88 (3), 503–507. doi:10.2106/jbjs.e.00103

Xiao, L., and Nasu, M. (2014). From regenerative dentistry to regenerative medicine: Progress, challenges, and potential applications of oral stem cells. *Stem cells cloning Adv. Appl.* 7, 89–99. doi:10.2147/sccaa.s51009

Yamada, Y., Nakamura-Yamada, S., Kusano, K., and Baba, S. (2019). Clinical potential and current progress of dental pulp stem cells for various systemic diseases in regenerative medicine: A concise review. *Int. J. Mol. Sci.* 20 (5), 1132. doi:10.3390/ijms20051132

Yamanaka, S. (2009). Elite and stochastic models for induced pluripotent stem cell generation. *Nature* 460 (7251), 49–52. doi:10.1038/nature08180

Yamaza, T., Kentaro, A., Chen, C., Liu, Y., Shi, Y., Gronthos, S., et al. (2010). Immunomodulatory properties of stem cells from human exfoliated deciduous teeth. *Stem Cell Res. Ther.* 1 (1), 5–11. doi:10.1186/scrt5

Yang, X., Lu, Z., Wu, H., Li, W., Zheng, L., and Zhao, J. (2018). Collagen-alginate as bioink for three-dimensional (3D) cell printing based cartilage tissue engineering. *Mater. Sci. Eng. C* 83, 195–201. doi:10.1016/j.msec.2017.09.002

Yang, X., Ma, Y., Guo, W., Yang, B., and Tian, W. (2019). Stem cells from human exfoliated deciduous teeth as an alternative cell source in bio-root regeneration. *Theranostics* 9 (9), 2694–2711. doi:10.7150/thno.31801

Zainal Ariffin, S. H., Kermani, S., Megat Abdul Wahab, R., Senafi, S., Zainal Ariffin, Z., and Abdul Razak, M. (2012). *In vitro* chondrogenesis transformation study of mouse dental pulp stem cells. *Sci. World J.* 2012, 1–7. doi:10.1100/2012/827149

Zehentner, B. K., Dony, C., and Burtscher, H. (1999). The transcription factor Sox9 is involved in BMP-2 signaling. *J. Bone Mineral Res.* 14 (10), 1734–1741. doi:10.1359/jbmr.1999.14.10.1734

Zhang, S., Hu, B., Liu, W., Wang, P., Lv, X., Chen, S., et al. (2020). Articular cartilage regeneration: The role of endogenous mesenchymal stem/progenitor cell recruitment and migration. *Seminars arthritis rheumatism* 50, 198–208. doi:10.1016/j.semarthrit.2019.11.001

Zhang, W., Walboomers, X. F., Shi, S., Fan, M., and Jansen, J. A. (2006). Multilineage differentiation potential of stem cells derived from human dental pulp after cryopreservation. *Tissue Eng.* 12 (10), 060928122958008–060928122958023. doi:10.1089/ten.2006.12.ft-220

Zhang, Y., Liu, X., Zeng, L., Zhang, J., Zuo, J., Zou, J., et al. (2019). Polymer fiber scaffolds for bone and cartilage tissue engineering. *Adv. Funct. Mater.* 29 (36), 1903279. doi:10.1002/adfm.201903279

Zuk, P. A., Zhu, M., Ashjian, P., De Ugarte, D. A., Huang, J. I., Mizuno, H., et al. (2002). Human adipose tissue is a source of multipotent stem cells. *Mol. Biol. Cell* 13 (12), 4279–4295. doi:10.1091/mbc.e02-02-0105

Zuk, P. A., Zhu, M., Mizuno, H., Huang, J., Futrell, J. W., Katz, A. J., et al. (2001). Multilineage cells from human adipose tissue: Implications for cell-based therapies. *Tissue Eng.* 7 (2), 211–228. doi:10.1089/107632701300062859

Friedenstein, A, Piatetzky-Shapiro, I, and Petrakova, K. Osteogenesis in transplants of bone marrow cells. *J Embryol Exp Morphol*, 1966 16:381-90.

frontiers | Frontiers in Bioengineering and Biotechnology

TYPE Original Research
PUBLISHED 07 March 2023
DOI 10.3389/fbioe.2023.1110703

OPEN ACCESS

EDITED BY
Andrea Banfi,
University of Basel, Switzerland

REVIEWED BY
Anjali P. Kusumbe,
University of Oxford, United Kingdom
Liangliang Kong,
Children's Hospital of Nanjing Medical University, China

*CORRESPONDENCE
Chuang Ma,
8212682@qq.com

†These authors have contributed equally to this work and share first authorship

SPECIALTY SECTION
This article was submitted to Tissue Engineering and Regenerative Medicine, a section of the journal Frontiers in Bioengineering and Biotechnology

RECEIVED 29 November 2022
ACCEPTED 24 February 2023
PUBLISHED 07 March 2023

CITATION
Wu S, Zhang L, Zhang R, Yang K, Wei Q, Jia Q, Guo J and Ma C (2023), Rat bone marrow mesenchymal stem cells induced by rrPDGF-BB promotes bone regeneration during distraction osteogenesis.
Front. Bioeng. Biotechnol. 11:1110703.
doi: 10.3389/fbioe.2023.1110703

Rat bone marrow mesenchymal stem cells induced by rrPDGF-BB promotes bone regeneration during distraction osteogenesis

Shuo Wu[1†], Lijie Zhang[2†], Ruidan Zhang[3†], Kang Yang[4], Qin Wei[5], Qiyu Jia[1], Jian Guo[1] and Chuang Ma[1*]

[1]Department of Microrepair and Reconstruction, the First Affiliated Hospital of Xinjiang Medical University, Urumqi, China, [2]Department of Neurology, the Second Affiliated Hospital of Xinjiang Medical University, Urumqi, China, [3]Guangdong New Omega Medical Centre, Guangzhou, China, [4]Hand and foot microsurgery of the third people's Hospital of Xinjiang Uygur Autonomous Region, Urumqi, China, [5]Animal Experiment Center of Xinjiang Medical University, Urumqi, China

Background: In the clinical treatment of large bone defects, distraction osteogenesis can be used. However, some patients may suffer from poor bone regeneration, or even delayed healing or non-union. Problems with the aggregation and proliferation of primary osteoblasts, or problems with the differentiation of primary osteoblasts will lead to poor bone regeneration. Therefore, supplementing exogenous primary osteoblasts and growth factors when using distraction osteogenesis may be a treatment plan with great potential.

Methods: Bone marrow mesenchymal stem cells (BMSCs) were extracted from rats and cultured. Subsequently, Recombinant Rat Platelet-derived Growth Factor BB (rrPDGF-BB) was used to induce bone marrow mesenchymal stem cells. At the same time, male adult rats were selected to make the right femoral distraction osteogenesis model. During the mineralization period, phosphate buffer salt solution (control group), non-induction bone marrow mesenchymal stem cells (group 1) and recombinant rat platelet-derived growth factor BB intervened bone marrow mesenchymal stem cells (group 2) were injected into the distraction areas of each group. Then, the experimental results were evaluated with imaging and histology. Statistical analysis of the data showed that the difference was statistically significant if $p < 0.05$.

Results: After intervention with recombinant rat platelet-derived growth factor BB on bone marrow mesenchymal stem cells, the cell morphology changed into a thin strip. After the cells were injected in the mineralization period, the samples showed that the callus in group 2 had greater hardness and the color close to the normal bone tissue; X-ray examination showed that there were more new callus in the distraction space of group 2; Micro-CT examination showed that there were more new bone tissues in group 2; Micro-CT data at week eight showed that the tissue volume, bone volume, percent bone volume, bone trabecular thickness, bone trabecular number and bone mineral density in group 2 were the largest, and the bone trabecular separation in group 2 was the smallest. There was a statistical difference between the groups ($p < 0.05$); HE staining confirmed that group 2 formed more blood vessels and chondrocytes earlier than the control group. At 8 weeks, the bone marrow cavity of group 2 was obvious, and some of them had been fused.

Conclusion: The study confirmed that injecting bone marrow mesenchymal stem cellsBB into the distraction space of rats can promote the formation of new bone in the distraction area and promote the healing of distraction osteogenesis.

KEYWORDS

BMSCs, distraction osteogenesis (DO), PDGF-BB, rat, osteogenesis, femur

1 Introduction

In the clinical practice, large bone defects can be treated with Ilizarov technology (Qin, 2021; Zheng et al., 2021). However, some patients had bone regeneration deficiency, which eventually led to delayed healing or even difficult healing (Borzunov and Shastov, 2019; Mi et al., 2021; Migliorini et al., 2021). Some scholars believe that the principle of poor bone regeneration is that there is a problem in the aggregation and proliferation of original osteoblasts, or there is a problem in the differentiation of original osteoblasts (Feng et al., 2016). Clinical studies have found that patients with primary osteoblast deficiency, severe trauma and severe tissue defects after radiotherapy will suffer from bone regeneration deficiency (Hamushan et al., 2020; Shen et al., 2021; Ye et al., 2021). Therefore, when using distraction osteogenesis to treat large bone defects, it may be a reasonable treatment plan to supplement exogenous original osteoblasts.

A large number of scholars have studied the principle of distraction osteogenesis. Some scholars reported that during distraction osteogenesis, BMSCs were recruited from the incubation period, and differentiated into osteoblasts or chondrocytes in the extended and mineralized periods (Ai-Aql et al., 2008; Dhaliwal et al., 2016), and a large number of callus was formed (Wang et al., 2013; Yuan-Zhe and Lee, 2018). Yang found that injecting mesenchymal stem cells into the distraction space can promote the formation of new bone tissue and shorten the mineralization time. Therefore, transplantation of BMSCs was a valuable regenerative therapy (Yang et al., 2017). However, the survival rate of BMSCs after transplantation was low, the differentiation was poor, and the regeneration ability was reduced (Ortinau et al., 2019). Some scholars proposed to enhance the activity of BMSCs through endogenous or exogenous methods to promote the proliferation of BMSCs, which may further promote bone repair.

Platelet-derived growth factor-BB (PDGF-BB) is considered to be a key regulator of tissue repair and regeneration. Studies have shown that PDGF-BB can promote cell mitosis (Gruber et al., 2003; Lee et al., 2013), chemotactic BMSCs and fibroblasts to reach the callus site (Heldin and Westermark, 1999; Ozaki et al., 2007), and promote tissue angiogenesis (Homsi and Daud, 2007). Some scholars reported that exogenous PDGF-BB was injected into the distraction space of rats, and the results showed that the volume of regenerated bone in the experimental group was significantly larger than that in the control group (Moore et al., 2009). Therefore, it was confirmed that PDGF-BB injection could promote the formation of new bone in the distraction space, accelerate the mineralization of bone tissue, and shorten the healing time. However, growth factor injection therapy has many disadvantages, such as the high price of growth factor, short and unstable half-life, easy infection caused by repeated injections, and difficult to grasp the injection dose and frequency. Therefore, it is particularly important to select an appropriate release control system. Our research group plans to inject the BMSCs induced by rrPDGF-BB into distraction space of rats to verify its osteogenic effect.

The main method of this study was to culture rat BMSCs *in vitro*, and use rrPDGF-BB to induce BMSCs. At the same time, the rat femur distraction osteogenesis model was made, and then the induced BMSCs were injected into the distraction space, then the experimental results were evaluated by imaging and histology. The results confirmed that the injection of BMSCs induced by rrPDGF-BB into the distraction space can promote the formation of new bone in the distraction area of rats. We expect that this study will promote the development of distraction osteogenesis technology.

2 Materials and methods

2.1 Experimental animals

120 male Sprague-Dawley (SD) rats, 48 of which were used to extract BMSCs (weight 120–150 g), 72 of which were used to build femoral distraction osteogenesis models (weight 350–400 g). The rats were purchased from Animal Experiment Center of Xinjiang Medical University [Certificate No: SYXK (Xin) 2018–0003]. The rats were raised in a standard and suitable environment for 7 days before surgery. The animal study was reviewed and approved by Ethics Committee of the First Affiliated Hospital of Xinjiang Medical University (NO. IACUC20190818-06). Written informed consent was obtained from the owners for the participation of their animals in this study.

2.2 Main instruments

Distraction osteogenesis external fixation device (Figure 1), designed by the key laboratory of the Institute of Engineering and Technology of Xinjiang University, mainly made of titanium alloy, 50.0 mm long, 10.0 mm wide, and 10.0 mm high; The end contains a rotating nut, which is used with an internal square wrench. The internal square wrench can be rotated 360° clockwise to increase the distraction space by 0.5 mm. External fixation device with four pieces of 1.0 × 200.0 mm self tapping threaded Kirschner wire is made of titanium alloy, with thread at the end and thread length of 12.0 mm. For the convenience of the following description, we mark the corresponding nail path of the external fixation device, which is marked by number 1–4 (Figure 1C).

2.3 Rat BMSCs culture

SD rats weighing 120–150 g were selected and anesthetized with 2% pentobarbital sodium (3 mg/100 g, Huaye Huanyu Chemical, Beijing, China). After the anesthesia took effect, the

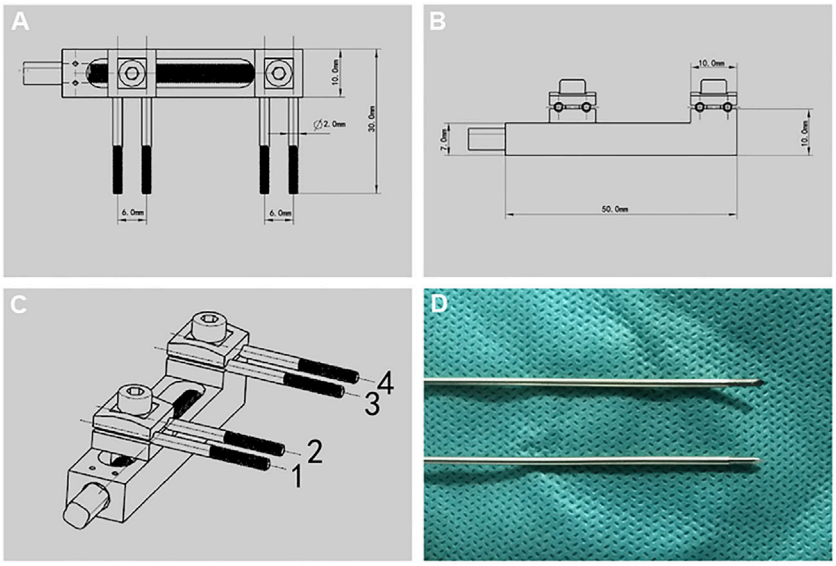

FIGURE 1
Design drawing of external fixation device and Kirschner wire. **(A-C)** Design drawing of external fixation device. **(D)** Threaded Kirschner wire matched with external fixation device.

rats were killed by cervical dislocation; After soaking in 75% ethanol (Caoshanhu, Jiangxi, China) for 10 min, transfer it to the super clean table (Sujing, Shanghai, China, SM-CJ-1D), cut the skin and subcutaneous tissue of rats, take out bilateral tibia, fibula and femur, and soak them in sterile phosphate buffer salt solution (PBS, Gibco, United States) containing 1% penicillin (Gibco, United States), Use sterile surgical scissors (Wilson, Shanghai, China) to cut off both ends of the bone, use a 5.0 mL syringe to absorb low sugar complete culture medium to repeatedly wash the bone marrow cavity, blow the bone marrow solution evenly repeatedly and then centrifugate it (2000 r/min, 10 min), wash it twice with PBS, discard the upper liquid, blow the lower bone marrow solution evenly and then inoculate it in the culture bottle (Corning, United States), The low sugar complete medium (Gibco, United States) containing 12% fetal bovine serum (Gibco, United States) was used for culture.

2.4 Flow cytometry identification of rat BMSCs

The third generation BMSCs were cultured, and when they filled 90% of the bottom of the culture bottle, they were fully digested with 0.25% trypsin (Gibco, United States). Divide the cell fluid into four tubes, ensuring that each tube has at least 2×10^5 cells were washed twice with PBS, then CD29-PE antibody (BD Biosciences, United States), CD34-PE antibody (Abcam, Cambridge, United Kingdom) and CD45-PE-Cy antibody (BD Biosciences, United States) were added into the test tube, and blank control was set in the fourth tube. Incubate at room temperature and away from light for 30 min, discard the upper liquid after centrifugation, then add 1.0 mL PBS into the test tube, and use flow cytometry (Beckman coulter, Germany) for analysis.

2.5 Rat BMSCs induced by rrPDGF-BB

Our previous study found that the concentration was 25 μg/L rrPDGF-BB (Catalog: 520-BB, R&D Systems, United States) has the best effect in inducing rat BMSCs for 3 days (Jiang et al., 2021a; Wei et al., 2021a; Jiang et al., 2021b; Wei et al., 2021b). The concentration of rrPDGF-BB configured in this study is 25 μg/L conditioned medium, use this conditioned medium to culture the third generation BMSCs, and observe the cells under light microscope (ZEISS Axio observer Z1, ZEISS, Germany).

2.6 Preparation of cell injection

Cultivate the BMSCs mentioned above, and when they fill the bottom of the culture bottle, fully digest them with trypsin, and prepare them into cell suspension with a concentration of 1×10^6/mL。 BMSCs cell suspension without induction was prepared by the same method for standby.

2.7 Model of distraction osteogenesis

Rats were fasted for 6 h before operation. 350–400 g male SD rats were selected and anesthetized with 2% pentobarbital sodium. After the anesthesia took effect, the rats were placed in the right lateral position. The operation area was shaved with an animal razor. After shaving, the operation area was disinfected with skin iodine for three times and sterile sheets were laid. A 3.0 cm strip incision was taken at the lateral side of the right femur of the rat. After the skin was cut according to the femoral course of the rat, a white line was visible, and the subcutaneous tissue and fascia were cut layer by layer (Figure 2A). Use vascular forceps to separate the surrounding

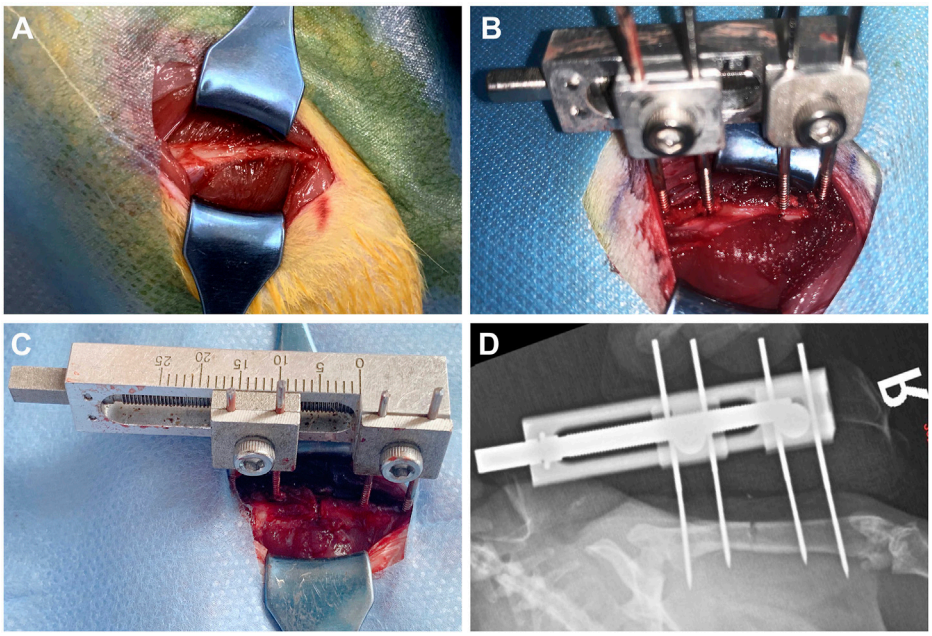

FIGURE 2
Schematic diagram of the operation of rat right femoral distraction osteogenesis model. **(A-C)** The surgical procedure. **(D)** X-ray examination after operation.

muscles and other soft tissues layer by layer, and use hooks to pull the surrounding tissues to protect the nerves, blood vessels, muscles, etc. A titanium alloy Kirschner wire with a diameter of 1.0 mm was drilled into the proximal femur perpendicular to the femur, marked as No. 1; Use the nail path of the external fixation device to match the corresponding position of the femur, and drill No. 3 Kirschner wire into the distal femur; Using the same method, drill in No. 2 and No. 4 Kirschner pins. After fixing firmly, install the external fixing device and adjust the external fixing device to a proper position (Figure 2B). At this time, pull the surrounding tissues with a draw hook to protect the soft tissues in the operation area. Pay attention to protecting the periosteum. At the middle of No. 3 and No. 4 Kirschner wires, cut the femur with a pendulum saw (YTZJ-B, Zhengda, Hangzhou, China). During osteotomy, wash the osteotomy area with low temperature normal saline to avoid thermal damage during osteotomy (Figure 2C). Use an internal square wrench to turn the nut of the external fixation device clockwise. The two ends of the femur are separated from each other under direct vision, indicating that the femur is completely disconnected, and the molding is successful (Wu et al., 2020; Liu Y. et al., 2021; Wu et al., 2021; Liu et al., 2022). Rinse the wound with normal saline, suture the wound layer by layer, bind it with sterile gauze, and complete the modeling.

2.8 Postoperative treatment

The rats were given normal diet 6 h after the operation, and were given painkillers and antibiotics to prevent infection until the third day after the operation. The wound was wiped with iodophor cotton balls at an interval of 2 days after surgery, and clean sterile gauze was replaced until the wound healed. When severe wound infection was found, debridement was performed on the infected rat wound in time.

2.9 Distraction process

After operation, every rat was raised in a single cage. The first 7 days were the rest period. After the rest period, the rats entered into the stretching period. Every 12 h, the internal square wrench was used to rotate the nut of the external fixation device 180° clockwise. The tensioning frequency was 0.25 mm/12 h (Figure 3). The distraction period was 14 days, and the expected distraction was 7.0 mm. After the end of the distraction, the scale of the external fixation device was observed. All rats basically obtained the expected distraction distance, and then the rats entered the mineralization period, Continue single cage feeding until the end of the experiment.

2.10 Cell injection into rats

72 rats were randomly divided into three groups; Control group: 0.3 mL PBS injection; group 1:0.3 mL BMSCs cell suspension was injected. Group 2:0.3 mL of BMSCs cell suspension induced by rrPDGF-BB was injected. Inject cells once on the first day of mineralization, the injection method: the rats were anesthetized and the injection area was disinfected. 0.3 mL cell suspension (the concentration was 1 × 106/mL) was drawn with a 1.0 mL syringe, and the needle of the syringe was inserted into the distraction area. There was a sense of penetration. No bleeding was found after the

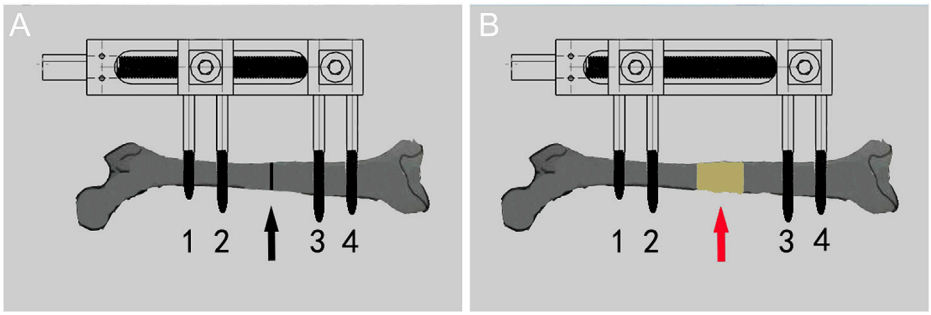

FIGURE 3
Diagram of the process of distraction osteogenesis in rats. **(A)** Before distraction the femur (black arrow shows osteotomy area). **(B)** After distraction the femur (red arrow shows the distraction area).

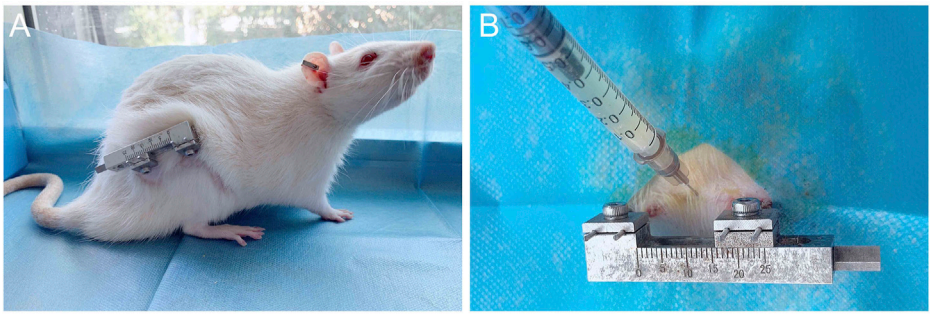

FIGURE 4
Post-operative picture of the rat and schematic diagram of injected cells. **(A)** Post-operative photos of rats with external fixation devices. **(B)** Schematic diagram of injected of cells into the distraction osteogenesis area of rat femur.

pump back, and then the cells were injected into the distraction area. The syringe was removed and the wound was pressed for 2min without significant bleeding, then disinfected again and wrapped in a sterile dressing (Figure 4B).

2.11 X-ray examination

X-ray was taken on all rats on the day after operation, after the end of distraction and at 2, 4, and 8 weeks of mineralization (Kodak DR7500, Department of Radiology, First Affiliated Hospital of Xinjiang Medical University, Urumqi, China).

2.12 Micro-CT examination

At the 8th week of mineralization period, three rats in each group were killed at random, and bilateral femoral specimens were taken. After cleaning the specimens, Micro-CT examination (Scanco Medical, Switzerland). Micro-CT program was used to calculate the data of each group, including the tissue volume, bone volume, percent bone volume, bone trabecular thickness, bone trabecular number, bone trabecular separation and bone mineral density, and statistical analysis was conducted.

2.13 Sample collection

At 2, 4, and 8 weeks of mineralization period, six rats in each group were randomly selected and sacrificed to collect femur specimens. The sample was fixed with 4% paraformaldehyde (Solarbio, Beijing, China) for 48 h, and then cleaned with PBS. After cleaning, pour in 10% EDTA decalcification solution (Solarbio, Beijing, China). It was estimated that decalcification will last for 4 weeks (Savi et al., 2017; Bogoevski et al., 2019; Dou et al., 2021; Alaeddini et al., 2022). When the samples was elastic, it indicated that decalcification was complete, and the samples was stored in 75% alcohol.

2.14 Histomorphological analysis

The decalcified samples were cleaned and then gradually dehydrated with alcohol, after which they were immersed in xylene (Sigma, Switzerland) and finally embedded in paraffin (Leica, Germany) (Guo et al., 2020; Nakamura et al., 2021; Marinopoulos et al., 2022). The samples were frozen at −20°C for 8 h, and then cut into 3.0 μm thick sections with a microtome (RM2135, Leica, Germany), removed with adhesion microscope slides (Citotest, Jiangsu, China) and baked in a 60°C oven.

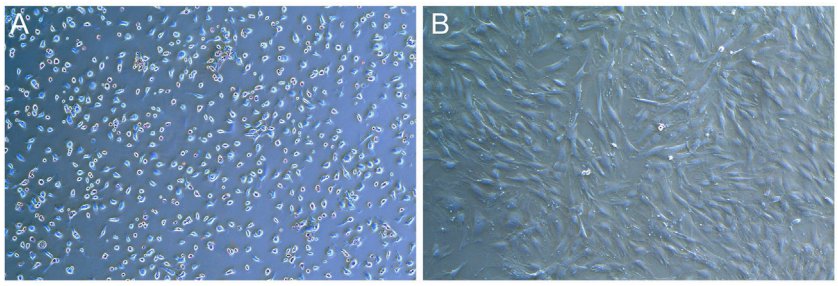

FIGURE 5
Photos of BMSCs in SD rats (X50). **(A)** Photos of primary cells. **(B)** Photos of the third generation cells.

2.15 HE staining

The slides containing the samples were hydrated step by step, dipped in hematoxylin dye solution (Sigma, Switzerland) for staining, washed with ultrapure water and then dipped with 1% hydrochloric acid ethanol (Sigma, Switzerland), washed again with ultrapure water and then re stained with eosin solution (Sigma, Switzerland), and the xylene was transparent after alcohol dehydration. Finally, cover the glass slide, seal the slides with neutral resin (Solarbio, Beijing, China), and observe under the light microscope after the slices were dried.

2.16 Statistical method

SPSS 26.0 statistical software was used for statistical analysis of data. The data were expressed by mean ± standard deviation (Mean + SD). Analysis of variance was used for comparison between groups. $p < 0.05$ was statistically significant.

3 Result

3.1 Morphological observation of rat BMSCs

Primary rat BMSCs adhered to the wall and grew as small, round or oval cells with regular morphology and slow cell growth (Figure 5A). After passage, the cells grew faster and began to spread in a spindle shape and round shape. In the third generation, cells proliferate in a swirl. The cells in the center of the whirlpool were dense, large in size, clear in outline, mostly flat spindle or irregular, and 1-3 nucleoli could be seen in the cells under high magnification (Figure 5B).

3.2 Purity identification of rat BMSCs by flow cytometry

Flow cytometry was used to detect the surface markers of BMSCs. The results showed that the third generation BMSCs expressed high CD29 (95.0%), low CD45 (3.6%) and CD34 (0.1%), the purity of BMSCs was high (Figure 6). The results were consistent with those reported in the literature (Cui et al., 2018; Zhao et al., 2018; Yang H. et al., 2020; Liu M. et al., 2021).

3.3 Observe induced cells

After the rat BMSCs of third generation were cultured in the medium containing rrPDGF-BB, the culture medium contained floating cells and cell fragments under the microscope on the first day of induction, which decreased after fluid change. The cell morphology changed from the initial oval shape to an elongated shape with no significant change in cell volume (Figure 7A). On the third day of induction, some cells died. Under the microscope, the cells were reduced in size and elongated in shape, showing a flat spindle shape. The cells were arranged in a circular or reticulated arrangement, with some cells growing together (Figure 7B).

3.4 Observation of rat activity

During the experiment, the spirit of the rats was good, the diet and sleep were good, and the activities were good. At the third week after operation, there was a strip scar on the lateral side of the right femur of the rats, which was well healed. The hair around the wound had grown and completely covered the wound (Figure 4A). When the skin around the wound was touched, the rats responded. The skin temperature was acceptable, and there was no leakage at the suture. The external fixation device was well fixed, and four titanium alloy Kirschner wires were vertically drilled into the femur, without looseness and falling off. The skin around the Kirschner wire had no inflammatory reaction such as pus overflowing, and the wound had crusted and healed well. The external fixation device was gently moved, and it was found that the fixation was good without loosening or displacement. The rats were gently placed on the ground, and the rats walked well with a slight sense of load. The knee joint and ankle joint of the rats were active, and the rest were normal.

3.5 X-ray examination

The X-ray examination was taken on the day after the operation, which showed that the femoral shaft was completely separated, and the alignment of the broken end was good (Figure 2D). The X-ray examination taken after the end of the distraction showed that the distraction had reached the expected length. During the distraction, the osteotomy end was gradually separated without dislocation, and there was no obvious callus formation in the distraction area. On the 14th day

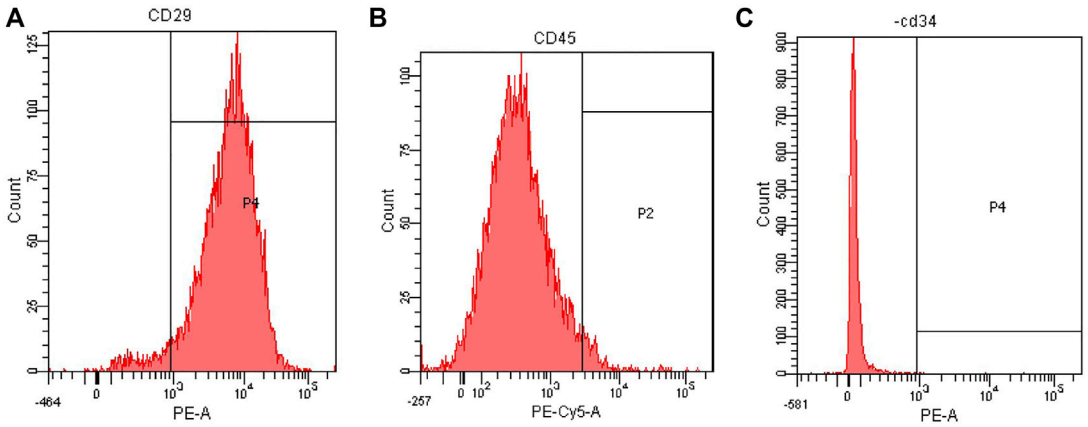

FIGURE 6
Flow cytometry analysis of rat BMSCs. **(A)** Expression of CD29. **(B)** Expression of CD45. **(C)** Expression of CD34.

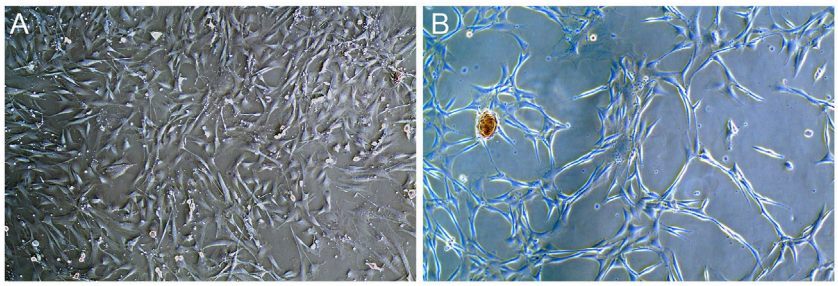

FIGURE 7
Photos of rrPDGF-BB induced BMSCs (X50). **(A)** One days after intervention. **(B)** Three days after intervention.

of mineralization period, callus formation was observed in the distraction area of groups 1 and 2, with uneven new bone formation and no continuous callus, and the density of callus in group 2 was higher than that in group 1. In the control group, the distraction area was bright without obvious callus formation. The osteotomy ends of the three groups were flat and clearly demarcated from the normal bone. On the 28th day of the mineralization period, callus formation was observed in the stretch area of the three groups, and the new callus was strip like or sheet like new bone, and the callus density in group 2 was greater than that in group 1, while the callus density in the control group was the smallest. The new bone in the distraction area of the three groups was cloudy, with low density, relatively continuous bone, uneven osteotomy end, and obvious boundary with normal bone. On the 56th day of mineralization period, uniform and continuous callus could be seen in the distraction area of groups 1 and 2 without obvious bright area, and the callus density of group 2 was higher than that of group 1, while the density of control group was the lowest. In group 2, the stretch area was dense and uniform, the bone was continuous, the osteotomy end was uneven, and the boundary with normal bone was blurred. In group 2, the bone marrow cavity was seen, but no bone marrow cavity recanalization was observed. The osteotomy ends of the control group and group 1 weren't smooth and had a clear boundary with the normal bone. In the control group, the new bone was discontinuous and there were transparent areas. The three groups of X-ray examination did not find the phenomenon of femoral bone non-union, bone defect and soft tissue incarceration (Figure 8).

3.6 Micro-CT examination

At the 8th week, the femur specimens of rats in each group were taken, and new bone was formed in the stretch area of the three groups, and the femurs were thickened. In the control group, the healing was poor, a small amount of callus was formed, and the broken end was not connected, and there was a certain gap that was not healed; In group 1, a large amount of callus was formed in the distraction area, and the broken end was partially connected, and no bone marrow cavity was reopened; In group 2, the healing was good, there were more callus in the distraction area, and the disconnected ends were connected, but no bone marrow cavity was reopened (Figure 9).

3.7 Micro-CT parameter analysis

The Micro-CT parameters of rat femur specimens were shown in Table 1 and Figure 10. The tissue volume, bone volume, percent

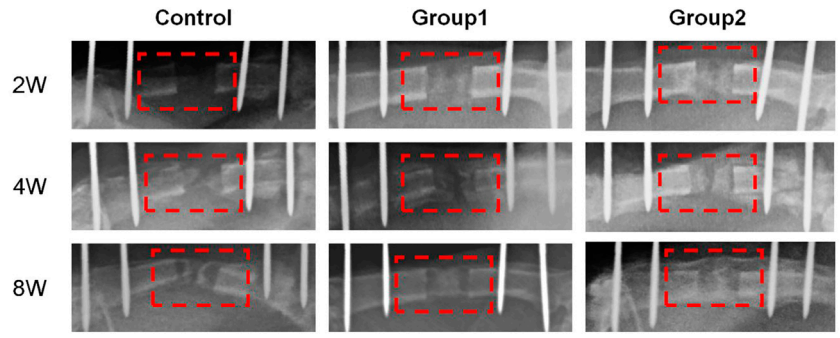

FIGURE 8
X-ray photos of femoral samples at different time points.

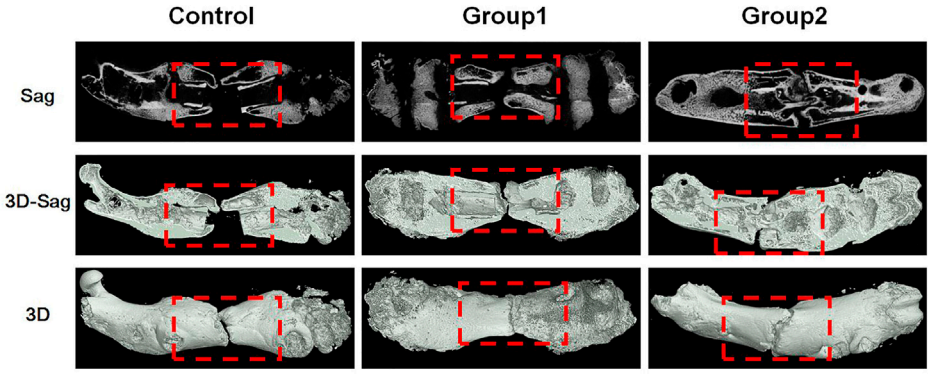

FIGURE 9
Micro-CT images of femurs in each group at the 8th week.

bone volume, bone trabecular thickness, bone trabecular number and bone mineral density of group 2 were the largest, followed by group 1, and the control group were the smallest, with statistical difference between groups ($p < 0.05$). The bone trabecular separation in the control group was the highest, followed by group 1 and group 2, and there were statistical differences between groups ($p < 0.05$).

3.8 General observation of samples

Femur samples at different time points were placed in a sterile sheet for observation (Figure 11). With the increase of time, the color of the distraction area gradually changed from brown to gray white, and the texture gradually became hard. On the 14th day of the mineralization period, the distraction area of the three groups had a clear boundary with the normal bone tissue, and the femur was elastic. With a little pressure, the femurs could be bent. The distraction area of the control group was brown red with soft texture, while the distraction area of groups 1 and groups 2 was brown with harder texture than the control group, and the distraction area of group 2 was harder than that of group 1. On the 28th day of the mineralization period, the new bone tissue in the distraction area of the control group was brown, with a clear boundary with the normal bone tissue, and the distraction area of group 1 and group 2 was gray white; The hardness of the new bone tissue in the distraction area of the three groups increased compared with that before. The hardness of group 2 was the highest, followed by group 1, and the hardness of the control group was the lowest. At the 56th day of mineralization, the distraction area of the control group was grayish white, with a clear boundary with normal bone tissue; In group 1 and group 2, the distraction area was white, with no obvious boundary with normal bone tissue; The hardness of the new bone tissue in the distraction area of the three groups was higher than before, the hardness of group 2 was the highest, followed by group 1, and the hardness of the control group was the lowest; In group 2, the texture of the distraction area was hard and the elasticity was poor. When the femur was bent, the femur was not easy to bend.

3.9 HE staining

Histological observation was carried out on rat samples of different groups at 2, 4, and 8 weeks respectively (Figure 12). At 2 weeks, fibroblasts and new blood vessels were mainly found in the distraction area. The most new blood vessels were found in the

TABLE 1 Micro-CT parameters of rat femora at week 8 (Mean + SD).

Sample	TV (mm^3)	BV (mm^3)	BV/TV (%)	Tb.Th (mm)	Tb.N (1/mm)	Tb.Sp (mm)	BMD (g/cm^3)
Control	148.668 ± 12.893	49.916 ± 8.701	0.334 ± 0.032	0.293 ± 0.036	1.120 ± 0.099	0.749 ± 0.075	0.326 ± 0.017
Group1	171.605 ± 13.900	77.498 ± 10.944	0.450 ± 0.029	0.348 ± 0.016	1.392 ± 0.279	0.554 ± 0.031	0.443 ± 0.049
Group2	198.315 ± 7.881	126.712 ± 14.820	0.638 ± 0.051	0.411 ± 0.033	1.734 ± 0.128	0.467 ± 0.042	0.602 ± 0.045
F	13.181	32.812	46.866	11.936	8.164	22.614	36.375
p	0.006	0.001	0.000	0.008	0.019	0.002	0.000

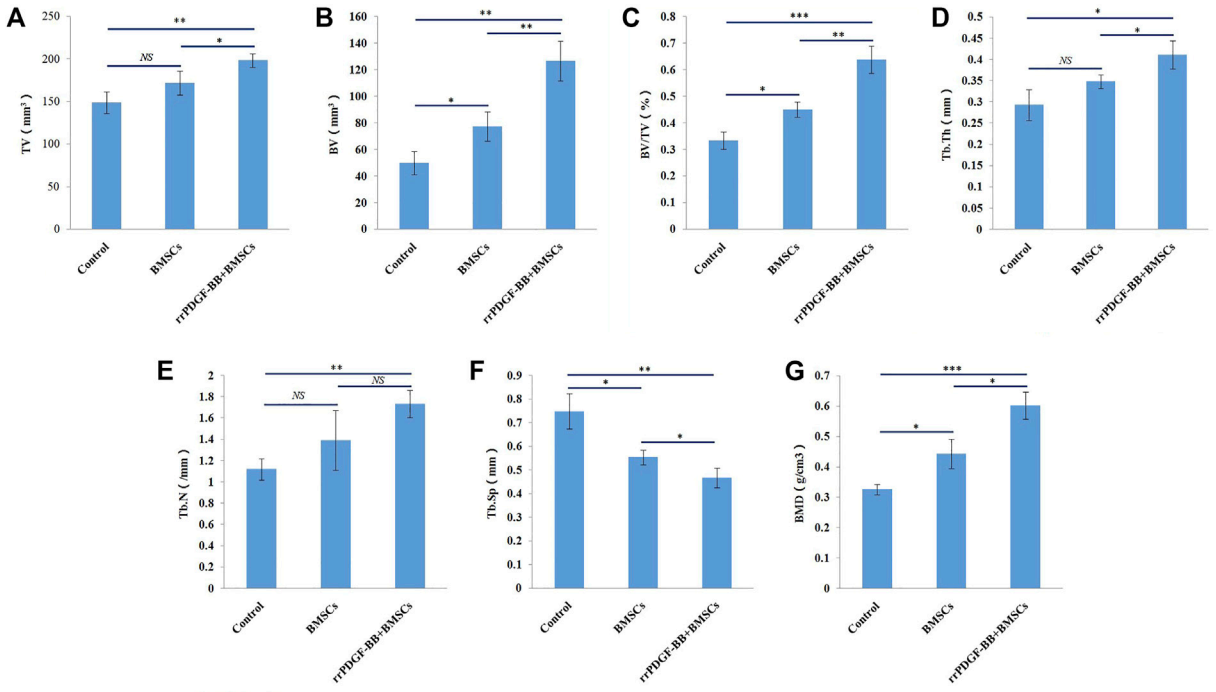

FIGURE 10
Micro-CT parameters of rat femora at week 8. **(A)** Micro-CT analyses of tissue volume (TV) in each group. **(B)** Micro-CT analyses of bone volume (BV) in each group. **(C)** Micro-CT analyses of percent bone volume (BV/TV) in each group. **(D)** Micro-CT analyses of trabecular thickness (Tb.Th) in each group. **(E)** Micro-CT analyses of trabecular number (Tb.N) in each group. **(F)** Micro-CT analyses of trabecular separation (Tb.Sp) in each group. **(G)** Micro-CT analyses of bone mineral density (BMD) in each group. ***p-value <0.001. **p-value <0.01. *p-value <0.05.

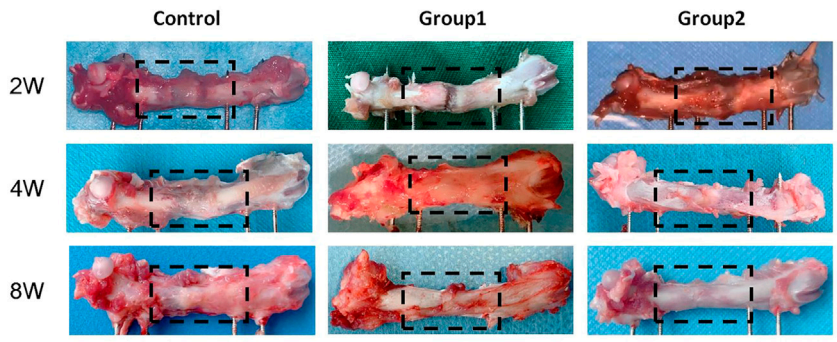

FIGURE 11
General picture of rat femur.

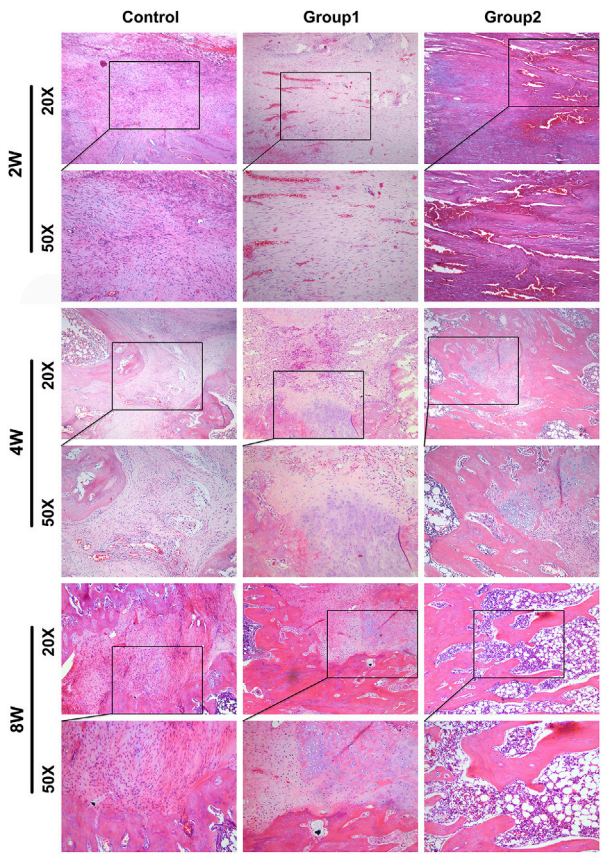

FIGURE 12
HE staining photos of femoral samples at different time points (X50).

distraction area of group 2, followed by group 1. In the control group, fibroblasts were mainly seen under microscope, and new blood vessels were few; In addition, a small amount of chondrocytes were generated in the distraction area of group 2. In the 4 weeks control group, fibroblasts were dominant under microscope, and the number of new blood vessels increased compared with that before; In group 1, fibroblasts were mainly seen under microscope, but the number was less than before, and there were new chondrocytes; In group 2, the new bone cells were mainly in the distraction area, the number of fibroblasts was less, and the number of chondrocytes was more than before. In the 8-week control group, the majority of the specimens were fibroblasts under microscope, and the number of new bone tissue was higher than before; group 1 was mainly composed of new bone tissue under microscope, with more chondrocytes and fewer fibroblasts than before. The new bone tissue had been connected into pieces and formed a few bone marrow cavities; In group 2, new bone tissue was mainly seen under microscope, no chondrocytes and fibroblasts were found, and bone marrow cavity was seen under microscope, part of which had been fused.

4 Discussion

Bone healing is a highly coordinated process, which is jointly affected by various growth factors and cells. Tissue engineering uses exogenous or endogenous growth factors, seed cells and scaffolds to simulate these healing processes. Many studies have described the effects of single factor and multi factor applications on bone healing (Hamushan et al., 2020; Shen et al., 2021; Ye et al., 2021; Han et al., 2022). Our study showed that injecting rrPDGF-BB into the distraction space during the mineralization period of distraction osteogenesis could promote the formation of new bone in the distraction area and promote healing.

In order to promote the healing of distraction osteogenesis, researchers in various countries have conducted a large number of experimental studies on it. Akçay found that the systemic application of vitamin E can stimulate the formation of new bone in rabbit distraction osteogenesis, thereby shortening the treatment time (Akçay et al., 2019); Acikan found that systemic application of melatonin can increase the formation of new bone in distraction osteogenesis (Acikan et al., 2018); Altay found that oxytocin can promote bone metabolism, increase new bone formation and promote bone healing in the distraction area (Altay et al., 2020); McDonald applied sclerostin antibody (Scl-Ab) in the rat model of distraction osteogenesis. The results showed that Scl-Ab treatment could promote bone formation and lead to bone regeneration with larger volume and higher strength. They believed that Scl-Ab had potential clinical value in preventing re fracture (McDonald et al., 2018); Jia found that mesenchymal stem cell exosomes can enhance the proliferation and osteogenesis of BMSCs, and promote the bone regeneration of distraction osteogenesis in aged rats (Jia et al., 2020). Tissue engineering is a better method to promote regeneration, so the combination of bone tissue engineering and distraction osteogenesis can promote the development of distraction osteogenesis (Yang et al., 2017; Roddy et al., 2018; Valtanen et al., 2021).

Some scholars had confirmed that BMSCs could be recruited into the distraction space, and then differentiated into osteoblasts or chondrocytes (Ai-Aql et al., 2008; Dhaliwal et al., 2016). This process was accompanied by callus formation (Wang et al., 2013; Yuan-Zhe and Lee, 2018), so BMSCs transplantation was a valuable regenerative therapy. Previous studies have shown that vasculature is the source of PDGFB. Vasculature plays a critical role in osteogenesis and bone diseases (Chen et al., 2021; Owen-Woods and Kusumbe, 2022), and vascular PDGF signalling is involved (Singh et al., 2019). Studies had confirmed that PDGF-BB could promote cell mitosis, chemotaxis of fibroblasts and BMSCs, promoted angiogenesis, promoted bone healing, etc., (Gruber et al., 2003; Ozaki et al., 2007). Our previous study found that the distraction space was gelatinlike tissue, and under the microscope, it was newly generated fibroblasts, new blood vessels, etc., (Wu et al., 2020). The new tissue in the distraction space can act as a scaffold material. Therefore, we believe that exogenous supplement of BMSCs and PDGF-BB can achieve the purpose of promoting healing.

After BMSCs were transplanted into the body, the differentiation was poor, the survival rate was low, and the regeneration potential was limited (Ortinau et al., 2019); Bowenpope made a rat model of distraction osteogenesis, and injected rhPDGF-BB of different density into the distraction area to verify the therapeutic effect of rhPDGF-BB on rat distraction osteogenesis (Bowenpope et al., 1984). However, the half-life of PDGF-BB is very short, and only continuous injection can achieve

the purpose of treatment, but it's expensive (Moore et al., 2009); In addition, there were problems such as fluid leakage during injection, so our research group first used rrPDGF-BB to intervene BMSCs, and then transplanted them. In addition, our previous *in vitro* experiments had confirmed that rrPDGF-BB of 25 μg/L significantly promoted differentiation of BMSCs, and once the concentration exceeded 50 μg/L, it would lead to cell death.

In our experiment, after we used rrPDGF-BB to induce with BMSCs, the cell morphology changed, and a circular or reticular structure appeared. We speculated that the cells had differentiated and had a preliminary vascular rudiment, which was consistent with the report of Heldin (Heldin and Westermark, 1999; Ozaki et al., 2007), and our previous research confirmed that PDGF-BB could promote the proliferation of rat BMSCs and induce BMSCs to differentiate into vascular endothelial cells (Jiang et al., 2021a; Jiang et al., 2021b), which was basically consistent with the results of this study. Then we transplanted the BMSCs induced by rrPDGF-BB into the distraction osteogenic area of rats, and then used general observation of samples, X-ray examination, Micro-CT examination and histological staining to verify its therapeutic effect. The results confirmed that injecting the BMSCs induced by rrPDGF-BB into the rat distraction space can promote the formation of new bone in the distraction area, which is consistent with the report of Moore (Moore et al., 2009; Del Rosario et al., 2015; Luvizuto et al., 2016; Gao et al., 2021; Komatsu et al., 2022). Moore studied the effect of PDGF-BB on bone repair, so Moore directly injected PDGF-BB into rats. Different from Moore, We studied the effect of BMSCs induced by PDGF-BB on bone repair, and our previous research confirmed that PDGF-BB can induce BMSCs to differentiate into osteoblasts (Wei et al., 2021b). In addition, some scholars showed that the effect of injecting stem cells in the distraction period had a better curative effect than the injection of stem cells in the mineralization period (Yang Y. et al., 2020). Therefore, choosing the appropriate dose of PDGF-BB to intervene in BMSCs and injecting BMSCs in the appropriate period will bring greater benefits, which is also our future research direction.

In conclusion, our study shows that injecting the BMSCs induced by rrPDGF-BB into the rat distraction space during the mineralization period of distraction osteogenesis can promote bone regeneration and healing. The results of this study have certain clinical value. However, whether BMSCs induced by PDGF-BB have differentiated *in vivo* has not been explored in this topic. Later, we will continue the research in this area, screen out the appropriate induction dose and time, and reduce the incidence of complications, so as to make further contributions to the research of distraction osteogenesis.

Data availability statement

The original contributions presented in the study are included in the article/supplementary material, further inquiries can be directed to the corresponding author.

Ethics statement

The animal study was reviewed and approved by Ethics Committee of the First Affiliated Hospital of Xinjiang Medical University.

Author contributions

SW and QW conceived and designed the study. SW, LZ, RZ, and KY collected the data. SW, QJ, and JG performed the research, analyzed data. SW, LZ, and RZ wrote the paper. CM reviewed and modified the article. All authors discussed the results and contributed to the final article. All authors read and approved the final article.

Funding

Work toward this research was supported by the National Natural Science Foundation of China (82260425 and 81760397) and Postgraduate Research and Innovation Project of Xinjiang Uygur Autonomous Region (CXCY2022012).

Conflict of interest

The authors declare that the research was conducted in the absence of any commercial or financial relationships that could be construed as a potential conflict of interest.

Publisher's note

All claims expressed in this article are solely those of the authors and do not necessarily represent those of their affiliated organizations, or those of the publisher, the editors and the reviewers. Any product that may be evaluated in this article, or claim that may be made by its manufacturer, is not guaranteed or endorsed by the publisher.

References

Acikan, I., Mehmet, G., Artas, G., Yaman, F., Deniz, G., Bulmus, O., et al. (2018). Systemic melatonin application increases bone formation in mandibular distraction osteogenesis. *Braz Oral Res.* 32, e85. doi:10.1590/1807-3107bor-2018.vol32.0085

Ai-Aql, Z. S., Alagl, A. S., Graves, D. T., Gerstenfeld, L. C., and Einhorn, T. A. (2008). Molecular mechanisms controlling bone formation during fracture healing and distraction osteogenesis. *J. Dent. Res.* 87 (2), 107–118. doi:10.1177/154405910808700215

Akçay, H., Kuru, K., Tatar, B., and Şimşek, F. (2019). Vitamin E promotes bone formation in a distraction osteogenesis model. *J. Craniofac Surg.* 30 (8), 2315–2318. doi:10.1097/scs.0000000000005685

Alaeddini, M., Bashizadehfakhar, H., Amirinia, F., Abbasi, S., Shamshiri, A. R., Etemad-Moghadam, S., et al. (2022). The effect of different combinations of fixatives and decalcifying agents on rat and rabbit hard tissues, a guide for histologic processing. *Acta histochem.* 124 (8), 151962. doi:10.1016/j.acthis.2022.151962

Altay, B., Dede, E., Özgul, Ö., Atıl, F., Koçyiğit İ, D., Orhan, K., et al. (2020). Effect of systemic oxytocin administration on new bone formation and distraction rate in rabbit mandible. *J. Oral Maxillofac. Surg.* 78 (7), 1171–1182. doi:10.1016/j.joms.2020.03.005

Bogoevski, K., Woloszyk, A., Blackwood, K., Woodruff, M. A., and Glatt, V. (2019). Tissue morphology and antigenicity in mouse and rat tibia: Comparing 12 different

decalcification conditions. *J. Histochem Cytochem* 67 (8), 545–561. doi:10.1369/0022155419850099

Borzunov, D. Y., and Shastov, A. L. (2019). Mechanical solutions to salvage failed distraction osteogenesis in large bone defect management. *Int. Orthop.* 43 (5), 1051–1059. doi:10.1007/s00264-018-4032-6

Bowenpope, D. F., Malpass, T. W., Foster, D. M., and Ross, R. (1984). Platelet-derived growth factor *in vivo*: Levels, activity, and rate of clearance. *Blood* 64 (2), 458–469. doi:10.1182/blood.v64.2.458.bloodjournal642458

Chen, J., Sivan, U., Tan, S. L., Lippo, L., De Angelis, J., Labella, R., et al. (2021). High-resolution 3D imaging uncovers organ-specific vascular control of tissue aging. *Sci. Adv.* 7 (6), eabd7819. doi:10.1126/sciadv.abd7819

Cui, Y., Huang, R., Wang, Y., Zhu, L., and Zhang, X. (2018). Down-regulation of LGR6 promotes bone fracture recovery using bone marrow stromal cells. *Biomed. Pharmacother.* 99, 629–637. doi:10.1016/j.biopha.2017.12.109

Del Rosario, C., Rodríguez-Évora, M., Reyes, R., Delgado, A., and Évora, C. (2015). BMP-2, PDGF-BB, and bone marrow mesenchymal cells in a macroporous β-TCP scaffold for critical-size bone defect repair in rats. *Biomed. Mater* 10 (4), 045008. doi:10.1088/1748-6041/10/4/045008

Dhaliwal, K., Kunchur, R., and Farhadieh, R. (2016). Review of the cellular and biological principles of distraction osteogenesis: An invivo bioreactor tissue engineering model. *J. Plastic Reconstr. Aesthetic Surg. Jpras* 69 (2), e19–e26. doi:10.1016/j.bjps.2015.11.003

Dou, Z., Chau, M., Muder, D., Vedung, T., and Nilsson, O. (2021). Optimized protocols for *in situ* hybridization, immunohistochemistry, and immunofluorescence on skeletal tissue. *Acta histochem.* 123 (5), 151747. doi:10.1016/j.acthis.2021.151747

Feng, G., Zheng, K., Song, D., Wu, S., Zhu, S., and Hu, J. (2016). Mesenchymal stem cells modified with Runt-related transcription factor 2 promote bone regeneration in rabbit mandibular distraction osteogenesis. *West China J. Stomatology* 34 (2), 125–129. doi:10.7518/hxkq.2016.02.004

Gao, S. Y., Lin, R. B., Huang, S. H., Liang, Y. J., Li, X., Zhang, S. E., et al. (2021). PDGF-BB exhibited therapeutic effects on rat model of bisphosphonate-related osteonecrosis of the jaw by enhancing angiogenesis and osteogenesis. *Bone* 144, 115117. doi:10.1016/j.bone.2019.115117

Gruber, R., Karreth, F., Frommlet, F., Fischer, M., and Watzek, G. (2003). Platelets are mitogenic for periosteum-derived cells. *J. Orthop. Res.* 21, 941–948. doi:10.1016/S0736-0266(03)00053-6

Guo, K., Wang, W., Liu, Z., Xu, W., Zhang, S., and Yang, C. (2020). Reliability of acellular decalcified and decalcified teeth as bone graft material: An experimental and pathological study in rats. *Int. J. Clin. Exp. Pathol.* 13 (5), 837–845.

Hamushan, M., Cai, W., Zhang, Y., Lou, T., Zhang, S., Zhang, X., et al. (2020). High-purity magnesium pin enhances bone consolidation in distraction osteogenesis model through activation of the VHL/HIF-1α/VEGF signaling. *J. Biomater. Appl.* 35 (2), 224–236. doi:10.1177/0885328220928550

Han, Z., He, X., Feng, Y., Jiang, W., Zhou, N., and Huang, X. (2022). Hsp20 promotes endothelial progenitor cell angiogenesis via activation of PI3K/akt signaling pathway under hypoxia. *Tissue Eng. Regen. Med.* 19, 1251–1266. doi:10.1007/s13770-022-00481-1

Heldin, C.-H., and Westermark, B. (1999). Mechanism of action and *in vivo* role of platelet-derived growth factor. *Physiol. Rev.* 79, 1283–1316. doi:10.1152/physrev.1999.79.4.1283

Homsi, J., and Daud, A. (2007). Spectrum of activity and mechanism of action of VEGF/PDGF inhibitors. *Cancer control J. Moffitt Cancer Cent.* 14, 285–294. doi:10.1177/107327480701400312

Jia, Y., Qiu, S., Xu, J., Kang, Q., and Chai, Y. (2020). Exosomes secreted by young mesenchymal stem cells promote new bone formation during distraction osteogenesis in older rats. *Calcif. Tissue Int.* 106 (5), 509–517. doi:10.1007/s00223-019-00656-4

Jiang, T., Ma, L., Li, Z., Shou, X., Duan, M., Wu, S., et al. (2021a). Platelet-derived growth factor BB induces bone marrow mesenchymal stem cells to differentiate into vascular endothelial cells. *Chin. J. Tissue Eng. Res.* 25 (25), 3937–3942. doi:10.12307/2021.001

Jiang, T., Wu, S., Li, Z., Shou, X., Ma, Y., Ma, C., et al. (2021b). Platelet-derived growth factor BB promotes the proliferation of bone marrow mesenchymal stem cells of Sprague-Dawley rats. *Chin. J. Tissue Eng. Res.* 25 (13), 1976–1981. doi:10.3969/j.issn.2095-4344.2188

Komatsu, K., Ideno, H., Shibata, T., Nakashima, K., and Nifuji, A. (2022). Platelet-derived growth factor-BB regenerates functional periodontal ligament in the tooth replantation. *Sci. Rep.* 12 (1), 3223. doi:10.1038/s41598-022-06865-6

Lee, M., Kwon, B.-J., Koo, M.-A., You, K., and Park, C. (2013). Mitogenesis of vascular smooth muscle cell stimulated by platelet-derived growth factor-bb is inhibited by blocking of intracellular signaling by epigallocatechin-3-O-gallate. *Oxidative Med. Cell. Longev.* 2013, 1–10. doi:10.1155/2013/827905

Liu, M., Ding, H., Wang, H., Wang, M., Wu, X., Gan, L., et al. (2021a). Moringa oleifera leaf extracts protect BMSC osteogenic induction following peroxidative damage by activating the PI3K/Akt/Foxo1 pathway. *J. Orthop. Surg. Res.* 16 (1), 150. doi:10.1186/s13018-021-02284-x

Liu, Y., Cai, F., Liu, K., Liu, J., Zhang, X., and Yusufu, A. (2021b). Cyclic distraction-compression dynamization technique enhances the bone formation during distraction osteogenesis. *Front. Bioeng. Biotechnol.* 9, 810723. doi:10.3389/fbioe.2021.810723

Liu, Y., Liu, J., Cai, F., Liu, K., Zhang, X., and Yusufu, A. (2022). Hypoxia during the consolidation phase of distraction osteogenesis promotes bone regeneration. *Front. Physiol.* 13, 804469. doi:10.3389/fphys.2022.804469

Luvizuto, E. R., Tangl, S., Dobsak, T., Reich, K., Gruber, R., Sonoda, C. K., et al. (2016). Effect of recombinant PDGF-BB on bone formation in the presence of β-tricalcium phosphate and bovine bone mineral matrix: A pilot study in rat calvarial defects. *BMC Oral Health* 16 (1), 52. doi:10.1186/s12903-016-0210-3

Marinopoulos, A. E., Ayres, S. C., Biswas, S., Huang, X., Mantena, S. R., Peterson, R. A., et al. (2022). Optimization of decalcification techniques for histologic examination of the rat maxillary and mandibular incisors for toxicity studies. *J. Histotechnol.* 45 (1), 2–9. doi:10.1080/01478885.2021.1974780

McDonald, M. M., Morse, A., Birke, O., Yu, N. Y. C., Mikulec, K., Peacock, L., et al. (2018). Sclerostin antibody enhances bone formation in a rat model of distraction osteogenesis. *J. Orthop. Res.* 36 (4), 1106–1113. doi:10.1002/jor.23726

Mi, J., Xu, J., Yao, H., Li, X., Tong, W., Li, Y., et al. (2021). Calcitonin gene-related peptide enhances distraction osteogenesis by increasing angiogenesis. *Tissue Eng. Part A* 27 (1-2), 87–102. doi:10.1089/ten.TEA.2020.0009

Migliorini, F., La Padula, G., Torsiello, E., Spiezia, F., Oliva, F., and Maffulli, N. (2021). Strategies for large bone defect reconstruction after trauma, infections or tumour excision: A comprehensive review of the literature. *Eur. J. Med. Res.* 26 (1), 118. doi:10.1186/s40001-021-00593-9

Moore, D. C., Ehrlich, M. G., McAllister, S. C., Machan, J. T., Hart, C. E., Voigt, C., et al. (2009). Recombinant human platelet-derived growth factor-BB augmentation of new-bone formation in a rat model of distraction osteogenesis. *J. Bone Jt. Surg. Am.* 91 (8), 1973–1984. doi:10.2106/jbjs.H.00540

Nakamura, T., Sumi, K., Tsuji, E., Hosotani, M., Namba, T., Ichii, O., et al. (2021). Novel polychrome staining distinguishing osteochondral tissue and bone cells in decalcified paraffin sections. *Cell. Tissue Res.* 385 (3), 727–737. doi:10.1007/s00441-021-03516-6

Ortinau, L., Wang, H., Lei, K., Deveza, L., Jeong, Y., Hara, Y., et al. (2019). Identification of functionally distinct Mx1+αSMA+ periosteal skeletal stem cells. *Cell. Stem Cell.* 25, 784–796. e5. doi:10.1016/j.stem.2019.11.003

Owen-Woods, C., and Kusumbe, A. (2022). Fundamentals of bone vasculature: Specialization, interactions and functions. *Semin. Cell. Dev. Biol.* 123, 36–47. doi:10.1016/j.semcdb.2021.06.025

Ozaki, Y., Nishimura, M., Sekiya, K., Suehiro, F., Kanawa, M., Nikawa, H., et al. (2007). Comprehensive analysis of chemotactic factors for bone marrow mesenchymal stem cells. *Stem cells Dev.* 16, 119–130. doi:10.1089/scd.2006.0032

Qin, S. (2021). Inspiration of ilizarov's invention, discovery and systematic innovation to the Chinese medical community: I would like to commemorate the centennial birthday of professor Ilizarov with this special issue. *Chin. J. Bone Jt. Surg.* 14 (06), 457–461. doi:10.3969/j.issn.2095-9958.2021.06.01

Roddy, E., DeBaun, M. R., Daoud-Gray, A., Yang, Y. P., and Gardner, M. J. (2018). Treatment of critical-sized bone defects: Clinical and tissue engineering perspectives. *Eur. J. Orthop. Surg. Traumatol.* 28 (3), 351–362. doi:10.1007/s00590-017-2063-0

Savi, F. M., Brierly, G. I., Baldwin, J., Theodoropoulos, C., and Woodruff, M. A. (2017). Comparison of different decalcification methods using rat mandibles as a model. *J. Histochem Cytochem* 65 (12), 705–722. doi:10.1369/0022155417733708

Shen, J., Sun, Y., Liu, X., Zhu, Y., Bao, B., Gao, T., et al. (2021). EGFL6 regulates angiogenesis and osteogenesis in distraction osteogenesis via Wnt/β-catenin signaling. *Stem Cell. Res. Ther.* 12 (1), 415. doi:10.1186/s13287-021-02487-3

Singh, A., Veeriah, V., Xi, P., Labella, R., Chen, J., Romeo, S. G., et al. (2019). Angiocrine signals regulate quiescence and therapy resistance in bone metastasis. *JCI Insight* 4 (13), e125679. doi:10.1172/jci.insight.125679

Valtanen, R. S., Yang, Y. P., Gurtner, G. C., Maloney, W. J., and Lowenberg, D. W. (2021). Synthetic and Bone tissue engineering graft substitutes: What is the future? *Injury* 52 (2), S72–S77. doi:10.1016/j.injury.2020.07.040

Wang, X., Wang, Y., Gou, W., Lu, Q., Peng, J., and Lu, S. (2013). Role of mesenchymal stem cells in bone regeneration and fracture repair: A review. *Int. Orthop.* 37 (12), 2491–2498. doi:10.1007/s00264-013-2059-2

Wei, Q., Maimai, A., Zhang, J., Wu, S., and Ma, C. (2021a). Experimental study of PDGF-BB inducing rabbit bone marrow mesenchymal stem cells to differentiate into osteoblasts. *J. Xinjiang Med. Univ.* 44 (03), 290–296. doi:10.3639/j.issn.1009-5551.2021.03.006

Wei, Q., Zhang, X., Ma, L., Li, Z., Shou, X., Duan, M., et al. (2021b). Platelet derived growth factor BB induces rat bone marrow mesenchymal stem cells to differentiate into osteoblasts. *Chin. J. Tissue Eng. Res.* 25 (19), 2953–2957. doi:10.3969/j.issn.2095-4344.2200

Wu, S., Maimai, A., Wei, Q., Chen, D., Feng, D., Abdulsalam, A., et al. (2020). Establishment of rat femoral distraction osteogenesis model. *Chin. J. Microsurg.* 43 (06), 578–582. doi:10.3760/cma.j.cn441206-20200528-00245

Wu, S., Wei, Q., Maimai, A., Chen, D., Lv, L., Li, X., et al. (2021). Effect of autogenous BMSCs modified by rrPDGF-BB gene on femoral distraction osteogenesis in rats. *Chin. J. Microsurg.* 44 (05), 526–534. doi:10.3760/cma.j.cn441206-20210608-00150

Yang, H., Wu, L., Deng, H., Chen, Y., Zhou, H., Liu, M., et al. (2020a). Anti-inflammatory protein TSG-6 secreted by bone marrow mesenchymal stem cells attenuates neuropathic pain by inhibiting the TLR2/MyD88/NF-κB signaling pathway in spinal microglia. *J. Neuroinflammation* 17 (1), 154. doi:10.1186/s12974-020-1731-x

Yang, Y., Lin, S., Wang, B., Gu, W., and Li, G. (2017). Stem cell therapy for enhancement of bone consolidation in distraction osteogenesis. *Bone & Jt. Res.* 6 (6), 385–390. doi:10.1302/2046-3758.66.bjr-2017-0023

Yang, Y., Pan, Q., Zou, K., Wang, H., Zhang, X., Yang, Z., et al. (2020b). Administration of allogeneic mesenchymal stem cells in lengthening phase accelerates early bone consolidation in rat distraction osteogenesis model. *Stem Cell. Res. Ther.* 11, 129. doi:10.1186/s13287-020-01635-5

Ye, L., Xu, J., Mi, J., He, X., Pan, Q., Zheng, L., et al. (2021). Biodegradable magnesium combined with distraction osteogenesis synergistically stimulates bone tissue regeneration via CGRP-FAK-VEGF signaling axis. *Biomaterials* 275, 120984. doi:10.1016/j.biomaterials.2021.120984

Yuan-Zhe, J., and Lee, J. H. (2018). Mesenchymal stem cell therapy for bone regeneration. *Clin. Orthop. Surg.* 10 (3), 271–278. doi:10.4055/cios.2018.10.3.271

Zhao, P., Xiao, L., Peng, J., Qian, Y. Q., and Huang, C. C. (2018). Exosomes derived from bone marrow mesenchymal stem cells improve osteoporosis through promoting osteoblast proliferation via MAPK pathway. *Eur. Rev. Med. Pharmacol. Sci.* 22 (12), 3962–3970. doi:10.26355/eurrev_201806_15280

Zheng, X., Qin, S., Guo, B., Shi, L., Zhao, J., and Wang, Z. (2021). Effect of Ilizarov method in treatment of femoral shortening and knee deformity. *Chin. J. Bone Jt. Surg.* 14 (06), 480–484. doi:10.3969/j.issn.2095-9958.2021.06.05

frontiers | Frontiers in Bioengineering and Biotechnology

TYPE Original Research
PUBLISHED 18 May 2023
DOI 10.3389/fbioe.2023.1181580

OPEN ACCESS

EDITED BY
Wai Hong Lo,
University of Connecticut, United States

REVIEWED BY
Debolina Ghosh,
UCONN Health, United States
Chinedu Ude,
University of Connecticut Health Center, United States

*CORRESPONDENCE
Pengfei Zheng,
zhengpengfei@njmu.edu.cn

†These authors have contributed equally to this work

RECEIVED 07 March 2023
ACCEPTED 09 May 2023
PUBLISHED 18 May 2023

CITATION
Qiang L, Fan M, Wang Y, Liu Y, Zhuang H, Guo R, Huang H, Ben Y, Wang D, Wu X, Wang J, Weng J and Zheng P (2023), Injectable hydrogel loaded with bilayer microspheres to inhibit angiogenesis and promote cartilage regeneration for repairing growth plate injury.
Front. Bioeng. Biotechnol. 11:1181580.
doi: 10.3389/fbioe.2023.1181580

Injectable hydrogel loaded with bilayer microspheres to inhibit angiogenesis and promote cartilage regeneration for repairing growth plate injury

Lei Qiang[1,2†], Minjie Fan[1†], Yiwei Wang[1†], Yihao Liu[1,3], Hanjie Zhuang[1], Ruoyi Guo[1], Hao Huang[2], Yulong Ben[1], Dalin Wang[4], Xiaoling Wu[5], Jinwu Wang[3], Jie Weng[2] and Pengfei Zheng[1*]

[1]Department of Orthopaedic Surgery, Children's Hospital of Nanjing Medical University, Nanjing, Jiangsu, China, [2]Key Laboratory of Advanced Technologies of Materials (MOE), School of Materials Science and Engineering, Southwest Jiaotong University, Chengdu, Sichuan, China, [3]Shanghai Key Laboratory of Orthopaedic Implant, Department of Orthopaedic Surgery, Shanghai Ninth People's Hospital, Shanghai Jiao Tong University School of Medicine, Shanghai, China, [4]Department of Orthopaedic Surgery, Nanjing First Hospital, Nanjing, Jiangsu, China, [5]School of Biomedical Engineering and Informatics, Nanjing Medical University, Nanjing, Jiangsu, China

Introduction: The repair and regeneration of growth plate injuries using tissue engineering techniques remains a challenge due to large bone bridge formation and low chondrogenic efficiency.

Methods: In this study, a bilayer drug-loaded microspheres was developed that contains the vascular endothelial growth factor (VEGF) inhibitor, Bevacizumab, on the outer layer and insulin-like growth factor-1 (IGF-1), a cartilage repair factor, on the inner layer. The microspheres were then combined with bone marrow mesenchymal stem cells (BMSCs) in the gelatin methacryloyl (GelMA) hydrogel to create a composite hydrogel with good injectability and biocompatibility.

Results: The in vitro drug-release profile of bilayer microspheres showed a sequential release, with Bevacizumab released first followed by IGF-1. And this hydrogel simultaneously inhibited angiogenesis and promoted cartilage regeneration. Finally, in vivo studies indicated that the composite hydrogel reduced bone bridge formation and improved cartilage regeneration in the rabbit model of proximal tibial growth plate injury.

Conclusion: This bilayer microsphere-based composite hydrogel with sequential controlled release of Bevacizumab and IGF-1 has promising potential for growth plate injury repair.

KEYWORDS

growth plate, bilayer microspheres, anti-angiogenesis, chondrogenic differentiation, hydrogel, tissue engineering

1 Introduction

Growth plate is the critical cartilage area at the end of long bones in children, responsible for controlling the longitudinal growth of bone (Kronenberg, 2003; Agirdil, 2020). Notably, the growth plate is avascular and devoid of nerves (Provot and Schipani, 2007; Villemure and Stokes, 2009), which limits their inherent ability to repair after injury. In such cases, the cartilage may be replaced by bone tissue, leading to the formation of bone bridge. The bone bridge could impede bone growth and result in significant complications, including length discrepancy and angular deformity, which could negatively impacts on the physical and mental wellbeing of affected children (McCarty et al., 2010; Cepela et al., 2016; Shaw et al., 2018). The current clinical treatment mainly involves osteotomy combined with filling the corresponding materials such as fat and bone cement. However, this approach has limited efficacy and a low success rate (Foster et al., 2000; Hasler and Foster, 2002). Thus, there is an urgent pressing need for new and more effective treatments for injuries to growth plates.

Recently, advancements in tissue engineering have enabled significant progress in the repair of injured growth plates. This is achieved by incorporating a combination of bone marrow mesenchymal stem cells (BMSCs) or chondrocytes and growth factors into biologically active scaffolds, aimed at constructing the growth-plate-regenerative cartilage that can replace the injured tissue and perform its original biological function (Xian and Foster, 2006; Shukrimi et al., 2013; Wang et al., 2021). For instance, Erickson et al. demonstrated the use of chitosan-genipin microgels loaded with stromal-cell derived factor-1α (SDF-1α) or transforming growth factor β3 (TGF-β3) (Erickson et al., 2021a). Li et al. showed the feasibility of repairing growth plate cartilage by loading BMSCs on extracellular matrix scaffolds (Li et al., 2017). Erickson et al. explored the use of alginate-chitosan hydrogels loaded with VEGF antibodies (Erickson et al., 2021b). Despite these promising results, these studies reported the challenges of achieving efficient chondrogenic differentiation and avoiding the formation of large bone bridges (Azarpira et al., 2015; Sundararaj et al., 2015; Li et al., 2017; Erickson et al., 2021a; Erickson et al., 2021b). Our hypothesis is that these challenges can be overcome by implementing a sequential approach that targets both the prevention of bone bridge formation and the promotion of chondrogenic differentiation in the early stages of injury. By targeting a series of cellular and molecular events following injury (Chung and Xian, 2014), and blocking or even reversing these pathological changes, it may be possible to achieve more effective regeneration and repair of growth plate cartilage.

Over the past two decades, extensive research using various animal models has been performed to gain a better understanding to the underlying pathophysiology of the bone bridge formation following injury (Zhou et al., 2004; Chung et al., 2009; Chung et al., 2011; Xie et al., 2014). The research has identified four different phases of injury repair: the inflammatory phase, the fibrogenic phase, the osteogenic phase, and the remodeling phase (Chung and Xian, 2014). The initial phase, lasting 1–3 days post-injury, is characterized by the infiltration of inflammatory cells and the upregulation of cytokines and mediators at the injury site. This constitutes the inflammatory phase of growth plate injury repair. In the subsequent fibrogenic phase, which lasts 3–7 days, osteoprogenitor cells infiltrate the injury site and secrete pro-angiogenic factors. This promotes the invasion of new blood vessels, a critical step in the formation of the bone bridge (Qiu et al., 2020; Chen et al., 2021). The fibrogenic phase is therefore a crucial stage in the repair process. One of the critical pro-angiogenic factors involved in the formation of new blood vessels is vascular endothelial growth factor (VEGF), which has been shown to play a key role in bone bridge formation (Hu and Olsen, 2016; Erickson et al., 2021b; Ye et al., 2021). To prevent bone bridge formation, it is therefore essential to inhibit the action of VEGF. The osteogenic phase commences around day 7 post-injury, as osteoprogenitor cells differentiate into osteoblasts and bony trabeculae begin to form. Finally, on day 14, bone remodeling is observed. Thus, in order to interrupt the pathological process of osteogenic differentiation and prevent bone bridge formation, it is crucial to inhibit osteogenic differentiation in the early stages of growth plate injury repair. In this study, we proposed to use the VEGF inhibitor Bevacizumab (Chase, 2008; Chung et al., 2014) to inhibit angiogenesis during the fibrogenic phase, interrupting the pathological process of osteogenic differentiation and preventing the eventual formation of bone bridge. In addition, we need to induce exogenous or endogenous stem cells to differentiate into chondrocytes in order to promote the regeneration of cartilage at the injury site. Insulin-like growth factor-1 (IGF-1), a commonly used cartilage repair factor, has the ability to promote chondrogenic differentiation, chondrocyte proliferation, and matrix synthesis (Lui et al., 2019; Cho et al., 2020). In light of the protracted nature of growth plate repair, it is imperative to maintain the optimal concentration of drugs in the affected area to ensure effective repair. To this end, we have proposed the utilization of microspheres to achieve sustained delivery of Bevacizumab and IGF-1. As a well-established system for sustained drug release, poly (lactic-co-glycolic acid) (PLGA) microspheres are capable of delivering the loaded drugs in a slow and continuous manner (Morille et al., 2016; Su et al., 2021; Chen et al., 2023).

In this study, we aim to address the long-standing challenge of growth plate injury repair through a novel approach. We propose the use of a bilayer drug-loaded PLGA microsphere system that comprises of Bevacizumab and IGF-1 to achieve sustained drug delivery to the injury site. The outer layer of the microsphere is loaded with Bevacizumab, which will be released first to inhibit early osteogenic differentiation and prevent the formation of a bone bridge. The inner layer of the microsphere contains IGF-1, which will be released slowly to promote chondrogenic differentiation and the regeneration of growth plate cartilage. Further, we encapsulate the bilayer drug-loaded PLGA microspheres in a composite hydrogel, composed of gelatin methacryloyl (GelMA) and bone marrow mesenchymal stem cells (BMSCs). This composite hydrogel can provide a favorable microenvironment for both drug delivery and cell proliferation, thus facilitating the repair and regeneration of growth plate cartilage after injury. In conclusion, this study provides a novel approach for growth plate injury repair by using a bilayer drug-loaded PLGA microsphere system combined with a composite hydrogel and the results of this study hold the potential to inform the development of a clinically viable treatment strategy for growth plate injuries.

2 Materials and methods

2.1 Materials

PLGA (lactide/glycolide ratio 50:50, MW 65 kDa) and poly (vinyl alcohol) (PVA) (88%, MW 31–50 kDa) were purchased from Sigma-Aldrich (St. Louis, MO, USA). IGF-1 and

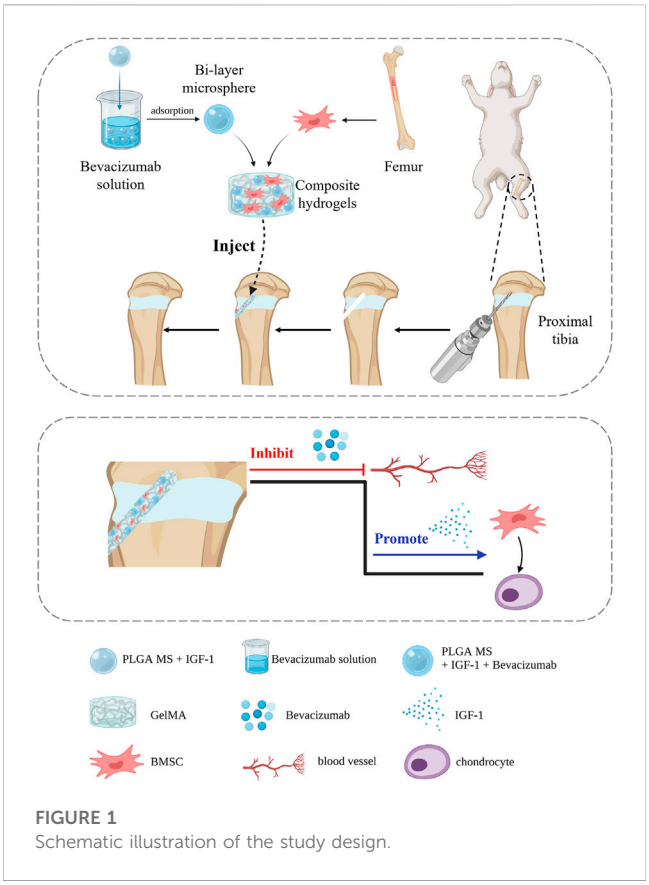

FIGURE 1
Schematic illustration of the study design.

Bevacizumab, Minimal Essential Medium (MEM), and phosphate-buffered solution (PBS) were obtained from Gibco (Grand Island, USA) and the RNA extraction kit was purchased from Omega Biotek (Georgia, USA). The cell counting kit 8 (CCK-8) was purchased from Abcam (UK); all were used as received. The study design is illustrated in Figure 1.

2.2 Synthesis and characterization of bilayer microspheres

In this study, microspheres were fabricated by the water-in-oil-in-water (w/o/w) double emulsion technique. Briefly, 200 mg of PLGA was dissolved in 4 mL of dichloromethane, and 500 μL of 100 μm IGF-1 solution and 150 μL of 6% gelatin were added to it. This was followed by emulsification at 10,000 rpm for 1 min by using a high-speed homogenizer. The resultant emulsion was added to 30 mL of 1% PVA solution and emulsified at 8,000 rpm for 2 min. This emulsion was added to 200 mL of 0.1% PVA solution and stirred at 1,000 rpm for 5 min, resulting in a double emulsion. Next, the emulsion was stirred in a fume hood for 4 h to evaporate dichloromethane. Finally, the solution was centrifuged to collect microspheres, and these microspheres were washed with distilled water four times and lyophilized to obtain monolayer microspheres loaded with IGF-1. Next, 100 mg of IGF-1-loaded monolayer microspheres were immersed in the PBS solution with 100 μg of Bevacizumab; after adsorption for 1 h and lyophilization, bilayer microspheres were obtained. Similarly, Bevacizumab-loaded monolayer microspheres were prepared by adding 100 mg of blank microspheres to the PBS solution containing 100 μg of Bevacizumab. The morphological characteristics of all microspheres were observed by scanning electron microscopy (SEM), and the mean size was measured. Encapsulation efficiency was calculated using the following equation: encapsulation efficiency (%) = (measured protein concentration/theoretical protein concentration) × 100 (Eswaramoorthy et al., 2012).

2.3 Fabrication and characterization of composite hydrogels

First, 10 g of gelatin (Sigma-Aldrich) was added to PBS at 50°C to prepare a 10% w/v homogeneous solution. Then, 10 ml of methacrylic anhydride (MA; Sigma-Aldrich) was slowly added dropwise into the gelatin solution with stirring, and the solution was allowed to react at 50°C for 3 h. Next, the resultant solution was packed into 3,500 Da dialysis bags and dialyzed in deionized water at 37°C for 5 days to remove unreacted MA and additional by-products. The dialysate was centrifuged at 3,000 rpm for 10 min, and the supernatant was lyophilized at −80°C for 6 days to obtain GelMA, which was stored at −20°C until further use.

Then, 1 g of GelMA was dissolved in 10 ml of deionized water to obtain a 100 mg/ml GelMA solution, and 0.2% (w/v) of the photoinitiator lithium phenyl-2,4,6-trimethylbenzoylphosphinate was added. Finally, BMSCs and PLGA microspheres were added at a concentration of (5×10^4)/ml and 5 mg/ml, respectively, to form the composite hydrogel loaded with PLGA microspheres and BMSCs, and it was cross-linked under Ultraviolet (UV) light. The following groups of hydrogels were prepared: (i) GP group: GelMA + BMSCs; (ii) GPB group: GelMA + BMSCs + PLGA microspheres loaded with Bevacizumab; (iii) GPI: GelMA + BMSCs + PLGA microspheres loaded with IGF-1; (iv) GPIB group: GelMA + BMSCs + bilayer PLGA microspheres.

The injectability of composite hydrogels was analyzed by injecting the prepolymer solution carrying red pen ink with a 1 mL syringe (needle diameter = 0.5 mm). The gelatin solidification time was measured as follows: the hydrogel was injected into the glass bottle that was then gently shaken. Subsequently, the tilting angle of the glass bottle was continuously changed to observe the flow of the prepolymer solution. When the glass bottle was tilted but the solution no longer flowed, the hydrogel was considered to have been formed, and this solidification time was recorded. The viscosity and shear rate of the prepolymer solution of each group was measured by using a modular compact rheometer. Scanning electron microscopy (SEM, TESCAN) was utilized to observe the morphology of composite hydrogels. The swelling capacity of composite hydrogels was evaluated as follows (Verma et al., 2007): First, all the hydrogels were lyophilized and weighed to determine the dry weight (Md). Then, the lyophilized hydrogels were soaked in PBS at 37°C for 24 h. After removing free water, the weight was marked as Mw. Mw/Md was the swelling ratio, and [(Mw - Md)/Mw]×100% was used to calculate the equilibrium water content (EWC).

2.4 Mechanical characterizations and release profile

The elastic modulus was determined by using a mechanical tester (Hengyi, Shanghai, China). The samples were subjected to

uniaxial compression testing at a steady strain rate of 1 mm/min and 0.1–5 Hz frequency at 25°C, and the elastic modulus was obtained by calculating the slope of the stress–strain curve for 0%–10% strain. Moreover, the original height of the sample before compression was recorded as H_0, and after the compression test, the final height of the sample was recorded as H_r. The ratio H_r/H_0 was used to measure the elasticity of the sample. The following rheological measurements were conducted at 37°C on a Haake Mars Modular Advanced Rheometer (Thermo Fisher Scientific, USA). At a fixed strain of 5%, a frequency sweep test was performed from 0.1 to 10 Hz to obtain the storage modulus (G′) and loss modulus (G″).

Next, 100 mg of the composite hydrogel from each group was immersed in 50 ml of PBS, and the drug release was analyzed in a shaker at 37°C. At predetermined time points, i.e., days 1, 3, 5, 7, 9, 11, 13, 15, 17, 19, and 21, 2 ml of the supernatant was collected and replaced with fresh PBS. The absorbance of the collected samples was measured by using a fluorescence spectrometer to evaluate the drug concentration and plot the *in vitro* drug release curve.

2.5 Cell viability, proliferation and adhesion

In a 96-well plate, BMSCs were seeded into the hydrogel of each group (5×10^3/well). The culture medium was removed on days 1, 4, and 7, and washed twice with PBS. Then, 90 μL of the medium and 10 μL of CCK-8 reagent were added to each well, followed by incubation in an incubator for 1 h in the dark. The absorbance values were detected at 450 nm using the enzyme marker. To assess the cell viability on the hydrogels, BMSCs with a density of 5×10^3 were seeded into a 12-well plate and co-incubated with hydrogels of each group for 24 h. Further, 5 μL of calcein-AM and 20 μL of PI were added to 10 mL of PBS to prepare the Live/Dead solution. Subsequently, 200 μL of the Live/Dead solution was added to each well, and incubated for 30 min at 37°C in the dark. After the solution was removed, images were captured by using a confocal laser scanning microscope (CLSM). BMSCs with a density of 5×10^3 were seeded into the hydrogels for 24 h, and the medium was removed. All the samples were immobilized by 4% paraformaldehyde for 30 min, permeabilized in 0.5% Triton X-100 for 15 min, and blocked in 1% BSA solution for 60 min. Then, to observe the cell adhesion on the hydrogels, these samples were stained with FITC-phalloidin and DAPI, and the images were obtained with a CLSM.

2.6 *In vitro* angiogenesis assay

To assess the anti-angiogenic effect of Bevacizumab, the tube formation assay was performed: 300 μL of Matrigel was added to each well in a 24-well Transwell plate and incubated at 37°C with 5% CO_2 for 4 h, and 100 μL of a suspension [(2×10^5)/mL] of human umbilical vein endothelial cells (HUVECs) was added to each well; this was followed by placing the Transwell chambers in the culture plate and incubating for 24 h. The hydrogels of each group were placed in the Transwell plate in the upper chamber of the culture plate. After 24 h of culture, random images were collected to observe the tubule formation, and the number of tubular branches was determined using the Image J software. Moreover, cells were collected and the total RNA was extracted using an RNA extraction kit. Then, RT-PCR was performed to detect the expression level of genes specific to angiogenesis, such as VEGF and HIF-1α. The endogenous control gene was GAPDH. The relative gene expression was measured by the $2^{-\Delta\Delta CT}$ method.

2.7 *In vitro* chondrogenic differentiation

To assess the chondrogenic differentiating effect of IGF-1, BMSCs were inoculated with a density of 2×10^4 in a 24-well Transwell plate. After 24 h of culture, the hydrogel of each group was placed in the upper chamber of the Transwell plate. Then, after 14 and 21 days of culture, cells were collected and the total RNA was extracted using an RNA extraction kit. Then, Reverse Transcription-polymerase Chain Reaction (RT-PCR) was performed to detect the expression levels of osteogenic genes—such as Runx2, Col1a1, and OPN—and chondrogenic genes—such as Col2a1, ACAN, and Sox-9—using GAPDH as an internal reference gene. The relative gene expression was measured by the $2^{-\Delta\Delta CT}$ method.

2.8 *In vivo* growth plate regeneration

Animal experiments were approved by the Ethics Committee of Nanjing Medical University. All experimental procedures on animals were carried out in accordance with the National Institutes of Health guide for the care and use of Laboratory animals. We purchased 40 6-week-old male New Zealand white rabbits, from Nanjing Medical University and randomly divided them into five groups, which included control, GP, GPB, GPI, and GPIB groups.

To study the role of hydrogels in the repair of growth plate injuries, referring to the modeling method of previous studies (Erickson et al., 2017), the proximal tibial growth plate injury model was established. After anesthetizing the rabbits, the surgical area from the medial malleolus to the pelvis was culled clean of fur and then sterilized with gauze soaked in povidone-iodine. A skin incision of about 2 cm was made from the medial gap of the knee joint toward the proximal tibia, and the soft tissue was separated to expose the growth plate of proximal tibia (Supplementary Figure S1A). An incision of approximately 0.5 cm was made from the growth plate to the lower end of the skin incision using a scalpel at the proximal tibia, and the surrounding fascia and soft tissue were scraped off. A 3-mm-diameter drill was used to drill a cortical window in the tibial stem at 10,000 rpm (Supplementary Figure S1B). Then, the drill was placed at an appropriate angle and oriented such that it penetrated through the cortical window up to the center of the growth plate (Supplementary Figure S1C). The appropriate depth of injury was ensured by measuring the entry length of the drill. After ensuring the injury to the growth plate, the drill channel was flushed with sterile saline through a syringe. Thus, the model was successfully established. Next, the hydrogel of each group was injected into the defect, and after closure with bone wax, the subcutaneous tissue was continuously stitched layer by layer, and the skin was sutured. After surgery, the rabbits were kept in separate cages without immobilizing the limbs. Penicillin was

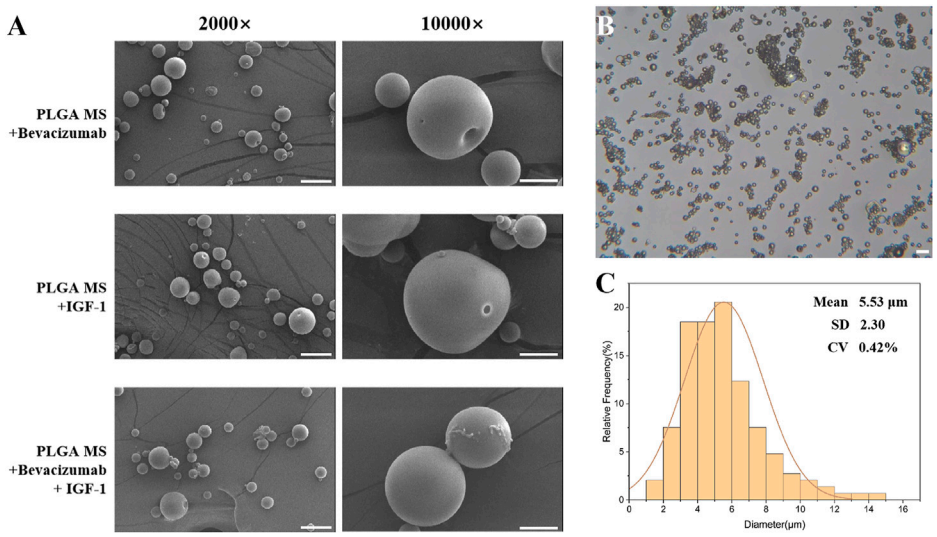

FIGURE 2
Characteristics of poly (lactic-co-glycolic acid) (PLGA) microspheres. **(A)** Scanning electron micrographs of PLGA microspheres; scale bar = 20 μm. **(B,C)** Particle size distribution of PLGA microspheres; scale bar = 20 μm.

intramuscularly injected daily at 20,000 units/kg for 3 days postoperatively to reduce the risk of infection. At 1 month after the surgery, half of the rabbits in each group were euthanized, while the rest were euthanized after 3 months. The histological sections of the lower limb were analyzed through HE staining. Additionally, the repair and regeneration of growth plate cartilage were evaluated by methods of Toluidine blue and Alcian blue staining.

2.9 Statistical analysis

The experimental data were expressed as mean ± standard deviation (Mean ± SD). The statistical analysis was performed using GraphPad Prism 8.0. Multi-group comparisons were analyzed by oneway analysis of variance (ANOVA) with the Tukey test. All statistical tests were evaluated as two-sided, and signifificance was set at $p < 0.05$.

3 Results

3.1 Fabrication and characterization of microspheres

In this study, the preparation of single-layer and bilayer poly (lactic-co-glycolic acid) (PLGA) microspheres loaded with Bevacizumab and insulin-like growth factor-1 (IGF-1) was carried out. Scanning electron microscopy (SEM) images revealed that the microspheres were well-formed with spherical shapes and smooth surfaces, without any signs of adhesion between the particles (Figure 2A). Particle size analysis showed that the average diameter of the microspheres was 5.53 ± 2.30 μm, with a low coefficient of variation (CV) of 0.42% (Figures 2B, C). The data showed that the fabricated PLGA microspheres have a 46.14%% encapsulation efficiency of IGF-1 (1,153.4143 ng of IGF-1 per mg of PLGA microspheres). These results indicate the successful preparation of the microspheres.

3.2 Fabrication and characterization of composite hydrogels

The composite hydrogels were prepared by incorporating the PLGA microspheres of each group into GelMA containing BMSCs. The injectability of the hydrogel was demonstrated in Figure 3B, where the composite hydrogel prepolymer solution was successfully injected using a syringe, followed by cross-linking with ultraviolet (UV) light irradiation. The shear thinning evaluation was conducted, with the results displayed in Figure 4C, which indicated that all the hydrogels exhibited shear thinning properties, thereby facilitating their injection using a syringe. The appearance of the composite hydrogel changed from translucent to opaque and milky white after cross-linking, as observed during the glass bottle tilting test, with a solidification time of 30 s (Figure 3C). The cross-sectional images of the hydrogels in all groups revealed similar sponge-like structures with porous morphologies (Figure 3A). This indicated that the incorporation of PLGA microspheres did not alter the original porous architecture of the GelMA hydrogel. Furthermore, under high magnification, no agglomerated microspheres were observed, showing that the microspheres were well distributed in the hydrogels. This interconnected porous structure could facilitate cell growth, the exchange of nutrients and metabolic wastes, and the construction of a regenerative microenvironment conducive to growth plate cartilage tissue repair.

The swelling properties of the hydrogels play a crucial role in facilitating the efficient exchange of nutrients and metabolic waste within cells. After being immersed in PBS for 24 h, the weight of

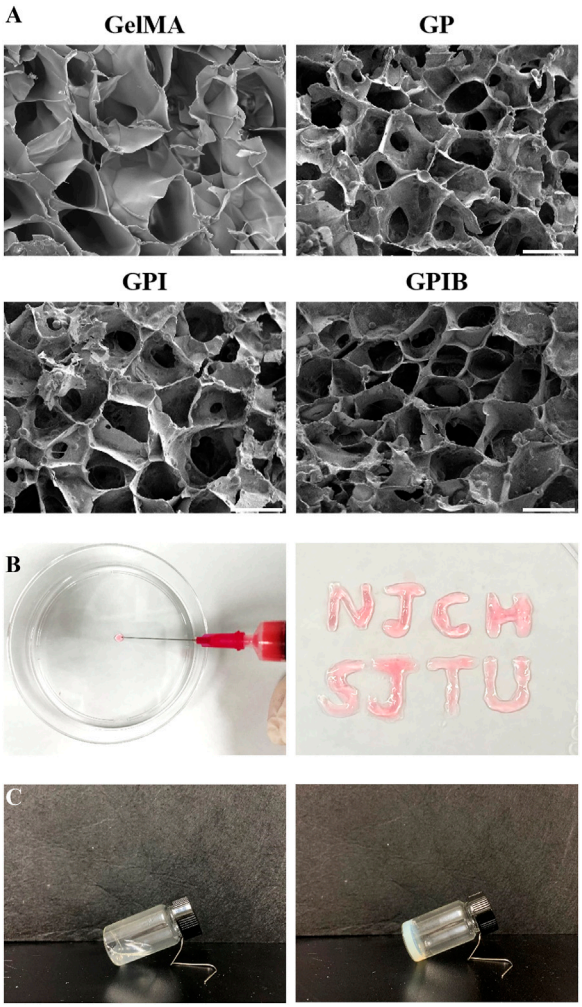

FIGURE 3
Characteristics of composite hydrogels. **(A)** Scanning electron micrographs of composite hydrogels in each group; scale bar = 50 μm. **(B)** Injectability of composite hydrogels. **(C)** Solidification of composite hydrogels.

hydrogels became about 10–15 times that before swelling, and there was a significant decrease in the swelling rate observed in the presence of microspheres (Figure 4A). Additionally, the equilibrium water content (EWC) dropped slightly from 92% to 89% with the addition of microspheres (Figure 4B), indicating an increase in the crosslink density. These results suggest that the GelMA hydrogel and microspheres exhibit a stable crosslinked relationship.

To investigate the effect of microspheres on the mechanical properties of hydrogels, mechanical tests were performed. As illustrated in Figure 4E, the addition of microspheres to GelMA hydrogel improved the mechanical properties of the composite hydrogels. However, as depicted in Figure 4F, the elasticity of composite hydrogels in the GPI group and GPIB group was weaker than that of pure GelMA, yet upon compression, the recovery height of the composite hydrogels was close to the original height, suggesting that the composite hydrogel also basically retained the good elasticity of GelMA. To investigate the effect of the addition of microspheres into the GelMA hydrogel on rheological properties, the strain sweep was conducted to measure the G′ and G″ data. Results showed that hydrogels of all groups had a relatively stable G′ and G″, signifying stable crosslinking. G′ was higher than G″, indicating rapid gelation of the composite hydrogels after crosslinking (Figure 4D).

3.3 *In vitro* release behaviour

The *in vitro* drug release behavior of hydrogels loaded with PLGA microspheres was analyzed. The results showed that the drug release pattern of hydrogels containing monolayer PLGA microspheres was consistent with a slow and sustained release profile, with no sudden burst effect observed within the first 24 h. On the other hand, the hydrogels loaded with bilayer microspheres exhibited a sequential release pattern, with approximately 80% of Bevacizumab being released in the first week, while only a lesser amount of IGF-1 was released. Over the following 2 weeks, the release of IGF-1 increased steadily and the cumulative release of IGF-1 was higher than that of Bevacizumab (Figure 5A). These findings suggest that the drug release pattern of bilayer microspheres differs from that of monolayer microspheres.

3.4 Biocompatibility of composite hydrogels *in vitro*

The hydrogels of each group were co-cultured with BMSCs, and their effects on the proliferation of BMSCs were determined using the CCK-8 assay. The results showed that the cell proliferation activity of each experimental group was slightly lower than that of the control group on days 1, 4, and 7, however, the differences between each experimental group and the control group were not statistically significant (Figure 5B). In addition, to assess the biocompatibility of hydrogels in each group, Live/Dead staining was performed on BMSCs after 24 h of culture. Results showed that the cell survival rate within the hydrogels of each group was high (Figure 5C), indicating that the hydrogels had no cytotoxicity and displayed good biocompatibility.

After 24 h of culture, FITC-phalloidin and DAPI were utilized to label the nucleus and actin cytoskeleton, and then, the morphology of BMSCs in the hydrogels was visualized using confocal laser scanning microscope (CLSM). The results indicated that BMSCs were distributed within the hydrogels and exhibited good attachment (Figure 5D). Additionally, the BMSCs cultured on the surface of the GelMA hydrogel displayed the spindle-like shape, while those on the surface of the composite hydrogels were polygonal. The change in cellular morphology indicated that the addition of microspheres enhanced cell adhesion. As shown in Figure 5E, the spreading area of the BMSCs in all experimental groups was larger than that of the blank group, and the difference was statistically significant ($p < 0.05$). This could be attributed to the fact that the addition of microspheres resulted in a rougher morphology of the composite

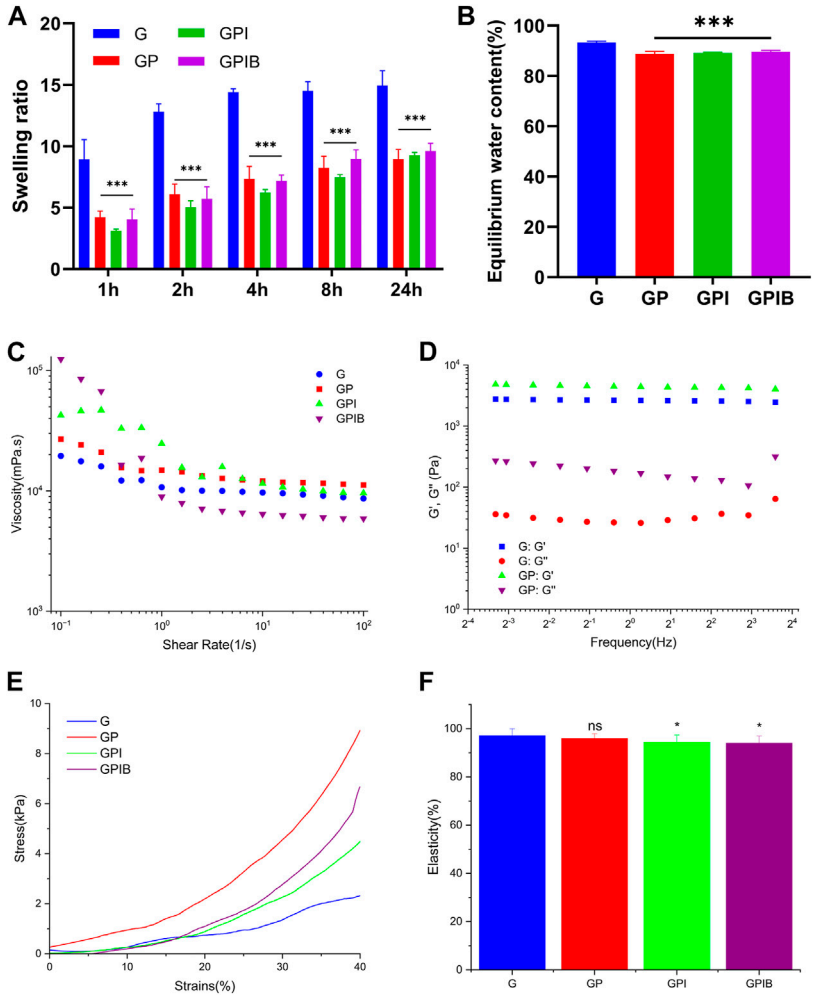

FIGURE 4
In vitro relevant tests of composite hydrogels. **(A)** Swelling ratio and **(B)** equilibrium water content of composite hydrogels in each group. **(C)** Viscosity and shear rate of prepolymer solution in each group. **(D)** Storage modulus (G′) and loss modulus (G″) of composite hydrogels in each group. **(E)** The stress-strain curve and **(F)** elasticity of composite hydrogels in each group. *, $p < 0.05$; **, $p < 0.01$; ***, $p < 0.001$; ns, no significance.

hydrogel, which facilitated cellular spreading. However, there was no statistically significant difference in the cellular spreading area among the experimental groups.

3.5 *In vitro* angiogenic and chondrogenic evaluation

As for tube formation assay *in vitro*, vessels formed by HUVECs loaded on Matrigel and cultured with the hydrogels of each group. IGF-1 is well-established to have an angiogenic effect, and the outcomes illustrated that HUVECs cultured with GPI hydrogels generated dense and complete tubule-like networks, which were more prominent than those produced by the control and GelMA groups. Conversely, the tubule network formed in the GPIB group exhibited sparsity and local fracturing (Figure 5F). And in terms of number of loops, the GPI group demonstrated significantly higher values in comparison to the control and GelMA groups, whereas the number of loops in the GPIB group was significantly lower (Figure 5G). Thus, it is reasonable to conclude that hydrogels of the GPIB group may have the ability to inhibit the tube formation of HUVECs.

Furthermore, to determine the expression of vasculogenic, osteogenic, and chondrogenic genes, RT-PCR was performed, which revealed that the expression of VEGF and HIF-1α was significantly lower ($p < 0.05$) in the GPB group and the bilayer microsphere group compared to the control and GP groups (Figure 5H). This indicates that Bevacizumab could suppress the expression of VEGF. Additionally, RT-PCR data revealed a decrease in osteogenic gene expression ($p < 0.05$) and an increase in chondrogenic gene expression ($p < 0.05$) in the GPI groups (Figure 5H).

3.6 *In vivo* growth plate regeneration performance

At 1 month and 3 months postoperatively, the specimens were removed and histologically sectioned and stained (Supplementary Figure S2). Histological staining in each group showed a significant

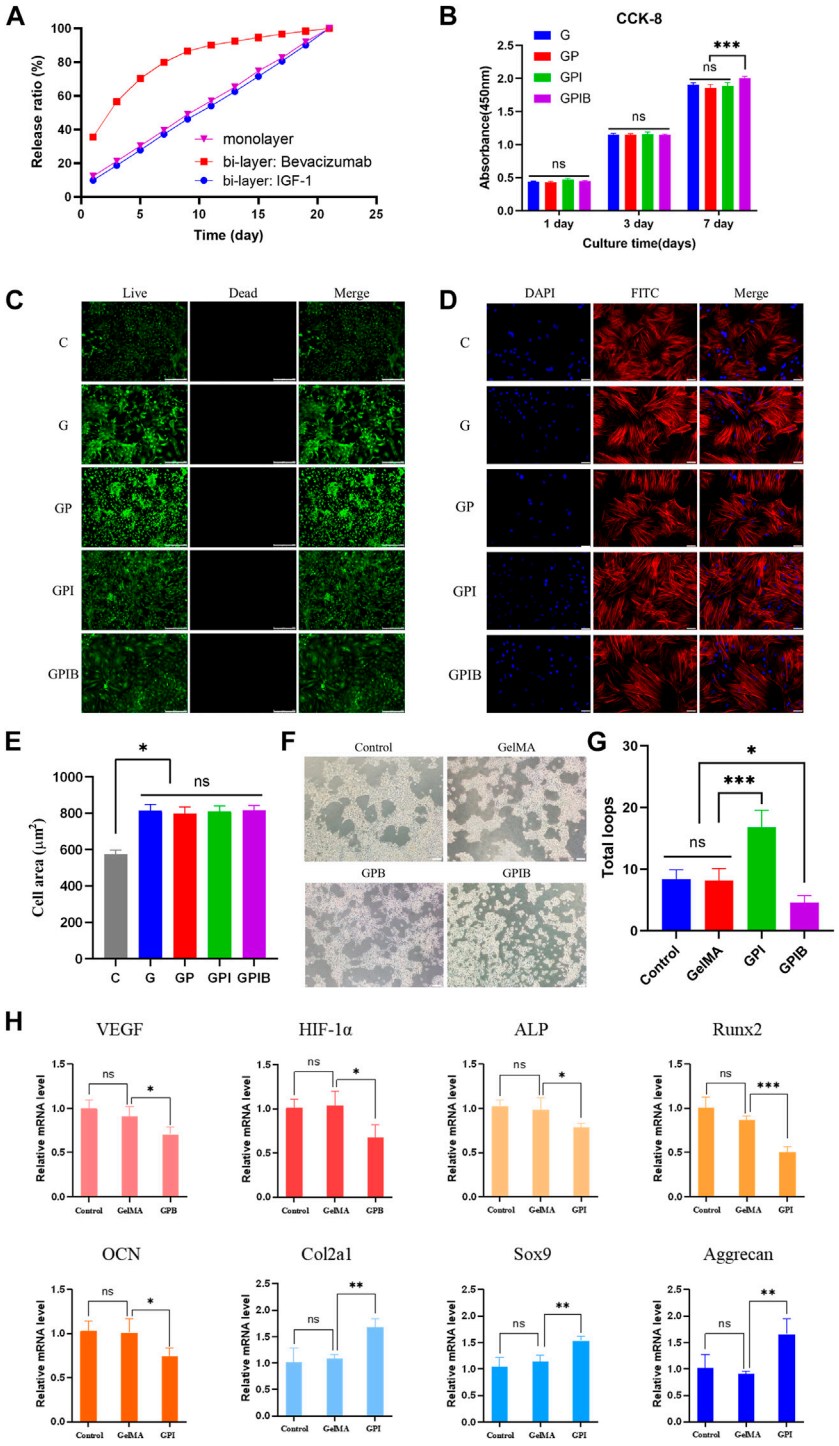

FIGURE 5
Effects of composite hydrogels on cell viability, morphology, and behavior. **(A)** *In vitro* drug release curve of composite hydrogels. **(B)** Cell proliferation of bone marrow mesenchymal stem cells (BMSCs) cultured on composite hydrogels in each group after culturing for 1, 3, and 7 days. **(C)** Live/Dead staining of BMSCs on composite hydrogels in each group after 24 h of culture; scale bar = 250 μm. **(D)** Confocal laser scanning microscope images of BMSCs cultured on composite hydrogels in each group after 24 h staining with FITC-phalloidin and DAPI; scale bar = 50 μm. **(E)** Quantitative analysis of the cell spreading area. **(F)** Tube formation assay images of HUVECs treated with PBS or composite hydrogels in each group; scale bar = 200 μm. **(G)** The number of total loops in HUVECs treated with PBS or composite hydrogels in each group; **(H)** RT-PCR analysis of angiogenesis-related genes (VEGF and HIF-1α) in HUVECs, and osteogenesis-related genes (Runx2, Col1a1, and OPN) and chondrogenesis-related genes (Col2a1, Sox9, and Aggrecan) in BMSCs. *, $p < 0.05$; **, $p < 0.01$; ***, $p < 0.001$; ns, no significance.

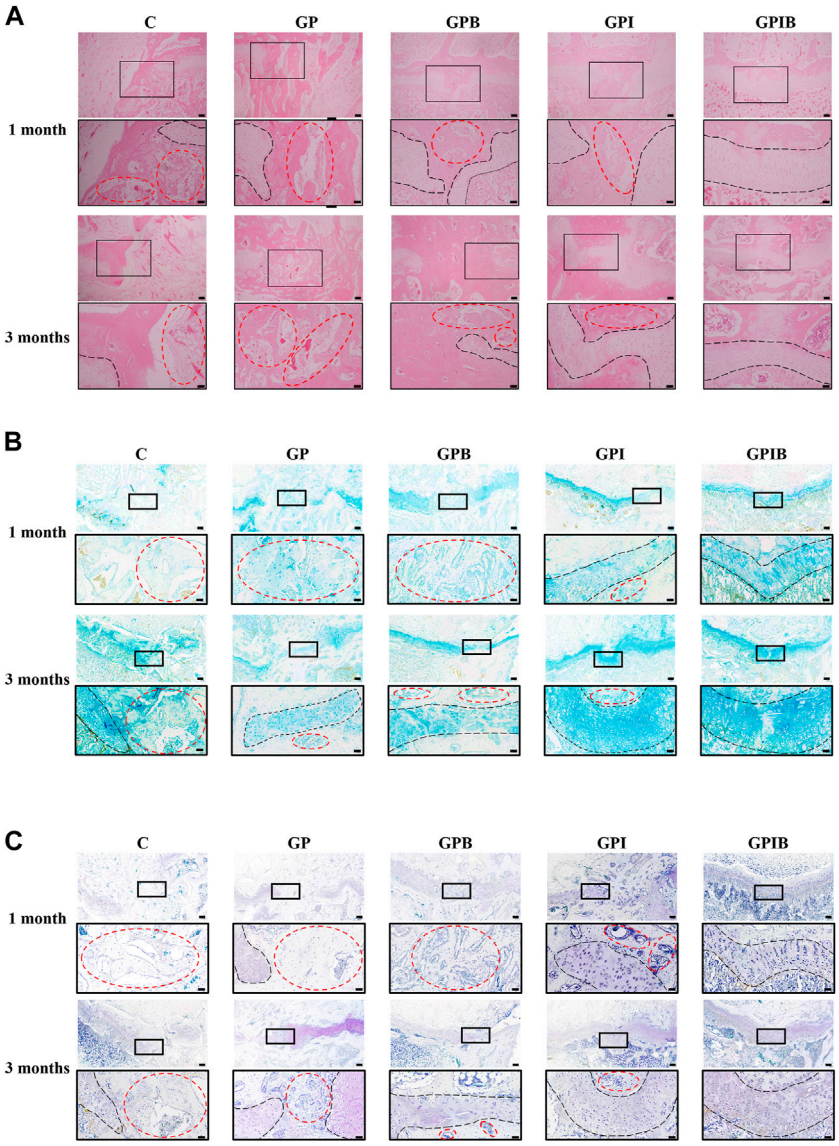

FIGURE 6
Repair effect of composite hydrogels on growth plate after injury. The HE **(A)**, AB **(B)** and TB **(C)** staining images of the injury site in the growth plate (scale bar = 200 μm). The boxed area represents the defect site and is enlarged below it (scale bar = 50 μm). The region marked by red dotted lines mainly represents bone tissue, and the region marked by black dotted lines mainly represents the growth plate cartilage.

formation of cartilage regeneration within the defect area in the GPI and GPIB groups compared to the control group (Figure 6A). Specifically, in the control and GP groups, bone bridge formation was significant and cartilage regeneration was limited at the injury site when compared to the uninjured site. And in the GPB group, bone bridge formation was less compared to the control and GP groups, while cartilage regeneration was still limited, indicating that although the extent of bone bridge formation was reduced, the regeneration of cartilage tissue remained insufficient. In the GPI group, cartilage regeneration was greater compared to the control and GP groups, but the regenerated cartilage displayed a discontinuous or irregular morphology, which may be attributed to the presence of bone tissue that limited the space for cartilage regeneration. Finally, in the GPIB group, prominent cartilage regeneration was observed with minimal bone tissue formation, and the regenerated cartilage exhibited a continuous and regular morphology that closely resembled that of uninjured growth plate cartilage.

Similar to the results of HE staining, AB and TB staining also showed that the control and GP groups had little cartilage formation and more bone and mesenchymal tissue infiltration in the injury site. The bone tissue formation was reduced in the GPB group compared to the control group, but regenerated cartilage was still less and appeared atypical. The GPI group showed typical cartilage regeneration, but the regenerated cartilage appeared intermittent or irregular, which was mainly due to bone bridge formation affecting the regeneration of cartilage. In contrast, the regenerated cartilage tissue in the GPIB group was more continuous, flatter, and more regular, much like the native growth plate cartilage (Figures 6B, C).

4 Discussion

In previous studies in which tissue engineering techniques were used for the repair and regeneration of growth plate cartilage, the challenges of the formation of large bone bridges and low chondrogenic efficiency remained (Sundararaj et al., 2015; Li et al., 2017; Erickson et al., 2021a). Through the analysis of the pathological processes following growth plate injury, we posited that the traditional focus on either promoting chondrogenic differentiation and cartilage regeneration or inhibiting the formation of bone bridges may be the underlying reason for the limited success in these efforts. As such, we proposed a novel approach, where the inhibition of osteogenic differentiation and bone bridge formation would be prioritized before promoting chondrogenic differentiation. The sequential and synergistic integration of these two processes was hypothesized to lead to more effective repair and regeneration of cartilage tissue following growth plate injury.

In this study, we aimed to address the aforementioned challenges associated with the repair and regeneration of growth plate cartilage using tissue engineering techniques. To this end, we proposed to first inhibit osteogenic differentiation and bone bridge formation, and then promote chondrogenic differentiation. However, the conventional single layer PLGA microspheres could not provide the desired sequential release of the drugs. Thus, a bilayer drug-loaded PLGA microsphere was adopted in this study, which allowed for sequential release of Bevacizumab and IGF-1. The results of the *in vitro* study showed that the bilayer microspheres were able to release Bevacizumab and IGF-1 in a sequential manner. In particular, the dominant release of Bevacizumab from the outer layer in the first week. Since the fibrogenic phase occurs mainly in the 1st week after growth plate injury, the dominant release of Bevacizumab from the bilayer microspheres in the 1st week can precisely and rapidly inhibit the local neovascularization to the maximum extent and achieve the inhibition of bone bridge formation at the source. Subsequently, the gradual increase in the release of IGF-1 from the inner layer continued to promote the differentiation of the stem cells involved in repair into cartilage, leading to cartilage tissue regeneration.

Furthermore, the composite hydrogel formed from the bilayer microspheres and BMSCs in GelMA showed good injectability and biocompatibility, and was able to effectively block pathological changes associated with bone bridge formation and induce differentiation of stem cells towards chondrocytes, thereby directly and indirectly promoting the regenerative repair of growth plate cartilage. These findings demonstrate the potential of the bilayer drug-loaded PLGA microspheres for the repair and regeneration of growth plate cartilage after injury.

The results of *in vitro* experiments demonstrated that Bevacizumab effectively inhibits angiogenesis, and IGF-1 induces chondrogenic differentiation of stem cells. After a growth plate injury, endogenous stem cells migrate to the injury site and are subjected to a microenvironment that is detrimental to cartilage regeneration, as a result of the inflammatory response and vascular invasion. The majority of the stem cells involved in tissue repair differentiate into osteoblasts under the influence of osteogenic factors, reducing the pool of stem cells available for chondrogenic differentiation and leading to a decrease in the amount of regenerated cartilage tissue. Hence, inhibiting bone bridge formation can indirectly enhance cartilage regeneration. The *in vivo* animal experiments showed that the bilayer microsphere group exhibited superior growth plate cartilage repair and a reduced extent of bone bridge formation due to the early-stage inhibition of angiogenesis (Wang et al., 2011; Chung et al., 2014). Additionally, IGF-1 facilitated the differentiation of stem cells into chondrogenic cells during the repair process, further augmenting the efficacy of cartilage repair (Moon et al., 2015; Sundararaj et al., 2015).

To sum up, the present study proposes a novel bilayer PLGA microsphere-based composite hydrogel for the repair and regeneration of growth plate cartilage following injury. The outer layer of the PLGA microspheres is loaded with Bevacizumab, which effectively inhibits angiogenesis, while the inner layer is loaded with IGF-1, which promotes chondrogenic differentiation of stem cells. By combining the bilayer PLGA microspheres with GelMA, a composite hydrogel was prepared that enables sequential release of the drugs and provides good injectability and biocompatibility. The results of both *in vitro* and *in vivo* experiments demonstrated that the composite hydrogel effectively inhibited bone bridge formation and promoted cartilage regeneration, thereby providing a promising strategy for the treatment of growth plate cartilage injuries.

Data availability statement

The original contributions presented in the study are included in the article/Supplementary Material, further inquiries can be directed to the corresponding author.

Ethics statement

The animal study was reviewed and approved by the Ethics Committee of Nanjing Children's Hospital Affiliated to Nanjing Medical University.

Author contributions

LQ: Conceptualization, Methodology, Writing—original draft. MF: Conceptualization, Methodology, Writing—original draft. YW: Data curation, Methodology, Investigation, Writing—review and editing. YL: Conceptualization, Methodology, Writing—original draft. HZ: Methodology, Formal analysis. RG: Data curation, Formal analysis. HH: Methodology, Validation. YB: Methodology, Validation. DW: Resources, Software. XW: Resources, Software. JwW: Methodology, Supervision. JiW: Methodology, Supervision. PZ: Conceptualization, Funding acquisition, Formal analysis, Supervision, Writing—review and editing. All authors listed have made a substantial, direct, and intellectual contribution to the work and approved it for publication.

Funding

This work was supported by Jiangsu Provincial Key Research and Development Program (CN) (grant number BE2019608);

Postdoctoral Research Foundation of China (2022M721685); Jiangsu Health Commission Medical Research Program (grant number 2020158); National Facility for Translational Medicine (Shanghai) Open Program (grant number TMSK-2021-304); Nanjing International Science and Technology Cooperation Program; Nanjing Medical Science and Technology Development Key Program (grant number ZKX18041); Nanjing Postdoctoral Research Funding Program.

Conflict of interest

The authors declare that the research was conducted in the absence of any commercial or financial relationships that could be construed as a potential conflict of interest.

Publisher's note

Supplementary material

The Supplementary Material for this article can be found online at: https://www.frontiersin.org/articles/10.3389/fbioe.2023.1181580/full#supplementary-material

References

Agirdil, Y. (2020). The Growth Plate: A physiologic overview. *EFORT Open Rev.* 5 (8), 498–507. doi:10.1302/2058-5241.5.190088

Azarpira, M. R., Shahcheraghi, G. H., Ayatollahi, M., and Geramizadeh, B. (2015). Tissue engineering strategy using mesenchymal stem cell-based chitosan scafolds in Growth Plate surgery: A preliminary study in rabbits. *Orthop. Traumatol. Surg. Res.* 101 (5), 601–605. doi:10.1016/j.otsr.2015.04.010

Cepela, D. J., Tartaglione, J. P., Dooley, T. P., and Patel, P. N. (2016). Classifications in brief: Salter-harris classification of pediatric physeal fractures. *Clin. Orthop. Relat. Res.* 474 (11), 2531–2537. doi:10.1007/s11999-016-4891-3

Chase, J. L. (2008). Clinical use of anti-vascular endothelial growth factor monoclonal antibodies in metastatic colorectal cancer. *Pharmacotherapy* 28, 23S–30S. doi:10.1592/phco.28.11-supp.23S

Chen, K., Liao, S., Li, Y., Jiang, H., Liu, Y., Wang, C., et al. (2021). Osteoblast-derived Egfl6 couples angiogenesis to osteogenesis during bone repair. *Theranostics* 11 (20), 9738–9751. doi:10.7150/thno.60902

Chen, L., Huang, X., Chen, H., Bao, D., Su, X., Wei, L., et al. (2023). Hypoxia-mimicking scaffolds with controlled release of DMOG and PTHrP to promote cartilage regeneration via the HIF-1α/YAP signaling pathway. *Int. J. Biol. Macromol.* 226, 716–729. doi:10.1016/j.ijbiomac.2022.12.094

Cho, H., Kim, J., Kim, S., Jung, Y. C., Wang, Y., Kang, B. J., et al. (2020). Dual delivery of stem cells and insulin-like growth factor-1 in coacervate-embedded composite hydrogels for enhanced cartilage regeneration in osteochondral defects. *J. Control Release* 327, 284–295. doi:10.1016/j.jconrel.2020.08.002

Chung, R., and Xian, C. J. (2014). Recent research on the Growth Plate: Mechanisms for Growth Plate injury repair and potential cell-based therapies for regeneration. *J. Mol. Endocrinol.* 53 (1), T45–T61. doi:10.1530/JME-14-0062

Chung, R., Foster, B. K., Zannettino, A. C., and Xian, C. J. (2009). Potential roles of growth factor pdgf-bb in the bony repair of injured Growth Plate. *Bone* 44 (5), 878–885. doi:10.1016/j.bone.2009.01.377

Chung, R., Foster, B. K., and Xian, C. J. (2011). Injury responses and repair mechanisms of the injured Growth Plate. *Front. Biosci. Sch. Ed.* 3 (1), 117–125. doi:10.2741/s137

Chung, R., Foster, B. K., and Xian, C. J. (2014). The potential role of vegf-induced vascularisation in the bony repair of injured Growth Plate cartilage. *J. Endocrinol.* 221 (1), 63–75. doi:10.1530/JOE-13-0539

Erickson, C. B., Shaw, N., Hadley-Miller, N., Riederer, M. S., Krebs, M. D., and Payne, K. A. (2017). A rat tibial Growth Plate injury model to characterize repair mechanisms and evaluate Growth Plate regeneration strategies. *J. Vis. Exp.* (125), 55571. doi:10.3791/55571

Erickson, C., Stager, M., Riederer, M., Payne, K. A., and Krebs, M. (2021). Emulsion-free chitosan-genipin microgels for Growth Plate cartilage regeneration. *J. Biomater. Appl.* 36 (2), 289–296. doi:10.1177/0885328221999894

Erickson, C. B., Newsom, J. P., Fletcher, N. A., Yu, Y., Rodriguez-Fontan, F., Weatherford, S. A., et al. (2021). Anti-vegf antibody delivered locally reduces bony bar formation following physeal injury in rats. *J. Orthop. Res.* 39 (8), 1658–1668. doi:10.1002/jor.24907

Eswaramoorthy, R., Chang, C. C., Wu, S. C., Wang, G. J., Chang, J. K., and Ho, M. L. (2012). Sustained release of pth(1-34) from plga microspheres suppresses osteoarthritis progression in rats. *Acta Biomater.* 8 (6), 2254–2262. doi:10.1016/j.actbio.2012.03.015

Foster, B. K., John, B., and Hasler, C. (2000). Free fat interpositional graft in acute physeal injuries: The anticipatory langenskiold procedure. *J. Pediatr. Orthop.* 20 (3), 282–285. doi:10.1097/01241398-200005000-00002

Hasler, C. C., and Foster, B. K. (2002). Secondary tethers after physeal bar resection: A common source of failure? *Clin. Orthop. Relat. Res.* 405 (405), 242–249. doi:10.1097/00003086-200212000-00031

Hu, K., and Olsen, B. R. (2016). Osteoblast-derived vegf regulates osteoblast differentiation and bone formation during bone repair. *J. Clin. Invest.* 126 (2), 509–526. doi:10.1172/JCI82585

Kronenberg, H. M. (2003). Developmental regulation of the Growth Plate. *Nature* 423 (6937), 332–336. doi:10.1038/nature01657

Li, W., Xu, R., Huang, J., Bao, X., and Zhao, B. (2017). Treatment of rabbit Growth Plate injuries with oriented ecm scaffold and autologous bmscs. *Sci. Rep.* 7, 44140. doi:10.1038/srep44140

Lui, J. C., Colbert, M., Cheung, C. S. F., Ad, M., Lee, A., Zhu, Z., et al. (2019). Cartilage-targeted igf-1 treatment to promote longitudinal bone growth. *Mol. Ther.* 27 (3), 673–680. doi:10.1016/j.ymthe.2019.01.017

McCarty, R. C., Xian, C. J., Gronthos, S., Zannettino, A. C., and Foster, B. K. (2010). Application of autologous bone marrow derived mesenchymal stem cells to an ovine model of Growth Plate cartilage injury. *Open Orthop. J.* 4, 204–210. doi:10.2174/1874325001004010204

Moon, P. D., Kim, M. H., Oh, H. A., Nam, S. Y., Han, N. R., Jeong, H. J., et al. (2015). Cysteine induces longitudinal bone growth in mice by upregulating igf-I. *Int. J. Mol. Med.* 36 (2), 571–576. doi:10.3892/ijmm.2015.2257

Morille, M., Toupet, K., Montero-Menei, C. N., Jorgensen, C., and Noel, D. (2016). Plga-based microcarriers induce mesenchymal stem cell chondrogenesis and stimulate cartilage repair in osteoarthritis. *Biomaterials* 88, 60–69. doi:10.1016/j.biomaterials.2016.02.022

Provot, S., and Schipani, E. (2007). Fetal Growth Plate: A developmental model of cellular adaptation to hypoxia. *Ann. N. Y. Acad. Sci.* 1117, 26–39. doi:10.1196/annals.1402.076

Qiu, P., Li, M., Chen, K., Fang, B., Chen, P., Tang, Z., et al. (2020). Periosteal matrix-derived hydrogel promotes bone repair through an early immune regulation coupled with enhanced angio- and osteogenesis. *Biomaterials* 227, 119552. doi:10.1016/j.biomaterials.2019.119552

Shaw, N., Erickson, C., Bryant, S. J., Ferguson, V. L., Krebs, M. D., Hadley-Miller, N., et al. (2018). Regenerative medicine approaches for the treatment of pediatric physeal injuries. *Tissue Eng. Part B Rev.* 24 (2), 85–97. doi:10.1089/ten.TEB.2017.0274

Shukrimi, A. B., Afizah, M. H., Schmitt, J. F., and Hui, J. H. (2013). Mesenchymal stem cell therapy for injured Growth Plate. *Front. Biosci. Sch. Ed.* 5 (2), 774–785. doi:10.2741/s407

Su, Y., Zhang, B., Sun, R., Liu, W., Zhu, Q., Zhang, X., et al. (2021). Plga-based biodegradable microspheres in drug delivery: Recent advances in research and application. *Drug Deliv.* 28 (1), 1397–1418. doi:10.1080/10717544.2021.1938756

Sundararaj, S. K., Cieply, R. D., Gupta, G., Milbrandt, T. A., and Puleo, D. A. (2015). Treatment of Growth Plate injury using igf-I-loaded plga scaffolds. *J. Tissue Eng. Regen. Med.* 9 (12), E202–E209. doi:10.1002/term.1670

Verma, V., Verma, P., Kar, S., Ray, P., and Ray, A. R. (2007). Fabrication of agar-gelatin hybrid scaffolds using a novel entrapment method for *in vitro* tissue

engineering applications. *Biotechnol. Bioeng.* 96 (2), 392–400. doi:10.1002/bit.21111

Villemure, I., and Stokes, I. A. (2009). Growth Plate mechanics and mechanobiology. A survey of present understanding. *J. Biomech.* 42 (12), 1793–1803. doi:10.1016/j.jbiomech.2009.05.021

Wang, C. J., Huang, K. E., Sun, Y. C., Yang, Y. J., Ko, J. Y., Weng, L. H., et al. (2011). Vegf modulates angiogenesis and osteogenesis in shockwave-promoted fracture healing in rabbits. *J. Surg. Res.* 171 (1), 114–119. doi:10.1016/j.jss.2010.01.045

Wang, X., Li, Z., Wang, C., Bai, H., Wang, Z., Liu, Y., et al. (2021). Enlightenment of Growth Plate regeneration based on cartilage repair theory: A review. *Front. Bioeng. Biotechnol.* 9, 654087. doi:10.3389/fbioe.2021.654087

Xian, C. J., and Foster, B. K. (2006). Repair of injured articular and Growth Plate cartilage using mesenchymal stem cells and chondrogenic gene therapy. *Curr. Stem Cell Res. Ther.* 1 (2), 213–229. doi:10.2174/157488806776956904

Xie, Y., Zhou, S., Chen, H., Du, X., and Chen, L. (2014). Recent research on the Growth Plate: Advances in fibroblast growth factor signaling in Growth Plate development and disorders. *J. Mol. Endocrinol.* 53 (1), T11–T34. doi:10.1530/JME-14-0012

Ye, L., Xu, J., Mi, J., He, X., Pan, Q., Zheng, L., et al. (2021). Biodegradable magnesium combined with distraction osteogenesis synergistically stimulates bone tissue regeneration via cgrp-fak-vegf signaling Axis. *Biomaterials* 275, 120984. doi:10.1016/j.biomaterials.2021.120984

Zhou, F. H., Foster, B. K., Sander, G., and Xian, C. J. (2004). Expression of proinflammatory cytokines and growth factors at the injured Growth Plate cartilage in young rats. *Bone* 35 (6), 1307–1315. doi:10.1016/j.bone.2004.09.014

frontiers | Frontiers in Bioengineering and Biotechnology

TYPE Review
PUBLISHED 31 August 2023
DOI 10.3389/fbioe.2023.1249860

OPEN ACCESS

EDITED BY
Lorenzo Fassina,
University of Pavia, Italy

REVIEWED BY
Brunella Grigolo,
Rizzoli Orthopedic Institute (IRCCS), Italy
Shi-Cong Tao,
Shanghai Jiao Tong University, China

*CORRESPONDENCE
Ming Dong,
dongm@dmu.edu.cn
Weidong Niu,
niu.wd.endo@dmu.edu.cn

†These authors have contributed equally to this work

RECEIVED 29 June 2023
ACCEPTED 21 August 2023
PUBLISHED 31 August 2023

CITATION
Liu R, Wu S, Liu W, Wang L, Dong M and Niu W (2023), microRNAs delivered by small extracellular vesicles in MSCs as an emerging tool for bone regeneration. *Front. Bioeng. Biotechnol.* 11:1249860. doi: 10.3389/fbioe.2023.1249860

microRNAs delivered by small extracellular vesicles in MSCs as an emerging tool for bone regeneration

Runyuan Liu†, Saixuan Wu†, Wanqing Liu, Lina Wang, Ming Dong* and Weidong Niu*

School of Stomatology, Dalian Medical University, Dalian, China

Bone regeneration is a dynamic process that involves angiogenesis and the balance of osteogenesis and osteoclastogenesis. In bone tissue engineering, the transplantation of mesenchymal stem cells (MSCs) is a promising approach to restore bone homeostasis. MSCs, particularly their small extracellular vesicles (sEVs), exert therapeutic effects due to their paracrine capability. Increasing evidence indicates that microRNAs (miRNAs) delivered by sEVs from MSCs (MSCs-sEVs) can alter gene expression in recipient cells and enhance bone regeneration. As an ideal delivery vehicle of miRNAs, MSCs-sEVs combine the high bioavailability and stability of sEVs with osteogenic ability of miRNAs, which can effectively overcome the challenge of low delivery efficiency in miRNA therapy. In this review, we focus on the recent advancements in the use of miRNAs delivered by MSCs-sEVs for bone regeneration and disorders. Additionally, we summarize the changes in miRNA expression in osteogenic-related MSCs-sEVs under different microenvironments.

KEYWORDS

microRNAs, small extracellular vesicles, bone regeneration, mesenchymal stem cells, angiogenesis, osteogenesis

1 Introduction

Bone tissue is a highly vascularized tissue, with abundant vessel networks that transport nutrients and oxygen (Anada et al., 2019). Bone repair after injury occurs in three stages: acute inflammation, bone repair, and remodeling (Claes et al., 2012). However, excessive inflammation negatively affects the osteogenic potential of cells. Therefore, the promotion of bone regeneration relies on angiogenesis, osteogenesis, and anti-inflammatory effect (Bucher et al., 2019).

Mesenchymal stem cells (MSCs) possess the necessary potential for bone regeneration, including homing and multi-lineage differentiation capability (Chen et al., 2021a). However, their transplantation encounters obstacles, such as long-term safety risks (Turinetto et al., 2016; Volarevic et al., 2018; Buduru et al., 2019), tumorigenicity (Miura et al., 2006; Ishihara et al., 2017), cellular senescence (Gong et al., 2020; Luo et al., 2021; Hu M. et al., 2022), and immunological rejection (Zhou et al., 2022a). Therefore, a promising cell-free therapy for bone defect repair and regeneration is extremely urgent. Recent research shown that MSCs stimulate osteogenic differentiation and vasculogenesis through paracrine signaling (Han et al., 2020).

Interestingly, the small extracellular vesicles (sEVs) released by MSCs are considered as the executors of this paracrine effect and have potential to replace MSC-based treatments in bone tissue engineering (Hade et al., 2021). Compared to organ transplantation and stem cell therapy, sEVs induce less immunological rejection and provide greater stability for application, transportation, and storage (Liu F. et al., 2019; Kim et al., 2021; Zheng et al., 2021; Tsai et al., 2022). The regenerative functions of MSCs-derived sEVs (MSCs-sEVs) depend on the proteins, lipids, DNA, RNA, and miRNAs they carry. Importantly, miRNAs are associated with bone homeostasis and angiogenesis. However, miRNA-based treatments have encountered challenges due to limited *in vivo* delivery efficiency. Recently, MSCs-sEVs have emerged as a viable tool for delivering therapeutic miRNAs (Zhu et al., 2020). As a natural delivery system, sEVs not only contain abundant miRNAs internally but also serve as carriers, enhancing the stability of encapsulated cargo, prolonging circulation periods, and facilitating transmembrane delivery. However, several challenges persist in the realm of MSCs-sEVs, including the presence of endogenous miRNAs, their potential impact on bone regeneration, and the successful encapsulation of osteogenic miRNAs within sEVs.

This review highlights the delivery of miRNAs by MSCs-sEVs to enhance angiogenesis, reduce inflammation, and promote osteogenesis (Figure 1). To begin with, we provide a concise overview of the biogenesis and functions of sEVs, which serve as nanocarriers for miRNAs. Next, we summarize the alterations in the expression of osteogenic-related miRNAs within MSCs-sEVs, observing diverse microenvironments. Lastly, we discuss the latest research findings concerning the delivery of miRNAs by MSCs-sEVs in the context of bone regeneration and bone-related diseases.

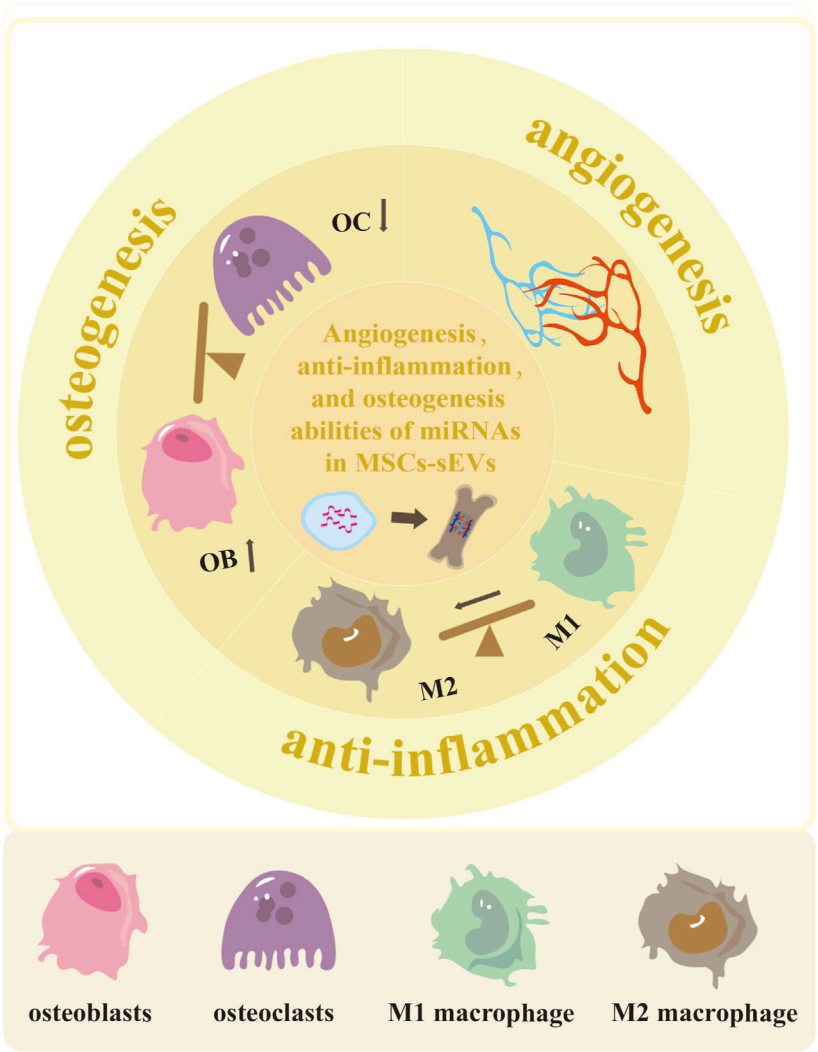

FIGURE 1
The potential of MSCs-sEVs-miRNAs in enhancing angiogenesis, reducing inflammation, and promoting osteogenesis. The miRNAs derived from MSCs-sEVs exhibit the ability to enhance vascular development and regeneration in cases of bone defects. They also have the potential to promote polarization of M2 macrophage, thus reducing inflammation. Additionally, these miRNAs can facilitate osteoblast differentiation while inhibiting osteoclast differentiation.

2 sEVs as nanocarriers for miRNAs

2.1 The biological properties and functions of sEVs

Extracellular vesicles (EVs) are intricate structures with double-layer lipid membrane, ranging in diameter from 40 to 160 nm. They are abundantly found in diverse body fluids being secreted by various cell types including bone mesenchymal stem cells (BMSCs) (Li X. et al., 2020), adipose mesenchymal stem cells (ASCs) (Fang and Liang, 2021), human umbilical cord mesenchymal stem cells (huc-MSCs) (Yang J. et al., 2020), and tumor cells (Kalluri and LeBleu, 2020). EVs can be classified into three distinct groups based on their size: large, medium, and small EVs. Moreover, they can be categorized according to their origin as microvesicles, apoptotic bodies, and exosomes. Microvesicles emerge through cell membrane budding, while apoptotic bodies generate during cell apoptosis (Tkach and Théry, 2016). Exosomes are produced via the formation of intracellular multivesicular bodies (MVBs) that encompass intraluminal vesicles (ILVs). These exosomes are then released through the fusion of MVBs with the plasma membrane and subsequent exocytosis (Gandham et al., 2020). In line with the latest guidelines recommending the use of "sEVs" instead of "exosomes," this review will adopt the term "sEVs". The isolation of sEVs can be achieved through various techniques, including differential ultracentrifugation, density gradient centrifugation, microfluidics (Cheng et al., 2021), size exclusion chromatography (Koh et al., 2018), immunoaffinity capture (Stam et al., 2021), or sEVs isolation kits (Macías et al., 2019). To characterize sEVs, their structures, size, and surface markers are examined using transmission electron microscopy (TEM), nanoparticle tracking analysis (NTA), and western blotting (Zhao et al., 2020).

sEVs display diverse physiological functions depending on their origins and contents. Recent research has revealed their crucial roles in various biological processes such as intercellular communication, angiogenesis, tissue regeneration, inflammation, and cancer metastasis (Lv et al., 2018; Ma et al., 2018; Mashouri et al., 2019; Brennan et al., 2020; Kalluri and LeBleu, 2020). Notably, sEVs can regulate the proliferation, differentiation, and apoptosis of target cells through multiple signaling pathways (Vinaiphat and Sze, 2020). For example, ASCs-sEVs activate the SMAD2/3 and SMAD1/5/9 pathways, promoting tendon stem cell proliferation, migration, and tenogenic differentiation (Liu H. et al., 2021). BMSCs-sEVs inhibit apoptosis and inflammation in RAW 264.7 cells via the BRD4/EZH2/TRAIL axis (Su et al., 2021). sEVs derived from dental pulp stem cells (DPSCs) promote cell migration and angiogenic differentiation (Ganesh et al., 2022), while blood serum-derived sEVs facilitate fibroblast migration, angiogenesis, and granulation tissue formation in diabetic mice (Chen et al., 2021b). Hepatocyte-derived sEVs contribute to liver regeneration by increasing sphingosine-1-phosphate synthesis (S1P) (Nojima et al., 2016). MSCs-sEVs alleviate inflammation by suppressing NLRP3 inflammasome activation and the TLR4/NF-κB signaling pathway (Zhang C. et al., 2022). However, carcinoma-associated fibroblasts (CAFs)-derived sEVs increase salivary adenoid cystic carcinoma lung metastasis by inducing lung pre-metastatic niche formation (Kong et al., 2019). Moreover, sEVs play a role in regulating bone metastasis. Prostate cancer-derived sEVs promote the progression of osteolytic lesions in bone metastasis by transferring miR-152–3p from prostate cancer cells to osteoclasts (Ma et al., 2021). Consequently, sEVs derived from various sources exhibit diverse effects, serving as therapeutic agents for tissue regeneration, inflammation suppression, and potential targets for treating cancer metastasis.

sEVs have emerged as valuable tools for both diagnosis and therapy in the treatment of various diseases. Their composition, including proteins, lipids, DNA, RNA, and miRNAs, contributes to their unique properties. sEVs are promising non-invasive diagnostic biomarkers for cancer, diabetes mellitus (Huang et al., 2022), and bone diseases (Li R. et al., 2022). For example, urinary sEVs have been utilized for the early detection of gastric cancer (Chen et al., 2022), hepatocellular carcinoma (Li et al., 2022c), and head and neck cancer (Hofmann et al., 2022). Additionally, the identification of differentially expressed miRNAs within sEVs offers illuminating insights into various processes related to bone diseases such as osteoarthritis, femoral head necrosis, and bone fracture healing (Li et al., 2022b). Consequently, the detection of sEVs has become a simple, non-invasive, highly sensitive, and cost-effective method for monitoring the emergence and progression of diseases.

In the treatment of various diseases, sEVs have demonstrated significant advantages due to their biocompatibility, high bioavailability, and ability to deliver therapeutic cargo to target cells. Stem cell-derived sEVs possess remarkable regenerative potential, making them highly applicable in therapeutic applications. Notably, MSCs-sEVs have been explored as nanotherapeutics for autoimmune and neurodegenerative disorders. MSCs-derived sEVs, for instance, have shown their ability to reduce demyelination and neuroinflammation (Riazifar et al., 2019). Meanwhile, ASCs-derived sEVs have accelerated wound healing by promoting re-epithelialization and reducing inflammation (Zhou et al., 2022b), while BMSCs-derived sEVs have exhibited potential in improving osteoarthritis by promoting cartilage repair and alleviating knee pain (He et al., 2020). Huc-MSCs-derived sEVs have exhibited potential in repairing Parkinson's disease by crossing the blood-brain barrier (BBB), reducing apoptosis, and preventing the loss of substantia nigra dopaminergic neuron (Chen et al., 2020). sEVs have also been detected in various body fluids. For example, bovine milk-derived sEVs have demonstrated the ability to alleviate colitis symptoms by modulating intestinal inflammatory responses (Han et al., 2022). Plasma-derived sEVs have shown the potential to promote the proliferation and migration of BMSCs while inhibiting inflammation-induced chondrocyte degeneration (Zhang Y. et al., 2022). Furthermore, saliva-derived sEVs have exhibited potential in promoting cutaneous wound healing by stimulating the proliferation, migration, and angiogenesis of human umbilical vein endothelial cells (HUVECs) (Mi et al., 2020). In addition, there is growing interest in using sEVs as delivery tools for therapeutic miRNAs, proteins, and drugs. For instance, miR-31–5p mimics loaded in milk-derived sEVs have demonstrated efficacy in promoting diabetic wound healing (Yan et al., 2022). Zha et al. (2020) reported that encapsulated VEGF plasmid gene within sEVs elevated vascularized osteogenesis *in vivo*. Qian et al. (2022) found that sEVs derived from neural stem cells inhibited glioma by transferring miR-124–3p. Moreover, doxorubicin-loaded

neutrophil-derived sEVs have shown potential in the treatment of glioma, brain diseases, and solid tumors (Wang J. et al., 2021). Overall, sEVs possess biocompatibility and exhibit extended circulation time by evading macrophage capture and clearance (Kamerkar et al., 2017). MSCs-derived sEVs offer significant potential in promoting angiogenic and osteogenic differentiation, making them a promising cell-free therapy for bone repair and regeneration (Heris et al., 2022).

2.2 sEVs transfer miRNAs into cells

miRNAs are initially transcribed into pre-miRNAs by RNA polymerase II and further processed by Drosha/DGCR8 to generate pri-miRNAs. These pri-miRNAs are exported to the cytoplasm through exportin-5 and mature into functional miRNAs. These mature miRNAs bind to the 3′ untranslated region (3′UTR) of target mRNAs, regulating various physiological and pathological processes through post-transcriptional silencing (Kim et al., 2009). However, the therapeutic potential of miRNAs is hindered by the lack of safe, effective, and stable delivery systems that protect them from degradation and facilitate cellular uptake.

Studies indicated that sEVs contain multiple miRNAs that can be transferred to target cells, influencing their functions. sEVs present potential advantages over other miRNA delivery strategies, including enhanced delivery efficiency and reduced degradation rates (Liang et al., 2021). Factors such as cell source, culture conditions, and sEV isolation techniques can influence the number of miRNAs in sEVs. Loading miRNAs into sEVs can be achieved either by modulating donor cells (endogenously) or by loading cargoes into sEVs *in vitro* (exogenously). Endogenous transfection methods involve modifying source cells to alter miRNA levels (Shojaati et al., 2019; Lou et al., 2020), while exogenous techniques include electroporation, co-incubation, sonication, and lipofectamine for sEVs derived from body fluids like blood, urine, saliva, and breast milk (Asadirad et al., 2019). Notably, the clinical implementation of electroporation (Zhang et al., 2017) for the direct transfer of miRNA mimics or inhibitors into sEVs encounters challenges such as exosome destruction, aggregation, and low loading efficiency (Wei Z. et al., 2021). Exo-Fect transfection has demonstrated high effectiveness, with over 50% transfection efficiency and lower co-localization with lysosomal and early endosomal compartments compared to other methods like heat shock or cholesterol modification of miRNAs (de Abreu et al., 2021). Nevertheless, since sEVs already naturally contain miRNAs and proteins, the efficient encapsulation of additional miRNAs remains unclear. To overcome these challenges and enhance the clinical translation of sEVs for miRNA delivery, further research is needed to optimize their utilization.

3 Variations in osteogenic-associated miRNAs expression within MSCs-sEVs under different microenvironments

Altered miRNA expression has been observed in stem cells derived from different sources and cultured under various conditions, as identified through miRNA microarray or high-throughput sequencing techniques. This article provides a summary of effects of osteogenic induction, hypoxic preconditioning, cellular senescence, and chemical or biomaterial microenvironments on the expression of osteogenic-associated miRNAs in MSCs-sEVs.

3.1 Osteogenic induction

Despite the potential of MSCs for multi-lineage differentiation, their application in tissue-engineering is limited due to low survival rates and differentiation efficiency. Osteogenic induction medium (OIM) can improve the stability, calcified nodules, and levels of ALP, OCN, OPN, and Runx2 in MSCs. Moreover, it affects the expression of miRNAs in MSCs-derived sEVs. For example, osteogenic induction of huc-MSCs resulted in 67 upregulated and 64 downregulated miRNAs in MSCs-derived sEVs during extended culture. These miRNAs target genes associated with bone growth and function, which are silenced. Notably, the gradually increasing expression of miR-2110 and miR-328–3p promoted osteogenesis by inhibiting the MAPK and PI3K-AKT-mTOR signaling pathways (Yahao and Xinjia, 2021). In BMSCs-sEVs, 8 miRNAs were downregulated, and 16 miRNAs were upregulated under osteoinductive culture, closely linked to bone formation by regulating the balance between Bmpr2/Acvr2b and smad1/5/9 phosphorylation (Liu A. et al., 2021). Moreover, OIM significantly altered miRNA expression over time, with miR-455–3p (Ma et al., 2022) and miR-27a-3p (Ren et al., 2021) continuing to increase on the 7th and 14th days in OIM, resulting in the downregulation of downstream targets HDAC2 and CRY2/ERK1/2. In conclusion, osteogenic induction can alter miRNA expression in sEVs, thereby impacting the osteogenic differentiation ability of sEVs.

3.2 Hypoxia preconditioning

Hypoxic pretreatment promotes the viability, proliferation, plasticity, and differentiation of BMSCs, while decreasing their apoptosis via the upregulation of HIF-1α (Luo et al., 2019) and downregulation of stress response-related genes p16 and extracellular signal-regulated kinase (Tsiapalis and Zeugolis, 2019). Recent studies have unveiled the capability of hypoxia preconditioning to elevate miRNA expression in sEVs derived from BMSCs (Shen et al., 2022). For instance, hypoxia preconditioning upregulated miR-126 in MSCs-sEVs via HIF-1α activation. This activation improved bone fracture healing through the miR-126/SPRED1/Ras/Erk signaling pathway (Liu et al., 2020a). Moreover, hypoxic MSCs-derived sEVs stimulate osteogenesis and promote new blood vessel growth in mice with bone deficiencies. During hypoxia, miRNA sequencing analysis demonstrated that elevated levels of miR-210–3p in sEVs. The upregulation of miR-210–3p facilitated vascularized bone regeneration by inhibiting the expression of EFNA3 and activating the PI3K/AKT pathway (Zhuang et al., 2022). Furthermore, MSCs-sEVs derived from the hypoxic preconditioning microenvironment induced the polarization of M1 to M2 phenotype by enriching miR-216a-5p

and activating the TLR4/NF-κB/PI3K/AKT axis (Liu et al., 2020b). It is important to note that prolonged periods of hypoxia or excessively low oxygen concentrations may impair the function of MSCs, despite the effectiveness of hypoxic preconditioning in optimizing the regenerative and therapeutic potential of MSCs.

3.3 Senescence

Senescence induces irreversible cell-cycle arrest, which in turn contributes to age-related bone fragility and loss. The composition of sEVs and their miRNAs in the bone marrow microenvironment may vary with age. Previous studies have revealed that BMSCs-sEVs from young and aged mice are rich in miRNAs, but the miRNA profile differs significantly, contributing to the dysfunction of stem cells associated with aging. Particularly, aged sEVs exhibited a significant increase in miR-183–5p expression. Transfection of miR-183–5p mimics into BMSCs induced osteoblast dysfunction by downregulating heme oxygenase-1 (Hmox1) activity (Davis et al., 2017). Xu et al. (2018) discovered elevated levels of miR-31a-5p in BMSCs-derived sEVs from aged rats compared to those from their younger counterparts. The enrichment of miR-31a-5p in sEVs regulated osteoblastic and osteoclastic activities, promoting bone resorption and inhibiting bone formation. This observation presents miR-31a-5p as a potential therapeutic modulator for age-related bone loss. Furthermore, sEVs derived from aged bone matrix stimulated adipogenesis and vascular calcification during bone resorption by upregulating the expression of miR-128–3p (Xu et al., 2020), miR-483–5p, and miR-2861 (Wang ZX. et al., 2022). In conclusion, as time progresses, sEVs enriched with specific miRNAs hinder bone formation, enhance bone resorption, and stimulate adipogenesis in bone marrow microenvironment. These molecules hold promise as valuable biomarkers for age-related bone diseases.

3.4 Chemical or biomaterials microenvironment

Both chemical elements and biomaterial structures can influence cell-to-cell communication, altering miRNA profiles and target gene expression in sEVs. For example, the incorporation of lithium (Li) into bioactive materials enhanced the proliferation, migration, and tube formation of HUVECs, thereby promoting angiogenesis during bone remodeling. This effect was achieved through the upregulation of miR-130a and activation of the PTEN/AKT signaling pathway in BMSCs-derived sEVs (Liu L. et al., 2019). Similarly, biocompatible titanium alloys supported the attachment of mineralized bone matrix and promoted cell-free bone regeneration by upregulating the expression of miR-146a-5p, miR-503–5p, miR-483–3p and miR-129–5p, while downregulating the expression of miR-32–5p, miR-133a-3p, and miR-204–5p. Coating cell-free titanium alloy scaffolds (Ti-scaffolds) with MSC-sEVs facilitated bone-forming outcomes comparable to those achieved with MSC-seeded Ti-scaffolds (Zhai et al., 2020). In another study, Fe_3O_4 nanoparticles were used to manufacture BMSCs-sEV, which were found to promote osteogenesis and angiogenesis by modulating miR-1260a/HDAC7/COL4A2 (Wu et al., 2021a). Similarly, the utilization of strontium (Sr) -containing biomaterials prompted the production of pro-angiogenic miR-146a cargoes within BMSCs-sEVs. These cargoes, in turn, inhibited the expression of Smad4 and NF2, leading to the development of engineered Sr-sEVs with dual-functional regulation for promoting both osteogenesis and angiogenesis in the context of vascularized bone regeneration (Liu L. et al., 2021). Additionally, 3D printing biomaterials loaded with human gingival MSCs-sEVs increased the expression of osteogenic and angiogenic markers such as RUNX2, VEGFA, OPN, and COL1A1, alongside enhanced expression of miR-2861 and miR-210 (Pizzicannella et al., 2019). Taken together, these studies suggest that even tiny bioactive elements or structures can significantly impact the expression of miRNAs in MSCs-sEVs, thereby playing a pivotal role in bone repair and regeneration.

4 miRNAs delivered by MSCs-sEVs in bone regeneration

Osteogenesis, angiogenesis, and inflammation are all essential processes involved in the healing of bone defects. miRNAs delivered by MSCs-sEVs and the associated signaling pathways play crucial roles in regulating the above processes (as depicted in Figure 2). These small molecules facilitate intercellular communication, enabling cells to exchange information and participate in the regulation of osteogenesis. Therefore, targeting sEVs-miRNAs and their related signaling pathways holds potential therapeutic opportunities for the treatment of bone injuries and diseases. The formation of blood vessel networks is crucial to supply the necessary nutrients and oxygen required for regulating bone remodeling. The expression of sEVs-miRNAs affects angiogenesis, thereby influencing osteogenesis (Yang et al., 2021). Furthermore, during the inflammatory phase of bone healing, researchers discovered that sEVs-miRNAs enhanced their immunomodulatory properties, leading to the suppression of pro-inflammatory markers and elevation of anti-inflammatory markers (Kang M. et al., 2022). These findings emphasized the importance of the pro-angiogenic and anti-inflammatory abilities of sEVs-miRNAs in promoting bone regeneration.

4.1 Facilitating osteoblastic differentiation

Researchers have been investigating the potential application of miRNA mimics or inhibitors to stimulate the proliferation, migration, and differentiation of osteoblasts in stem cells. They have discovered that incorporating these miRNAs into MSCs-sEVs is an effective method for promoting bone formation. For example, BMSCs-sEVs containing miR-21–5p enhanced the differentiation of osteoblasts and increased ALP activity in hFOB1.19 cells (You et al., 2022). Similarly, miR-126–5p and miR-150–5p enriched apical papilla-derived sEVs (SCAP-sEVs) facilitated migration and tube formation of HUVECs, promoted differentiation of MC3T3-E1 cells, and improved bone regeneration (Jing et al., 2022). BMSCs-sEVs were also found to support hBMSCs migration and osteogenesis by transporting miR-20a (Liu et al., 2021d).

These sEVs containing miRNAs operate by binding to the 3′ untranslated region (3′UTR) of downstream targets and mediating

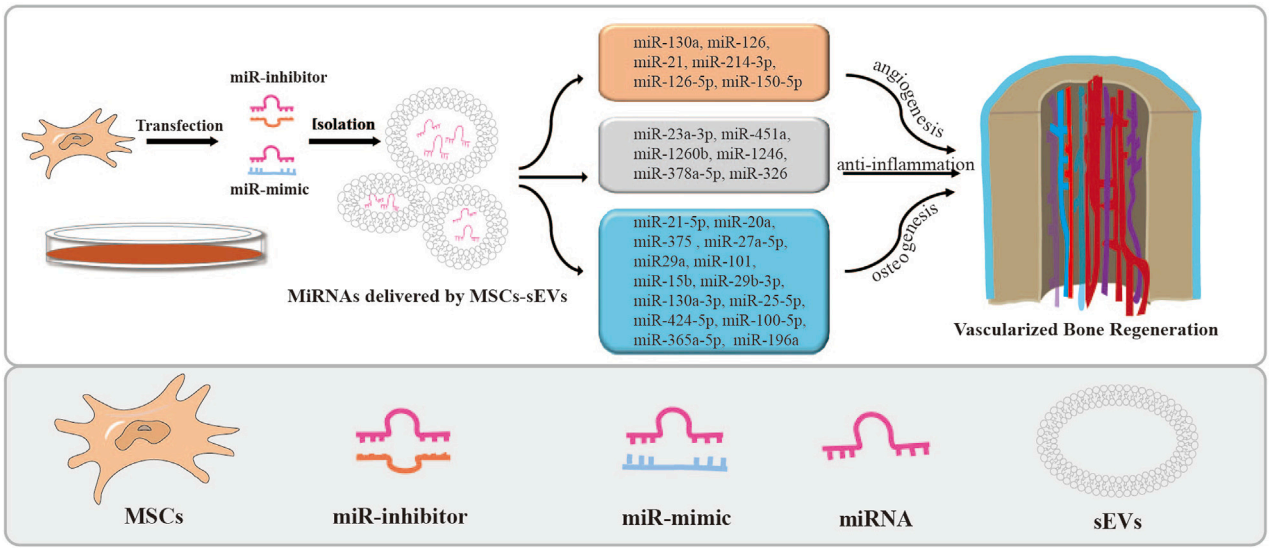

FIGURE 2
MSCs-sEVs deliver miRNAs by transfection and their applications. The miRNA mimics or inhibitors were transfected into stem cells to overexpress or knock down the expression of miRNAs in MSCs-sEVs. Then, miRNAs loaded in MSCs-sEVs enhance angiogenesis and bone regeneration.

various signaling pathways. Compared to BMSCs-sEVs, BMSCs-derived sEVs loaded with miR-21–5p inhibited KLF3, a negative factor in osteogenic differentiation, resulting in enhanced osteoblastic differentiation and ALP activity in target cells (You et al., 2022). BMSCs-sEVs containing miR29a promoted angiogenesis and osteogenesis in a VASH1-dependent manner (Lu et al., 2020). Another research unveiled that sEVs derived from BMSCs, abundant in miR-27a-5p, induced the differentiation of osteoblast cells while suppressing autophagy, leading to bone formation by targeting Atg4B (Li X. et al., 2021). In a calvarial defect model, sEVs derived from miR-375-overexpressing hASCs promoted bone regenerative capacity by binding to insulin-like growth factor binding protein 3 (IGFBP3) (Chen et al., 2019).

MSCs-derived sEVs containing distinct miRNAs can facilitate or inhibit osteogenic differentiation by regulating various signaling pathways. For example, miR-101 encapsulated in BMSCs-sEVs facilitate osteogenic differentiation by repressing FBXW7 to regulate the HIF1α/FOXP3 axis (Li Y. et al., 2021). BMSC-sEVs containing miR-196a targeted Dkk1 to activate Wnt/β-catenin pathway (Peng et al., 2021). Meanwhile, BMSCs-sEVs loaded with miR-140–3p targeted plexin B1 (plxnb1), thereby promoting the osteoblastogenesis function via the plexin B1/RhoA/ROCK signaling pathway (Wang N. et al., 2022). BMSC-sEVs loaded with miR-15b impaired WWP1-mediated KLF2 ubiquitination and inactivated the NF-κB signaling pathway (Li Y. et al., 2020). Moreover, miR-29b-3p encapsulated in BMSCs-sEVs enhanced neovascularization at fracture sites by modulating PTEN/PI3K/AKT (Yang et al., 2022) and KDM5A/SOCS1/NF-κB axes (Zhang et al., 2020b). The overexpression of miR-130a-3p in ASCs-sEVs promoted osteogenic differentiation by mediating SIRT7/Wnt/β-catenin axis (Yang S. et al., 2020). The above studies demonstrate the potential of sEVs-delivered miRNAs in promoting vascularized bone regeneration.

However, it is important to note that some sEVs containing miRNAs have been identified as inhibitors of osteogenesis. For example, the overexpression of miR-25–5p (Lan et al., 2022), miR-424–5p (Wei Y. et al., 2021), and miR-100–5p (Yang et al., 2021) in sEVs inhibited osteogenesis by targeting RUNX2, OCN, ALP, and OPN levels through the SMAD2/ERK, WIF1/Wnt/β-catenin, and BMPR2/Smad1/5/9 signaling pathways, respectively. Huc-MSC-sEVs promoted the proliferation and osteogenesis of BMSCs by suppressing miR-365a-5p via the SAV1/YAP signaling pathway (Kuang et al., 2021). In addition, Long non-coding RNAs (LncRNAs) interact with miRNA and mRNA molecules through the competing endogenous RNA regulatory mechanism in bone repair and regeneration (Yang Y. et al., 2020). Acting as molecular sponges, LncRNAs competitively absorb miRNAs, thereby alleviating their inhibitory impact on target mRNAs and elevating the expression of those specific targets (Liu et al., 2022). For example, overexpressing lncRNA-KCNQ1OT1 in ASCs-sEVs silenced miR-141–5p expression, reducing cytotoxicity and apoptosis of osteoblasts, thus improving osteoporosis (Wang SZ. et al., 2021). Similarly, BMSCs-sEVs containing lnc-H19 absorbed miR-106, thereby promoting osteogenesis through the miR-106-Angpt1-Tie2/NO signaling pathway (Behera et al., 2021). Overall, MSCs-sEVs facilitate osteoblastic differentiation through lncRNA-miRNA-mRNA networks. However, a judicious selection of specific miRNAs is necessary, considering their potential to either promote or inhibit osteogenesis. The main miRNAs-mRNAs networks highlighted in the above studies are summarized in Table 1.

4.2 Inhibiting osteoclast differentiation

MSCs-sEVs-miRNAs inhibit osteoclast differentiation, which negatively impacts bone healing by causing bone resorption. For

TABLE 1 MSC-sEVs delivered miRNAs can regulate many signaling pathways to facilitate osteogenic differentiation.

Stem cells	Delivered miRNAs	Target cells	Target gene	Functions	Signal pathway	Refs
BMSCs	miR-101	MSCs	FBXW7	augment osteogenic differentiation	HIF1α/FOXP3	Li et al. (2021c)
	miR-196a	HFOB1.19	Dkk1	promote osteogenic differentiation	Wnt/β-catenin	Peng et al. (2021)
	miR-140–3p	BMSCs	plxnb1	promote bone formation	plexin B1/RhoA/ROCK	Wang et al. (2022a)
	miR-15b	BMSCs	WWP1	increase ALP activity and osteogenic differentiation-related marker expression	NF-κB	Li et al. (2020c)
	miR-29b-3p	HUVECs BMSCs	PTEN	enhance neovascularization at the fracture site	PI3K/AKT	Yang et al. (2022)
	miR-29b-3p	hFOB1.19	KDM5A	promote angiogenesis and facilitate fracture healing	SOCS1/NF-κB	Zhang et al. (2020b)
	miR-25–5p	BMSCs	SMAD2	promote BMSC osteogenesis	SMAD2/ERK	Lan et al. (2022)
	miR-424–5p	BMSCs	WIF1	attenuate osteogenic development	WIF1/Wnt/β-catenin	Wei et al. (2021a)
	miR-100–5p	HUVECs BMSCs	BMPR2	inhibit osteogenesis of hBMSCs and angiogenesis of HUVECs	BMPR2/Smad1/5/9	Yang et al. (2021)
HUC-MSC	miR-365a-5p	BMSCs	SAV1	promote the proliferation and osteogenesis of BMSCs	SAV1/YAP	Kuang et al. (2021)
ASCs	miR-130a-3p	ADSCs	SIRT7	promote osteogenic differentiation	Wnt/β-catenin	Yang et al. (2020c)

instance, the transfection of miR-27a (Wang Y. et al., 2022) and miR-21 (Hu et al., 2022b) into MSCs increased their expression levels in sEVs, leading to decreased osteoclasts numbers and tartrate-resistant acid phosphatase (Trap) levels through the DKK2/Wnt/β-catenin signaling pathway, ultimately increasing bone mineral density. Similarly, ASCs-sEVs enriched with miR-21–5p and let-7b-5p significantly inhibited osteoclast differentiation, promoted BMSCs migration, and reduced bone resorption (Lee et al., 2021). The abundance of miR-6924–5p in BMSCs-sEVs inhibited osteoclast formation and enhanced bone healing by targeting OCSTAMP and CXCL12 (Feng et al., 2021). Furthermore, gingival tissue-derived MSCs-sEVs-miR-1260b inhibited osteoclastogenic activity by targeting the Wnt5a/RANKL pathway (Nakao et al., 2021). These sEVs-delivery systems exhibit promise for improving bone regeneration by activating osteoblastic differentiation while inhibiting osteoclast differentiation.

4.3 Promoting angiogenesis

The growth of blood vessels and the high expression of angiogenic factors are crucial for bone repair (Zhang L. et al., 2020). sEVs play a significant role in promoting vascularized bone regeneration by modulating the expression of miRNAs and multiple signaling pathways. BMSCs-sEVs can promote the expression of proangiogenic cytokines, including VEGF, platelet endothelial cell adhesion molecule-1 (CD31), and HIF-1α, leading to improved vascular development and regeneration in bone defects through the upregulation of the miR-21/NOTCH1/DLL4 signaling axis (Zhang et al., 2021c; Hu H. et al., 2022). The overexpression of miR-130a in BMSCs-sEVs facilitates bone formation and enhances the pro-angiogenic potential of HUVECs by stimulating the PTEN/AKT signaling pathway (Liu L. et al., 2019). The high expression of BMSCs-sEVs-miR-126 enhances angiogenesis by targeting PIK3R2, which activated the PI3K/Akt signaling pathway (Zhang L. et al., 2021). Encapsulation of BMSCs-derived sEVs in scaffolds extends their delivery and released time. sEVs-loaded hydrogels release miR-21, which targets SPRY2 and accelerates both osteogenesis and angiogenesis (Wu et al., 2021b). However, sEVs-miR-214–3p results in impaired angiogenic potential and decreased bone mineral density (Wang X. et al., 2021), highlighting the importance of downregulating this miRNA in sEVs to promote vascularized bone regeneration. Overall, these findings shed light on the regulatory roles of sEVs containing miRNA in angiogenesis during the process of bone remodeling, further emphasizing their potential in bone tissue engineering.

4.4 Reducing inflammation

sEVs carrying miRNAs hold significant potential in modulating the bone healing process by regulating the polarization state of host macrophages. The polarization of macrophages plays an essential role in bone healing. M1-type macrophages induce persistent inflammation and tissue degradation, while M2-type

TABLE 2 miRNAs delivered by MSCs-sEVs in bone-related diseases.

Bone diseases	Stem cells	Delivered miRNAs	Target cells	Target gene/Signal pathway	Functions	Refs
BF	BMSCs	miR-136–5p	BMSCs, osteoblasts	Wnt/β-catenin	facilitate bone fracture healing	(Hu et al., 2021a; Yu et al., 2021)
		miR-19b		WWP1/Smurf2/KLF5		
		miR-25, miR-29b-3p		SMURF1/Runx2, VapB/Wnt/β-catenin,PTEN/PI3K/AKT		
		miR-335				
OP	BMSCs	miR29a	HUVECs	VASH1	promote angiogenesis and osteogenesis	Lu et al. (2020)
	BMSCs	miR-21–5p	hFOB1.19 cells	KLF3	enhance proliferation and osteoblastic differentiation	You et al. (2022)
	BMSCs	miR-146a	MC3T3-E1 cells	Rtn4/miR-146a	inhibit the viability of cells and promote their apoptosis	Cao et al. (2020)
	BMSCs	miR-34c	hFOB1.19 cells	SATB2	enhance osteoblast activity in osteoporotic mice	Yang et al. (2019)
	BMSCs	miR-186	BMSCs	Hippo signaling pathway	promote osteogenesis in OVX rats	Li et al. (2021a)
	huc-MSCs	miR-1263	BMSCs	Mob1/Hippo	inhibit BMSC apoptosis and prevent OP	Yang et al. (2020a)
	MSCs	miR-27a	Osteoblasts, osteoclasts	DKK2/Wnt/β-catenin	improve bone damage recovery and decrease bone resorption	Wang et al. (2022b)
OA	SMSCs	miR-212–5p	chondrocyte	Runx2	attenuate inflammation, degeneration, and degradation	Wang et al. (2021d), Zheng et al. (2022b)
		miR-155–5p		ELF3		
	BMSCs	miR-125a-5p	chondrocyte	E2F2	accelerate migration and alleviate degradation	Xia et al. (2021)
	BMSCs	miR-206, miR-127–3p, and miR-9-5p	osteoblasts,	Elf3, CDH11, SDC1	ameliorate inflammation and inhibit apoptosis	(Jin et al., 2020; Huang et al., 2021b)
			chondrocyte			
	BMSCs	miR-326	chondrocyte	HDAC3/STAT1/NF-κB p65	inhibit pyroptosis of chondrocytes and cartilage	Xu and Xu (2021)
	BMSCs	miR-122–5p, miR-206	chondrocyte	Sesn2/Nrf2, GIT1	repress autophagy and apoptosis	(Liu et al., 2018; Zhang and Jin, 2022)
ONFH	BMSCs	miR-185–3p	BMSCs	PI3K/Akt, Wnt signaling pathways	regulate osteogenesis-related signaling pathways	Zhu et al. (2022)
		miR-1b-5p				
		miR-129b-5p				
		miR-223–5p				
	BMSCs	miR-224–3p	HUVECs	FIP200	downregulation of miR-224–3p promotes the angiogenesis	Xu et al. (2019)
	$CD34^+$ stem cells	miR-26a	HUVECs,	ALP, RUNX2, COL I	increase the bone integrity and vessel density	Zuo et al. (2019)
			BMSCs			
	huc-MSCs,	miR-21–5p	hFOB1.19 cells, HUVECs, BMSCs	SOX5, EZH2	augment angiogenesis and osteogenesis	(Nan et al., 2021; Fang et al., 2022)
	ASCs	miR-378		Sufu, Shh		
	hiPSC-MSCs,	miR-135b	MG-63	PDCD4	inhibit cell apoptosis and promote cell proliferation	(Kuang et al., 2019; Zhang et al., 2020c)
	BMSCs,	miR-150	U-2 cells, osteoblasts	GREM1/NF-κ		
	huc-MSCs	miR-21	MLO-Y4	BPTEN/AKT		

macrophages promote anti-inflammatory responses and enhance tissue repair (Mao et al., 2022). The capacity of sEVs to transport and transfer miRNAs renders them a promising avenue for biomedical research. Studies have demonstrated the potential of sEVs in attenuating inflammation and promoting bone tissue repair. For instance, sEVs derived from BMSCs transfected with miR-23a-3p mimics promoted M2 macrophage polarization, reduced inflammation by inhibiting the IRF1 and NF-κB pathways, and improved tendon-bone healing. This was further evidenced by an increased ratio of bone volume to total volume (BV/TV), upregulated collagen type II alpha 1 levels, and improved bone healing outcomes (Li Z. et al., 2022). Similarly, ASCs-sEVs enriched with miR-451a significantly promoted bone healing and facilitated the shift from M1 macrophages to M2 macrophages, thereby inhibiting inflammation via miR-451a/MIF signaling pathway (Li R. et al., 2022). Furthermore, BMSCs-sEVs overexpressing miR-181b facilitated M2 macrophage polarization and osteointegration by suppressing PRKCD while activating p-AKT (Liu et al., 2021e). Additionally, gingival MSCs-derived sEVs containing miR-1260b inhibited osteoclastogenesis and periodontal bone resorption by inducing anti-inflammatory M2 macrophage polarization and repressing Wnt5a/RANKL pathway (Nakao et al., 2021). Dental pulp stem cells derived sEVs (DPSC-sEVs) enhanced T-cell modulatory function, restored the balance between Th17 cells and Treg cells, suppressed inflammation, and accelerated alveolar bone healing by transferring miR-1246 and inhibiting Nfat5 expression (Zhang et al., 2021b). Lastly, huc-MSCs-derived sEVs containing miR-378a-5p (Cai et al., 2021) and miR-326 (Wang et al., 2020) inhibited the expression of interleukin (IL)-18, IL-1β, Caspase-1, and NLRP3 inflammasomes. These findings suggest that miRNAs enriched in MSCs-sEVs possess the capability to regulate macrophage polarization and suppress inflammation, thereby promoting bone regeneration.

5 miRNAs delivered by MSCs-sEVs in bone-related diseases

MSCs and their sEVs have shown promising potential as therapeutic agents for bone-related diseases. They can transfer various types of information, regulate immune responses, inhibit cell apoptosis, induce differentiation, and promote tissue regeneration (Malekpour et al., 2022). The miRNAs found in MSCs-sEVs play a crucial role in maintaining the balance between osteoblasts and osteoclasts, promoting angiogenesis, and aiding in bone restoration. Table 2 outlines the important roles of miRNAs from MSCs-sEVs in various bone-related conditions such as bone fractures, osteoporosis, osteoarthritis, and osteonecrosis of the femoral head.

5.1 Bone fracture

Bone fracture healing is a complex process, involving the coordinated actions of osteoclasts for bone resorption and osteoblasts for bone formation. Recent studies have highlighted the role of miRNAs encapsulated within BMSCs-sEVs in enhancing neovascularization and bone formation at the fracture site through various complicated signaling pathways. For example, BMSCs-sEVs carrying miR-136–5p promoted osteoblast differentiation and facilitated fracture healing by targeting LRP4 and activating the Wnt/β-catenin signaling pathway (Yu et al., 2021). Another miRNA, miR-19b, abundant in BMSC-sEVs, facilitated bone cell mineralization, and enhanced neovascularization at the fracture site through the WWP1/Smurf2/KLF5/β-catenin signaling pathway (Huang et al., 2021a). Additionally, BMSC-sEVs secrete miR-25 (Jiang et al., 2020), miR-29b-3p (Yang et al., 2022), and miR-335 (Hu H. et al., 2021), which have demonstrated the ability to enhance the proliferation, migration, and differentiation of osteoblasts *in vitro*. *In vivo*, these miRNAs accelerate bone fracture healing through three distinct pathways: SMURF1/Runx2, VapB/Wnt/β-catenin, and PTEN/PI3K/AKT axes, respectively. Collectively, these findings suggest that MSCs-sEVs-encapsulated miRNAs may offer valuable insights into the disappearance of fracture lines, callus formation, and overall fracture healing process.

5.2 Osteoporosis

Osteoporosis (OP) is a degenerative bone disease caused by an imbalance in bone remodeling cycle, resulting in an increased risk and susceptibility to bone fractures (Brown, 2017). Recent *in vitro* experiments have demonstrated that certain miRNAs carried by MSCs-sEVs could impact the prognosis of OP. In postmenopausal osteoporotic rats, the expression of BMSCs-sEVs-miR-27a-3p and miR-196b-5p was relatively reduced (Lai et al., 2022), but these miRNAs actually accelerated osteogenesis and reduced bone resorption in OP. Upregulating BMSCs-sEVs containing miR-150–3p (Qiu et al., 2021), miR29a (Lu et al., 2020), and miR-21–5p (You et al., 2022) also stimulate angiogenesis and osteogenesis, presenting a novel therapeutic strategy for treating OP. Conversely, downregulating miR-146a in BMSCs-sEVs enhance the viability of MC3T3-E1 cells and prevent their apoptosis (Cao et al., 2020). BMSCs-derived sEVs containing MALAT1 boost osteoblast activity in osteoporotic mice by inhibiting the expression of miR-34c and promoting the expression of SATB2 (Yang et al., 2019). Mechanistically, miR-186 loaded BMSCs-sEVs facilitate osteogenesis in osteoporotic rats through the Hippo signaling pathway (Li L. et al., 2021). Further research revealed that sEVs derived from huc-MSCs prevent OP by inhibiting BMSCs apoptosis and regulating the miR-1263/Mob1/Hippo signaling pathway (Yang BC. et al., 2020). Overall, MSCs-sEVs carrying specific miRNAs have emerged as a promising therapy for OP, as they promote bone damage recovery and reduce bone resorption through various signaling pathways (Wang Y. et al., 2022).

5.3 Osteoarthritis

Osteoarthritis (OA) is a chronic inflammatory disease characterized by the degeneration of chondrocytes, bone sclerosis, and inflammation. Numerous studies have demonstrated the crucial roles of MSCs-sEVs-miRNAs in promoting chondrocyte migration and proliferation (Zhu et al., 2017). In OA tissues, the expression of miR-212–5p and miR-155–5p in synovial mesenchymal stem cells

derived sEVs (SMSCs-sEVs) was found to be downregulated. Conversely, upregulated miR-212–5p and miR-155–5p (Wang Z. et al., 2021) in SMSC-sEVs could attenuate inflammation, chondrocyte degeneration, and degradation (Zheng T. et al., 2022). Similarly, MSCs-sEVs enriched with miR-125a-5p exhibited the ability to enhance chondrocyte migration and alleviate extracellular matrix degradation by targeting E2F2 (Xia et al., 2021). BMSC-sEVs encapsulating miR-206, miR-127–3p, and miR-9-5p could ameliorate inflammation and inhibit apoptosis by reducing Elf3 (Huang et al., 2021b), CDH11 (Dong et al., 2021), and SDC1 (Jin et al., 2020), respectively. BMSC-sEVs delivering miR-326 could inhibit chondrocyte pyroptosis and cartilage degradation by targeting HDAC3 through the STAT1/NF-κB p65 axis (Xu and Xu, 2021). Furthermore, recent studies have revealed the involvement of sEVs-lncRNAs in the pathological processes of OA through their interaction with miRNAs. For instance, the lncRNA NEAT1 and lncRNA-KLF3-AS1 delivered by MSCs-sEVs could suppress chondrocyte autophagy and apoptosis and decelerated the progression of OA by modulating the miR-122–5p/Sesn2/Nrf2 (Zhang and Jin, 2022) and miR-206/GIT1 (Liu et al., 2018) axes. In summary, miRNAs and lncRNAs loaded in MSCs-sEVs hold promise in effectively reducing inflammation, alleviating cartilage degradation, and promoting bone regeneration by modulating downstream targets and signaling pathways, thus providing potential therapeutic strategies for the treatment of OA.

5.4 Osteonecrosis of the femoral head

Osteonecrosis of the femoral head (ONFH) is a bone disease caused by impaired blood supply and necrosis of the marrow in the femoral head. Recently, studies have shown that the levels of miRNAs in sEVs might be altered during the progression of ONFH (Li et al., 2018). For example, miRNA sequencing revealed decreased expression of miR-185–3p and miR-1b-5p, while miR-129b-5p and miR-223–5p were upregulated in sEVs from femoral tissue in ONFH patients. These changes closely related to classical osteogenesis-related signaling pathways, including PI3K/Akt and Wnt signaling pathways (Zhu et al., 2022). Furthermore, elevated expression of sEVs-miR-100–5p in ONFH inhibits osteogenesis and angiogenesis through the BMPR2/SMAD1/5/9 signaling pathway (Yang et al., 2021). In contrast, in ONFH, the expression of miR-224–3p is downregulated in BMSCs-sEVs, which leads to increased angiogenesis by upregulating FIP200 (Xu et al., 2019). Overall, miRNAs promoting disease progression are upregulated, while those inhibiting disease progression are downregulated in ONFH.

Osteogenesis and angiogenesis are crucial for ONFH treatment, and miRNAs encapsulated within MSC-sEVs play a pivotal role in this process. For example, overexpressing miR-26a in MSCs-sEVs can protect the femoral head by enhancing integrity and density of vessels (Zuo et al., 2019). Recent studies indicated that huc-MSCs-sEVs delivering miR-21–5p promote angiogenesis and osteogenesis by suppressing SOX5 and EZH2 expression (Fang et al., 2022). Other findings suggested that ASCs-sEVs carrying miR-378 accelerate bone regeneration and angiogenesis, inhibiting ONFH progression by targeting Sufu to upregulate the Shh signaling pathway (Nan et al., 2021). Moreover, BMSCs-sEVs delivering miR-148a-3p mimics could enhance BMSCs viability and promote osteogenic differentiation to alleviate ONFH by inhibiting SMURF1 and subsequently increasing SMAD7 and BCL2 expression (Huang S. et al., 2020). Additionally, overexpressing miR-122–5p in sEVs increased osteoblasts proliferation and differentiation in the femoral head via the SPRY2/RTK/Ras/MAPK signaling pathway (Liao et al., 2019).

Osteocyte apoptosis may contribute to bone resorption, trigger osteoporosis, cause microfractures, result in femoral head hypoxia and ischemia, and ultimately lead to ONFH (Xu et al., 2021). Recent reports suggested that sEVs containing miRNAs prevent ONFH by inhibiting osteocyte apoptosis (Li G. et al., 2020). For example, human-induced pluripotent stem cell-derived MSCs-sEVs (hiPSC-MSC-sEVs) could inhibit cell apoptosis, promote cell proliferation, and alleviate the bone loss in ONFH by transferring miR-135b (Zhang et al., 2020c). BMSCs-sEVs delivering miR-150 could alleviate ONFH by suppressing osteoblast apoptosis through the GREM1/NF-κB signal pathway (Zheng LW. et al., 2022). Additionally, sEVs derived from huc-MSCs reduced osteocyte apoptosis in ONFH via the miR-21-PTEN-AKT signaling pathway (Kuang et al., 2019). In conclusion, the miRNAs delivered by MSC-sEVs play a pivotal role in promoting angiogenesis, reducing apoptosis, and facilitating vascularized bone formation in ONFH. This mechanism holds potential as a therapeutic strategy for treating ONFH.

6 Conclusion and future perspectives

In summary, bone repair and regeneration rely on the development of bone and blood vessels. MSCs show significant potential for bone regeneration due to their self-renewal and multilineage differentiation capacity (Huang CC. et al., 2020). However, MSCs therapies face obstacles such as high costs, limited sources, and strict storage requirements. Therefore, it is crucial to develop cell-free or acellular approaches to promote bone regeneration.

miRNAs play a crucial role in regulating osteoblast-osteoclast interactions and offer substantial clinical potential (Hu et al., 2022c). However, the lack of effective delivery systems has limited the use of miRNA-based therapeutics. sEVs have emerged as ideal delivery systems due to their ability to maintain miRNA stability during storage. However, sEVs are quickly cleared *in vivo*, which hampers their ability to reach the target site. To overcome this challenge, scaffolds can provide long-term preservation and sustained release of sEVs. For instance, MSCs-sEVs were lyophilized on a microporous bio-glass scaffold, resulting in controlled release, heightened expression of osteogenic-related markers, and enhanced bone repair efficiency (Liu A. et al., 2021). To ensure prolonged retention and controlled release of sEVs, researchers have developed cell-free metal-organic frameworks functionalized with hASCs-sEVs (Kang Y. et al., 2022). These sEVs-loaded composite scaffolds have shown the ability to accelerate blood supply, osteogenic differentiation, and bone reconstruction over an extended period.

However, a major challenge in sEVs research is the impurity and low abundance of conventionally produced sEVs. Three-dimensional (3D) cultures have proven more effective than two-dimensional (2D) cultures in producing sEVs by preventing cell

adhesion to culture flask surfaces. sEVs produced from 3D-cultured MSCs exhibit potential in suppressing inflammation and enhancing therapeutic effects in bone regeneration by the upregulation of miRNAs. The upregulation of miRNAs is thought to be caused by the hypoxic conditions in the center of the 3D spheroidal structure (Zhang et al., 2021b). Other findings have shown that combining tangential flow filtration (TFF) with 3D cell cultures can increase the concentration of sEVs in cell culture supernatants, resulting in higher yields of biologically active sEVs and improved transferability of therapeutic siRNAs (Haraszti et al., 2018). Furthermore, the creation of specific sEVs-mimetics (EMs) through sequential mechanical extrusion of cells offers a rapid method for producing large quantities of sEVs, thereby enhancing manufacturing efficiency compared to traditional methods (Zha et al., 2020).

Ultimately, challenges in using sEVs for bone regeneration are their uncertain distribution and lack of targeting ability in the bone microenvironment. Recent research suggested that click chemistry, physical surface modification, and genetic engineering can help sEVs accumulate at the target site and enhance their therapeutic efficacy (Jiang et al., 2022). Several bone-targeting delivery strategies have been developed, including attaching the bone-targeting peptide SDSSD to the membrane of sEVs for specifically delivery to osteoblasts and the promotion of bone formation (Cui et al., 2022). Additionally, C-X-C motif chemokine receptor 4 (CXCR4) positive bone-targeted sEVs could be recruited by BMSCs and released miR-188 to promote osteogenesis and decrease cortical bone porosity for age-related bone loss (Hu Y. et al., 2021). Although the isolation, delivery, and targeted modification of sEVs are relatively well-documented, further research is necessary to understand the mechanisms by which sEVs deliver functional miRNAs to recipient cells. Therefore, it is important to consider good manufacturing practices, stability, loading efficiency, and targeted delivery of sEV-encapsulated miRNAs for bone repair and regeneration.

Author contributions

RL and SW drafted the review; RL, WL, and LW collected the references and designed the table; RL drew the figures; MD and WN read and approved the final manuscript. All authors contributed to the article and approved the submitted version.

Funding

This study was supported by grants from the Provincial Basic Scientific Research Project of Liaoning Education Department (LJKZ0841); Science and Technology Plan of Liaoning Province (2021JH2/10300027); National Natural Science Foundation of China (82270971; 82100998); Liaoning Province Doctor Startup Foundation (2022-BS-237); Dalian Science and Technology Innovation Fund (2022JJ13SN063).

Conflict of interest

The authors declare that the research was conducted in the absence of any commercial or financial relationships that could be construed as a potential conflict of interest.

Publisher's note

All claims expressed in this article are solely those of the authors and do not necessarily represent those of their affiliated organizations, or those of the publisher, the editors and the reviewers. Any product that may be evaluated in this article, or claim that may be made by its manufacturer, is not guaranteed or endorsed by the publisher.

References

Anada, T., Pan, C. C., Stahl, A. M., Mori, S., Fukuda, J., Suzuki, O., et al. (2019). Vascularized bone-mimetic hydrogel constructs by 3D bioprinting to promote osteogenesis and angiogenesis. *Int. J. Mol. Sci.* 20, 1096. doi:10.3390/ijms20051096

Asadirad, A., Hashemi, S. M., Baghaei, K., Ghanbarian, H., Mortaz, E., Zali, M. R., et al. (2019). Phenotypical and functional evaluation of dendritic cells after exosomal delivery of miRNA-155. *Life Sci.* 219, 152–162. doi:10.1016/j.lfs.2019.01.005

Behera, J., Kumar, A., Voor, M. J., and Tyagi, N. (2021). Exosomal lncRNA-H19 promotes osteogenesis and angiogenesis through mediating Angpt1/Tie2-NO signaling in CBS-heterozygous mice. *Theranostics* 11, 7715–7734. doi:10.7150/thno.58410

Brennan, M., Layrolle, P., and Mooney, D. J. (2020). Biomaterials functionalized with MSC secreted extracellular vesicles and soluble factors for tissue regeneration. *Adv. Funct. Mater* 30, 1909125. doi:10.1002/adfm.201909125

Brown, C. (2017). Osteoporosis: staying strong. *Nature* 550, S15–s17. doi:10.1038/550S15a

Bucher, C. H., Schlundt, C., Wulsten, D., Sass, F. A., Wendler, S., Ellinghaus, A., et al. (2019). Experience in the adaptive immunity impacts bone homeostasis, remodeling, and healing. *Front. Immunol.* 10, 797. doi:10.3389/fimmu.2019.00797

Buduru, S. D., Gulei, D., Zimta, A. A., Tigu, A. B., Cenariu, D., and Berindan-Neagoe, I. (2019). The potential of different origin stem cells in modulating oral bone regeneration processes. *Cells* 8, 29. doi:10.3390/cells8010029

Cai, X., Zhang, Z. Y., Yuan, J. T., Ocansey, D. K. W., Tu, Q., Zhang, X., et al. (2021). hucMSC-derived exosomes attenuate colitis by regulating macrophage pyroptosis via the miR-378a-5p/NLRP3 axis. *Stem Cell Res. Ther.* 12, 416. doi:10.1186/s13287-021-02492-6

Cao, G., Meng, X., Han, X., and Li, J. (2020). Exosomes derived from circRNA Rtn4-modified BMSCs attenuate TNF-α-induced cytotoxicity and apoptosis in murine MC3T3-E1 cells by sponging miR-146a. *Biosci. Rep.* 40, BSR20193436. doi:10.1042/bsr20193436

Chen, H., Huang, C., Wu, Y., Sun, N., and Deng, C. (2022). Exosome metabolic patterns on aptamer-coupled polymorphic carbon for precise detection of early gastric cancer. ACS Nano *Online ahead print* 16, 12952–12963. doi:10.1021/acsnano.2c05355

Chen, H. X., Liang, F. C., Gu, P., Xu, B. L., Xu, H. J., Wang, W. T., et al. (2020). Exosomes derived from mesenchymal stem cells repair a Parkinson's disease model by inducing autophagy. *Cell Death Dis.* 11, 288. doi:10.1038/s41419-020-2473-5

Chen, L., Luo, W., Wang, Y., Song, X., Li, S., Wu, J., et al. (2021a). Directional homing of glycosylation-modified bone marrow mesenchymal stem cells for bone defect repair. *J. Nanobiotechnology* 19, 228. doi:10.1186/s12951-021-00969-3

Chen, L., Qin, L., Chen, C., Hu, Q., Wang, J., and Shen, J. (2021b). Serum exosomes accelerate diabetic wound healing by promoting angiogenesis and ECM formation. *Cell Biol. Int.* 45, 1976–1985. doi:10.1002/cbin.11627

Chen, S., Tang, Y., Liu, Y., Zhang, P., Lv, L., Zhang, X., et al. (2019). Exosomes derived from miR-375-overexpressing human adipose mesenchymal stem cells promote bone regeneration. *Cell Prolif.* 52, e12669. doi:10.1111/cpr.12669

Cheng, S., Li, Y., Yan, H., Wen, Y., Zhou, X., Friedman, L., et al. (2021). Advances in microfluidic extracellular vesicle analysis for cancer diagnostics. *Lab. Chip* 21, 3219–3243. doi:10.1039/d1lc00443c

Claes, L., Recknagel, S., and Ignatius, A. (2012). Fracture healing under healthy and inflammatory conditions. *Nat. Rev. Rheumatol.* 8, 133–143. doi:10.1038/nrrheum.2012.1

Cui, Y., Guo, Y., Kong, L., Shi, J., Liu, P., Li, R., et al. (2022). A bone-targeted engineered exosome platform delivering siRNA to treat osteoporosis. *Bioact. Mater* 10, 207–221. doi:10.1016/j.bioactmat.2021.09.015

Davis, C., Dukes, A., Drewry, M., Helwa, I., Johnson, M. H., Isales, C. M., et al. (2017). MicroRNA-183-5p increases with age in bone-derived extracellular vesicles, suppresses

bone marrow stromal (stem) cell proliferation, and induces stem cell senescence. *Tissue Eng. Part A* 23, 1231–1240. doi:10.1089/ten.TEA.2016.0525

de Abreu, R. C., Ramos, C. V., Becher, C., Lino, M., Jesus, C., da Costa Martins, P. A., et al. (2021). Exogenous loading of miRNAs into small extracellular vesicles. *J. Extracell. Vesicles* 10, e12111. doi:10.1002/jev2.12111

Dong, J., Li, L., Fang, X., and Zang, M. (2021). Exosome-encapsulated microRNA-127-3p released from bone marrow-derived mesenchymal stem cells alleviates osteoarthritis through regulating CDH11-mediated wnt/β-catenin pathway. *J. Pain Res.* 14, 297–310. doi:10.2147/jpr.S291472

Fang, J., and Liang, W. (2021). ASCs -derived exosomes loaded with vitamin A and quercetin inhibit rapid senescence-like response after acute liver injury. *Biochem. Biophys. Res. Commun.* 572, 125–130. doi:10.1016/j.bbrc.2021.07.059

Fang, S., Liu, Z., Wu, S., Chen, X., You, M., Li, Y., et al. (2022). Pro-angiognetic and pro-osteogenic effects of human umbilical cord mesenchymal stem cell-derived exosomal miR-21-5p in osteonecrosis of the femoral head. *Cell Death Discov.* 8, 226. doi:10.1038/s41420-022-00971-0

Feng, W., Jin, Q., Ming-Yu, Y., Yang, H., Xu, T., You-Xing, S., et al. (2021). MiR-6924-5p-rich exosomes derived from genetically modified Scleraxis-overexpressing PDGFRα(+) BMMSCs as novel nanotherapeutics for treating osteolysis during tendon-bone healing and improving healing strength. *Biomaterials* 279, 121242. doi:10.1016/j.biomaterials.2021.121242

Gandham, S., Su, X., Wood, J., Nocera, A. L., Alli, S. C., Milane, L., et al. (2020). Technologies and standardization in research on extracellular vesicles. *Trends Biotechnol.* 38, 1066–1098. doi:10.1016/j.tibtech.2020.05.012

Ganesh, V., Seol, D., Gomez-Contreras, P. C., Keen, H. L., Shin, K., and Martin, J. A. (2022). Exosome-based cell homing and angiogenic differentiation for dental pulp regeneration. *Int. J. Mol. Sci.* 24, 466. doi:10.3390/ijms24010466

Gong, L., Chen, B., Zhang, J., Sun, Y., Yuan, J., Niu, X., et al. (2020). Human ESC-sEVs alleviate age-related bone loss by rejuvenating senescent bone marrow-derived mesenchymal stem cells. *J. Extracell. Vesicles* 9, 1800971. doi:10.1080/20013078.2020.1800971

Hade, M. D., Suire, C. N., and Suo, Z. (2021). Mesenchymal stem cell-derived exosomes: applications in regenerative medicine. *Cells* 10, 1959. doi:10.3390/cells10081959

Han, G., Cho, H., Kim, H., Jang, Y., Jang, H., Kim, D. E., et al. (2022). Bovine colostrum derived-exosomes prevent dextran sulfate sodium-induced intestinal colitis via suppression of inflammation and oxidative stress. *Biomater. Sci.* 10, 2076–2087. doi:10.1039/d1bm01797g

Han, Y., Gong, T., Zhang, C., and Dissanayaka, W. L. (2020). HIF-1α stabilization enhances angio-/vasculogenic properties of SHED. *J. Dent. Res.* 99, 804–812. doi:10.1177/0022034520912190

Haraszti, R. A., Miller, R., Stoppato, M., Sere, Y. Y., Coles, A., Didiot, M. C., et al. (2018). Exosomes produced from 3D cultures of MSCs by tangential flow filtration show higher yield and improved activity. *Mol. Ther.* 26, 2838–2847. doi:10.1016/j.ymthe.2018.09.015

He, L., He, T., Xing, J., Zhou, Q., Fan, L., Liu, C., et al. (2020). Bone marrow mesenchymal stem cell-derived exosomes protect cartilage damage and relieve knee osteoarthritis pain in a rat model of osteoarthritis. *Stem Cell Res. Ther.* 11, 276. doi:10.1186/s13287-020-01781-w

Heris, R. M., Shirvaliloo, M., Abbaspour-Aghdam, S., Hazrati, A., Shariati, A., Youshanlouei, H. R., et al. (2022). The potential use of mesenchymal stem cells and their exosomes in Parkinson's disease treatment. *Stem Cell Res. Ther.* 13, 371. doi:10.1186/s13287-022-03050-4

Hofmann, L., Medyany, V., Ezić, J., Lotfi, R., Niesler, B., Röth, R., et al. (2022). Cargo and functional profile of saliva-derived exosomes reveal biomarkers specific for head and neck cancer. *Front. Med. (Lausanne)* 9, 904295. doi:10.3389/fmed.2022.904295

Hu, H., Hu, X., Li, L., Fang, Y., Yang, Y., Gu, J., et al. (2022a). Exosomes derived from bone marrow mesenchymal stem cells promote angiogenesis in ischemic stroke mice via upregulation of MiR-21-5p. *Biomolecules* 12, 883. doi:10.3390/biom12070883

Hu, H., Wang, D., Li, L., Yin, H., He, G., and Zhang, Y. (2021a). Role of microRNA-335 carried by bone marrow mesenchymal stem cells-derived extracellular vesicles in bone fracture recovery. *Cell Death Dis.* 12, 156. doi:10.1038/s41419-021-03430-3

Hu, L., Guan, Z., Tang, C., Li, G., and Wen, J. (2022b). Exosomes derived from microRNA-21 overexpressed adipose tissue-derived mesenchymal stem cells alleviate spine osteoporosis in ankylosing spondylitis mice. *J. Tissue Eng. Regen. Med.* 16, 634–642. doi:10.1002/term.3304

Hu, L., Xie, X., Xue, H., Wang, T., Panayi, A. C., Lin, Z., et al. (2022c). MiR-1224-5p modulates osteogenesis by coordinating osteoblast/osteoclast differentiation via the Rap1 signaling target ADCY2. *Exp. Mol. Med.* 54, 961–972. doi:10.1038/s12276-022-00799-9

Hu, M., Xing, L., Zhang, L., Liu, F., Wang, S., Xie, Y., et al. (2022d). NAP1L2 drives mesenchymal stem cell senescence and suppresses osteogenic differentiation. *Aging Cell* 21, e13551. doi:10.1111/acel.13551

Hu, Y., Li, X., Zhang, Q., Gu, Z., Luo, Y., Guo, J., et al. (2021b). Exosome-guided bone targeted delivery of Antagomir-188 as an anabolic therapy for bone loss. *Bioact. Mater* 6, 2905–2913. doi:10.1016/j.bioactmat.2021.02.014

Huang, C. C., Kang, M., Lu, Y., Shirazi, S., Diaz, J. I., Cooper, L. F., et al. (2020a). Functionally engineered extracellular vesicles improve bone regeneration. *Acta Biomater.* 109, 182–194. doi:10.1016/j.actbio.2020.04.017

Huang, J. P., Chang, C. C., Kuo, C. Y., Huang, K. J., Sokal, E. M., Chen, K. H., et al. (2022). Exosomal microRNAs miR-30d-5p and miR-126a-5p are associated with heart failure with preserved ejection fraction in STZ-induced type 1 diabetic rats. *Int. J. Mol. Sci.* 23, 7514. doi:10.3390/ijms23147514

Huang, S., Li, Y., Wu, P., Xiao, Y., Duan, N., Quan, J., et al. (2020b). microRNA-148a-3p in extracellular vesicles derived from bone marrow mesenchymal stem cells suppresses SMURF1 to prevent osteonecrosis of femoral head. *J. Cell Mol. Med.* 24, 11512–11523. doi:10.1111/jcmm.15766

Huang, Y., Xu, Y., Feng, S., He, P., Sheng, B., and Ni, J. (2021a). miR-19b enhances osteogenic differentiation of mesenchymal stem cells and promotes fracture healing through the WWP1/Smurf2-mediated KLF5/β-catenin signaling pathway. *Exp. Mol. Med.* 53, 973–985. doi:10.1038/s12276-021-00631-w

Huang, Y., Zhang, X., Zhan, J., Yan, Z., Chen, D., Xue, X., et al. (2021b). Bone marrow mesenchymal stem cell-derived exosomal miR-206 promotes osteoblast proliferation and differentiation in osteoarthritis by reducing Elf3. *J. Cell Mol. Med.* 25, 7734–7745. doi:10.1111/jcmm.16654

Ishihara, S., Inman, D. R., Li, W. J., Ponik, S. M., and Keely, P. J. (2017). Mechano-signal transduction in mesenchymal stem cells induces prosaposin secretion to drive the proliferation of breast cancer cells. *Cancer Res.* 77, 6179–6189. doi:10.1158/0008-5472.Can-17-0569

Jiang, Y., Li, J., Xue, X., Yin, Z., Xu, K., and Su, J. (2022). Engineered extracellular vesicles for bone therapy. *Nano Today* 44, 101487. doi:10.1016/j.nantod.2022.101487

Jiang, Y., Zhang, J., Li, Z., and Jia, G. (2020). Bone marrow mesenchymal stem cell-derived exosomal miR-25 regulates the ubiquitination and degradation of Runx2 by SMURF1 to promote fracture healing in mice. *Front. Med. (Lausanne)* 7, 577578. doi:10.3389/fmed.2020.577578

Jin, Z., Ren, J., and Qi, S. (2020). Exosomal miR-9-5p secreted by bone marrow-derived mesenchymal stem cells alleviates osteoarthritis by inhibiting syndecan-1. *Cell Tissue Res.* 381, 99–114. doi:10.1007/s00441-020-03193-x

Jing, X., Wang, S., Tang, H., Li, D., Zhou, F., Xin, L., et al. (2022). Dynamically bioresponsive DNA hydrogel incorporated with dual-functional stem cells from apical papilla-derived exosomes promotes diabetic bone regeneration. *ACS Appl. Mater Interfaces* 14, 16082–16099. doi:10.1021/acsami.2c02278

Kalluri, R., and LeBleu, V. S. (2020). The biology, function, and biomedical applications of exosomes. *Science* 367, eaau6977. doi:10.1126/science.aau6977

Kamerkar, S., LeBleu, V. S., Sugimoto, H., Yang, S., Ruivo, C. F., Melo, S. A., et al. (2017). Exosomes facilitate therapeutic targeting of oncogenic KRAS in pancreatic cancer. *Nature* 546, 498–503. doi:10.1038/nature22341

Kang, M., Huang, C. C., Gajendrareddy, P., Lu, Y., Shirazi, S., Ravindran, S., et al. (2022a). Extracellular vesicles from TNFα preconditioned MSCs: effects on immunomodulation and bone regeneration. *Front. Immunol.* 13, 878194. doi:10.3389/fimmu.2022.878194

Kang, Y., Xu, C., Meng, L., Dong, X., Qi, M., and Jiang, D. (2022b). Exosome-functionalized magnesium-organic framework-based scaffolds with osteogenic, angiogenic and anti-inflammatory properties for accelerated bone regeneration. *Bioact. Mater* 18, 26–41. doi:10.1016/j.bioactmat.2022.02.012

Kim, G. U., Sung, S. E., Kang, K. K., Choi, J. H., Lee, S., Sung, M., et al. (2021). Therapeutic potential of mesenchymal stem cells (MSCs) and MSC-derived extracellular vesicles for the treatment of spinal cord injury. *Int. J. Mol. Sci.* 22, 13672. doi:10.3390/ijms222413672

Kim, V. N., Han, J., and Siomi, M. C. (2009). Biogenesis of small RNAs in animals. *Nat. Rev. Mol. Cell Biol.* 10, 126–139. doi:10.1038/nrm2632

Koh, Y. Q., Almughlliq, F. B., Vaswani, K., Peiris, H. N., and Mitchell, M. D. (2018). Exosome enrichment by ultracentrifugation and size exclusion chromatography. *Front. Biosci. (Landmark Ed.* 23, 865–874. doi:10.2741/4621

Kong, J., Tian, H., Zhang, F., Zhang, Z., Li, J., Liu, X., et al. (2019). Extracellular vesicles of carcinoma-associated fibroblasts creates a pre-metastatic niche in the lung through activating fibroblasts. *Mol. Cancer* 18, 175. doi:10.1186/s12943-019-1101-4

Kuang, M. J., Huang, Y., Zhao, X. G., Zhang, R., Ma, J. X., Wang, D. C., et al. (2019). Exosomes derived from Wharton's jelly of human umbilical cord mesenchymal stem cells reduce osteocyte apoptosis in glucocorticoid-induced osteonecrosis of the femoral head in rats via the miR-21-PTEN-AKT signalling pathway. *Int. J. Biol. Sci.* 15, 1861–1871. doi:10.7150/ijbs.32262

Kuang, M. J., Zhang, K. H., Qiu, J., Wang, A. B., Che, W. W., Li, X. M., et al. (2021). Exosomal miR-365a-5p derived from HUC-MSCs regulates osteogenesis in GIONFH through the Hippo signaling pathway. *Mol. Ther. Nucleic Acids* 23, 565–576. doi:10.1016/j.omtn.2020.12.006

Lai, G., Zhao, R., Zhuang, W., Hou, Z., Yang, Z., He, P., et al. (2022). BMSC-derived exosomal miR-27a-3p and miR-196b-5p regulate bone remodeling in ovariectomized rats. *PeerJ* 10, e13744. doi:10.7717/peerj.13744

Lan, Y., Xie, H., Jin, Q., Zhao, X., Shi, Y., Zhou, Y., et al. (2022). Extracellular vesicles derived from neural EGFL-Like 1-modified mesenchymal stem cells improve acellular bone regeneration via the miR-25-5p-SMAD2 signaling axis. *Bioact. Mater* 17, 457–470. doi:10.1016/j.bioactmat.2022.01.019

Lee, K. S., Lee, J., Kim, H. K., Yeom, S. H., Woo, C. H., Jung, Y. J., et al. (2021). Extracellular vesicles from adipose tissue-derived stem cells alleviate osteoporosis through osteoprotegerin and miR-21-5p. *J. Extracell. Vesicles* 10, e12152. doi:10.1002/jev2.12152

Li, G., Liu, H., Zhang, X., Liu, X., Zhang, G., and Liu, Q. (2020a). The protective effects of microRNA-26a in steroid-induced osteonecrosis of the femoral head by repressing EZH2. *Cell Cycle* 19, 551–566. doi:10.1080/15384101.2020.1717043

Li, L., Zhou, X., Zhang, J. T., Liu, A. F., Zhang, C., Han, J. C., et al. (2021a). Exosomal miR-186 derived from BMSCs promote osteogenesis through hippo signaling pathway in postmenopausal osteoporosis. *J. Orthop. Surg. Res.* 16, 23. doi:10.1186/s13018-020-02160-0

Li, R., Li, D., Wang, H., Chen, K., Wang, S., Xu, J., et al. (2022a). Exosomes from adipose-derived stem cells regulate M1/M2 macrophage phenotypic polarization to promote bone healing via miR-451a/MIF. *Stem Cell Res. Ther.* 13, 149. doi:10.1186/s13287-022-02823-1

Li, X., Chen, R., Li, Y., Wang, P., Cui, Y., Yang, L., et al. (2021b). miR-27a-5p-Abundant small extracellular vesicles derived from epimedium-preconditioned bone mesenchymal stem cells stimulate osteogenesis by targeting Atg4B-mediated autophagy. *Front. Cell Dev. Biol.* 9, 642646. doi:10.3389/fcell.2021.642646

Li, X., Zheng, Y., Hou, L., Zhou, Z., Huang, Y., Zhang, Y., et al. (2020b). Exosomes derived from maxillary BMSCs enhanced the osteogenesis in iliac BMSCs. *Oral Dis.* 26, 131–144. doi:10.1111/odi.13202

Li, Y., Huang, P., Nasser, M. I., Wu, W., Yao, J., and Sun, Y. (2022b). Role of exosomes in bone and joint disease metabolism, diagnosis, and therapy. *Eur. J. Pharm. Sci.* 176, 106262. doi:10.1016/j.ejps.2022.106262

Li, Y., Wang, J., Ma, Y., Du, W., Feng, H., Feng, K., et al. (2020c). Retracted article: microRNA-15b shuttled by bone marrow mesenchymal stem cell-derived extracellular vesicles binds to WWP1 and promotes osteogenic differentiation. *Arthritis Res. Ther.* 22, 269. doi:10.1186/s13075-020-02316-7

Li, Y., Wang, J., Ma, Y., Du, W., Feng, K., and Wang, S. (2021c). miR-101-loaded exosomes secreted by bone marrow mesenchymal stem cells requires the FBXW7/HIF1α/FOXP3 axis, facilitating osteogenic differentiation. *J. Cell Physiol.* 236, 4258–4272. doi:10.1002/jcp.30027

Li, Y., Wu, J., Li, E., Xiao, Z., Lei, J., Zhou, F., et al. (2022c). TP53 mutation detected in circulating exosomal DNA is associated with prognosis of patients with hepatocellular carcinoma. *Cancer Biol. Ther.* 23, 439–445. doi:10.1080/15384047.2022.2094666

Li, Z., Li, Q., Tong, K., Zhu, J., Wang, H., Chen, B., et al. (2022d). BMSC-derived exosomes promote tendon-bone healing after anterior cruciate ligament reconstruction by regulating M1/M2 macrophage polarization in rats. *Stem Cell Res. Ther.* 13, 295. doi:10.1186/s13287-022-02975-0

Li, Z., Yang, B., Weng, X., Tse, G., Chan, M. T. V., and Wu, W. K. K. (2018). Emerging roles of MicroRNAs in osteonecrosis of the femoral head. *Cell Prolif.* 51, e12405. doi:10.1111/cpr.12405

Liang, Y., Duan, L., Lu, J., and Xia, J. (2021). Engineering exosomes for targeted drug delivery. *Theranostics* 11, 3183–3195. doi:10.7150/thno.52570

Liao, W., Ning, Y., Xu, H. J., Zou, W. Z., Hu, J., Liu, X. Z., et al. (2019). BMSC-derived exosomes carrying microRNA-122-5p promote proliferation of osteoblasts in osteonecrosis of the femoral head. *Clin. Sci. (Lond)* 133, 1955–1975. doi:10.1042/cs20181064

Liu, A., Lin, D., Zhao, H., Chen, L., Cai, B., Lin, K., et al. (2021a). Optimized BMSC-derived osteoinductive exosomes immobilized in hierarchical scaffold via lyophilization for bone repair through Bmpr2/Acvr2b competitive receptor-activated Smad pathway. *Biomaterials* 272, 120718. doi:10.1016/j.biomaterials.2021.120718

Liu, F., Hu, S., Yang, H., Li, Z., Huang, K., Su, T., et al. (2019a). Hyaluronic acid hydrogel integrated with mesenchymal stem cell-secretome to treat endometrial injury in a rat model of asherman's syndrome. *Adv. Healthc. Mater* 8, e1900411. doi:10.1002/adhm.201900411

Liu, H., Zhang, M., Shi, M., Zhang, T., Lu, W., Yang, S., et al. (2021b). Adipose-derived mesenchymal stromal cell-derived exosomes promote tendon healing by activating both SMAD1/5/9 and SMAD2/3. *Stem Cell Res. Ther.* 12, 338. doi:10.1186/s13287-021-02410-w

Liu, J., Yao, Y., Huang, J., Sun, H., Pu, Y., Tian, M., et al. (2022). Comprehensive analysis of lncRNA-miRNA-mRNA networks during osteogenic differentiation of bone marrow mesenchymal stem cells. *BMC Genomics* 23, 425. doi:10.1186/s12864-022-08646-x

Liu, L., Liu, Y., Feng, C., Chang, J., Fu, R., Wu, T., et al. (2019b). Lithium-containing biomaterials stimulate bone marrow stromal cell-derived exosomal miR-130a secretion to promote angiogenesis. *Biomaterials* 192, 523–536. doi:10.1016/j.biomaterials.2018.11.007

Liu, L., Yu, F., Li, L., Zhou, L., Zhou, T., Xu, Y., et al. (2021c). Bone marrow stromal cells stimulated by strontium-substituted calcium silicate ceramics: release of exosomal miR-146a regulates osteogenesis and angiogenesis. *Acta Biomater.* 119, 444–457. doi:10.1016/j.actbio.2020.10.038

Liu, W., Huang, J., Chen, F., Xie, D., Wang, L., Ye, C., et al. (2021d). MSC-derived small extracellular vesicles overexpressing miR-20a promoted the osteointegration of porous titanium alloy by enhancing osteogenesis via targeting BAMBI. *Stem Cell Res. Ther.* 12, 348. doi:10.1186/s13287-021-02303-y

Liu, W., Li, L., Rong, Y., Qian, D., Chen, J., Zhou, Z., et al. (2020a). Hypoxic mesenchymal stem cell-derived exosomes promote bone fracture healing by the transfer of miR-126. *Acta Biomater.* 103, 196–212. doi:10.1016/j.actbio.2019.12.020

Liu, W., Rong, Y., Wang, J., Zhou, Z., Ge, X., Ji, C., et al. (2020b). Exosome-shuttled miR-216a-5p from hypoxic preconditioned mesenchymal stem cells repair traumatic spinal cord injury by shifting microglial M1/M2 polarization. *J. Neuroinflammation* 17, 47. doi:10.1186/s12974-020-1726-7

Liu, W., Yu, M., Chen, F., Wang, L., Ye, C., Chen, Q., et al. (2021e). A novel delivery nanobiotechnology: engineered miR-181b exosomes improved osteointegration by regulating macrophage polarization. *J. Nanobiotechnology* 19, 269. doi:10.1186/s12951-021-01015-y

Liu, Y., Lin, L., Zou, R., Wen, C., Wang, Z., and Lin, F. (2018). MSC-derived exosomes promote proliferation and inhibit apoptosis of chondrocytes via lncRNA-KLF3-AS1/miR-206/GIT1 axis in osteoarthritis. *Cell Cycle* 17, 2411–2422. doi:10.1080/15384101.2018.1526603

Lou, G., Chen, L., Xia, C., Wang, W., Qi, J., Li, A., et al. (2020). MiR-199a-modified exosomes from adipose tissue-derived mesenchymal stem cells improve hepatocellular carcinoma chemosensitivity through mTOR pathway. *J. Exp. Clin. Cancer Res.* 39, 4. doi:10.1186/s13046-019-1512-5

Lu, G. D., Cheng, P., Liu, T., and Wang, Z. (2020). BMSC-derived exosomal miR-29a promotes angiogenesis and osteogenesis. *Front. Cell Dev. Biol.* 8, 608521. doi:10.3389/fcell.2020.608521

Luo, S., Xiao, S., Ai, Y., Wang, B., and Wang, Y. (2021). Changes in the hepatic differentiation potential of human mesenchymal stem cells aged *in vitro*. *Ann. Transl. Med.* 9, 1628. doi:10.21037/atm-21-4918

Luo, Z., Wu, F., Xue, E., Huang, L., Yan, P., Pan, X., et al. (2019). Hypoxia preconditioning promotes bone marrow mesenchymal stem cells survival by inducing HIF-1α in injured neuronal cells derived exosomes culture system. *Cell Death Dis.* 10, 134. doi:10.1038/s41419-019-1410-y

Lv, L. L., Feng, Y., Wen, Y., Wu, W. J., Ni, H. F., Li, Z. L., et al. (2018). Exosomal CCL2 from tubular epithelial cells is critical for albumin-induced tubulointerstitial inflammation. *J. Am. Soc. Nephrol.* 29, 919–935. doi:10.1681/asn.2017050523

Ma, H., Li, M., Jia, Z., Chen, X., and Bu, N. (2022). MicroRNA-455-3p promotes osteoblast differentiation via targeting HDAC2. Inj. *S0020-* 1383, 3636–3641. doi:10.1016/j.injury.2022.08.047

Ma, Q., Liang, M., Wu, Y., Dou, C., Xu, J., Dong, S., et al. (2021). Small extracellular vesicles deliver osteolytic effectors and mediate cancer-induced osteolysis in bone metastatic niche. *J. Extracell. Vesicles* 10, e12068. doi:10.1002/jev2.12068

Ma, T., Chen, Y., Chen, Y., Meng, Q., Sun, J., Shao, L., et al. (2018). MicroRNA-132, delivered by mesenchymal stem cell-derived exosomes, promote angiogenesis in myocardial infarction. *Stem Cells Int.* 2018, 1–11. doi:10.1155/2018/3290372

Macías, M., Rebmann, V., Mateos, B., Varo, N., Perez-Gracia, J. L., Alegre, E., et al. (2019). Comparison of six commercial serum exosome isolation methods suitable for clinical laboratories. Effect in cytokine analysis. *Clin. Chem. Lab. Med.* 57, 1539–1545. doi:10.1515/cclm-2018-1297

Malekpour, K., Hazrati, A., Zahar, M., Markov, A., Zekiy, A. O., Navashenaq, J. G., et al. (2022). The potential use of mesenchymal stem cells and their derived exosomes for orthopedic diseases treatment. *Stem Cell Rev. Rep.* 18, 933–951. doi:10.1007/s12015-021-10185-z

Mao, J. Y., Chen, L., Cai, Z. W., Qian, S. T., Liu, Z. M., Zhao, B. F., et al. (2022). Advanced biomaterials for regulating polarization of macrophages in wound healing. *Adv. Funct. Mater.* 32, 2111003. doi:10.1002/adfm.202111003

Mashouri, L., Yousefi, H., Aref, A. R., Ahadi, A. M., Molaei, F., and Alahari, S. K. (2019). Exosomes: composition, biogenesis, and mechanisms in cancer metastasis and drug resistance. *Mol. Cancer* 18, 75. doi:10.1186/s12943-019-0991-5

Mi, B., Chen, L., Xiong, Y., Yan, C., Xue, H., Panayi, A. C., et al. (2020). Saliva exosomes-derived UBE2O mRNA promotes angiogenesis in cutaneous wounds by targeting SMAD6. *J. Nanobiotechnology* 18, 68. doi:10.1186/s12951-020-00624-3

Miura, M., Miura, Y., Padilla-Nash, H. M., Molinolo, A. A., Fu, B., Patel, V., et al. (2006). Accumulated chromosomal instability in murine bone marrow mesenchymal stem cells leads to malignant transformation. *Stem Cells* 24, 1095–1103. doi:10.1634/stemcells.2005-0403

Nakao, Y., Fukuda, T., Zhang, Q., Sanui, T., Shinjo, T., Kou, X., et al. (2021). Exosomes from TNF-α-treated human gingiva-derived MSCs enhance M2 macrophage polarization and inhibit periodontal bone loss. *Acta Biomater.* 122, 306–324. doi:10.1016/j.actbio.2020.12.046

Nan, K., Zhang, Y., Zhang, X., Li, D., Zhao, Y., Jing, Z., et al. (2021). Exosomes from miRNA-378-modified adipose-derived stem cells prevent glucocorticoid-induced osteonecrosis of the femoral head by enhancing angiogenesis and osteogenesis via targeting miR-378 negatively regulated suppressor of fused (Sufu). *Stem Cell Res. Ther.* 12, 331. doi:10.1186/s13287-021-02390-x

Nojima, H., Freeman, C. M., Schuster, R. M., Japtok, L., Kleuser, B., Edwards, M. J., et al. (2016). Hepatocyte exosomes mediate liver repair and regeneration via sphingosine-1-phosphate. *J. Hepatol.* 64, 60–68. doi:10.1016/j.jhep.2015.07.030

Peng, Z., Lu, S., Lou, Z., Li, Z., Li, S., Yang, K., et al. (2021). Exosomes from bone marrow mesenchymal stem cells promoted osteogenic differentiation by delivering

miR-196a that targeted Dickkopf-1 to activate Wnt/β-catenin pathway. *Bioengineered* 1, 1996015. doi:10.1080/21655979.2021.1996015

Pizzicannella, J., Diomede, F., Gugliandolo, A., Chiricosta, L., Bramanti, P., Merciaro, I., et al. (2019). 3D printing PLA/gingival stem cells/EVs upregulate miR-2861 and -210 during osteoangiogenesis commitment. *Int. J. Mol. Sci.* 20, 3256. doi:10.3390/ijms20133256

Qian, C., Wang, Y., Ji, Y., Chen, D., Wang, C., Zhang, G., et al. (2022). Neural stem cell-derived exosomes transfer miR-124-3p into cells to inhibit glioma growth by targeting FLOT2. *Int. J. Oncol.* 61, 115. doi:10.3892/ijo.2022.5405

Qiu, M., Zhai, S., Fu, Q., and Liu, D. (2021). Bone marrow mesenchymal stem cells-derived exosomal MicroRNA-150-3p promotes osteoblast proliferation and differentiation in osteoporosis. *Hum. Gene Ther.* 32, 717–729. doi:10.1089/hum.2020.005

Ren, L. R., Yao, R. B., Wang, S. Y., Gong, X. D., Xu, J. T., and Yang, K. S. (2021). MiR-27a-3p promotes the osteogenic differentiation by activating CRY2/ERK1/2 axis. *Mol. Med.* 27, 43. doi:10.1186/s10020-021-00303-5

Riazifar, M., Mohammadi, M. R., Pone, E. J., Yeri, A., Lässer, C., Segaliny, A. I., et al. (2019). Stem cell-derived exosomes as nanotherapeutics for autoimmune and neurodegenerative disorders. *ACS Nano* 13, 6670–6688. doi:10.1021/acsnano.9b01004

Shen, K., Duan, A., Cheng, J., Yuan, T., Zhou, J., Song, H., et al. (2022). Exosomes derived from hypoxia preconditioned mesenchymal stem cells laden in a silk hydrogel promote cartilage regeneration via the miR-205-5p/PTEN/AKT pathway. *Acta Biomater.* 143, 173–188. doi:10.1016/j.actbio.2022.02.026

Shojaati, G., Khandaker, I., Funderburgh, M. L., Mann, M. M., Basu, R., Stolz, D. B., et al. (2019). Mesenchymal stem cells reduce corneal fibrosis and inflammation via extracellular vesicle-mediated delivery of miRNA. *Stem Cells Transl. Med.* 8, 1192–1201. doi:10.1002/sctm.18-0297

Stam, J., Bartel, S., Bischoff, R., and Wolters, J. C. (2021). Isolation of extracellular vesicles with combined enrichment methods. *J. Chromatogr. B Anal. Technol. Biomed. Life Sci.* 1169, 122604. doi:10.1016/j.jchromb.2021.122604

Su, Y., Song, X., Teng, J., Zhou, X., Dong, Z., Li, P., et al. (2021). Mesenchymal stem cells-derived extracellular vesicles carrying microRNA-17 inhibits macrophage apoptosis in lipopolysaccharide-induced sepsis. *Int. Immunopharmacol.* 95, 107408. doi:10.1016/j.intimp.2021.107408

Tkach, M., and Théry, C. (2016). Communication by extracellular vesicles: where we are and where we need to go. *Cell* 164, 1226–1232. doi:10.1016/j.cell.2016.01.043

Tsai, H. I., Wu, Y., Liu, X., Xu, Z., Liu, L., Wang, C., et al. (2022). Engineered small extracellular vesicles as a FGL1/PD-L1 dual-targeting delivery system for alleviating immune rejection. *Adv. Sci. (Weinh)* 9, e2102634. doi:10.1002/advs.202102634

Tsiapalis, D., and Zeugolis, D. I. (2019). Hypoxia preconditioning of bone marrow mesenchymal stem cells before implantation in orthopaedics. *J. Am. Acad. Orthop. Surg.* 27, e1040–e1042. doi:10.5435/jaaos-d-19-00044

Turinetto, V., Vitale, E., and Giachino, C. (2016). Senescence in human mesenchymal stem cells: functional changes and implications in stem cell-based therapy. *Int. J. Mol. Sci.* 17, 1164. doi:10.3390/ijms17071164

Vinaiphat, A., and Sze, S. K. (2020). Advances in extracellular vesicles analysis. *Adv. Clin. Chem.* 97, 73–116. doi:10.1016/bs.acc.2019.12.003

Volarevic, V., Markovic, B. S., Gazdic, M., Volarevic, A., Jovicic, N., Arsenijevic, N., et al. (2018). Ethical and safety issues of stem cell-based therapy. *Int. J. Med. Sci.* 15, 36–45. doi:10.7150/ijms.21666

Wang, G., Yuan, J., Cai, X., Xu, Z., Wang, J., Ocansey, D. K. W., et al. (2020). HucMSC-exosomes carrying miR-326 inhibit neddylation to relieve inflammatory bowel disease in mice. *Clin. Transl. Med.* 10, e113. doi:10.1002/ctm2.113

Wang, J., Tang, W., Yang, M., Yin, Y., Li, H., Hu, F., et al. (2021a). Inflammatory tumor microenvironment responsive neutrophil exosomes-based drug delivery system for targeted glioma therapy. *Biomaterials* 273, 120784. doi:10.1016/j.biomaterials.2021.120784

Wang, N., Liu, X., Tang, Z., Wei, X., Dong, H., Liu, Y., et al. (2022a). Increased BMSC exosomal miR-140-3p alleviates bone degradation and promotes bone restoration by targeting Plxnb1 in diabetic rats. *J. Nanobiotechnology* 20, 97. doi:10.1186/s12951-022-01267-2

Wang, S. Z., Jia, J., and Chen, C. H. (2021b). lncRNA-KCNQ1OT1: A potential target in exosomes derived from adipose-derived stem cells for the treatment of osteoporosis. *Stem Cells Int.* 2021, 1–17. doi:10.1155/2021/7690006

Wang, X., Li, X., Li, J., Zhai, L., Liu, D., Abdurahman, A., et al. (2021c). Mechanical loading stimulates bone angiogenesis through enhancing type H vessel formation and downregulating exosomal miR-214-3p from bone marrow-derived mesenchymal stem cells. *Faseb J.* 35, e21150. doi:10.1096/fj.202001080RR

Wang, Y., Zhou, X., and Wang, D. (2022b). Mesenchymal stem cell-derived extracellular vesicles inhibit osteoporosis via MicroRNA-27a-induced inhibition of DKK2-mediated wnt/β-catenin pathway. *Inflammation* 45, 780–799. doi:10.1007/s10753-021-01583-z

Wang, Z., Yan, K., Ge, G., Zhang, D., Bai, J., Guo, X., et al. (2021d). Exosomes derived from miR-155-5p-overexpressing synovial mesenchymal stem cells prevent osteoarthritis via enhancing proliferation and migration, attenuating apoptosis, and modulating extracellular matrix secretion in chondrocytes. *Cell Biol. Toxicol.* 37, 85–96. doi:10.1007/s10565-020-09559-9

Wang, Z. X., Luo, Z. W., Li, F. X., Cao, J., Rao, S. S., Liu, Y. W., et al. (2022c). Aged bone matrix-derived extracellular vesicles as a messenger for calcification paradox. *Nat. Commun.* 13, 1453. doi:10.1038/s41467-022-29191-x

Wei, Y., Ma, H., Zhou, H., Yin, H., Yang, J., Song, Y., et al. (2021a). miR-424-5p shuttled by bone marrow stem cells-derived exosomes attenuates osteogenesis via regulating WIF1-mediated Wnt/β-catenin axis. *Aging (Albany NY)* 13, 17190–17201. doi:10.18632/aging.203169

Wei, Z., Chen, Z., Zhao, Y., Fan, F., Xiong, W., Song, S., et al. (2021b). Mononuclear phagocyte system blockade using extracellular vesicles modified with CD47 on membrane surface for myocardial infarction reperfusion injury treatment. *Biomaterials* 275, 121000. doi:10.1016/j.biomaterials.2021.121000

Wu, D., Chang, X., Tian, J., Kang, L., Wu, Y., Liu, J., et al. (2021a). Bone mesenchymal stem cells stimulation by magnetic nanoparticles and a static magnetic field: release of exosomal miR-1260a improves osteogenesis and angiogenesis. *J. Nanobiotechnology* 19, 209. doi:10.1186/s12951-021-00958-6

Wu, D., Qin, H., Wang, Z., Yu, M., Liu, Z., Peng, H., et al. (2021b). Bone mesenchymal stem cell-derived sEV-encapsulated thermosensitive hydrogels accelerate osteogenesis and angiogenesis by release of exosomal miR-21. *Front. Bioeng. Biotechnol.* 9, 829136. doi:10.3389/fbioe.2021.829136

Xia, Q., Wang, Q., Lin, F., and Wang, J. (2021). miR-125a-5p-abundant exosomes derived from mesenchymal stem cells suppress chondrocyte degeneration via targeting E2F2 in traumatic osteoarthritis. *Bioengineered* 12, 11225–11238. doi:10.1080/21655979.2021.1995580

Xu, H., and Xu, B. (2021). BMSC-derived exosomes ameliorate osteoarthritis by inhibiting pyroptosis of cartilage via delivering miR-326 targeting HDAC3 and STAT1//NF-κB p65 to chondrocytes. *Mediat. Inflamm.* 2021, 1–26. doi:10.1155/2021/9972805

Xu, H. J., Liao, W., Liu, X. Z., Hu, J., Zou, W. Z., Ning, Y., et al. (2019). Down-regulation of exosomal microRNA-224-3p derived from bone marrow-derived mesenchymal stem cells potentiates angiogenesis in traumatic osteonecrosis of the femoral head. *Faseb J.* 33, 8055–8068. doi:10.1096/fj.201801618RRR

Xu, K., Lu, C., Ren, X., Wang, J., Xu, P., and Zhang, Y. (2021). Overexpression ofHIF-1α enhances the protective effect of mitophagy on steroid-induced osteocytes apoptosis. *Environ. Toxicol.* 36, 2123–2137. doi:10.1002/tox.23327

Xu, R., Shen, X., Si, Y., Fu, Y., Zhu, W., Xiao, T., et al. (2018). MicroRNA-31a-5p from aging BMSCs links bone formation and resorption in the aged bone marrow microenvironment. *Aging Cell* 17, e12794. doi:10.1111/acel.12794

Xu, T., Luo, Y., Wang, J., Zhang, N., Gu, C., Li, L., et al. (2020). Exosomal miRNA-128-3p from mesenchymal stem cells of aged rats regulates osteogenesis and bone fracture healing by targeting Smad5. *J. Nanobiotechnology* 18, 47. doi:10.1186/s12951-020-00601-w

Yahao, G., and Xinjia, W. (2021). The role and mechanism of exosomes from umbilical cord mesenchymal stem cells in inducing osteogenesis and preventing osteoporosis. *Cell Transpl.* 30, 096368972110574. doi:10.1177/09636897211057465

Yan, C., Chen, J., Wang, C., Yuan, M., Kang, Y., Wu, Z., et al. (2022). Milk exosomes-mediated miR-31-5p delivery accelerates diabetic wound healing through promoting angiogenesis. *Drug Deliv.* 29, 214–228. doi:10.1080/10717544.2021.2023699

Yang, B. C., Kuang, M. J., Kang, J. Y., Zhao, J., Ma, J. X., and Ma, X. L. (2020a). Human umbilical cord mesenchymal stem cell-derived exosomes act via the miR-1263/Mob1/Hippo signaling pathway to prevent apoptosis in disuse osteoporosis. *Biochem. Biophys. Res. Commun.* 524, 883–889. doi:10.1016/j.bbrc.2020.02.001

Yang, J., Chen, Z., Pan, D., Li, H., and Shen, J. (2020b). <p>Umbilical cord-derived mesenchymal stem cell-derived exosomes combined pluronic F127 hydrogel promote chronic diabetic wound healing and complete skin regeneration</p>. *Int. J. Nanomedicine* 15, 5911–5926. doi:10.2147/ijn.S249129

Yang, J., Gao, J., Gao, F., Zhao, Y., Deng, B., Mu, X., et al. (2022). Extracellular vesicles-encapsulated microRNA-29b-3p from bone marrow-derived mesenchymal stem cells promotes fracture healing via modulation of the PTEN/PI3K/AKT axis. *Exp. Cell Res.* 412, 113026. doi:10.1016/j.yexcr.2022.113026

Yang, S., Guo, S., Tong, S., and Sun, X. (2020c). Exosomal miR-130a-3p regulates osteogenic differentiation of Human Adipose-Derived stem cells through mediating SIRT7/Wnt/β-catenin axis. *Cell Prolif.* 53, e12890. doi:10.1111/cpr.12890

Yang, W., Zhu, W., Yang, Y., Guo, M., Qian, H., Jiang, W., et al. (2021). Exosomal miR-100-5p inhibits osteogenesis of hBMSCs and angiogenesis of HUVECs by suppressing the BMPR2/Smad1/5/9 signalling pathway. *Stem Cell Res. Ther.* 12, 390. doi:10.1186/s13287-021-02438-y

Yang, X., Yang, J., Lei, P., and Wen, T. (2019). LncRNA MALAT1 shuttled by bone marrow-derived mesenchymal stem cells-secreted exosomes alleviates osteoporosis through mediating microRNA-34c/SATB2 axis. *Aging (Albany NY)* 11, 8777–8791. doi:10.18632/aging.102264

Yang, Y., Yujiao, W., Fang, W., Linhui, Y., Ziqi, G., Zhichen, W., et al. (2020d). The roles of miRNA, lncRNA and circRNA in the development of osteoporosis. *Biol. Res.* 53, 40. doi:10.1186/s40659-020-00309-z

You, M., Ai, Z., Zeng, J., Fu, Y., Zhang, L., and Wu, X. (2022). Bone mesenchymal stem cells (BMSCs)-derived exosomal microRNA-21-5p regulates Kruppel-like factor 3

(KLF3) to promote osteoblast proliferation *in vitro*. *Bioengineered* 13, 11933–11944. doi:10.1080/21655979.2022.2067286

Yu, H., Zhang, J., Liu, X., and Li, Y. (2021). microRNA-136-5p from bone marrow mesenchymal stem cell-derived exosomes facilitates fracture healing by targeting LRP4 to activate the Wnt/β-catenin pathway. *Bone Jt. Res.* 10, 744–758. doi:10.1302/2046-3758.1012.Bjr-2020-0275.R2

Zha, Y., Lin, T., Li, Y., Zhang, X., Wang, Z., Li, Z., et al. (2020). Exosome-mimetics as an engineered gene-activated matrix induces *in-situ* vascularized osteogenesis. *Biomaterials* 247, 119985. doi:10.1016/j.biomaterials.2020.119985

Zhai, M., Zhu, Y., Yang, M., and Mao, C. (2020). Human mesenchymal stem cell derived exosomes enhance cell-free bone regeneration by altering their miRNAs profiles. *Adv. Sci. (Weinh)* 7, 2001334. doi:10.1002/advs.202001334

Zhang, C., Huang, Y., Ouyang, F., Su, M., Li, W., Chen, J., et al. (2022a). Extracellular vesicles derived from mesenchymal stem cells alleviate neuroinflammation and mechanical allodynia in interstitial cystitis rats by inhibiting NLRP3 inflammasome activation. *J. Neuroinflammation* 19, 80. doi:10.1186/s12974-022-02445-7

Zhang, D., Lee, H., Zhu, Z., Minhas, J. K., and Jin, Y. (2017). Enrichment of selective miRNAs in exosomes and delivery of exosomal miRNAs *in vitro* and *in vivo*. *Am. J. Physiol. Lung Cell Mol. Physiol.* 312, L110–l121. doi:10.1152/ajplung.00423.2016

Zhang, L., Jiao, G., Ren, S., Zhang, X., Li, C., Wu, W., et al. (2020a). Exosomes from bone marrow mesenchymal stem cells enhance fracture healing through the promotion of osteogenesis and angiogenesis in a rat model of nonunion. *Stem Cell Res. Ther.* 11, 38. doi:10.1186/s13287-020-1562-9

Zhang, L., Ouyang, P., He, G., Wang, X., Song, D., Yang, Y., et al. (2021a). Exosomes from microRNA-126 overexpressing mesenchymal stem cells promote angiogenesis by targeting the PIK3R2-mediated PI3K/Akt signalling pathway. *J. Cell Mol. Med.* 25, 2148–2162. doi:10.1111/jcmm.16192

Zhang, S., and Jin, Z. (2022). Bone mesenchymal stem cell-derived extracellular vesicles containing long noncoding RNA NEAT1 relieve osteoarthritis. *Oxid. Med. Cell Longev.* 2022, 1–21. doi:10.1155/2022/5517648

Zhang, X., Wang, W., Wang, Y., Zhao, H., Han, X., Zhao, T., et al. (2020b). Extracellular vesicle-encapsulated miR-29b-3p released from bone marrow-derived mesenchymal stem cells underpins osteogenic differentiation. *Front. Cell Dev. Biol.* 8, 581545. doi:10.3389/fcell.2020.581545

Zhang, X., You, J. M., Dong, X. J., and Wu, Y. (2020c). Administration of mircoRNA-135b-reinforced exosomes derived from MSCs ameliorates glucocorticoid-induced osteonecrosis of femoral head (ONFH) in rats. *J. Cell Mol. Med.* 24, 13973–13983. doi:10.1111/jcmm.16006

Zhang, Y., Chen, J., Fu, H., Kuang, S., He, F., Zhang, M., et al. (2021b). Exosomes derived from 3D-cultured MSCs improve therapeutic effects in periodontitis and experimental colitis and restore the Th17 cell/Treg balance in inflamed periodontium. *Int. J. Oral Sci.* 13, 43. doi:10.1038/s41368-021-00150-4

Zhang, Y., Wang, X., Chen, J., Qian, D., Gao, P., Qin, T., et al. (2022b). Exosomes derived from platelet-rich plasma administration in site mediate cartilage protection in subtalar osteoarthritis. *J. Nanobiotechnology* 20, 56. doi:10.1186/s12951-022-01245-8

Zhang, Y., Xie, Y., Hao, Z., Zhou, P., Wang, P., Fang, S., et al. (2021c). Umbilical mesenchymal stem cell-derived exosome-encapsulated hydrogels accelerate bone repair by enhancing angiogenesis. *ACS Appl. Mater Interfaces* 13, 18472–18487. doi:10.1021/acsami.0c22671

Zhao, S., Mi, Y., Guan, B., Zheng, B., Wei, P., Gu, Y., et al. (2020). Tumor-derived exosomal miR-934 induces macrophage M2 polarization to promote liver metastasis of colorectal cancer. *J. Hematol. Oncol.* 13, 156. doi:10.1186/s13045-020-00991-2

Zheng, L. W., Lan, C. N., Kong, Y., Liu, L. H., Fan, Y. M., and Zhang, C. J. (2022a). Exosomal miR-150 derived from BMSCs inhibits TNF-α-mediated osteoblast apoptosis in osteonecrosis of the femoral head by GREM1/NF-κB signaling. *Regen. Med.* 17, 739–753. doi:10.2217/rme-2021-0169

Zheng, Q., Zhang, S., Guo, W. Z., and Li, X. K. (2021). The unique immunomodulatory properties of MSC-derived exosomes in organ transplantation. *Front. Immunol.* 12, 659621. doi:10.3389/fimmu.2021.659621

Zheng, T., Li, Y., Zhang, X., Xu, J., and Luo, M. (2022b). Exosomes derived from miR-212-5p overexpressed human synovial mesenchymal stem cells suppress chondrocyte degeneration and inflammation by targeting ELF3. *Front. Bioeng. Biotechnol.* 10, 816209. doi:10.3389/fbioe.2022.816209

Zhou, Y., Wen, L. L., Li, Y. F., Wu, K. M., Duan, R. R., Yao, Y. B., et al. (2022a). Exosomes derived from bone marrow mesenchymal stem cells protect the injured spinal cord by inhibiting pericyte pyroptosis. *Neural Regen. Res.* 17, 194–202. doi:10.4103/1673-5374.314323

Zhou, Y., Zhang, X. L., Lu, S. T., Zhang, N. Y., Zhang, H. J., Zhang, J., et al. (2022b). Human adipose-derived mesenchymal stem cells-derived exosomes encapsulated in pluronic F127 hydrogel promote wound healing and regeneration. *Stem Cell Res. Ther.* 13, 407. doi:10.1186/s13287-022-02980-3

Zhu, L., Shi, Y., Liu, L., Wang, H., Shen, P., and Yang, H. (2020). Mesenchymal stem cells-derived exosomes ameliorate nucleus pulposus cells apoptosis via delivering miR-142-3p: therapeutic potential for intervertebral disc degenerative diseases. *Cell Cycle* 19, 1727–1739. doi:10.1080/15384101.2020.1769301

Zhu, W., Zhang, F., Lu, J., Ma, C., Shen, L., Hu, D., et al. (2022). The analysis of Modified Qing' E Formula on the differential expression of exosomal miRNAs in the femoral head bone tissue of mice with steroid-induced ischemic necrosis of femoral head. *Front. Endocrinol. (Lausanne)* 13, 954778. doi:10.3389/fendo.2022.954778

Zhu, Y., Wang, Y., Zhao, B., Niu, X., Hu, B., Li, Q., et al. (2017). Comparison of exosomes secreted by induced pluripotent stem cell-derived mesenchymal stem cells and synovial membrane-derived mesenchymal stem cells for the treatment of osteoarthritis. *Stem Cell Res. Ther.* 8, 64. doi:10.1186/s13287-017-0510-9

Zhuang, Y., Cheng, M., Li, M., Cui, J., Huang, J., Zhang, C., et al. (2022). : Small extracellular vesicles derived from hypoxic mesenchymal stem cells promote vascularized bone regeneration through the miR-210-3p/EFNA3/PI3K pathway, *Acta biomaterialia*. Online ahead of print. doi:10.1016/j.actbio.2022.07.015

Zuo, R., Kong, L., Wang, M., Wang, W., Xu, J., Chai, Y., et al. (2019). Exosomes derived from human CD34(+) stem cells transfected with miR-26a prevent glucocorticoid-induced osteonecrosis of the femoral head by promoting angiogenesis and osteogenesis. *Stem Cell Res. Ther.* 10, 321. doi:10.1186/s13287-019-1426-3

10.3389/fbioe.2023.1249860

Glossary

MSCs	Mesenchymal stem cells
sEVs	Small extracellular vesicles
miRNAs	microRNAs
MSCs-sEVs	MSCs-derived small extracellular vesicles
BMSCs	Bone mesenchymal stem cells
ASCs	Adipose mesenchymal stem cells
huc-MSCs	Human umbilical cord mesenchymal stem cells
EVs	Extracellular vesicles
MVBs	Multivesicular bodies
ILVs	Intraluminal vesicles
TEM	Transmission electron microscopy
NTA	Nanoparticle tracking analysis
S1P	Sphingosine-1-phosphate synthesis
EZH2	Enhancer of zeste homolog 2
TRAIL	TNF-related apoptosis-inducing ligand
NLRP3	NOD-, LRR- and pyrin domain-containing 3
TLR4	Toll-like receptor 4
NF-κB	Nuclear factor-kappa B
CAFs	Carcinoma-associated fibroblasts
BBB	Blood-brain barrier
HUVECs	Human umbilical vein endothelial cells
DOX	Doxorubicin
DGCR8	DiGeorge syndrome critical region 8
3′UTR	3′ untranslated region
mRNAs	Messenger RNAs
OA	Osteoarthritis
OIM	Osteogenic induction medium
ALP	Alkaline phosphatase
OCN	Osteocalcin
OPN	Osteopontin
Runx2	Runt-related transcription factor 2
PI3K	Phosphoinositide 3-kinase
Akt	Protein kinase B
mTOR	Mammalian target of rapamycin
Bmpr2	Bone morphogenetic protein receptor type 2
Acvr2b	Activin receptor type-2B
HDAC2	Histone deacetylase 2
CRY2	Cryptochrome 2
ERK1/2	Extracellular signal-regulated kinase 1 and 2
HIF-1α	Hypoxia-inducible factor 1 alpha
EFNA3	Ephrin-A3
Hmox1	Heme oxygenase-1
Li	Lithium
Ti	Titanium
HDAC7	Histone deacetylase 7
COL4A2	Collagen type IV alpha 2 chain
NF2	Neurofibromin 2
Sr	Strontium
CD31	Platelet endothelial cell adhesion molecule-1
NOTCH1	Neurogenic locus notch homolog protein 1
DLL4	Delta-like ligand 4
SPRY2	Sprouty RTK signaling antagonist 2
IRF1	Interferon regulatory factor 1
BV/TV	Ratio of bone volume to total volume
MIF	Macrophage migration inhibitory factor
PRKCD	Protein kinase C delta
RANKL	Receptor activator of nuclear factor kappa-B ligand
DPSC-sEVs	Dental pulp stem cells derived sEVs
Nfat5	Nuclear factor of activated T-cells 5
IL	Interleukin
SCAP-sEVs	Apical papilla-derived sEVs
KLF3	Kruppel-like factor 3
VASH1	Vasohibin-1
Atg4B	Autophagy-related 4B cysteine peptidase
IGFBP3	Insulin-like growth factor binding protein 3
FBXW7	Fbox and WD repeat domain-containing 7
FOXP3	Forkhead box p3
KLF2	Kruppel-like factor 2
KDM5A	Lysine demethylase 5A
SOCS1	Suppressors of cytokine signaling 1
SAV1	Salvador family WW domain-containing protein 1
YAP	Yes-associated protein
NO	Nitric oxide
DKK2	Dickkopf WNT signaling pathway inhibitor 2
CXCL12	C-X-C motif chemokine ligand 12
Trap	Tartrate-resistant acid phosphatase
OP	Osteoporosis
SATB2	Special AT-rich sequence-binding protein 2
Mob1	Mps one binder kinase activator-like 1
ONFH	Osteonecrosis of the femoral head
SOX5	SRY-box transcription factor 5
EZH2	Enhancer of zeste homolog 2

RTK	Receptor tyrosine kinase
MAPK	Mitogen-activated protein kinase
LRP4	Low-density lipoprotein receptor-related protein 4
KLF5	Krüppel-like factor 5
hiPS	Human-induced pluripotent stem cell
VapB	VAMP-associated protein B
OA	Osteoarthritis
SMSCs	Synovial mesenchymal stem cells
CDH11	Cadherin-11
SDC1	Syndecan-1
HDAC3	Histone deacetylase 3
NEAT1	Nuclear enriched abundant transcript 1
Nrf2	Nuclear factor erythroid 2-related factor 2
3D	Three-dimensional
2D	Two-dimensional
TFF	Tangential flow filtration
EMs	sEVs-mimetics
CXCR4	C-X-C motif chemokine receptor 4

frontiers | Frontiers in Bioengineering and Biotechnology

TYPE Review
PUBLISHED 07 September 2023
DOI 10.3389/fbioe.2023.1238181

OPEN ACCESS

EDITED BY
Nora Bloise,
University of Pavia, Italy

REVIEWED BY
Anjali P. Kusumbe,
University of Oxford, United Kingdom
Karthik Sivaraman,
Manipal Academy of Higher Education, India

*CORRESPONDENCE
Baohong Zhao,
bhzhao@cmu.edu.cn

RECEIVED 11 June 2023
ACCEPTED 29 August 2023
PUBLISHED 07 September 2023

CITATION
Gao J, Jiang L and Zhao B (2023), Median mandibular flexure—the unique physiological phenomenon of the mandible and its clinical significance in implant restoration.
Front. Bioeng. Biotechnol. 11:1238181.
doi: 10.3389/fbioe.2023.1238181

Median mandibular flexure—the unique physiological phenomenon of the mandible and its clinical significance in implant restoration

Jing Gao, Lulu Jiang and Baohong Zhao*

Center of Implantology School and Hospital of Stomatology, China Medical University, Liaoning Province Key Laboratory of Oral Diseases, Shenyang, China

Mandibular flexure, characterized by unique biomechanical behaviors such as elastic bending and torsion under functional loading, has emerged as a crucial factor in oral clinical diagnosis and treatment. This paper presents a comprehensive review of the current research status on mandibular flexure, drawing insights from relevant studies retrieved from the PubMed database (www.ncbi.nlm.nih.gov/pubmed), including research conclusions, literature reviews, case reports, and authoritative reference books. This paper thoroughly explores the physiological mechanisms underlying mandibular flexure, discussing different concurrent deformation types and the essential factors influencing this process. Moreover, it explores the profound implications of mandibular flexure on clinical aspects such as bone absorption around dental implants, the precision of prosthesis fabrication, and the selection and design of superstructure materials. Based on the empirical findings, this review provides crucial clinical recommendations. Specifically, it is recommended to exert precise control over the patients mouth opening during impression-taking. Those with a high elastic modulus or bone-tissue-like properties should be prioritized when selecting superstructure materials. Moreover, this review underscores the significance of customizing framework design to accommodate individual variations in facial morphology and occlusal habits. Future research endeavors in this field have the potential to advance clinical diagnosis and treatment approaches, providing opportunities for improvement.

KEYWORDS

median mandibular flexure, implant restoration, deformation, factors, clinical significance

Abbreviations: MF, mandibular flexure; MMF, median mandibular flexure; MOF, maximum occlusal force; MFUB, mandibular flexure upper border; ICP, intercuspal position; NiTi C.R., nickel-titanium Centric Relation.

1 Introduction

Weinmann and Sicher. (1955) demonstrated for the first time in 1955 that the cohesion of the traction condyle can cause the mandible to bend and deform due to the contraction of the lateral pterygoid muscle. In 1973, (Goodkind and Heringlake, 1973), designated this bending phenomenon as mandibular flexure (MF). In recent years, researchers interest in the physiological deformation of the mandible has gradually grown.

MF is a unique and complex physiological phenomenon of the mandible involving the interaction of numerous head and neck muscles (Sivaraman et al., 2016; Azpiazu-Flores et al., 2022). Generally, researchers (Regli and Kelly, 1967; Hylander, 1984) concur that the primary factor attributed to MF is the contraction of the pterygoid muscle; the platysma, mylohyoid, and superior constrictor also play a role in condyle convergence (Hylander, 1984). As the muscle attached to the mandible contracts, the tension it exerts on the mandible changes both the mandibles morphology and the teeth relative positioning. Hylanders experimental findings regarding the biological behavior of the mandible in adult rhesus monkeys reveal four jaw deformation types in MF (Hylander, 1984; Sivaraman et al., 2016) (As shown in Figure 1.).

1. Symphyseal bending associated with median convergence, or corporal approximation: this type of strain is associated with the contraction of the lateral pterygoid muscle during jaw opening movements.
2. Dorsoventral shear: this produces a shearing force in the sagittal plane and is a result of the vertical components of muscle forces from the lateral pterygoid muscles and their action forces at the condyles. The magnitude of the shear force depends on the points of application. The amount of shear force is equal on both sides of the mandible during symmetrical loading, while the amount of deformation differs between the working and balancing sides during unilateral loading.
3. Corporal rotation: this occurs during rotation of the body of the mandible, usually during the lower stroke of mastication. The resultant force causes narrowing of the dental arch.
4. Anteroposterior shear: this is induced by the contraction of the lateral components of the jaw-elevating muscles. It appears late in the power stroke, and the bending moment increases from the posterior to the anterior region."

Among the various mandibular deformations, the median mandibular flexure (MMF) is the most influential mandibular deformation mode on implant restoration. Most researchers have reached an initial consensus on the mechanism of mandibular deformation: the "U"-shaped or horseshoe-shaped mandible functions as a curvilinear beam that supports bilateral and unilateral loads. The lateral pterygoid muscles contract to initiate mandibular movement. In conjunction with the

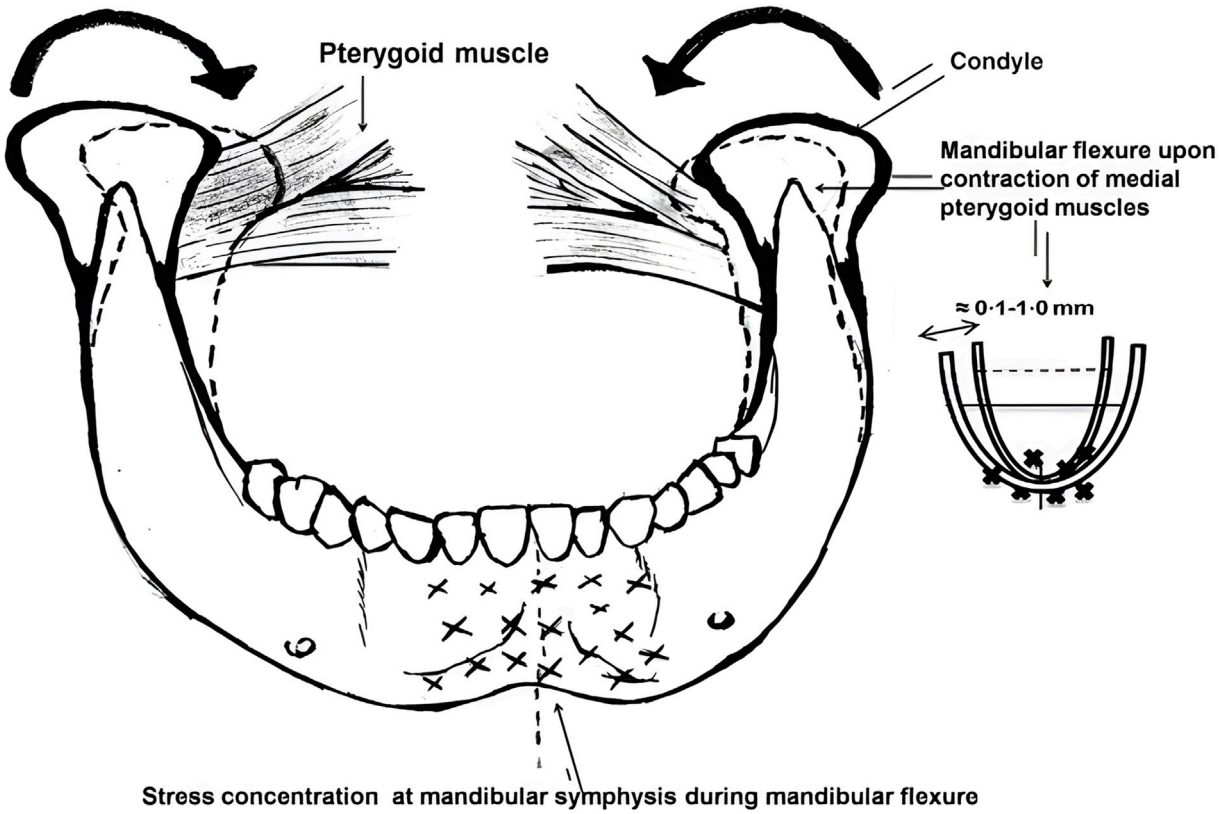

FIGURE 1
Medial rotation of the mandible and decrease in arch width during mandibular flexure caused by contraction of lateral pterygoid muscle (Sivaraman et al., 2016).

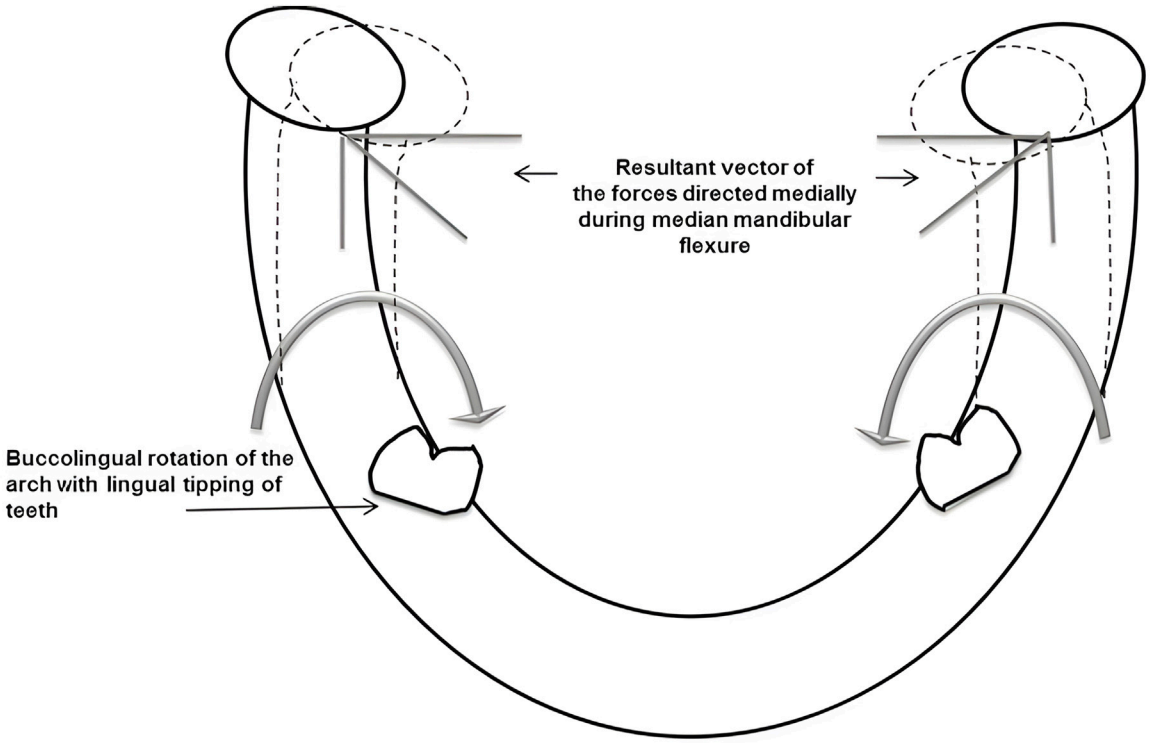

FIGURE 2
Bucco-lingual tipping of the teeth in lower arch and stress concentration at mandibular symphysis area during mandibular flexure (Sivaraman et al., 2016).

sagittal movement of the posterior segment, the medial pull on the mandibular condyle facilitates mandibular flexion around the mandibular symphysis. As depicted in Figure 2, the tension exerted by these attached structures induces changes in the mandibular shape, resulting in a narrower arch and affecting the teeth relative positioning within the mandibular arch (Sivaraman et al., 2016). Therefore, functional flexure of the mandible is worthy of significant biomechanical consideration. Torsional stresses may develop within the mandibular dental arch due to the rigid splinting of natural teeth or the integration of implants via fixed trans-arch bridges. Due to the adaptable nature of the periodontal ligament, these stresses can be compensated for in the case of natural teeth. Significantly, such stresses may also manifest in the superstructure of restorations, potentially leading to ceramic fractures and adhesive failures (Fischman, 1990).

Clinicians must be aware of mandibular deformation, and while there have been notable advances in MF-related research, this area remains relatively understudied, primarily due to technical and methodological limitations. Thus, the authors comprehensively reviewed the literature from 1955 to 2023, including review papers, clinical trials, biomechanical experiments, and case reports. This review aimed to thoroughly explore the mechanisms of MMF and its clinical significance and shed light on the preventative measures clinicians should consider. Moreover, this review endeavored to present novel research ideas and avenues for advancing our understanding of MMF.

2 MMF

2.1 Deformation caused by MMF

The jaw deforms in at least three directions due to non-masticatory physiological movements, with a deformation range of a few microns to 1 mm and an average value of approximately 0.073 mm (Shinkai et al., 2004; Covani et al., 2011). Furthermore, approximately 2% of patients can experience more than 4 mm elastic displacement of the mandibular condyles during mandibular movement (Linkow and Ghalili, 1999).

During jaw opening and protrusion, the bilateral pterygoid muscles can narrow the mandibular arch by contraction (Manzi et al., 2013). In their study using oral impressions with varying degrees of mandibular opening, Regli CP et al. found that deformation had a positive correlation with opening degree and extension distance (Regli and Kelly, 1967). In addition, Ioanid N demonstrated no change in the width of the mandible up to a mouth opening of 28%, after which the change in width was directly proportional to the mouth opening (Ioanid et al., 2017). Using intraoral scanning, Gülsoy M. demonstrated that MMF values increased linearly from the anterior to the posterior mandible in both dentulous and edentulous individuals (Gülsoy et al., 2022). The posterior portion of the mandibular foramen is more susceptible to elastic deformation, whereas the region between the bilateral mental foramen is relatively stable and less prone to deformation (English, 1993). These findings align with Carl E. Mischs observations, indicating that the cohesive mobility of the first molar can reach

TABLE 1 Deformation of the most distal implants in edentulous patients during mandibular movement (Sesma et al., 1996).

Mandibular movement	Deformation types		
	Condyles convergence (mm)	Corporal rotation (°)	Dorsoventral shear (mm)
Jaw opening movement	0.1–0.04	0.05–0.11	0.04–0.09
Mandibular protrusion movement	0.01–0.02	0.03–0.08	0.03–0.05
Mandibular lateral movement	0.02–0.05	0.03–0.15	0.05–0.1

0.8 mm, while that of the mandibular ascending ramus can reach 1.5 mm (Carl, 2005).

In addition to opening and protrusion, flexural movement occurs during lateral and retrusion movements. Hobkirk JA et al. measured relative motion and force transmission between dental osseointegrated implants in the edentulous mandibular premolar region using sensors connected to the implants. It was observed that forces during lateral deflections were significantly less than during open-mouth and closed-mouth movements (Hobkirk and Schwab, 1991), with an average of approximately 0.243–0.257 mm (ElSyad et al., 2019). Moreover, centric relation position (C.R.) is also associated with some amount of mandibular flexure. The study by Omar and Wise measured mandibular flexure in the horizontal plane, recorded using an "anterior jig", chin-point guidance and patient-exerted muscle forces. The study found that horizontal mandibular retraction forces in the centric relation recordings resulted in an increase in the width of the dental arch (Omar and Wise, 1981; Ioanid et al., 2017).

2.2 MMF concurrent deformation types

(Law et al., 2012) reported discovering three deformation patterns in the MMF: symphyseal bending, corporal rotation, and dorsoventral shear. (Abdel-Latif et al., 2000). adopted a displacement sensor to measure the displacement of the most distal implants in patients with the implant-supported fixed denture in the edentulous mandible during lateral, opening, and clenching movements. The distance between the most distal implants on the left and right sides was the variable of convergence between the condyles. Meanwhile, the relative rotation of the left and right mandibular bodies projected on the median sagittal plane was used as the dorsoventral shear, and the rotation of the most distal implant was taken as the corporals degree of rotation. They discovered that the cohesive deformation caused by MMF was 0.04 mm, the degree of body rotation was 60°, and the dorsal-ventral incision was 19°. In addition, (Sesma et al., 1996), placed a displacement sensor close to the implants midline to measure the mandible deformation caused by MMF. Table 1 demonstrates the results.

2.3 Factors influencing MMF

2.3.1 Gender

In forensic medicine, the accuracy of mandibular ramus flexure for gender judgment can range from 50% to 80% (Hazari et al., 2016). Remarkably, the Korean populations MF upper border (MFUB) has the highest accuracy in gender discrimination analysis. It has been used in forensic science and law to determine the gender of the Korean population (Lin et al., 2014). Experimentally, Johnson RB et al. observed gender differences in MF, with females generally exhibiting greater flexure than males. This disparity could be attributed to variations in bone density, hormonal influences, and masticatory musculature (Johnson et al., 2009). However, numerous researchers have stated that there is no significant correlation between gender and the deformation of MMF and that the influence of gender on MF may be negligible when compared to other factors, such as occlusal force magnitude, mandibular morphology, and dental occlusion (Wolf et al., 2019; Gülsoy et al., 2022). Also demonstrated that the difference is not statistically significant despite the MMF deformation degree observed in female subjects being greater than in male subjects (Gülsoy et al., 2022). Hence, the possible link between MF and gender remains a topic of ongoing research and discussion.

2.3.2 Age

Age plays a pivotal role in MF, as changes in mandibular bone composition and structure occur with age. Numerous studies have shown that aging is associated with many typical cell-intrinsic factors within the skeleton (Rebelo-Marques et al., 2018) and intrinsic changes in osteolymphatic endothelial cells leading to their lack of stress response to genotoxic agents in the aging skeleton (Biswas et al., 2023); age-dependent perturbation of the vascular niche can also affect skeletal and hematopoietic regeneration in aging animals (Chen et al., 2021). Due to decreased bone mineral density and changes in bone architecture, MF is frequently increased in the elderly (Hobkirk and Schwab, 1991). According to experimental studies, advanced age is associated with elevated levels of MF during functional movements, which impacts the stability and longevity of restorations and implants (Smith et al., 2005).

2.3.3 Bone density

Mandibular bone density is a critical factor influencing the extent of MF. Studies were conducted by (Hylander, 1984; White et al., 2016) to investigate the effect of bone density on MF during functional movements. A strain gauge was employed to measure the extent of MF during functional movement in both experiments involving a cohort of patients with varying bone density. The existence of an inverse correlation between bone density and MF was confirmed by the experiments. Individuals with greater bone density typically exhibit diminished flexure, as denser bones can better withstand mechanical stress during functional movements (Hylander, 1984).

2.3.4 Musculature strength

The ability of the mandible to flex under load is directly linked to the muscle forces exerted on it (Koolstra and van Eijden, 2005), and the direction and intensity of the muscle forces influence the pattern of MF during various functional activities (Lobbezoo et al., 2004). Strong masticatory muscles can generate greater chewing forces. As the muscles contract with greater force, the mandibles bending moment increases, leading to greater flexure (Rafferty et al., 2008). In addition, Green SE et al. examined the impact of muscle imbalances on MF. They found that weaker or unbalanced musculature could increase MF and potential complications in implant-supported prostheses (Green et al., 2020).

According to the positive correlation between masticatory muscle strength and occlusal force (van der Bilt et al., 2006; Ebadian et al., 2020) evaluated the relationship between mandibular occlusal force (MOF) and MMF in a cohort of adult participants, revealing that MOF and MMF are critical and effective factors in the success of prosthetic restorations. Nonetheless, (Canabarro Sde and Shinkai, 2006), employed a distinct methodology in their study, which collected bilateral MOF measurements using transarch force transducers positioned in the first molar region. The mandibular occlusal surface impressions were obtained at rest (R), maximal opening (O), and maximal inclination (P). The degree of MF was then computed using these impressions. This approach discovered no significant association between MMF and MOF in this group of dentate adults.

2.3.5 Symphyseal bone height

MF deformation is influenced by the height of the symphyseal bone, which represents the region where the two-halves of the mandible meet. (Chen et al., 2000) investigated the relationship between the symphyseal bone height and MF during functional movements. The study found a significant positive association between the symphyseal bone height and decreased MF. Individuals with a greater symphyseal bone height exhibited improved stability of the mandible during functional movements, leading to reduced flexure (Canabarro Sde et al., 2006).

2.3.6 Lower gonial angle

The lower gonial angle, formed between the mandibular ramus and the mandibular body, is another significant factor affecting MF. A smaller angle is associated with greater mandibular flexibility, contributing to higher MF levels (Shinkai et al., 2004). In contrast, a larger angle increases stability and decreases flexure during functional movements (Suresh, 2005).

2.3.7 Facial type

The population can be classified into three main facial types: short-faced, medium-faced, and long-faced. There is a significant correlation between the vertical facial pattern and the thickness of the masseter muscle, resulting in varying masticatory muscle strength among face types. Robust or thick masticatory muscles impose an increased mechanical load on the jaws, stimulating suture growth and bone alignment, ultimately leading to lateral jaw growth (Van Spronsen et al., 1992; Satiroğlu et al., 2005; Prasad et al., 2013) measured experimentally the variation in the distance between bilateral first molars at the maximum open and resting positions for three facial types in the South Indian population. The findings revealed a correlation between facial pattern variation and MMF values, with the short facial type displaying the highest MMF levels, followed by the medium and long facial types. Moreover, (Custodio et al., 2011), study involved measuring MMF values among three distinct facial types, concluding that vertical facial type affected MF. However, there are also contradictory studies. Shinkai RS et al. analyzed the correlation between the three facial types and MMF in a Brazilian population using impression-making and found no relationship between MMF and vertical facial morphology (Shinkai et al., 2007). In conclusion, the correlation between MMF and facial type is still debatable and requires further investigation.

3 The impact of MMF on implant restoration

MMF is one of the essential clinical factors affecting the design of dentures and their subsequent clinical effects. Its undesirable consequences include 1) the inability to passively position the prosthesis due to an imprecise impression; 2) screw or superstructure fracture; 3) bone loss surrounding the distal implants; and 4) fatigue and fracture of metal materials due to repeated compression (Mijiritsky et al., 2022). Therefore, a comprehensive understanding of the clinical significance of this biological phenomenon in implant restorations and the precise diagnostic and therapeutic protocols followed are essential for prolonging denture longevity and improving patient satisfaction.

3.1 Accuracy of making impressions

In order to create a clinical impression, a certain degree of opening is required. The traditional wide-opening impression technique will cause muscle contraction, resulting in the cohesion of the mandible and the reduction of the dental archs width, which ranges between 0.011 mm and 0.232 mm (Wolf et al., 2019). Furthermore, the teeth will be positioned more lingually than the intercuspal position (ICP). Additionally, the pressure placed on a patients jaw by dentists during an impression can cause changes to the mandibles width. If the mandibular impression is made at the opening stage, the restoration made on the corresponding working model can only achieve a proper fit at the opening stage. The mismatches will induce significant differences between the final restoration and the patients oral condition, preventing the passive fit of the final fixed and removable dentures. When the denture is worn to perform functions, the teeth and restorations are susceptible to undesirable stress, causing occlusal interference, pain and discomfort, bone resorption, gingivitis, and other complications.

Therefore, when making impressions, controlling the patients extent of opening is crucial. Using the closed-mouth technique to make an impression can minimize the contraction of the masticatory muscles and reduce mandibular deformation. When making an impression, (Gates and Nicholls, 1981), believed that applying a horizontal retraction force to the mandible could prevent width reduction. (Omar and Wise, 1981). suggested that any opening and protrusive movements exceeding 20 mm should be avoided when making impressions to minimize the amount of change in the width of the mandibular arch.

3.2 Recording centric relation

During patient-guided Centric Relation (C.R.) registration or functional procedures, MF may impact the restorations fit, leading to challenges in achieving proper occlusal contact (Sivaraman et al., 2016). The horizontal plane MF can cause a discrepancy between the cusp indentation in the jaw registration record and the cusp position on the dental cast (Kan et al., 1999). Due to the lingual movement of the mandibular teeth, the occlusal relationship may be inaccurately represented, and prostheses fabricated from such records may exhibit occlusal interference. The results of Omar and Wise's study showed greater mandibular flexure when centric relationships are recorded by patient-guided muscular movements (Omar and Wise, 1981). To minimize this discrepancy, it is advisable to utilize the "closed mouth" impression technique and the C.R. technique, as the dentist directs, for recording. Additionally, the closed-mouth occlusal double arch method, supported by (Tylman, 1989), can help in avoiding the MF effect associated with the open-mouth technique.

3.3 Implant supported overdenture

MF, which can impact the fit of removable implant-supported overdentures, should be considered during fabrication. For the fabrication of implant frameworks, computer-aided design/computer-aided manufacturing (CAD/CAM) is a superior option. However, it is also susceptible to MF (Kan et al., 1999; Torsello et al., 2008) due to its large camera head, which may necessitate a wide lower jaw opening for insertion. Future mitigation of the impact of MF on the CAD/CAM technique may be possible due to ongoing progress in this aspect (Sivaraman et al., 2016).

3.4 The segmented design of the fixed implant-supported superstructure

In the context of fixed prostheses, MF can pose particular challenges. The segmented design of the superstructure for implant-supported fixed dentures in edentulous patients is currently debated. (Martin-Fernandez et al., 2018). experiments revealed that a one-piece superstructure provides the optimal biomechanical environment for mandibular movement. In contrast, the two-piece and three-piece models exert greater stress on restoration components during protrusion and opening, respectively. Moreover, a study utilized three-dimensional finite element analysis to investigate the impact of MF on the segmental design of fixed frameworks for edentulous implants. According to the study, the greatest stress in one-piece framework restorations occurred around the distal implants on both sides, progressively decreasing toward more mesial positions. In two-piece framework restorations, the greatest stress was observed surrounding the lateral incisor location. The three-piece framework restorations exhibited greater stress than the one-piece and two-piece frameworks, where the maximum stress was observed around the canine location. Thus, patients with edentulous implant-supported fixed restorations may benefit from a non-segmented framework without a cantilever, as it provides an optimal biomechanical environment (Gao et al., 2022). These findings support the theory that an inflexible full-arch prosthesis can provide additional resistance, thereby offsetting the effects of MF, particularly in cases with a single unilateral posterior framework (Naini and Nokar, 2009; Zaugg et al., 2012).

However, more researchers prefer a segmented superstructure design for edentulous patients. Zarone F et al. suggested that the flexibility of the implant-restored mandible is affected by at least two factors: the position of the implants and the type of prosthetic superstructure. As a result of mandibular functional flexure in mandibular full-arch fixed prostheses supported by osseointegrated implants, a substantial amount of stress develops in the more distal implants and the superstructure at the symphysis (Zarone et al., 2003). In this way, the segmented framework can better adapt to the physiologic curvature characteristics of the mandible, guarantee accurate and passive implant placement, and increase the restorations service life (Suedam et al., 2009; Marin et al., 2015; Azpiazu-Flores et al., 2022). When using a cross-arch implant-supported fixed denture to restore edentulous jaws, failure to consider MMF can lead to mechanical and biological complications, resulting in pain and discomfort for the patient. With more implants connected by rigid splints and a longer dental arch, the risk of MMF negatively affecting implant or restoration prognosis increases. (Marin et al., 2015). demonstrated that dividing the superstructure into two parts at the symphyseal region only reduces stress caused by MMF, whereas dividing it into three parts is more effective in mitigating the effect of mandibular rotation and achieving superior clinical outcomes. Other clinical trials (Paez et al., 2003) demonstrated that separating the superstructure from the midline reduces patient pain and discomfort, further improving when the superstructure is divided into three parts. Furthermore, (Nokar and Baghai Naini, 2010), confirmed that stress on each restoration component and the jaw differs between two-segment and three-segment superstructures when occlusal forces are applied at different positions (two static bites of the incisal and right molar clenching). Table 2 summarizes the findings. Consequently, the authors propose that a two-piece superstructure provides a more favorable biomechanical environment for molar occlusion, whereas a three-piece superstructure is more suited for incisor occlusion.

The segmental design of the superstructure remains controversial in light of these findings. In addition, it is essential to tailor the restorations design to the patients occlusal habits, including group functional occlusion, canine protection, and balanced occlusion, to maximize the restorations longevity. Therefore, additional exhaustive and in-depth research is required to confirm the results.

3.5 Bone resorption

Studies have shown that MMF is a major factor in implant and superstructure loosening in implant-supported fixed dentures (Sivaraman et al., 2016). This phenomenon is caused primarily by the differences between natural teeth and dental implants (Azpiazu-Flores et al., 2022). Through the periodontal ligament, natural teeth have a close integration with the alveolar bone, which allows for the adjustment and buffering of bite forces and provides sensory feedback to protect the alveolar bone. During functional

TABLE 2 When the bite force is loaded at different positions (two static bites of incisal and right molar clenching), the maximum stress point and deformation of the two-piece and three-piece superstructure (Nokar and Baghai Naini, 2010).

Clenching	Superstructure design	Maximum stress values (MPa)	Deformation (mm)
Incisal clenching (INC)	Two- piece superstructure	Condylar region, masseter attachment, buccal cortical bone of the most mesial implant (29.1)	Mandibular angle (0.6) Symphyseal region (0.45)
	Three- piece superstructure	Buccal cortical bone of the most mesial implant (20.1)	Mandibular angle (0.55) Symphyseal region (0.3)
Right molar clenching (RMOL)	Two- piece superstructure	Mandibular ramus, condyle, the lingual aspect of cortical bone around the most distal implant on the right side (104.7)	Mandibular angle and lower edge of Symphyseal region (0.3)
	Three-piece superstructure	Lingual aspect of cortical bone around the most distal implant on the right side (62.5)	Mandibular angle (0.5) Symphyseal region (0.6)

movement, teeth exhibit a degree of physiological activity (approximately 28 μm vertically (Borg and Grondahl, 1996) and 56–75 μm horizontally (Wenzel and Gröndahl, 1995)). Dental implants, on the other hand, integrate directly with the alveolar bone via osseointegration (Varthis et al., 2019), resulting in limited mobility (with a maximum vertical and horizontal range of only 2–3 μm) (Borg and Grondahl, 1996). These differences decrease peri-implant tissue adaptability and tolerance compared to natural teeth.

Due to micromovements, MMF may cause microdamage at the crestal region and suboptimal osseointegration around implants. During mandibular movement, MMF flexes and twists with the median joint as the pivot; considerable stress is generated in the neck of the implant and the midline of the superstructure (Hobkirk and Havthoulas, 1998), leading to bone compression and subsequent loss (Zarone et al., 2003; Hobkirk and Schwab, 1991) discovered posterior implants in cantilever situations may experience stress-induced microdamage at the bone-implant interface due to MF. Lindquist et al., using stereoscopic intra-oral radiography, discovered pronounced crestal bone loss around anterior implants compared to posterior implants in the symphysis region. It was primarily due to the restricting effect of the splint at the primary point of flexure (Lindquist et al., 1988). Moreover, it has been observed that using fewer implants can result in localized force distribution patterns (Marin et al., 2015). To address this, researchers advocate increasing the number of implants in edentulous jaws, with feasible placement in the posterior regions based on anatomical and surgical considerations, to minimize cantilever situations and excessive spacing between implants (Gao et al., 2022). Fixed implants and flexible connectors are discouraged in the anterior region, and two or more independent restorations are preferred (Borg and Grondahl, 1996). It is recommended to use freestanding mandibular posterior osseointegrated implants with fixed restorations featuring shorter spans or stress relievers attached to the abutment to optimize the treatment outcome when implant size or bone quality is problematic.

3.6 Selection of superstructure materials

MMF plays a crucial role in selecting materials for implant denture superstructures. Implant-supported rigid splints can limit the extent of MF, and the degree of inhibition is proportional to the number of connected implants and the materials stiffness (Favot et al., 2014; Abadzhiev et al., 2017) reported that MMF contributes to chronic pain syndrome in edentulous patients with implant-supported fixed restorations. (Favot et al., 2014). conducted three-dimensional finite element analysis to compare mandibular deformations in edentulous patients with restored occlusion using four different materials (zirconia, titanium, gold, and nickel-titanium (NiTi)). The results indicated that mandibular deformation decreases with increasing material stiffness, with NiTi exhibiting the best adaptation to MF throughout all chewing stages, followed by gold, titanium, and zirconium oxide. Matching the elastic modulus of the superstructure material to that of bone tissue or employing a material with a high elastic modulus comparable to that of bone tissue is crucial for avoiding stress on the bone tissue around the distal implant and minimizing potential complications such as discomfort, pain, and bone resorption caused by excessive stress.

4 Conclusion

Clinicians must implement appropriate preventive measures and precise clinical techniques to minimize mandibular flexure during diagnosis and treatment of implant restorations. A careful regulation of the degree of a patients mouth opening during impression-taking and consideration of a superstructure material with a high elastic modulus comparable to the elastic modulus of bone tissue can contribute to the achievement of optimal restorations while preserving the health of periodontal tissue and bone tissue. However, there are ongoing discussions regarding the choice of segmental design for the superstructure of implant-supported fixed dentures in edentulous patients. Exploring adjustments to implant denture design based on different facial types and occlusal habits can yield valuable insights and references that can be used to optimize clinical diagnosis and treatment.

Author contributions

JG: conceptualization-lead, investigation-equal, writing—original, draft-lead LJ: data curation-equal, methodology-equal, writing—review and editing-equal,project administration-equal BZ: conceptualization-equal, data curation-equal, funding acquisition-equal, project

administration-equal, writing—review and editing-equal. All authors contributed to the article and approved the submitted version.

Funding

This study was funded by the National Natural Science Foundation of China [grant number 82071151], Natural Science Foundation of Liaoning Province, China [grant numbers 20170541059].

Acknowledgments

Throughout the writing of this dissertation I have received a great deal of support and assistance. I would first like to thank my supervisor, BZ and teacher, LJ, whose expertise was invaluable in formulating the research questions and methodology. Your insightful feedback pushed me to sharpen my thinking and brought my work to a higher level. The authors would like to thank National Natural Science Foundation for helpful funding on topics related to this work.

Conflict of interest

The authors declare that the research was conducted in the absence of any commercial or financial relationships that could be construed as a potential conflict of interest.

Publisher's note

References

Abadzhiev, M., Todorov, G., and Kamberov, K. (2017). Mandibular flexure – a REASON FOR CHRONIC PAIN SYNDROME IN EDENTULOUS PATIENT RESTORED WITH FIXED ZRO2 CONSTRUCTION OVER IMPLANTS, INSERTED IN NATURAL BONE AND BONE GRAFT AREA. Case report. *Annu. Proceeding Sci. Pap.* 23, 1432–1440. doi:10.5272/jimab.2017231.1432

Abdel-Latif, H. H., Hobkirk, J. A., and Kelleway, J. P. (2000). Functional mandibular deformation in edentulous subjects treated with dental implants. *Int. J. Prosthodont* 13, 513–519.

Azpiazu-Flores, F. X., Mata-Mata, S. J., and Lee, D. J. (2022). Detection of mandibular flexure with a dental plaster verification device: A clinical report with video recording. *J. Prosthet. Dent.* S0022-3913 (22), 105–106. doi:10.1016/j.prosdent.2022.01.039

Biswas, L., Chen, J., De Angelis, J., Singh, A., Owen-Woods, C., Ding, Z., et al. (2023). Lymphatic vessels in bone support regeneration after injury. *Cell* 186 (2), 382–397. doi:10.1016/j.cell.2022.12.031

Borg, E., and Grondahl, H. G. (1996). On the dynamic range of different x-ray photon detectors in intra-oral radiography. A comparison of image quality in film, charge-coupled device and storage phosphor systems. *Dentomaxillofac Radiol.* 25, 82–88. doi:10.1259/dmfr.25.2.9446978

Canabarro Sde, A., and Shinkai, R. S. (2006). Medial mandibular flexure and maximum occlusal force in dentate adults. *Int. J. Prosthodont* 19 (2), 177–182.

Carl, E. (2005). "Misch. The completely edentulous mandible: treatment plans for fixed restorations," in *Misch C.E. Dental implant prosthetics* (St. Louis: Elsevier Mosby), 602.

Chen, D. C., Lai, Y. L., Chi, L. Y., and Lee, S. Y. (2000). Contributing factors of mandibular deformation during mouth opening. *J. Dent.* 28, 583–588.

Chen, J., Sivan, U., Tan, S. L., Lippo, L., De Angelis, J., Labella, R., et al. (2021). High-resolution 3D imaging uncovers organ-specific vascular control of tissue aging. *Sci. Adv.* 7 (6), eabd7819. doi:10.1126/sciadv.abd7819

Covani, U., Ricci, M., Bozzolo, G., Mangano, F., Zini, A., and Barone, A. (2011). Analysis of the pattern of the alveolar ridge remodelling following single tooth extraction. *Clin. Oral Implants Res.* 22 (8), 820–825. doi:10.1111/j.1600-0501.2010.02060.x

Custodio, W., Gomes, S. G., Faot, F., Garcia, R. C., and Del Bel Cury, A. A. (2011). Occlusal force, electromyographic activity of masticatory muscles and mandibular flexure of subjects with different facial types. *J. Appl. Oral Sci.* 19 (4), 343–349. doi:10.1590/s1678-77572011005000008

Ebadian, B., Abolhasani, M., Heidarpour, A., Ziaei, M., and Jowkar, M. (2020). Assessment of the relationship between maximum occlusal force and median mandibular flexure in adults: A clinical trial study. *J. Indian Prosthodont Soc.* 20 (1), 76–82. doi:10.4103/jips.jips_282_19

ElSyad, M. A., Alameldeen, H. E., and Elsaih, E. A. (2019). Four-implant-supported fixed prosthesis and milled bar overdentures for rehabilitation of the edentulous mandible: A 1-year randomized controlled clinical and radiographic study. *Int. J. Oral Maxillofac. Implants* 34, 1493–1503. doi:10.11607/jomi.7667

English, C. E. (1993). Biomechanical concerns with fixed partial dentures involving implants. *Implant Dent.* 2, 221–241. doi:10.1097/00008505-199312000-00002

Favot, L. M., Berry-Kromer, V., Haboussi, M., Thiebaud, F., and Ben Zineb, T. (2014). Numerical study of the influence of material parameters on the mechanical behaviour of a rehabilitated edentulous mandible. *J. Dent.* 42 (3), 287–297. doi:10.1016/j.jdent.2013.11.027

Fischman, B. (1990). The rotational aspect of mandibular flexure. *J. Prosthet. Dent.* 64, 483–485. doi:10.1016/0022-3913(90)90049-i

Gao, J., Li, X., He, J., Jiang, L., and Zhao, B. (2022). The effect of mandibular flexure on the design of implant-supported fixed restorations of different facial types under two loading conditions by three-dimensional finite element analysis. *Front. Bioeng. Biotechnol.* 10, 928656. doi:10.3389/fbioe.2022.928656

Gates, G. N., and Nicholls, J. I. (1981). Evaluation of mandibular arch width change. *J. Prosthet. Dent.* 46, 385–392. doi:10.1016/0022-3913(81)90443-1

Goodkind, R. J., and Heringlake, C. B. (1973). Mandibular flexure in opening and closing movements. *J. Pros. Dent.* 30, 134–138. doi:10.1016/0022-3913(73)90046-2

Green, S. E., Johnson, A. B., Williams, E. F., and Davis, G. H. (2020). Impact of muscle imbalances on mandibular flexure. *J. Oral Rehabil.* 47 (9), 1081–1087.

Gülsoy, M., Tuna, S. H., and Pekkan, G. (2022). Evaluation of median mandibular flexure values in dentulous and edentulous subjects by using an intraoral digital scanner. *J. Adv. Prosthodont* 14 (1), 32–44. doi:10.4047/jap.2022.14.1.32

Hazari, P., Hazari, R. S., Mishra, S. K., Agrawal, S., and Yadav, M. (2016). Is there enough evidence so that mandible can be used as a tool for sex dimorphism? A systematic review. *J. Forensic Dent. Sci.* 8 (3), 174. doi:10.4103/0975-1475.195111

Hobkirk, J. A., and Havthoulas, T. K. (1998). The influence of mandibular deformation, implant numbers, and loading position on detected forces in abutments supporting fixed implant superstructures. *J. Prosthet. Dent.* 80, 169–174. doi:10.1016/s0022-3913(98)70106-4

Hobkirk, J. A., and Schwab, J. (1991). Mandibular deformation in subjects with osseointegrated implants. *Int. J. Oral Maxillofac. Implants* 6 (3), 319–328.

Hylander, W. L. (1984). Stress and strain in the mandibular symphysis of primates: A test of competing hypotheses. *Am. J. Phys. Anthropol.* 64, 1–46. doi:10.1002/ajpa.1330640102

Ioanid, N., Ţănculescu, O., Luca, O., MârţuStefanache, M. A., Doscas, A. R., Ciofu, M., et al. (2017). Study on mandibular medial flexure value (MMF) for natual tooth and dental implant support. *Ro J. Oral Rehabil.* 9, 99–108.

Johnson, R. B., White, J. S., and Andersson, E. M. (2009). Gender differences in mandibular flexure. *J. Prosthet. Dent.* 101 (5), 307–314.

Kan, J. Y., Rungcharassaeng, K., Bohsali, K., Goodacre, C. J., and Lang, B. R. (1999). Clinical methods for evaluating implant framework fit. *J. Prosthet. Dent.* 81 (1), 7–13. doi:10.1016/s0022-3913(99)70229-5

Koolstra, J. H., and van Eijden, T. M. (2005). Combined finite-element and rigid-body analysis of human jaw joint dynamics. *J. Dent. Res.* 84 (1), 2431–2439. doi:10.1016/j.jbiomech.2004.10.014

Law, C., Bennani, V., Lyons, K., and Swain, M. (2012). Mandibular flexure and its significance on implant fixed prostheses: A review. *J. Prosthodont* 21 (3), 219–224. doi:10.1111/j.1532-849X.2011.00798.x

Lin, C., Jiao, B., Liu, S., Guan, F., Chung, N. E., Han, S. H., et al. (2014). Sex determination from the mandibular ramus flexure of Koreans by discrimination function analysis using three-dimensional mandible models. *Forensic Sci. Int.* 236, 191.e1–6. doi:10.1016/j.forsciint.2013.12.015

Lindquist, L., Rockler, B., and Carlsson, G. (1988). Bone resorption around fixtures in edentulous patients treated with mandibular fixed tissue integrated prostheses. *J. Prosthet. Dent.* 59, 59–63. doi:10.1016/0022-3913(88)90109-6

Linkow, L. I., and Ghalili, R. (1999). Ramus hinges for excessive movements of the condyles: A new dimension in mandibular tripodal subperiosteal implants. *J. Oral Implantol.* 25, 11–17. doi:10.1563/1548-1336(1999)025<0011:RHFEMO>2.3.CO;2

Lobbezoo, F., Van der Glas, H. W., Van Kampen, F. M., Bosman, F., and van der Bilt, A. (2004). The effects of jaw clenching and jaw relaxation on the human masseter muscle. *Arch. Oral Biol.* 49 (4), 281–286.

Manzi, M. R., Manzano, R., and Pimentel, A. C. (2013). Medial mandibular flexure related to biomechanical failures of implant-supported fixed prosthesis with rigid connection distal to the mental foramen. *Dent. Press Implantol.* 7, 43–50.

Marin, D. O., Dias Kde, C., Paleari, A. G., Pero, A. C., Arioli Filho, J. N., and Compagnoni, M. A. (2015). Split-framework in mandibular implant-supported prosthesis. *Case Rep. Dent.* 2015, 1–5. doi:10.1155/2015/502394

Martin-Fernandez, E., Gonzalez-Gonzalez, I., deLlanos-Lanchares, H., Mauvezin-Quevedo, M. A., Brizuela-Velasco, A., and Alvarez-Arenal, A. (2018). Mandibular flexure and peri-implant bone stress distribution on an implant-supported fixed full-arch mandibular prosthesis: 3D finite element analysis. *Biomed. Res. Int.* 2018, 1–9. doi:10.1155/2018/8241313

Mijiritsky, E., Shacham, M., Meilik, Y., and Dekel-Steinkeller, M. (2022). Clinical influence of mandibular flexure on oral rehabilitation: narrative review. *Int. J. Environ. Res. Public Health* 19 (24), 16748. doi:10.3390/ijerph192416748

Naini, R. B., and Nokar, S. (2009). Three-dimensional finite element analysis of the effect of 1-piece superstructure on mandibular flexure. *Implant Dent.* 18 (5), 428–437. doi:10.1097/ID.0b013e3181ad8d87

Nokar, S., and Baghai Naini, R. (2010). The effect of superstructure design on stress distribution in peri-implant bone during mandibular flexure. *Int. J. Oral Maxillofac. Implants* 25 (1), 31–37.

Omar, R., and Wise, M. D. (1981). Mandibular flexure associated with muscle force applied in the retruded axis position. *J. Oral Rehabil.* 8, 209–221. doi:10.1111/j.1365-2842.1981.tb00495.x

Paez, C. Y., Barco, T., Roushdy, S., and Andres, C. (2003). Split-frame implant prosthesis designed to compensate for mandibular flexure: A clinical report. *J. Prosthet. Dent.* 89 (4), 341–343. doi:10.1067/mpr.2003.57

Prasad, M., Hussain, M. Z., Shetty, S. K., Kumar, T., Khaur, M., George, S., et al. (2013). Median mandibular flexure at different mouth opening and its relation to different facial types: A prospective clinical study. *J. Nat. Sci. Biol. Med.* 4, 426–430. doi:10.4103/0976-9668.117028

Rafferty, K. L., Liu, Z. J., Ye, W., and Major, P. W. (2008). Head posture and the morphology of the first cervical vertebra (Atlas). *Spine* 33 (1), 76–82.

Rebelo-Marques, A., De Sousa Lages, A., Andrade, R., Ribeiro, C. F., Mota-Pinto, A., Carrilho, F., et al. (2018). Aging hallmarks: the benefits of physical exercise. *Front. Endocrinol. (Lausanne).* 9, 258. doi:10.3389/fendo.2018.00258

Regli, C. P., and Kelly, E. K. (1967). The phenomenon of decreased mandibular arch width in opening movements. *J. Prosthet. Dent.* 17 (1), 49–53. doi:10.1016/0022-3913(67)90050-9

Satiroğlu, F., Arun, T., and Işik, F. (2005). Comparative data on facial morphology and muscle thickness using ultrasonography. *Eur. J. Orthod.* 27, 562–567. doi:10.1093/ejo/cji052

Sesma, N., Ribeiro, F. C., and Zanetti, A. L. (1996). Delexão mandibular e suas relações com próteses e implantes osseointegrados. *Rev. Assoc. Paul. Cir. Dent.* 50, 73–77.

Shinkai, R. S., Canabarro Sde, A., Schmidt, C. B., and Sartori, E. A. (2004). Reliability of a digital image method for measuring medial mandibular flexure in dentate subjects. *J. Appl. Oral Sci.* 12 (4), 358–362. doi:10.1590/s1678-77572004000400020

Shinkai, R. S., Lazzari, F. L., Canabarro, S. A., Gomes, M., Grossi, M. L., Hirakata, L. M., et al. (2007). Maximum occlusal force and medial mandibular flexure in relation to vertical facial pattern: A cross-sectional study. *Head. Face Med.* 3, 18. doi:10.1186/1746-160X-3-18

Sivaraman, K., Chopra, A., and Venkatesh, S. B. (2016). Clinical importance of median mandibular flexure in oral rehabilitation: A review. *J. Oral Rehabil.* 43, 215–225. doi:10.1111/joor.12361

Smith, J. M., Johnson, R. B., and Anderson, E. M. (2005). Age-related changes in mandibular flexure determined using implant strain gauge analysis. *J. Oral Rehabil.* 32 (2), 117–122.

Suedam, V., Souza, E. A., Moura, M. S., Jacques, L. B., and Rubo, J. H. (2009). Effect of abutment's height and framework alloy on the load distribution of mandibular cantilevered implant-supported prosthesis. *Clin. Oral Implants Res.* 20 (2), 196–200. doi:10.1111/j.1600-0501.2008.01609.x

Suresh, S. H. (2005). An analysis of mandibular flexure on mouth opening for dentate subjects: in vivo study. dissertation. Chennai: The Tamilnadu: Dr. M.G.R. Medical University.

Torsello, F., Di Torresanto, V. M., Ercoli, C., and Cordaro, L. (2008). Evaluation of the marginal precision of one-piece complete arch titanium frameworks fabricated using five different methods for implant-supported restorations. *Clin. Oral Implants Res.* 19, 772–779. doi:10.1111/j.1600-0501.2008.01555.x

Tylman, G. L. (1989). *Tylman's theory and practice of fixed prosthodontics*. St. Louis: Ishiyaku Euro America, 407–417.

van der Bilt, A., van Kampen, F. M., Cune, M. S., and Bosman, F. (2006). Relationship between maximal bite force and facial morphology in young adults. *J. Dent. Res.* 85 (3), 243–246.

Van Spronsen, P. H., Weijs, W. A., Prahl-Andersen, Valk J. B., and Van Ginkel, F. C. (1992). A comparison of jaw muscle cross-sections of long-face and normal adults. *J. Dent. Res.* 71, 1279–1285. doi:10.1177/00220345920710060301

Varthis, S., Tarnow, D. P., and Randi, A. (2019). Interproximal open contacts between implant restorations and adjacent teeth. prevalence-causes-possible solutions. *J. Prosthodont* 28, 806–810. doi:10.1111/jopr.12980

Weinmann, J. P., and Sicher, H. (1955). Bone and bones: fundamentals of bone biology. *Am. J. Med. Sci.* 42, 394–395. doi:10.1097/00007611-194708000-00022

Wenzel, A., and Gröndahl, H. G. (1995). Direct digital radiography in the dental office. *Int. Dent. J.* 45 (1), 27–34.

White, J. S., Johnson, A. B., Williams, E. F., and Davis, G. H. (2016). Relationship between bone density and mandibular flexure. *J. Dent. Res.* 95 (3), 345–350.

Wolf, L., Bergauer, B., Adler, W., Wichmann, M., and Matta, R. E. (2019). Three-dimensional evaluation of mandibular deformation during mouth opening. *Int. J. Comput. Dent.* 22 (1), 21–27.

Zarone, F., Apicella, A., Nicolais, L., Aversa, R., and Sorrentino, R. (2003). Mandibular flexure and stress build-up in mandibular full-arch fixed prostheses supported by osseointegrated implants. *Clin. Oral Implants Res.* 14 (1), 103–114. doi:10.1034/j.1600-0501.2003.140114.x

Zaugg, B., Hämmerle, C. H., Palla, S., and Gallo, L. M. (2012). Implant-supported mandibular splinting affects temporomandibular joint biomechanics. *Clin. Oral Implants Res.* 23, 897–901. doi:10.1111/j.1600-0501.2011.02241.x

frontiers | Frontiers in Bioengineering and Biotechnology

TYPE Original Research
PUBLISHED 12 October 2023
DOI 10.3389/fbioe.2023.1268176

OPEN ACCESS

EDITED BY
Livia Visai,
University of Pavia, Italy

REVIEWED BY
Girish Pattappa,
University Medical Center Regensburg, Germany
Andreas Martin Seitz,
Ulm University Medical Center, Germany

*CORRESPONDENCE
Britt Wildemann,
Britt.Wildemann@med.uni-jena.de

RECEIVED 27 July 2023
ACCEPTED 11 September 2023
PUBLISHED 12 October 2023

CITATION
Dabaghi M, Eras V, Kaltenhaeuser D, Ahmed N and Wildemann B (2023), Allografts for partial meniscus repair: an *in vitro* and *ex vivo* meniscus culture study.
Front. Bioeng. Biotechnol. 11:1268176.
doi: 10.3389/fbioe.2023.1268176

Allografts for partial meniscus repair: an *in vitro* and *ex vivo* meniscus culture study

Mohammad Dabaghi[1], Volker Eras[2], Daniel Kaltenhaeuser[2], Norus Ahmed[2] and Britt Wildemann[1]*

[1]Experimental Trauma Surgery, Department of Trauma, Hand and Reconstructive Surgery, Jena University Hospital, Friedrich Schiller University Jena, Jena, Germany, [2]German Institute for Cell and Tissue Replacement (DIZG, gemeinnützige GmbH), Berlin, Germany

The purpose of this study was to evaluate the treatment potential of a human-derived demineralized scaffold, Spongioflex® (SPX), in partial meniscal lesions by employing *in vitro* models. In the first step, the differentiation potential of human meniscal cells (MCs) was investigated. In the next step, the ability of SPX to accommodate and support the adherence and/or growth of MCs while maintaining their fibroblastic/chondrocytic properties was studied. Control scaffolds, including bovine collagen meniscus implant (CMI) and human meniscus allograft (M-Allo), were used for comparison purposes. In addition, the migration tendency of MCs from fresh donor meniscal tissue into SPX was investigated in an *ex vivo* model. The results showed that MCs cultured in osteogenic medium did not differentiate into osteogenic cells or form significant calcium phosphate deposits, although AP activity was relatively increased in these cells. Culturing cells on the scaffolds revealed increased viability on SPX compared to the other scaffold materials. Collagen I synthesis, assessed by ELISA, was similar in cells cultured in 2D and on SPX. MCs on micro-porous SPX (weight >0.5 g/cm^3) exhibited increased osteogenic differentiation indicated by upregulated expression of ALP and RUNX2, while also showing upregulated expression of the chondrogen-specific SOX9 and ACAN genes. Ingrowth of cells on SPX was observed after 28 days of cultivation. Overall, the results suggest that SPX could be a promising biocompatible scaffold for meniscal regeneration.

KEYWORDS

meniscus lesion, biocompatible scaffold, allograft, collagen meniscus implant, knee

1 Introduction

Human menisci are cartilaginous structures that provide cushioning to the knee joint by increasing the contact area of the tibiofemoral joint. The meniscus is composed of chondrocytes and fibroblasts that are embedded in an extracellular matrix composed of collagen, proteoglycans, glycoproteins and elastin (Chevrier et al., 2009; Makris et al., 2011). Meniscal lesions are a frequent occurrence in the workplace, during sports, and in daily activities. This may arise from the amalgamation of axial loading and rotational force, resulting in a shear load on the meniscus (Hede et al., 1990; Messner and Gao, 1998; Mather et al., 2015; Cao and Chen, 2022). The symptoms of meniscus lesions include pain, swelling, and difficulty moving the knee joint. In certain instances, the tear may result in the knee locking or catching when bent (Cao and Chen, 2022). A diagnosis is typically made through a physical exam and imaging, such as X-rays or MRI scans (Laible et al., 2013; Zhang, 2022).

Due to their poor vascularization particularly in their innermost regions, the menisci have a limited capacity for healing in the event of injury. In the past, a complete meniscectomy was performed as the standard of care. This would temporarily relieve symptoms, but in the long run, it would carry a higher risk of osteoarthritis (McDermott and Amis, 2006). Modern arthroscopic treatments typically focus on meniscal sutures or repairs, with a meniscectomy reserved for cases where such repairs are not possible. Some of the conventional treatment options for meniscus lesions include fixation devices, which are utilized to repair the meniscus tear and stabilize the joint (Brucker et al., 2010; Seo et al., 2020) and abrasion, which is a technique used to remove damaged tissue from the meniscus (Longo et al., 2012).

Over the past decades, regenerative medicine has come into focus to restore the specialized functions of the menisci. Several studies were conducted to develop and test materials for meniscus regeneration including hydrogels, polymer based fibers and scaffolds (Ronge et al., 2014; Vadodaria et al., 2019). The hydrogels can provide a supportive environment for the cells to regenerate (Romanazzo et al., 2018; Sasaki et al., 2018; Bansal et al., 2021), while the nanofibers can facilitate cell adhesion and proliferation (Hutmacher, 2001; Holloway et al., 2010; Holloway et al., 2014; Vadodaria et al., 2019). Additionally, the scaffolds provide a structure for the cells to attach to while allowing for the growth of new tissue (Whitehouse et al., 2017; Winkler et al., 2020; Angele et al., 2021; Hutchinson and Rodeo, 2022; Winkler et al., 2022). Each of these materials has the potential to improve the healing process and to restore the functionality of the meniscus. Only a few materials have been approved for human use. These include meniscal allografts (Cavendish et al., 2020) and cell-free biocompatible meniscus scaffolds (Scotti et al., 2013; Lombardo et al., 2021; Hutchinson and Rodeo, 2022).

Allograft transplantation is a procedure where healthy donor tissue is transplanted into the patient's knee joint. The utilization of allogeneic materials for the treatment of meniscal lesions has been practiced for a considerable period of time (Kean et al., 2017). These materials are believed to serve as a scaffold for tissue regeneration and repair. However, the long-term outcomes of this technique, particularly in terms of chondroprotection and osteoarthritis prevention, have not yet been demonstrated (Bilgen et al., 2018). The potential disadvantages of this method include concerns about the availability of tissue, the immunological response, disease transmission, and the size of the graft (Scotti et al., 2013).

The use of a cell-free biomaterial for the restoration and replacement of a portion of the meniscus is supported by the potential for cell repopulation within the scaffold. The potential migration of cells from the synovium and meniscal residues, and the subsequent tissue integration, can lead to a post-implantation cell-based outcome (Scotti et al., 2013; Lu et al., 2022; Taghiyar et al., 2023). Veronesi et al. summarized the preclinical and clinical studies on the use of scaffolds for the treatment of partial meniscus lesions (Veronesi et al., 2021). Based on this review, only two scaffolds are approved for human use. The synthetic Actifit® and the organic bovine collagen meniscus implant (CMI). As the initial regenerative technique, CMI was proposed as a treatment option for meniscal tissue regeneration in clinical practice (Stone et al., 1992; Zaffagnini et al., 2015). Initially, the clinical results of CMI implantation for partial meniscal regeneration were described as satisfactory (Buma et al., 2007). However, some studies have reported long-term shrinkage of the CMI, complete degradation, or the formation of scar tissue (Martinek et al., 2006; Scotti et al., 2013; Zaffagnini et al., 2015). A recent systematic review has revealed that the use of CMI as a singular effective treatment option for meniscal defects cannot be recommended for routine clinical application due to a lack of supporting evidence and a relatively high failure rate (Kohli et al., 2022).

The complexities and limitations of treating meniscal lesions, as well as the unsatisfactory outcomes of current procedures, necessitate the application of improved technologies and the use of biocompatible materials for innovative treatments. In this study, we investigated *in vitro* the suitability of a human-derived demineralized cancellous bone scaffold, called Spongioflex® (SPX) for the treatment of partial meniscal lesions. Due to the different porosities of the native cancellous bone, SPX can be produced with different porosities. The SPX with a lower porosity has a higher weight (>0.5 g/cm^3), while the SPX with higher porosity has a lower weight (<0.5 g/cm^3). Demineralization of cancellous bone leads to elastic and flexible tissue properties. These properties give SPX a sponge like behavior which allows it to act as a shock absorber in addition to the scaffold properties. A recent case study on a patient with bilateral medial meniscal lesions revealed that SPX block implants resulted in rapid implant integration with good radiographic and functional outcomes after a short term follow up of 6 and 12 months respectively (right and left meniscus) (Behrendt, 2023). In the present study, we first investigated the differentiation of fresh meniscal cells (MCs) isolated from human donors in different culture and differentiation media. Secondly, we aimed to determine whether SPX provides a biocompatible scaffold that is capable of accommodating MCs for their regeneration while still preserving their fibroblastic and chondrocytic characteristics. Moreover, the migration tendency of MCs from fresh donor meniscal tissue into SPX was investigated in an *ex vivo* model.

2 Materials and methods

2.1 Scaffolds

The commercially available human bone allograft tissues used in this study were provided by the German Institute for Cell and Tissue Replacement (DIZG, gemeinnützige GmbH, Berlin, Germany). All human tissues were acquired from nonprofit tissue recovery partners after informed consent. Grafts were sterilized using a validated, GMP-compliant process and were approved as medicinal products under §21 and §21a of the German Medicinal Products Act. For sterilization, tissues were fully submerged in a validated tissue-preserving sterilization solution (2% peracetic acid, 96% ethanol, water for injection; ratio v/v/v 2/1/1) and incubated with constant agitation at low pressure and room temperature for 4 h (Pruss et al., 2001). Subsequently, tissues were rinsed in a washing process using water for injection. Prior to sterilization, SPX was cut from cancellous bone and freed from bone marrow and lipids. The density was then measured in the mineralized state. A hydrochloric acid-based demineralization step renders SPX suitable for sterilization. Demineralization of cancellous bone leads to elastic and flexible tissue properties. These properties give SPX a sponge like behavior which allows it

to act as a shock absorber as well as a scaffold. Meniscal allograft tissue was prepared from human donor knees (Donors: 7 males, aged between 40 and 73 years). After opening the knee capsule, remnants of blood, fat, muscle and connective tissue were removed. Subsequently, the menisci were visually evaluated, and the intact menisci underwent sterilization. Commercially, SPX is available in a freeze-dried state and meniscal allografts are in a deep-frozen state. In this study, the meniscal allografts were thawed and SPX was rehydrated prior to use.

The bovine Collagen Meniscus Implant, CMI (Stryker, MI, United States), served as control scaffold.

The following scaffolds were used:

- SPX with macro pores: SPX (<0.5 g/cm^3)
- SPX with micro pores: SPX (>0.5 g/cm^3)
- Meniscus allograft: M-Allo
- Collagen Mencius Implant: CMI

2.2 Tissue harvest, cell isolation, and cell culture

Menisci (complete or parts) from 25 donors were harvested: 15 male and 10 female donors (22 patients with gonarthrosis and three patients with post-traumatic gonarthrosis) aged between 56 and 84 years. According to the Pauli classification (Pauli et al., 2011) the menisci used were grade 2–4, without calcium deposits. Approval was obtained from the ethics committee of Jena University Hospital (Umbrella Application: 2018_1158_1-Material, Addendum: 21.08.2020) and written informed consent was obtained from all patients. To isolate meniscal cells (MC), tissues were washed with phosphate-buffered Dulbecco's saline (DPBS, Sigma-Aldrich, Darmstadt, Germany) and sliced into tiny fragments measuring 1–2 mm^3 using a surgical scalpel. They were then treated with Pronase E (Merck, Darmstadt, Germany) for 30 min followed by Collagenase P (Sigma-Aldrich, Darmstadt, Germany) overnight, filtered through a cell strainer, centrifuged, and washed three times with DPBS. Cells were re-suspended in DMEM (PanBiotech, Aidenbach, Germany) supplemented with 10% v/v FBS (Capricorn Scientific, Ebsdorfergrund, Germany), 100 U/mL penicillin and 100 µg/mL streptomycin (Pen/Strep, Gibco, Thermo Fisher Scientific GmbH, Karlsruhe, Germany), counted, and cultured at 37°C in an incubator with 5% CO_2 for 1–2 weeks until the confluency reached more than 80%. Cells were then trypsinized, harvested, counted, and re-suspended in cryomedium (consisting of 10% DMSO, 20% FBS, and 1% Pen/Strep) for cryopreservation. Cells in passage three to four were used for the following experiments.

2.3 Cell differentiation

MCs (4×10^4 per well) were cultured in 24-well plates using four different culture media, namely, normal culture medium (DMEM supplemented with 10% FBS and 1% Pen/Strep), fibroblast medium/DMEM-AS (DMEM supplemented with 10% FBS, 1% Pen/Strep, and 0.17 mM L-Ascorbic acid (Sigma-Aldrich, Darmstadt, Germany), Chondrogenic culture medium (Chondrocyte Basal Medium with 10% FCS supplemented with 10% Chondrocyte growth medium SupplementMix (PromoCell, Heidelberg, Germany, and 1% Pen/Strep), and Osteogenic medium (DMEM supplemented with 0.5 mM L-Ascorbic acid, 10 mM β-Glycerophosphate disodium salt hydrate from Sigma-Aldrich, Darmstadt, Germany, 10 µM Calciumchlorid from Roth, Karlsruhe, Germany, 100 nM Dexamethasone from Sigma-Aldrich, Darmstadt, Germany). Media were changed at days 1, 4, 7, and 10. The viability of cells was measured using PrestoBlue® Cell Viability Reagent (Invitrogen, Life Technologies Corporation, CA, United States) following the manufacturer protocol at days 1, 7, and 14. The old medium was removed from the wells, and 500 µL per well of PrestoBlue® Cell Viability Reagent, diluted 1:10 with the same medium, was added. MCs were incubated for 2 h at 37°C. Measurements were performed in triplicates in a 96-well plate at 570 nm using a plate reader (Epoch, BioTek, CA, United States). The Alkaline Phosphatase (AP) activity of MCs at day 14 was assessed by measuring the absorbance of 4-Nitrophenol at a wavelength of 405 nm, which was released from MCs into the culture supernatants following the incubation with p-nitrophenylphosphate substrate for 30 min at 37°C. Calcium phosphate deposits were assessed by staining the fixed MCs with Alizarin Red S 0.5% (v/v diluted in distilled water) for 10 min at room temperature. Subsequently a solution of 1 g sodium dodecyl sulfate dissolved in 20 mL of 5 mM hydrochloric acid was added, and incubated for 10–20 min to solubilize the stain for quantitation. The absorbance of the solution was measured at 405 nm wavelength using a plate reader (Epoch, BioTek, CA, United States). Human osteosarcoma SAOS-2 cell line served as positive control for the AP-activity measurement and Alizarin Red staining. Cell viability and AP activity experiments were performed in triplicate and repeated with cells from 4 donors. The Alizarin Red staining was performed in duplicate and repeated with cells from 2 donors.

2.4 Flow cytometry

Fresh isolated MCs cultured at 37°C in a humidified 5% CO_2 environment were trypsinised when they reached 80% confluency. MCs (5×10^5) were incubated (30–45 min at room temperature in the dark) with mouse anti-human fluorochrome-conjugated antibodies (from Human Mesenchymal Stem Cell Multi-Color Flow Kit, R&D SYSTEMS, MN, United States) targeting surface markers, namely, CD105/Endoglin-PerCP, CD146/MCAM-CFS, and CD90/Thy1-APC. As a negative marker, a mouse anti-human antibody against CD45 was used. Mouse IgG1 and IgG2A served as isotype controls. Following the incubation, excess antibody was removed by washing the cells with 2 mL of Staining Buffer from the same kit mentioned above. The final cell pellet was resuspended in 200–400 µL of the staining buffer from the kit for flow cytometric analysis using the BD FACSAria™ Fusion (BD Bioscience, Belgium) with FSC/SSC gating and FlowJo v10.8.1 software.

2.5 MC on scaffold culture

For each replication, MCs from three different donors in their second to third passages were pooled in equal numbers. SPX (<0.5 g/cm^3 or >0.5 g/cm^3), Meniscus Allograft (M-Allo) and CMI underwent shaping into a cylindrical form by employing a surgical biopsy punch

TABLE 1 List of primer sequences for the target genes used for qRT-PCR.

Target genes forward and reverse primer sequences reported by TIB MOLBIOL
ACTB _ Forward 5'-AAGCCACCCCACTTCTCTC-3' Reverse 5'-GCTATCACC TCCCCTGTG-3'
GAPDH _ Forward 5'-GAAGGTGAAGGTCGGAGTC-3' Reverse 5'-TCGCTCCTG GAAGATGGTG-3'
ACAN _ Forward 5'-ACTCTGGGTTTTCGTGACTCT-3' Reverse 5'-ACACTC AGCGAGTTGTCATG-3'
RUNX2 _ Forward 5'-TGGTTACTGTCATGGCGGG-3' Reverse 5'-TCTCAGATC GTTGAACCTTGC-3'
ALP _ Forward 5'-ACCACCACGAGAGTGAACC-3' Reverse 5'-CGTTGTCTG AGTACCAGTCC-3'
COL1 _ Forward 5'-GGGCCAAGACGAAGACATC-3' Reverse 5'-CAGATCACG TCATCGCACAAC-3'
COL2 _ Forward 5'-TGGACGCCATGAAGGTTTTCT-3' Reverse 5'-TGGGAG CCAGATTGTCATC-3'
SOX9 _ Forward 5'-AGCGAACGCACATCAAGAC-3' Reverse 5'-CTGTAGGCG ATCTGTTGG-3'

with a 5 mm diameter. Samples were placed in a 48-well plate and pretreated overnight in DMEM culture medium supplemented with 10% FBS, 1% Pen/Strep. MCs (4×10^4 per well) suspended in 10 µL culture medium were gently added on top of the scaffolds and the wells were filled with DMEM culture medium supplemented with 10% FBS, 1% Pen/Strep up to 100 µL. The 48-well plate was incubated at 37°C for 1 h, after which 400 µL culture medium was added to each well. After 24 h, the scaffolds were carefully removed from the wells and transferred into a new one. This step was performed to exclude the cells that were not attached to the scaffolds. Cells with grafts were cultured for 7 days with a medium change every 2–3 days. Cells in 2D culture served as a control. Cell viability experiments were performed in triplicate and repeated with 3 pools of cells from 9 donors.

2.6 Scaffolds tight-fit in meniscus blocks, *ex vivo* model for partial meniscus repair

Fresh meniscal tissues (4 donors) were cut into wedge-shaped pieces of almost equal size and punched using a 5 mm diameter surgical biopsy punch. Four different scaffolds (SPX <0.05 g/cm^3, >0.05 g/cm^3, SPX, M-Allo, and CMI) were tight-fit added into the punched meniscus blocks and placed in 24-well plates filled with culture medium (DMEM supplemented with 10% FBS, 1% Pen/Strep). Meniscus cylinders taken from the biopsy punches of the fresh menisci were also cultured in the same medium as a control. The cultivation lasted for 7 or 28 days, with the medium being changed every 2–3 days. Cell viability experiments were performed in triplicate.

2.7 Enzyme-linked immunosorbent assay (ELISA)

The concentrations of human Pro-Collagen I α 2 (Pro-Col1) and human Pro-Collagen II α 1 (Pro-Col2) in supernatants from MCs cultured in different differentiation media (from day 14 post cultivation) and MCs cultured with scaffolds (from days 1 and 7 post cultivation) were measured using the Human Pro-Collagen I alpha 1 DuoSet ELISA kit, Human Pro-Collagen II DuoSet ELISA kit and DuoSet ELISA Ancillary Reagent Kit 2 (R&D SYSTEMS, MN, United States). The procedure of the assay was conducted according to the manufacturer's instructions.

2.8 RNA extraction, cDNA synthesis, and quantitative real-time polymerase chain reaction (qPCR)

RNA from monolayer-cultured MCs was extracted using the RNeasy Plus Mini Kit (Qiagen, Hilden, Germany). MCs cells cultured on scaffolds were extracted with a combination of the Trizol method (Invitrogen, Life Technologies Corporation, CA, United States) and chloroform extraction, followed by using RNeasy Plus Mini Kit. The concentration of the RNA was determined by measuring the absorbance of a diluted sample of the RNA at 260 and 280 nm using a NanoDrop™ 2000c (Thermo Fisher Scientific GmbH, Karlsruhe, Germany) after re-suspending it in RNase-free water. The RNA was placed in liquid nitrogen and stored at −80°C. Reverse transcription of 100 ng of RNA from each sample into cDNA was conducted with the qScript® cDNA SuperMix reverse transcription kit (from Quantabio, Beverly, MA, United States) using a polymerase chain reaction (PCR) method, as per the manufacturer's protocol.

The gene expression levels of Beta actin (*ACTB*), Glyceraldehyde 3-phosphate dehydrogenase (*GAPDH*), Aggrecan (*ACAN*), Runt-related transcription factor 2 (*RUNX2*), Alkaline phosphatase (*ALP*), Collagen Type I Alpha 2 (*COL1*), Collagen Type II Alpha 1 (*COL2*), SRY-Box Transcription Factor 9 (*SOX9*) were determined using the PerfeCTa SYBR Green SuperMix kit (Quantabio, Beverly, MA, United States) and human-specific primers from TIB MOLBIOL Syntheselabor GmbH, Berlin, Germany (Table 1). The qRT-PCR was performed on Rotor-Gene Q (Qiagen, Hilden, Germany) according to the manufacturer's instructions. Relative expression was calculated according to the $2^{-\Delta\Delta CT}$ method, and results were normalized to the arithmetic average of *ACTB* and *GAPDH* expression.

2.9 Histology

After 7 or 28 days of MC culture on scaffolds or within the meniscus, samples were fixed in 4% Paraformaldehyde for 24–48 h and were paraffin embedded. Samples were cut into 5 µm sections. The samples were then stained with DAPI (Thermo Fisher Scientific GmbH, Karlsruhe, Germany) and assessed under the microscope (Keyence BZ-810 Fluorescence Microscope). Experiments were replicated four times. For quantitative analysis, two slides per sample were used and all stained cells within the scaffolds were counted.

2.10 Statistical analyses

All data were presented as median with interquartile range (IQR) or mean ± standard error of the mean (SEM). Due to the

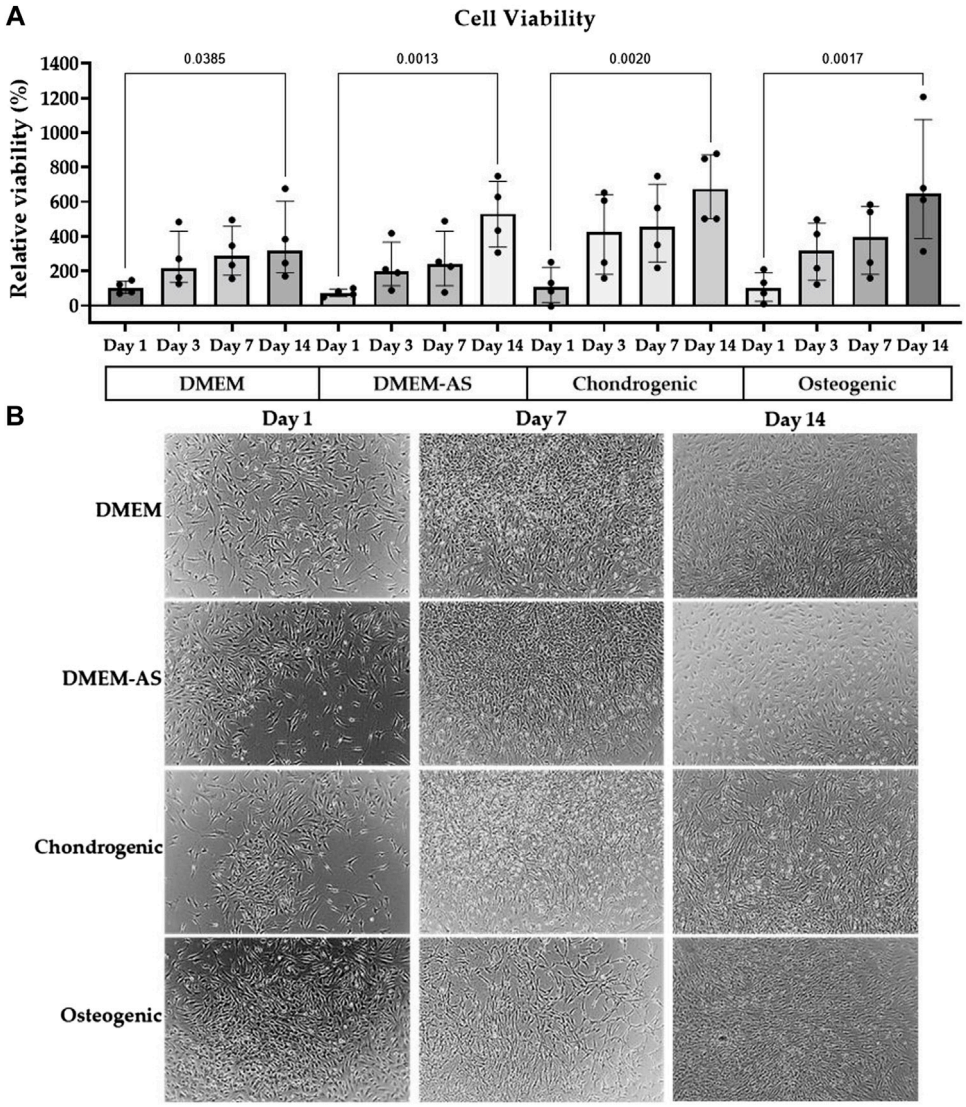

FIGURE 1
MCs viability and morphology in differentiation media. The viability of MCs increased over time when cultured in various media **(A)**, and their morphology stayed consistent **(B)**. The bar graph is based on the results of four experiments (n = 4) with the median (IQR) displayed in the bars.

small sample size and the non-parametric distribution of the data, statistical differences between samples were analyzed using nonparametric One-Way ANOVA test with GraphPad Prism software version 9.3.1 (San Diego, CA, United States). The effect size was calculated using Cohn´s d (Cohen, 1988) and for all statistically significant differences this was d > 0.8, meaning a large effect.

3 Results

3.1 Viability of MCs cultured in different culture media (differentiation media)

The viability assay, which was also used as an indirect measure of cell number, showed the viability/cell number of MCs, cultured in four different media (DMEM, DMEM-AS, chondrogenic and osteogenic) at four time points (day 1, 3, 7 and 14, Figure 1A). Viability values were normalized to the viability of MCs cultured in DMEM at day 1. The results showed that MCs grew at a similar rate. A significant increase in MCs viability was observed in all four media at day 14 compared to day 1 ($p \leq 0.0385$, see figure for exact p-values). Moreover, the morphology of MCs in differentiation media was visualized by light microscopy at different time intervals (Figure 1B). No morphological changes were observed over time.

3.2 Osteogenic differentiation

MCs cultured in osteogenic medium had a relatively higher alkaline phosphatase (AP) activity than the MCs cultured in other media at day 14 (Figure 2A). Alizarin Red staining showed that

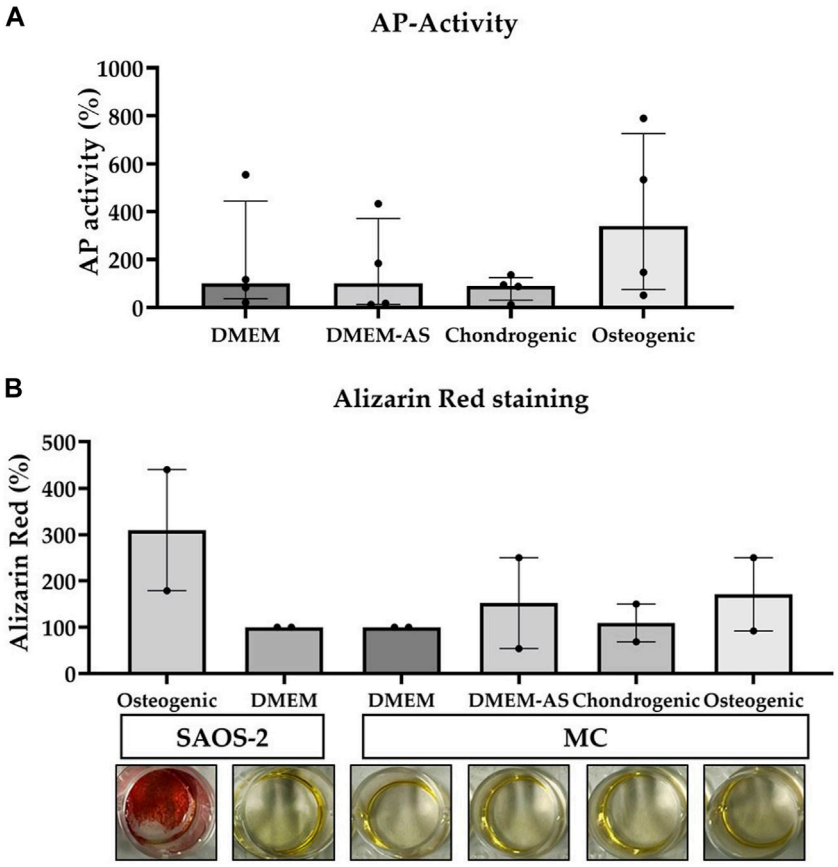

FIGURE 2
The AP-activity of MCs and their production of calcium phosphate deposits measured when cultured in various media. Osteogenic medium resulted in a relatively higher AP-activity of MCs compared to other media **(A)**. The calcium phosphate deposits produced by MCs cultured in the different media were less than those produced by SAOS-2 cells in osteogenic medium **(B)**. The data is based on four (n = 4) and two (n = 2) experiments respectively. The bars represent median (IQR). AP: alkaline phosphatase, MC: meniscal cell.

calcium phosphate deposition (evidence of osteogenic differentiation) of SAOS-2 cells cultured in osteogenic medium was higher than that of MCs cultured in DMEM, DMEM-AS, chondrogenic, and osteogenic media at day 14 (Figure 2B). In contrast, MCs exhibited no major difference in the amount of calcium phosphate deposits when cultured in different media.

3.3 Pro-Col1 and 2 production by MCs cultured in differentiation media and MCs surface markers

MCs cultured in osteogenic medium for 14 days produced significantly more Pro-Col1 than MCs cultured in DMEM and chondrogenic medium ($p \leq 0.0313$, exact p-values see Figure 3). Culturing MCs in DMEM-AS resulted in greater amounts of Pro-Col1 than MCs cultured in chondrogenic medium ($p = 0.045$). The levels of Pro-Col2 were below the detection limit in all samples as determined by ELISA. Flow cytometric analysis revealed that CD90 was expressed on the majority of cells (88.1%), whereas CD105 and CD146 were expressed on only 7.5% and 0.7% of cells, respectively (surface markers for mesenchymal stromal cells). CD 45 (marker for nucleated hematopoietic cells) was expressed on 0.4% of cells (n = 4).

3.4 Expression of osteogenic and chondrogenic genes in MCs cultured in differentiation media

The qPCR analysis of MCs cultured in differentiation media revealed no notable alterations in the expression of osteogenic and chondrogenic genes after 14 days of culture (Figure 4). It should be mentioned that not all genes were expressed in all samples and that the results showed a high variation. *COL2* expression was not detected.

3.5 Viability of MCs cultured on scaffolds and their Pro-Col1 and 2 production levels

The viability/cell number of MCs cultured in 2D, on SPX with micropores, SPX with macropores, M-Allo, and CMI at different time intervals (days 1, 4, and 7) indicated a time-dependent increase in the viability of MCs cultured in 2D and on both SPX porosities (Figure 5A). In contrast, cells cultured on M-Allo and CMI displayed reduced viability by day 7. On day 1, the viability/cell number of 2D cultured MCs was significantly higher than that of MCs cultured on M-Allo, and CMI scaffolds ($p = 0.0082$ and $p = 0.009$, respectively). Only 16% ± 2% (mean ± SEM) viability was detected when measuring

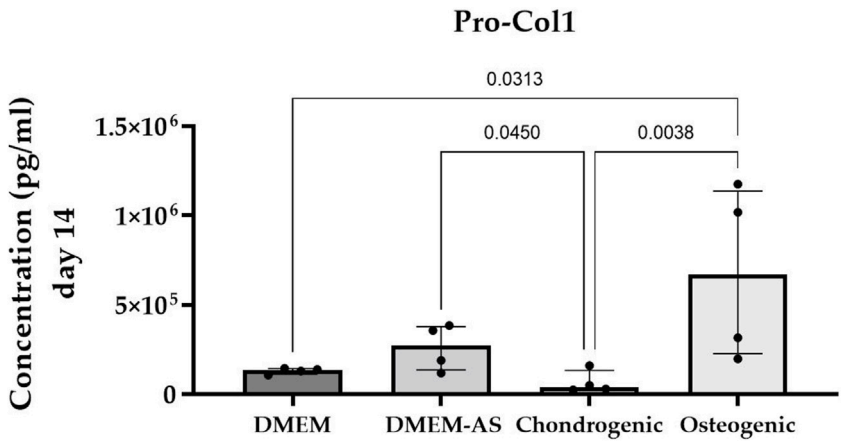

FIGURE 3
Cultivation of MCs in osteogenic medium resulted in higher production of Pro-Col1 compared with MCs cultured in other media. Bar graph showing the median (IQR) of results from four experiments (n = 4).

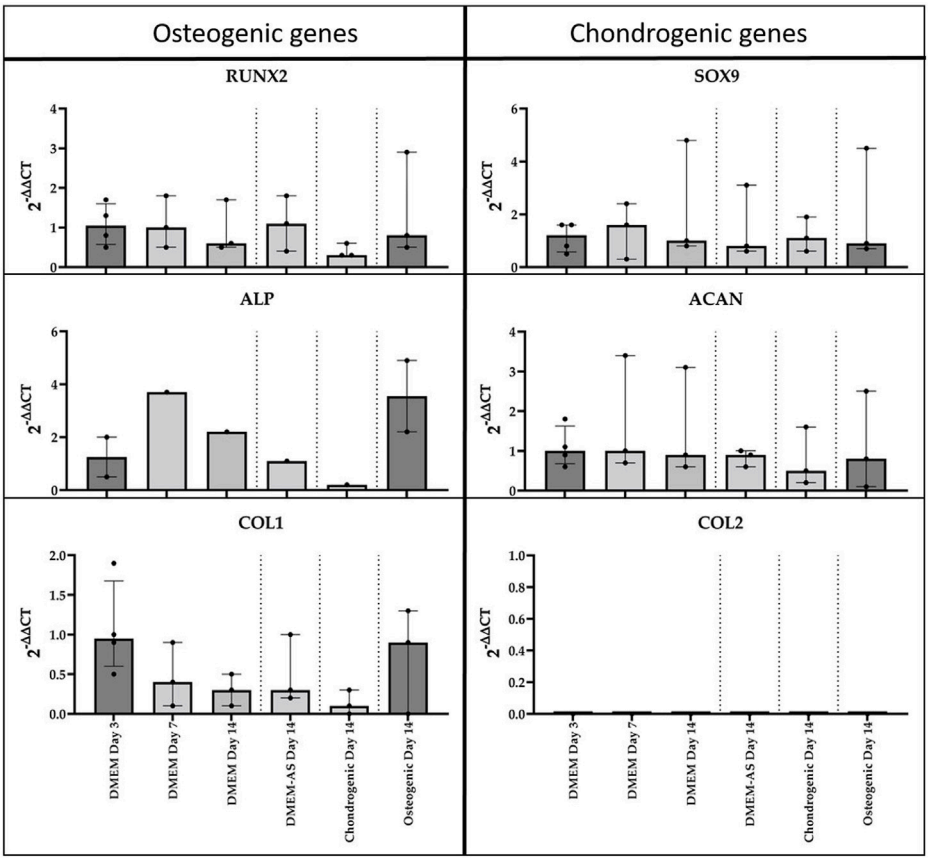

FIGURE 4
qPCR analysis of cDNA of RUNX2, ALP, COL1, SOX9, ACAN, and COL2 genes in monolayer MCs culture in various media (n = 3). Data all presented as median (IQR).

the viability of the cells in the "transferred" wells (the wells in which the scaffolds had been inserted into on day 0) of the scaffolds on day 1 (n = 3). Meaning, approximately 16% of cells were lost during the transfer of the scaffold between day 0 and day 1. Furthermore, the viability of 2D-cultured MCs was significantly higher than the viability of MCs cultured on CMI (day 7; p = 0.014). The Pro-Col1 concentration in the

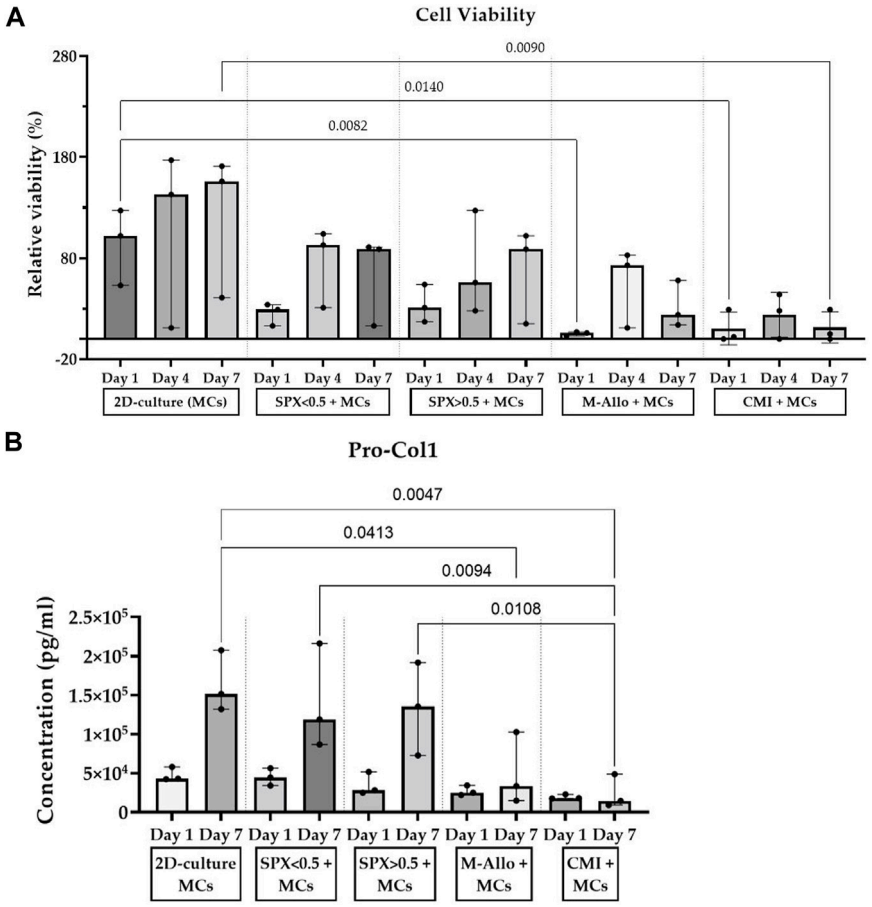

FIGURE 5
(A) Viability results show an increase in MCs cultured on SPX and in 2D culture for 7 days. **(B)** MCs cultured on SPX produced higher amounts of Pro-Col1 than MCs cultured on CMI. Viability values are normalized to the viability of 2D-culture MCs at day 1, n = 3, bars represent median (IQR). SPX: spongioflex®, M-Allo: meniscus allograft, CMI: collagen meniscus implant, Col1: collagen 1, MCs: meniscal cells.

supernatants of MCs cultured in 2D conditions and on SPX (both porosities) was higher at day 7 compared with day 1, although the differences were not statistically significant (Figure 5B). Moreover, Pro-Col1 levels in 2D cultured MCs were significantly higher than those of MCs cultured on M-Allo and CMI at day 7 (exact *p*-values see figure). In addition, the levels of Pro-Col1 in the supernatant of micro- and macro-pores SPX were also significantly higher than in the supernatant of MCs cultured on CMI. In all samples, the Pro-Col2 levels were below the detection limit.

3.6 Expression of osteogenic and chondrogenic genes in MCs cultured on scaffolds

The expression of osteogenic and chondrogenic related genes showed that MCs cultured on micro-pores SPX have the highest expression of analyzed genes (e.g., *RUNX2*, *ALP* and *SOX9* significantly higher compared to 2D culture, see Figure 6 for exact *p*-values). The expression level of *Col1* in MCs on SPX (both porosities) was significantly higher than in fresh meniscus. *SOX9* expression level was highest in fresh meniscus. Low expression values or no gene expression was observed when MCs were cultured on CMI. This is due to the low cell number and RNA values in these cultures. Further details on the gene expression and significant differences are shown in Figure 6.

3.7 Histological DAPI staining of MCs cultured on scaffolds

DAPI staining of paraffin-embedded sections of various scaffolds cultured with MCs showed the presence of MCs in SPX (both porosities) (Figure 7). No cells were seen in CMI with MCs after 7 days of cultivation. It was not possible to distinguish whether MCs grew on M-Allo because the DAPI staining was seen in M-Allo without culture with MCs.

3.8 Viability of meniscal tissues cultured with scaffolds (*ex vivo* meniscus model)

The viability of fresh human meniscal tissue blocks (cultured with micro-pores SPX, macro-pores SPX, M-Allo, and CMI) was

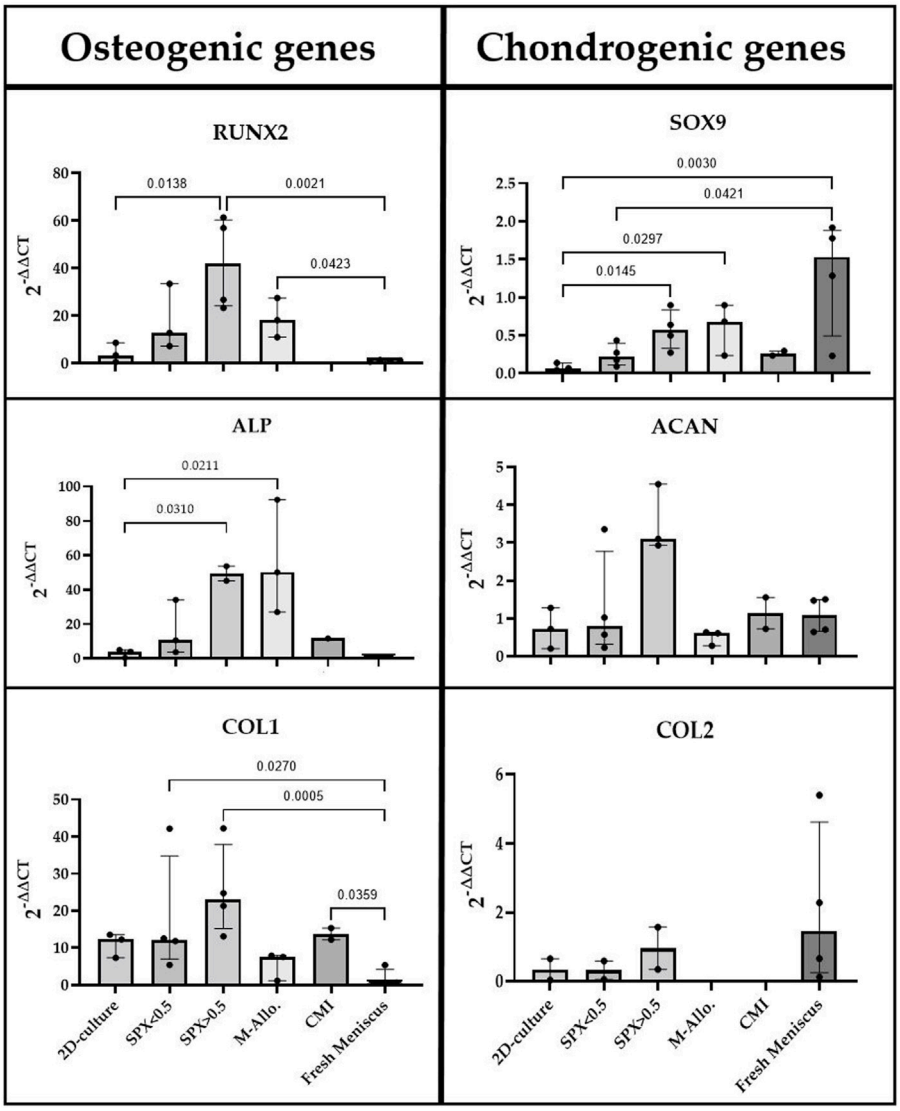

FIGURE 6
qPCR analysis of cDNA of RUNX2, ALP, COL1, SOX9, ACAN, and COL2 genes in monolayer MCs culture, MCs in fresh meniscus, and MCs cultured on SPX, M-Allo, and CMI (n = 3–5). Data all presented as median (IQR). SPX: spongioflex®, M-Allo: meniscus allograft, CMI: collagen meniscus implant.

measured using the PrestoBlue® viability assay. Although the viability values were not directly comparable due to the differences in size and cell numbers of the fresh meniscus blocks, the findings suggest that, at least within a 7-day timeframe, the scaffolds do not exhibit cytotoxic effects on the meniscal cells (Figure 8). This was determined by observing that the viability of the tissue blocks was not altered over the 7 days in culture.

3.9 Expression of osteogenic and chondrogenic genes in *ex vivo* meniscus with scaffolds

To analyze the gene expression, the scaffolds were removed from the menisci and the RNA was separately isolated. Osteogenic and chondrogenic genes were expressed in the cultured fresh meniscal tissue (Figure 9). The expression of these genes was found to be low or not detectable in the separated scaffold samples after 7 days of culture, partially due to the low amount of isolated RNA. On the other hand, the expression of *RUNX2*, *ALP*, *SOX9*, and *ACAN* in migrated cells in SPX (both porosities) and CMI after 28 days of co-cultivation was higher than that after 7 days of cultivation.

3.10 Histological DAPI staining of *ex vivo* meniscus with scaffolds

DAPI staining demonstrated that not until 28 days after culturing the scaffolds in the meniscus, MCs migrate from the meniscus to the SPX. (Figure 10). Quantification of the number of cells that migrated into the scaffolds showed ingrowth of cells in

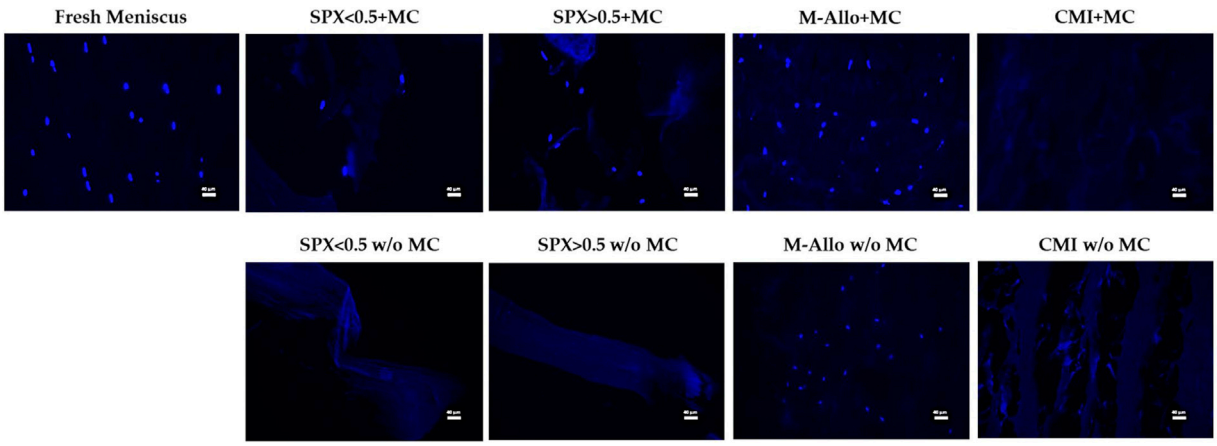

FIGURE 7
Fluorescent images of MCs in fresh meniscus and cultured on different scaffolds stained with DAPI. Scale bars in the images equal 40 μm. SPX: spongioflex®, M-Allo: meniscus allograft, CMI: collagen meniscus implant, MC: meniscal cell, w/o: without.

SPX (both micro- and macro-pores) and in CMI (60 ± 46 cells for macro-pores SPX, 57 ± 53 cells for micro-pores SPX, and 53 ± 19 for CMI, n = 4).

4 Discussion

The meniscus has a low regeneration potential and the current regenerative therapies are limited, often resulting in an unsatisfactory treatment or, as a last resort, to the resection of the meniscus. This *in vitro* and *ex vivo* study aimed to investigate a possible grafting material for meniscus regeneration. Human meniscal cells or meniscal tissue was cultured with different grafting materials to invesitgate cell ingrowth and differentiation. Two types of human allografts were used: SPX (demineralized cancellous bone) with different porosities (porosity approximated by the weight, macro-pores: <0.5 g/cm^3 and micro-pores: >0.5 g/cm^3) and M-Allo. CMI served as the control material, as it is also made of collagen. Cells cultured on SPX showed an increase in viability over 7 days, whereas those on M-Allo or CMI were less viable. The synthesis of the extracellular matrix protein collagen I was comparable between cells in 2D and cells on SPX. Cell ingrowth was only detectable for cells cultured on SPX. *Ex vivo* organ culture showed that cells had not grown into the scaffolds after 7 days, resulting in no detectable gene expression. However, MCs were able to migrate from the meniscal tissue to the SPX within 28 days. Gene expression analysis showed that the expression of *RUNX2*, *ALP*, *SOX9*, and *ACAN* increased in cells that migrated from meniscal tissue to SPX (both micro- and macro-pores) and CMI after 28 days of co-cultivation. The porous scaffold provided attractive conditions for cell growth within 7 days, but a longer time (28 days) was required to stimulate cell migration from the surrounding tissue in an *ex vivo* culture.

The cells used in this study were isolated from human donor menisci (complete or parts). The menisci were harvested from patients with gonarthrosis and the menisci were grade 2–4 without calcium deposits based on the Pauli classification

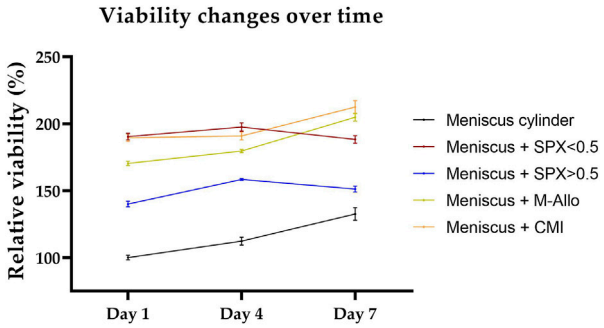

FIGURE 8
Viability of meniscus blocks cultured with different scaffolds over a period of 7 days in DMEM culture medium. Viability values are normalized to the viability of the meniscal cylinder at day 1. n = 4, bars represent mean ± SEM. SPX: spongioflex®, M-Allo: meniscus allograft, CMI: collagen meniscus implant.

(Pauli et al., 2011). This resulted in an inhomogeneous cell population as seen in the different areas of the meniscus. Verdonk et al. published one of the first studies on human meniscal cell characteristics and demonstrated their distinct phenotype and improved fibrochondogenic properties when cultured in 3D (Verdonk et al., 2005). Using flow cytometry, they characterized human meniscal cells and the cell-associated extracellular matrix and distinguished different cell types. Depending on the donor, they found a high variability of collagen I, II and aggrecan. A high variability in gene expression was also seen in other studies (Liang et al., 2017; Crawford et al., 2020) and might further be explained by the inhomogeneous structure of the meniscus. According to Zheng et al., different cell sources such as bone marrow mesenchymal stem cells, adipose-derived stem cells, and articular chondrocytes demonstrate diverse proliferative behaviors, distinct biochemical and biomechanical attributes, and varying gene expression profiles (Zheng et al., 2023). The variations in gene expression

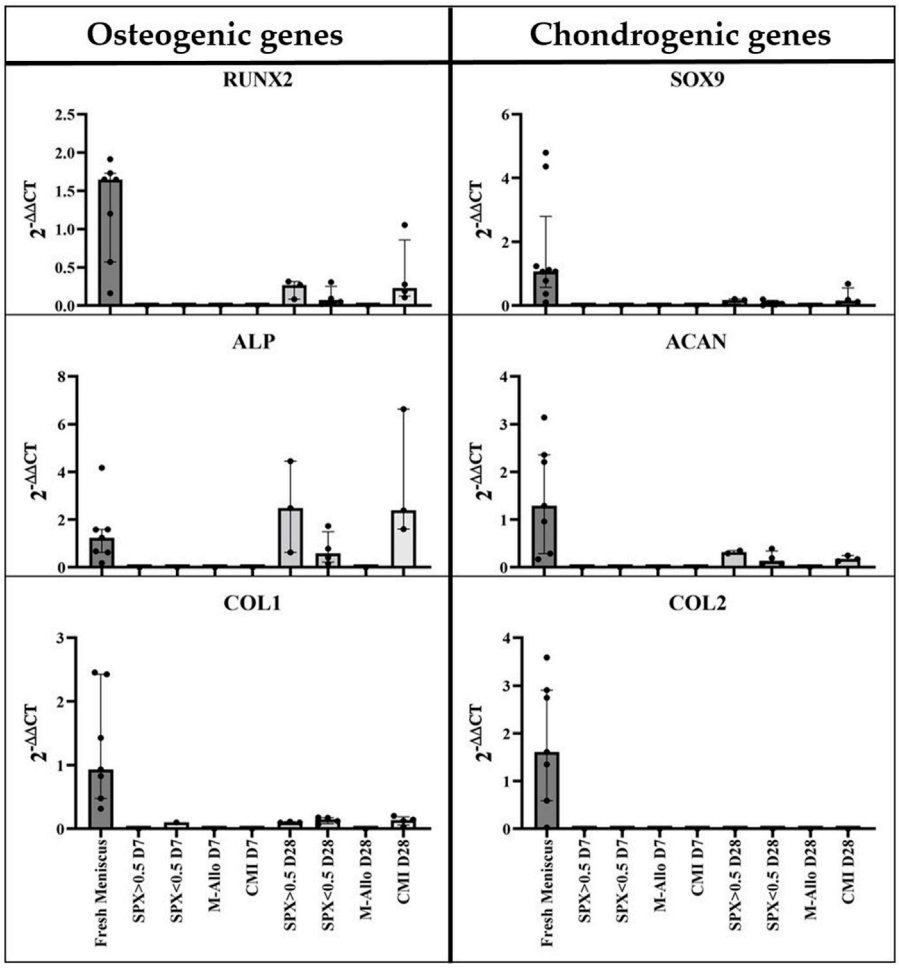

FIGURE 9
qPCR analysis of cDNA of RUNX2, ALP, COL1, SOX9, ACAN, and COL2 genes in MCs in fresh meniscus and in migrated MCs into SPX, M-Allo, and CMI (n = 7 for fresh meniscus and n = two to five for scaffold). Data all presented as median (IQR). SPX: spongioflex®, M-Allo: meniscus allograft, CMI: collagen meniscus implant.

seen in these experiments can therefore be explained by the different donors and different regions of the meniscus. In addition, the natural structural differences in the meniscus with varying proportions of different cell types in distinct regions could influence our results. As a limitation of this study, no mechanical stimulation of the constructs was performed. Mechanical loading has a proven role in enhancing fibrochondrocyte differentiation and might affect the cells in the scaffolds as summarized in a review by Ma et al. (Ma et al., 2022a). It impacts the cell behavior and especially the gene expression, particularly of extracellular matrix proteins. For instance, it has been demonstrated to enhance the differentiation of fibrochondrocytes derived from Bone Marrow Mesenchymal Stem cells (BMSCs) in fibrin constructs, leading to an upregulation of COL1 expression (Connelly et al., 2010). Furthermore, studies have indicated that mechanical stimulation can increase the levels of aggrecan, COL1, and COL2 in chondrocytes (Shadi et al., 2022). Sex-specific differences were seen in the reaction of engineered menisci depending in the mechanical stimuli (Ma et al., 2022b).

Liang et al. investigated the expression of osteogenic genes after 21 days of culturing meniscus fibrochondrocytes, discovering no differences in the modified culturing environment. Similarly, their cells were negative for the Alizarin red stain, as was the case in this study (Liang et al., 2017). In contrast, Fu et al. found an osteogenic differentiation of meniscal cells 14 days after culturing under osteogenic conditions (Fu et al., 2016). Both studies used cells at passage 3 but with different time points and Liang et al. also added TGFβ1 and FGF-2 to the medium. Culturing the MCs for 7 days in osteogenic medium resulted in no osteogenic differentiation, although the control cells (SAOS2) showed a strong Alizarin red stain in this study. Osteogenic differentiation is an important aspect, and the reason for the different osteogenic gene expression should be investigated further, as an osteogenic differentiation of the cells within the meniscus graft would be an unwanted effect. Furthermore, the lack of COL2 expression in MCs cultured in the different media might be due to the cultivation period being too short.

Analyzing cell surface markers showed that almost all cells isolated from the meniscus expressed CD90, but only a few cells were positive for CD105 or CD146. Recent studies investigated the phenotype of meniscal cells using flow cytometry and single cell

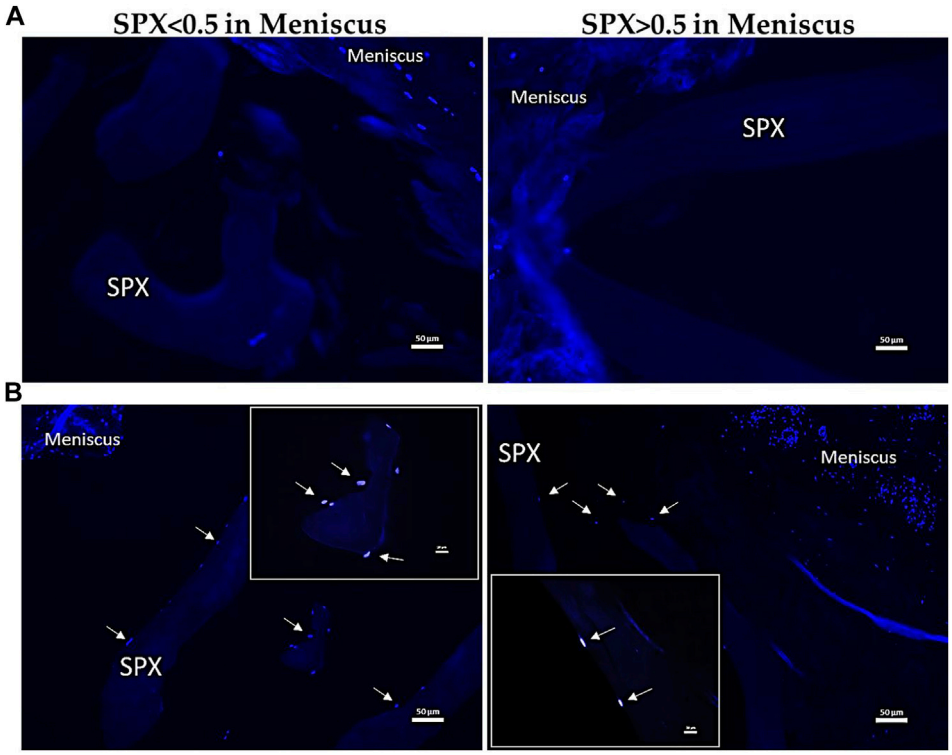

FIGURE 10
Fluorescent images of MCs in meniscus blocks containing SPX for 7 **(A)** and 28 **(B)** days stained with DAPI. The arrows indicate the migration of MCs from the surrounding meniscal tissue. Scale bars in the images equal 50 µm in A and B respectively. SPX: spongioflex®.

sequencing. They found regional differences with high amounts of CD90-positive cells and up to seven independent cell clusters (Sun et al., 2020; Wang et al., 2022). The low amount of CD146-positive cells in this study might indicate towards a special phenotype found in degenerated menisci: degenerated meniscus progenitor cells (DegP) (Sun et al., 2020). Interestingly, Verdonk et al. found a low amount of CD105 and CD44 positive cells but an increase in this surface marker when cells were cultured in alginate (Verdonk et al., 2005). Cellular properties are different depending on the localization, the degeneration of the meniscus (Fu et al., 2022), and culture conditions (fibronectin coating, physioxia vs. hyperoxia) that can be modified to enhance the progenitor phenotype of isolated meniscal cells (Pattappa et al., 2022). The cells used in this study were isolated from the entire meniscal tissue obtained without separation of different meniscal areas and further isolation of the progenitor cells. Moreover, the meniscal tissue was obtained from surgery and the menisci showed signs of alterations. Attention was paid to using only tissue areas with fewer alterations for cell isolation and the *ex vivo* meniscus model, but it cannot be excluded that the cells were affected and do not fully resemble healthy meniscal cells. The variation in the results can be explained by the variations described for affected meniscal tissue (Bradley et al., 2023). This would also be the case in the clinical situation where the scaffold would be implanted into injured meniscus at different regions. However, this approach might explain the high variation in the data as the cell populations might be very inhomogeneous.

The majority of the extracellular matrix of a native meniscal tissue is composed mainly of collagen I and a smaller amount of collagen II and glycosaminoglycans, which serve as a substrate for cell migration and proliferation (Chen et al., 2015; Lyons et al., 2019; Ruprecht et al., 2019; Zhong et al., 2020; Bansal et al., 2021). Biocompatible materials have been shown to facilitate cell adhesion, promote cell growth, and stimulate collagen deposition (Murakami et al., 2017; Baek et al., 2019). Despite large interconnected pores of the porous SPX, only a few of the suspended cells were actually able to pass through, and the majority of the cells remained stuck in the scaffolds. Nevertheless, the cell viability assay indicated that not all of the trapped cells were able to adhere to the inner surfaces of the scaffolds and were possibly unable to form the intercellular connections and extracellular matrix necessary for survival.

Our results showed that despite many of the cells being able to adhere to the scaffolds on day 0, a proportion died and were consequently removed from the scaffolds. This was likely due to the increased stress caused by the transfer of the scaffolds into a new well and the medium exchange procedure. Additionally, the cells were not able to produce an adequate amount of extracellular matrix within 24 h of seeding. In this study, we demonstrated that as opposed to M-Allo and CMI, SPX also promotes meniscal cell growth and proliferation and stimulates the synthesis of the extracellular matrix protein collagen I. One possible explanation for the lack of cell growth on M-Allo could be the high density of this scaffold, which prevented the cells from initially penetrating inside. Previous studies have also reported high collagen synthesis when different types of stem cells were cultured on biocompatible scaffolds, including bone marrow-derived mesenchymal stem

cells, primary MCs, and peripheral blood-derived mesenchymal stem cells (Lyons et al., 2019; Mao et al., 2022; Barceló et al., 2023). The ability of these scaffolds to promote collagen I production is an important finding that could have significant clinical implications. These results suggest that biocompatible materials might be a promising approach for meniscal tissue development and regeneration.

Culturing MCs on SPX with low porosity appears to enhance differentiation of the cells into an osteogenic phenotype, as might be expected from the upregulation of the ALP and RUNX2 genes. However, the expression of the ACAN gene, which is considered a chondrogen-specific gene in these cells, was also relatively upregulated. One possible explanation for the upregulation of osteogenic genes could be the influence of scaffold architecture and pore size on the cells. Studies have reported the effects of architectural or topographical factors on the gene and protein expressions of mesenchymal stem/stromal cells, the tendency of the cells to have a specific phenotype and on the cell proliferation (Zhang et al., 2016; Olvera et al., 2017; Barceló et al., 2023). One has to keep in mind that the cells used in this study were from menisci with a degeneration grade of two to four according to the Pauli classification (Pauli et al., 2011), without calcium deposition. It can be speculated that a proportion of the cells are already primed for osteogenic differentiation might be isolated and cultured, which could explain the higher expression of the osteogenic marker.

A recent study investigated the suitability of a scaffold made out of polyglycolic acid (PGA) fibers as a meniscus graft *in vitro* (Cojocaru et al., 2020). The human meniscal cells cultured on the scaffolds revealed a good viability/proliferation until day 7, with a slight decrease at day 14. This is in accordance with the cells showing an increase in cell viability when cultured on SPX for 7 days. Culturing the cells in 2D or on PGA with human serum or platelet concentrate resulted in the regulation of gene expression. A clear comparison with the present data is not possible due to the different conditions, but it displays the effects of culturing conditions and scaffolds on the cells.

For the *ex vivo* meniscus model the scaffolds were used in a tight-fit manner to ensure a tight contact between scaffold and donor meniscus. In the clinical situation of partial meniscus repair, the surgeon would also aim for a very close contact between the scaffold and the meniscal tissue to allow the invasion of the cells into the scaffold and therefore the regeneration procedure. The *ex vivo* meniscus model showed no ingrowth of cells into the scaffolds over a period of 7 days. The time frame might have been too short to let the cells migrate out of the meniscus matrix into the scaffold. The decision for the 7-day time point was made to reduce the risk of cell death in the *ex vivo* meniscal tissue and is a time point previously used in comparable experiments (Kang et al., 2006; Freymann et al., 2012; Zhang et al., 2016; Kwak et al., 2017; Ruprecht et al., 2019). In contrast, the 28-day cultivation of SPX in meniscal tissue resulted in ingrowth of MCs into SPX. The higher cell migration from the meniscus into the scaffolds from day 7 to day 28 is in accordance with previous observations using porcine menisci and porcine meniscus-derived matrix (Ruprecht et al., 2019). The lack of cell migration on day 7 might be explained by too weak or absent migration-stimulating signals during the 7 days and therefore the cells embedded in the dense extracellular matrix of the meniscus were not stimulated to grow out. However, the 28-day period was sufficient to stimulate cell ingrowth into the SPX. The analysis of gene expression showed that the expression of RUNX2, ALP, SOX9, and ACAN was increased in cells that migrated from meniscal tissue to SPX (both micro- and macro-porous) and CMI after 28 days of co-cultivation. This indicates that a greater number of cells were able to migrate into the scaffolds. However, it remains uncertain whether the cells differentiated into an osteogenic or chondrogenic lineage, and it appears that more time might be required for the cells to undergo this process.

5 Conclusion

In conclusion, this study investigated the potential of meniscal regeneration using graft materials by *in vitro* and *ex vivo* experiments. The results indicate that the use of SPX as a graft material is promising for meniscal tissue regeneration. Consistent with our findings, a case study indicated that the utilization of SPX block implants in a patient with bilateral medial meniscal lesions resulted in rapid integration of the implant, along with favorable radiographic and functional outcomes (Behrendt, 2023). Cells cultured on SPX showed increased viability and synthesis of the extracellular matrix protein collagen I compared with other materials. Consistent with this, the *ex vivo* organ culture demonstrated that meniscal cells exhibited migration from the surrounding tissue and successfully grew on the SPX scaffold within a 28-day period.

The study also highlights the importance of donor variation and the inhomogeneous structure of the meniscus, which may contribute to differences in gene expression and the cellular properties. The results suggest that meniscal cell phenotype and behavior may be influenced by factors such as cultivation conditions, scaffold architecture, and pore size.

Overall, the biocompatible materials show potential to promote cell growth, proliferation, and collagen production, which are critical for meniscal tissue regeneration. Further studies are required to optimize scaffold design, culturing conditions, and migration-stimulating signals to improve the efficacy of meniscal regeneration therapies.

Data availability statement

The original contributions presented in the study are included in the article/Supplementary Material, further inquiries can be directed to the corresponding author.

Ethics statement

The use of human tissue was approved by Ethics Committee of Jena University Hospital (Umbrella Application: 2018_1158_1-Material, Addendum: 21.08.2020). The studies were conducted in accordance with the local legislation and institutional requirements. The participants provided their written informed consent to participate in this study.

Author contributions

MD: Data curation, Formal Analysis, Investigation, Methodology, Visualization, Writing–original draft. VE: Project administration, Resources, Writing–review and editing, Conceptualization. DK: Resources, Writing–review and editing. NA: Writing–review and editing. BW: Conceptualization, Funding acquisition, Project administration, Resources, Supervision, Writing–review and editing.

Funding

The author(s) declare financial support was received for the research and publication of this article. The study received funding from the German Institute for Cell and Tissue Replacement (DIZG, gemeinnützige GmbH).

Acknowledgments

We wish to acknowledge Birgit Lemser, Waltraud Palm and Yvonne Hofmann for their exceptional technical assistance and Manuela Thierbach and Stefan Pentzold for valuable scientific advice during the project. We would also like to thank the surgeons, especially Dr. Felix Kohler, and Norbert Kinitz for their support in tissue collection.

Conflict of interest

E, DK, and NA are employees of the German Institute for Cell and Tissue Replacement (DIZG gemeinnützige GmbH), a nonprofit provider of sterile allografts.

The remaining authors declare that the research was conducted in the absence of any commercial or financial relationships that could be construed as a potential conflict of interest.

Publisher's note

References

Angele, P., Docheva, D., Pattappa, G., and Zellner, J. (2021). Cell-based treatment options facilitate regeneration of cartilage, ligaments and meniscus in demanding conditions of the knee by a whole joint approach. *Knee Surg. Sports Traumatol. Arthrosc.* 30, 1138–1150. doi:10.1007/s00167-021-06497-9

Baek, J., Lotz, M. K., and D'Lima, D. D. (2019). Core–shell nanofibrous scaffolds for repair of meniscus tears. *Tissue Eng. Part A* 25 (23-24), 1577–1590. doi:10.1089/ten.tea.2018.0319

Bansal, S., Floyd, E. R., Kowalski, M., Aikman, E., Elrod, P., Burkey, K., et al. (2021). Meniscal repair: the current state and recent advances in augmentation. *J. Orthop. Research®* 39 (7), 1368–1382. doi:10.1002/jor.25021

Barceló, X., Eichholz, K. F., Gonçalves, I. F., Garcia, O., and Kelly, D. J. (2023). Bioprinting of structurally organized meniscal tissue within anisotropic melt electrowritten scaffolds. *Acta Biomater.* 158, 216–227. doi:10.1016/j.actbio.2022.12.047

Behrendt, S. (2023). MRI follow up of bilateral partial meniscal substitution with a demineralized bone block. A case report. *Radiol. Case Rep.* 18 (1), 21–26. doi:10.1016/j.radcr.2022.09.091

Bilgen, B., Jayasuriya, C. T., and Owens, B. D. (2018). Current concepts in meniscus tissue engineering and repair. *Adv. Healthc. Mater.* 7 (11), 1701407. doi:10.1002/adhm.201701407

Bradley, P. X., Thomas, K. N., Kratzer, A. L., Robinson, A. C., Wittstein, J. R., DeFrate, L. E., et al. (2023). The interplay of biomechanical and biological changes following meniscus injury. *Curr. Rheumatol. Rep.* 25 (2), 35–46. doi:10.1007/s11926-022-01093-3

Brucker, P. U., Favre, P., Puskas, G. J., von Campe, A., Meyer, D. C., and Koch, P. P. (2010). Tensile and shear loading stability of all-inside meniscal repairs: an *in vitro* biomechanical evaluation. *Am. J. Sports Med.* 38 (9), 1838–1844. doi:10.1177/0363546510368131

Buma, P., Van Tienen, T., and Veth, R. (2007). The collagen meniscus implant. *Expert Rev. Med. Devices* 4 (4), 507–516. doi:10.1586/17434440.4.4.507

Cao, J., and Chen, B. (2022). Function, injury, and treatment for meniscus. *Highlights Sci. Eng. Technol.* 8, 263–271. doi:10.54097/hset.v8i.1145

Cavendish, P., DiBartola, A. C., Everhart, J. S., Kuzma, S., Kim, W. J., and Flanigan, D. C. (2020). Meniscal allograft transplantation: A review of indications, techniques, and outcomes. *Knee Surg. Sports Traumatol. Arthrosc.* 28, 3539–3550. doi:10.1007/s00167-020-06058-6

Chen, Y-C., Chen, R-N., Jhan, H-J., Liu, D-Z., Ho, H-O., Mao, Y., et al. (2015). Development and characterization of acellular extracellular matrix scaffolds from porcine menisci for use in cartilage tissue engineering. *Tissue Eng. Part C. Methods* 21 (9), 971–986. doi:10.1089/ten.tec.2015.0036

Chevrier, A., Nelea, M., Hurtig, M. B., Hoemann, C. D., and Buschmann, M. D. (2009). Meniscus structure in human, sheep, and rabbit for animal models of meniscus repair. *J. Orthop. Res.* 27 (9), 1197–1203. doi:10.1002/jor.20869

Cohen, J. (1988). *Statistical power analysis for the behavioral sciences*. Milton Park, Abingdon: Routledge.

Cojocaru, D. G., Hondke, S., Krüger, J. P., Bosch, C., Croicu, C., Florescu, S., et al. (2020). Meniscus-shaped cell-free polyglycolic acid scaffold for meniscal repair in a sheep model. *J. Biomed. Mater. Res. Part B Appl. Biomaterials* 108 (3), 809–818. doi:10.1002/jbm.b.34435

Connelly, J. T., Vanderploeg, E. J., Mouw, J. K., Wilson, C. G., and Levenston, M. E. (2010). Tensile loading modulates bone marrow stromal cell differentiation and the development of engineered fibrocartilage constructs. *Tissue Eng. Part A* 16 (6), 1913–1923. doi:10.1089/ten.tea.2009.0561

Crawford, M. D., Hellwinkel, J. E., Aman, Z., Akamefula, R., Singleton, J. T., Bahney, C., et al. (2020). Microvascular anatomy and intrinsic gene expression of menisci from young adults. *Am. J. Sports Med.* 48 (13), 3147–3153. doi:10.1177/0363546520961555

Freymann, U., Endres, M., Neumann, K., Scholman, H-J., Morawietz, L., and Kaps, C. (2012). Expanded human meniscus-derived cells in 3-D polymer–hyaluronan scaffolds for meniscus repair. *Acta Biomater.* 8 (2), 677–685. doi:10.1016/j.actbio.2011.10.007

Fu, W., Chen, S., Yang, R., Li, C., Gao, H., Li, J., et al. (2022). Cellular features of localized microenvironments in human meniscal degeneration: A single-cell transcriptomic study. *Elife* 11, e79585. doi:10.7554/elife.79585

Fu, W., Xie, X., Li, Q., Chen, G., Zhang, C., Tang, X., et al. (2016). Isolation, characterization, and multipotent differentiation of mesenchymal stem cells derived from meniscal debris. *Stem Cells Int.* 2016, 1–9. doi:10.1155/2016/5093725

Hede, A., Jensen, D. B., Blyme, P., and Sonne-Holm, S. (1990). Epidemiology of meniscal lesions in the knee: 1,215 open operations in Copenhagen 1982-84. *Acta Orthop. Scand.* 61 (5), 435–437. doi:10.3109/17453679008993557

Holloway, J. L., Lowman, A. M., and Palmese, G. R. (2010). Mechanical evaluation of poly (vinyl alcohol)-based fibrous composites as biomaterials for meniscal tissue replacement. *Acta Biomater.* 6 (12), 4716–4724. doi:10.1016/j.actbio.2010.06.025

Holloway, J. L., Lowman, A. M., VanLandingham, M. R., and Palmese, G. R. (2014). Interfacial optimization of fiber-reinforced hydrogel composites for soft fibrous tissue applications. *Acta Biomater.* 10 (8), 3581–3589. doi:10.1016/j.actbio.2014.05.004

Hutchinson, I. D., and Rodeo, S. A. (2022). The current role of biologics for meniscus injury and treatment. *Curr. Rev. Musculoskelet. Med.* 15 (6), 456–464. doi:10.1007/s12178-022-09778-z

Hutmacher, D. W. (2001). Scaffold design and fabrication technologies for engineering tissues—State of the art and future perspectives. *J. Biomaterials Sci. Polym. Ed.* 12 (1), 107–124. doi:10.1163/156856201744489

Kang, S. W., Sun-Mi, S., Jae-Sun, L., Eung-Seok, L., Kwon-Yong, L., Sang-Guk, P., et al. (2006). Regeneration of whole meniscus using meniscal cells and polymer scaffolds

in a rabbit total meniscectomy model. *J. Biomed. Mater. Res. Part A Official J. Soc. Biomaterials* 77 (4), 659–671. doi:10.1002/jbm.a.30579

Kean, C. O., Brown, R. J., and Chapman, J. (2017). The role of biomaterials in the treatment of meniscal tears. *PeerJ* 5, e4076. doi:10.7717/peerj.4076

Kohli, S., Schwenck, J., and Barlow, I. (2022). Failure rates and clinical outcomes of synthetic meniscal implants following partial meniscectomy: A systematic review. *Knee Surg. Relat. Res.* 34 (1), 27. doi:10.1186/s43019-022-00155-1

Kwak, H. S., Nam, J., Lee, J. H., Kim, H. J., and Yoo, J. J. (2017). Meniscal repair *in vivo* using human chondrocyte-seeded PLGA mesh scaffold pretreated with platelet-rich plasma. *J. Tissue Eng. Regen. Med.* 11 (2), 471–480. doi:10.1002/term.1938

Laible, C., Stein, D. A., and Kiridly, D. N. (2013). Meniscal repair. *JAAOS-Journal Am. Acad. Orthop. Surg.* 21 (4), 204–213. doi:10.5435/jaaos-21-04-204

Liang, Y., Idrees, E., Andrews, S. H., Labib, K., Szojka, A., Kunze, M., et al. (2017). Plasticity of human meniscus fibrochondrocytes: A study on effects of mitotic divisions and oxygen tension. *Sci. Rep.* 7 (1), 12148–12213. doi:10.1038/s41598-017-12096-x

Lombardo, M. D., Mangiavini, L., and Peretti, G. M. (2021). Biomaterials and meniscal lesions: current concepts and future perspective. *Pharmaceutics* 13 (11), 1886. doi:10.3390/pharmaceutics13111886

Longo, U. G., Campi, S., Romeo, G., Spiezia, F., Maffulli, N., and Denaro, V. (2012). Biological strategies to enhance healing of the avascular area of the meniscus. *Stem Cells Int.* 2012, 1–7. doi:10.1155/2012/528359

Lu, J., Huang, J., Jin, J., Xie, C., Xue, B., Lai, J., et al. (2022). The design and characterization of a strong bio-ink for meniscus regeneration. *Int. J. Bioprinting* 8 (4), 600. doi:10.18063/ijb.v8i4.600

Lyons, L. P., Hidalgo Perea, S., Weinberg, J. B., Wittstein, J. R., and McNulty, A. L. (2019). Meniscus-derived matrix bioscaffolds: effects of concentration and cross-linking on meniscus cellular responses and tissue repair. *Int. J. Mol. Sci.* 21 (1), 44. doi:10.3390/ijms21010044

Ma, Z., Li, D. X., Kunze, M., Mulet-Sierra, A., Westover, L., and Adesida, A. B. (2022b). Engineered human meniscus in modeling sex differences of knee osteoarthritis *in vitro*. *Front. Bioeng. Biotechnol.* 10, 823679. doi:10.3389/fbioe.2022.823679

Ma, Z., Vyhlidal, M. J., Li, D. X., and Adesida, A. B. (2022a). Mechano-bioengineering of the knee meniscus. *Am. J. Physiol. Cell. Physiol.* 323 (6), C1652–C1663. doi:10.1152/ajpcell.00336.2022

Makris, E. A., Hadidi, P., and Athanasiou, K. A. (2011). The knee meniscus: structure–function, pathophysiology, current repair techniques, and prospects for regeneration. *Biomaterials* 32 (30), 7411–7431. doi:10.1016/j.biomaterials.2011.06.037

Mao, B., Zhang, Z., Lai, S., Zhang, K., Li, J., and Fu, W. (2022). Demineralized cortical bone matrix augmented with peripheral blood-derived mesenchymal stem cells for rabbit medial meniscal reconstruction. *Front. Bioeng. Biotechnol.* 10, 855103. doi:10.3389/fbioe.2022.855103

Martinek, V., Ueblacker, P., Bräun, K., Nitschke, S., Mannhardt, R., Specht, K., et al. (2006). Second generation of meniscus transplantation: in-vivo study with tissue engineered meniscus replacement. *Archives Orthop. Trauma Surg.* 126, 228–234. doi:10.1007/s00402-005-0025-1

Mather, R. C., III, Garrett, W. E., Cole, B. J., Hussey, K., Bolognesi, M. P., Lassiter, T., et al. (2015). Cost-effectiveness analysis of the diagnosis of meniscus tears. *Am. J. Sports Med.* 43 (1), 128–137. doi:10.1177/0363546514557937

McDermott, I., and Amis, A. (2006). The consequences of meniscectomy. *J. bone Jt. Surg. Br.* 88 (12), 1549–1556. doi:10.1302/0301-620x.88b12.18140

Messner, K., and Gao, J. (1998). The menisci of the knee joint. Anatomical and functional characteristics, and a rationale for clinical treatment. *J. Anat.* 193 (2), 161–178. doi:10.1046/j.1469-7580.1998.19320161.x

Murakami, T., Otsuki, S., Nakagawa, K., Okamoto, Y., Inoue, T., Sakamoto, Y., et al. (2017). Establishment of novel meniscal scaffold structures using polyglycolic and poly-l-lactic acids. *J. Biomaterials Appl.* 32 (2), 150–161. doi:10.1177/0885328217713631

Olvera, D., Sathy, B. N., Carroll, S. F., and Kelly, D. J. (2017). Modulating microfibrillar alignment and growth factor stimulation to regulate mesenchymal stem cell differentiation. *Acta Biomater.* 64, 148–160. doi:10.1016/j.actbio.2017.10.010

Pattappa, G., Reischl, F., Jahns, J., Schewior, R., Lang, S., Zellner, J., et al. (2022). Fibronectin adherent cell populations derived from avascular and vascular regions of the meniscus have enhanced clonogenicity and differentiation potential under physioxia. *Front. Bioeng. Biotechnol.* 9, 789621. doi:10.3389/fbioe.2021.789621

Pauli, C., Grogan, S. P., Patil, S., Otsuki, S., Hasegawa, A., Koziol, J., et al. (2011). Macroscopic and histopathologic analysis of human knee menisci in aging and osteoarthritis. *Osteoarthr. Cartil.* 19 (9), 1132–1141. doi:10.1016/j.joca.2011.05.008

Pruss, A., Baumann, B., Seibold, M., Kao, M., Tintelnot, K., von Versen, R., et al. (2001). Validation of the sterilization procedure of allogeneic avital bone transplants using peracetic acid–ethanol. *Biologicals* 29 (2), 59–66. doi:10.1006/biol.2001.0286

Romanazzo, S., Vedicherla, S., Moran, C., and Kelly, D. (2018). Meniscus ECM-functionalised hydrogels containing infrapatellar fat pad-derived stem cells for bioprinting of regionally defined meniscal tissue. *J. Tissue Eng. Regen. Med.* 12 (3), e1826–e1835. doi:10.1002/term.2602

Rongen, J. J., van Tienen, T. G., van Bochove, B., Grijpma, D. W., and Buma, P. (2014). Biomaterials in search of a meniscus substitute. *Biomaterials* 35 (11), 3527–3540. doi:10.1016/j.biomaterials.2014.01.017

Ruprecht, J. C., Waanders, T. D., Rowland, C. R., Nishimuta, J. F., Glass, K. A., Stencel, J., et al. (2019). Meniscus-derived matrix scaffolds promote the integrative repair of meniscal defects. *Sci. Rep.* 9 (1), 8719. doi:10.1038/s41598-019-44855-3

Sasaki, H., Rothrauff, B. B., Alexander, P. G., Lin, H., Gottardi, R., Fu, F. H., et al. (2018). *In vitro* repair of meniscal radial tear with hydrogels seeded with adipose stem cells and TGF-β3. *Am. J. Sports Med.* 46 (10), 2402–2413. doi:10.1177/0363546518782973

Scotti, C., Hirschmann, M. T., Antinolfi, P., Martin, I., and Peretti, G. M. (2013). Meniscus repair and regeneration: review on current methods and research potential. *Eur. Cells Mater.* 26, 150–170. doi:10.22203/ecm.v026a11

Seo, S-S., Kim, C-W., Lee, C-R., Park, D-H., Kwon, Y-U., Kim, O-G., et al. (2020). Second-look arthroscopic findings and clinical outcomes of meniscal repair with concomitant anterior cruciate ligament reconstruction: comparison of suture and meniscus fixation device. *Archives Orthop. Trauma Surg.* 140, 365–372. doi:10.1007/s00402-019-03323-3

Shadi, M., Talaei-Khozani, T., Sani, M., Hosseinie, R., Parsaei, H., and Vojdani, Z. (2022). Optimizing artificial meniscus by mechanical stimulation of the chondrocyte-laden acellular meniscus using ad hoc bioreactor. *Stem Cell. Res. Ther.* 13 (1), 382. doi:10.1186/s13287-022-03058-w

Stone, K. R., Rodkey, W. G., Webber, R., McKinney, L., and Steadman, J. R. (1992). Meniscal regeneration with copolymeric collagen scaffolds: *in vitro* and *in vivo* studies evaluated clinically, histologically, and biochemically. *Am. J. Sports Med.* 20 (2), 104–111. doi:10.1177/036354659202000202

Sun, H., Wen, X., Li, H., Wu, P., Gu, M., Zhao, X., et al. (2020). Single-cell RNA-seq analysis identifies meniscus progenitors and reveals the progression of meniscus degeneration. *Ann. rheumatic Dis.* 79 (3), 408–417. doi:10.1136/annrheumdis-2019-215926

Taghiyar, L., Asadi, H., and Baghaban Eslaminejad, M. (2023). A bioscaffold of decellularized whole osteochondral sheet improves proliferation and differentiation of loaded mesenchymal stem cells in a rabbit model. *Cell. Tissue Bank.* doi:10.1007/s10561-023-10084-2

Vadodaria, K., Kulkarni, A., Santhini, E., and Vasudevan, P. (2019). Materials and structures used in meniscus repair and regeneration: A review. *Biomedicine* 9 (1), 2. doi:10.1051/bmdcn/2019090102

Verdonk, P. C., Forsyth, R., Wang, J., Almqvist, K. F., Verdonk, R., Veys, E. M., et al. (2005). Characterisation of human knee meniscus cell phenotype. *Osteoarthr. Cartil.* 13 (7), 548–560. doi:10.1016/j.joca.2005.01.010

Veronesi, F., Di Matteo, B., Vitale, N. D., Filardo, G., Visani, A., Kon, E., et al. (2021). Biosynthetic scaffolds for partial meniscal loss: A systematic review from animal models to clinical practice. *Bioact. Mater* 6 (11), 3782–3800. doi:10.1016/j.bioactmat.2021.03.033

Wang, J., Roberts, S., Li, W., and Wright, K. (2022). Phenotypic characterization of regional human meniscus progenitor cells. *Front. Bioeng. Biotechnol.* 10, 1003966. doi:10.3389/fbioe.2022.1003966

Whitehouse, M. R., Howells, N. R., Parry, M. C., Austin, E., Kafienah, W., Brady, K., et al. (2017). Repair of torn avascular meniscal cartilage using undifferentiated autologous mesenchymal stem cells: from *in vitro* optimization to a first-in-human study. *Stem Cells Transl. Med.* 6 (4), 1237–1248. doi:10.1002/sctm.16-0199

Winkler, P. W., Faber, S., Balke, M., Metzlaff, S., Niethammer, T. R., Roessler, P. P., et al. (2022). Germany has a high demand in meniscal allograft transplantation but is subject to health economic and legal challenges: A survey of the German knee society. *Knee Surg. Sports Traumatol. Arthrosc.* 30 (7), 2352–2357. doi:10.1007/s00167-022-06889-5

Winkler, P. W., Rothrauff, B. B., Buerba, R. A., Shah, N., Zaffagnini, S., Alexander, P., et al. (2020). Meniscal substitution, a developing and long-awaited demand. *J. Exp. Orthop.* 7, 55–15. doi:10.1186/s40634-020-00270-6

Zaffagnini, S., Grassi, A., Marcheggiani Muccioli, G. M., Bonanzinga, T., Nitri, M., Raggi, F., et al. (2015). MRI evaluation of a collagen meniscus implant: A systematic review. *Knee Surg. Sports Traumatol. Arthrosc.* 23, 3228–3237. doi:10.1007/s00167-014-3155-6

Zhang, M. (2022). Classification, risk factors, diagnoses, and examination for six-type meniscus tears. *Highlights Sci. Eng. Technol.* 8, 454–462. doi:10.54097/hset.v8i.1192

Zhang, Z-Z., Jiang, D., Ding, J-X., Wang, S-J., Zhang, L., Zhang, J-Y., et al. (2016). Role of scaffold mean pore size in meniscus regeneration. *Acta Biomater.* 43, 314–326. doi:10.1016/j.actbio.2016.07.050

Zheng, R., Song, D., Ding, Y., Sun, B., Lu, C., Mo, X., et al. (2023). A comparative study on various cell sources for constructing tissue-engineered meniscus. *Front. Bioeng. Biotechnol.* 11, 1128762. doi:10.3389/fbioe.2023.1128762

Zhong, G., Yao, J., Huang, X., Luo, Y., Wang, M., Han, J., et al. (2020). Injectable ECM hydrogel for delivery of BMSCs enabled full-thickness meniscus repair in an orthotopic rat model. *Bioact. Mater.* 5 (4), 871–879. doi:10.1016/j.bioactmat.2020.06.008

frontiers | Frontiers in Bioengineering and Biotechnology

TYPE Original Research
PUBLISHED 07 December 2023
DOI 10.3389/fbioe.2023.1301454

OPEN ACCESS

EDITED BY
Lorenzo Fassina,
University of Pavia, Italy

REVIEWED BY
Livia Visai,
University of Pavia, Italy
Nora Bloise,
University of Pavia, Italy

*CORRESPONDENCE
Reza Sanaei,
reza.sanaei@unimelb.edu.au

RECEIVED 25 September 2023
ACCEPTED 27 November 2023
PUBLISHED 07 December 2023

CITATION
Sanaei R, Pagel CN, Ayodele BA, Lozanovski B, Beths T, Leary M, Shidid D, Kastrati E, Elambasseril J, Bühner U, Williamson T, Ryan S and Brandt M (2023), Reducing the prosthesis modulus by inclusion of an open space lattice improves osteogenic response in a sheep model of extraarticular defect. *Front. Bioeng. Biotechnol.* 11:1301454. doi: 10.3389/fbioe.2023.1301454

Reducing the prosthesis modulus by inclusion of an open space lattice improves osteogenic response in a sheep model of extraarticular defect

Reza Sanaei[1]*, Charles Neil Pagel[1], Babatunde A. Ayodele[1], Bill Lozanovski[2], Thierry Beths[1], Martin Leary[2], Darpan Shidid[2], Endri Kastrati[2,3], Joe Elambasseril[2], Ulrich Bühner[4], Tom Williamson[2,3], Stewart Ryan[1] and Milan Brandt[2]

[1]Melbourne Veterinary School, Faculty of Science, The University of Melbourne, Parkville, VIC, Australia, [2]RMIT Centre for Additive Manufacturing, RMIT University, Carlton, VIC, Australia, [3]Stryker Australia Pty Ltd., St Leonards, NSW, Australia, [4]Stryker Leibinger GmbH & Co., KG, Freiburg, Germany

Introduction: Stress shielding is a common complication following endoprosthetic reconstruction surgery. The resulting periprosthetic osteopenia often manifests as catastrophic fractures and can significantly limit future treatment options. It has been long known that bone plates with lower elastic moduli are key to reducing the risk of stress shielding in orthopedics. Inclusion of open space lattices in metal endoprostheses is believed to reduce the prosthesis modulus potentially improving stress shielding. However, no *in vivo* data is currently available to support this assumption in long bone reconstruction. This manuscript aims to address this hypothesis using a sheep model of extraarticular bone defect.

Methods: Initially, CT was used to create a virtual resection plan of the distal femoral metaphyses and to custom design endoprostheses specific to each femur. The endoprostheses comprised additively manufactured Ti6Al4V-ELI modules that either had a solid core with a modulus of ~120 GPa (solid implant group) or an open space lattice core with unit cells that had a modulus of 3–6 GPa (lattice implant group). Osteotomies were performed using computer-assisted navigation followed by implantations. The periprosthetic, interfacial and interstitial regions of interest were evaluated by a combination of micro-CT, back-scattered scanning electron microscopy (BSEM), as well as epifluorescence and brightfield microscopy.

Results: In the periprosthetic region, mean pixel intensity (a proxy for tissue mineral density in BSEM) in the caudal cortex was found to be higher in the lattice implant group. This was complemented by BSEM derived porosity being lower in the lattice implant group in both caudal and cranial cortices. In the interfacial and interstitial regions, most pronounced differences were observed in the axial interfacial perimeter where the solid implant group had greater bone coverage. In contrast, the lattice group had a greater coverage in the cranial interfacial region.

Conclusion: Our findings suggest that reducing the prosthesis modulus by inclusion of an open-space lattice in its design has a positive effect on bone

material and morphological parameters particularly within the periprosthetic regions. Improved mechanics appears to also have a measurable effect on the interfacial osteogenic response and osteointegration.

KEYWORDS

stress shielding, endoprosthesis, osteointegration, Ti6Al4V-ELI, lattice, additive manufacturing, load bearing

1 Introduction

Endoprosthetic reconstruction is one of the cornerstones of limb salvage surgery requiring extensive resection of bone. Current indications include osseous or soft-tissue tumors encroaching on bone, periprosthetic infections as well as the surgical management of arthritic and trauma patients (Hennessy et al., 2020). Based on current projections, by 2040, annual hip and knee replacement surgeries, in the US alone, are predicted to reach over 1.4 and 3.4 million respectively (Singh et al., 2019). Endoprostheses are commonly affected by complications such as mechanical and soft-tissue failure, periprosthetic infection and fractures as well as aseptic loosening, which may lead to subsequent revisions or limb amputation (Abu El Afieh et al., 2022). While the rate of complications associated with endoprostheses is not dissimilar to alternatives such as allogenic reconstructions (Albergo et al., 2017), it is beneficial to explore the possibility of limiting these adverse events. This is paramount especially when considering patients requiring chemo- and/or radiotherapeutic treatments who are at a higher risk of such complications (Novikov et al., 2019; Fujiwara et al., 2020; Abu El Afieh et al., 2022).

Early data suggests that altering the implant design to introduce porosity is the key to alleviating some of the risk (Ji et al., 2020; Guder et al., 2021). Effective incorporation of a surface lattice can improve post-operative soft-tissue and bone integration reducing surgical dead space and thus the risk of infection (Chen et al., 2009; Guder et al., 2021). The resulting improved soft tissue integration is thought to be associated with improved function and a reduced risk of soft tissue failure (Chen et al., 2009; Guder et al., 2021).

It has been suggested previously that titanium implants that incorporate open space lattice architectures in their design, have favorable osteoconductive properties, yielding excellent osteointegration when used in the reconstruction of long bones (Li et al., 2016; Crovace et al., 2020). Good quality osteointegration improves load sharing with the periprosthetic bone protecting the device from mechanical failure and premature loosening (Mavrogenis et al., 2009; Apostu et al., 2018; Ji et al., 2020). Moreover, the engineered porosity (if substantial) reduces device's elastic modulus, which has been suggested to result in enhanced osteogenesis and reduced stress shielding of the periprosthetic bone (Huiskes et al., 1992; Sumner and Galante, 1992; Nouri and Hodgson, 2010; Moghaddam et al., 2016; Caffrey et al., 2018). Stress shielding is a common complication of endoprosthetic reconstruction surgery and is significant not only because of associated surgical failure, but also due to the resulting periprosthetic osteopenia, which significantly limits future treatment options (Nagels et al., 2003; Tagliero et al., 2020; Braig et al., 2021; Cho et al., 2021; Bendich et al., 2022). Selecting an appropriate prosthesis modulus is crucial to achieving the best possible functional and long-term outcomes for patients with medical implants because it ensures that the mechanical properties of the artificial implant closely match those of the surrounding natural tissues and bones, preventing issues like stress shielding and subsequent implant loosening, or implant failure that may arise if the prosthesis is too rigid or too flexible compared to the natural tissue.

Notwithstanding this rationale, many legislative agencies around the world still do not allow for routine incorporation of lattices into implants due to a dearth of *in vivo* and clinical data on their effectiveness and safety. Thus, further research is required to establish the therapeutic profile and safety of this approach in the design and manufacturing of endoprostheses. This work was undertaken to test the hypothesis that reducing the prosthesis modulus by incorporating a three-dimensional (3D) open-space lattice into its core structure, will improve host osteogenic response in load bearing locations and prevent stress shielding of the periprosthetic bone. To our knowledge, there are no previous studies that have directly investigated this hypothesis using a controlled *in vivo* model in a long bone.

Here, we describe our findings following experimental reconstruction of distal femoral extraarticular defects in a sheep model where two distinct structural designs of different moduli are compared. A sheep model was selected due to the relatively large size of bones in sheep and thus similar biomechanics to humans. To overcome the challenges associated with surgical planning and fitting of highly customized and geometrically complex endoprostheses, bone resections were performed using a robot-assisted approach followed by manual fitting of the prostheses. Our research questions were:

(1) Is a reduction in prosthesis modulus associated with an improved quantity and quality of periprosthetic cortical bone?
(2) Is a reduction in prosthesis modulus associated with an improved osteointegration, i.e., quantity and quality of interfacial and interstitial bone?

2 Materials and methods

2.1 Animals

A total of nine 2-year-old castrated male Merino sheep (42–56 kg body weight on arrival) were used for this study which were housed and maintained in the animal house facility of the Melbourne Veterinary School, The University of Melbourne, Victoria, Australia. Sheep were kept in groups of maximum 4 animals per pen and provided with a once-a-day ratio of pellets. Dry hay and water were provided *ad libitum*. An

acclimatization period of at least 2 weeks was observed before subjecting the animals to any procedures. Four animals were randomly assigned to each of the two groups receiving either the solid- or lattice-core prostheses. Each holding pen contained a mix of sheep from both experimental groups. One of the animals in the lattice group was euthanized early on due to the incidence of a spiral fracture distal to the implant during the recovery period and had to be replaced by an additional animal (hence nine animals were used in total). The use of all animals in this study was approved by the Animal Ethics Committee of the Faculty of Veterinary and Agricultural Sciences, the University of Melbourne (Infonetica # 10442). All work was conducted in compliance with the Australian Code for the Care and Use of Animals for Scientific Purposes (2013).

Each animal was anaesthetized twice, once at the time of the initial CT scans for planning purposes and once at the time of surgery. All intravenous drugs and fluids were administered via an 18G over-the-needle catheter placed in a cephalic vein. For the surgeries, following an intravenous administration of midazolam (0.3 mg/kg), general anesthesia was induced using an intravenous bolus of propofol (4–6 mg/kg). A prophylactic antibiotic (cefazolin, 20 mg/kg IV) was administered at this time and repeated every 90 min thereafter. This was followed by IM administration of procaine penicillin G (15 mg/kg once daily) for 3 postoperative days.

Anesthetic maintenance was provided with isoflurane in oxygen (20–50 mL/kg/min) via an endotracheal tube. Intraoperative analgesia consisted of intravenous methadone (0.2 mg/kg) every 4 h, a constant rate infusion (CRI) of ketamine (10 mg/kg/min) and epidural morphine (0.1 mg/kg). The CRI was preceded by a bolus of ketamine (1 mg/kg, IV) at the time of surgical site preparation. The first dose of methadone was also given at this stage. At the end of the procedure and before turning off the isoflurane, a subcutaneous dose of meloxicam (1 mg/kg) was administered. A fentanyl patch (0.2 mg/kg/h) was placed on the antebrachium at this time and kept for 72 h. Following recoveries, animals were individually housed in a divided pen for 5 days (2 animals per pen) before being returned to the flock. Further postoperative pain management was provided by buprenorphine (0.01 mg/kg IM q12 h) and meloxicam (1 mg/kg PO q24 h) for a total of 5 days. Sheep were provided with a rubber matting postoperatively for the duration of the study.

The anesthesia protocol for the planning CT scans were similar to the surgeries, but methadone was replaced with butorphanol (0.2 mg/kg IV) with no further intraprocedural or postprocedural analgesia. All animals were subjected to intravital fluorochrome labelling of bone using alizarin red (25 mg/kg IV) and calcein (10 mg/kg IV), 20 and 5 days respectively before being euthanized at 12 weeks. Euthanasia was performed by a lethal IV administration of pentobarbital.

2.2 Imaging and pre-planning

For each animal, computed tomography (CT) using a Siemens Somatom Emotion 16 (Siemens Healthineers, Germany) was used to scan the right hind limbs. The CT images were then used to create a representative 3D map of the distal femur in a custom surgical planning software based on the MITK framework (DKFZ, Germany). A "reference" plan was created based on an average femoral bone geometry (lateral aspect), on which a curved osteotomy geometry was defined. For each sheep, the generated femur geometry was aligned to the reference plan, as to create a curvilinear lateral metaphyseal defect that was identical in all 9 femora (one sheep was excluded from the study due to a postoperative fracture).

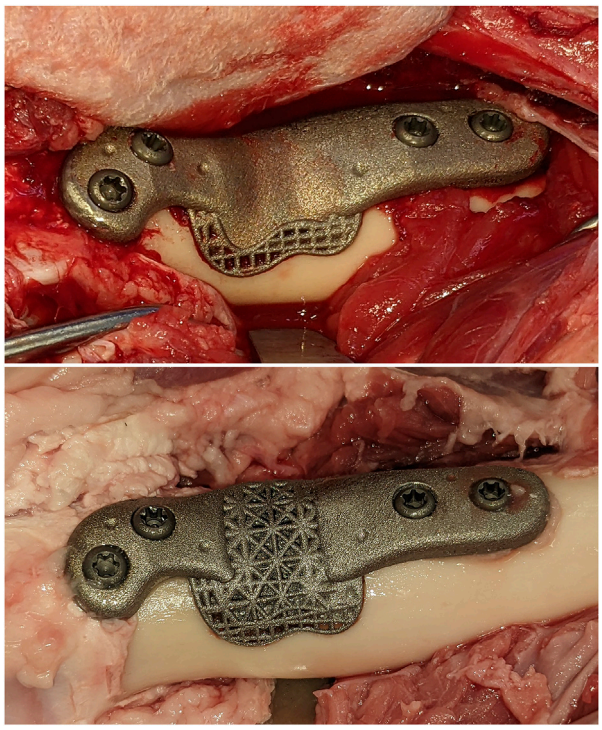

FIGURE 1
The solid and open-lattice prostheses within the surgically created defects. An identical interfacial lattice was incorporated into the bone facing aspects of both prosthesis designs.

2.3 The design of the endoprostheses

Two types of endoprostheses were used in this study. Both designs had an identical convex bone interface matching the curvature of the pre-planned osteotomies. The curvature of the interface tapered into a proximal and distal flange each accommodating two fixation screws (total of 4 screws) resembling a bone plate with an expanded middle segment (Figure 1). The implants were designed to either have a solid core with a unit cell size of 2 mm as interfacial lattice (which faced the bone defect) or a lattice core within an identical interfacial lattice. The core lattice consisted of a gradient face-centered cubic with z-strut (FCCZ) lattice structure with a unit cell size of 4 × 4 × 4 mm. The surface-intersecting unit cells were modified to fit the geometric boundaries of the core. Strut diameter was linearly graded (0.7 mm–0.325 mm) as to avoid strut distortion from an excessive thermal gradient at the points of their connection with the flanges and to avoid stress concentrations when under loading. The interfacial lattice comprised a FCCZ lattice structure with a unit cell size of 2 × 2 × 2 mm. The strut diameter had a similar

gradient (0.7 mm–0.325 mm in diameter). The solid core was estimated to have a 120 GPa modulus whereas the unit cells of the lattices had a 3–6 GPa modulus. For reference, the modulus of the ovine femur is about 22 GPa (Erickson et al., 2002).

Each endoprosthesis was additively manufactured out of Ti6Al4V-ELI (grade 23 titanium) powder in a SLM®125 machine (SLM Solutions, Germany) using a layer thickness of 30μm, scan speed of 375 mm/s, laser power of 100 W and a hatch distance of 130 μm. Following the manual removal of all support beams and a light deburring, implants were cleaned by dry-ice blasting (60 s per side). Further cleaning was performed using three 1-h cycles of ultrasonic cleaning in deionized water at 80°C and a diluted alkaline cleaning solution (Micro-90®, Cole-Parmer®, Illinois, United States). Each cycle was followed by a rinse in deionized water and submersion in a fresh batch of water and detergent. A fourth and final 1-h cycle in deionized water concluded the post-processing of implants.

2.4 Robotic resection and implantation

Surgical access to the distal femur was achieved via a lateral approach. To synchronize the pre-planned resection map with the actual bone, intra-operative registration was carried out to link four identifiable landmarks (medial and lateral condyles, trochlear groove, and part way up the femoral shaft) with corresponding fiducial points in the virtual 3D map of the same animal using a custom software. This was followed by the surgeon "painting" the surface of the bone with 50–150 additional fiducial points for the iterative closest point (ICP)-based final registration. Following registration and robotic osteotomies, prostheses were manually fit into each defect. Two 3.5 mm cortical screws (Stryker AxSOS 3 3.5 mm cortex screw, self-tapping, Stryker, United States) were used proximally, and two 4 mm trabecular screws (Stryker AxSOS 3 4.0 mm cancellous screw, full thread self-tapping, Stryker, United States) were used distally to secure each implant (Figure 1). The surgical site was then irrigated and closed in multiple layers. We set and adhered to a 2-week time limit for the whole process, from the planning CT to implantations, to simulate the realistic requirements of a clinical setting.

2.5 Microcomputed tomography

Following euthanasia at 12 weeks, femora were resected *en bloc* following perfusion fixation with 10% neutral buffered formalin (NBF) through a femoral artery catheter. Samples were defleshed as necessary, downsized and subjected to further fixation by submersion in 10% NBF for 7 days. Next, samples were washed using 3 changes of PBS while being agitated on a shaking plate (<60 RPM) for a total of 2 h. They were then placed in 50% ethanol at 4°C for 3 nights before being transferred to 70% ethanol. Micro-computed tomography (micro-CT) was performed using a Phoenix v|tome|x s240 CT system (GE Research, New York, USA) at an isometric resolution of 34.5 μm/voxel, with a peak voltage of 180 kV, current of 130 μA, integration time of 500 m, frame averaging of 3, image skip of 2, and a copper filter of 0.1 mm to reduce beam hardening. Datasets were rotated and cropped based on consistent

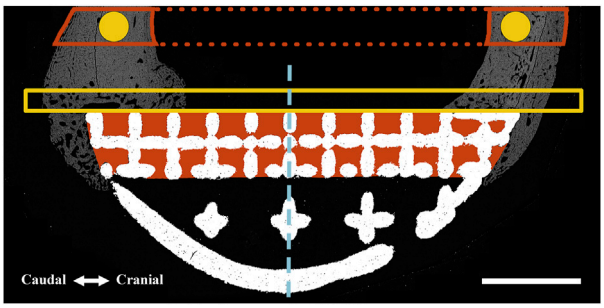

FIGURE 2
Regions of interest (ROIs) were defined for one-dimensional (perimeter) and two-dimensional (surface area and pixel density) measurements using an identical method for both BSEM (shown) and brightfield microscopy images. A similar method was used for volumetric analyses using micro-CT datasets (where measurements were performed). The interfacial ROI demarcated by the yellow box spanned the axial perimeter of the implant and extended for an extra 3 mm in both caudal and cranial directions and measured 1 mm in width. This region was further divided into cranial (Cr.Ax) and caudal (Cd.Ax) ROIs (dashed line depicts border). To take account of the periosteal reaction, the small caudal and cranial perimeters of the interfacial lattice were also analyzed; each started from the respective caudal or cranial end of the implant to the corresponding abaxial extent of the interfacial lattice. Area shaded in red depicts the interstitial ROI drawn by tracing the interior of the interfacial lattice. These ROIs were divided into cranial (Cr) and caudal (Cd) parts and were separately analyzed (dashed line depicts border). In the case of the full-lattice prostheses, a second interstitial ROI was defined by tracing the abaxial open lattice. The latter did not have an equivalent ROI in the solid prosthesis. The highlighted circles (1.5 mm in diameter) are periprosthetic ROIs (5 mm away from the prostheses) within the center of the original caudal and cranial cortices ignoring the periosteal and endosteal calluses. The full thickness of the caudal and cranial periprosthetic cortices were also traced (new cortex) and separately analyzed. Marrow diameter was measured within the area depicted by the dotted red lines. Scale bar equals 5 mm.

landmarks in DataViewer version 1.5.6.2 64-bit (Bruker Micro CT, Aartselaar, Belgium) before being imported into CT Analyzer software version 1.13.11.0 (Bruker Micro CT, Aartselaar, Belgium Bruker, RRID:SCR_021338) for analysis. Volumes of interest (VOIs) were defined within the caudal and cranial periprosthetic cortices using similar criteria as those shown for histomorphometry in Figure 2. Due to the presence of metal related artefacts, the interfacial and interstitial VOIs were deemed unsuitable for quantitative analysis.

2.6 Histological processing

Following micro-CT, dehydration was carried out at 4°C using graded concentrations of ethanol with 15 min of vacuum applied after each change to remove trapped air bubbles. Dehydration took a total of 5 weeks. Clearing was performed using two changes of toluene for a total of 7 days. Samples were embedded using a modified method previously described (Emmanual et al., 1987). Briefly, cleared samples were infiltrated with the thin methyl methacrylate (MMA) solution (destabilized MMA + 1% dibutyl phthalate + 0.05% [w/v] benzoyl peroxide) for 3 weeks followed by the thick MMA solution (destabilized MMA + 1% dibutyl phthalate + 3% [w/v] benzoyl peroxide) before being polymerized at 15°C.

Polymerized blocks were incubated overnight at 35°C and 40°C on separate days before further processing.

Embedded samples were orientated and trimmed as necessary to allow reproducible identification of sample landmarks and the proximal and distal limits of the implants. Further trimming was performed to remove the medial cortices. Blocks were marked at 2 mm intervals starting proximally at the level of the first screw closest to the center (histological section 1) all the way to the level of the corresponding screw in the distal flange (histological section 9). Blocks were glued to chucks and cut perpendicular to the long axis of bone using an IsoMet low speed saw (Buehler, Illinois Tool Works Inc., IL, United States) fitted with an IsoMet precision blade (IsoMet Blade, 15HC, 127 mm). Sections selected for brightfield, and fluorescence microscopy (histological sections 3, 5, 8) were glued to plexiglass and ground to a 50 µm thickness on a series of silicone carbide sandpapers and diamond suspensions using a custom-built planar microgrinder (Sanaei, 2023). Prepared sections were polished using diamond suspensions on polishing cloths using the same setup. When backscattered electron microscopy (BSEM) was intended (histological sections 4, 6), 2 mm blocks were ground until planar followed by polishing and carbon coating.

2.7 Microscopy

Sections prepared for BSEM were coated with a 20 nm carbon layer under a high vacuum (Safematic CCU-010 HV, Safematic Switzerland). BSEM images were obtained using a backscattered detector and electron beam setting of 10 kV voltage and 20 nA current at 10 mm working distance and 300X magnification (FEI Teneo Volumescope, Thermo Fisher Scientific, Hillsboro, OR, United States). BSEM image tiles were stitched using MAPS (ThermoFisher Scientific, MA, United States, RRID:SCR_024446). Stitched image files were downsized eighty percent for further analysis.

To identify the fluorochrome labels (histological sections 5, 8), unstained sections were scanned using the ×10 objective lens in a ZEISS Axioscan 7 slide scanner (Carl Zeiss AG, Oberkochen, Germany). FITC and Cy3 filters were used to detect calcein and alizarin labels respectively. Brightfield microscopic images (histological sections 3, 5, 8) were obtained following Masson-Goldner staining using the ×10 objective lens in the same slide scanner.

2.8 Static histomorphometry

ImageJ (National Institutes of Health, Bethesda, MD, United States, RRID:SCR_003070) was used for morphometric analysis of prepared BSEM and brightfield images by first defining standardized regions of interest (ROIs) within the periprosthetic, interfacial (bordering the implant) and interstitial regions (within implant pores) as shown in Figure 2. Bone area fraction and porosity were measured following segmentation of bone tissue as previously described (Dempster et al., 2013). Pixel intensity of bone tissue within each ROI (BSEM) was measured following identification by segmentation and expressed as cortical density (Ct.Dn). The percentage of implant surfaces spanned by bone tissue was also determined for the axial (facing the long axis of bone) as well as caudal and cranial interfacial perimeters (Figure 2).

2.9 Dynamic histomorphometry

Dynamic histomorphometry using the fluorescent labels alizarin red (red) and calcein (green) was performed to determine the extent and rates of mineralization and bone formation in the interfacial and interstitial ROIs shown in Figure 2 using histological sections 5, 8. Fluorescent images from each of the regions of interest were imported into ImageJ. Random fields from each ROI were exported as Tiff files after merging red and green channels, which were read into OsteoMeasure System, Version 4.10 (OsteoMetrics, Decatur, GA, USA, RRID:SCR_024447). The total bone surface, along with the bone surfaces labelled with either alizarin red or calcein (single labelled surfaces; sLS) and the bone surfaces labelled with both alizarin red and calcein (double labelled surfaces; dLS) were traced for each ROI. The dynamic histomorphometric parameters were derived by the OsteoMeasure software from the primary indices using the standard ASBMR nomenclature (Dempster et al., 2013).

2.10 Statistics

All measurements were performed by blinded operators where possible. Data analysis was performed by a different group of authors than those who conceptualized, allocated animals or ran the experiments. SPSS Statistics version 28 (IBM Corp©, Armonk, NY, United States, RRID:SCR_016479) was used for all analyses. Graphs were prepared using the Python (RRID:SCR_008394) data visualization libraries, Matplotlib and Seaborn (Hunter, 2007; Waskom et al., 2017). For each variable, the group means were compared using an Independent Samples *t*-Test. No significance threshold was set due to the exploratory nature of this work, a small sample size ($n = 4$) and current recommendations (Leopold and Porcher, 2017; Amrhein et al., 2019; Vail and Avidan, 2022). For effect size, Hedge's g is reported which has been automatically corrected for the small sample size bias by SPSS Statistics. An effect size < 0.2 was considered small, > 0.5 was considered moderate and > 0.8 was considered large. Standard Error of Mean and Standard Error of Difference have been presented in graphs and tables respectively.

3 Results

Other than the one sheep that sustained a fracture during the immediate postoperative period, the recoveries were without incident. All animals were fully weight bearing on the operated limb within 2–3 weeks of surgeries. All prostheses were highly stable and well-integrated into the host bone during histological preparations and downsizing. The periosteal callus was usually more pronounced in the caudal region except for one animal in the solid implant group where it was more pronounced in the cranial region. In one case (lattice implant group), an ossicle was found within the caudal region which might have been caused by the lodgment of bone chips and particles produced at the time of osteotomies (osteotomies were always accompanied and followed by irrigation).

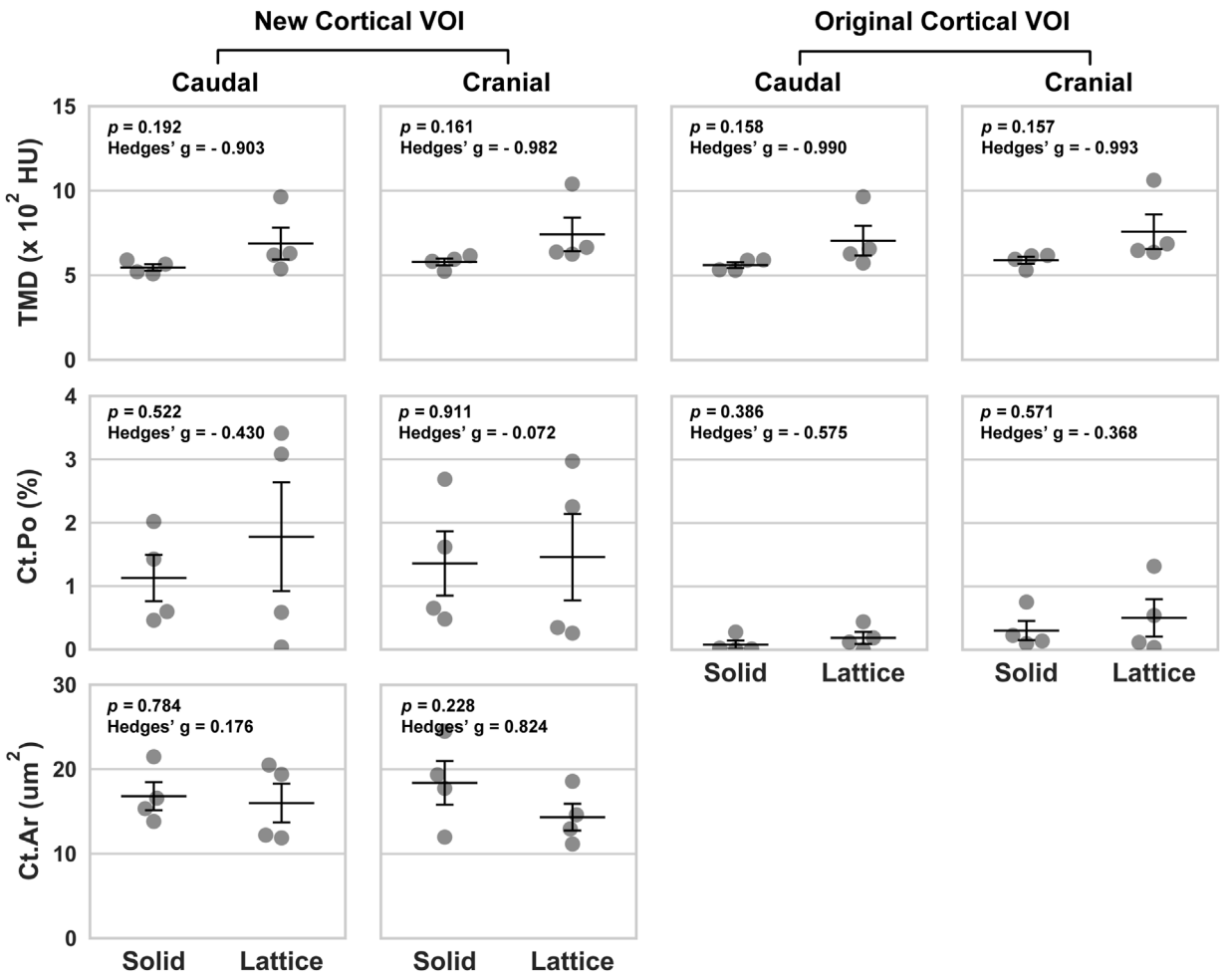

FIGURE 3
Volumetric data based on four periprosthetic VOIs following micro-CT imaging. The VOIs were defined using similar landmarks to those used for BSEM and brightfield analyses (Figure 2). Original cortical VOIs are a subset of the new cortical VOIs. Cortical area (Ct.Ar) was calculated by dividing the primary cortical bone volume values (Ct.V) by stack height (voxel size X number of slices per stack). As such, the presented Ct.Ar is a 3D driven index and is used as a proxy for the single dimensional cortical thickness (Bouxsein et al., 2010). TMD, tissue mineral density; Ct.Po, cortical porosity; $n = 4$; error bars represent SEM.

3.1 Periprosthetic ROIs

3.1.1 Micro-CT

Data from the caudal and cranial periprosthetic VOIs is presented in Figure 3. The main differences observed between the two groups related to bone material density measurements (tissue mineral density; TMD). TMD appeared to be higher in the lattice group in all four caudal and cranial VOIs when compared to the control solid implant group. However, while similar between the two groups in the caudal VOI, cortical area (Ct.Ar) appeared to be lower in the cranial VOI of the lattice group.

3.1.2 Back-scattered SEM

Back-scattered scanning electron microscopy (BSEM) was used to evaluate the periprosthetic cortical ROIs within histological section 4 (section 6 images shown in Figure 4). Analysis of pixel greyscale intensities (used as a proxy for cortical mineral density; Ct.Dn) indicated that here too, the lattice group had higher values in all 4 periprosthetic ROIs which was however only notable in histological section 6 (Figures 5A, B). Interestingly, cortical porosity (Ct.Po) values complemented this finding, being lower in the lattice group, this time, only in histological section 4 (Figure 5). Cortical thickness (Ct.Th), like micro-CT, appeared to be lower in the cranial cortex of the lattice implant group in histological section 4 with similar values in all other three ROIs.

3.2 Osteointegration: interfacial ROIs

To evaluate the effect of reduced modulus on osteointegration, interfacial ROIs (Figure 2) were histologically assessed and various area and perimeter as well as dynamic indices measured (Tables 1, 2). Static parameters were measured using BSEM images from histological sections 4 and 6 as well as Masson-Goldner-stained histological sections 3, 5 and 8 (section 3 images shown in Figure 6). Where BSEM was used, pixel intensity is also reported. Histological section 3 was only used for perimeter measurements. Osteoid measurements

10.3389/fbioe.2023.1301454

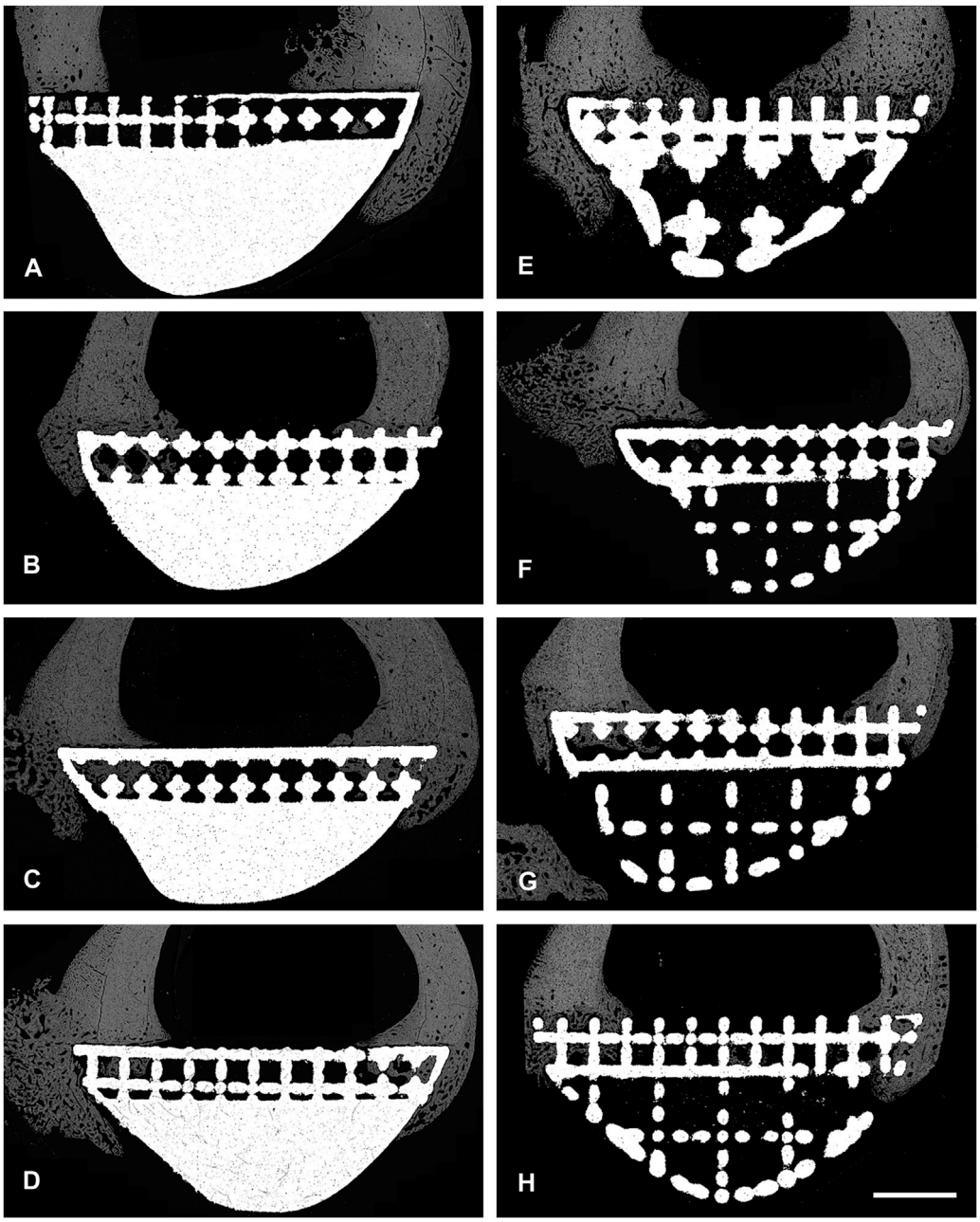

FIGURE 4
BSEM images from histological section 6. Grey signal indicates mineral. Cranial cortex is to the right side of each image. **(A–D)** solid implant group. **(E–H)** lattice implant group. Scale bar = 5 mm.

were only completed for histological section 5. Dynamic histomorphometry was completed for histological sections 5 and 8.

Histology showed that the interfacial lattices in both implant groups were overall in contact with the host bone, marrow or fibrous tissue depending on location. Periosteal and endosteal callus was being remodeled and replaced with mature lamellar bone. A fibrous tissue capsule was found surrounding all abaxial surfaces which was continuous with the callus and occasionally continued onto the axial interface of the implants (facing the osteotomy defects). In many areas, evidence of intramembranous ossification could be seen at the interface of this layer and the newly formed bone. In some areas of the implant site, calcified cartilage was observed, indicating the presence of endochondral ossification in the newly formed bone. There was no evidence of inflammation or foreign body reaction in any of the sections.

While many indices were similar between the two groups, it was found that the axial interfacial perimeters were more thoroughly covered by bone in the solid implant group in histological sections 3 and 8 (Table 1). The cranial interfacial perimeters, on the other hand, were more extensively spanned by bone in the lattice implant group in histological section 8. Of the dynamic derived parameters, while mineral apposition rate (MAR) was higher in the lattice implant group, statistical analysis remained unequivocal (Table 2).

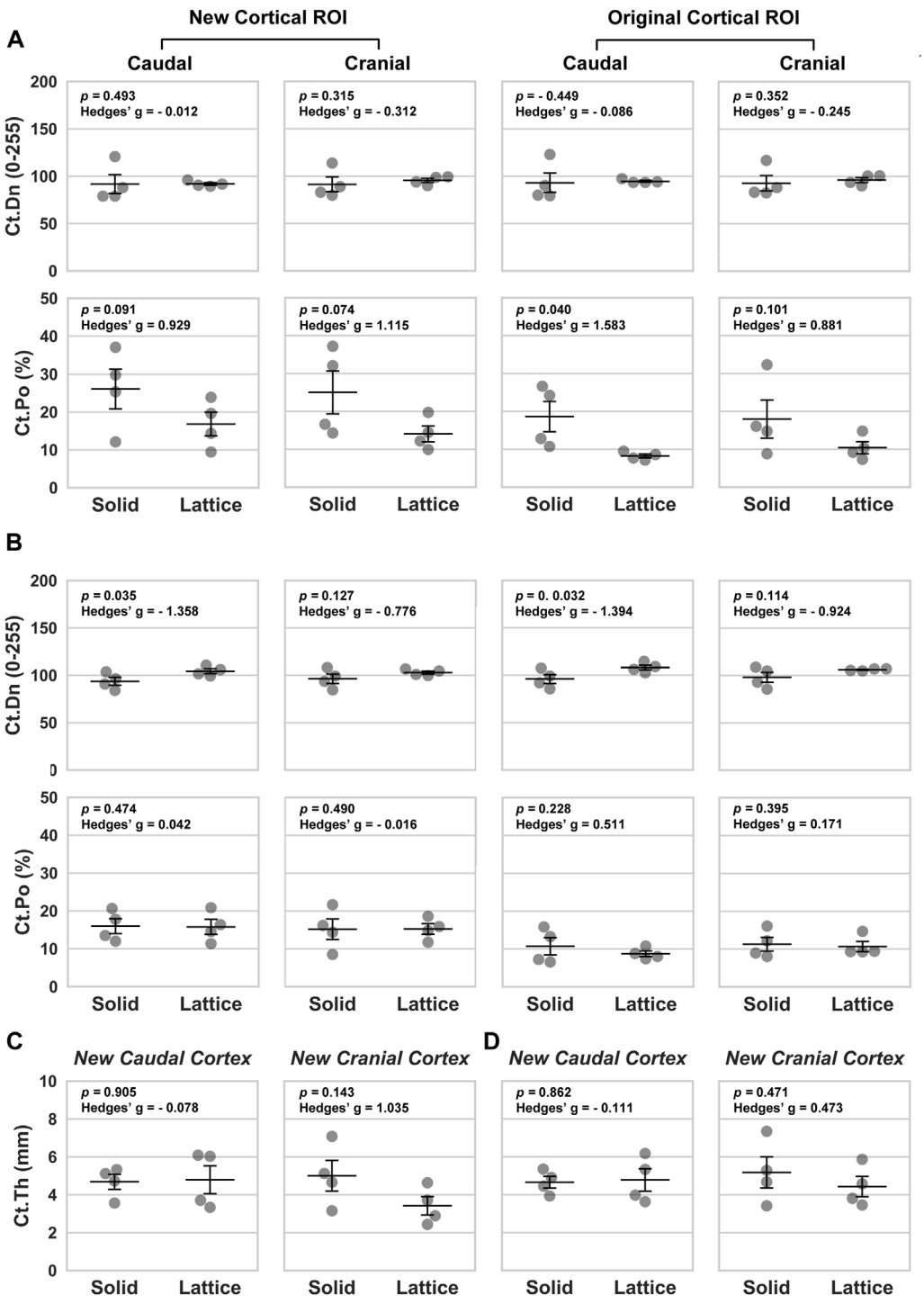

FIGURE 5
Morphological parameters based on four periprosthetic ROIs defined for BSEM images. **(A, C)** Data from histological section 4. **(B, D)** Data from histological section 6. Ct.Dn, cortical density; Ct.Po, cortical porosity; Ct.Th, cortical thickness. Data analyzed using a one-tailed Independent Samples *t*-Test; Hedges' g values indicate effect size; $n = 4$; error bars represent SEM.

3.3 Osteointegration: interstitial ROIs

Static histomorphometry was performed for histological sections 4, 5 and 6 (Table 3). Dynamic histomorphometry was performed for histological sections 5 and 8 (Table 4). Our analyses did not point to any clear differences between the two groups here. Evidence of bony ingrowth into the core of the lattice implant group was apparent in 3 instances across 2 sections that were evaluated for this purpose. This could not be directly compared with the solid group for obvious reasons.

10.3389/fbioe.2023.1301454

TABLE 1 Comparison of derived static interfacial parameters between the lattice and solid implant groups.

Index	Section/ ROI	Two-tailed p	Hedges' g[a]	Mean difference[a]	Std. Err of diff	Lower 95% CI of diff	Upper 95% CI of diff
B.Ar/T.Ar (%)	4/Cd.Ax	0.406	−0.55	−14.55	16.3	−54.43	25.32
	5/Cd.Ax	0.419	−0.53	−9.21	10.62	−35.19	16.77
	6/Cd.Ax	0.963	−0.03	−0.27	5.65	−14.09	13.55
	4/Cr.Ax	0.060	0.05	0.6	7.69	−18.21	19.4
	5/Cr.Ax	0.542	0.40	5.98	9.25	−16.66	28.61
	6/Cr.Ax	0.397	0.56	5.54	6.07	−9.32	20.4
	5/Cd.Ax	0.327	−0.66	−14.15	13.25	−46.58	18.27
	5/Cr.Ax	0.852	−0.12	−2.33	11.94	−31.54	26.88
Bone Density (0–255)	4/Cd.Ax	0.772	0.19	2.61	8.61	−18.45	23.67
	6/Cd.Ax	0.255	−0.77	−5.86	4.66	−17.25	5.54
	4/Cr.Ax	0.932	−0.06	−0.69	7.7	−19.54	18.16
	6/Cr.Ax	0.302	−0.69	−4.66	4.13	−14.75	5.44
Perimeter Spanned by Bone (%)	3/Ax	0.015	2.08	16.41	4.84	4.56	28.27
	4/Ax	0.685	0.26	5.74	13.46	−27.19	38.67
	5/Ax	0.840	−0.13	−2.81	13.35	−35.49	29.87
	6/Ax	0.711	0.24	5.08	13.06	−26.89	37.05
	8/Ax	0.296	0.703	22.24	19.43	−25.31	69.80
	3/Cd	0.222	−0.84	−31.22	22.90	−87.26	24.82
	4/Cd	0.834	−0.14	−11.46	51.11	−153.92	131.01
	5/Cd	0.214	−0.85	−35.90	25.86	−99.18	27.37
	6/Cd	0.599	0.34	20.27	36.54	−69.15	109.69
	8/Cd	0.391	0.61	3.52	3.52	−7.68	14.72
	3/Cr	0.599	−0.34	−20.86	37.61	−112.90	71.17
	4/Cr	0.581	0.36	32.55	55.81	−104.02	169.11
	5/Cr	0.904	−0.08	−4.14	33.02	−84.93	76.65
	6/Cr	0.785	−0.18	−21.12	73.92	−201.98	159.75
	8/Cr	0.037	−1.64	−64.65	24.18	−123.81	−5.48

[a]Negative values indicate higher lattice values.
Ax, axial; Cd, caudal; Cr, cranial; Cd.Ax, caudal axial ROI; Cr.Ax, cranial axial ROI.

4 Discussion

Our study reveals that that at the 12-week mark post-surgery, both open-lattice and solid core prostheses remain intact and are well integrated with the host tissues largely to the same extent. This points to a favorable characteristic of titanium lattices that when strategically incorporated into endoprostheses, can help minimize surgical dead space and improve both bone and soft tissue integration (research question 2). Notably, the results of our analyses suggest that modifying the prosthesis modulus of elasticity has a measurable effect on the periprosthetic and interfacial bone. The incorporation of an open lattice structure to minimize the implant modulus effectively reduces stress shielding of the surrounding bone, as predicted (research question 1).

Overall, the small sample size made statistical interpretations challenging. We have reported all *p* values in conjunction with the corresponding effect sizes (Hedge's g) and have avoided flagging any results as statistically significant or otherwise as suggested by other groups (Leopold and Porcher, 2017; Amrhein et al., 2019; Vail and Avidan, 2022). We felt that this is appropriate due to the exploratory nature of this work and the small group size that would have led to a high risk of type II errors (Leopold and Porcher, 2017; Amrhein et al., 2019; Vail and Avidan, 2022). In this respect, the effect sizes should be paid special attention to. Given the early evaluations

TABLE 2 Comparison of dynamic interfacial parameters between the lattice and solid implant groups.

Index	Section #	Two-tailed p	Hedges' g[a]	Mean difference[a]	Std. Err of diff	Lower 95% CI of diff	Upper 95% CI of diff
sL/BS (%)	5	0.894	−0.08	−1.50	10.83	−28.01	25.01
	8	0.349	0.62	16.92	16.66	−23.86	57.69
dL/BS (%)	5	0.495	0.45	4.00	5.50	−9.46	17.46
	8	0.270	0.77	7.83	6.21	−8.75	24.41
MAR (μm/day)	5	0.157	−0.99	−0.58	0.36	−1.47	0.30
	8	0.42	−0.58	−9.54	10.12	−41.74	22.66
BFR (μm/day)	5	0.518	−0.42	−0.05	0.08	−0.24	0.13
	8	0.499	−0.47	−0.36	0.47	−1.84	1.12
BFR/BS (μm^3/μm^2/day)	5	0.794	−0.17	−0.00	0.01	−0.03	0.03
	8	0.526	−0.41	−0.02	0.03	−0.09	0.05

[a]Negative values indicate higher lattice values.

(12 weeks), and considering the reported effect sizes, these results are indeed promising.

4.1 The periprosthetic ROIs

Our micro-CT and BSEM evaluations suggest that the periprosthetic cortices in the lattice implant group had a higher mineral density/pixel intensity than the equivalent regions in the solid implant group. BSEM-derived porosity measurements complemented this finding, being lower in the lattice implant group. Micro-CT-derived porosity, nevertheless, did not appear to follow any meaningful patterns. To resolve this conflict, it must be noted that micro-CT of large metallic implants is frequently affected by photon starvation and beam hardening artefacts, which was also the case in our study so much so that we were unable to use our datasets for the purpose of interfacial and interstitial evaluations without risking significant error. BSEM, on the other hand, has far greater resolution and is not at all impacted by the presence of metals. As such, more weight is placed on BSEM-derived porosity measurements in interpreting the results. Specifically, in the caudal cortex, one of the two sections evaluated by BSEM showed markedly higher mean pixel intensity (a proxy for tissue mineral density) in the lattice implant group, indicating denser bone formation (p = 0.035, Hedges' g = −1.358). Additionally, both caudal and cranial cortices in one of the two evaluated sections exhibited lower porosity in the lattice implant group (caudal: p = 0.091, Hedges' g = 0.929; cranial: p = 0.074, Hedges' g = 1.115). Furthermore, the central ROI within the caudal cortex, excluding the callus, also showed less porosity in the lattice implant group (p = 0.040, Hedges' g = 1.583). These findings suggest that the lattice implant's open structure may contribute to greater bone density and reduced porosity, potentially indicating improved bone integration and remodeling around the implant site.

The above-mentioned differences in pixel intensity and porosity support our hypothesis that an implant with a lattice architecture and thus lower modulus shares more load with the host bone and therefore stimulates the osteogenic response when compared to a similarly designed higher modulus solid implant. This notion is in accord with previous studies describing the effects of stress shielding associated with bone plates (Tonino et al., 1976; Moyen et al., 1978; Uhthoff and Finnegan, 1983; Uhthoff et al., 1993).

A perplexing aspect of our findings was the observed differences between the cranial and caudal VOIs/ROIs. Importantly, despite bone density and porosity differences supporting our hypothesis, the cranial periprosthetic Ct.Ar (micro-CT) and Ct.Th (BSEM–histological section 4) values were smaller in the lattice implant group in comparison to the control group. Previously, a biomechanical study by Woo et al. proposed that bone plate induced stress shielding manifests in the form of cortical thinning rather than diminished mechanical properties of the bone tissue *per se* (Woo et al., 1976). It must, however, be noted that based on current understanding, the latter characteristic is attributed to bone mineralization and bone porosity (Hart et al., 2017), both of which allude to the onset of a gradual bone loss in the solid implant group in our study. Contrary to the conclusion proposed by Woo et al., other experimental results confirm our opinion that porosity is a key variable that increases by stress shielding (Tonino et al., 1976; Moyen et al., 1978; Uhthoff and Finnegan, 1983; Uhthoff et al., 1993). Bone mineralization is also thought to respond to strain based on available data (Skedros et al., 1994; Isaksson et al., 2009).

Under physiological conditions, the disparities in loading conditions between different regions in bone often result in regional differences in cortical thickness, structural organization and/or mineralization (Skedros et al., 1994; Skedros et al., 2019). Of note, the natural curvature of the femur in this distal location results in the generation of eccentric axial compression and bending when loaded during normal weight bearing and locomotion exposing the caudal and cranial cortices to compressive and tensile strains respectively. The current observation that the cranial cortex was thinner in the lattice implant group than the solid implant group may be partially explained if one assumes a more pronounced host response to compressive than tensile strains. Zhong et al. have previously shown that *in vitro*, compressive strains are significantly more potent than tensile strains in stimulating Wnt

10.3389/fbioe.2023.1301454

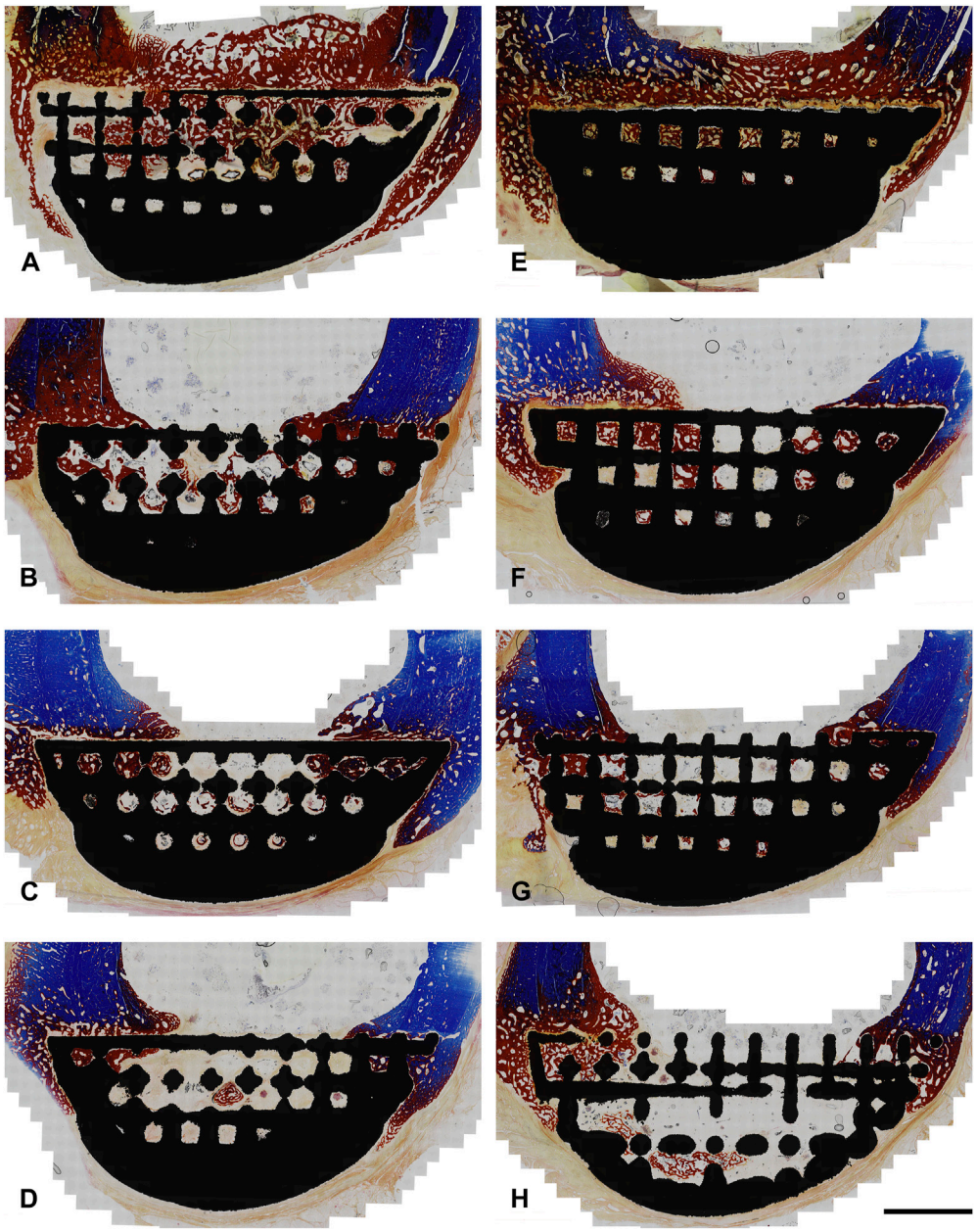

FIGURE 6
Photomicrographs from histological section 3 (Masson-Goldner Trichrome; original magnification ×10). Sections are from the boundary between the interfacial lattice and the implant core (lattice core is exposed in the bottom right image). Regions stained in blue are mineralized bone whereas regions stained in red are either osteoid or bone tissue that is partially mineralized. Cranial cortex is to the right side of each image. **(A–D)** solid implant group; **(E–H)** lattice implant group. Scale bar equals 5 mm.

signaling in osteoblasts (Zhong et al., 2013). Wnt signaling is a well-known pro-osteoblastic pathway that positively regulates bone formation and accrual (Kim et al., 2013).

That said, it has been suggested that in the sheep tibia, loading-induced regional changes in bone mass are not closely linked to local strain magnitude and as such inference of functional loading history from bone shape should be done judiciously (Wallace et al., 2014). It is also possible that the complex contour of the prostheses used here introduces a different strain distribution pattern to these assumptions. Callus buttressing is another factor that should be considered when interpreting these results. All femora evaluated had a more extensive callus caudally. It must be also noted that from the viewpoint of biomechanics, a sole reduction in cortical thickness or area can sometimes be associated with an increase in flexural and torsional rigidity (Uhthoff et al., 1993). As we did not complete a mechanical study, this remains to be determined by future investigations. Finite element analysis may also be useful to shed light on these findings.

TABLE 3 Comparison of derived static interstitial parameters between the lattice and solid implant groups.

Index	Section/ ROI	Two-tailed p	Hedges' g[a]	Mean difference[a]	Std. Err of diff	Lower 95% CI of diff	Upper 95% CI of diff
B.Ar/T.Ar (%)	4/Cd	0.633	−0.31	−4.09	8.13	−24	15.81
	5/Cd	0.684	−0.26	−3.88	9.06	−26.05	18.29
	6/Cd	0.475	−0.47	−4.01	5.26	−16.89	8.87
	4/Cr	0.422	−0.53	−5.47	6.34	−20.98	10.05
	5/Cr	0.840	0.13	1.02	4.81	−10.75	12.78
	6/Cr	0.350	−0.62	−3.96	3.91	−13.54	5.61
O.Ar/B.Ar (%)	5/Cd	0.430	−0.56	−1.74	1.92	−7.80	4.32
	5/Cr	0.999	0.00	−0.01	10.56	−25.84	25.83
Bone Density (0–255)	4/Cd	0.608	0.33	3.75	6.95	−13.24	20.75
	6/Cd	0.284	−0.72	−3.52	2.99	−10.85	3.8
	4/Cr	0.960	0.03	0.33	6.35	−15.21	15.88
	6/Cr	0.660	−0.28	−1.53	3.31	−9.62	6.56

[a]Negative values indicate higher lattice values.
Cd, caudal; Cr, cranial.

TABLE 4 Comparison of dynamic interstitial parameters between the lattice and solid implant groups.

Index	Section #	Two-tailed p	Hedges' g[a]	Mean difference[a]	Std. Err of diff	Lower 95% CI of diff	Upper 95% CI of diff
sL/BS (%)	5	0.689	−0.26	−9.78	23.27	−66.72	47.15
	8	0.222	0.93	32.69	21.56	−34.02	99.40
dL/BS (%)	5	0.645	0.30	4.45	9.18	−18.02	26.91
	8	0.349	0.62	7.49	7.37	−10.55	25.53
MAR (μm/day)	5	0.626	−0.32	−0.65	1.24	−4.09	2.78
	8	0.222	0.84	1.82	1.33	−1.44	5.08
BFR (μm/day)	5	0.543	−0.40	−0.07	0.10	−0.36	0.27
	8	0.209	0.86	0.14	0.10	−0.11	0.40
BFR/BS (μm^3/ μm^2/day)	5	0.599	−0.34	−0.01	0.01	−0.04	0.03
	8	0.273	0.74	0.01	0.01	−0.01	0.03

[a]Negative values indicate higher lattice values.

4.2 Osteointegration

Evaluation of the interfacial ROIs seemed to indicate that osteointegration varied slightly across the interface; a better bone-prosthesis contact was observed in the axial perimeter for the solid implant group and in the cranial perimeter for the lattice implant group. No difference was observed between the two groups within the interstitial ROIs though the lattice core allowed for some bone ingrowth which could be considered an advantage of this design. While the difference in modulus and the resulting change in mechanics can help explain the subtle differences observed, the presence of an identical interfacial lattice in both prosthesis designs may be the key in understanding these findings. This interfacial lattice was included in both designs to take advantage of osteointegration and better load sharing in both groups hence a more relevant comparison. Variation of congruence at implant-bone interface is a well-known issue impacting the validity of research on the biomechanics of bone plate-type implants (Pilliar et al., 1979; Uhthoff et al., 1993). Having a similar interface across the groups also enabled us to assess the effect of modulus on osteointegration. This, however, has likely minimized the gap between the two groups as the interfacial lattice has a lower modulus than the solid core. Thus, a modulus gradient in the solid prosthesis is expected with lower modulus aspects being in direct contact with the host bone which can explain the observed overall similarities between the two groups in this region.

4.3 Limitations

Other than the small sample size, the similarity between the two implant designs, both having an identical interfacial lattice, can be considered a limiting factor in the current model as discussed before. Additionally, this study includes observations following a 12-week period. This is a short timeline considering the permanent nature of endoprostheses in an actual clinical setting. We based our 12-week time point for this study on the report that most of the loss in bone rigidity occurs within the first 8 weeks following plate buttressing with histological changes becoming more and more obvious in the subsequent weeks (Uhthoff et al., 1993). While invaluable insight is gained from this study, longer observations are required to thoroughly investigate our hypothesis.

4.4 Conclusion

The study demonstrates that reducing the prosthesis modulus by inclusion of a load-bearing open-space lattice in its design can effectively reduce stress shielding of the periprosthetic bone. This can potentially reduce the risk of periprosthetic osteopenia long term hence the risk of fractures. The modified biomechanical profile can also change the interfacial osteogenic response and the resulting osteointegration. This has significant implications for orthopedic implant design, suggesting that strategically incorporating load-bearing open-lattice structures into endoprostheses could enhance surgical outcomes and long-term stability by optimizing bone-implant interactions. Combined with the advantages of 3D computer aided design and additive manufacturing in patient customization and therefore the resulting improved bone fit, it is our opinion that use of lattices should be an indispensable part of many future applications of the technology in joint and bone reconstruction surgeries.

Data availability statement

The raw data supporting the conclusion of this article will be made available by the authors, without undue reservation.

Ethics statement

The animal study was approved by the Animal Ethics Committee of the Faculty of Veterinary and Agricultural Sciences, The University of Melbourne, Australia (Infonetica # 10442). The study was conducted in accordance with the local legislation and institutional requirements.

Author contributions

RS: Data curation, Formal Analysis, Investigation, Methodology, Visualization, Writing–original draft. CP: Data curation, Formal Analysis, Investigation, Methodology, Writing–original draft. BA: Investigation, Methodology, Writing–review and editing. BL: Investigation, Writing–review and editing. TB: Investigation, Methodology, Writing–review and editing. ML: Conceptualization, Funding acquisition, Writing–review and editing. DS: Investigation, Writing–review and editing. EK: Investigation, Writing–review and editing. JE: Investigation, Writing–review and editing. UB: Data curation, Funding acquisition, Investigation, Methodology, Project administration, Writing–review and editing. TW: Data curation, Investigation, Methodology, Software, Writing–review and editing. SR: Data curation, Investigation, Methodology, Project administration, Writing–review and editing. MB: Conceptualization, Funding acquisition, Methodology, Project administration, Supervision, Writing–review and editing.

Funding

The author(s) declare financial support was received for the research, authorship, and/or publication of this article. The project was co-funded by the Department of Industry, Science, Energy and Resources (Innovative Manufacturing CRC Ltd.) and Stryker Australia Pty Ltd (IMCRC/STR/18092017).

Acknowledgments

We thank Dr. Aisha Tarar for technical assistance with histomorphometry. We also thank the Biological Optical Microscopy Platform, The University of Melbourne, and specifically Ms. Kalyan Shobhana and Dr. Shane Doris Cheung for their support and assistance in optical microscopy. BSEM imaging was performed at Ian Holmes Imaging Centre, Bio21 Molecular Science and Biotechnology Institute, The University of Melbourne. The authors acknowledge the facilities, and the scientific and technical assistance of the RMIT Advanced Manufacturing Precinct.

Conflict of interest

UB was employed by Stryker. EK and TW became Stryker employees following the completion of the study. ML, DS, EK, JE, UB, TW, and MB are co-authors on patent applications related to the technology used for this work. The authors declare that this study received funding from Stryker Australia Pty Ltd. The funder was involved in the study design and animal experiments but not in data analysis and interpretations.

The remaining authors declare that the research was conducted in the absence of any commercial or financial relationships that could be construed as a potential conflict of interest.

Publisher's note

References

Abu El Afieh, J., Gray, M., Seah, M., and Khan, W. (2022). Endoprosthetic reconstruction in Ewing's sarcoma patients: a systematic review of postoperative complications and functional outcomes. *J. Clin. Med.* 11 (15), 4612. doi:10.3390/jcm11154612

Albergo, J. I., Gaston, C. L., Aponte-Tinao, L. A., Ayerza, M. A., Muscolo, D. L., Farfalli, G. L., et al. (2017). Proximal tibia reconstruction after bone tumor resection: are survivorship and outcomes of endoprosthetic replacement and osteoarticular allograft similar? *Clin. Orthop. Relat. Res.* 475 (3), 676–682. doi:10.1007/s11999-016-4843-y

Amrhein, V., Greenland, S., and McShane, B. (2019). Scientists rise up against statistical significance. *Nature* 567 (7748), 305–307. doi:10.1038/d41586-019-00857-9

Apostu, D., Lucaciu, O., Berce, C., Lucaciu, D., and Cosma, D. (2018). Current methods of preventing aseptic loosening and improving osseointegration of titanium implants in cementless total hip arthroplasty: a review. *J. Int. Med. Res.* 46 (6), 2104–2119. doi:10.1177/0300060517732697

Bendich, I., Lawrie, C. M., Riegler, V., Barrack, R. L., and Nunley, R. M. (2022). The impact of component design and fixation on stress shielding after modern total knee arthroplasty. *J. Arthroplasty* 37 (6), S221–s225. doi:10.1016/j.arth.2022.01.074

Bouxsein, M. L., Boyd, S. K., Christiansen, B. A., Guldberg, R. E., Jepsen, K. J., and Müller, R. (2010). Guidelines for assessment of bone microstructure in rodents using micro-computed tomography. *J. Bone Min. Res.* 25 (7), 1468–1486. doi:10.1002/jbmr.141

Braig, Z. V., Tagliero, A. J., Rose, P. S., Elhassan, B. T., Barlow, J. D., Wagner, E. R., et al. (2021). Humeral stress shielding following cemented endoprosthetic reconstruction: an under-reported complication? *J. Surg. Oncol.* 123 (2), 505–509. doi:10.1002/jso.26300

Caffrey, J. P., Alonso, E., Masuda, K., Hunt, J. P., Carmody, C. N., Ganey, T. M., et al. (2018). Strains in trussed spine interbody fusion implants are modulated by load and design. *J. Mech. Behav. Biomed. Mater* 80, 203–208. doi:10.1016/j.jmbbm.2018.02.004

Chen, G. J., Wang, Z., Bai, H., Li, J. M., and Cai, H. (2009). A preliminary study on investigating the attachment of soft tissue onto micro-arc oxidized titanium alloy implants. *Biomed. Mater* 4 (1), 015017. doi:10.1088/1748-6041/4/1/015017

Cho, B. W., Kwon, H. M., Hong, Y. J., Park, K. K., Yang, I. H., and Lee, W. S. (2021). Anatomical tibial component is related to more medial tibial stress shielding after total knee arthroplasty in Korean patients. *Knee Surg. Sports Traumatol. Arthrosc.* 29 (3), 710–717. doi:10.1007/s00167-020-05869-x

Crovace, A. M., Lacitignola, L., Forleo, D. M., Staffieri, F., Francioso, E., Di Meo, A., et al. (2020). 3D biomimetic porous titanium (Ti6Al4V ELI) scaffolds for large bone critical defect reconstruction: an experimental study in sheep. *Anim. (Basel)* 10 (8), 1389. doi:10.3390/ani10081389

Dempster, D. W., Compston, J. E., Drezner, M. K., Glorieux, F. H., Kanis, J. A., Malluche, H., et al. (2013). Standardized nomenclature, symbols, and units for bone histomorphometry: a 2012 update of the report of the ASBMR Histomorphometry Nomenclature Committee. *J. Bone Min. Res.* 28 (1), 2–17. doi:10.1002/jbmr.1805

Emmanual, J., Hornbeck, C., and Bloebaum, R. D. (1987). A polymethyl methacrylate method for large specimens of mineralized bone with implants. *Stain Technol.* 62 (6), 401–410. doi:10.3109/10520298709108030

Erickson, G. M., Catanese, J., 3rd, and Keaveny, T. M. (2002). Evolution of the biomechanical material properties of the femur. *Anat. Rec.* 268 (2), 115–124. doi:10.1002/ar.10145

Fujiwara, T., Ebihara, T., Kitade, K., Setsu, N., Endo, M., Iida, K., et al. (2020). Risk factors of periprosthetic infection in patients with tumor prostheses following resection for musculoskeletal tumor of the lower limb. *J. Clin. Med.* 9 (10), 3133. doi:10.3390/jcm9103133

Guder, W. K., Hardes, J., Nottrott, M., Podleska, L. E., and Streitburger, A. (2021). Highly cancellous titanium alloy (TiAl6V4) surfaces on three-dimensionally printed, custom-made intercalary tibia prostheses: promising short-to intermediate-term results. *J. Pers. Med.* 11 (5), 351. doi:10.3390/jpm11050351

Hart, N. H., Nimphius, S., Rantalainen, T., Ireland, A., Siafarikas, A., and Newton, R. U. (2017). Mechanical basis of bone strength: influence of bone material, bone structure and muscle action. *J. Musculoskelet. Neuronal Interact.* 17 (3), 114–139.

Hennessy, D. W., Raskin, K. A., Schwab, J. H., and Lozano-Calderon, S. A. (2020). Endoprosthetic reconstruction of the upper extremity in oncologic surgery. *J. Am. Acad. Orthop. Surg.* 28 (8), e319–e327. doi:10.5435/JAAOS-D-19-00219

Huiskes, R., Weinans, H., and van Rietbergen, B. (1992). The relationship between stress shielding and bone resorption around total hip stems and the effects of flexible materials. *Clin. Orthop. Relat. Res.* 274, 124–134. doi:10.1097/00003086-199201000-00014

Hunter, J. D. 2007, Matplotlib: a 2D graphics environment. *Comput. Sci. Eng.* 9(3), 90–95. doi:10.1109/mcse.2007.55

Isaksson, H., Tolvanen, V., Finnilä, M. A., Iivarinen, J., Tuukkanen, J., Seppänen, K., et al. (2009). Physical exercise improves properties of bone and its collagen network in growing and maturing mice. *Calcif. Tissue Int.* 85 (3), 247–256. doi:10.1007/s00223-009-9273-3

Ji, T., Yang, Y., Tang, X., Liang, H., Yan, T., Yang, R., et al. (2020). 3D-printed modular hemipelvic endoprosthetic reconstruction following periacetabular tumor resection: early results of 80 consecutive cases. *J. Bone Jt. Surg. Am.* 102 (17), 1530–1541. doi:10.2106/JBJS.19.01437

Kim, J. H., Liu, X., Wang, J., Chen, X., Zhang, H., Kim, S. H., et al. (2013). Wnt signaling in bone formation and its therapeutic potential for bone diseases. *Ther. Adv. Musculoskelet. Dis.* 5 (1), 13–31. doi:10.1177/1759720x12466608

Leopold, S. S., and Porcher, R. (2017). Editorial: the minimum clinically important difference—the least we can do. *Clin. Orthop. Relat. Res.* 475 (4), 929–932. doi:10.1007/s11999-017-5253-5

Li, G., Wang, L., Pan, W., Yang, F., Jiang, W., Wu, X., et al. (2016). *In vitro* and *in vivo* study of additive manufactured porous Ti6Al4V scaffolds for repairing bone defects. *Sci. Rep.* 6, 34072. doi:10.1038/srep34072

Mavrogenis, A. F., Dimitriou, R., Parvizi, J., and Babis, G. C. (2009). Biology of implant osseointegration. *J. Musculoskelet. Neuronal Interact.* 9 (2), 61–71.

Moghaddam, N. S., Skoracki, R., Miller, M., Elahinia, M., and Dean, D. (2016). Three dimensional printing of stiffness-tuned, nitinol skeletal fixation hardware with an example of mandibular segmental defect repair. *Procedia CIRP* 49, 45–50. doi:10.1016/j.procir.2015.07.027

Moyen, B. J., Lahey, P. J., Jr., Weinberg, E. H., and Harris, W. H. (1978). Effects on intact femora of dogs of the application and removal of metal plates. A metabolic and structural study comparing stiffer and more flexible plates. *J. Bone Jt. Surg. Am.* 60 (7), 940–947. doi:10.2106/00004623-197860070-00012

Nagels, J., Stokdijk, M., and Rozing, P. M. (2003). Stress shielding and bone resorption in shoulder arthroplasty. *J. Shoulder Elb. Surg.* 12 (1), 35–39. doi:10.1067/mse.2003.22

Nouri, A., and Hodgson, P. D. (2010). "Biomimetic porous titanium scaffolds for orthopedic and dental applications," in *Biomimetics learning from nature*. EditorA. Mukherjee, InTech.

Novikov, D., Cohen, D., Swanson, D., Vojdani, S., and Khan, F. (2019). A meta-analysis of outcomes in total hip arthroplasty recipients following pelvic irradiation. *J. Arthroplasty* 34 (7), 1546–1552. doi:10.1016/j.arth.2019.02.047

Pilliar, R. M., Cameron, H. U., Binnington, A. G., Szivek, J., and Macnab, I. (1979). Bone ingrowth and stress shielding with a porous surface coated fracture fixation plate. *J. Biomed. Mater Res.* 13 (5), 799–810. doi:10.1002/jbm.820130510

Sanaei, R. (2023). A customized 3D-printed histological microgrinder for the study of metallic endoprostheses. *J. Histotechnol.*, 1–9. doi:10.1080/01478885.2023.2205617

Singh, J. A., Yu, S., Chen, L., and Cleveland, J. D. (2019). Rates of total joint replacement in the United States: future projections to 2020-2040 using the national inpatient sample. *J. Rheumatol.* 46 (9), 1134–1140. doi:10.3899/jrheum.170990

Skedros, J. G., Bloebaum, R. D., Mason, M. W., and Bramble, D. M. (1994). Analysis of a tension/compression skeletal system: possible strain-specific differences in the hierarchical organization of bone. *Anat. Rec.* 239 (4), 396–404. doi:10.1002/ar.1092390406

Skedros, J. G., Su, S. C., Knight, A. N., Bloebaum, R. D., and Bachus, K. N. (2019). Advancing the deer calcaneus model for bone adaptation studies: *ex vivo* strains obtained after transecting the tension members suggest an unrecognized important role for shear strains. *J. Anat.* 234 (1), 66–82. doi:10.1111/joa.12905

Sumner, D. R., and Galante, J. O. (1992). Determinants of stress shielding: design versus materials versus interface. *Clin. Orthop. Relat. Res.* 274, 202–212. doi:10.1097/00003086-199201000-00020

Tagliero, A. J., Bukowski, B. R., Rose, P. S., Morrey, M. E., Elhassan, B. T., Barlow, J. D., et al. (2020). High incidence of complications associated with shoulder girdle reconstruction utilizing a Stryker proximal humerus cap endoprosthesis following Tikhoff-Linberg resections. *Int. Orthop.* 44 (11), 2449–2455. doi:10.1007/s00264-020-04576-z

Tonino, A. J., Davidson, C. L., Klopper, P. J., and Linclau, L. A. (1976). Protection from stress in bone and its effects. Experiments with stainless steel and plastic plates in dogs. *J. Bone Jt. Surg. Br.* 58 (1), 107–113. doi:10.1302/0301-620x.58b1.1270486

Uhthoff, H. K., and Finnegan, M. (1983). The effects of metal plates on post-traumatic remodelling and bone mass. *J. Bone Jt. Surg. Br.* 65 (1), 66–71. doi:10.1302/0301-620x.65b1.6822605

Uhthoff, H. K., Foux, A., Yeadon, A., McAuley, J., and Black, R. C. (1993). Two processes of bone remodeling in plated intact femora: an experimental study in dogs. *J. Orthop. Res.* 11 (1), 78–91. doi:10.1002/jor.1100110110

Vail, E. A., and Avidan, M. S. (2022). Trials with 'non-significant' results are not insignificant trials: a common significance threshold distorts reporting and interpretation of trial results. *Br. J. Anaesth.* 129 (5), 643–646. doi:10.1016/j.bja.2022.06.023

Wallace, I. J., Demes, B., Mongle, C., Pearson, O. M., Polk, J. D., and Lieberman, D. E. (2014). Exercise-induced bone formation is poorly linked to local strain magnitude in the sheep tibia. *PLoS One* 9 (6), e99108. doi:10.1371/journal.pone.0099108

Waskom, M., Botvinnik, O., and O'Kane, D. (2017). "*mwaskom/seaborn: seaborn v0.8.1, Zenodo*".).

Woo, S. L., Akeson, W. H., Coutts, R. D., Rutherford, L., Doty, D., Jemmott, G. F., et al. (1976). A comparison of cortical bone atrophy secondary to fixation with plates with large differences in bending stiffness. *J. Bone Jt. Surg. Am.* 58 (2), 190–195. doi:10.2106/00004623-197658020-00005

Zhong, Z., Zeng, X. L., Ni, J. H., and Huang, X. F. (2013). Comparison of the biological response of osteoblasts after tension and compression. *Eur. J. Orthod.* 35 (1), 59–65. doi:10.1093/ejo/cjr016

frontiers | Frontiers in Bioengineering and Biotechnology

TYPE Original Research
PUBLISHED 01 February 2024
DOI 10.3389/fbioe.2024.1339530

OPEN ACCESS

EDITED BY
Lorenzo Fassina,
University of Pavia, Italy

REVIEWED BY
Cheng Hu,
Sichuan University, China
Zhen Yang,
Peking University People's Hospital, China

*CORRESPONDENCE
Ruiming Liang,
rmliang97@163.com
Li Zheng,
zhengli224@163.com
Shixing Luo,
shixingluo2018@hotmail.com

†These authors have contributed equally to this work

RECEIVED 16 November 2023
ACCEPTED 19 January 2024
PUBLISHED 01 February 2024

CITATION
Luo S, Shang Y, Qin Z, Zhou B, Lu C, Qu Y, Zhao J, Liang R, Zheng L and Luo S (2024), A novel cartilage-targeting MOF-HMME-RGD sonosensitizer combined with sonodynamic therapy to enhance chondrogenesis and cartilage regeneration.
Front. Bioeng. Biotechnol. 12:1339530.
doi: 10.3389/fbioe.2024.1339530

A novel cartilage-targeting MOF-HMME-RGD sonosensitizer combined with sonodynamic therapy to enhance chondrogenesis and cartilage regeneration

Shanchao Luo[1,2,3†], Yifeng Shang[1†], Zainen Qin[1†], Bo Zhou[1], Chun Lu[4], Yangyang Qu[1], Jinmin Zhao[1,2], Ruiming Liang[1,2*], Li Zheng[1,2*] and Shixing Luo[1,3*]

[1]Guangxi Engineering Center in Biomedical Materials for Tissue and Organ Regeneration, International Joint Laboratory on Regeneration of Bone and Soft Tissues, Guangxi Key Laboratory of Regenerative Medicine, Collaborative Innovation Center of Regenerative Medicine and Medical Bioresource Development and Application Co-constructed by the Province and Ministry, The First Affiliated Hospital of Guangxi Medical University, Nanning, Guangxi, China, [2]Department of Orthopaedics Trauma and Hand Surgery, The First Affiliated Hospital of Guangxi Medical University, Nanning, Guangxi, China, [3]Department of Orthopedics, The Ninth Affiliated Hospital of Guangxi Medical University, Guangxi Medical University, Nanning, Guangxi, China, [4]School of Materials and Environment, Guangxi Minzu University, Nanning, Guangxi, China

Articular cartilage regeneration is still a difficult task due to the cartilage's weak capacity for self-healing and the effectiveness of the available therapies. The engineering of cartilage tissue has seen widespread use of stem cell-based therapies. However, efficient orientation of line-specific bone marrow mesenchymal stem cells (BMSCs) to chondrogenesis and maintenance of chondrogenic differentiation challenged stem cell-based therapy. Herein, we developed a Fe-based metal-organic framework (MOF) loaded with hematoporphyrin monomethyl ether (HMME) and cartilage-targeting arginine-aspartate-glycine (RGD) peptide to form MOF-HMME-RGD sonosensitizer to regulate BMSCs chondrogenic differentiation for cartilage regeneration via the modulation of reactive oxygen species (ROS). By using sonodynamic therapy (SDT), the MOF-HMME-RGD demonstrated favorable biocompatibility, could generate a modest amount of ROS, and enhanced BMSCs chondrogenic differentiation through increased accumulation of glycosaminoglycan, an ECM component specific to cartilage, and upregulated expression of key chondrogenic genes (*ACAN*, *SOX9*, and *Col2a1*). Further, transplanted BMSCs loading MOF-HMME-RGD combined with SDT enhanced cartilage regeneration for cartilage defect repair after 8 weeks into treatment. This synergistic strategy based on MOF nanoparticles provides an instructive approach to developing alternative sonosensitizers for cartilage regeneration combined with SDT.

KEYWORDS

articular cartilage regeneration, stem cell therapy, metal-organic framework, sonosensitizers, sonodynamic therapy

1 Introduction

Articular cartilage, a thin tissue layer, effectively distributes loads by its unique extracellular matrix components, including collagen and chondroitin sulfate. This structural composition serves to safeguard the subchondral bone from excessive stress. (Gao et al., 2021). Due to its aneural, avascular, and alymphatic nature, severe cartilage damage or trauma is difficult to self-repair (Dai et al., 2015; Liu et al., 2021). The stem cell-based treatment using multipotent stem cells, which can be guided towards chondrogenic development, has found extensive use in the field of cartilage tissue engineering (Gugjoo et al., 2016; Lee and Wang, 2017). However, the efficient orientation of line-specific BMSCs to chondrogenesis and maintenance of chondrogenic differentiation challenged stem cell-based therapy (Shi et al., 2019).

It has been reported that moderate ROS is important for cell growth and differentiation. During the process of chondrogenesis, the involvement of ROS is of significant importance as they actively contribute to the stimulation of cell proliferation and the facilitation of differentiation in BMSCs while simultaneously preventing the onset of an inflammatory response (Kim et al., 2010; Lu et al., 2019; Wu et al., 2023a). Previous studies showed that the ROS level was specifically high in developing chondrocytes of the embryonic limb, and chondrocyte maturation was accompanied by a progressive decrease in catalase activity in growing cartilage (Salas-Vidal et al., 1998; Schnabel et al., 2006). Regarding *in vitro* chondrogenic differentiation, ROS generation was increased during induction (Jallali et al., 2007; Heywood and Lee, 2017). In addition, varieties of nanomaterials and hydrogels were capable of effectively promoting the chondrogenic differentiation of BMSCs due to the increasing generation of ROS (Lu et al., 2019; Cai et al., 2020; Wu et al., 2023b). Sonodynamic therapy (SDT) is a promising therapeutic modality that utilizes ultrasound (US) to induce sonoluminescence. This process activates sonosensitizers, leading to the generation of ROS, including hydroxyl radicals and singlet oxygen. SDT represents an ultrasound-based approach for the treatment of cartilage-related conditions, offering a new paradigm in the field of cartilage therapy (Uddin et al., 2016; Truong Hoang et al., 2022). The use of sonosensitizer-enabled SDT has been shown to effectively enhance the repair of articular cartilage lesions (Wu et al., 2023b). This approach has many advantages, including non-invasiveness, the ability to penetrate deep into the tissue, high therapeutic efficacy, and little occurrence of adverse effects (Vahedi et al., 2021). For SDT, the selection of appropriate sonosensitizers is critical.

Organic sonosensitizers like porphyrins, phthalocyanines, fluoroquinolone (FQ) antibiotics, phenothiazine compounds, *etc.*, with special groups producing sonosensitive activity by the US, have attracted much attention because of their easy monitoring, clear structure, stable chemical and physical properties, and evaluation of drug metabolism (Li et al., 2021). In particular, the porphyrins derivatives hematoporphyrin monomethyl ether (HMME) which is a second-generation hematoporphyrin (HP)-related sensitizer can produce a sensitive reaction to convert oxygen into ROS under US irradiation and has been continuously used as US-responsive sonosensitizer in SDT with the advantage of high quantum yield in the ROS generation, good selective retention and long-term retention in tissue (Huang et al., 2018; Li et al., 2021; Song et al., 2023). Furthermore, HMME was a hydrolysis product of endogenous hemoglobin with good biocompatibility, sonosensitizing ability, and emissive properties. Previous research has confirmed that HMME has been widely used in SDT by US irradiation for medication of ROS-related diseases, including antitumor treatment, sonodynamic antimicrobial chemotherapy, and neovascularization theranostics. It can easily control the amount of ROS production by regulating the concentration of HMME and several the sonodynamic parameters including ultrasonic intensity, irradiation duration and frequency. Wen et al. successfully synthesized polymeric nanoparticles, namely, CAT@HA-HMME NPs, whereby HMME was used as a representative organic sonosensitize (Wen et al., 2022). These nanoparticles were designed to exhibit prolonged blood circulation and disintegration inside tumor sites, hence enhancing the efficacy of sonodynamic treatment. Yao et al. constructed ferrite-encapsulated nanoparticles that are sensitive to low-intensity focused ultrasoun (Yao et al., 2021). These nanoparticles were created via HMME-mediated SDT and were designed for theranostics targeting neovascularization in atherosclerotic plaques. Xu reported the synthesis of Fe-HMME coordination particles (FeCPs) by the assembly of HMME with Fe (III) ions (Xu et al., 2020). These particles were then loaded with the anticancer medication doxorubicin to enable a combination therapy approach using SDT and chemotherapy for the treatment of deep-seated tumors. Nonetheless, HMME-based nanoparticles remain unsatisfactory because of poor water solubility, poor light stability, low efficient delivery, rapid metabolism, fast clearance, *etc.*, resulting in reduced bioavailability and restricted absorption into the body (Huang et al., 2018; Wen et al., 2022). These aforementioned limitations give rise to suboptimal pharmacokinetics and a lack of therapeutic efficacy in the context of SDT. Hence, the development of novel techniques is important to get optimal SDT using organic sonosensitizers.

Metal-organic frameworks (MOFs) are a category of porous coordination polymers that have garnered significant attention due to their growing and practical applications. The formation of coordination bonds is facilitated by the coordination of metal ions or clusters with functional organic ligands, resulting in the creation of these frameworks (Wen et al., 2023). MOFs have attracted extensive research interest and have been widely used in drug delivery due to the unique features of facile synthesis, diverse compositions, adjustable porosity, high surface areas, easy surface functionalization, good dispersibility, high loading capacities, and tunable biocompatibility (Jiang et al., 2023). In our previous studies, we developed pH-responsive MOFs modified by hyaluronic acid (HA) loaded with anti-inflammatory protocatechuic acid (PCA) for osteoarthritis therapy (Xiong et al., 2020) and zinc-based MOFs with antibacterial and anti-inflammatory properties for promoting wound healing (Chen et al., 2022). It was found that the porous structure of MOFs can prevent the self-quenching of organic acoustic molecules and promote the rapid diffusion of ROS, thus increasing the quantum yield of ROS by leveraging the benefits offered by the linker-to-metal charge transfer mechanism (Xie et al., 2022). Thus, MOFs may be promising carriers for HMME in SDT applications.

Herein, we developed MOF-based multifunctional therapeutic nanoparticles loading with HMME and arginine-aspartate-glycine

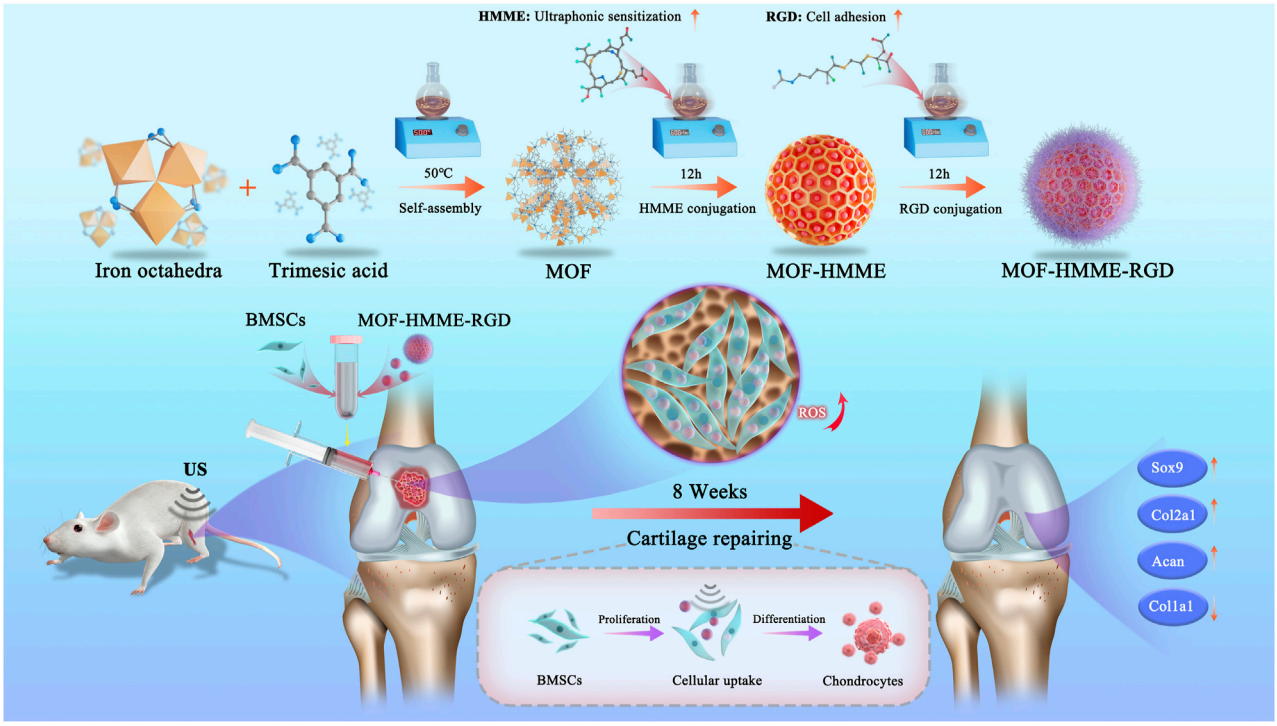

SCHEME 1
Schematic illustrations of MOF-HMME-RGD synthesis and the potential therapeutic mechanisms of the multifunctional combined strategy.

(RGD) (MOF-HMME-RGD) with a combination of SDT for cartilage regeneration in an attempt to regulate chondrogenic differentiation of BMSCs by producing moderate ROS (Scheme 1). HMME can serve as sonosensitizers to produce ROS (e.g., singlet oxygen) via US stimulation. The RGD peptide is well recognized as a particular binding site for integrin receptors, which are key regulators of cell-extracellular and cell-cell microenvironment communication (Koh et al., 2022). Therefore, it is anticipated that MOF-HMME-RGD would enhance cell viability, stimulate the production of proteoglycans, and facilitate the restoration of cartilage by expediting the lineage-specific differentiation of BMSCs towards chondrogenic lineage and cartilage regeneration. This strategy based on MOF nanoparticles provides an instructive approach to developing alternative sonosensitizers for cartilage regeneration combined with SDT.

2 Materials and methods

2.1 Synthesis of MOF-HMME-RGD nanoparticles (NPs)

2.1.1 Preparation of metal-organic frameworks (MOFs) NPs

Metal-organic frameworks nanoparticles were synthesized utilizing a technique that was derived from prior research, with some adjustments made to the procedure (Cai et al., 2017). A mixture was prepared by combining 40 mL of a 2 mM $FeCl_3$ solution (dissolved in methanol) with 40 mL of 1.2 mM 1, 3, 5-benzene tricarboxylic acid (trimesic acid, BTC) solution (also dissolved in methanol). The mixture was subjected to vigorous stirring for 10 min. The solution was put into a heated oil bath maintained at a temperature of 50°C and allowed to undergo a reaction for 90 min. Subsequently, the solution underwent centrifugation for 12 min at a rotational speed of 12,000 revolutions per minute (rpm) using a centrifuge (Eppendorf 5810R, Germany). Following centrifugation, the resulting pellet was subjected to three consecutive washes with deionized water. The MOFs NPs were ultimately acquired by the process of freeze-drying in a freeze dryer and kept at a temperature of 4°C.

2.1.2 Preparation of modified MOF-HMME NPs

5 mL MOF methanol solution (1.0 mg/mL) and 5 mL HMME methanol solution (1.0 mg/mL) were mixed under ultrasonic conditions. Then, the aforementioned solution was subjected to agitation at ambient temperature for 12 h. Subsequently, the obtained mixtures were subjected to centrifugation at a rotational speed of 10,000 rpm for 5 min, and followed by a triple rinsing procedure using ethanol and deionized water. The resultant product was obtained via the process of centrifugation and then designated as MOF-HMME. Thereafter, the resulting product was reconstituted by adding 5 mL ultrapure water and stored at 4°C.

2.2 Preparation of modified MOF-HMME-RGD NPs

The methanol solution containing 5 mg MOF-HMME NPs and the solution containing 0.5 mg RGD (5 mg/mL) were mixed under sonication conditions and placed at a constant temperature of 37°C

for 12 h in a shaker. The MOF-HMME-RGD was obtained by centrifugation to remove the unloaded RGD. Finally, MOF-HMME-RGD NPs were resuspended with 5 mL ultrapure water and stored at 4°C.

2.3 Characterization of MOF-HMME-RGD

The morphology and structure of MOF-HMME-RGD nanoparticles were examined using transmission electron microscopy (TEM) and X-ray diffraction (XRD) techniques, respectively. The TEM analysis was conducted using a Hitachi instrument from Japan, while the XRD analysis was performed using a MiniFlex 600 instrument, also from Japan. The absorption spectra of nanoparticles (NPs) in phosphate-buffered saline (PBS) were measured using a UV-visible spectrophotometer (Shimadzu, UV-2700, Japan). The average particle size and zeta potential of nanoparticles in a PBS solution were measured using Nano-ZS equipment manufactured by Malvern Panalytical in China. The HMME releasing behaviors from MOF-HMME-RGD were investigated. 200 μg MOF-HMME-RGD was dissolved in 1 mL of PBS buffer and then placed at 37°C with or without ultrasound stimulation under thermostatic shaking. The HMME concentration in the buffer was measured uniformly using a UV spectrophotometer at 0, 10, 30, 60, 120, 180 min, and the drug release rate (Q) was further calculated.

$$Q(\%) = \left(C_t V_0 + \sum_{i=1}^{t-1} C_i V_i \right) \Big/ W \times 100$$

C_t and C_i in equation represent the concentration of HMME in the tth and i^{th} collected samples, respectively. V_0 and V_i represent the original volume in the simulated system and the volume of the i^{th} sampling, respectively (V_0 = 1 mL; V_i = 1 mL), and W is the total amount of drug HMME in the simulated system.

2.4 Detection of singlet oxygen

The single oxygen generated by MOFs, HMME, MOF-HMME, MOF-HMME-RGD was measured by a chemical probe 1, 3-diphenylisobenzofuran (DPBF). Typically, 10 μL 10 mM DPBF ethanol solution was added to 1.0 mL of PBS, and MOFs, HMME, MOF-HMME, and MOF-HMME-RGD were immersed into the above solution under ultrasound stimulation with a frequency of 1.0 MHz, a sound intensity of 0.35 W/cm^2, a duty cycle of 60%. Finally, the absorbance of DPBF at a wavelength of 410 nm was assessed using a microplate reader.

2.5 Cell isolation and culture

The animal experiments conducted in this study were approved by the Animal Ethics Committee standards of Guangxi Medical University, by Protocol Number 201903034. The animals were euthanized with the administration of sodium pentobarbital. BMSCs were obtained from the femoral marrow of neonatal Sprague-Dawley (SD) rats, as described in previous work. (Gao et al., 2023). BMSCs were cultivated in α-minimal essential medium (α-MEM, Biosharp, China) with 1% penicillin/streptomycin antibiotics (Biosharp, China) and 10% fetal bovine serum (Tianhang, China). The cells were subjected to incubation at a temperature of 37°C under an atmosphere containing 5% carbon dioxide. The medium was replenished at regular intervals of every 3 days.

2.6 Intracellular ROS detection

The measurement of intracellular ROS generation was conducted using a probe kit containing 2′,7′-dichlorofluorescein diacetate (DCFH-DA) obtained from Thermo Fisher Scientific, located in the United States. The BMSCs were cultured in 6-well plates with a density of 2 × 10^5 cells per well. The fluorescent probe DCFH-DA can enter cells and undergo cleavage upon oxidation by ROS. Subsequently, it is de-esterified by endogenous esterases and transformed into the fluorescent molecule 2′,7′-dichlorofluorescein (DCF). In summary, the cells that had undergone treatment were gathered and reconstituted with a diluted solution of DCFH-DA (10 μM). Subsequently, the cells had an incubation phase of 20 min at a temperature of 37°C inside a regulated cell incubator. The cells underwent centrifugation, followed by three rounds of washing, and were then resuspended using a serum-free cell culture medium. The quantification of ROS inside the intracellular environment was conducted utilizing a fluorescence spectrophotometer. The excitation wavelength used was 488 nm, while the emission wavelength utilized was 525 nm.

2.7 Cell viability and cell apoptosis assay

The optimal concentration of HMME incorporated in MOF-HMME-RGD, along with the ultrasonic intensity, irradiation duration, and frequency, were determined based on the results obtained from the cell viability analysis performed using the 3-(4,5-dimethylthiazol-2-yl)-2,5-diphenyltetrazolium bromide (MTT) assay provided by Gibco, United States. The BMSCs were cultured in 6-well plates with a density of 2×10^5 cells per well. The absorbance value at 490 nm was measured using the microplate reader from Thermo Fisher Scientific, United States. Subsequently, the computation of cell viability was conducted. The treatment parameters which the most substantial support for cells proliferation were chosen for the subsequent experiment. The experiment was divided into five groups: (1) Control group; (2) T group: BMSCs were cultured in the chondrogenic medium; (3)TU group: BMSCs were cultured in chondrogenic medium with ultrasound stimulation; (4)TMU group: BMSCs were cultured in chondrogenic medium containing MOF-HMME-RGD (C_{HMME} = 1 μg/mL) with ultrasound stimulation; (5) Nac-TMU group: BMSCs were cultured in chondrogenic medium containing MOF-HMME-RGD (C_{HMME} = 1 μg/mL) and NAC (a ROS scavenger) with ultrasound stimulation. The cultured BMSCs were carried out with ultrasound stimulation by a medical ultrasound physiotherapy instrument (WELLD, China). The treatment parameters of LIPUS were: free mode, switching ratio of 60%, frequency of 1 MHz, ultrasound intensity of 0.35 W/cm^2,

irradiation time of 60 s, and irradiation frequency of once a day. The apoptosis of the BMSCs with ultrasound stimulation was determined with the Annexin V-EGFP/PI apoptosis kit (KeyGEN BioTECH, Nanjing, China) by a flow cytometer (BD FACSCalibur, USA).

2.8 Intracellular uptake of MOF-HMME-RGD

The BMSCs were cultured in 6-well plates with a density of 3×10^4 cells per well. After 12 h of incubation, the cells were cultured with 3 mL medium containing FITC-labeled MOF-HMME-RGD (C_{HMME} = 1 μg/mL). Samples were collected and observed using fluorescence microscopy at 4h, 1d, and 3d.

2.9 Biochemical assays

To further explore the synergistic effect of MOF-HMME-RGD on BMSCs chondrogenesis with SDT, the cells were cultured in chondrogenic medium containing 10 ng mL^{-1} transforming growth factor-β1 (TGF-β1, PeproTech, USA), 50 μg mL^{-1} ascorbic acid (Solarbio, China), 50 mg mL^{-1} insulin-transferrin-selenium (Gibco, USA), 100 nmol mL^{-1} dexamethasone (Solarbio, China) at 5% CO_2, 37°C for 14 days. The BMSCs were cultured in 6-well plates with a density of 2×10^5 cells per well. The experiment was divided into five groups: (1) Control group; (2) T group: BMSCs were cultured in the chondrogenic medium; (3)TU group: BMSCs were cultured in chondrogenic medium with ultrasound stimulation; (4)TMU group: BMSCs were cultured in chondrogenic medium containing MOF-HMME-RGD (C_{HMME} = 1 μg/mL) with ultrasound stimulation; (5) Nac-TMU group: BMSCs were cultured in chondrogenic medium containing MOF-HMME-RGD (C_{HMME} = 1 μg/mL) and NAC (a ROS scavenger) with ultrasound stimulation. The treatment parameters of LIPUS were: free mode, switching ratio of 60%, frequency of 1 MHz, ultrasound intensity of 0.35 W/cm^2, irradiation time of 60 s, and irradiation frequency of once a day.

The cells were subjected to a series of procedures at each time point. Firstly, they were washed three times with a PBS solution. Subsequently, the cells were digested with a 1.0 mL solution of proteinase K, which had a concentration of 20 mg/mL. This digestion process took place at a temperature of 56°C for 10 h. The purpose of these procedures was to quantify the levels of DNA and glycosaminoglycan (GAG) present in the cells. DNA contents were measured using the Hoechst 33,258 dye with DNA from the calf thymus as a standard. The GAG contents were quantified using dimethyl methylene blue (DMMB) chloride methods, and optical density was tested at 525 nm. The quantification of GAG secretion was performed using a calibration curve based on the absorbance of chondroitin sulfate, and the results were normalized to account for the total DNA content.

2.10 Quantitative real-time polymerase chain reaction (qRT-PCR) analysis

Quantitative real-time polymerase chain reaction (qRT-PCR) was used to evaluate the expression levels of cartilage-specific genes (*Acan*, *Sox9*, *Col2a1*, *Col1a1*) in BMSCs. The BMSCs were cultured in 6-well plates with a density of 2×10^5 cells per well in chondrogenic medium for 14 days. The treatment parameters of LIPUS were: free mode, switching ratio of 60%, frequency of 1 MHz, ultrasound intensity of 0.35 W/cm^2, irradiation time of 60 s, and irradiation frequency of once a day. The process of reverse transcription (RT) was conducted to convert total RNA into complementary DNA (cDNA) using a Prime Script RT kit manufactured by Takara in Japan. The qRT-PCR experiment was performed using the Fast Start universal SYBR Green Master Mix (Roche, Germany) on a detection system. The PCR cycling protocol included an initial denaturation step at a temperature of 95°C for 180 s, followed by a series of 40 cycles, including denaturation at 95°C for 3 s and annealing at 60°C for 30 s. The primer sequences for both the forward and reverse directions were documented in Table 1. The quantification of mRNA expression levels was conducted by using GAPDH as an internal control and using the threshold cycle (Ct) technique to determine the values represented as $R = 2^{-\Delta\Delta CT}$.

TABLE 1 Primers in qRT-PCR analysis.

Genes	Primers	Sequences
GAPDH	Forward	AGGCCGGTGCTGAGTATGTC
	Reverse	TGCCTGCTTCACCACCTTCT
Acan	Forward	CCGCTGGTCTGATGGACACT
	Reverse	AGGTGTTGGGGTCTGTGCAA
Col2α1	Reverse	TGCCTGCTTCACCACCTTCT
	Reverse	ACCCCTCTCTCCCTTGTCAC
Col1α1	Forward	GAGAGGTGAACAAGGTCCCG
	Reverse	AAACCTCTCTCGCCTCTTGC
SOX9	Forward	TCGGTGAAGAATGGGCAAGC
	Reverse	CTGAGATTGCCCGGAGTGCT

2.11 Animal procedure

The animal experiments conducted in our research were conducted according to the ethical guidelines established by the Animal Ethics Committee of Guangxi Medical University (Protocol Number: 201,903,034). In this investigation, a cohort of 24 Sprague-Dawley rats, aged between 8 and 10 weeks and weighing around 200 g, was used. Following the administration of general anesthesia using a 2% solution of sodium pentobarbital at a dosage of 30 mg/kg, a controlled experiment was conducted to create a defect only inside the cartilage tissue. The observed defect had a diameter of 3 mm and a depth of 2 mm, and it was located inside the articular cartilage area of the distal femoral condyle in the knee joint. The Sprague-Dawley rats were allocated into four groups using a random assignment method. The study consisted of four experimental groups: (1) Control group: untreated cartilage defect model, (2) BMSCs group: treated with implantation of 10×10^6 BMSCs, (3) BMSCs + US group: treated with implantation of 10×10^6 BMSCs and ultrasound stimulation, (4) SDT group: treated with implantation of

10×10^6 BMSCs uptaking MOF-HMME-RGD NPs and ultrasound stimulation. The treatment parameters of LIPUS were: free mode, switching ratio of 60%, frequency of 1 MHz, intensity of 0.35 W/cm^2, 1 min per exposure, and one exposure every other day.

2.12 Gross observation, histological staining, and grading

The femoral condyle's articular cartilage, which had undergone repair, was collected for macroscopic examination and grading at two specific time intervals: 4 weeks and 8 weeks after the surgical intervention. A morphological evaluation of cartilage regeneration was performed by three impartial assessors who were blinded to the experimental groups. The evaluation was completed in accordance with the grading method established by the International Cartilage Repair Society (ICRS).

After doing a first visual inspection, the femoral condyles were fixed by immersing them in a 4% paraformaldehyde solution for 48 h. Subsequently, decalcification was carried out using an aqueous solution with a pH of 7.2, consisting of 10% (v/v) ammonium hydroxide and 14% (w/v) EDTA. This decalcification process was facilitated by an ultrasonic machine manufactured by Medite in Germany and lasted for 2 weeks. Following the process of dehydration using graded ethanol, the samples underwent paraffin embedding and were then sectioned into slices measuring 3 mm in thickness. The samples underwent staining using safranin O/fast green and the hematoxylin-eosin (HE) kit (Solarbio, Peking, China). The immunohistochemical staining technique was used to analyze the expression of *Col2a1* using a specific *Col2a1* antibody (Bioss, Peking, China) and the Biotin-Streptavidin HRP Detection System. The specimens were visually examined and collected using an optical microscope (BX 63, Olympus, Japan). The articular cartilage that underwent repair in each experimental group was evaluated and rated using the Modified O'Driscoll Score (MODS). Three independent observers who were unaware of the research settings, assessed the histological evaluation scale. (Betz et al., 2017).

2.13 Statistical analysis

The data underwent analysis using SPSS 22.0 (SPSS Inc., Chicago, Illinois, USA) and were afterward published as mean ± standard deviation. The statistical significance between groups was assessed using a significance level of $p < 0.05$. The study used a one-way analysis of variance (ANOVA) to investigate the differences between two cohorts, followed by a *post hoc* analysis using the Least Significant Difference (LSD) approach.

3 Results

3.1 Preparation and characterization of MOF-HMME-RGD

The synthesis of the multifunctional MOF-HMME-RGD was carried out according to the methodology depicted in Scheme 1. We obtained MOF-HMME-RGD by stepwise stirring reaction under mild conditions. The compound [Fe (BTC)] (BTC: 1,3,5-benzene dicarboxylate) consists of clusters of iron octahedra that are connected by a shared vertex μ3-O, with the connection facilitated by the BTC moieties. The TEM images (Figure 1A) revealed that the MOF, MOF-HMME, and MOF-HMME-RGD samples exhibited a distinct spherical morphology with uniform size distribution. The mean diameters of the MOF, MOF-HMME, and MOF-HMME-RGD were 131.12 ± 4.59 nm,169.41 ± 19.16 nm, and 236.44 ± 20.34 nm (Figure 1B), respectively, which indicates that all three samples exhibited a reasonably narrow size distribution, with no statistically significant differences observed between them. In addition, the average zeta potentials of MOF, MOF-HMME, and MOF-HMME-RGD were −5.03 ± 0.23 mV, −17.87 ± 2.22 mV and −34.93 ± 0.67 mV (Figure 1C), respectively. Figure 1D presented the XRD pattern of the MOF, MOF-HMME, and MOF-HMME-RGD. The X-ray diffraction patterns exhibited distinct diffraction peaks, all of which were successfully attributed to a cubic crystal structure. This observation aligns with the findings documented in previous studies. The introduction of HMME and RGD did not induce any alterations in the crystalline structure of Fe-BTC nanoparticles (metal-organic framework). In order to conduct a more comprehensive examination of the optical characteristics, UV-visible spectroscopy was employed to ascertain the loading quantities of HMME within the MOF NPs. The absorption spectra of MOF, MOF-HMME, and MOF-HMME-RGD were shown in Figure 1E. The MOFs had no obvious photoabsorption in a wide range (300–500 nm). The MOF-HMME and MOF-HMME-RGD NPs had maximum absorption peaks at 390 nm after the incorporation of HMME due to π-π stacking, and loading RGD did not affect the absorption peak of MOF-HMME-RGD. The HMME releasing behaviors from MOF-HMME-RGD were investigated in Figure 1F. The HMME releasing from MOF-HMME-RGD under ultrasonic stimulation reached the maximum in 180 min and the cumulative release was 77.41%, while that in the MOF-HMME-RGD without ultrasonic stimulation was 13.18%.

3.2 Cell viability assessment of MOF-HMME-RGD

The determination of the ideal concentration of HMME loaded in MOF-HMME-RGD, as well as the ultrasonic intensity, irradiation time, and frequency, was based on the results of cell viability assessed via the MTT assay. The cellular viability exhibited an upward trend as the concentration of HMME encapsulated within MOF-HMME-RGD remained below 1.0 μg, after which they decreased significantly (Figure 2A). For the optimal treatment time, the cellular viability was increased when the ultrasound intensity was maintained at 0.35 W/cm^2 (Figure 2B), and the irradiation time was less than 60 s (Figure 2C), which dropped considerably afterward. When different ultrasound frequencies were performed each day, there was the highest cell viability when cells were treated with ultrasound once a day (Figure 2D), and cell viability was greatly reduced in 2 days of irradiation compared to only 1 day of irradiation (Figure 2E). Thus, ultrasound intensity of 0.35 W/cm^2, irradiation time of 60 s, and

10.3389/fbioe.2024.1339530

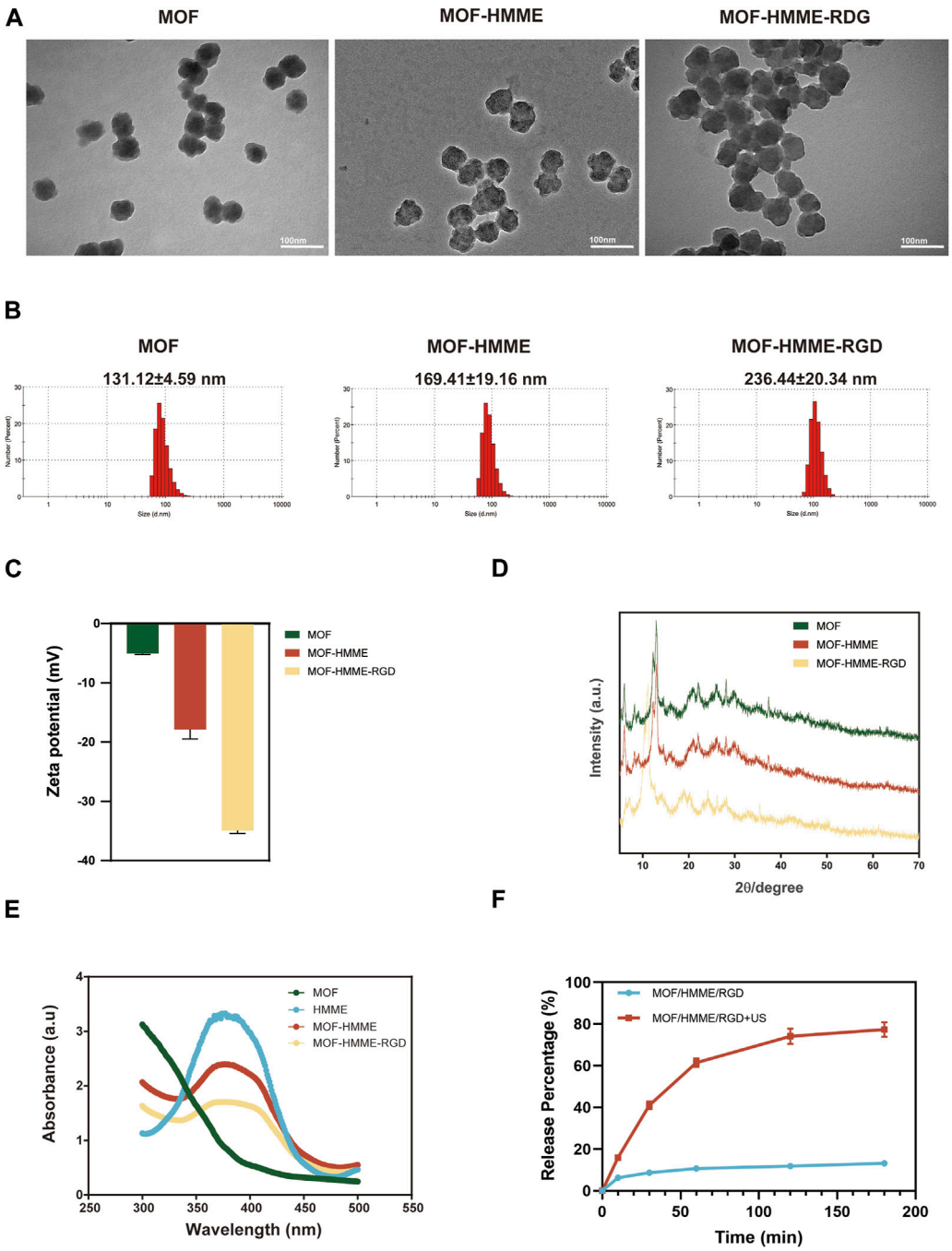

FIGURE 1
The characterizations of MOF-HMME-RGD. **(A)** TEM images, scale bar = 100 nm. **(B)** Particle size and **(C)** zeta potentials were tested by a Malvern particle size analyzer. **(D)** X-ray diffraction (XRD) analysis. **(E)** UV spectra of MOF-HMME-RGD. **(F)** The HMME releasing behaviors from MOF-HMME-RGD.

irradiation frequency of once a day, which provided the most substantial support for the proliferation of cells, were chosen for the subsequent experiment.

As shown in Figure 2F, the TMU group had the highest cell viability under ultrasound stimulation, and cell viability was significantly reduced after the addition of ROS scavenger NAC in the Nac-TMU group. This result indicated that the MOF-HMME-RGD with ultrasound stimulation significantly increased the cell viability.

3.3 Intracellular ROS generation of MOF-HMME-RGD

To explore the source of ROS, the capability of singlet oxygen generation by MOF-HMME-RGD was detected by a chemical probe 1, 3-diphenylisobenzofuran (DPBF) at 410 nm. As illustrated in Figure 3A, the production level of singlet oxygen in MOF-HMME-RGD and MOF-HMME is much higher than that in MOF when irradiated by ultrasound, as demonstrated by the characteristic

10.3389/fbioe.2024.1339530

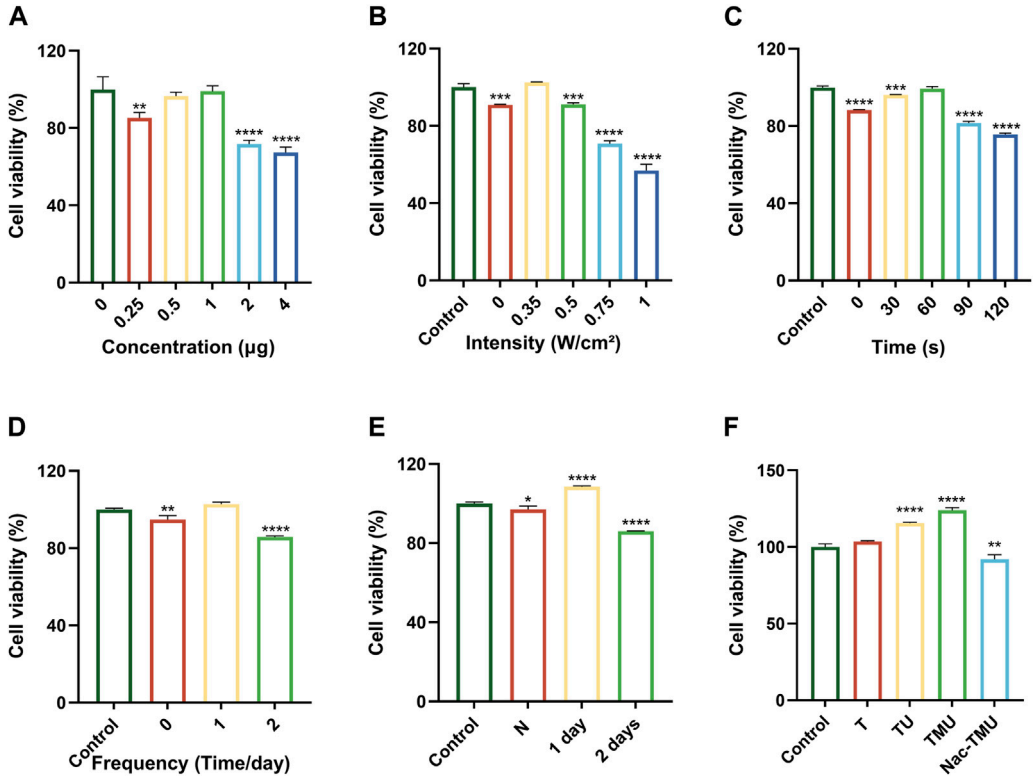

FIGURE 2
Cell viability assay **(A)** Viability of BMSCs cultured in different concentrations of HMME loaded in MOF-HMME-RGD for 24 h. **(B)** Viability of BMSCs with different ultrasound intensities. **(C)** Viability of BMSCs with different ultrasound times (0.35 W/cm^2 ultrasound intensity). **(D)** Viability of BMSCs with different irradiation frequencies once a day. **(E)** Viability of BMSCs at different ultrasound intervals. **(F)** Viability of BMSCs cultured in optimal conditions. Mean ± SD, n = 3. * symbol compared with control group, $^{**}p < 0.01$, $^{***}p < 0.001$, and $^{****}p < 0.0001$.

absorption peak of DPBF decreased with the increase of irradiation time. Besides, the decrease in absorbance of the MOF-HMME-RGD group was quicker than that of the MOF-HMME group, which may be due to the synergistic effect of HMME and RGD to produce more singlet oxygen. In contrast, MOF cannot decline the absorption of DPBF, indicating that MOFs are not able to generate singlet oxygen.

The cellular uptake behavior of MOF-HMME-RGD was investigated in BMSCs for 3 days. The nucleus was subjected to blue fluorescence staining using 4′,6-diamidino-2-phenylindole (DAPI), whereas the MOF-HMME-RGD was labeled with green fluorescence using FITC. As shown in Figure 3B, the cytoplasm exhibited a distribution of MOF-HMME-RGD at the 4-h time point, indicating the effective endocytosis of MOF-HMME-RGD by BMSCs.

During chondrogenesis, appropriate ROS are required for cell growth and differentiation of BMSCs. In order to verify the ROS generation capacity of MOF-HMME-RGD mediated by ultrasound, intracellular ROS production in BMSCs was measured using a chemical probe DCFH-DA. The compound DCFH-DA has the ability to undergo a reaction with ROS, resulting in the formation of 2′,7′-dichlorofluorescein (DCF). This reaction leads to the emission of green fluorescence. As shown in Figure 3C, there was lower fluorescence in the control group and the T group. However, the highest green fluorescence was found in the TMU group and decreased in the Nac-TMU group, which was treated with a ROS scavenger, the N-acetyl cysteine (NAC), indicating that the intracellular ROS can be produced by MOF-HMME-RGD nanoparticles and ROS generation capacity of MOF-HMME-RGD can be enhanced with ultrasound irradiation.

The apoptosis of the BMSCs with ultrasound stimulation was determined to investigate the effect of ROS generation by MOF-HMME-RGD nanoparticles on cell apoptosis. As shown in Figure 3D, the percentage of cell apoptosis in the MOF-HMME + US irradiation (6.48%) and MOF-HMME-RGD + US irradiation (5.54%) was lower than that in the MOF-HMME (8.79%) and MOF-HMME-RGD (8.21%), indicating ROS generation by MOF-HMME-RGD nanoparticles was not cause more apoptosis.

3.4 MOF-HMME-RGD combined with SDT promoted chondrogenic differentiation of BMSCs

The evaluation of GAG, a key component of the ECM present in cartilage, was conducted through the utilization of the DMMB test. As shown in Figure 4A and Figure 4B, MOF-HMME-RGD increased the GAG content via ultrasound by 73.1% and 68.4% on days 7 and 14 compared to the T group, respectively. However, GAG secretion was significantly decreased with the amount by

10.3389/fbioe.2024.1339530

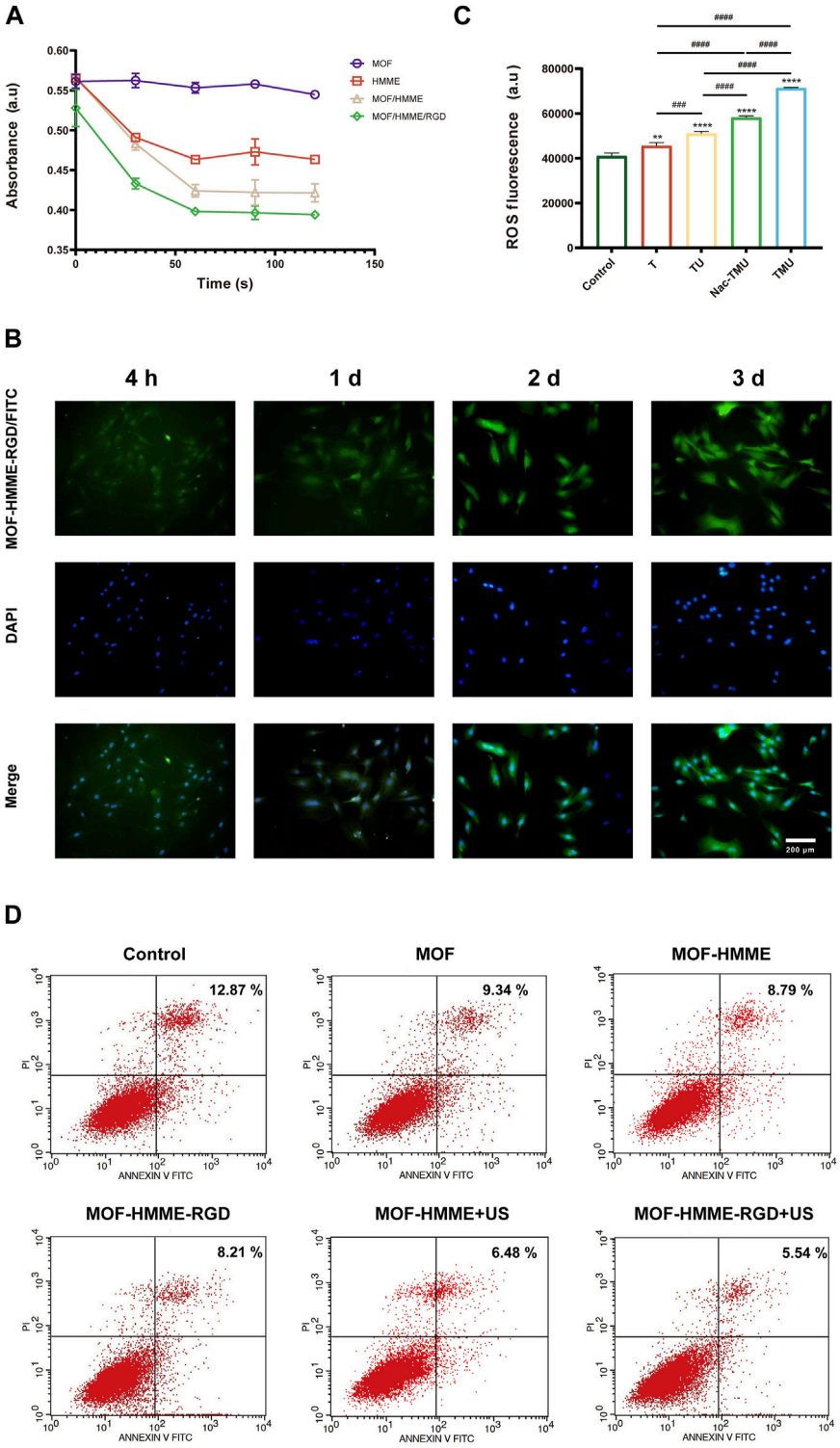

FIGURE 3
ROS generation of MOF-HMME-RGD. **(A)** The capability of singlet oxygen generation was tested by a chemical probe DPBF under different ultrasound times. **(B)** Cellular uptake of MOF-HMME-RGD (MOF-HMME-RGD/FITC: green, DAPI: blue). (Scale bar = 200 μm). **(C)** Intracellular ROS production was assessed with a DCFH-DA probe. **(D)** The apoptosis of the BMSCs with ultrasound stimulation was determined by flow cytometry. Mean ± SD, n = 3. * symbol compared with control group, $^{**}p < 0.01$, $^{***}p < 0.001$, and $^{****}p < 0.0001$, and # symbol compared between groups, $^{\#}p < 0.05$, $^{\#\#}p < 0.01$, $^{\#\#\#}p < 0.001$, and $^{\#\#\#\#}p < 0.0001$.

10.3389/fbioe.2024.1339530

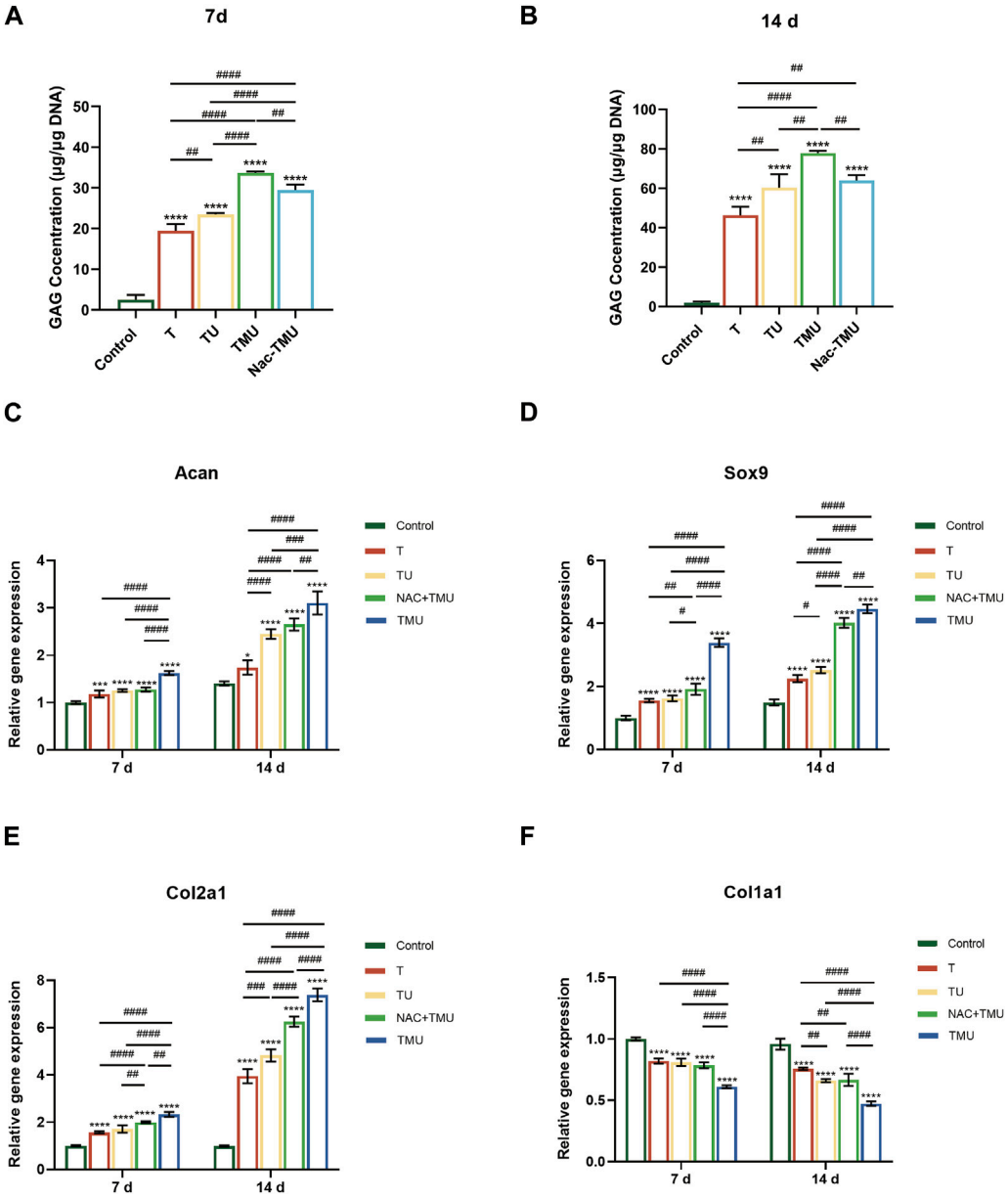

FIGURE 4
MOF-HMME-RGD combined with SDT promoted chondrogenic differentiation of BMSCs. **(A,B)** Secretion of GAG was evaluated by using DMMB assay for 7 days **(B)** and 14 days **(C)**. **(C–F)** The expression levels of *ACAN*, *SOX9*, *Col2a1*, and *Col1a1* in BMSCs were examined by qRT-PCR for 7 and 14 days. Mean ± SD, n = 3, * symbol compared with control group, $^{**}p < 0.01$, $^{***}p < 0.001$, and $^{****}p < 0.0001$, and # symbol compared between groups, $^{\#}p < 0.05$, $^{\#\#}p < 0.01$, $^{\#\#\#}p < 0.001$, and $^{\#\#\#\#}p < 0.0001$.

12.5% and 17.8% on days 7 and 14, respectively, in the Nac-TMU group treated with NAC. Thus, MOF-HMME-RGD could promote the secretion of GAG in BMSCs under ultrasound treatment.

To further explore the synergistic effect of MOF-HMME-RGD on BMSCs chondrogenesis with SDT, the cartilage-specific genes of BMSCs were examined by qRT-PCR (Figures 4C–F). The levels of chondrogenic markers *ACAN*, *SOX9*, and *Col2a1* exhibited a notable increase in the T, TU, Nac-TMU, and TMU groups as compared to the control group. This increase was more pronounced in the TMU group. However, the gene expression of fibrocartilage marker *Col1a1* was significantly downregulated in the TMU group.

3.5 MOF-HMME-RGD and BMSCs combined with SDT promoted cartilage defect repair *in vivo*

In order to assess the potential for cartilage regeneration, a study was conducted using MOF-HMME-RGD and BMSCs as therapeutic agents to repair cartilage lesions of 3 mm × 3 mm×2 mm on the distal femoral condyle surface of Sprague-Dawley rats (Figure 5A). The cartilage regeneration was evaluated comprehensively after 4 weeks or 8 weeks of treatment, respectively. As shown in Figure 5B, there was nearly no inflammation, and synovial hyperplasia was observed for all implanted BMSCs compared to the control group, only with neo-

10.3389/fbioe.2024.1339530

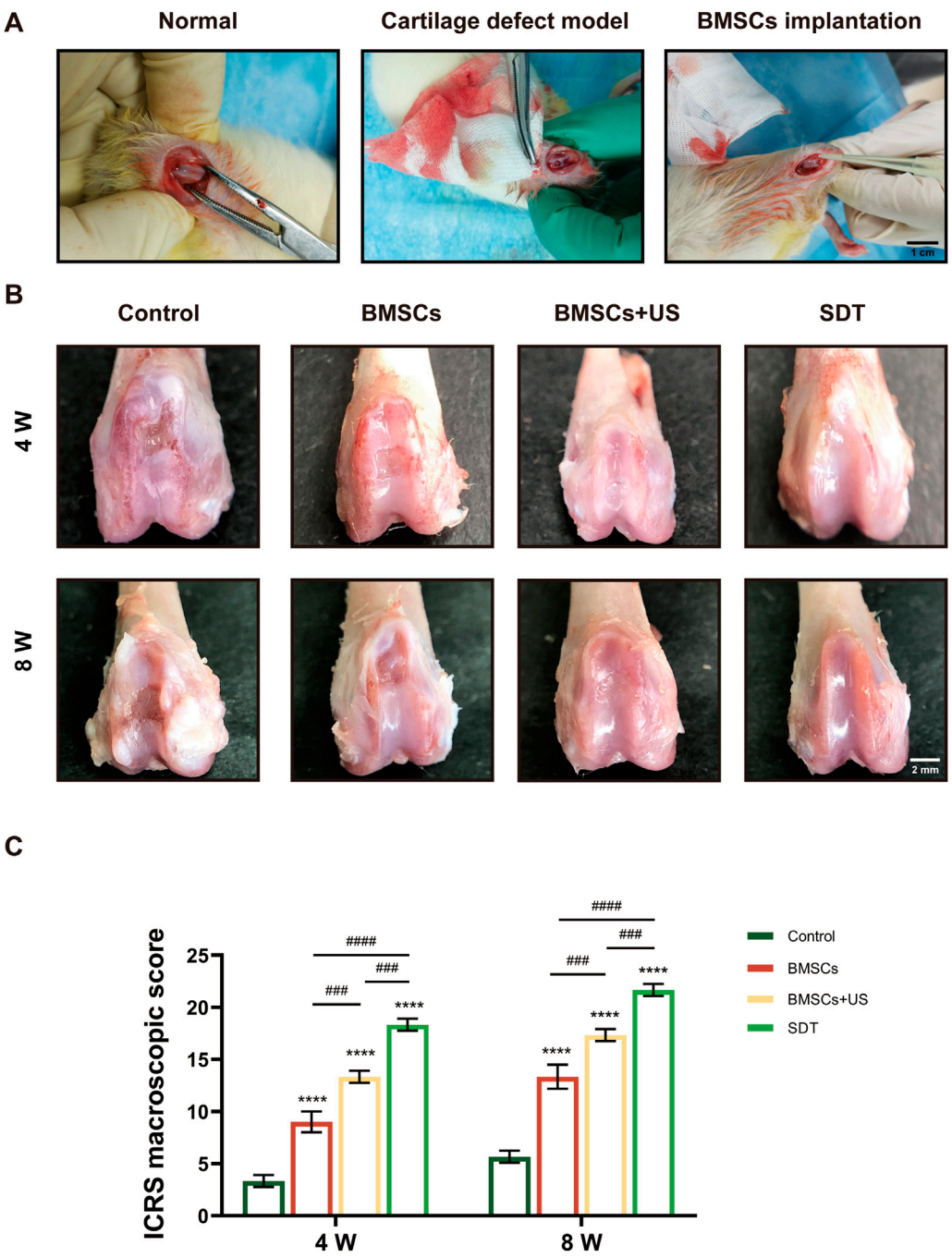

FIGURE 5
Macroscopic observation and scores of therapeutic effects of cartilage defect *in vivo*. **(A)** Animal operation at the articular cartilage site of the distal femoral condyle of the knee in adult SD rats. **(B)** Macroscopic observation of repaired cartilage after 4 weeks and 8 weeks of treatment. **(C)** The corresponding International Cartilage Repair Society (ICRS) macroscopic score. Mean ± SD, n = 3, * symbol compared with control group, $^{**}p < 0.01$, $^{***}p < 0.001$, and $^{****}p < 0.0001$, and # symbol compared between groups, $^{\#}p < 0.05$, $^{\#\#}p < 0.01$, $^{\#\#\#}p < 0.001$, and $^{\#\#\#\#}p < 0.0001$.

cartilage tissue regenerated. Thin fibrous tissue with distinct borders was observed in the control group, indicating poor cartilage self-healing ability. Gross examination of knee joints (Figure 5C) showed that fibrous cartilage tissue formed within the defective area both in the BMSCs and BMSCs + US groups after 4 weeks and 8 weeks of repair. In contrast, smooth white repair tissue with indistinguishable borders could be observed in the SDT group, indicating a superior therapeutic effect. The ICRS macroscopic scores at 4 weeks and 8 weeks post-repair indicated that the SDT group had scores of 18.3 and 21.7, respectively. These values were found to be greater than those observed in the other groups. (Figure 5C).

In addition, the diseased sections underwent analysis by various staining techniques, including HE staining, safranin O/fast green staining, and immunohistochemistry staining, in order to assess

10.3389/fbioe.2024.1339530

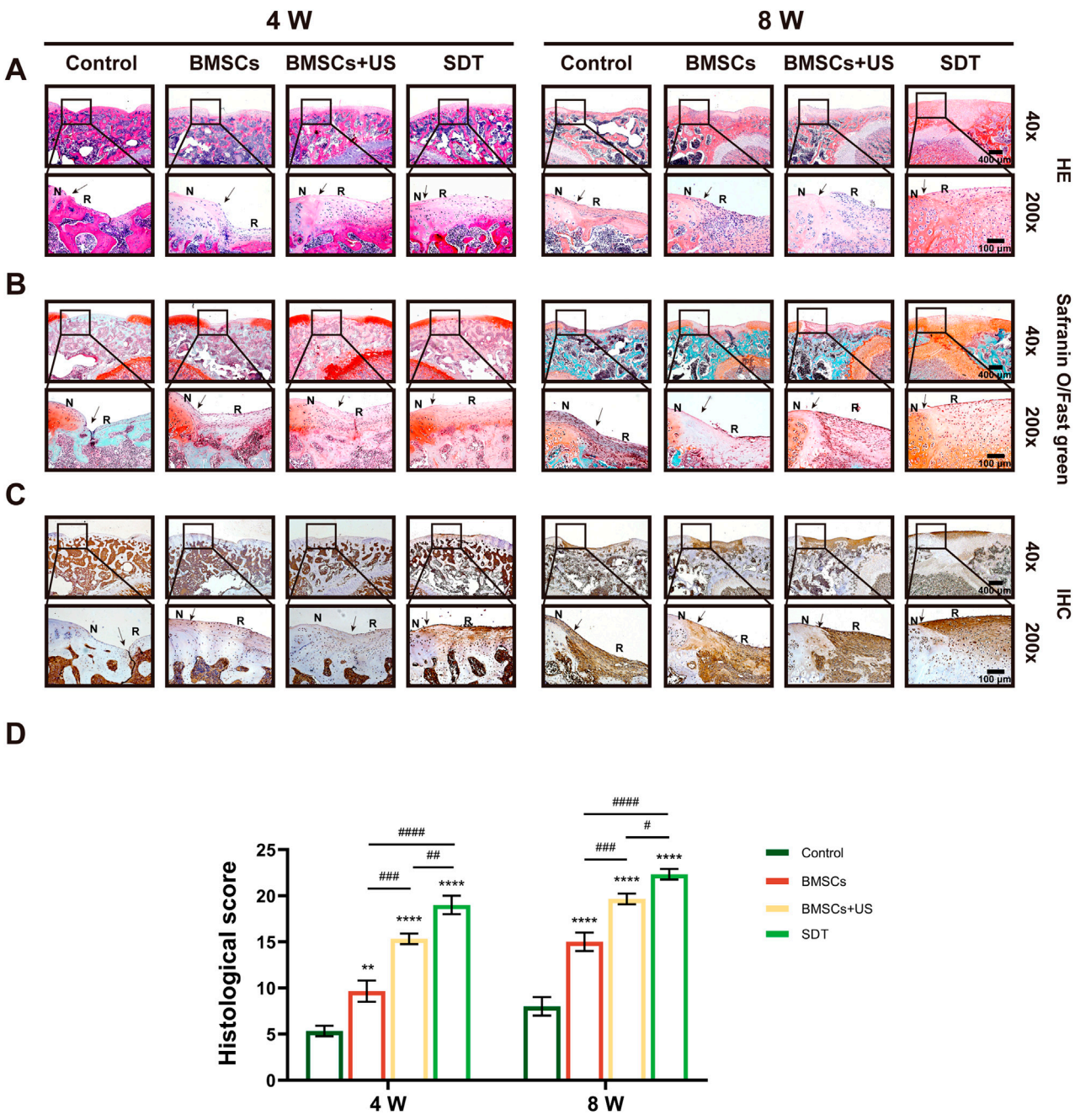

FIGURE 6
Histological observation of therapeutic effects of cartilage defect *in vivo*. **(A)** HE staining, **(B)** Safranin O/fast green staining, and **(C)** Immunohistochemical staining of tissue sections of knee joints with different magnifications. The black arrows show the edges of the repaired cartilage. N: normal cartilage; R: repaired cartilage. **(D)** The histological score of repaired cartilage. Mean ± SD, n = 3, * symbol compared with control group, $^{**}p < 0.01$, $^{***}p < 0.001$, and $^{****}p < 0.0001$, and # symbol compared between groups, $^{\#}p < 0.05$, $^{\#\#}p < 0.01$, $^{\#\#\#}p < 0.001$, and $^{\#\#\#\#}p < 0.0001$.

the efficacy of cartilage repair. It found that the control group formed fibrous tissue in the defect area, creating a large residual gap with the original cartilage. A small number of round or oval depressed cells with the characteristics of chondrocytes and predominantly fibrous tissue were visible on the irregular surface of specimen sections from the BMSCs group. However, a large amount of newly formed cartilage tissue could be observed in specimen sections from the SDT group, whereas neo-cartilage tissue and a small amount of fibrous tissue could be observed in the BMSCs + US group (Figure 6A). In a similar vein, the SDT group exhibited the presence of tissue resembling hyaline cartilage, displaying favorable integration with the surrounding tissues as seen by safranin O/fast green staining in comparison to the other groups (Figure 6B). The technique of immunohistochemical staining was employed to ascertain the presence of *Col2a1* expression within the neo-cartilage tissue. As shown in Figure 6C, the repair area of the control group exhibited

negative staining, whereas the group treated with BMSCs displayed a small amount of positive staining. However, the BMSCs + US group and SDT group stained strongly positive, indicating the formation of hyaline cartilage-like tissue. The histological grade was used to assess cartilage healing using histological investigation, hence corroborating the obtained findings (Figure 6D). The histology score in the SDT group at 8 weeks after surgery was 22.33 ± 0.82 scores, which exhibited a statistically significant increase compared to the other three groups.

4 Discussion

It has been reported that moderate ROS are important for cell growth and differentiation (Liu et al., 2023). During chondrogenesis, ROS are required for cell growth and differentiation of BMSCs (Lu et al., 2019). SDT has emerged as a potentially effective therapeutic modality that has garnered significant interest in recent years. It involves the use of ultrasound to induce sonoluminescence and activate sonosensitizers. The process of activation results in the generation of highly detrimental ROS, such as singlet oxygen and hydroxyl radicals. SDT has developed as a potential US-based treatment option for cartilage-related conditions, offering a new paradigm in cartilage therapy (Vahedi et al., 2021). In our study, we synthesized a good biodegradable, biocompatible sonosensitizer MOF-HMME-RGD to regulate chondrogenic differentiation of BMSCs for cartilage regeneration via the modulation of ROS.

The use of sonosensitizers in the context of SDT has been shown to effectively enhance the treatment of articular cartilage abnormalities (Cook et al., 2001; Xia et al., 2017; He et al., 2024). This approach has many advantages, including non-invasiveness, the ability to penetrate deep into the tissue, high therapeutic efficacy, and little occurrence of adverse effects. However, many sonosensitizers in clinical applications are still limited by the difficulties of non-biodegradation, poor water solubility, low efficient delivery, and potential biosafety issues (Nguyen Cao et al., 2023). We synthesized a good biodegradable, biocompatible sonosensitizer MOF-HMME-RGD, which significantly promoted the cell viability of BMSCs under ultrasound stimulation (Figure 3F). This is mainly due to the composition of MOF-HMME-RGD, including MOFs, hydrolysis products of endogenous hemoglobin HMME, and RGD peptide, which had good biocompatibility and biodegradability. On day 14, the expression levels of chondrogenic genes (*ACAN*, *SOX9*, and *Col2a1*) were found to be 1.21, 1.99, and 6.46-fold higher, respectively, in the MOF-HMME-RGD group (Figures 4C–E). The histological observations provided further confirmation of the regeneration of tissue resembling hyaline cartilage inside the intra-articular setting (Figures 6A–C), as well as the enhanced repair of cartilage defects after damage. The findings suggested that MOF-HMME-RGD exhibited good biocompatibility and low cytotoxicity, hence promoting cellular proliferation and differentiation towards the hyaline cartilage phenotype, which is crucial for chondrogenesis.

The regulation of ROS is an additional significant element that influences the process of chondrogenic differentiation (Bai et al., 2019). In recent years, accumulating studies indicated that ROS were signaling molecules, and a regulated basal level of ROS was necessary and had the advantage of cell functions, such as cell survival, proliferation, and differentiation (Li et al., 2017). ROS are essential for chondrogenesis, and ROS generation was increased in the early stage of chondrogenesis (Heywood and Lee, 2017). The MOF-HMME-RGD exhibited dual functionality as both sonosensitizers and ROS producers when subjected to ultrasonic stimulation. The percentage of cell apoptosis in MOF-HMME-RGD + US irradiation (5.54%) was low, indicating ROS generation by MOF-HMME-RGD nanoparticles was not cause more apoptosis. The T group, which did not have ultrasonic irradiation and thus lacked the ability to produce ROS, had little impact on the process of chondrogenic differentiation and cartilage regeneration. This conclusion is supported by the results obtained from GAG analysis (Figures 4A, B), qRT-PCR measurements (Figures 5C–E), and histological assessments (Figures 6A–C). For the TMU group exposed to ultrasound stimulation, it was observed that there was an increase in intracellular ROS in TMU (Figure 3C), which was associated with the capability to generate singlet oxygen generation detected by the chemical probe DPBF (Figure 3A). During the process of MSCs chondrogenic differentiation, the generated ROS as second messengers mediate the cellular alterations (glycolysis, oxidative metabolism), including alterations in molecules (proteins, nucleic acids, sugars, and lipids) that were essential for promoting differentiation (Li et al., 2017). As a result, MOF-HMME-RGD + SDT resulted in an upregulation of chondrogenic genes (*ACAN*, *SOX9* and *Col2a1*) (Figures 4C–E) and evidently promoted the cartilage regeneration (Figure 5B, Figures 6A–C). After treatment of NAC, which was a direct scavenger for ROS, a notable decrease in the accumulation of glycosaminoglycan, a cartilage-specific ECM component, was observed. Additionally, the expression of cartilage-specific genes was successfully inhibited, hence reducing the impact on chondrogenic differentiation. Our study suggested that ROS generation of MOF-HMME-RGD plays a critical role in BMSCs chondrogenesis and cartilage regeneration.

5 Conclusion

In summary, we synthesized a good biodegradable, biocompatible sonosensitizer MOF-HMME-RGD to regulate the chondrogenic differentiation of BMSCs for cartilage regeneration. The MOF-HMME-RGD NPs have the ability to generate a moderate level of ROS via the process of sonodynamic treatment. This leads to enhanced chondrogenic differentiation of BMSCs by promoting the accumulation of glycosaminoglycan, a particular ECM component found in cartilage. Furthermore, the upregulation of crucial chondrogenic genes, such as *ACAN*, *SOX9*, and *Col2a1*, occurs as a result. Moreover, the combination of transplanted BMSCs and SDT shows an augmented capacity for promoting cartilage regeneration in the context of repairing cartilage defects. This beneficial effect was seen after a duration of 8 weeks of therapeutic intervention. This study presents a synergistic technique that utilizes MOF nanoparticles as a basis for generating

alternative sonosensitizers for the purpose of cartilage regeneration in conjunction with SDT.

Data availability statement

The original contributions presented in the study are included in the article/Supplementary material, further inquiries can be directed to the corresponding authors.

Ethics statement

The animal study was approved by the Animal Ethics Committee standards of Guangxi Medical University. The study was conducted in accordance with the local legislation and institutional requirements.

Author contributions

ShanL: Data curation, Investigation, Conceptualization, Formal Analysis, Software, Writing–original draft. YS: Data curation, Formal Analysis, Investigation, Visualization, Writing–original draft. ZQ: Conceptualization, Data curation, Formal Analysis, Writing–review and editing. BZ: Investigation, Project administration, Writing–review and editing. CL: Methodology, Software, Writing–review and editing. JZ: Conceptualization, Funding acquisition, Resources, Writing–review and editing. RL: Conceptualization, Data curation, Investigation, Methodology, Resources, Writing–review and editing. LZ: Conceptualization, Project administration, Writing–review and editing. ShiLuo: Conceptualization, Investigation, Validation, Writing–review and editing.

Funding

The author(s) declare financial support was received for the research, authorship, and/or publication of this article. This study was financially supported by the Guangxi Science and Technology Major Project (Grant No. GuikeAA19254002), the Guangxi Scientific Research and Technological Development Foundation (Grant No. GuikeAB21220062), and the National Natural Science Foundation of China (Grant No. 81972120 and 82360425).

Conflict of interest

The authors declare that the research was conducted in the absence of any commercial or financial relationships that could be construed as a potential conflict of interest.

Publisher's note

All claims expressed in this article are solely those of the authors and do not necessarily represent those of their affiliated organizations, or those of the publisher, the editors and the reviewers. Any product that may be evaluated in this article, or claim that may be made by its manufacturer, is not guaranteed or endorsed by the publisher.

References

Bai, Y., Gong, X., Dou, C., Cao, Z., and Dong, S. (2019). Redox control of chondrocyte differentiation and chondrogenesis. *Free Radic. Biol. Med.* 132, 83–89. doi:10.1016/j.freeradbiomed.2018.10.443

Betz, V. M., Keller, A., Foehr, P., Thirion, C., Salomon, M., Rammelt, S., et al. (2017). BMP-2 gene activated muscle tissue fragments for osteochondral defect regeneration in the rabbit knee. *J. Gene Med.* 19 (9-10). doi:10.1002/jgm.2972

Cai, H., Ma, J., Xu, X., Chu, H., Zhang, D., and Li, J. (2020). Sulfonated glycosaminoglycan bioinspired carbon dots for effective cellular labelling and promotion of the differentiation of mesenchymal stem cells. *J. Mater Chem. B* 8 (26), 5655–5666. doi:10.1039/d0tb00795a

Cai, W., Gao, H., Chu, C., Wang, X., Wang, J., Zhang, P., et al. (2017). Engineering phototheranostic nanoscale metal-organic frameworks for multimodal imaging-guided cancer therapy. *ACS Appl. Mater Interfaces* 9 (3), 2040–2051. doi:10.1021/acsami.6b11579

Chen, Y., Cai, J., Liu, D., Liu, S., Lei, D., Zheng, L., et al. (2022). Zinc-based metal organic framework with antibacterial and anti-inflammatory properties for promoting wound healing. *Regen. Biomater.* 9, rbac019. doi:10.1093/rb/rbac019

Cook, S. D., Salkeld, S. L., Popich-Patron, L. S., Ryaby, J. P., Jones, D. G., and Barrack, R. L. (2001). Improved cartilage repair after treatment with low-intensity pulsed ultrasound. *Clin. Orthop. Relat. Res.* 391 (391 Suppl. l), S231–S243. doi:10.1097/00003086-200110001-00022

Dai, L., Zhang, X., Hu, X., Liu, Q., Man, Z., Huang, H., et al. (2015). Silencing of miR-101 prevents cartilage degradation by regulating extracellular matrix–related genes in a rat model of osteoarthritis. *Mol. Ther.* 23 (8), 1331–1340. doi:10.1038/mt.2015.61

Gao, J., Liang, Y., Chen, J., Shen, H., and Liu, H. (2023). CXCR4 enhances the inhibitory effects of bone mesenchymal stem cells on lung cell apoptosis in a rat model of smoking-induced COPD. *Apoptosis* 28 (3-4), 639–652. doi:10.1007/s10495-022-01800-6

Gao, T., Boys, A. J., Zhao, C., Chan, K., Estroff, L. A., and Bonassar, L. J. (2021). Non-destructive spatial mapping of glycosaminoglycan loss in native and degraded articular cartilage using confocal Raman microspectroscopy. *Front. Bioeng. Biotechnol.* 9, 744197. doi:10.3389/fbioe.2021.744197

Gugjoo, M. B., Amarpal, H., Sharma, G. T., Aithal, H. P., and Kinjavdekar, P. (2016). Cartilage tissue engineering: role of mesenchymal stem cells along with growth factors and scaffolds. *Indian J. Med. Res.* 144 (3), 339–347. doi:10.4103/0971-5916.198724

He, W., Li, C., Zhao, S., Li, Z., Wu, J., Li, J., et al. (2024). Integrating coaxial electrospinning and 3D printing technologies for the development of biphasic porous scaffolds enabling spatiotemporal control in tumor ablation and osteochondral regeneration. *Bioact. Mater.* 34, 338–353. doi:10.1016/j.bioactmat.2023.12.020

Heywood, H. K., and Lee, D. A. (2017). Bioenergetic reprogramming of articular chondrocytes by exposure to exogenous and endogenous reactive oxygen species and its role in the anabolic response to low oxygen. *J. Tissue Eng. Regen. Med.* 11 (8), 2286–2294. doi:10.1002/term.2126

Huang, J., Liu, F., Han, X., Zhang, L., Hu, Z., Jiang, Q., et al. (2018). Nanosonosensitizers for highly efficient sonodynamic cancer theranostics. *Theranostics* 8 (22), 6178–6194. doi:10.7150/thno.29569

Jallali, N., Ridha, H., Thrasivoulou, C., Butler, P., and Cowen, T. (2007). Modulation of intracellular reactive oxygen species level in chondrocytes by IGF-1, FGF, and TGF-β1. *Connect. Tissue Res.* 48 (3), 149–158. doi:10.1080/03008200701331516

Jiang, Q., Gao, X., Zhang, W., and Chen, Z. (2023). Recent progress in metal-organic framework-based sonosensitizers for sonodynamic tumor therapy. *Biomater. Sci.* 11 (13), 4452–4470. doi:10.1039/d3bm00556a

Kim, K. S., Choi, H. W., Yoon, H. E., and Kim, I. Y. (2010). Reactive oxygen species generated by NADPH oxidase 2 and 4 are required for chondrogenic differentiation. *J. Biol. Chem.* 285 (51), 40294–40302. doi:10.1074/jbc.m110.126821

Koh, R. H., Kim, J., Kim, S. H. L., and Hwang, N. S. (2022). RGD-incorporated biomimetic cryogels for hyaline cartilage regeneration. *Biomed. Mater* 17 (2), 024106. doi:10.1088/1748-605x/ac51b7

Lee, W. Y., and Wang, B. (2017). Cartilage repair by mesenchymal stem cells: clinical trial update and perspectives. *J. Orthop. Transl.* 9, 76–88. doi:10.1016/j.jot.2017.03.005

Li, D., Yang, Y., Li, D., Pan, J., Chu, C., and Liu, G. (2021). Organic sonosensitizers for sonodynamic therapy: from small molecules and nanoparticles toward clinical development. *Small* 17 (42), e2101976. doi:10.1002/smll.202101976

Li, Q., Gao, Z., Chen, Y., and Guan, M. X. (2017). The role of mitochondria in osteogenic, adipogenic and chondrogenic differentiation of mesenchymal stem cells. *Protein Cell.* 8 (6), 439–445. doi:10.1007/s13238-017-0385-7

Liu, L., Mondal, A. M., and Liu, X. (2023). Crosstalk of moderate ROS and PARP-1 contributes to sustainable proliferation of conditionally reprogrammed keratinocytes. *J. Biochem. Mol. Toxicol.* 37 (2), e23262. doi:10.1002/jbt.23262

Liu, Y., Shah, K. M., and Luo, J. (2021). Strategies for articular cartilage repair and regeneration. *Front. Bioeng. Biotechnol.* 9, 770655. doi:10.3389/fbioe.2021.770655

Lu, Z., Liu, S., Le, Y., Qin, Z., He, M., Xu, F., et al. (2019). An injectable collagen-genipin-carbon dot hydrogel combined with photodynamic therapy to enhance chondrogenesis. *Biomaterials* 218, 119190. doi:10.1016/j.biomaterials.2019.05.001

Nguyen Cao, T. G., Truong Hoang, Q., Hong, E. J., Kang, S. J., Kang, J. H., Ravichandran, V., et al. (2023). Mitochondria-targeting sonosensitizer-loaded extracellular vesicles for chemo-sonodynamic therapy. *J. Control Release* 354, 651–663. doi:10.1016/j.jconrel.2023.01.044

Salas-Vidal, E., Lomeli, H., Castro-Obregon, S., Cuervo, R., Escalante-Alcalde, D., and Covarrubias, L. (1998). Reactive oxygen species participate in the control of mouse embryonic cell death. *Exp. Cell. Res.* 238 (1), 136–147. doi:10.1006/excr.1997.3828

Schnabel, D., Salas-Vidal, E., Narvaez, V., Sanchez-Carbente Mdel, R., Hernandez-Garcia, D., Cuervo, R., et al. (2006). Expression and regulation of antioxidant enzymes in the developing limb support a function of ROS in interdigital cell death. *Dev. Biol.* 291 (2), 291–299. doi:10.1016/j.ydbio.2005.12.023

Shi, Y., Hu, X., Zhang, X., Cheng, J., Duan, X., Fu, X., et al. (2019). Superoxide dismutase 3 facilitates the chondrogenesis of bone marrow-derived mesenchymal stem cells. *Biochem. Biophys. Res. Commun.* 509 (4), 983–987. doi:10.1016/j.bbrc.2019.01.042

Song, X., Zhang, Q., Chang, M., Ding, L., Huang, H., Feng, W., et al. (2023). Nanomedicine-enabled sonomechanical, sonopiezoelectric, sonodynamic, and sonothermal therapy. *Adv. Mater* 2023, e2212259. doi:10.1002/adma.202212259

Truong Hoang, Q., Ravichandran, V., Nguyen Cao, T. G., Kang, J. H., Ko, Y. T., Lee, T. I., et al. (2022). Piezoelectric Au-decorated ZnO nanorods: ultrasound-triggered generation of ROS for piezocatalytic cancer therapy. *Chem. Eng. J.* 435, 135039. doi:10.1016/j.cej.2022.135039

Uddin, S. M., Richbourgh, B., Ding, Y., Hettinghouse, A., Komatsu, D. E., Qin, Y. X., et al. (2016). Chondro-protective effects of low intensity pulsed ultrasound. *Osteoarthr. Cartil.* 24 (11), 1989–1998. doi:10.1016/j.joca.2016.06.014

Vahedi, P., Hosainzadegan, H., Brazvan, B., Roshangar, L., Shafaei, H., and Salimnejad, R. (2021). Treatment of cartilage defects by Low-intensity pulsed ultrasound in a sheep model. *Cell. Tissue Bank.* 22 (3), 369–378. doi:10.1007/s10561-020-09880-x

Wen, M., Yu, N., Wu, S., Huang, M., Qiu, P., Ren, Q., et al. (2022). On-demand assembly of polymeric nanoparticles for longer-blood-circulation and disassembly in tumor for boosting sonodynamic therapy. *Bioact. Mater* 18, 242–253. doi:10.1016/j.bioactmat.2022.03.009

Wen, X., Lin, L., and Li, S. (2023). Current trends in MOF (Metal-Organic framework) and metal X-ides. *Int. J. Mol. Sci.* 24 (13), 11188. doi:10.3390/ijms241311188

Wu, S., Zhang, H., Wang, S., Sun, J., Hu, Y., Liu, H., et al. (2023a). Ultrasound-triggered *in situ* gelation with ROS-controlled drug release for cartilage repair. *Mater Horiz.* 10, 3507–3522. doi:10.1039/d3mh00042g

Wu, S., Zhang, H., Wang, S., Sun, J., Hu, Y., Liu, H., et al. (2023b). Ultrasound-triggered *in situ* gelation with ROS-controlled drug release for cartilage repair. *Mater Horiz.* 10 (9), 3507–3522. doi:10.1039/d3mh00042g

Xia, P., Wang, X., Qu, Y., Lin, Q., Cheng, K., Gao, M., et al. (2017). TGF-β1-induced chondrogenesis of bone marrow mesenchymal stem cells is promoted by low-intensity pulsed ultrasound through the integrin-mTOR signaling pathway. *Stem Cell. Res. Ther.* 8 (1), 281. doi:10.1186/s13287-017-0733-9

Xie, Z., Lyu, Z., Wang, J., Li, A., and François-Xavier Corvini, P. (2022). Ultrafine-Mn2O3@N-doped porous carbon hybrids derived from Mn-MOFs: dual-reaction centre catalyst with singlet oxygen-dominant oxidation process. *Chem. Eng. J.* 429, 132299. doi:10.1016/j.cej.2021.132299

Xiong, F., Qin, Z., Chen, H., Lan, Q., Wang, Z., Lan, N., et al. (2020). pH-responsive and hyaluronic acid-functionalized metal-organic frameworks for therapy of osteoarthritis. *J. Nanobiotechnology* 18 (1), 139. doi:10.1186/s12951-020-00694-3

Xu, H., Yu, N., Zhang, J., Wang, Z., Geng, P., Wen, M., et al. (2020). Biocompatible Fe-Hematoporphyrin coordination nanoplatforms with efficient sonodynamic-chemo effects on deep-seated tumors. *Biomaterials* 257, 120239. doi:10.1016/j.biomaterials.2020.120239

Yao, J., Yang, Z., Huang, L., Yang, C., Wang, J., Cao, Y., et al. (2021). Low-intensity focused ultrasound-responsive ferrite-encapsulated nanoparticles for atherosclerotic plaque neovascularization theranostics. *Adv. Sci. (Weinh).* 8 (19), e2100850. doi:10.1002/advs.202100850

frontiers | Frontiers in Bioengineering and Biotechnology

TYPE Review
PUBLISHED 29 February 2024
DOI 10.3389/fbioe.2024.1366398

OPEN ACCESS

EDITED BY
Livia Visai,
University of Pavia, Italy

REVIEWED BY
George S. Hussey,
University of Pittsburgh, United States
Agnes Silvia Klar,
University Children's Hospital Zurich, Switzerland

*CORRESPONDENCE
Fangchun Jin,
jinfangchun@xinhuamed.com.cn

†These authors have contributed equally to this work

RECEIVED 06 January 2024
ACCEPTED 19 February 2024
PUBLISHED 29 February 2024

CITATION
Wang Y, Lu X, Lu J, Hernigou P and Jin F (2024), The role of macrophage polarization in tendon healing and therapeutic strategies: Insights from animal models.
Front. Bioeng. Biotechnol. 12:1366398.
doi: 10.3389/fbioe.2024.1366398

The role of macrophage polarization in tendon healing and therapeutic strategies: Insights from animal models

Yicheng Wang[1†], Xiao Lu[2,3†], Jianxi Lu[2,3], Philippe Hernigou[4] and Fangchun Jin[1*]

[1]Department of Pediatric Orthopedics, Xin Hua Hospital Affiliated to Shanghai Jiao Tong University School of Medicine, Shanghai, China, [2]Shanghai Bio-lu Biomaterials Co., Ltd., Shanghai, China, [3]Shanghai Technology Innovation Center of Orthopedic Biomaterials, Shanghai, China, [4]University Paris East, Orthopedic Hospital Geoffroy Saint Hilaire, Paris, France

Tendon injuries, a common musculoskeletal issue, usually result in adhesions to the surrounding tissue, that will impact functional recovery. Macrophages, particularly through their M1 and M2 polarizations, play a pivotal role in the inflammatory and healing phases of tendon repair. In this review, we explore the role of macrophage polarization in tendon healing, focusing on insights from animal models. The review delves into the complex interplay of macrophages in tendon pathology, detailing how various macrophage phenotypes contribute to both healing and adhesion formation. It also explores the potential of modulating macrophage activity to enhance tendon repair and minimize adhesions. With advancements in understanding macrophage behavior and the development of innovative biomaterials, this review highlights promising therapeutic strategies for tendon injuries.

KEYWORDS

macrophage polarization, tendon healing, M1 and M2 macrophage, tissue repair, inflammatory response, therapeutic strategies, biomaterials in tendon repair, animal models

1 Introduction

Tendons, dense connective tissues responsible for transferring force from muscles to bones, play a crucial role in movement by storing elastic energy and withstanding immense tensile forces. (Docheva et al., 2015). Various injury mechanisms, such as acute overload, tearing, overuse, or age-related degeneration, can lead to tendon injuries. (Thomopoulos et al., 2015). Despite significant advancements in surgical and rehabilitation techniques, tendon repair may encounter postoperative complications. (Voleti et al., 2012). Tendon adhesion, a major complication following tendon injury, affects approximately 40% of patients after surgery, restricting tendon gliding ability and potentially leading to lifelong disability. (de Putter et al., 2012; Titan et al., 2019).

To understand tendon adhesion and healing, it is essential to firstly explore tendon biology, focusing on its collagen composition. Natural tendons are characterized by a sophisticated hierarchy of collagen intermingled with tenocytes and non-collagenous elements. (Benjamin et al., 2008). The tendon as a whole is wrapped in a thin layer called the epitenon. Beneath this layer are the fascicles, aligned with the tendon's length and visible post-dissection, each surrounded by the endotenon, which also provides blood and nerve supply to the tendon. (Voleti et al., 2012).

Based on this structural foundation, we examine the detailed composition of tendon fascicles, crucial components of tendon architecture. Tendon fascicles consist of collagen fibers interspersed with tenocytes and are identifiable under optical microscopy at about 10 μm in diameter. (Screen et al., 2004). Electron microscopy further uncovers collagen fibrils, marked by periodic crimping in relaxed states. (Sharma and Maffulli, 2005). At a more minute level, microfibrils, formed from cross-linked tropocollagen molecules, lay the foundation of this structure, with tropocollagen being a water-soluble triple helix of polypeptide chains. (Screen et al., 2004). These complex structures, down to tropocollagen, are essential for understanding tendon response to stress and repair initiation.

The critical issue of tendon adhesion following injury or surgery was a key focus of current study. (Legrand et al., 2017). Further research has been dedicated to understanding the genesis and prevention of these adhesion, particularly in healing intrasynovial flexor tendons. (Voleti et al., 2012). Animal studies have shed light on critical elements influencing tendon repair and adhesion development, including initial injury severity, quality of surgical repair, and the significance of mechanical loading. (Thomopoulos et al., 2015). While mechanical loading facilitates collagen type III synthesis and boosts growth factor levels as well as cellular and matrix activities at the injury site, its excess can compromise healing. (Wong et al., 2009). Additionally, prolonged immobility is also implicated in adhesion development, as evidenced in various animal models. (Wong et al., 2014).

In the context of these findings, adhesion prevention has become a central goal in tendon repair research, especially considering its role in functional recovery, as adhesions can complicate the healing process and impair functional recovery. (Hu et al., 2023). In light of this, researchers have come to realize that the immune system plays an important role in tendon healing and adhesion formation, many studies have focused on how to modulate the immune response at the injured site. (Chisari et al., 2020). Bao et al. (Bao et al., 2024) expand the horizon of the anti-inflammatory effects primarily driven by sympathetic nerve through β2 adrenergic signals on macrophages, and made a history of using sympathetic stimulation to significantly prevent macrophage-mediated peritendious inflammation. In this context, the role of macrophages, particularly their involvement in the inflammatory response and modulation of the healing process, has garnered increasing attention. This focus stems from the understanding that inflammatory processes, driven largely by macrophages, are critical in the formation of adhesions during tendon healing. (Sunwoo et al., 2020). Additionally, researchers have recognized the significant impact of macrophages on tendon healing and adhesion formation, leading to a shift in focus towards understanding how macrophages specifically regulate tendon adhesion. (Xu et al., 2020) (Table 1).

The natural healing process of injured tendons involves three consecutive and overlapping stages: the inflammatory phase, proliferative phase, and remodeling phase. (Nichols et al., 2019). During the inflammatory phase, cytokines derived from platelets signal an elevation in vascular permeability, attracting circulating inflammatory cells, including phagocytic neutrophils, monocytes, and macrophages, to the injury site. (Marsolais et al., 2001; Chisari et al., 2020). The subsequent proliferative phase is characterized by the release of growth factors, such as vascular endothelial growth factor and members of the transforming growth factor beta (TGF-β) family, stimulating angiogenesis, granulation tissue formation, and fibroblast proliferation. (Wong et al., 2009). In the final remodeling phase, newly synthesized collagen fibers realign along the longitudinal axis of the tendon until they can withstand load. This process may take up to 2 years to complete. (Lomas et al., 2015).

In the context of macrophage-mediated regulation, the dominance of macrophages becomes significant beyond the initial 24-h period following injury. (Wong et al., 2009). Understanding how macrophages modulate the inflammatory and proliferative phases, and their potential impact on the subsequent remodeling phase, is essential for unraveling the intricacies of tendon healing. As we delve into the macrophage-specific aspects of tendon healing, the focus shifts towards strategies that enhance intrinsic healing while minimizing the impact of extrinsic healing, with the ultimate goal of improving the functional recovery of tendons (Stauber et al., 2020).

2 Pathology of macrophage-mediated adhesion

Macrophages are key components of the human innate immune system, widely distributed across connective tissues and various solid organs (Murray, 2017). Their high heterogeneity and plasticity enable them to play diverse roles in human diseases, driven by their ability to differentiate into distinct phenotypes under varying stimuli in the local microenvironment (Mosser and Edwards, 2008; Mould et al., 2019).

Classically activated macrophages, or M1 macrophages, emerge under the induction of lipopolysaccharide (LPS), interferon-gamma (IFN-γ), or tumor necrosis factor-alpha (TNF-α) (Di Benedetto et al., 2019). These M1 macrophages are known for their involvement in phagocytosis and display pro-inflammatory characteristics, essential in the body's response to pathogens and injury.

Conversely, alternative activated macrophages, or M2 macrophages, develop in response to interleukin-4 (IL-4) or interleukin-13 (IL-13) (Viola et al., 2019). These M2 macrophages exhibit anti-inflammatory and pro-healing functions, playing a vital role in tissue repair and regeneration. Notably, M2 macrophages are further subclassified into M2a, M2b, M2c, and M2d subtypes, each characterized by unique activation stimuli, molecular expressions, and functional attributes (Paoli et al., 2014).

Furthermore, Lehner et al (Lehner et al., 2019) have identified a specific population of tissue-resident macrophages in murine and human tendons. These macrophages are key to phagocytosis, inflammatory cytokine secretion, and extracellular matrix-related proteins, playing a crucial role in tendon health and response to injury. Fujii et al. (2022) extend this understanding in the context of anterior cruciate ligament reconstruction (ACLR) in mice, identifying two distinct macrophage populations that infiltrate the tendon/bone interface post-surgery: the $CD9^+$ IL1+ and CX3CR1+ CCR2+ macrophages. The $CD9^+$ IL1+ macrophages peak 1 day after surgery with a highly inflammatory profile, transitioning later to a homeostatic state, while the CX3CR1+ CCR2+ macrophages accumulate more gradually and express interferon signature genes that might suppress bone formation. In addition, Li et al. (2023) provides the first evidence that

TABLE 1 The effect of macrophage targeted therapies on the healing tendons in animal models.

Injured tissue	Intervention	Effect on macrophage	Effect on tendon healing
Murine Supraspinatus Tendons	CCR2 Knockout (CCR2KO)	Reduced macrophage infiltration	Improved biomechanical properties (higher load-to-failure and stiffness) Eliasberg et al. (2023)
Murine Achilles Tendons	Acute Achilles tenotomy and repair	A shift to M2 macrophages coordinating ECM deposition and tissue repair	Agent of degradation and repair in injured tendon tissue Sugg et al. (2014)
Murine Supraspinatus Tendons	Mechanical stimulation	Macrophage M2 polarization	Promoted MSCs chondrogenesis, and improved matrix formation Wang et al. (2023a)
Murine Flexor Digitorum Longus Tendons	Neutralization of active TGF-β1 and genetic manipulation	Reduced TGF-β1 production by macrophages	Attenuation of peritendinous adhesion formation Li et al. (2023)
Murine Flexor Digitorum Longus Tendons	COX siRNAs and Pla1a/Etv1 axis-related treatments	M2 macrophage polarization, increasing Pla1a protein secretion	Enhanced tendon healing Jing et al. (2023)
Murine Supraspinatus Tendons	polarized Macrophages and their derived exosomes	Exosome production and subsequent effects on FAPs	Reduced muscle atrophy and fatty infiltration Liu et al. (2023)
Murine Achilles Tendons	Extracellular vesicle-educated macrophages	M2-like immunophenotypic shift in EEMs	Improved mechanical properties of the healing tendon Chamberlain et al. (2019)
Murine Achilles Tendons	TDSCs seeded in Small Intestinal Submucosa scaffolds	Promotion of M2 macrophage polarization	Reduced adhesions and regulated ECM formation Mao et al. (2022)
Murine Achilles Tendons	Nano-micro fibrous woven scaffolds	Promotion of M2 macrophage polarization	Better tissue organization, reduced inflammatory response Cai et al. (2023)
Murine Achilles Tendons	Wnt3a-modified nanofiber scaffolds	Promotion of M2 macrophage polarization	Accelerated tendon healing, increased mechanical strength, reduced inflammatory response Wei et al. (2023)
Murine Achilles Tendons	Extracellular vesicles from inflammation-primed adipose-derived stem cells	Inhibiting M1 polarization and promoting an M1-to-M2 transition	Reduced inflammation, increased tendon cell proliferation, and improved collagen production Shen and Lane, (2023)
Murine Achilles Tendons	PDTC-loaded electrospun membranes	Inhibition of NF-κB pathway in macrophages	Reduced peritendinous adhesion and inflammation Lu et al. (2023)
Murine Peritendinous tissue	JSH-23-loaded PLA membranes	Inhibition of NF-κB phosphorylation and polarization	Tendon healing enhancement Wang et al. (2022)
Murine Achilles Tendons	Lipid nanoparticle-assisted miR29a delivery via core-shell nanofibers	Promotion of M2 macrophage polarization	Improved collagen composition and alignment, higher mechanical strength Chen et al. (2022)

macrophages are a primary source of TGF-β1, which is crucial in recruiting stem cell and make it differentiate into myofibroblasts to the surrounding site of injured tendon. This breakthrough sheds light on a crucial antiadhesion landmark of drug therapies, as it identifies an accurate cellular target to reduce peritendinous adhesion by manipulating the TGF-β1 pathway.

In normal tendon tissue, both in the outer membrane and inner fibrous layers, macrophages are sparsely distributed. (de la Durantaye et al., 2014). However, this changes during the acute inflammatory phase following tendon injury. (Wong et al., 2009). In such instances, injured tendon tissue releases chemokines, including C-C chemokine ligand 2 (CCL2), which recruit immune cells, predominantly macrophages. (Sugg et al., 2014). This influx of macrophages leads to the further release of chemokines and cytokines, amplifying the inflammatory response and playing a crucial role in the initial phase of tendon healing. (Marsolais et al., 2001) (Figure 1).

The C-C chemokine receptor type 2 (CCR2) is particularly significant in this context, as it plays a vital role in the activation of macrophages, especially those exhibiting pro-inflammatory characteristics. (Liu et al., 2017). Utilizing CCR2 knockout models, researchers have demonstrated reduced recruitment of monocytes and a subsequent decrease in the inflammatory environment at wound healing sites. (Willenborg et al., 2012). This discovery has prompted exploration into CCR2 inhibition as a potential therapeutic approach, with studies in various conditions, including traumatic brain injury and nonalcoholic fatty liver disease, showing promising results. (Morganti et al., 2015; Flores-Toro et al., 2020). In tendon healing, particularly in the context of rotator cuff repair in CCR2 knockout mice models, there has been an observed decline in macrophage infiltration and suppression of interferon pathways. (Eliasberg et al., 2023).

Recent insights into macrophage-mediated adhesion pathology reveal the significant role of macrophage-secreted Secreted Phosphoprotein 1 (SPP1) in aggravating tendon adhesions. (Liu et al., 2022). Moreover, the interaction of SPP1 with fibroblasts, via cytokine secretion and cellular communication, leads to enhanced fibroblast activation and migration, further exacerbating adhesion

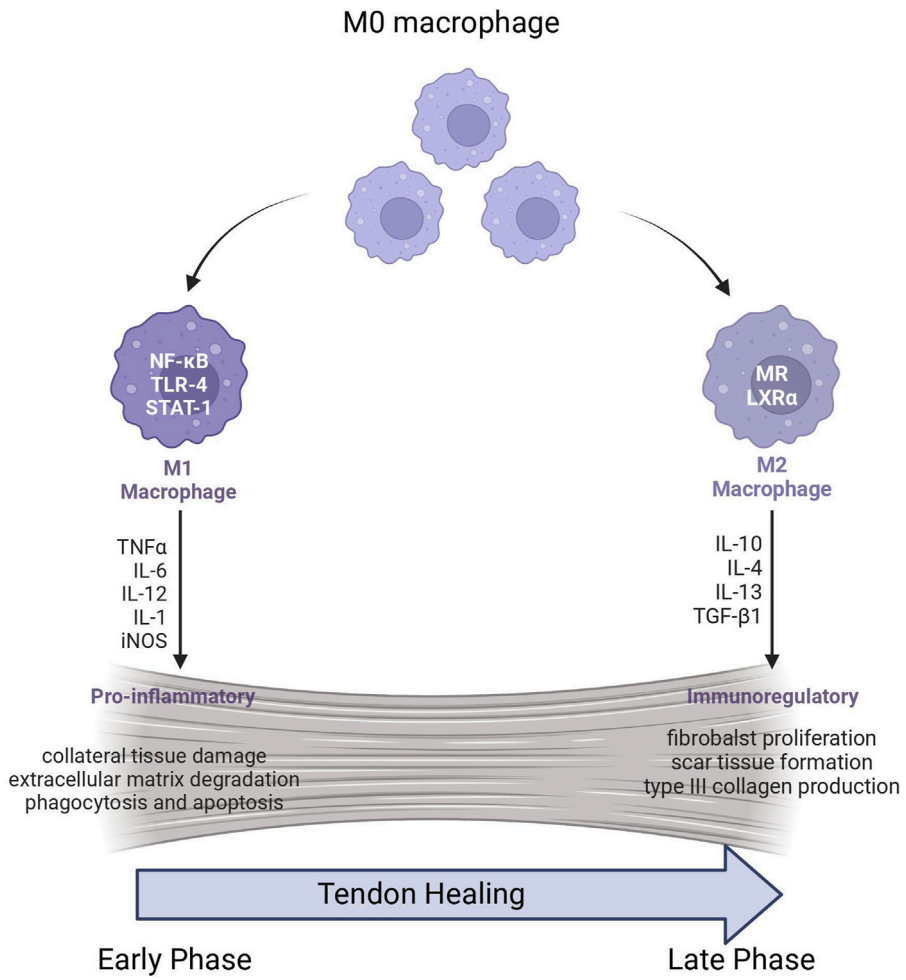

FIGURE 1
Macrophage polarization in Tendon healing.

formation. (Kapur et al., 2019). Wang et al. (Wang et al., 2024) further reveal that elevated SPP1 expression in macrophages enhanced fibroblasts activation to myofibroblasts through CD44 positive feedback pathway, which indicates a crucial cascade amplification between macrophages and myofibroblasts in the field of in inflammatory hyperplasia.

3 M1 macrophage-mediated adhesion mechanisms

In the early stages of tendon healing, the infiltrating macrophages at the site of injury are predominantly of the M1 phenotype (Sunwoo et al., 2020). Their concentration significantly increases within the first 2 weeks of tendon healing, and they localize to the newly formed tendon tissue and areas of tissue remodeling (Marsolais et al., 2001; Sugg et al., 2014). M1 macrophages contribute to the propagation of inflammatory responses by releasing a range of pro-inflammatory cytokines and mediators, such as interleukin-1 (IL-1), IL-6, IL-12, tumor necrosis factor-alpha (TNF-α), and reactive nitrogen and oxygen species (Barrientos et al., 2008; Koh and DiPietro, 2011). While they exhibit stronger microbicidal properties, M1 macrophages also have an increased potential for causing collateral damage to surrounding healthy tissues (Chamberlain et al., 2011; Sica and Mantovani, 2012). Additionally, M1 macrophages contribute to the degradation of the extracellular matrix, engaging in processes such as phagocytosis of cellular debris and apoptosis (Mosser and Edwards, 2008).

Given the pivotal role of M1 macrophages in the early stages of tendon healing, it is important to understand the underlying mechanisms that regulate their activity. One such critical aspect is epigenetic regulation, particularly through DNA methylation (Chen et al., 2023). Crucial DNA methyltransferases like DNA methyltransferase 3b (DNMT3b) and DNMT1 are involved in the polarization of these macrophages. DNMT3b inhibits peroxisome proliferator activated receptor (PPAR)γ1, a regulator of the anti-inflammatory M2 phenotype, thereby promoting the M1 phenotype crucial for the early inflammatory response in tendon healing (Yang et al., 2014). DNMT1 contributes by mediating the hypermethylation of genes that are essential for the pro-inflammatory activities of M1 macrophages (Denis et al., 2011). This intricate regulation of gene expression through epigenetic mechanisms underscores the complexity of M1 macrophage behavior in tendon healing and their critical role in initiating the

inflammatory response that is essential for early stages of tissue repair.

Furthermore, the emerging role of non-coding RNAs (ncRNAs) in macrophage polarization is gaining attention (Ning and Liu, 2013). MicroRNAs (miRNAs) and other ncRNAs, such as long non-coding RNAs (lncRNAs) and circular RNAs (circRNAs), are significant regulators of macrophage behavior. For example, under the stimulation of IL-13 or TGF-β, miR-155 targets IL-13Rα1 and SMAD2, leading to a bias towards M1-like gene expression (Louafi et al., 2010). Beyond miRNAs, there is increasing interest in the role of long non-coding RNAs (lncRNAs) (Wang et al., 2020). LncRNA cyclooxygenase-2 (cox-2), for instance, is more prevalently expressed in LPS-induced M1 macrophages than in IL-4-induced M2 macrophages, and its suppression results in a decrease in M1 macrophage markers (Ye et al., 2018). Additionally, circular RNAs (circRNAs), which have a unique covalently closed loop structure, are also being studied for their relationship with macrophage polarization. Notably, circRNA Cdyl has been found to promote M1 polarization by inhibiting the nuclear translocation of interferon regulatory factor 4 (IRF4) (Song et al., 2022). In a similar vein, circRNA PPM1F is known to enhance the NF-κB signaling pathway following LPS stimulation, promoting M1 polarization (Zhang et al., 2020). This highlights the growing importance of understanding ncRNA-mediated regulation in macrophages, particularly in the context of their role in tissue healing and adhesion mechanisms.

Besides, an increasing number of studies indicate that M1 macrophages may influence the tissue microenvironment through the secretion of exosomes, which function to transport molecules containing biological information (Momen-Heravi et al., 2014). Lou et al. (2023) discovered that miRNA-155-5p, which is highly expressed in exosomes derived from M1-polarized macrophages, exerts antiangiogenic effects by targeting the GDF6-Akt axis, ultimately impacting the healing process in diabetic conditions.

4 M2 macrophage-mediated adhesion mechanisms

In contrast to M1 macrophages, M2 macrophages play a significant role in promoting fibroblast proliferation and stimulation of new tissue deposition. (Mantovani et al., 2002; Sun et al., 2023). The increase in the concentration of M2 macrophages primarily occurs in the later stages of the tendon healing process, especially in the region where the tendon extracellular matrix is located (Nichols et al., 2019). Sugg et al. (2014) found that in healing mouse tendons, the concentration of M2 macrophages within the first 28 days post-injury was similar to that of normal, uninjured tendon tissue. However, after 28 days of tendon injury, there was a significant increase in M2 macrophages, becoming the predominant macrophage phenotype at the site of injury. Wang L. et al. (2023) found that mechanical stimulation promotes the polarization of macrophages into the M2 phenotype and secretion of elevated levels of TGF-β1, ultimately, facilitates the chondrogenic differentiation of MSCs and enhances the process of tendon to bone healing in an acute rotator cuff repair model. Interestingly, while the study found that TGF-β1 secreted by M2 macrophages promotes tendon repair, another study revealed a potential drawback of TGF-β1, as it may contribute to tendon adhesion. The research findings by Li et al. (2023) suggest that TGF-β1 derived from M2 macrophages recruits mesenchymal stem cells and promotes the formation of myofibroblasts in tendon adhesion. Besides, due to its association with the inhibition of pro-inflammatory cytokines including IL-1β, IL-8, GM-CSF, and TNF-α, TGF-β1 is involved in terminating the inflammatory response during tendon healing, with M2 macrophages playing a role in this process (Fadok et al., 1998). Another research has been demonstrated that M2 macrophages facilitate tendon healing by secreting phospholipase A1 member A (Pla1a) (Jing et al., 2023). The secretion of Pla1a not only promotes tendon cell proliferation and reduces apoptosis but also leads to decreased Etv1 expression. This dual action of Pla1a, regulated by M2 macrophages, plays a critical role in reducing tendon adhesion and enhancing cell viability.

Contrasting with the earlier discussed role of M1 macrophage-derived exosomes, Liu et al (Liu et al., 2023) found that exosomes derived from M2 macrophages uniquely influence the differentiation of fibro-adipogenic progenitors, highlighting their distinct role in tendon healing mechanisms. The study provides detailed insights into the dynamic interactions between these exosomes and fibro-adipogenic progenitors, emphasizing that M2 macrophages significantly promote brown/beige fat differentiation, a crucial factor for effective muscle regeneration and reducing fatty infiltration.

M2 macrophage could also be associated with an elevated propensity for scar tissue formation. Wojciak et al (Wojciak and Crossan, 2008) found that the existence of inflammatory cells within the synovial sheath and epitenon during the healing process of tendons prompts synovial fibroblasts and epitenon cells to augment their fibronectin synthesis, thereby establishing a framework that facilitates the subsequent formation of adhesions. Moreover, an elevated M2 macrophage activity was detected in the fibrotic healing process observed in murine flexor digitorum longus tendons with Type II Diabetes (Ackerman et al., 2017). These fibrotic tendons displayed diminished biomechanical strength when compared to the repaired tendons of the nondiabetic control group. This excessive fibrosis could potentially be attributed to the excessive production of TGF-β1 by the M2 macrophages, which has been associated with the development of pathological fibrotic conditions in various tissues (Colwell et al., 2005).

In summary, the complex role of M2 macrophage is greatly due to the distinction between intrinsic and extrinsic healing processes in tendon repair. Intrinsic healing, originating from within the tendon, involves tenocytes and internal collagen synthesis, aiming for the restoration of normal tendon structure and function (Stauber et al., 2020). This contrasts with extrinsic healing, where repair is facilitated by external cells including fibroblasts and macrophages, often leading to the formation of adhesion (Voleti et al., 2012). Therefore, while M2 macrophages are integral to anti-inflammatory responses and promote tissue remodeling, which is beneficial in early stages of tendon repair, their prolonged predominance in later stages can inevitably promote extrinsic healing. Excessive M2 activity may lead to an imbalance in the healing process, deviating from the desired intrinsic repair pathway. Thus, in developing therapeutic strategies for tendon injuries, a critical

goal is to modulate macrophage activity to encourage a balance that supports intrinsic healing, while mitigating the risk of excessive extrinsic tissue formation. This balance is essential for optimal tendon recovery, emphasizing the need for precise temporal and spatial control of macrophage phenotypes during the healing process.

5 Reprogramming of M1 to M2 transition

An increasing amount of evidence suggests that macrophages exhibit a vast spectrum of phenotypes and functions, shaped by specific differentiation signals, surrounding cell types, and the molecular context of different tissues. (Williams et al., 2018; Lehner et al., 2019). This diversity is more intricately understood through advanced technologies such as single-cell RNA-seq and single-cell mass cytometry by time of flight, which allow for the analysis of macrophage phenotypes with unprecedented resolution. (Murray, 2017; Arlauckas et al., 2021). These studies reveal that macrophages exist in a continuum of numerous subtypes, emphasizing the complexity of their roles in various physiological contexts. While the classification of macrophages into M1 and M2 phenotypes provides a useful framework, it serves primarily as a starting point for exploring the regulation of the optimal balance between inflammation and regeneration during tendon healing.

5.1 Interaction between MSCs and macrophages in M1 to M2 reprogramming

Delving into the mechanisms of macrophage transformation, particularly the reprogramming from the M1 to M2 transition, it is crucial to understand the dynamic interplay of macrophages within the healing environment. A significant aspect of this reprogramming is the interaction between macrophages and mesenchymal stromal/stem cells (MSCs), which has been shown to critically influence tendon healing (Maggini et al., 2010). MSCs modulate macrophage behavior by inhibiting M1 markers such as TNF-α and iNOS, and promoting M2 polarization, thereby resulting in improved tendon and ligament healing (Abumaree et al., 2013). A recent study revealed that MSCs facilitated the transition of monocytes into macrophages, heightened the response to microbial stimuli, shifted naive macrophages towards an M1 state, and simultaneously reduced the activity of already activated M1 macrophages while promoting M2 macrophage activation (Vasandan et al., 2016). Despite the current lack of complete understanding regarding the mechanisms underlying MSC-induced macrophage polarization at various stages, several studies have identified certain key factors. For instance, Németh et al. (2009) found that MSCs preconditioned with LPS or TNF-α can modify macrophage behavior through the release of prostaglandin E2 (PGE2), which interacts with macrophages through the EP2 and EP4 receptors. Another study by Chamberlain et al. (2019) showed that macrophage can be educated with extracellular vesicles (EVs) instead of direct coculture with MSCs, suggesting a paracrine-mediated mechanism by which MSCs polarize macrophages. Injured tendons treated with these EV-educated macrophages exhibited improved mechanical properties, reduced inflammation, and earlier angiogenesis, therefore result in superior tendon healing. He et al. (2019) demonstrated that exosomes derived from MSCs can drive macrophages towards M2 polarization. Depletion of MSC-derived exosomes resulted in a reduction in the M2 phenotype of macrophages, suggesting that MSC transplantation induces M2 polarization of macrophages and facilitates wound healing through the transfer of microRNAs within exosomes (Figure 2).

5.2 Comprehensive insights of biomaterials and mechanical stimuli in macrophage polarization

The pivotal role of biomaterials and scaffolds in directing macrophage polarization, a crucial aspect of tendon healing, cannot be overstated. Recent studies have highlighted that material cues can induce macrophage polarization towards either a pro-inflammatory or pro-resolving phenotype, which in turn leads to prolonged inflammation or tendon regeneration, respectively (Lin et al., 2018). (Hotchkiss et al., 2016) highlighted the significance of biomaterials' chemical properties in this context, finding that different titanium-based surfaces affect macrophage activation. This study underscores the influence of surface properties on macrophage behavior and tissue remodeling. Wang et al. (2022) demonstrated that phosphorylation of NF-κB is an excellent unidirectional molecular switch to M1, which gives a insightful solutions to the long-standing challenge of selective control of macrophage polarization. Lu et al. (2023) inhibited M1 macrophages by NF-κB inhibitor PDTC to significantly reduce tendon adhesion formation and promote tendon healing, which firstly makes a record in peritendinous adapted treatment. Further, the physical structure of biomaterials plays a crucial role in macrophage phenotype modulation. Notably, the elongated shape of M2 macrophages compared to M1 macrophages has been leveraged to influence macrophage polarization (Tylek et al., 2020). McWhorter et al. (McWhorter et al., 2013) demonstrated that macrophage elongation, induced by aligned topography, leads to M2 polarization, a process inhibited by disrupting actin or myosin. Chen et al. (Chen et al., 2010) and Luu et al. (Luu et al., 2015) further explored this concept, observing maximal elongation and anti-inflammatory cytokine production in macrophages on substrates with 400–500 nm wide grooves.

The elasticity of substrates also impacts macrophage behavior, with studies showing that different stiffness levels affect activation and cytokine profiles. (Patel et al., 2012). Comparisons of 2D and 3D collagen matrices revealed that 3D environments are more conducive to pro-resolving cytokine secretion, suggesting their suitability for future studies in macrophage polarization. (Friedemann et al., 2017). The influence of mechanical loading on macrophage polarization during tendon healing is another crucial aspect. Blomgran et al. (Blomgran et al., 2016) found that mechanical loading delays the shift from M1 to M2 macrophages and Treg cells during tendon healing in rats by influencing the inflammatory response. This delay in macrophage polarization, caused by mechanical loading, potentially impacts the timing and quality of tendon repair. Conversely, Schoenenberger et al. (Schoenenberger et al., 2020) reported that mechanical loading tends to promote a shift toward an M2-like macrophage phenotype, considered beneficial for tissue healing. These insights highlight the need for further evaluation in biomaterial design to

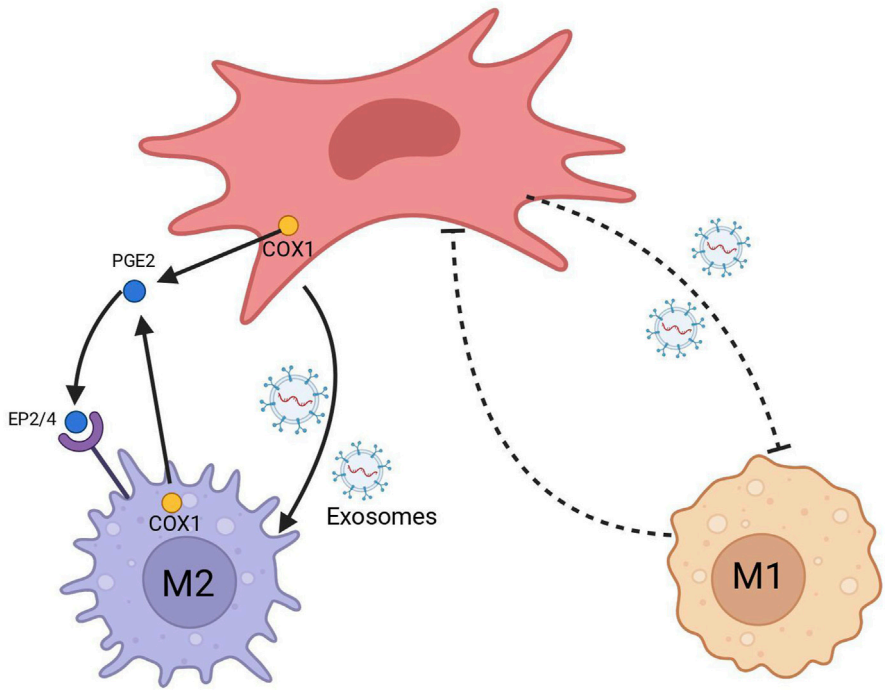

FIGURE 2
MSC interacts with Macrophage.

modulate macrophage polarization for improved tendon healing outcomes. Understanding the interplay among biomaterials, mechanical stimuli, and macrophage behavior is vital for advancing tendon repair strategies.

5.3 Exploring specific biomaterials in macrophage polarization and tendon healing

With the growing focus on manipulating the inflammatory response via biomaterials and scaffolds, considerable research has been directed towards developing various materials. These materials, each with unique attributes and mechanisms, are pivotal in influencing macrophage polarization, underlining their importance in tendon healing advancements. Small Intestinal Submucosa (SIS), as a naturally occurring decellularized matrix material, has been used to treat tendon defects in animals and has shown the ability to enhance tendon tissue regeneration. (Gilbert et al., 2007; Zhang et al., 2019). Mao et al. (Mao et al., 2022) seeded tendon-derived stem cells (TDSCs) onto a hydrogel coating of SIS to promote proliferation and enhance their adhesion and differentiation capabilities. In a 12-week rat Achilles tendon defect model, the combination of SIS scaffold and TDSCs promoted tendon regeneration and induced polarization of macrophages towards the M2 phenotype at the injured site, demonstrating their ability to modulate the immune micro-environment.

Derived from the natural macromolecule amniotic membrane, the decellularized amniotic membrane is another naturally derived biomaterials that has gained prominence due to its unique characteristics. (Tenenhaus, 2017). A recent study highlights the effectiveness of using decellularized amniotic membrane in tendon sheath repair to prevent adhesion. (Liu et al., 2018). This approach is marked by its ability to reduce inflammation and tissue swelling, as well as minimize adhesion formation. Additionally, the amniotic membrane group demonstrated enhanced biomechanical properties in the early postoperative phase compared to control groups. Studies have shown that biologically derived materials, such as decellularized surgical meshes, influence macrophage polarization, with a higher presence of M2 macrophages correlating with positive tissue remodeling outcomes. (Brown et al., 2012). Besides, functional biomaterials developed from naturally derived polysaccharides for tissue regeneration and pharmaceutical application have shown their role on altering macrophage phenotypes and influencing the immune response and tissue healing by recognizing cell membrane receptors. (Li and Bratlie, 2021). These findings suggest the potential of decellularized amniotic membrane as an effective biological material for tendon sheath reconstruction, contributing to improved healing and functionality while decreasing adhesion risks by modulating macrophage activity towards a constructive remodeling phenotype.

Recent trends in research have shown an increased focus on synthetic biomaterials over naturally derived ones. This shift reflects the versatile and customizable nature of synthetic materials, which offers broader possibilities for manipulating macrophage polarization in tendon healing. Cai et al. (Cai et al., 2023) developed a novel high-strength nano-micro fibrous woven

scaffold with native-like anisotropic structure and immunoregulatory function for tendon tissue engineering application. This scaffold, made from polylactic acid and silk fibroin, effectively modulate the polarization of macrophages towards the M2 phenotype, demonstrating significant immunomodulatory capabilities. Additionally, research involving a Wnt3a-modified nanofiber scaffold, as demonstrated in a study, further underscores the potential of material-based approaches in modulating macrophage polarization. (Wei et al., 2023). This scaffold, designed to deliver the Wnt3a protein, not only facilitated the early functional recovery of Achilles tendon injuries in rats but also promoted the transition from an M1-dominated macrophage microenvironment to an M2-dominated one at the injury site, thus supporting tendon regeneration through an immunomodulatory mechanism. Similarly, a study by Shen et al. (Shen and Lane, 2023) revealed that extracellular vesicles from primed adipose-derived stem cells can effectively modulate the macrophage response towards M2 polarization, aiding in reducing inflammation and enhancing tendon healing, providing a complementary biological approach to the material-based strategies.

A notable advancement in tendon repair is highlighted in the work of Cai et al. (Cai et al., 2022), where the synergistic combination of self-healing hydrogel and siRNA nanoparticles presents a groundbreaking approach in macrophage modulation. This innovative design integrates the mechanical resilience and biocompatibility of hydrogels with the targeted gene-silencing capability of siRNA nanoparticles. Furthermore, the influence of biomaterial degradation products on macrophage behavior is a critical factor in peritendinous adhesion. (Wang S. et al., 2023). The findings suggest that the degradation of polylactide nanofibers could potentially modulate the inflammatory response and aid in tissue remodeling through the STAT6 signaling pathway. Their breakthrough of mechanism about Polylactic acid degradation related M2 polarization around tendon can address previously immunoreactivity challenging problems within the field of re-adhesion.

Naturally derived biomaterials such as Small Intestinal Submucosa (SIS) and decellularized amniotic membrane are known for their biocompatibility and anti-inflammatory properties, which are advantageous in reducing inflammation and adhesion in tendon healing. On the other hand, synthetic materials like polylactic acid and silk fibroin scaffolds are notable for their customizability and control over macrophage responses. While natural materials bring biological compatibility, synthetic alternatives offer tailored functionality, though they might require intricate engineering for optimal biocompatibility. This contrast emphasizes the need for careful material selection in tendon repair, based on specific therapeutic objectives.

5.4 The role of molecular pathway NF-κB in macrophage polarization

Furthermore, the understanding of macrophage polarization in tendon healing extends beyond material-based strategies to molecular mechanisms. In this realm, the role of NF-κB as a transcription factor is crucial. NF-κB plays a significant role in promoting the classical activation of macrophages, typically associated with the M1 phenotype. (Chen et al., 2017; Fan et al., 2020). Lu et al. (Lu et al., 2023) encapsulated the NF-κB inhibitor PDTC in electrospun polylactic acid (PLA) membranes, demonstrating that inhibiting NF-κB in macrophages can reduce tendon adhesion formation. Wang et al. (Wang et al., 2022) used the selective NF-κB inhibitor JSH-23 to demonstrate its role in macrophage polarization and the release of inflammatory cytokines. They confirmed that phosphorylation of NF-κB contributes to M1 polarization and the release of pro-inflammatory cytokines. Moreover, Chen et al. (Chen et al., 2022) loaded miR-29a into lipid nanoparticles incorporated into electrospun fiber membranes, finding that miR-29a downregulated NF-κB p65 expression and nuclear translocation at the injury site, promoting M2 polarization and inhibiting inflammation. These studies highlight the importance of targeting molecular pathways such as NF-κB to modulate macrophage behavior, providing insight into the complex interplay of cellular and molecular mechanisms in tendon healing.

However, it is crucial to maintain a balanced macrophage response during tendon healing. While promoting M2 polarization can suppress early inflammatory responses, excessive M2 activity may lead to adverse outcomes, such as the formation of adhesive tissues due to heightened fibroblast proliferation and excessive extracellular matrix deposition. (Colwell et al., 2005; Ackerman et al., 2017). Conversely, M1 macrophages, despite their potential for causing collateral tissue damage, are indispensable for effective tendon repair. Studies have shown that reducing M1 macrophages and neutrophils excessively does not improve Achilles tendon healing, whereas a moderate decrease in the M1/M2 ratio appears to be optimal for the healing process. (Chamberlain et al., 2011). This underscores the importance of a balanced M1 and M2 macrophage presence for optimal tendon recovery.

6 Conclusion

In conclusion, while this review has highlighted significant advancements in understanding macrophage polarization in tendon healing and adhesion mechanisms, the path forward calls for focused exploration. Future research should aim to unravel the complex molecular pathways influencing macrophage behavior, particularly the role of non-coding RNAs. Additionally, the development and clinical application of innovative biomaterials that can modulate macrophage activity presents a promising avenue for enhancing tendon repair and reducing adhesion formation. These focused areas of research hold the potential to significantly advance our understanding and treatment of tendon injuries.

Author contributions

YW: Conceptualization, Investigation, Writing–original draft, Formal Analysis, Writing–review and editing. XL:

Conceptualization, Writing–original draft, Data curation, Writing–review and editing. JL: Conceptualization, Supervision, Writing–review and editing. PH: Conceptualization, Methodology, Writing–review and editing. FJ: Conceptualization, Funding acquisition, Supervision, Writing–review and editing.

Funding

The author(s) declare that financial support was received for the research, authorship, and/or publication of this article. This work is supported by 2021 Shanghai Jiao Tong University "Jiaotong University Star" Program Medical-Industrial Cross-Research Fund (Grant No. YG2021QN47) Shanghai Health Care Commission Clinical Research Special Project for Health Industry (Grant No. 202240106).

Conflict of interest

Authors XL and JL are employed by Shanghai Bio-lu Biomaterials Co., Ltd.

The remaining authors declare that the research was conducted in the absence of any commercial or financial relationships that could be construed as a potential conflict of interest.

Publisher's note

References

Abumaree, M. H., Al Jumah, M. A., Kalionis, B., Jawdat, D., Al Khaldi, A., Abomaray, F. M., et al. (2013). Human placental mesenchymal stem cells (pMSCs) play a role as immune suppressive cells by shifting macrophage differentiation from inflammatory M1 to anti-inflammatory M2 macrophages. *Stem Cell Rev. Rep.* 9, 620–641. doi:10.1007/s12015-013-9455-2

Ackerman, J. E., Geary, M. B., Orner, C. A., Bawany, F., and Loiselle, A. E. (2017). Obesity/Type II diabetes alters macrophage polarization resulting in a fibrotic tendon healing response. *PLOS ONE* 12, e0181127. doi:10.1371/journal.pone.0181127

Arlauckas, S., Oh, N., Li, R., Weissleder, R., and Miller, M. A. (2021). Macrophage imaging and subset analysis using single-cell RNA sequencing. *Nanotheranostics* 5, 36–56. doi:10.7150/ntno.50185

Bao, R., Wang, S., Liu, X., Tu, K., Liu, J., Huang, X., et al. (2024). Neuromorphic electro-stimulation based on atomically thin semiconductor for damage-free inflammation inhibition. *Nat. Commun.* 15, 1327. doi:10.1038/s41467-024-45590-8

Barrientos, S., Stojadinovic, O., Golinko, M. S., Brem, H., and Tomic-Canic, M. (2008). PERSPECTIVE ARTICLE: growth factors and cytokines in wound healing. *Wound Repair Regen.* 16, 585–601. doi:10.1111/j.1524-475X.2008.00410.x

Benjamin, M., Kaiser, E., and Milz, S. (2008). Structure-function relationships in tendons: a review. *J. Anat.* 212, 211–228. doi:10.1111/j.1469-7580.2008.00864.x

Blomgran, P., Blomgran, R., Ernerudh, J., and Aspenberg, P. (2016). A possible link between loading, inflammation and healing: immune cell populations during tendon healing in the rat. *Sci. Rep.* 6, 29824. doi:10.1038/srep29824

Brown, B. N., Londono, R., Tottey, S., Zhang, L., Kukla, K. A., Wolf, M. T., et al. (2012). Macrophage phenotype as a predictor of constructive remodeling following the implantation of biologically derived surgical mesh materials. *Acta Biomater.* 8, 978–987. doi:10.1016/j.actbio.2011.11.031

Cai, C., Zhang, X., Li, Y., Liu, X., Wang, S., Lu, M., et al. (2022). Self-healing hydrogel embodied with macrophage-regulation and responsive-gene-silencing properties for synergistic prevention of peritendinous adhesion. *Adv. Mater.* 34, 2106564. doi:10.1002/adma.202106564

Cai, J., Liu, J., Xu, J., Li, Y., Zheng, T., Zhang, T., et al. (2023). Constructing high-strength nano-micro fibrous woven scaffolds with native-like anisotropic structure and immunoregulatory function for tendon repair and regeneration. *Biofabrication* 15, 025002. doi:10.1088/1758-5090/acb106

Chamberlain, C. S., Clements, A. E. B., Kink, J. A., Choi, U., Baer, G. S., Halanski, M. A., et al. (2019). Extracellular vesicle-educated macrophages promote early Achilles tendon healing. *Stem Cells* 37, 652–662. doi:10.1002/stem.2988

Chamberlain, C. S., Leiferman, E. M., Frisch, K. E., Wang, S., Yang, X., van Rooijen, N., et al. (2011). The influence of macrophage depletion on ligament healing. *Connect. Tissue Res.* 52, 203–211. doi:10.3109/03008207.2010.511355

Chen, C., Liu, T., Tang, Y., Luo, G., Liang, G., and He, W. (2023). Epigenetic regulation of macrophage polarization in wound healing. *Burns Trauma* 11, tkac057. tkac057. doi:10.1093/burnst/tkac057

Chen, S., Jiang, S., Zheng, W., Tu, B., Liu, S., Ruan, H., et al. (2017). RelA/p65 inhibition prevents tendon adhesion by modulating inflammation, cell proliferation, and apoptosis. *Cell Death Dis.* 8, e2710. doi:10.1038/cddis.2017.135

Chen, S., Jones, J. A., Xu, Y., Low, H.-Y., Anderson, J. M., and Leong, K. W. (2010). Characterization of topographical effects on macrophage behavior in a foreign body response model. *Biomaterials* 31, 3479–3491. doi:10.1016/j.biomaterials.2010.01.074

Chen, W., Chen, Y., Ren, Y., Gao, C., Ning, C., Deng, H., et al. (2022). Lipid nanoparticle-assisted miR29a delivery based on core-shell nanofibers improves tendon healing by cross-regulation of the immune response and matrix remodeling. *Biomaterials* 291, 121888. doi:10.1016/j.biomaterials.2022.121888

Chisari, E., Rehak, L., Khan, W. S., and Maffulli, N. (2020). The role of the immune system in tendon healing: a systematic review. *Br. Med. Bull.* 133, 49–64. doi:10.1093/bmb/ldz040

Colwell, A. S., Phan, T.-T., Kong, W., Longaker, M. T., and Lorenz, P. H. (2005). Hypertrophic scar fibroblasts have increased connective tissue growth factor expression after transforming growth factor-β stimulation. *Plast. Reconstr. Surg.* 116, 1387–1390. doi:10.1097/01.prs.0000182343.99694.28

de la Durantaye, M., Piette, A. B., van Rooijen, N., and Frenette, J. (2014). Macrophage depletion reduces cell proliferation and extracellular matrix accumulation but increases the ultimate tensile strength of injured Achilles tendons. *J. Orthop. Res.* 32, 279–285. doi:10.1002/jor.22504

Denis, H., Ndlovu, 'M. N., and Fuks, F. (2011). Regulation of mammalian DNA methyltransferases: a route to new mechanisms. *EMBO Rep.* 12, 647–656. doi:10.1038/embor.2011.110

de Putter, C. E., Selles, R. W., Polinder, S., Panneman, M. J. M., Hovius, S. E. R., and van Beeck, E. F. (2012). Economic impact of hand and wrist injuries: health-care costs and productivity costs in a population-based study. *JBJS* 94, e56. doi:10.2106/JBJS.K.00561

Di Benedetto, P., Ruscitti, P., Vadasz, Z., Toubi, E., and Giacomelli, R. (2019). Macrophages with regulatory functions, a possible new therapeutic perspective in autoimmune diseases. *Autoimmun. Rev.* 18, 102369. doi:10.1016/j.autrev.2019.102369

Docheva, D., Müller, S. A., Majewski, M., and Evans, C. H. (2015). Biologics for tendon repair. *Adv. Drug Deliv. Rev.* 84, 222–239. doi:10.1016/j.addr.2014.11.015

Eliasberg, C. D., Carballo, C. B., Piacentini, A., Caughey, S., Havasy, J., Khan, M., et al. (2023). Effect of CCR2 knockout on tendon biomechanical properties in a mouse model of delayed rotator cuff repair. *J. Bone Jt. Surg.* 105, 779–788. doi:10.2106/JBJS.22.01160

Fadok, V. A., Bratton, D. L., Konowal, A., Freed, P. W., Westcott, J. Y., and Henson, P. M. (1998). Macrophages that have ingested apoptotic cells *in vitro* inhibit proinflammatory cytokine production through autocrine/paracrine mechanisms involving TGF-beta, PGE2, and PAF. doi:10.1172/JCI1112

Fan, H., Wu, Q., Peng, L., Li, D., Dong, Y., Cao, M., et al. (2020). Phyllolobium chinense fisch flavonoids (PCFF) suppresses the M1 polarization of LPS-stimulated RAW264.7 macrophages by inhibiting NF-κB/iNOS signaling pathway. *Front. Pharmacol.* 11, 864. doi:10.3389/fphar.2020.00864

Flores-Toro, J. A., Luo, D., Gopinath, A., Sarkisian, M. R., Campbell, J. J., Charo, I. F., et al. (2020). CCR2 inhibition reduces tumor myeloid cells and unmasks a checkpoint inhibitor effect to slow progression of resistant murine gliomas. *Proc. Natl. Acad. Sci.* 117, 1129–1138. doi:10.1073/pnas.1910856117

Friedemann, M., Kalbitzer, L., Franz, S., Moeller, S., Schnabelrauch, M., Simon, J.-C., et al. (2017). Instructing human macrophage polarization by stiffness and glycosaminoglycan functionalization in 3D collagen networks. *Adv. Healthc. Mater.* 6, 1600967. doi:10.1002/adhm.201600967

Fujii, T., Wada, S., Carballo, C. B., Bell, R. D., Morita, W., Nakagawa, Y., et al. (2022). Distinct inflammatory macrophage populations sequentially infiltrate bone-to-tendon

interface tissue after anterior cruciate ligament (ACL) reconstruction surgery in mice. *JBMR Plus* 6, e10635. doi:10.1002/jbm4.10635

Gilbert, T. W., Stewart-Akers, A. M., Simmons-Byrd, A., and Badylak, S. F. (2007). Degradation and remodeling of Small intestinal Submucosa in canine Achilles tendon repair. *JBJS* 89, 621–630. doi:10.2106/JBJS.E.00742

He, X., Dong, Z., Cao, Y., Wang, H., Liu, S., Liao, L., et al. (2019). MSC-derived exosome promotes M2 polarization and enhances cutaneous wound healing. *Stem Cells Int.* 2019, 1–16. doi:10.1155/2019/7132708

Hotchkiss, K. M., Reddy, G. B., Hyzy, S. L., Schwartz, Z., Boyan, B. D., and Olivares-Navarrete, R. (2016). Titanium surface characteristics, including topography and wettability, alter macrophage activation. *Acta Biomater.* 31, 425–434. doi:10.1016/j.actbio.2015.12.003

Hu, J., Liu, S., and Fan, C. (2023). Applications of functionally-adapted hydrogels in tendon repair. *Front. Bioeng. Biotechnol.* 11, 1135090. doi:10.3389/fbioe.2023.1135090

Jing, J., Qian Qian, Y., Jie, S., and You Lang, Z. (2023). Macrophages regulated by cyclooxygenases promote tendon healing via Pla1a/Etv1 axis. *Chem. Eng. J.* 477, 147144. doi:10.1016/j.cej.2023.147144

Kapur, R., Kasetty, G., Rebetz, J., Egesten, A., and Semple, J. W. (2019). Osteopontin mediates murine transfusion-related acute lung injury via stimulation of pulmonary neutrophil accumulation. *Blood* 134, 74–84. doi:10.1182/blood.2019000972

Koh, T. J., and DiPietro, L. A. (2011). Inflammation and wound healing: the role of the macrophage. *Expert Rev. Mol. Med.* 13, e23. doi:10.1017/S1462399411001943

Legrand, A., Kaufman, Y., Long, C., and Fox, P. M. (2017). Molecular biology of flexor tendon healing in relation to reduction of tendon adhesions. *J. Hand Surg.* 42, 722–726. doi:10.1016/j.jhsa.2017.06.013

Lehner, C., Spitzer, G., Gehwolf, R., Wagner, A., Weissenbacher, N., Deininger, C., et al. (2019). Tenophages: a novel macrophage-like tendon cell population expressing CX3CL1 and CX3CR1. *Dis. Model. Mech. Dmm.* 12, 041384. doi:10.1242/dmm.041384

Li, Y., Wang, X., Hu, B., Sun, Q., Wan, M., Carr, A., et al. (2023). Neutralization of excessive levels of active TGF-β1 reduces MSC recruitment and differentiation to mitigate peritendinous adhesion. *Bone Res.* 11, 24. doi:10.1038/s41413-023-00252-1

Li, Z., and Bratlie, K. M. (2021). The influence of polysaccharides-based material on macrophage phenotypes. *Macromol. Biosci.* 21, 2100031. doi:10.1002/mabi.202100031

Lin, J., Zhou, W., Han, S., Bunpetch, V., Zhao, K., Liu, C., et al. (2018). Cell-material interactions in tendon tissue engineering. *Acta Biomater.* 70, 1–11. doi:10.1016/j.actbio.2018.01.012

Liu, C., Yu, K., Bai, J., Tian, D., and Liu, G. (2018). Experimental study of tendon sheath repair via decellularized amnion to prevent tendon adhesion. *PLOS ONE* 13, e0205811. doi:10.1371/journal.pone.0205811

Liu, J., Huang, Y., Gong, Y., Liu, Q., Lin, J., Liu, J., et al. (2022). CTHRC1+ fibroblasts are stimulated by macrophage-secreted SPP1 to induce excessive collagen deposition in keloids. *Clin. Transl. Med.* 12, e1115. doi:10.1002/ctm2.1115

Liu, J., Xue, Y., Dong, D., Xiao, C., Lin, C., Wang, H., et al. (2017). CCR2– and CCR2+ corneal macrophages exhibit distinct characteristics and balance inflammatory responses after epithelial abrasion. *Mucosal Immunol.* 10, 1145–1159. doi:10.1038/mi.2016.139

Liu, M., Ng, M., Phu, T., Bouchareychas, L., Feeley, B. T., Kim, H. T., et al. (2023). Polarized macrophages regulate fibro/adipogenic progenitor (FAP) adipogenesis through exosomes. *Stem Cell Res. Ther.* 14, 321. doi:10.1186/s13287-023-03555-6

Lomas, A. J., Ryan, C. N. M., Sorushanova, A., Shologu, N., Sideri, A. I., Tsioli, V., et al. (2015). The past, present and future in scaffold-based tendon treatments. *Adv. Drug Deliv. Rev.* 84, 257–277. doi:10.1016/j.addr.2014.11.022

Lou, R., Chen, J., Zhou, F., Zhang, T., Chen, X., Wang, C., et al. (2023). Exosomal miRNA-155-5p from M1-polarized macrophages suppresses angiogenesis by targeting GDF6 to interrupt diabetic wound healing. *Mol. Ther. - Nucleic Acids* 34, 102074. doi:10.1016/j.omtn.2023.102074

Louafi, F., Martinez-Nunez, R. T., and Sanchez-Elsner, T. (2010). MicroRNA-155 targets SMAD2 and modulates the response of macrophages to transforming growth factor-β. *J. Biol. Chem.* 285, 41328–41336. doi:10.1074/jbc.M110.146852

Lu, M., Wang, S., Wang, H., Xue, T., Cai, C., Fan, C., et al. (2023). Pyrrolidine dithiocarbamate-loaded electrospun membranes for peritendinous anti-adhesion through inhibition of the nuclear factor-κb pathway. *Acta Biomater.* 155, 333–346. doi:10.1016/j.actbio.2022.10.004

Luu, T. U., Gott, S. C., Woo, B. W. K., Rao, M. P., and Liu, W. F. (2015). Micro- and nanopatterned topographical cues for regulating macrophage cell shape and phenotype. *ACS Appl. Mater. Interfaces* 7, 28665–28672. doi:10.1021/acsami.5b10589

Maggini, J., Mirkin, G., Bognanni, I., Holmberg, J., Piazzón, I. M., Nepomnaschy, I., et al. (2010). Mouse bone marrow-derived mesenchymal stromal cells turn activated macrophages into a regulatory-like profile. *PLOS ONE* 5, e9252. doi:10.1371/journal.pone.0009252

Mantovani, A., Sozzani, S., Locati, M., Allavena, P., and Sica, A. (2002). Macrophage polarization: tumor-associated macrophages as a paradigm for polarized M2 mononuclear phagocytes. *Trends Immunol.* 23, 549–555. doi:10.1016/S1471-4906(02)02302-5

Mao, X., Yao, L., Li, M., Zhang, X., Weng, B., Zhu, W., et al. (2022). Enhancement of tendon repair using tendon-derived stem cells in Small intestinal Submucosa via M2 macrophage polarization. *Cells* 11, 2770. doi:10.3390/cells11172770

Marsolais, D., Côté, C. H., and Frenette, J. (2001). Neutrophils and macrophages accumulate sequentially following Achilles tendon injury. *J. Orthop. Res.* 19, 1203–1209. doi:10.1016/S0736-0266(01)00031-6

McWhorter, F. Y., Wang, T., Nguyen, P., Chung, T., and Liu, W. F. (2013). Modulation of macrophage phenotype by cell shape. *Proc. Natl. Acad. Sci.* 110, 17253–17258. doi:10.1073/pnas.1308887110

Momen-Heravi, F., Bala, S., Bukong, T., and Szabo, G. (2014). Exosome-mediated delivery of functionally active miRNA-155 inhibitor to macrophages. *Nanomedicine Nanotechnol. Biol. Med.* 10, 1517–1527. doi:10.1016/j.nano.2014.03.014

Morganti, J. M., Jopson, T. D., Liu, S., Riparip, L.-K., Guandique, C. K., Gupta, N., et al. (2015). CCR2 antagonism alters brain macrophage polarization and ameliorates cognitive dysfunction induced by traumatic brain injury. *J. Neurosci.* 35, 748–760. doi:10.1523/JNEUROSCI.2405-14.2015

Mosser, D. M., and Edwards, J. P. (2008). Exploring the full spectrum of macrophage activation. *Nat. Rev. Immunol.* 8, 958–969. doi:10.1038/nri2448

Mould, K. J., Jackson, N. D., Henson, P. M., Seibold, M., and Janssen, W. J. (2019). Single cell RNA sequencing identifies unique inflammatory airspace macrophage subsets. *JCI Insight* 4, e126556. doi:10.1172/jci.insight.126556

Murray, P. J. (2017). Macrophage polarization. *Annu. Rev. Physiol.* 79, 541–566. doi:10.1146/annurev-physiol-022516-034339

Németh, K., Leelahavanichkul, A., Yuen, P. S. T., Mayer, B., Parmelee, A., Doi, K., et al. (2009). Bone marrow stromal cells attenuate sepsis via prostaglandin E2–dependent reprogramming of host macrophages to increase their interleukin-10 production. *Nat. Med.* 15, 42–49. doi:10.1038/nm.1905

Nichols, A. E. C., Best, K. T., and Loiselle, A. E. (2019). The cellular basis of fibrotic tendon healing: challenges and opportunities. *Transl. Res.* 209, 156–168. doi:10.1016/j.trsl.2019.02.002

Ning, P., and Liu, D. W. (2013). Advances in the research of the role of MicroRNAs in wound healing. *Zhonghua Shao Shang za zhi* 29 (4), 374–377.

Paoli, F. D., Staels, B., and Chinetti-Gbaguidi, G. (2014). Macrophage phenotypes and their modulation in atherosclerosis. *Circ. J.* 78, 1775–1781. doi:10.1253/circj.CJ-14-0621

Patel, N. R., Bole, M., Chen, C., Hardin, C. C., Kho, A. T., Mih, J., et al. (2012). Cell elasticity determines macrophage function. *PLOS ONE* 7, e41024. doi:10.1371/journal.pone.0041024

Schoenenberger, A. D., Tempfer, H., Lehner, C., Egloff, J., Mauracher, M., Bird, A., et al. (2020). Macromechanics and polycaprolactone fiber organization drive macrophage polarization and regulate inflammatory activation of tendon *in vitro* and *in vivo*. *Biomaterials* 249, 120034. doi:10.1016/j.biomaterials.2020.120034

Screen, H. R. C., Lee, D. A., Bader, D. L., and Shelton, J. C. (2004). An investigation into the effects of the hierarchical structure of tendon fascicles on micromechanical properties. *Proc. Inst. Mech. Eng. H.* 218, 109–119. doi:10.1243/095441104322984004

Sharma, P., and Maffulli, N. (2005). Basic biology of tendon injury and healing. *Surgeon* 3 (5), 309–316. doi:10.1016/s1479-666x(05)80109-x

Shen, H., and Lane, R. A. (2023). Extracellular vesicles from primed adipose-derived stem cells enhance Achilles tendon repair by reducing inflammation and promoting intrinsic healing. *Stem Cells* 41, 617–627. doi:10.1093/stmcls/sxad032

Song, H., Yang, Y., Sun, Y., Wei, G., Zheng, H., Chen, Y., et al. (2022). Circular RNA Cdyl promotes abdominal aortic aneurysm formation by inducing M1 macrophage polarization and M1-type inflammation. *Mol. Ther.* 30, 915–931. doi:10.1016/j.ymthe.2021.09.017

Stauber, T., Blache, U., and Snedeker, J. G. (2020). Tendon tissue microdamage and the limits of intrinsic repair. *Matrix Biol.* 85 (86), 68–79. doi:10.1016/j.matbio.2019.07.008

Sugg, K. B., Lubardic, J., Gumucio, J. P., and Mendias, C. L. (2014). Changes in macrophage phenotype and induction of epithelial-to-mesenchymal transition genes following acute Achilles tenotomy and repair. *J. Orthop. Res.* 32, 944–951. doi:10.1002/jor.22624

Sun, J., Ju, F., Jin, J., Wang, H. L., Li, Z. J., Sun, Y. C., et al. (2023). M2 macrophage membrane-mediated biomimetic-nanoparticle carrying COX-siRNA targeted delivery for prevention of tendon adhesions by inhibiting inflammation. *Small* 19, 2300326. doi:10.1002/smll.202300326

Sunwoo, J. Y., Eliasberg, C. D., Carballo, C. B., and Rodeo, S. A. (2020). The role of the macrophage in tendinopathy and tendon healing. *J. Orthop. Res.* 38, 1666–1675. doi:10.1002/jor.24667

Tenenhaus, M. (2017). The use of dehydrated human amnion/chorion membranes in the treatment of burns and complex wounds: current and future applications. *Ann. Plast. Surg.* 78, S11–S13. doi:10.1097/SAP.0000000000000983

Thomopoulos, S., Parks, W. C., Rifkin, D. B., and Derwin, K. A. (2015). Mechanisms of tendon injury and repair. *J. Orthop. Res.* 33, 832–839. doi:10.1002/jor.22806

Titan, A. L., Foster, D. S., Chang, J., and Longaker, M. T. (2019). Flexor tendon: development, healing, adhesion formation, and contributing growth factors. *Plast. Reconstr. Surg.* 144, 639e–647e. doi:10.1097/PRS.0000000000006048

Tylek, T., Blum, C., Hrynevich, A., Schlegelmilch, K., Schilling, T., Dalton, P. D., et al. (2020). Precisely defined fiber scaffolds with 40 μm porosity induce elongation driven M2-like polarization of human macrophages. *Biofabrication* 12, 025007. doi:10.1088/1758-5090/ab5f4e

Vasandan, A. B., Jahnavi, S., Shashank, C., Prasad, P., Kumar, A., and Prasanna, S. J. (2016). Human Mesenchymal stem cells program macrophage plasticity by altering their metabolic status via a PGE2-dependent mechanism. *Sci. Rep.* 6, 38308. doi:10.1038/srep38308

Viola, A., Munari, F., Sánchez-Rodríguez, R., Scolaro, T., and Castegna, A. (2019). The metabolic signature of macrophage responses. *Front. Immunol.* 10, 1462. doi:10.3389/fimmu.2019.01462

Voleti, P. B., Buckley, M. R., and Soslowsky, L. J. (2012). Tendon healing: repair and regeneration. *Annu. Rev. Biomed. Eng.* 14, 47–71. doi:10.1146/annurev-bioeng-071811-150122

Wang, L., Li, S., Xiao, H., Zhang, T., Liu, Y., Hu, J., et al. (2023a). TGF-β1 derived from macrophages contributes to load-induced tendon-bone healing in the murine rotator cuff repair model by promoting chondrogenesis. *Bone Jt. Res.* 12, 219–230. doi:10.1302/2046-3758.123.BJR-2022-0368.R1

Wang, P., Yin, B., Su, Y. J., and Jia, C. Y. (2020). Research advances in healing mechanism of chronic refractory wounds mediated by long non-coding RNA. *Zhonghua Shao Shang Za Zhi Zhonghua Shaoshang Zazhi Chin. J. Burns* 36, 758–761. doi:10.3760/cma.j.cn501120-20190526-00254

Wang, S., Lu, M., Cao, Y., Tao, Z., Sun, Z., Liu, X., et al. (2023b). Degradative polylactide nanofibers promote M2 macrophage polarization via STAT6 pathway in peritendinous adhesion. *Compos. Part B Eng.* 253, 110520. doi:10.1016/j.compositesb.2023.110520

Wang, S., Lu, M., Wang, W., Yu, S., Yu, R., Cai, C., et al. (2022). Macrophage polarization modulated by NF-κB in polylactide membranes-treated peritendinous adhesion. *Small* 18, 2104112. doi:10.1002/smll.202104112

Wang, S., Xiao, Y., Tian, J., Dai, B., Tao, Z., Liu, J., et al. (2024). Targeted macrophage CRISPR-cas13 mRNA editing in immunotherapy for tendon injury. *Adv. Mater.*, 2311964. doi:10.1002/adma.202311964

Wei, Y., Yun, X., Guan, Y., Cao, S., Li, X., Wang, Y., et al. (2023). Wnt3a-Modified nanofiber scaffolds facilitate tendon healing by driving macrophage polarization during repair. *ACS Appl. Mater. Interfaces* 15, 9010–9023. doi:10.1021/acsami.2c20386

Willenborg, S., Lucas, T., van Loo, G., Knipper, J. A., Krieg, T., Haase, I., et al. (2012). CCR2 recruits an inflammatory macrophage subpopulation critical for angiogenesis in tissue repair. *Blood* 120, 613–625. doi:10.1182/blood-2012-01-403386

Williams, J. W., Giannarelli, C., Rahman, A., Randolph, G. J., and Kovacic, J. C. (2018). Macrophage biology, classification, and phenotype in cardiovascular disease. *J. Am. Coll. Cardiol.* 72, 2166–2180. doi:10.1016/j.jacc.2018.08.2148

Wojciak, B., and Crossan, J. F. (2008). The accumulation of inflammatory cells in synovial sheath and epitenon during adhesion formation in healing rat flexor tendons. *Clin. Exp. Immunol.* 93, 108–114. doi:10.1111/j.1365-2249.1993.tb06505.x

Wong, J. K. F., Lui, Y. H., Kapacee, Z., Kadler, K. E., Ferguson, M. W. J., and McGrouther, D. A. (2009). The cellular biology of flexor tendon adhesion formation: an old problem in a new paradigm. *Am. J. Pathol.* 175, 1938–1951. doi:10.2353/ajpath.2009.090380

Wong, J. K. F., Metcalfe, A. D., Wong, R., Bush, J., Platt, C., Garcon, A., et al. (2014). Reduction of tendon adhesions following administration of adaprev, a hypertonic solution of mannose-6-phosphate: mechanism of action studies. *PLoS ONE* 9, e112672. doi:10.1371/journal.pone.0112672

Xu, H.-T., Lee, C.-W., Li, M.-Y., Wang, Y.-F., Yung, P. S.-H., and Lee, O. K.-S. (2020). The shift in macrophages polarisation after tendon injury: a systematic review. *J. Orthop. Transl.* 21, 24–34. doi:10.1016/j.jot.2019.11.009

Yang, X., Wang, X., Liu, D., Yu, L., Xue, B., and Shi, H. (2014). Epigenetic regulation of macrophage polarization by DNA methyltransferase 3b. *Mol. Endocrinol.* 28, 565–574. doi:10.1210/me.2013-1293

Ye, Y., Xu, Y., Lai, Y., He, W., Li, Y., Wang, R., et al. (2018). Long non-coding RNA cox-2 prevents immune evasion and metastasis of hepatocellular carcinoma by altering M1/M2 macrophage polarization. *J. Cell. Biochem.* 119, 2951–2963. doi:10.1002/jcb.26509

Zhang, C., Han, X., Yang, L., Fu, J., Sun, C., Huang, S., et al. (2020). Circular RNA circPPM1F modulates M1 macrophage activation and pancreatic islet inflammation in type 1 diabetes mellitus. *Theranostics* 10, 10908–10924. doi:10.7150/thno.48264

Zhang, X., Fang, Z., Cho, E., Huang, K., Zhao, J., Jiang, J., et al. (2019). Use of a novel, reinforced, low immunogenic, porcine Small intestine Submucosa patch to repair a supraspinatus tendon defect in a rabbit model. *Biomed. Res. Int.* 2019, 1–12. doi:10.1155/2019/9346567

Frontiers in
Bioengineering and Biotechnology

Accelerates the development of therapies, devices, and technologies to improve our lives

A multidisciplinary journal that accelerates the development of biological therapies, devices, processes and technologies to improve our lives by bridging the gap between discoveries and their application.

Discover the latest Research Topics

See more →

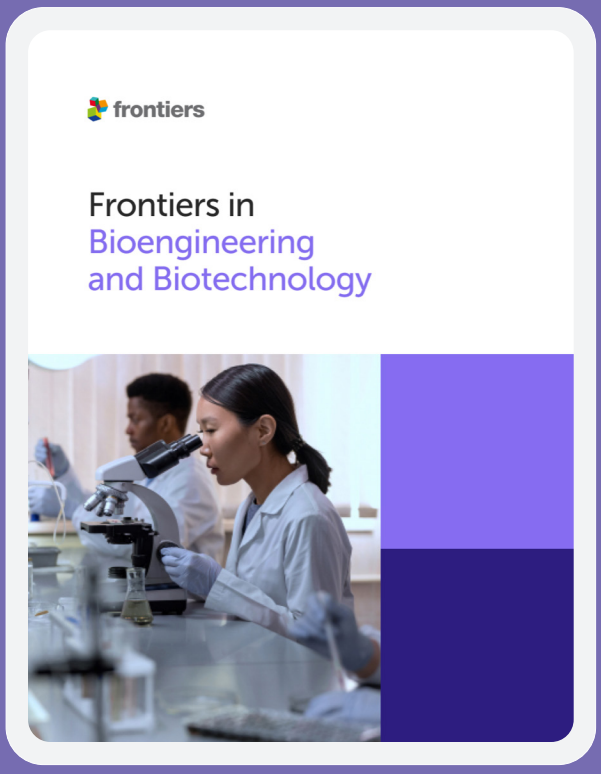

Frontiers

Avenue du Tribunal-Fédéral 34
1005 Lausanne, Switzerland
frontiersin.org

Contact us

+41 (0)21 510 17 00
frontiersin.org/about/contact